LBL-24200
UC-403

LAWRENCE
BERKELEY LABORATORY
DEC 7 1988
LIBRARY AND
DOCUMENTS SECTION

Annual Report 1987

For Reference
Not to be taken from this room

Earth Sciences Division

September 1988

LAWRENCE BERKELEY LABORATORY
UNIVERSITY OF CALIFORNIA
BERKELEY, CALIFORNIA 94720

LBL-24200 c.1

Prepared for the U.S. Department of Energy under Contract No. DE-AC03-76SF00098

DISCLAIMER

This document was prepared as an account of work sponsored by the United States Government. While this document is believed to contain correct information, neither the United States Government nor any agency thereof, nor the Regents of the University of California, nor any of their employees, makes any warranty, express or implied, or assumes any legal responsibility for the accuracy, completeness, or usefulness of any information, apparatus, product, or process disclosed, or represents that its use would not infringe privately owned rights. Reference herein to any specific commercial product, process, or service by its trade name, trademark, manufacturer, or otherwise, does not necessarily constitute or imply its endorsement, recommendation, or favoring by the United States Government or any agency thereof, or the Regents of the University of California. The views and opinions of authors expressed herein do not necessarily state or reflect those of the United States Government or any agency thereof or the Regents of the University of California.

EARTH SCIENCES DIVISION ANNUAL REPORT 1987

Lawrence Berkeley Laboratory
1 Cyclotron Road
Berkeley, CA 94720

September 1988

Prepared for the U.S Department of Energy under Contract No. DE-AC03-76SF00098

ACKNOWLEDGMENTS

This work was supported through U.S. Department of Energy Contract No. DE-AC03-76SF00098 by (1) the DOE Assistant Secretary for Energy Research, Office of Basic Energy Sciences; (2) the DOE Office of Civilian Radioactive Waste Management, Office of Geologic Repositories; (3) the DOE Assistant Secretary for Conservation and Renewable Energy, Office of Renewable Technology and Office of Advanced Conservation Technology; (4) the DOE Assistant Secretary for Fossil Energy, Office of Petroleum Resources; (5) the U.S. Nuclear Regulatory Commission, Office of Nuclear Regulatory Research; (6) the Environmental Protection Agency; (7) the U.S. Department of Interior; (8) the U.S. Department of Defense; (9) the California State Lands Commission and the University of California; (10) the California Consortium for Crustal Studies, the University of Southern California, and the University of California at Berkeley under National Science Foundation sponsorship.

CONTENTS

INTRODUCTION **1**

GEOCHEMISTRY **3**

Nuclide Migration from Areal Sources into a Fracture
J. Ahn, P.L. Chambré, T.H. Pigford, and W.W.-L. Lee **5**

Evidence for the Structural Difference between Rhyolitic and Basaltic Glasses and Its Effect on Hydrothermal Alteration Kinetics
J.A. Apps **8**

The Thermodynamic Properties and Stability of Bayerite in Relation to Gibbsite and Their Solubilities in Alkaline Aqueous Media
J.A. Apps **14**

The Thermodynamic Properties of Some Borosilicates
J.A. Apps **19**

Thermodynamic Properties of Silicate Materials
I.S.E. Carmichael, V.C. Kress, and D.A. Snyder **25**

Some Effects of Data-Base Variations on Numerical Simulations of Uranium Migration
C.L. Carnahan **29**

Waste Dissolution with Diffusion, Advection, and Chemical Reaction
P.L. Chambré, C.H. Kang, W.W.-L. Lee, and T.H. Pigford **33**

Numerical Simulation of the Alteration of Sodium Bentonite by Diffusion of Ionic Groundwater Components
J.S. Jacobsen and C.L. Carnahan **36**

Mechanisms of Mobility Control with Foams
A.I. Jiménez, K.S. Udell, and C.J. Radke **39**

Time-Dependent Nuclide Transport through Backfill into a Fracture
C.H. Kang, P.L. Chambré, W.W.-L. Lee, and T.H. Pigford **42**

Contaminant Transport from an Array of Sources
C.L. Kim, P.L. Chambré, W.W.-L. Lee, and T.H. Pigford **43**

Transmission Electron Microscope Studies on Aspects of Stress-Related Heterogeneous Dissolution
A. Meike **47**

Carbonate Complexation of Americium(III) in Aqueous Solution
H. Nitsche, E.M. Standifer, and R.J. Silva **54**

Solubility Studies for the Potential High-Level Nuclear Waste Repository at Yucca Mountain, Nevada
H. Nitsche, S.C. Lee, R.C. Gatti, D.B. Tucker, and E.M. Standifer **59**

Reaction of Uranium Chloride with Zirconium Alloy: A Chemical Model System for Spent-Fuel/Cladding Reactions
D.L. Perry and K.M. Ogle **61**

Reactions of Chalcopyrite in Acidic Aqueous Media
D.L. Perry and K.M. Ogle **63**

Potentiostatic Measurement of the Diffusion Coefficient of UO_2^{2+} in Carbonate Media
D.L. Perry, S.L. Phillips, and J.D. Chung **65**

Prediction of Mineral Solubilities in Aqueous Mixed Electrolytes to Temperatures up to 300°C
K.S. Pitzer and R.T. Pabalan **68**

Geochemical Investigations of Fractured Heated Rock
H.A. Wollenberg and S. Flexser **73**

GEOMECHANICS 77

Hollow-Cylinder Tests for Studying Fractures around Underground Openings
R.T. Ewy, N.G.W. Cook, and L.R. Myer **79**

Fracture Stiffness and Aperture As a Function of Applied Stress
D.L. Hopkins, N.G.W. Cook, and L.R. Myer **81**

Fracture Mechanics Applied to Faulting and Earthquake Rupture
J.M. Kemeny and N.G.W. Cook **85**

Permeability of Shale at Elevated Temperatures and Pressures
L.R. Myer and T.L. Christian **88**

Elastic Interface Waves Along a Fracture
L.J. Pyrak-Nolte and N.G.W. Cook **91**

Direct Three-Dimensional Observations of Microfracturing in Indiana Limestone
Z. Zheng, F.M. Doyle, L.R. Myer, and N.G.W. Cook **93**

GEOPHYSICS 97

A Three-Dimensional Structural Model for the Long Valley Caldera, California
S.F. Carle and N.E. Goldstein **99**

Multicomponent VSPs at Cajon Pass and the Salton Sea
T.M. Daley, T.V. McEvilly, and E.L. Majer **103**

The Development of Seismological Techniques for the Real-Time Mapping of Grout Injections
E.L. Majer and R.L. Haught **108**

CCS: Center for Computational Seismology
E.L. Majer, T.V. McEvilly, and L.R. Johnson **112**

Controlled Seismic Cross-Hole Experiments for Fracture Characterization
E.L. Majer, J.E. Peterson, and J.C.S. Long **114**

Summary of CALCRUST Program
T.V. McEvilly and D.A. Okaya **117**

Transfer-Function Estimation for Natural Electromagnetic Fields
H.F. Morrison and E.A. Nichols **122**

Three-Dimensional Interpretation of Magnetotelluric Data in Long Valley, California
S.K. Park, C. Torres-Verdin, and H.F. Morrison **125**

Self-Potential Anomalies Due to Contaminated Aquifers
M.J. Wilt **129**

Fracture Detection Using Low-Frequency Cross-Hole Electromagnetic Techniques
Q. Zhou, A. Becker, N.E. Goldstein, H.F. Morrison, and K.H. Lee **132**

RESERVOIR ENGINEERING AND HYDROGEOLOGY 139

Expert Systems As Tools for the Nuclear Repository Program
D. Billaux, M. Uszynski, and S.M. Benson **141**

A Casting Technique for Determining the Geometry of Voids in a Fracture
D. Billaux, L. van Vliet, and S. Gentier **143**

CHANGE: A Numerical Model for Three-Dimensional Modeling of Channelized Flow in Rock
D. Billaux and J.C.S. Long **146**

A Multi-Feedzone Wellbore Simulator
G. Bjornsson and G.S. Bodvarsson **149**

Preliminary Calculations of the Effects of Air and Liquid-Water Drilling on Moisture Conditions in Unsaturated Rocks
G.S. Bodvarsson, A. Niemi, A. Spencer, and M.P. Attanayake **152**

Equivalent Permeability of Statistically Simulated Single Fractures
K. Coakley, K. Muralidhar, J.C.S. Long, and L.R. Myer **157**

Analysis of Pressure, Enthalpy, and CO_2 Transients in Well BR21, Ohaaki, New Zealand
S.W. Gaulke and G.S. Bodvarsson **161**

Statistical Modeling of a Three-Dimensional Fracture Network
K. Hestir, D. Billaux, J.-P. Chiles, and J.C.S. Long **165**

Fracture Modeling at the Nevada Test Site
K. Hestir, K. Karasaki, and K. Grossenbacher **168**

Dissolution and Transport of Slightly Water-Soluble Gasoline Components in Groundwater
H.-Y.N. Holman and I. Javandel **172**

Modification to TRINET: A Three-Dimensional Advection-Dispersion Code for Fracture Networks
K. Karasaki **175**

Studies of Hierarchically Fractured Media
K. Karasaki, J.M. Polek, and J.C.S. Long **176**

The Genesis of Shear Fracture Zones in Brittle Rock
J.M. Kemeny and J.C.S. Long **180**

The NAGRA-DOE Cooperative Research Program
J.C.S. Long, E.L. Majer, K. Karasaki, K. Pruess, C.L. Carnahan, J.S. Jacobsen, K. Hestir, D. Billaux, J. Peterson, L.R. Myer, and C.F. Tsang **185**

Hydrodynamics of a Vertical Hydraulic Fracture
T.N. Narasimhan **189**

DYNAMIX: A Multidimensional, Multiple-Species Chemical-Transport Model for Redox-Driven Transport in Geologic Media
T.N. Narasimhan and C.W. Liu **191**

Capillary Hystersis Model Development and Application to Flow in Fractured Rocks
A. Niemi and G.S. Bodvarsson **193**

Unsaturated-Zone Thermal-Energy Storage: Model Development and Field Validation
A. Nir, C. Doughty, and C.F. Tsang **197**

A Simple Weighted Nonlinear Least-Squares Method for Estimating Michaelis-Menten or Langmuir Isotherm Constants
P. Persoff **199**

Groupings of Organic Waste Chemicals for Studies of Deep Subsurface Disposal
S.L. Phillips, F.V. Hale, and C.F. Tsang **201**

An Analytical Solution for Heat Transfer at a Moving Boiling Front
K. Pruess, C. Calore, R. Celati, and Y.S. Wu **204**

On Fluid and Heat Flow in Deep Zones of Vapor-Dominated Geothermal Reservoirs
K. Pruess, R. Celati, C. Calore, and G. Cappetti **207**

On the Validity of an Effective-Continuum Approximation for Multiphase Fluid and Heat Flow in Fractured Porous Media
K. Pruess, J.S.Y. Wang, and Y.W. Tsang **209**

Geologic and Reservoir-Engineering Studies of The Geysers Geothermal Field
M. Ripperda, G.S. Bodvarsson, S. Gaulke, and S.E. Halfman **212**

A Borehole Fluid-Conductivity Logging Method for the Determination of Fracture-Inflow Parameters
C.F. Tsang **214**

Channeling Characteristics of Flow and Solute Transport through a Rough-Surfaced Fracture
Y.W. Tsang, C.F. Tsang, F.V. Hale, L. Moreno, and I. Neretnieks **218**

Tracer Transport in Fractured Media: A Variable-Aperture Channel Approach
Y.W. Tsang and C.F. Tsang **221**

Reservoir Studies of the Seltjarnarnes Geothermal Field, Iceland
H. Tulinius, A.L. Spencer, G.S. Bodvarsson, H. Kristmansdottir, T. Thorsteinsson, and A.E. Sveinbjornsdottir **223**

Vertical and Lateral Movement of Partially Saturated Fluid Flow Near a Fault Zone
J.S.Y. Wang and T.N. Narasimhan **229**

Monitoring of Subsurface Contaminants with Borehole/Surface Resistivity Measurements: Field Results
M.J. Wilt, C.F. Tsang, I. Javandel, S.C. Lee, and H.F. Morrison **234**

APPENDIXES 239

Appendix A: Abstracts of Journal Articles **239**

Appendix B: LBL Reports, Book Contributions, Conference Papers **244**

INTRODUCTION

Scientists and engineers of the Earth Sciences Division, following the mission of a multipurpose National Laboratory, conduct research on a wide variety of topics relevant to the nation's energy development programs. This report summarizes the activities for 1987. The Earth Sciences Division has developed unique expertise in several research areas. This expertise is due in part to the special resources and facilities available to researchers at the Lawrence Berkeley Laboratory and in part to the Laboratory's commitment to technical and scientific excellence. In addition to the permanent Laboratory staff, University faculty members, postdoctoral fellows, students, and visiting scientists participate in many investigations. Each year, several Ph.D. and Masters theses are founded in research within the Division. Interlaboratory cooperation within the U.S. Department of Energy system and collaboration with other research institutions provide access to unmatched intellectual and technological resources for the study of complex problems.

Much of the Division's research deals with the physical and chemical properties and processes in the Earth's crust, from the partially saturated, low-temperature near-surface environment to the high-temperature environments characteristic of regions where magmatic-hydrothermal processes are active. Strengths in laboratory and field instrumentation, numerical modeling, and in situ measurement allow study of the transport of mass and heat through geologic media—studies that now include the appropriate chemical reactions and the hydraulic-mechanical complexities of fractured rock systems. Related and parallel laboratory and field investigations address the effects of temperature, pressure, stresses, pore fluids, and fractures on the elastic and electrical properties of rock masses. These studies are concerned with rock behavior in the brittle and ductile crustal regimes, and they drive the development of improved geomechanical and geophysical tools and techniques for mapping and characterizing heterogeneity in the subsurface. Prompted by Congressional concern over the decline in basic research in the petroleum industry due to the low price of oil, the Division has increased its emphasis on the application of fluid transport modeling and subsurface imaging methods to problems related to discovery and recovery of petroleum.

This Annual Report presents summaries of research activities grouped according to the principal disciplines of the Earth Sciences Division: Geochemistry, Geomechanics, Geophysics, and Reservoir Engineering and Hydrogeology. We are proud to be able to bring you this report, which we hope will convey not only a description of the Division's scientific activities but also a sense of the enthusiasm and excitement present today in the Earth Sciences.

GEOCHEMISTRY

Investigators in the Geochemistry group address problems that arise due to chemical reactions in the earth's crust. These problems usually involve interactions between subsurface aqueous fluids and the surrounding geologic media—both the chemical alteration of rock and soil by fluids and the chemical reactions that occur within the fluids. Many of these reactions occur during the transport of fluids; accordingly, our studies have a strong impact on the disposal of radioactive and toxic wastes. The successful containment of waste species is heavily dependent on the movement of dissolved chemical species in groundwaters. As a part of this overall study, separate investigations are conducted in areas of radiochemistry, inorganic chemistry, and surface chemistry in support of geologic transport models and codes that require such data.

Research in the Geochemistry group covers several themes related to geochemical reactions and transport. Several programs address field-oriented research, with the geochemical aspects being strongly coupled with groundwater migration. All this research contains large components of aqueous analytical chemistry, chemical-species modeling, and hydrochemistry. To date it has yielded considerable basic research regarding several coupled geochemical systems in general, as well as data that will help in the understanding of the geochemical processes as a whole. Other research in the group is related to geochemical and chemical modeling aspects of nuclear waste repositories—specifically, how radionuclide species dissolve, react, and migrate under repository conditions.

The Geochemistry group also conducts basic research as it relates to geologic processes— processes that occur in the earth's crust and in the upper mantle. Thermodynamic studies of liquid silicate minerals are in progress, along with studies of NaCl in steam. Thermodynamically coupled processes are being modeled, along with chemical species, as a function of different experimental parameters, such as pH, temperature, and oxidation potentials. Basic research is also in progress that concerns interfacial geologic chemical reactions; these reactions address both solid-liquid and solid-gas surface reactions of geologic processes, such as petroleum-precursor reactions with rocks and minerals, carbon dioxide reactions with geologic materials, and aqueous solution chemical alteration of geologic surfaces.

Nuclide Migration from Areal Sources into a Fracture

J. Ahn, P.L. Chambré, T.H. Pigford, and W.W.-L. Lee

Within a nuclear waste repository constructed in rock, it may be necessary to place a waste package across a rock fracture, or a rock fracture may develop some time after a waste package has been emplaced. It is necessary to predict the spatial and temporal distribution of radionuclides from a line of waste packages facing a rock fracture, since such fractures are now considered to be the main pathways along which released radionuclides can re-enter the biosphere. The situation studied is shown in Fig. 1, where a line of waste packages, here assumed to be corroded and releasing radionuclides, is exposed to a planar rock fracture in a fluid-saturated porous rock.

ANALYTIC SOLUTIONS—A SINGLE AREAL SOURCE

Consider an areal source, as shown in Fig. 1. After a radionuclide is released, several transport processes are important in determining its eventual fate. One is advection in the rock fracture. Another is transverse dispersion in the planar fracture. We established in an earlier study that longitudinal dispersion is of rather minor significance (Ahn et al., 1985). The radionuclide can sorb to the rock surface in the fracture, and it can migrate by diffusion into pores in the rock. The latter process is known as "matrix penetration" in nuclear waste disposal. After a nuclide has migrated into a pore, it is exposed to a large amount of surface, and sorption can take place. These transport processes can be described in the following coupled differential equations. The governing equation for the mass balance of nuclides in water in the rock fracture is

$$R_f \frac{\partial N}{\partial t} + v \frac{\partial N}{\partial z} - D_T \frac{\partial^2 N}{\partial x^2} + R_f \lambda N + q/b = 0$$

$$t > 0,\ z > 0,\ -\infty < x < \infty\,. \qquad (1)$$

where $N(x,z,t)$ is the nuclide concentration in the water in the rock fracture at time t and at location (x,z) [m nuclide/l^3 fracture water], K_f is the nuclide distribution coefficient [(m nuclide/l^2 fracture wall) / (m nuclide/l^3 fracture water)], $2b$ is the aperture of the fracture [l], v is the pore velocity in the fracture [l/t], D_T is the transverse dispersion coefficient [l^2/t], λ is the nuclide's decay constant [t^{-1}], R_f is the dimensionless retardation coefficient in the fracture, defined as $R_f = 1 + K_f/b$, and q is the diffusive flux into the rock matrix [$m/l^2\ t$]. We write a similar mass balance for the nuclide inside the porous rock matrix:

$$R_p \frac{\partial M}{\partial t} - D_p \frac{\partial^2 M}{\partial y^2} + R_p \lambda M = 0$$

$$t > 0,\ y > b,\ z > 0,\ -\infty < x < \infty, \qquad (2)$$

where $M(x,y,z,t)$ is the concentration of the nuclide in the matrix-pore water [m nuclide/l^3 pore water], D_p is the nuclide diffusion coefficient in the rock matrix [l^2/t], R_p is a dimensionless retardation coefficient defined as $R_p = 1 + a_p K_p/\epsilon$, K_p is a distribution coefficient in dimensions of [(m nuclide/l^2 pore surface)/(m nuclide/l^3 pore water)], a_p is the pore surface area per unit volume of rock [l^2 pore surface/l^3 rock matrix], and ϵ is the matrix porosity.

The two governing equations are coupled by two relationships. The first is flux continuity at the surface of the rock fracture:

$$q(x,z,t) = -\epsilon D_p \frac{\partial M}{\partial y}\Big]_{y=b}$$

$$t > 0, z > 0,\ -\infty < x < \infty\,. \qquad (3)$$

We solve the governing equations, (1) and (2), subject to (3) and the following initial conditions

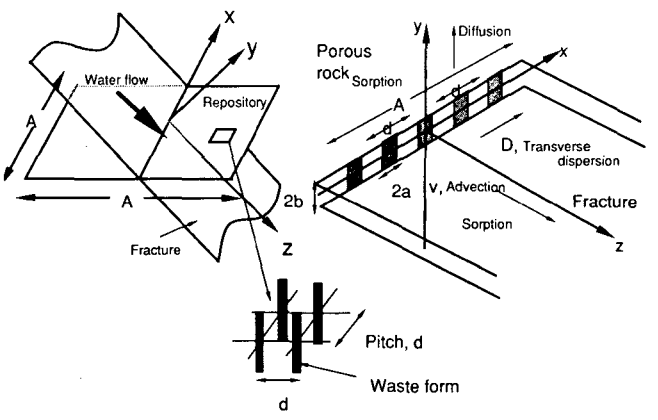

Figure 1. Schematic diagram of a planar fracture intersecting a repository, showing the processes considered in the model. [XBL 886-2140]

$$N(x,z,0) = 0 \quad z > 0, -\infty < x < \infty, \quad (4)$$

$$M(x,y,z,0) = 0 \quad y > b, z > 0, -\infty < x < \infty, \quad (5)$$

and boundary conditions

$$N(x,0,t) = \phi(t)[h(x + a) - h(x - a)] \quad t > 0, -\infty < x < \infty \quad (6)$$

$$N(x,\infty,t) = 0 \quad t > 0, -\infty < x < \infty, \quad (7)$$

$$N(\pm\infty,z,t) = 0 \quad z > 0, t > 0, \quad (8)$$

$$M(x,b,z,t) = N(x,z,t) \quad t > 0, z > 0, \quad -\infty < x < \infty, \quad (9)$$

$$M(x, +\infty,z,t) = 0 \quad t > 0, z > 0, \quad -\infty < x < \infty, \quad (10)$$

where $\phi(t)$ represents the time-dependent concentration at the surface of an areal source and can be in the form $N^\circ e^{-\lambda t}\{h(t) - h(t - T)\}$, with h(·) the Heaviside step function and N° the initial concentration. Equation (6) states that the center of an areal source of dimensions $2a \times 2b$ is located at the origin of the system. Equation (9) states the concentration continuity at the rock/fracture interface. The solution to the above system of governing equations is given in Ahn et al. (1987) and is summarized below.

$$N(x,z,t) = N^\circ F(b,z,t)G(x;\theta,a,0) \quad t \geqslant 0, -\infty < x < \infty, \quad (11)$$

$$M(x,y,z,t) = N^\circ F(y,z,t)G(x;\theta,a,0) \quad t \geqslant 0, y \geqslant b, z \geqslant 0, -\infty < x < \infty, \quad (12)$$

where

$$F(y,z,t) = f(y,z,t) - e^{-\lambda T} f(y,z,t-T), \quad (13)$$

$$f(y,z,t) = e^{-\lambda t} h(t - ZA) \cdot \operatorname{erfc}\left[\frac{Z + B(y - b)}{2\sqrt{t - ZA}}\right], \quad (14)$$

$$G(x;\theta,a,x_1) = \frac{1}{2} \cdot \left[\operatorname{erf}\left(\frac{x - x_1 + a}{2\theta}\right) - \operatorname{erf}\left(\frac{x - x_1 - a}{2\theta}\right)\right], \quad (15)$$

$$Z = \frac{R_f z}{vA}, \quad A = \frac{bR_f}{\epsilon\sqrt{D_p R_p}},$$

$$B = \sqrt{R_p/D_p}, \quad \theta = \sqrt{\frac{zD_T}{v}}. \quad (16)$$

These equations give the concentration field of the radionuclide in both the fracture and the rock matrix as a function of space and time.

ANALYTIC SOLUTION—MULTIPLE AREAL SOURCES

If there are multiple areal sources along the fracture, as shown in Fig. 1, the solution is obtained by superposing the solutions for single areal sources. For areal sources each of width $2a$ separated by a *pitch* d, and with the same release characteristics, the solution is

$$M(x,y,z,t,m) = N^\circ F(y,z,t) \sum_{k=1}^{m} G(x;\theta,a,x_k), \quad (17)$$

where m is the number of areal sources and x_k is the location of the center of the kth areal source on the transverse axis x and is given by

$$x_k = d[k - (m + 1)/2], \quad k = 1,\ldots, m.$$

NUMERICAL ILLUSTRATIONS

We now provide numerical illustrations of Eq. (17). In Fig. 2 we show the normalized concentration profile in the transverse direction. The ordinate shows the concentration predicted by Eq. (17) normalized by the concentration predicted by an infinitely long source, defined as

$$M^{\infty}(y,z,t) = N^{\circ}(2a/d)F(y,z,t) . \qquad (18)$$

Combining Eqs. (17) and (18) as shown in the ordinate of Fig. 2 gives

$$\frac{M(x,y,z,t,m)}{M^{\infty}(y,z,t)} = (d/2a)\sum_{k=1}^{m} G(x;\theta,a,x_k) . \qquad (19)$$

The normalized concentrations in Fig. 2 are for four values of the distance parameter $\theta = \sqrt{(zD_T)/v}$ and for ten areal sources separated on 10-m centers, or a total "repository" of 100 m. The following parameter values were used in the calculations:

a, half-width of the areal sources, 0.14 m,
b, half-aperture of the fracture, 0.005 m,
d, pitch or separation between areal sources, 10 m,
m, number of areal sources, 10,
D_p, diffusion coefficient, 10−2 m2/y,
D_T, transverse dispersion coefficient, 0.05 m^2/y,
R_f, fracture retardation coefficient, 1,
R_p, matrix retardation coefficient, 100,
v, pore velocity, 10 m/y,
N°, source strength, 1,
ϵ, porosity, 0.01.

The differences between the concentration fields predicted by the two models are illustrated more clearly in Fig. 3. Here the concentration ratio of Eq. (19) is plotted against the distance parameter, with a constant spacing of 10 m apart, for the number of areal sources up to 80.

Near the areal sources—i.e., for small values of θ—the plumes are evident, and the concentration field for discrete areal sources differs considerably from that for the infinitely long source. The "peaks" are the local plumes, opposite the location of the areal sources, and the "valleys" are where the local plumes are absent, opposite the region in between areal sources. However, farther away from the areal sources, $\theta \approx 3$ m, the plumes from the areal sources have merged completely because of transverse dispersion. At greater distances and until the concentration ratio becomes less than unity in Fig. 3, the simpler, infinite-source model predicts the concentration field just as well as the detailed areal-source model. For larger values of θ, when the concentration ratio becomes less than unity, the infinite-source model predicts a concentration that is higher than is accurate but on the conservative side. In this region the concentration field can be predicted accurately by replacing the discrete areal sources with a single finite-areal source of equivalent strength and with the same overall dimensions as the array of discrete sources. These observations are independent of nuclide, rock type, and time.

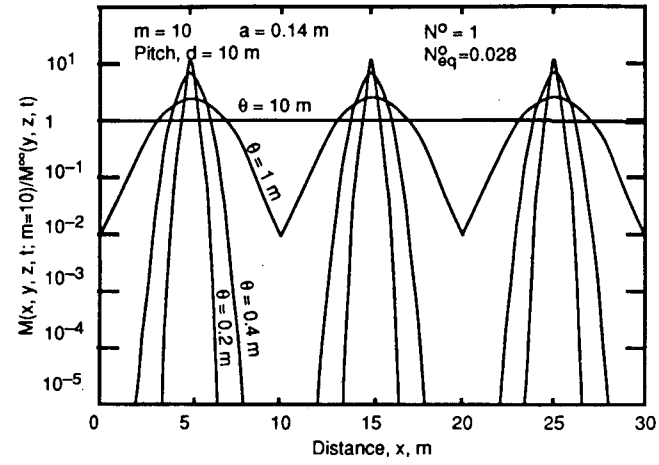

Figure 2. The relative nuclide concentration as a function of the transverse coordinate for four values of the distance parameter. [XBL 886-2141]

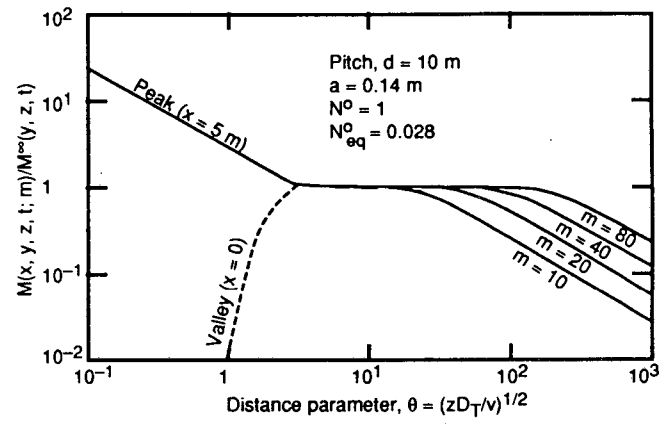

Figure 3. The effect of the number of areal sources on relative nuclide concentration as a function of the distance parameter. The peaks and valleys are defined in Fig. 2. [XBL 886-2142]

CONCLUSIONS

We present analytic solutions for the dispersion of radionuclides released from multiple areal sources into a rock fracture. We illustrate the analytic solutions with graphical display of plumes. We pose the question of when such detailed solutions have to be used and when simpler mathematical approximations can be used to obtain reasonably accurate predictions. From the numerical implementation of the analytic solutions, we find that three regions exist, defined in terms of a distance parameter $\theta = \sqrt{(zD_T)/v}$. For the parameter values used in this study, at $\theta \geqslant 3$ m the detailed multiple-areal-source solution should be used to give accurate predictions of the concentration field. For values of θ between 3 and 100 m, the concentration field predicted by a simpler infinite-line source model is identical. For values of θ greater than 100 m, the simpler infinite-line source model overestimates conservatively, and an equivalent single finite-areal source will yield the correct concentration field.

REFERENCES

Ahn, J., Chambré, P.L., and Pigford, T.H., 1985. Nuclide migration through a planar fissure with matrix diffusion. Lawrence Berkeley Laboratory Report LBL-19429.

Ahn, J., Chambré, P.L., Pigford, T.H., and Lee, W.W.-L., 1987. Radionuclide dispersion from multiple patch sources into a rock fracture. Lawrence Berkeley Laboratory Report LBL-23425.

Evidence for the Structural Difference between Rhyolitic and Basaltic Glasses and Its Effect on Hydrothermal Alteration Kinetics

J.A. Apps

Rocks containing either acid or mafic glass possess potential advantages over other rocks as hosts for radioactive waste. Because glasses are unstable, they will react with dissolving radioactive waste under hydrothermal conditions to produce secondary minerals capable of entrapping harmful radioelements. Natural silicic glasses are found at two sites in the western United States: the Hanford Reservation, Washington, and the Nevada Test Site (NST). At Hanford, a glass mesostasis occurs in the basalts of the Pasco Basin; at the NTS, vitrophyres are interbedded with massive devitrified ash fall and welded tuff beds. This summary—a condensation of a paper presented at a symposium (Apps, 1987)—addresses some of the contrasting alteration mechanisms between acid rhyolitic glasses and glasses of basaltic or mafic composition.

THERMODYNAMICS OF GLASSES IN RELATION TO HYDRATION AND DEVITRIFICATION

Natural glasses are composed mainly of SiO_2, ranging from 40 to 80 wt%, but also include various amounts of other network builders, principally Al_2O_3, and network modifiers, such as Na_2O, K_2O, CaO, MgO, and FeO. Together, these constituents usually make up over 95 wt% of the total composition.

When exposed to water, glasses have a tendency to alter by a variety of mechanisms. Wu (1980) categorized glasses into four types depending on their alteration behavior when exposed to steam at elevated temperature: those that (a), do not hydrate; (b), hydrate; (c), dissolve in the aqueous phase, and (d), devitrify or crystallize. Because all glasses could eventually crystallize to a more stable phase assemblage, the last category is a manifestation of more rapid crystallization kinetics.

The temperature-composition diagrams in Fig. 1 portray an arbitrary pseudobinary system with a stoichiometric anhydrous silicate as one end member and water as the other end member. The temperature range extends from about −50°C to beyond the melting point of the stoichiometric crystalline silicate. The pressure is arbitrarily set between 1 bar and 400 bars, a range expected to include most waste repository conditions.

Features common to all diagrams are a pseudobinary immiscibility loop between the vapor (steam) and liquid (silicate melt) phases, culminating in a critical phase, a solidus curve with respect to the

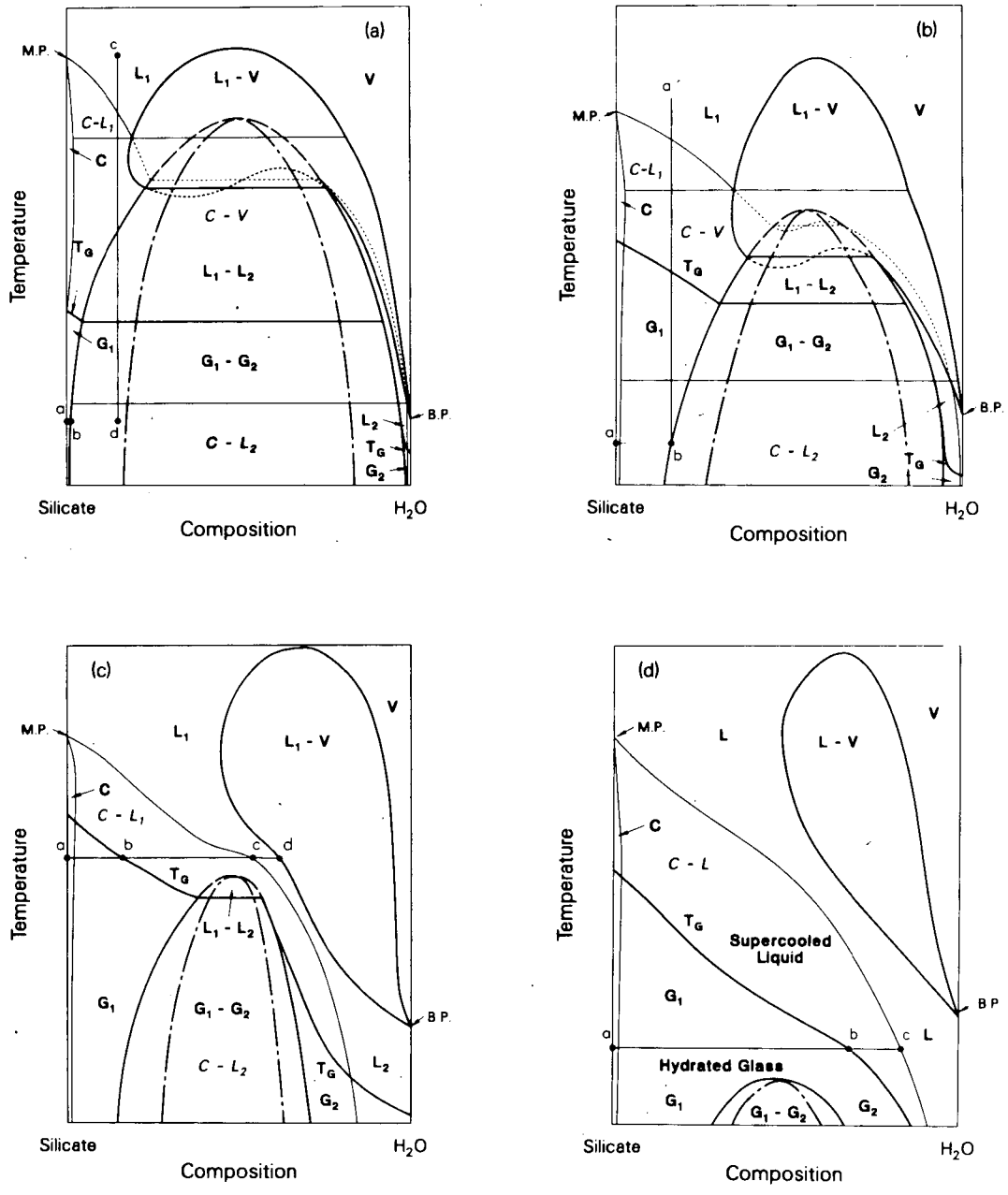

Figure 1. Hypothetical pseudobinary temperature composition diagrams to illustrate **(a)** the metastable field of a nonhydrated glass in equilibrium with the aqueous phase, **(b)** the metastable field of hydrated silcate glass in equilibrium with the aqueous phase, **(c)** the hydration and liquifaction of an alkali silicate glass by steam, and **(d)** the hydration and dissolution of an alkali silicate glass by a liquid aqueous phase. Italic letters designate stable phase equilibria with respect to the crystalline solid. C = crystalline solid; G = glass; L = liquid; V = vapor. [XBL 887-10358]

stable essentially stoichiometric solid and the liquid (i.e., melt + water) phase, and a subsolidus pseudobinary solvus leading to the formation of coexisting supercooled water-rich and water-poor melts (or glasses). Evidence for the existence of the binary solvus is based on the assumption that glasses have a finite equilibrium solubility and a finite and definable saturation limit with respect to hydration. Superimposed on the supercooled liquid field is the glass transition. Apart from the pseudobinary misci-

bility loop, all stable phase transitions are indicated by light lines, whereas metastable transitions are indicated by heavy lines.

Figure 1a represents Wu's second case, in which an anhydrous glass exposed to a steam atmosphere will hydrate to an inconsequential extent before saturation, as indicated by path a–b. This case may be representative of very high silica glasses, such as tektites or vitreous silica. A "superhydrated" unstable glass could in principle be produced in the system by quenching a hydrated melt along path c–d.

In Figure 1b, it is assumed that the glass will hydrate to a significant extent, which may arise by the quenching of a hydrous melt along path a–b or by hydration in contact with either a vapor or a liquid aqueous phase along path a–b. Rhyolitic or rhyodacitic glasses most probably follow path a′–b during hydration in closed systems.

Silicate glasses containing high concentrations of alkali metals are represented in Figs. 1c and 1d. In these cases, the glass will actually liquefy or dissolve in the presence of an aqueous phase. Figure 1c represents the situation of liquifaction in the presence of steam, as indicated along path a–d. The glass will first hydrate along a–b, undergo a transition to a supercooled liquid at b, become a stable liquid at c, and eventually become saturated at d with respect to the aqueous (steam) phase. Figure 1d shows the corresponding case in which the glass is dissolved by an aqueous liquid along path a–b–c. These last two cases have not been observed to occur naturally.

Wu's fourth category may be represented by basaltic glasses in nature. With falling temperature, a hypothetical stoichiometric silicate mimicing a basaltic melt in composition would, on cooling, recrystallize to form stable hydrated phases in the pseudobinary cross section. Metastable equilibrium hydration in the glass would be transient, because hydration would so lower the activation energy of devitrification that devitrification would immediately follow.

Field observations by many workers show that rhyolitic and basaltic glasses behave quite differently during hydration and devitrification. Natural rhyodacitic and rhyolitic glasses containing between 65 and 80 wt% silica will hydrate under earth-surface conditions, apparently without destruction of the SiO_4/AlO_4 tetrahedral framework and with only partial or even no loss of interstitial alkali cations. The saturation hydration level of rhyolitic glasses is about 5 wt% H_2O+ at 0–25°C. However, the saturation hydration of basaltic glasses within the same temperature range is unknown. In synthetic systems, covering a wider range of compositions, vitreous silica hydrates less than alkali silicate glasses under comparable conditions. This suggests that the saturation hydration in natural glasses could well be sensitive to composition.

KINETICS OF HYDRATION AND DEVITRIFICATION

The rate of natural glass hydration has been determined both experimentally and from field observations. Hydration in obsidians and perlites appears to be a diffusion-controlled process following a parabolic rate law. This process is sufficiently uniform and slow at earth surface temperatures that it has found application as a dating method for obsidian artifacts and for rhyolitic or obsidian flows.

Rhyolitic glasses undergo significant density and optical changes when they hydrate. This leads to localized stress concentrations at the interface between the hydrated and unhydrated glass, which is sufficient in some cases to cause optical strain or even fracturing. Evidence that hydration induces fracturing has also been observed in basaltic glasses. The fracturing permits access of water to the glass interior and facilitates transport of chemical components in and out of the glass, thus accelerating both hydration and devitrification.

According to Friedman and Long (1976), increasing SiO_2 and H_2O content in obsidian increases the diffusion rate of water, whereas increasing CaO and MgO decreases the rate of diffusion. The effect of minor changes in CaO and MgO content on hydration rate appears to be substantial. This suggests that basaltic glass hydration rates would be at least two and possibly three orders of magnitude slower than for a typical obsidian, which is consistent with the field observations by Muffler et al. (1969) and Scheidegger (1973).

In synthetic silica-metal oxide glass systems, the evidence of Yoko et al. (1983) and Moriya and Nogami (1980) indicates that substitution of up to 10 wt% Al_2O_3, MgO, or CaO for SiO_2 in a 20 wt% NaO_2SiO_2 glass decreases the hydration rate by as much as 500 times.

Although the evidence that basaltic glass will hydrate is equivocal at best, there is plenty of evidence that basaltic glass will devitrify to form secondary smectites and zeolites. The process by which basaltic glass alters to secondary minerals is known as palagonitization. It is most frequently observed when the glass is exposed to seawater under essentially "open system" conditions. Palagonitization may involve initial hydration of a thin rind less than

50 μm thick. The thin rind induces high stresses in the adjacent unaltered glass and leads to the formation of an array of microcracks penetrating the glass ahead of the "hydration" zone (Morgenstein and Riley, 1974). Rapid devitrification of the "hydrated" rind then produces a palagonite layer, which is poorly coherent, spalls, and leaves more fresh glass exposed for hydration. Repeated cycles lead to the formation of a cumulative alteration layer that in some cases possesses characteristics remiscent of Liesegang banding.

Many investigators have found that the net rate of basalt glass alteration in nature is linear and not parabolic. Experimental studies on basaltic glasses are also consistent with field evidence. The palagonite layer does not therefore act as a rate-controlling diffusive barrier.

At repository temperatures, rhyolitic glasses devitrify through dissolution in and precipitation from the aqueous phase. Field evidence in hydrothermally altering acid vitroclastic tuffs and basalts clearly shows, through the presence of secondary clays and zeolites in pores, fractures, and vesicles, that it is important in the 25–400°C range and probably dominates alternative devitrification mechanisms in most situations.

The hydration of rhyolitic glass will substantially decrease the activation energy of devitrification, thereby permitting measurable devitrification to proceed at much lower temperatures. Friedman and Long (1984) calculate that a hydrated rhyolitic glass will devitrify at 200°C at about the same rate that an anhydrous glass will at 600°C. The relative rates of devitrification of natural glass in the host rock of a waste repository may therefore be strongly dependent on its hydration rate and saturation level. Lofgren (1968) has tentatively established that rhyolitic glasses devitrify about four orders of magnitude slower than the hydration process.

EVIDENCE FOR STRUCTURAL DIFFERENCES BETWEEN RHYOLITIC AND BASALTIC GLASSES

Field and laboratory studies show that fundamental differences exist between basaltic and rhyolitic glasses in their manner of alteration in the presence of an aqueous phase. Both thermodynamic and spectroscopic evidence indicates that the differences may be attributed to a structural dissimilarity between the two glasses.

Navrotsky and her coworkers (e.g., McMillan et al., 1982; Navrotsky et al., 1982; Navrotsky et al., 1985a,b) have investigated the heats of solution of silicate glasses in molten lead borate. Their observations suggest that alkali earths, particularly Ca and Mg, interact much more strongly with the aluminosilicate framework and tend to destabilize the structure, with the potential for separation into a very silica-rich phase and a silica-poor phase, respectively.

The significance of these findings in relation to rhyolitic and basaltic glasses is evident. Thus the rhyolitic glass, whose aluminosilicate structure is charge compensated with the alkali metals, will be more stable and less likely to break down than a basaltic glass containing substantial amounts of alkali earths. The weaker structure of the latter would also have a tendency to react more rapidly and devitrify.

The tendency toward immiscibility in the charge-compensated alkali earth aluminosilicate melt systems also suggests that significant structural differences may exist between the two melts, for which there appears to be independent supporting evidence. X-ray scattering studies of albitic ($NaAlSi_3O_8$) and anorthitic ($CaAl_2Si_2O_8$) glasses by Taylor and Brown (1978a,b) and Taylor et al. (1980) led those investigators to conclude that albite glass possesses an open structure composed of linked six-membered tetrahedral rings, whereas anorthitic glass is perceived to contain four-membered tetrahedral rings. The former structure is quite open and could allow the diffusive penetration of water or permit ion exchange of potassium for sodium, whereas the latter structure's smaller ring size could inhibit diffusion of water and/or cations through the lattice.

Further circumstantial evidence that significant structural differences may exist in natural glasses of different chemical compositions is found in the existence of an immiscibility phenomenon in the corresponding liquid state (Philpotts, 1976) and in the demonstration that certain glasses can decompose spinodally. In subsequent work, Philpotts has made a thorough study of the formation of immiscible melts in basalts and gives evidence suggesting a corresponding structural discontinuity between basaltic and rhyolitic glasses.

Evidence for spinodal decomposition in natural glasses in the composition range of interest is much more tenuous. However, Manankov (1979) has examined glasses of basic composition after annealing them at 500–750°C and found that they decomposed spinodally into calcium-rich and calcium-poor phases. Similarly, Barron (1981), in modeling spinodal decomposition in synthetic silicate systems, concludes that a subsolidus diopside-quartz melt immiscibility occurs 100–150°C below the diopside liquidus in both diopside-nepheline-quartz and diopside-leucite-quartz systems. Again, we may note

the potential immiscible separation of Ca(-Mg)-rich and Ca(-Mg)-poor silicate liquids.

IMPLICATION OF GLASS COMPOSITION AND STRUCTURE ON THE RADIOACTIVE WASTE BURIAL IN ROCKS CONTAINING IGNEOUS GLASS

Hydrothermal alteration in a waste repository under present design concepts considered by the United States Department of Energy will range from ambient temperature to as high as 250°C. Most field observations and experimental studies of natural glass alteration are at earth-surface temperatures. No studies have been made on basaltic glass hydrothermal alteration at significantly elevated temperatures. In fact, almost nothing is known of the relative kinetics of hydration and devitrification with increasing temperature in such glasses. We must speculate that increasing temperature will accelerate these processes in basaltic glasses.

The composition of the glass mesostasis in basaltic rocks can be quite variable, depending on the history of the magma and its mode of cooling. In large flood basalt flows, cooling is slow, and the residual magmatic liquid can become highly enriched in silica. Although the silica content of the glass mesostasis may be as low as 65% wt% SiO_2, some basalt flows in Iceland contain glass mesostases with SiO_2 concentrations as high as 80 wt% (Kacandes et al., 1986). This is precisely the range of silica concentrations over which melt miscibility may occur (Philpotts and Doyle, 1982). Thus the mode of hydrothermal alteration of glass in basaltic flows may vary depending on its composition.

We may summarize the available evidence for glass alteration mechanisms in a repository environment in schematic diagrams as illustrated in Figs. 2 and 3 for rhyolitic and basaltic glasses, respectively. These diagrams are subject to modification as various issues and uncertainties are resolved.

ACKNOWLEDGMENTS

I am indebted to Mr. D. Snyder, University of California, Berkeley, and Dr. A.F. White, United States Geological Survey, for their critical review of the paper from which this summary is drawn.

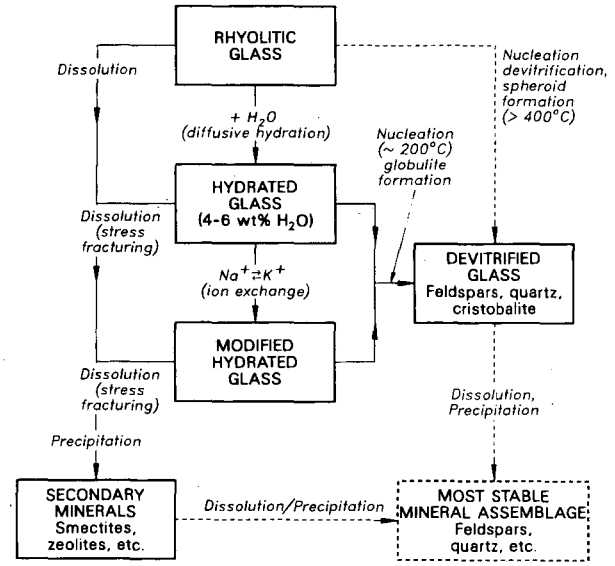

Figure 2. Schematic diagram to show the decomposition paths of rhyolitic glass when exposed to the aqueous phase. [XCG 871-6730]

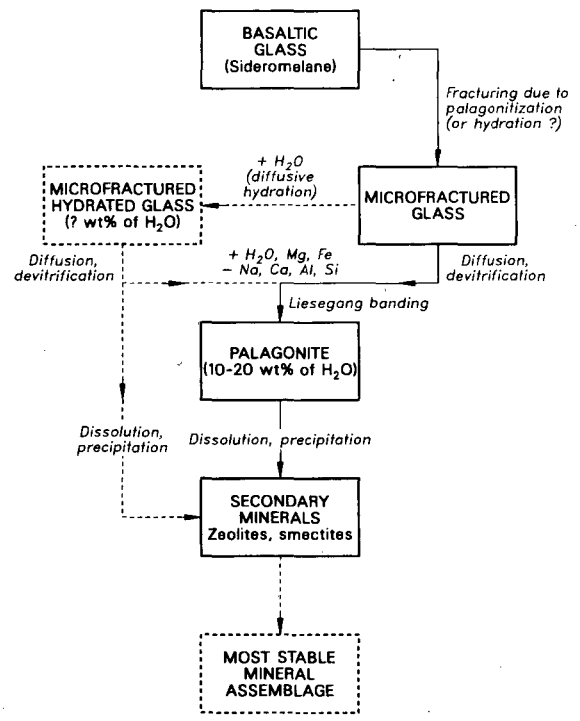

Figure 3. Schematic diagram to show the decomposition paths of basaltic glass when exposed to the aqueous phase. [XCG 871-6731]

REFERENCES

Apps, J.A., 1987. Alteration of natural glass in radioactive waste repository host rocks. Presented at the Symposium on Glass and Ceramics for Nuclear Repositories, Madrid, Spain, May 21–22, 1985. Lawrence Berkeley Laboratory Report LBL-22871.

Barron, L.M., 1981. The calculated geometry of silicate liquid immiscibility. Geochim. Cosmochim. Acta, v. 45, p. 495–512.

Friedman, I., and Long, W., 1976. Hydration rate of obsidian. Science, v. 191, p. 347–352.

Friedman, I., and Long W., 1984. Volcanic glasses, their origins and alteration processes. J. Non-Cryst. Solids, v. 67, p. 127–133.

Kacandes, G.H., Ulmer, G.C., and Grandstaff, D. E. 1986. Icelandic geothermal fields as an analog for nuclear waste isolation in Columbia Plateau (Washington, USA) basalt. *In* Fifth International Symposium on Water-Rock Interaction, Reykjavik, Iceland. Extended Abstracts. p. 302–305.

Lofgren, G.E., 1968. Experimental devitrification of rhyolite glass (Ph.D. thesis). Stanford University, 99 p.

Manankov, A.V., 1979. Mechanism of liquid immiscibility in silicate systems. Doklady Akad. Nauk SSSR, v. 246, p. 102–105.

McMillan, P., Piriou, B., and Navrotsky, A., 1982. A raman spectroscopic study of glasses along the joins silica-calcium aluminate, silica-sodium aluminate, and silica-potassium aluminate. Geochim. Cosmochim. Acta, v. 46, p. 2021–2037.

Morgenstein, M., and Riley, T., 1974. Hydration-rind dating of basaltic glass: A new method for archaeological chronologies. Asian Perspectives, p. 145–159.

Moriya, Y., and Nogami, M., 1980. Hydration of silicate glass in steam atmosphere. J. Non-Cryst. Solids, v.39, p. 667–672.

Muffler, L.P., Short, J.M., Terry, E.G., and Smith, V.C., 1969. Chemistry of fresh and altered basaltic glass from the upper Triassic Hound Island Volcanos, Southeastern Alaska. Am. J. Sci., v. 267, p. 196–209.

Navrotsky, A., Peraudeau, G., McMillan, P., and Coutures, J.-P., 1982. A thermochemical study of glasses and crystals along the joins silica-calcium aluminate and silica-sodium aluminate. Geochim. Cosmochim. Acta, v. 46, p. 2039–2047.

Navrotsky, A., Geisinger, K.L., McMillan, P., and Gibbs, G.V., 1985a. The tetrahedral framework in glasses and melts – Inferences from molecular orbital calculations and implications for structure, thermodynamics and physical properties. Phys. Chem. Miner., v. 11, p. 284–298.

Navrotsky, A., Hervig, R.L., Roy, B.N., and Huffman, M. 1985b. Thermochemical studies of silicate, aluminosilicate, and borosilicate glasses. High Temp. Sci., v. 19, p. 133–149.

Philpotts, A.R., 1976. Silicate liquid immiscibility: Its probable extent and petrogenetic significance. Am. J. Sci., v. 276, p. 1147–1177.

Philpotts, A.R., and Doyle, C.D., 1982. Effect of magma oxidation state on the extent of silicate liquid immiscibility in a tholeiitic basalt. Am. J. Sci., v. 283, p. 967–096.

Scheidegger, K.F., 1973. Volcanic ash layers in deep sea sediments and their petrological significance. Earth Planet. Sci. Lett., v. 17, p. 397–407.

Taylor, M., and Brown, G., 1978a. Structure of mineral glasses—I. The feldspar glasses $NaAlSi_3O_8$, $KAlSi_3O_8$, $CaAl_2Si_2O_8$. Geochim. Cosmochim. Acta, v. 43, p. 61–75.

Taylor, M., and Brown, G., 1978b. Structure of mineral glasses—II. The $SiO_2-NaAlSiO_4$ Join. Geochim. Cosmochim. Acta, v. 43, p. 1467–1473.

Taylor, M., Brown, G., and Fenn, P., 1980. Structure of mineral glasses—III. $NaAlSi_3O_8$ supercooled liquid at 805°C and the effects of thermal history. Geochim. Cosmochim. Acta, v. 44, p. 109–117.

Wu, C.-K., 1980. Stable silicate glasses containing up to 10 weight percent of water. J. Non-Cryst. Solids, v. 41, p. 381–398.

Yoko, T., Huang, Z., Kamiya, K., and Sakka, S., 1983. Hydration of silicate glasses by water vapor at high temperatures. Glastechnische Berichte, XIII Internationaler Glaskongress, July 4–9, 1983, Hamburg. Deutschen Glastechnischen Gesellschaft, Frankfurt am Main, p. 650–655.

The Thermodynamic Properties and Stability of Bayerite in Relation to Gibbsite and Their Solubilities in Alkaline Aqueous Media

J.A. Apps

In this article, the thermodynamic properties of bayerite are derived from solubility data in alkaline solutions and from available data on heats of decomposition. The observed spread in measured Bayer process gibbsite solubilities is then related to precipitation mechanisms during the Bayer process recovery stage, the implications of using Bayer process gibbsite for solubility measurements in dilute aqueous solution are considered, and a qualitative estimate is made regarding the kinetics of bayerite conversion to gibbsite.

THE DERIVATION OF BAYERITE THERMOCHEMICAL PROPERTIES

Bayerite solubility measurements have been reported several times in the literature, e.g., Fricke (1928, 1929), Russell et al. (1955), Chistyakova (1964), Hem and Roberson (1967), and Lyapunov et al. (1973). To test whether a consistent solubility product reflecting equilibrium with respect to a gibbsite polymorph might control the aluminum concentration in experiments involving the precipitation of aluminum hydroxide from solution and in natural systems, the experimental results of the above cited papers and others were re-evaluated to obtain values of log $K_{s4}(Al(OH)_3)$, representing the reaction

$$Al(OH)_3 + OH^- = Al(OH)_4^-$$

The log $K_{s4}(Al(OH)_3)$ data from the various studies are plotted in Fig. 1 as a function of reciprocal temperature. Included in the figure are curves showing the calculated log K_{s4} (gibbsite), as determined in Apps et al. (1986), and log K_{s4} (bayerite), as determined below. Also included for comparison are log K_{s4} (boehmite) and log K_{s4} (diaspore) from Apps et al. (1986), where log K_{s4} for these two minerals reflects the reaction

$$AlOOH + OH^- + H_2O = Al(OH)_4^-$$

The measurements by Fricke (1928, 1929), Russell et al. (1955), Chistyakova (1964), and Lyapunov et al. (1973) display a fairly consistent trend and most probably reflect bayerite solubility. However, the solubility products of synthetic and natural gibbsite by May et al. (1979), of a bauxite by Raupach (1963), of "aluminum hydroxide" by Thompson (1955), and of freshly precipitated bayerite (Hem and Roberson, 1967) lie well above this trend. The data by Sato (1954) involving the precipitation of gibbsite on gibbsite seeds over 120 hours show a trend similar to that of Russell et al. (1955) for the β trihydrate. In contrast, the solubilities of Arkansas and Surinam bauxites at 150°C from Taylor et al. (1927) fall below the gibbsite solubility curve, suggesting a reaction of natural gibbsite converting to boehmite.

A regression analysis of the data by Fricke (1928, 1929), Russell et al. (1955), and Chistyakova (1964) was made to calculate the thermodynamic properties of the bayerite dissolution reaction

$$\underset{\text{bayerite}}{Al(OH)_3} + OH^- = Al(OH)_4^-$$

It is assumed that the data reflect bayerite solubility and that the heat capacity of bayerite is the same as for gibbsite. The derived thermodynamic properties of bayerite are summarized in Table 1.

These data were calculated using the revised thermodynamic properties of the OH^- ion computed from the electrolyte model described by Tanger and Helgeson (1988) and the thermodynamic properties of the aluminate ion, $Al(OH)_4^-$, derived in Apps et al. (1986). The heat capacity of the bayerite dissolution reaction is assumed constant over the range 0–100°C.

The calculated entropy, S°_{298}, is rather higher than expected for a polymorph of gibbsite, for which S°_{298} = 16.36 cal·gfw^{-1}·K^{-1} (Hemingway et al., 1977). However, alternative interpretations using other data sets yielded less plausible results. In all probability, the true value of the entropy for bayerite lies between the calculated value and that of gibbsite. If so, bayerite probably has a somewhat larger heat capacity than assumed.

Several studies of the enthalpy of decomposition of both bayerite and gibbsite have been made, e.g., Fricke and Severin (1932), Herrmann and Stipetić (1950), Eyraud et al. (1955), Michel (1957), Mukaibo et al. (1969), and Strobel and Henning (1972). Such studies permit rough estimates of the enthalpy of transition for the reaction bayerite = gibbsite, and hence the enthalpy of formation, $\Delta H^\circ_{f,298}$(bayerite), given the corresponding value for $\Delta H^\circ_{f,298}$(gibbsite).

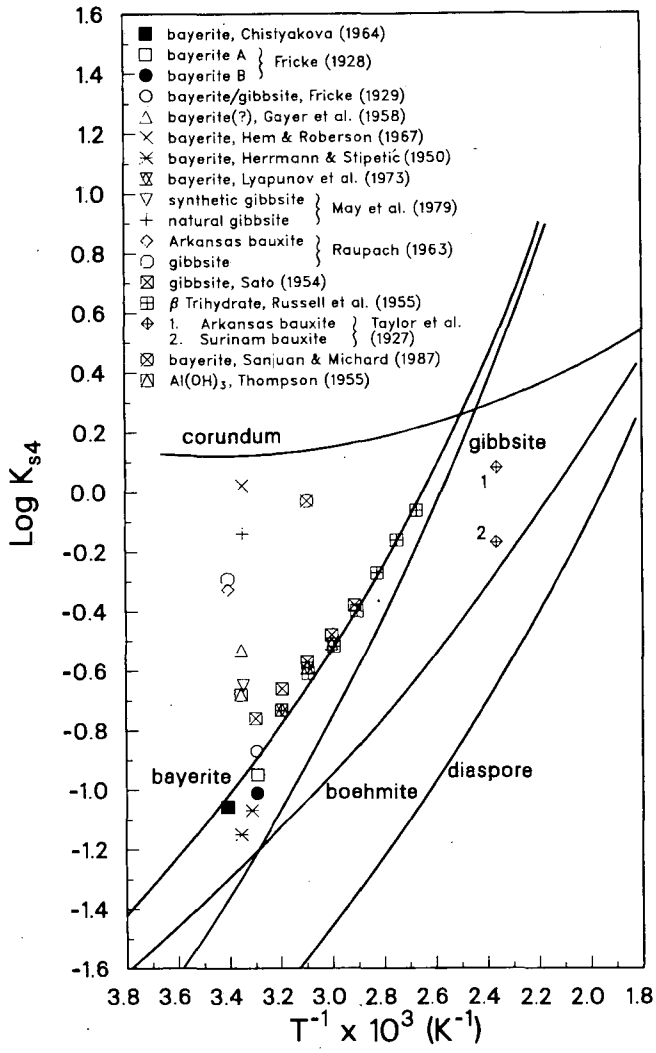

Figure 1. The solubility product log $K_{s4}(Al(OH)_3)$ as a function of reciprocal temperature. [XCG 877-11332].

Table 1. Calculated thermodynamic properties of bayerite trihydrate from data by Fricke (1928, 1929), Russell et al. (1955), Chistyakova (1964), and Lyapunov et al. 1973.

Parameter	Unit	Value
$C^{\circ}_{p,298}$	cal·gfw^{-1}·K^{-1}	+23.005[a]
S°_{298}	cal·gfw^{-1}·K^{-1}	+18.972
$\Delta H^{\circ}_{f,298}$	kcal·gfw^{-1}	−307.829
$\Delta G^{\circ}_{f,298}$	kcal·gfw^{-1}	−275.570
log $K^{\circ}_{f,298}$	—	+201.995

[a]Obtained using the Maier-Kelley heat capacity function for gibbsite reported by Helgeson et al. (1978).

Because the thermal decomposition of different bayerite and gibbsite samples rarely results in identical decomposition products, such an approach will produce questionable estimates of the heat of transition and the derived thermodynamic properties of bayerite. The average value for the heat of transition, $\Delta H^{\circ}_{r,T}$, from the literature sources, normalized to the gram formula weight (gfw) = $Al_2O_3{\cdot}3H_2O$, is −2.28 ± 1.05 kcal.

Of greater value are the data obtained from heat-of-solution determinations of bayerite and gibbsite in hydrofluoric acid. These measurements are summarized by Fricke and Wullhorst (1932) and probably permit the best estimate of $\Delta H^{\circ}_{f,298}$ (bayerite). Unfortunately, the temperature at which the HF dissolution measurements were conducted was not recorded. The most trustworthy data give 2.4 ± 0.52 kcal for the enthalpy of transition, normalized to gfw = $Al_2O_3{\cdot}3H_2O$ or −1.2 ± 0.26 kcal for gfw = $Al(OH)_3$. This is in excellent agreement with the estimate of −1.24 kcal for the same reaction using the thermodynamic properties of bayerite derived from the solubility measurements.

Although the limited solubility and calorimetric data appear to be in satisfactory accord, it should be emphasized that the available data are for the most part incomplete, and the materials utilized in the experiments are often inadequately characterized. In particular, the higher solubilities of precipitates also giving bayerite x-ray diffraction patterns, e.g., Hem and Roberson (1970), must reflect the effect of smaller particle sizes, as suggested by Parks (1972).

Because of its tendency to decompose to gibbsite in alkaline solution, the estimated bayerite solubility cannot be as precisely determined as that of gibbsite. Yet in alkaline solutions, bayerite never has a solubility less than the minimum observed for gibbsite, supporting the generally held belief that bayerite is the less stable polymorph over the range of temperatures and pressures studied.

A COMPARISON OF MEASURED BAYERITE AND GIBBSITE SOLUBILITIES IN ALKALINE SOLUTIONS

A comparison of the measured solubilities of bayerite and gibbsite in alkaline solutions provides an insight into the potential mechanisms involved in gibbsite formation and in the persistence of bayerite. In Fig. 2 are plotted log K_{s4} values derived from the precipitation or dissolution of gibbsite, bayerite, or unspecified aluminum hydroxides versus $1/T$ (K^{-1}). The data are divided into three categories: (1) those from experiments involving equilibration with gibbsite from undersaturation, designated with open

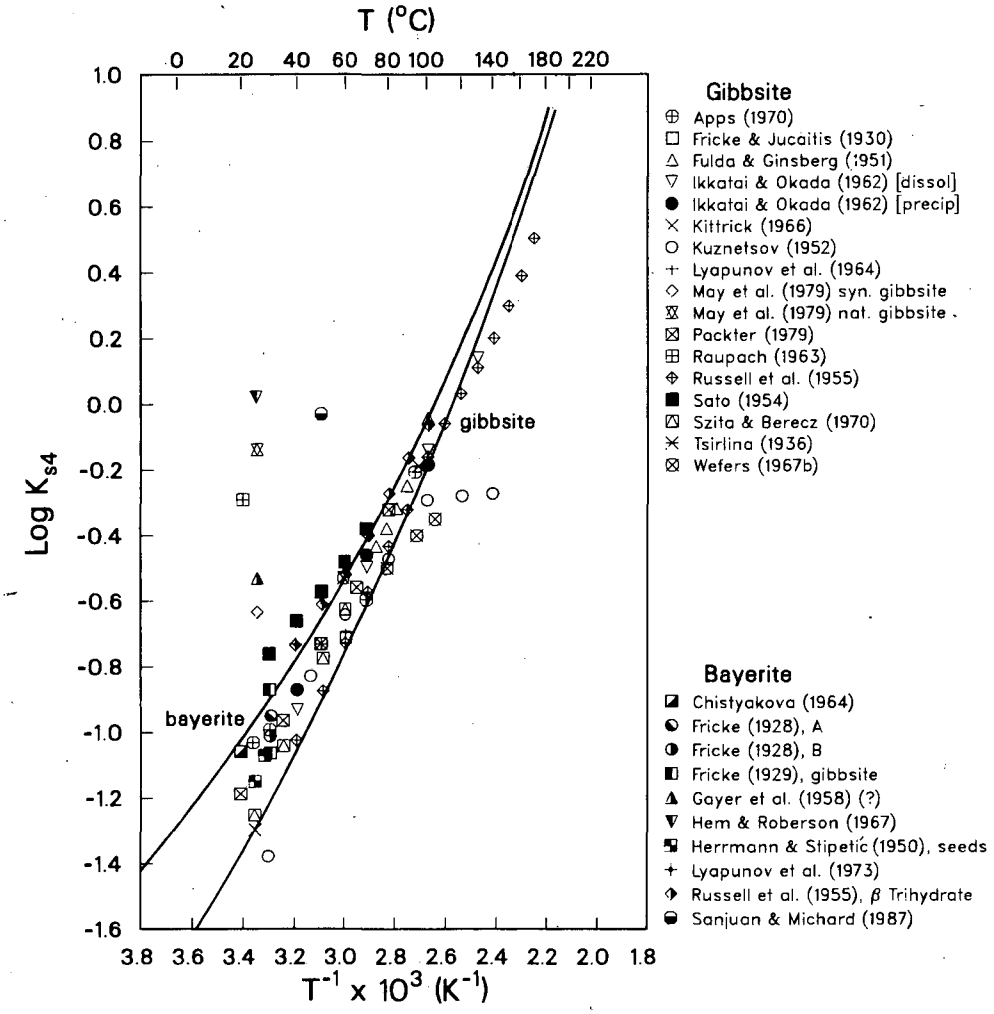

Figure 2. Comparison of the solubility products, K_{s4}, of gibbsite and bayerite, plotted as a function of reciprocal temperature. [XCG 878-11364]

symbols; (2) those from equilibration of gibbsite from oversaturation, designated with filled symbols; and (3) those from equilibration experiments from oversaturation or undersaturation where bayerite was identified as the participating phase, designated with partially filled symbols. The continuous lines in the figure represent the calculated gibbsite solubilities given in Apps et al. (1986) and the bayerite solubilities estimated in this article.

The broad scatter in the solubility measurements of gibbsite may be attributed to the mechanism by which gibbsite is produced during the Bayer process for treating bauxitic aluminum ores. In this process, a concentrated sodium aluminate liquor ($\leqslant$ 200 g^{-1} Na_2O) is cooled from as high as 250°C to approximately 50–60°C, diluted, and seeded with gibbsite crystals. The solution, which is supersaturated with respect to gibbsite, precipitates aluminum hydroxide onto the seeds. According to Calvet et al. (1951), this process is not one of simple crystal growth but instead involves the accretion of pseudocolloidal particles that have grown on "active centers," or nuclei. These "active centers" are introduced in trace amounts with poorly crystallized material associated with the well-crystallized gibbsite seeds. The interpretation by Calvet et al. (1951) is supported by SEM photographs by Bloom and Weaver (1982), who found that "untreated samples contained abundant globular surface material." The identity of the surface-active material remains in doubt. Van Straten (1984) also observed "an irregular layer with poor contrast on top of the [gibbsite] seed" when he studied the precipitation of $Al(OH)_3$ on gibbsite seeds in alkaline solutions between 25 and 90°C.

The tendency for bayerite to precipitate from alkaline solutions supersaturated with respect to gibbsite and then convert to gibbsite is well known (Geiling and Glocker, 1943; Brosset, 1952; Ginsberg et al., 1962; Bye and Robinson, 1964; Barnhisel and Rich, 1965; Wefers, 1967; Hemingway, 1982; Van Straten et al., 1984; Van Straten and de Bruyn, 1984). Moreover, Calvet et al. (1951) claim that a mixture of bayerite and gibbsite precipitates in synthetic solutions at 35°C, whereas Ginsberg et al. (1962) have shown that either a gel or bayerite forms initially from caustic aluminate solutions but that the bayerite transforms to gibbsite in the presence of alkali metal ions. At 20°C this transition takes about 60 days to complete in sodium hydroxide at pH = 12.5. At 60°C, in the presence of potassium hydroxide, the reaction is complete in 48 hours. In a series of detailed precipitation experiments conducted on aluminum hydroxide in alkaline solutions, Van Straten confirmed the observed precipitation sequence of hydroxides as a function of aluminum concentration and pH (Van Straten, 1984; Van Straten et al., 1984; Van Straten and de Bruyn, 1984). This sequence, amorphous $Al(OH)_3$—pseudoboehmite—bayerite—gibbsite, depends on a complex interplay of homogeneous and heterogeneous nucleation and growth reactions that depend on the degree of supersaturation of the solution and on temperature. Van Straten and de Bruyn (1984) provide semiquantitative evidence that bayerite precipitation is favored over a wider range of $p(OH)^-$ at lower temperature, but as the temperature is raised, both the gibbsite and the pseudoboehmite precipitation fields increase at the expense of the bayerite field.

The short-term secular equilibrium concentration of aluminum coexisting with aluminum hydroxide precipitate on gibbsite seed crystals in strong sodium aluminate solutions has also been studied by Sato (1954). The calculated solubility products, log K_{s4}, after 120 hours and at temperatures between 30 and 70°C, are also plotted in Fig. 2, where they bound the upper limits of all measurements of gibbsite solubility except for those on synthetic and natural gibbsite by May et al. (1979) and on gibbsite by Raupach (1963) in dilute alkaline solutions at 25°C and 20°C, respectively. Commercial Bayer process gibbsite, recovered from the pregnant liquor, would presumably possess a surface-active layer of even higher solubility than that determined by Sato, because of the need to optimize precipitation rates from the pregnant liquor. This probably accounts for the enhanced solubility of synthetic gibbsite observed by Raupach (1963), May et al. (1979), and Sanjuan and Michard (1987).

According to Van Straten (1984) and Van Straten et al. (1984), the precipitate of both bayerite and gibbsite in alkaline solutions in the low-supersaturation region is second order with respect to $[H^+]$ and $[Al(OH)_4^-]$, hence

$$-\frac{dc}{dt} = KrO(t)[H^+]^2[Al(OH)_4^-]^2$$

where c refers to the concentration of the solute species, H^+ or $Al(OH)_4^-$, Kr is the rate constant, and $O(t)$ is a surface-area term. The activation energy for the growth rate of bayerite is estimated to be between 14 and 19 kcal·mole^{-1} (Van Straten and de Bruyn 1984).

If, as is observed by Wefers (1967), gibbsite forms in alkaline solutions through epitaxial growth on precursor bayerite somatoids, the recrystallization of a metastable layer of bayerite to gibbsite must take place through dissolution and reprecipitation. The rate at which this occurs is very temperature sensitive. Thus, for example, Kittrick (1966) estimated that it would take about several years to equilibrate Bayer process gibbsite in ~ 0.01 N sodium hydroxide solution at 25°C, but Russell et al. (1955) equilibrated gibbsite in only 264 hours in 0.5 – 8 N sodium hydroxide at 40°C; an increase in the rate of over two orders of magnitude.

Finally, it should be noted that many ionic species will retard the rate of precipitation, as would be expected in natural systems.

We can now examine the consequences of using untreated Bayer process gibbsite to measure its solubility in dilute acid or alkaline solutions at temperatures less than 50°C. Because the surface-active material on Bayer process gibbsite may be more soluble than bayerite, a solubility product exceeding that of bayerite may be obtained when measuring its solubility in dilute solution. Furthermore, the quantity of aluminum that must dissolve to attain equilibrium is very small, particularly if a high pulp density is used. Sometimes, less than a monolayer of surface material would have dissolved before attainment of secular equilibrium! Unless some mechanism accelerates the dissolution or recrystallization of the surface layer, it would remain essentially intact during short-term experiments lasting only a few weeks (e.g., Raupach, 1963; May et al., 1979; and Sanjuan and Michard, 1987). Bloom and Weaver (1982) recognized the impact that this surface layer might have on the measurement of gibbsite solubility at 30°C in dilute acid solution and took steps to remove it beforehand. In contrast, Kittrick (1966) exposed synthetic gibbsite to dilute alkaline solutions

over a period of years before the true solubility of gibbsite was approached (Apps et al., 1986).

REFERENCES

Apps, J.A., 1970. The stability field of analcime (Ph.D. thesis). Harvard University, 347 p.

Apps. J.A., Neil, J.M., and Jun, C.-H., 1986. Thermochemical properties of gibbsite, boehmite, diaspore and the aluminate ion between 0 and 350°C. Lawrence Berkeley Laboratory Report LBL-21482, 304 p.

Barnhisel, R.I., and Rich, C.I., 1965. Gibbsite, bayerite and nordstrandite formation as affected by anions, pH and mineral surfaces. Soil Science Society of America Proceedings 1965, p. 531–534.

Bloom, P.R., and Weaver, R.M., 1982. Effect of the removal of reactive surface material on the solubility of synthetic gibbsites, Clays Clay Miner., v. 50, p. 281–286.

Brosset, C., 1952. On the reactions of the aluminium ion with water. Acta Chemica Scandinavica, v. 6, p. 910–940.

Bye, G.C., and Robinson, J.G., 1964. Crystallization processes in aluminum hydroxide gels. Kolloid Z.Z. Polym., v. 198, p. 53–60.

Calvet, E., Boivinet, P., Thibon, H., and Maillard, A., 1951. Etude microcalorimetrique de la "décomposition" des solutions alumino-sodiques. Mémoires Présentés à la Société Chimique, p. 402–415.

Chistyakova, A.A., 1964. Some data on the system Na_2–Al_2O_3–H_2O. Tsvetn. Metall. [English translation], v. 37, p. 58–63.

Eyraud, C., Goton, R., Trambouze, Y., Tran Huu The, and Prettre, M., 1955. Etude de la décomposition des hydrates d'alumin par analyse enthalpique différentielle. C. R. Acad. Sci., v. 240, p. 862–864.

Fricke, R., 1929. Einige Gesichtspunkte zu den Wandlungen der Oxydhydrate. Kolloid Z., v. 49, p. 229–243.

Fricke, R., and Jucaitis, P., 1930. Untersuchungen uber die Gleichgewichte in den Systemen $Al_2O_3 \cdot Na_2O \cdot H_2O$ and $Al_2O_3 \cdot K_2O \cdot H_2O$. Z. Anorg. Allg. Chem., v. 191, p. 129–149.

Fricke, R., and Severin, H., 1932. Uber die Zersetzungsdrücke kristallisierter Hydroxyde inbesondere von Aluminium und Beryllium. Z. Anorg. Allg. Chem., v. 205, p. 287–308.

Fricke, R., and Wullhorst, B., 1932. Die Energiedifferenzen verschiedener Modifikationen der kristallisierten Hydroxyde von Beryllium und Aluminium und die Bildungswärmen von kristallisiertem Zinc und Berylliumhydroxyd. Z. Anorg. Allg. Chem., v. 205, p. 127–144.

Geiling, S., and Glocker, R., 1943. Die Atomanordnung in Aluminiumhydroxydgel. Z. Electrochem., v. 49, p. 269–273.

Helgeson, H.C., Delany, J.M., Nesbitt, H.W., and Bird, D.K., 1978. Summary and critique of the thermodynamic properties of rock forming minerals. Am. J. Sci., v. 278-A, 229 p.

Hem, J.D., and Roberson, C.E., 1967. Form and stability of aluminum hydroxide complexes in dilute solution. *In* Chemistry of Aluminum in Natural Water, U.S. Geol. Survey Walter-Supply Paper 1827-A, 55 p.

Hemingway, B.S., 1982. Gibbs free energies of formation for bayerite, nordstrandite, $Al(OH)^{2+}$, and $Al(OH)_2^+$, aluminum mobility and the formation of bauxites and laterites. *In* S.K. Saxena (ed.), Advances in Geochemistry (Chapter 9). Springer Verlag, New York, p. 285–316.

Hemingway, B.S., Robie, R.A., Fisher, J.R., and Wilson, W.H., 1977. Heat capacities of gibbsite, $Al(OH)_3$, between 13 and 480 K and magnesite, $MgCO_3$, between 13 and 380 K and their standard entropies at 289.15 K, and the heat capacities of benzoic acid between 12 and 316 K. J. Res. U.S. Geol. Survey, v. 5, no. 6, p. 797–806.

Herrmann, E., and Stipetić, J., 1950. Der Ausrührvorgang von Tonerdehydrat nach BAYER als Keimbildungsproblem. Z. Anorg. Chem., v. 262, p. 258–287.

Kittrick, J.A., 1966. The free energy of formation of gibbsite and $Al(OH)_4^-$ from solubility measurements. Soil Science Society of America Proceedings, v. 30, no. 5, p. 595–598.

Lyapunov, A.N., Kryzhanovskii, M.M., Grigor'eva, G.N., Medvedeva, V.I., and Varzina, A.G., 1973. Increasing the decomposition rate and improving the quality of aluminum hydroxide. Tsvetn. Metall. [English translation], p. 36–39.

May, H.M., Helmke, P.A., and Jackson, M.L., 1979. Gibbsite solubility and thermodynamic properties of hydroxy-aluminum ions in aqueous solution at 25°C. Geochim. Cosmochim. Acta, v. 43, p. 861–868.

Michel, M., 1957. Etude calorimétrique de la décomposition thermique des trihydrates d'alumine. C. R. Acad. Sci., Paris, v. 244, p. 73–74.

Mukaibo, T., Takahashi, Y., and Yamada, K., 1969. The heat capacity and heat of dehydration of the hydrated aluminas. Proceedings, First International Conference on Calorimetry and Thermodynamics, Warsaw, August 31–September 4, 1969, p. 375–380.

Parks, G.A., 1972. Free energies of formation and aqueous solubilities of aluminum hydroxides and oxide hydroxides at 25°C. Am. Mineral., v. 57, p. 1163–1189.

Raupach, M., 1963. Solubility of simple aluminum compounds expected in soils, I. Hydroxides and oxyhydroxides. Australian J. Soil Res., v. 1, p. 28–35.

Russell, A.S., Edwards, J.D., and Taylor, C.S., 1955. Solubility and density of hydrated alumina in NaOH solutions. J. Metals, v. 7, p. 1123–1128.

Sanjuan, B., and Michard, G., 1987. Aluminum hydroxide solubility in aqueous solutions containing fluoride ions at 50°C. Geochim. Cosmochim. Acta, v. 51, p. 1823–1831.

Sato, T., 1954. Hydrolysis of sodium aluminate solution. XIII. Effect of decomposition temperature [in Japanese]. J. Chem. Soc. Japan., Ind. Chem. Sec. v. 57, p. 805–808.

Tanger, J.C., and Helgeson, H.C., 1988. Calculation of the thermodynamic and transport properties of aqueous species at high pressures and temperature: I. Revised equation of state for the standard partial molal properties of ions and electrolytes. Am. J. Sci., in press.

Taylor, C.S., Tosterud, M., and Edwards, J.D., 1927. The physical chemistry of aluminum. Aluminum Company of America Report R-95, 75 p.

Thompson, L.C.A., 1955. The equilibrium of aluminum hydroxide, uranium peroxide dihydrate and urano-uranate hydrate in acidic and alkaline media at 25°C. Unpublished dissertation, Wayne State University, Detroit, Michigan, 69 p.

Van Straten, H.A., 1984. Formation of solid phases from supersaturated aluminate solutions (Ph.D. thesis). University of Utrecht, Holland, 153 p.

Van Straten, H.A., and de Bruyn, P.L., 1984. Precipitation from supersaturated aluminate solutions. II. Role of temperature. J. Colloid Interface Sci., v. 102, p. 260–277.

Van Straten, H.A., Holtkamp, B.T.W., and de Bruyn, P.L., 1984. Precipitation from supersaturated aluminate solutions. I. Nucleation and growth of solid phases at room temperature. J. Colloid Interface Sci., v. 98, p. 342–362.

Wefers, K., 1967. Zur chemischen Technologie des Bauxitaufschlusses. Teil 1: Das System Na_2O–Al_2O_3–H_2O. Metall., v. 25, no. 5, p. 422–431.

The Thermodynamic Properties of Some Borosilicates

J.A. Apps

A request by the Environmental Protection Agency to characterize the fate of a strong sodium borate-sodium hydroxide waste solution containing minor organic constituents when injected into a deep saline aquifer in a sedimentary formation gave rise to an attempt to determine the thermodynamic properties of several borosilicates. The possibility existed that one or more borosilicates might precipitate through interaction of the waste steam with argillaceous sandstones and shales. Borosilicates are also of interest when considering the post-burial hydrothermal alteration of high-level radioactive processing waste, which has been manufactured into borosilicate glass castings. Finally, there is some interest in the possibility that borosilicates may form scale in power plants in which water is treated with sodium borate to control pH and retard corrosion.

Borosilicates are of widespread, though relatively uncommon, occurrence in nature. With the exception of datolite, very little is known about their thermochemical properties. Five borosilicates were chosen for evaluation: axinite, danburite, datolite, dumortierite, and howlite. All but dumortierite contain calcium.

Table 1 summarizes the chemical formulas used in this study; all are based on crystallographic studies. Both dumortierite and axinite are given idealized formulas. In nature, their chemical compositions are variable. Axinite has significant iron and manganese substituted for calcium.

Axinite and datolite are the most frequently observed borosilicates, usually the product of metasomatism of mafic volcanics, and presumably the result of post-consolidation separation and concentration of borate residues in the aqueous phase. Danburite is somewhat less common but is found in a wider range of geothermal environments, including skarns and marine evaporites. With few exceptions dumortierite tends to be restricted to pegmatites, the end result of magmatic crystallization, or to the ini-

Table 1. Structural formulas of borosilicates whose thermodynamic properties are evaluated in this report.

Mineral	Formula	Source
Axinite	$Ca_3Al_2[BO_3][Si_4O_{12}](OH)$	Ito and Takeuchi (1952)
Danburite	$CaB_2Si_2O_8$	Phillips et al. (1974)
Datolite	$CaB[SiO_4](OH)$	Foit et al. (1973)
Dumortierite	$Si_3B[Al_{6.75}\square_{0.25}O_{17.25}(OH)_{0.75}]$	Moore and Araki (1978)
Howlite	$Ca_2SiB_5O_9(OH)_5$	Finney et al. (1970)

tial stages of magmatization. Howlite is found only in marine and saline lake evaporites. Tourmaline was omitted from the evaluation because of its variable composition, which would have necessitated treatment of solid solutions and the introduction of additional chemical components in the system. There is also no evidence that it will form at temperatures below 100°C in the natural environment.

APPROACH TO THE CALCULATION OF THERMODYNAMIC PROPERTIES

To compute the equilibrium relations among minerals over the full range of temperatures, pressures, and bulk compositions found in nature, certain thermodynamic parameters must be known for the participating minerals. These conventionally include the molal volume (V°), the entropy at 298 K (S°_{298}), the enthalpy of formation at 298 K ($\Delta H^\circ_{f,298}$), and the variation of heat capacity with temperature ($C^\circ_p(T)$). For consistency with previous studies by Helgeson and his coworkers (e.g., Helgeson et al., 1978), the Maier-Kelley heat-capacity function is used for $C^\circ_p(T)$ (Maier and Kelley, 1932).

Because of the paucity of thermodynamic information on the selected borosilicates, recourse had to be made to iterative approximations using a variety of sources of data. The strategy adopted is as follows:

1. Survey the literature describing the natural occurrences of calcium borosilicates and dumortierite.
2. Summarize the paragenetic associations of the calcium borosilicate minerals and dumortierite with other minerals containing boron, calcium, silicon, and aluminum.
3. Identify natural occurrences where borosilicate minerals coexist. Construct schematic activity diagrams that are topologically compatible with the observed coexistences.
4. Generate quantitative activity diagrams as a function of

$$\log \frac{[Ca^{2+}]}{[H^+]^2} \text{ versus } \log [SiO_2(aq)]$$

at 50°C intervals to 300°C, displaying the stability fields of calcium silicates and calcium aluminosilicates observed to coexist with the selected calcium borosilicates. Estimate the range of log ($[Ca^{2+}]/[H]^{2+}$), log $[SiO_2(aq)]$, and log ($[Al^{3+}]/[H]^{3+}$), where calcium borosilicates are observed.
5. Calculate the molal volumes (V°), entropies (S°_{298}), and heat capacities ($C^\circ_p(T)$) for those borosilicates for which no data currently exist.
6. Utilize all available calorimetric, phase equilibrium, and solubility measurements, together with field observations of paragenetic assemblages, to compute the thermodynamic properties of the calcium borosilicates in sequence.
7. Calculate the solubility products of the borosilicates at 25, 60, 100, 150, 200, 250, and 300°C.
8. Construct activity diagrams as a function of log $[Ca^{2+}]/[H^+]^2$ versus log $[SiO_2\ (aq)]$ and versus log $[B(OH)_3\ (aq)]$ at 50° intervals to 300°C to display the stability fields of the borosilicates. Evaluate the stability fields in the context of observed paragenetic associations of borosilicates with each other and with associated minerals, and adjust $\Delta G^\circ_{f(T)}$ of the participating minerals accordingly.
9. Where possible, perform further independent tests of the validity of the computed thermodynamic data.

Although the literature review was not exhaustive, nearly thirty references to the natural occurrences of the selected borosilicate were consulted. Table 2 shows the borosilicate coexistences that were found.

Many of the occurrences of axinite and datolite also included minerals typical of calcium-rich environments, e.g., epidote, zoisite, clinozoisite, grossular, prehnite, wollastonite, vesuvianite, and idocrase. This suggested that an understanding of the stability fields of at least some of these minerals and the temperature ranges over which they were observed to be stable would form a logical basis for estimating the approximate chemical potentials of CaO, Al_2O_3, and SiO_2. Accordingly, activity diagrams for plotting log $([Ca^{2+}]/[H^+]^2)$ versus log $[SiO_2(aq)]$ were constructed at 50°C intervals to 300°C. Figure 1 illustrates the stability relations of the participating members at 250°C. Most of the thermodynamic data used in the computation of the diagram were derived from Haas et al. (1981).

Calorimetric measurements of the thermodynamic properties of the borosilicates are limited to the low-temperature heat-capacity measurements and entropy determinations on danburite and datolite by Agoshkov et al. (1978) and the heat capacity and enthalpy measurements on danburite and datolite by Zhdanov et al. (1978).

Phase-equilibria studies include that by Kurshakova (1975), who determined the temperature and boracic acid content of the coexisting aqueous phase for the divariant reaction

$$\underset{\text{wollastonite}}{CaSiO_3} + B(OH)_3(aq) = \underset{\text{datolite}}{CaB[SiO_4](OH)} + \underset{\text{water}}{H_2O}$$

which permitted her to calculate $\Delta G^{\circ}_{f,298}$(datolite). Another phase-equilibrium study used in this study is that by Eugster and Wise (1963) on the reaction

$$\underset{\text{datolite}}{2CaB[SiO_4](OH)} + \underset{\text{quartz}}{SiO_2} = \underset{\text{danburite}}{CaB_2Si_2O_8} + \underset{\text{wollastonite}}{CaSiO_3} + \underset{\text{water}}{H_2O}$$

Table 2. Borosilicate mineral coexistences reported in the literature.

Mineral coexistences	No. of observations
Axinite-datolite	5
Axinite-danburite	1
Axinite-dumortierite	1
Danburite-howlite	1
Danburite-datolite-axinite	2(?)

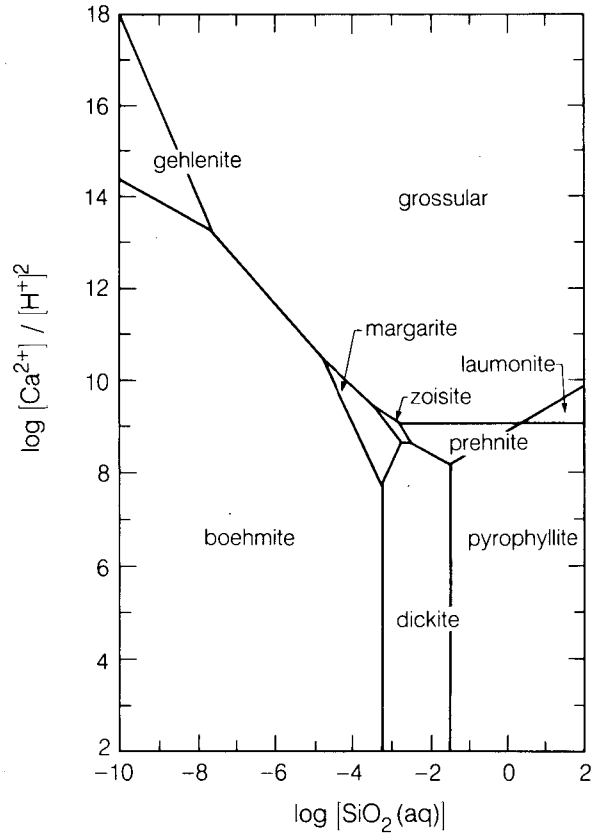

Figure 1. Activity diagram showing part of the system H_2O–CaO–Al_2O_3–SiO_2 at T = 250°C, P = 40 bar. [XBL 883-10102]

The Maier-Kelley heat-capacity functions and entropies of all minerals for which data were not already available were calculated using the empirical equations found by Helgeson et al. (1978) to give reasonable approximations of the correct values. The molal volumes of other minerals were calculated from their mineral densities, rather than from crystallographic data. The methods used in calculating the remaining thermodynamic parameters are summarized in the logic diagram illustrated in Fig. 2. The resulting data are summarized in Table 3.

Difficulties were encountered in reconciling the postulated environmental conditions for the two observed howlite occurrences, i.e., buried playa deposits and marine evaporite deposits. Furthermore, there are conflicting data in the literature for the thermodynamic properties of some of the coexisting sodium, sodium-calcium, and calcium borates, which are required for estimating the solubility of howlite; further study is necessary. A tentative estimate of howlite solubility was established through an assumption that the danburite coexists with quartz

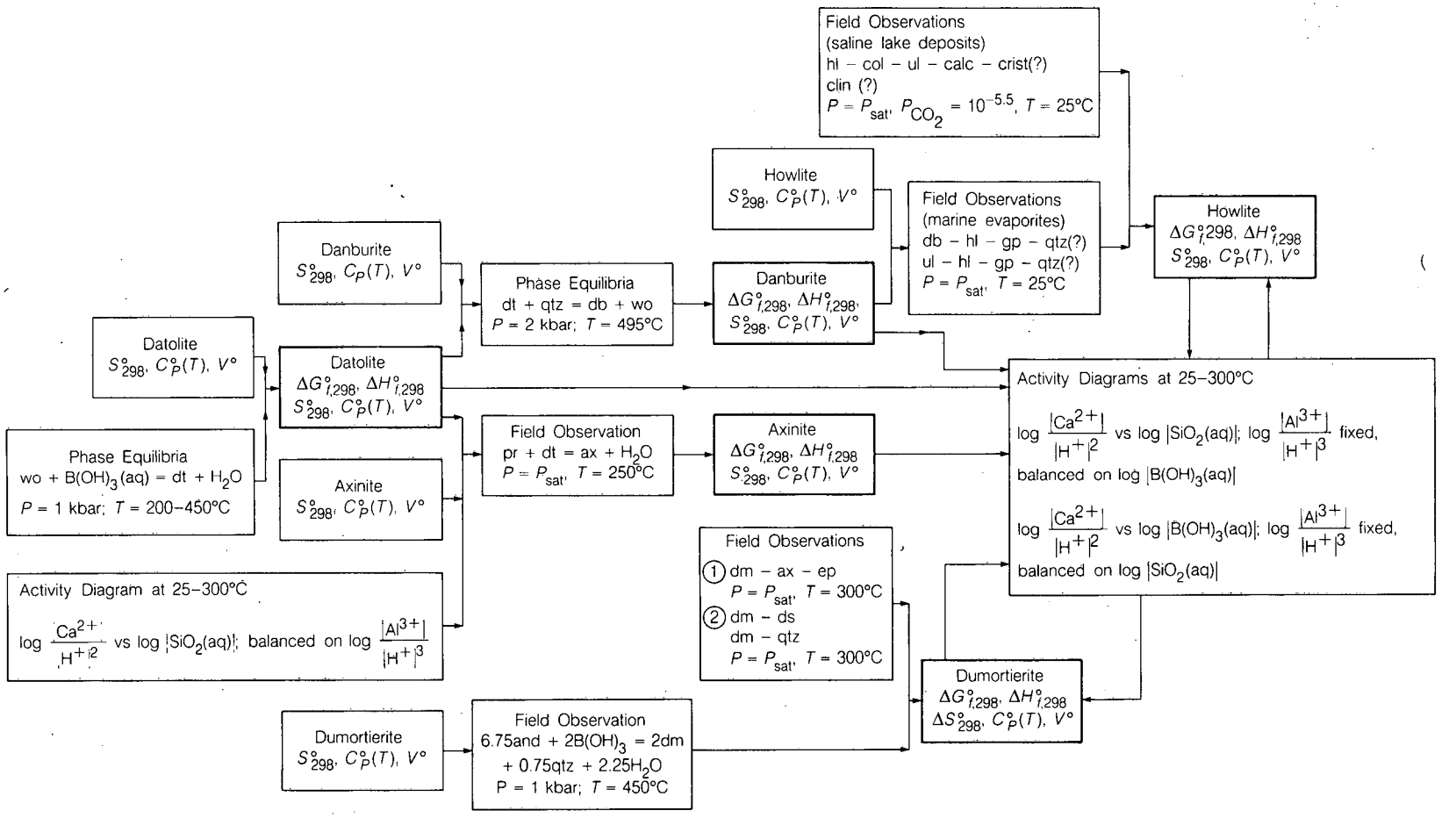

Figure 2. Logic diagram to show the sequence of steps used to calculate the thermodynamic properties of some borosilicates. [XBL 883-10100]

in marine evaporites. Table 3 summarizes all thermodynamic data computed in this study. Calculated solubility products for the borosilicates are given in Table 4. These may be incorporated under certain conditions into the EQ3 code database. The activity diagrams in Fig. 3 display the stability fields of borosilicates calculated at 25°C. These diagrams are generally consistent with field observations and available calorimetric and phase-equilibrium data.

One would be optimistic to suppose that the maximum errors in the computed solubility products do not exceed two log units. Certainly the results of this study should form the basis for designing additional experiments involving phase equilibrium, solubility, and calorimetric measurements from which the thermodynamic properties of borosilicates might be studied further. A more complete discussion of the study is given in Apps et al. (1988), which includes details about the uncertainties in the interpretations and a complete listing of all sources of information used in the computations. Further investigation of the thermodynamic properties of the borosilicates will probably be needed as new information becomes available. For the lastest data, please call (415) 486-5193.

Table 3. Summary of thermodynamic properties of some borosilicates at 298.15 K and 1 bar.

Mineral name	Formula	Gram formula weight (g)	$\Delta G^{\circ}_{f,298}$ (kcal·gfw^{-1})	$\Delta H^{\circ}_{f,298}$ (kcal·gfw^{-1})	S°_{298} (cal·gfw^{-1}·K^{-1})	$V^{\circ a}$ (cm^3·gfw^{-1})	$C^{\circ}_{p,T}$ coefficients a	b × 10^3	c × 10^{-5}
Axinite	$Ca_3Al_2BO_3[Si_4O_{12}](OH)$	554.353	−1882.768	−1997.783	84.89	168.50	119.11	46.06	−27.11
Danburite	$CaB_2Si_2O_8$	245.867	−874.165	−928.063	36.98[b]	81.41	35.57[c]	51.94[c]	−7.48[c]
Datolite	$CaB[SiO_4](OH)$	159.980	−551.000	−589.076	26.33[b]	53.15	34.62[c]	16.48[c]	−7.51[c]
Dumortierite	$Si_3B[Al_{6.75}\square_{0.25}O_{17.25}(OH)_{0.75}]$	565.937	−2066.995	−2196.555	79.08	168.43	137.28	40.29	−39.63
Howlite	$Ca_2SiB_5O_9(OH)_5$	391.327	−1421.930	−1535.876	70.51	151.68	93.21	46.36	−22.07

[a]calculated from measured specific gravity

[b]Agoshkov et al. (1978)

[c]Zhdanov et al. (1978)

Reference reactions used in the computation of S°_{298} and $C^{\circ}_{p,T}$ Maier-Kelley coefficients.

Axinite

$$\underset{\text{axinite}}{Ca_3Al_2BO_3[Si_4O_{12}](OH)} = \underset{\text{datolite}}{CaB[SiO_4](OH)} + \underset{\text{portlandite}}{2CaO} + \underset{\text{corundum}}{Al_2O_3} + \underset{\text{quartz}}{3SiO_2}.$$

Dumortierite

$$\underset{\text{dumortierite}}{Si_3B[Al_{6.75}\square_{0.25}O_{17.25}(OH)_{0.75}]} + \underset{\text{portlandite}}{CaO} + \underset{\text{structural water}}{0.125\ H_2O} = \underset{\text{datolite}}{CaB[SiO_4](OH)} + \underset{\text{corundum}}{3.375\ Al_2O_3} + \underset{\text{quartz}}{2SiO_2}$$

Howlite

$$\underset{\text{howlite}}{Ca_2SiB_5O_9(OH)_5} + \underset{\text{portlandite}}{3CaO} + \underset{\text{quartz}}{4SiO_2} = \underset{\text{datolite}}{5CaB[SiO_4](OH)}$$

Table 4. Solubility products of borosilicate minerals.

	Log K_{sp} [a]				
T(°C)	Axinite	Danburite	Datolite	Dumortierite	Howlite
0	47.988	4.383	9.216	52.176	22.192
25	42.232	4.428	8.685	41.257	21.362
60	35.427	4.341	8.017	28.378	20.200
100	29.020	4.113	7.343	16.282	18.905
150	23.457	3.712	6.600	3.933	17.339
200	16.255	3.198	5.907	−6.770	15.775
250	11.790	2.621	5.260	−16.065	14.254
300	7.155	1.984	4.624	−24.529	12.777

[a]Solubility reactions are

$Ca_3Al_2BO_3[Si_4O_{12}](OH) + 12H^+ = 2Al^{3+} + B(OH)_3(aq) + 3Ca^{2+} + 4SiO_2(aq) + 5H_2O$

$CaB_2Si_2O_8 + 2H^+ + 2H_2O = 2B(OH)_3(aq) + Ca^{2+} + 2SiO_2(aq)$

$Si_3B[Al_{6.75}\square_{0.25}O_{17.25}(OH)_{0.75}] + 20.25H^+ = 6.75Al^{3+} + B(OH)_3(aq) + 3SiO_2(aq) + 9H_2O$

$Ca_2SiB_5O_9(OH)_5 + 4H^+ + 3H_2O = 5B(OH)_3(aq) + 2Ca^{2+} + SiO_2(aq)$.

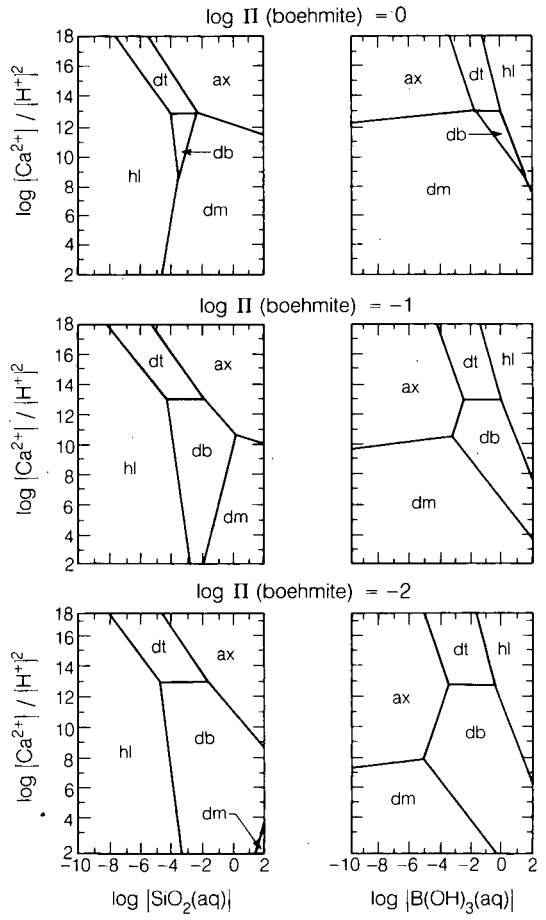

Figure 3. Activity diagrams showing selected borosilicate stability fields in the system H_2O–CaO–B_2O_3–Al_2O_3–SiO_2 at T = 25°C, P = 1 bar. [XBL 883-10101]

ACKNOWLEDGMENTS

The assistance of N. Chuma, N. Lim, and L. Liu in literature searches and data compilation is gratefully acknowledged. Calculations were facilitated through their use of the computer codes DIAGRAM, originally written by Professor T.H. Brown, University of British Columbia, SUPCRT, developed by Professor H.C. Helgeson and his coworkers at the University of California, Berkeley, and EQ3, developed by T.J. Wolery and his coworkers at the Lawrence Livermore National Laboratory.

REFERENCES

Agoshkov, V.M., Semenov, Yu. V., Malinko, S.V., and Khodakovskiy, I.L., 1978. Enthalpies of datolite and danburite between 298.15 and 973.15 K. Geochem. Int., v. 1977, p. 142–147

Apps, J.A., Jun, C.-H., and Chuma, N., 1988. The modeling of the chemical interactions of hazardous waste streams with groundwater and sedimentary host rocks in the injection zones of deep disposal wells. Lawrence Berkeley Laboratory Report LBL-24759 (in preparation).

Eugster, H.P., and Wise, W.S., 1963. Synthesis and stability of datolite and danburite. Schweiz. Mineral. Petrogr. Mitt., v. 43, p. 135–152.

Finney, J.J., Kumbasar, I., Konnert, J.A., and Clark, J.R., 1970. Crystal structure of the calcium silicoborate, howlite. Am. Mineral., v. 55 p. 716–728.

Foit, F.F., Phillips, M.W., and Gibbs, G.V., 1973. A refinement of the crystal structure of datolite, $CaBSiO_4(OH)$. Am. Mineral., v. 58, p. 909–914.

Haas, J.L., Robinson, G.R., Jr., and Hemingway, B.S., 1981. Thermodynamic calculations for selected phases in the system CaO–Al_2O_3–SiO_2–H_2O at 101.325 kPa (1 atm) between 273.15 and 1800 K. J. Phys. Chem. Ref. Data, v. 10, p. 575–635.

Helgeson, H.C., Delany, J.M., Nesbitt, H.W., and Bird, D.K., 1978. Summary and critique of the thermodynamic properties of rock forming minerals. Am. J. Sci., v. 278-A, 229 p.

Ito, T. and Takeuchi, Y., 1942. The crystal structure of axinite. Acta Crystallogr., v. 5, p. 202–208.
Kurshakova, L.P., 1975. Calculations of free energy of datolite formation according to experimental data (in Russian). Geokhimiya, p. 1029–1034
Maier, C.G., and Kelley, K.K., 1932. An equation for the representation of high temperature heat content data. J. Am. Chem. Soc., v. 54, p. 3243–3246
Moore, P.B., and Araki, T., 1978. Dumortierite, $Si_3B[Al_{6.75}\square_{0.25}O_{17.25}(OH)_{0.75}]$: A detailed structure analysis. Neues Jahrb. Mineral., Abh., v. 132, p. 231–241.
Phillips, M.W., Gibbs, G.V., and Ribbe, P.H., 1974. The crystal structure of danburite: A comparison with anorthite, albite and reedmergnerite. Am. Mineral., v. 59, p. 79–85.
Zhdanov, V.M., Turdakin, V.A., Arutyunov, U.S., Semenov, Yu.V., Malinko, S.V., and Khodakovskiy, I.L., 1978. Low temperature specific heat, standard entropy, and elastic parameters of datolite and danburite. Geochem. Int., v. 1977, p. 135– 141.

Thermodynamic Properties of Silicate Materials

I.S.E. Carmichael, V.C. Kress, and D.A. Snyder

Our program continues to focus on the experimental determination of the thermodynamic and physical properties of molten silicates. This past year we have concentrated on redox equilibria in multicomponent silicate liquids and on high-temperature calorimetry. These will be discussed separately.

STOICHIOMETRY OF THE IRON OXIDATION REACTION IN SILICATE MELTS

Iron is unique among the major constituents of natural silicate melts in that it is present in significant portions in more than one oxidation state. The distribution of iron between ferric and ferrous species provides a means by which variations in the chemical potential of oxygen, a quite mobile species, can profoundly influence the structure, rheology, and chemical composition of an evolving magma.

As a first approximation one may consider the oxidation of iron according to the reaction

$$2FeO^{melt} + \frac{1}{2}O_2 = Fe_2O_3^{melt} \qquad (1)$$

from which we may define an equilibrium constant:

$$K_1 \equiv \frac{[a^{melt}_{Fe_2O_3}]}{[a^{melt}_{FeO}]^2 \cdot [f_{O_2}]^{1/2}}, \qquad (2)$$

where a denotes the activity of the subscripted species in the melt phase. Assuming a standard state consisting of the pure component at P and T makes the equilibrium constant K_1 a function of pressure and temperature alone. If one makes the additional assumption that the ferric and ferrous components mix ideally, then a plot of $\ln(X_{Fe_2O_3} / X^2_{FeO})$ (where X_i denotes the mole fraction of the subscripted species i in the melt phase) against $\ln(f_{O_2})$ should be linear, with a slope of one-half. Deviations from such simple behavior will reflect nonideal mixing in ferric and/or ferrous components.

Sack et al. (1980) found that an excellent fit to observations could be obtained using a simple empirical expression of the form

$$\ln\left(\frac{X^{liq}_{Fe_2O_3}}{X^{liq}_{FeO}}\right) = a \ln f_{O_2} + \frac{b}{T} + c + \sum_i d_i X_i \,, \qquad (3)$$

where a, b, and d_i are regression coefficients and the sum is over the oxide components i. Kilinc et al. (1983) refined the compositional parameters d_i by supplementing the data base of Sack et al. (1980) with 46 additional experiments (in air) on compositions ranging from those of nephelinite to rhyolite.

Recent high-precision determinations of the ferric/ferrous distribution in mid-ocean ridge basalt (MORB) glasses (Christie et al., 1986) suggest that submarine basalts equilibrate under far more reducing conditions than had been previously believed. Using reaction (3) with the regression coefficients of Kilinc et al. (1983), Christie et al. (1986) estimated quench oxygen fugacities up to 3 $\log_{10}$ units below the nickel-nickel oxide (NNO) oxygen buffer. These

results suggest that MORBs are among the most reduced lavas on Earth. The most reduced experiments in the regression of Kilinc et al. (1983) were equilibrated at oxygen fugacities close to the fayalite-magnetite-quartz (FMQ) buffer (0.78 $\log_{10}$ units below NNO). The conclusions of Christie et al. (1986) are, therefore, based on an extrapolation of the regression of Kilinc et al. (1983) outside the range of experimental calibration.

It has been suggested (Mysen et al., 1984, 1985; Virgo and Mysen, 1985), on the basis of Mössbauer data, that the ferric ion undergoes a coordination change from four- to sixfold as $Fe^{3+}/(Fe^{2+}+Fe^{3+})$ is decreased below one-half. A ferric coordination shift will be accompanied by a change in the chemical potential of the ferric component and its derivatives. Such a coordination shift would, therefore, likely be expressed macroscopically as a change in the slope of $\ln(X_{Fe_2O_3}/X_{FeO})$ against $\ln f_{O_2}$. Existence of such a slope break would suggest that it is incorrect to apply the regression of Kilinc et al. (1983) at oxygen fugacities below FMQ.

To resolve this issue, and better define the stoichiometry of the oxidation reaction in silicate melts, we have performed ferric/ferrous equilibrium experiments on a limited number of compositions spanning a much larger and more complete range of f_{O_2} than had been previously attempted.

Experimental Technique

Starting materials consisted of fused natural rock glasses including andesite, MORB, nephelinite, and ugandite compositions. Glass fragments were welded onto 4-mm loops of 5-mil $Pt^{90\%}Rh^{10\%}$ wire and suspended in the hot spot of a vertical quench furnace. Oxygen fugacity was imposed by a furnace atmosphere consisting of a CO/CO_2 gas mixture (Deines et al., 1974).

Run products were analyzed for major and minor elements on an eight-channel ARL-EMX electron microprobe at the University of California, Berkeley. Ferrous iron contents were determined using wet chemical techniques. Ferric iron is calculated from the difference between total iron and iron in the ferrous state.

Results

Figures 1a to 1d are plots of $\ln(X_{Fe_2O_3}/X_{FeO})$ against $\ln f_{O_2}$ at roughly 1360°C and for four of the compositions studied. The significance of the solid and broken curves in these plots will be discussed later. These new data are entirely consistent with earlier results (Sack et al., 1980), which suggest that $\ln(X_{Fe_2O_3}/X_{FeO})$, rather than $\ln(X_{Fe_2O_3}/X^2_{FeO})$, is linear in $\ln(f_{O_2})$.

There is no indication of a slope break in any of the plots in Fig. 1, suggesting that there is probably no abrupt change in melt properties over the range of oxygen fugacities examined. This observation does not rule out a possible ferric ion coordination change within this range. A gradual coordination shift, distributed over a somewhat larger range of $Fe^{3+}/(Fe^{2+}+Fe^{3+})$, could conceivably explain the fact that $\ln(X_{Fe_2O_3}/X_{FeO})$ rather than $\ln(X_{Fe_2O_3}/X^2_{FeO})$ is linear in $\ln f_{O_2}$.

It is quite remarkable that both the slope and curvature of the plot of $\ln(X_{Fe_2O_3}/X_{FeO})$ versus $\ln f_{O_2}$ seem to be largely independent of composition over the range considered. The significance of this observation is highlighted by considering an asymmetric Margules formulation of the iron oxidation reaction in silicate melts (Sack et al., 1980):

$$\ln\left(\frac{X^{liq}_{Fe_2O_3}}{(X^{liq}_{FeO})^2}\right) = \frac{1}{2}\ln f_{O_2} - \frac{\Delta H_1}{RT} + \frac{\Delta S_1}{R} - \frac{1}{RT} \times \sum_i (W_{i,Fe_2O_3} - 2W_{i,FeO})X_i - \frac{1}{2RT}\sum_i\sum_j W_{i,j}X_iX_j\,, \quad (4)$$

where ΔH_1 and ΔS_1 are the enthalpy and entropy of reaction (1), respectively, R is the universal gas constant, and T is in Kelvin. In this thermodynamic formulation the deviation from ideality described above lies in the Margules mixing terms ($W_{i,j}$). The fact that the observed nonideal behavior is largely independent of bulk composition suggests that this nonideality must reside primarily in the W_{FeO,Fe_2O_3} and $W_{Fe_2O_3,FeO}$ terms. This is consistent with a suggestion made by Virgo and Mysen (1985) that clusters with Fe_3O_4 stoichiometry may be present in the melt at intermediate oxygen fugacities. An ideal mixing model involving partial association of ferric and ferrous components to a Fe_3O_4 cluster produces curves with the sort of overall slope observed in the experiments, but the shape of the curves so produced are significantly convex upward. This is not in accord with observations. As an alternative solution we investigated iron oxidation reactions for ferric-ferrous clusters of more general stoichiometry. We found that a model of the form

$$FeO + 0.232O_2 = FeO_{1.464} \quad (5)$$

reproduces the observed response of the ferric/ferrous ratio to f_{O_2} without resorting to ferric-ferrous regular solution parameters. It should be

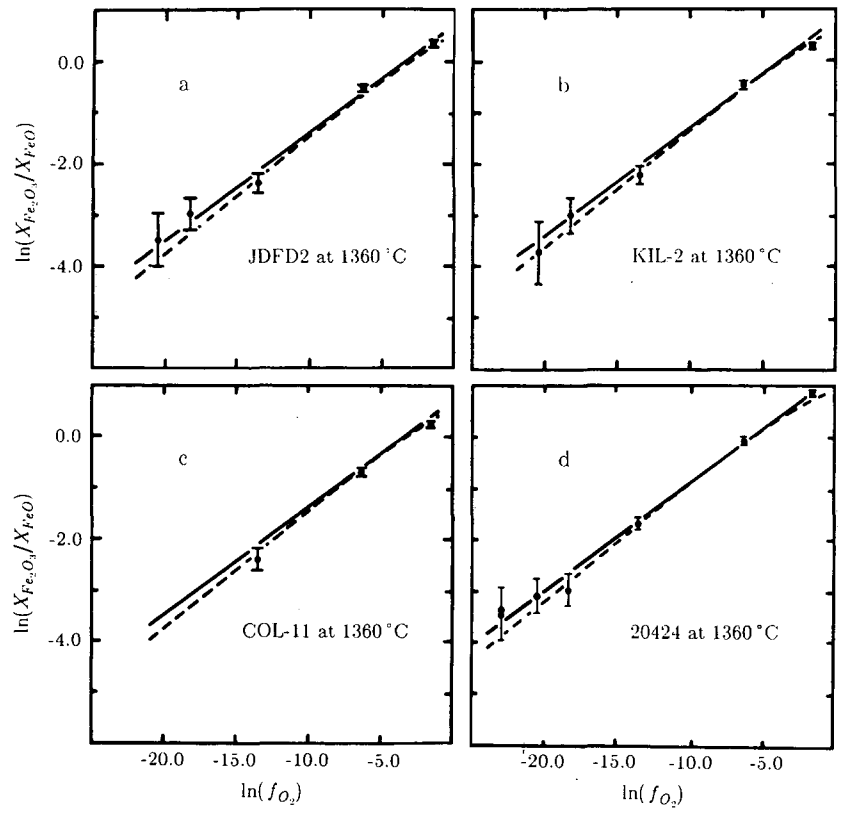

Figure 1. Plot of $\ln(X^{melt}_{Fe_2O_3}/X^{melt}_{FeO})$ versus $\ln f_{O_2}$ for four compositions at 1360°C. Error bars represent estimated analytical error. The broken lines are predicted using the model in Table 1; the solid lines are predicted from the model in Table 2. [XBL 886-2277]

emphasized that the $FeO_{1.464}$ cluster postulated above may or may not correspond to species existing in the melt. The primary value of the formulation represented by reaction (5) is that it allows a more ideal thermodynamic mixing model to be applied, for poorly constrained nonideal mixing terms may lead to significant errors on extrapolation. By casting compositions in terms of FeO and $FeO_{1.464}$ components, these nonideal mixing terms are avoided, resulting in simpler and more mathematically stable thermodynamic formulations (Ghiorso, 1985).

The broken curves in Figs. 1a to 1d are calculated from a model of the form

$$\ln\left(\frac{X^{liq}_{FeO_{1.464}}}{X^{liq}_{FeO}}\right) = 0.232 \ln f_{O_2} + \frac{b}{T} + c + \sum_i d_i X_i \,, \tag{6}$$

with coefficients from Table 1. Equation (6) reproduces the experimental data with a standard error of 0.3 natural log units.

Table 1. Values and standard errors for coefficients in Eq. (6):

$$\ln X^{liq}_{FeO_{1.464}}/X^{liq}_{FeO} = 0.232 \ln f_{O_2} + \frac{b}{T} + c + \sum_i d_i X_i .$$

Coefficient	Value	Standard error
b ($b/T(K)$)	12588	772
c constant	−6.47	0.47
$d_{Al_2O_3}$	−3.39	1.11
d_{CaO}	3.92	0.48
d_{Na_2O}	9.02	1.54
d_{K_2O}	9.25	1.46
R^2	0.956	
Standard error	0.295	

Alternatively, the results presented in this study confirm that the simple empirical formulation presented in Sack et al. (1980) remains valid to oxygen fugacities as low as those defined by the iron-wüstite assemblage. Stepwise regression of our data, along with the data base of Kilinc et al. (1983) and Sack et al. (1980), yields the coefficients listed in Table 2. The solid curves in Figs. 1a to 1d are produced using these coefficients.

Application of the revised values for the coefficients in Eq. (3) in Table 2 to the ferric-ferrous determinations of Christie et al. (1986) yields estimated values of $\ln f_{O_2}$ between 0.03 and 0.25 $\log_{10}$ units higher than those predicted using the coefficients of Kilinc et al. (1983). This difference is quite small and does not challenge the validity of the conclusions reached by Christie et al. (1985).

Conclusion

We have reaffirmed that the logarithm of the ferric/ferrous ratio is linear in $\ln f_{O_2}$ to a high degree of precision. The slope of this line is independent of composition over a wide range and is valid to oxygen fugacities as low as iron-wüstite. Such behavior is consistent with an empirical thermodynamic formulation involving oxidation of FeO to a completely associated $FeO_{1.464}$ component. In addition, we present refined values for coefficients in the empirical equation of Sack et al. (1980) that define a more precise relation between ferric/ferrous ratio, oxygen fugacity, temperature, and bulk composition.

Table 2. Values and standard errors for coefficients in Eq. (3):

$$\ln X^{liq}_{Fe_2O_3}/X^{liq}_{FeO} = a \ln f_{O_2} + \frac{b}{T} + c + \sum_i d_i X_i .$$

Coefficient	Value	Standard error
a ($a \ln f_{O_2}$)	0.2113	0.0033
b ($b/T(K)$)	11201	659
c constant	−2.92	0.95
d_{CaO}	3.45	0.41
d_{Na_2O}	8.06	1.32
d_{K_2O}	8.12	1.24
R^2	0.961	
Standard error	0.252	

HIGH-TEMPERATURE CALORIMETRY

Calorimetrically determined thermodynamic data have proved useful in making quantitative predictions of phase equilibria in both synthetic (Greenberg, et al., 1985; Hastie and Bonnell, 1985) and natural systems (Ghiorso et al., 1983) as well as in predicting the heat budgets in the upper mantle during magma genesis. We have continued our efforts to determine these data in the temperature range from 1800 to 2800 K.

Work in this past year has been focused on calibration of the high-temperature drop calorimeter. Two systems of the apparatus need careful calibration: the high-temperature photoelectric pyrometer and the enthalpy of the calorimetry vessel. The enthalpy of the vessel has now been determined and is given by

$$H = a + bT + cT^2 + dT^3 , \qquad (7)$$

where H is the enthalpy in kilojoules, T is the temperature in degrees centigrade ($18 < T < 29$), and a, b, c, and d are regressed parameters with the following values: $a = -1094.5046$, $b = 60.2704$, $c = 0.2706$, and $d = 9.1486 \times 10^{-5}$. A preliminary calibration of the photoelectric pyrometer has also been completed. This calibration was performed against a Type-S thermocouple. This calibration is preliminary to a more accurate determination using the thermal arrest method at the Pt point is executed. The calibration using the more accurate technique is underway.

REFERENCES

Christie, D.M., Carmichael, I.S.E., and Langmuir, C.H., 1986. Oxidation states of mid-ocean ridge basalt glasses. Earth Planet. Sci. Lett., v. 79, p. 397–411.

Deines, P., Nafziger, R.H., Ulmer, G.C., and Woermann, E., 1974. Temperature-oxygen fugacity tables for selected gas mixtures in the system C–H–O at one atmosphere total pressure. Bull. Earth Miner. Sci. Exp. Stn., v. 88, p. 1–129.

Ghiorso, M.S,. 1985. Chemical mass transfer in magmatic processes I. Thermodynamic relations and numerical algorithms. Contrib. Mineral. Petrol., v. 90, p. 107–120.

Ghiorso, M.S., Carmichael, I.S.E., Rivers, M.L., and Sack, R.O., 1983. The Gibbs free energy of mixing of natural silicate liquids; an expanded regular solution approximation for the calculation of magmatic intensive variables. Contrib. Mineral. Petrol., v. 84, p. 107–145.

Greenberg, J.P., Weare, J.H., and Harvie, C.E., 1985. An equilibrium computation algorithm for complex highly nonideal systems. High Temp. Sci., v. 20, p. 141–162.

Hastie, J.W. and Bonnell, D.W., 1985. A predictive phase equilibrium model for multicomponent oxide mixtures. Part II. Oxides of Na-K-Ca-Mg-Al-Si. High Temp. Sci., v. 19, p. 275–306.

Kilinc, A., Carmichael, I.S.E., Rivers, M.L., and Sack, R.O., 1983. The ferric-ferrous ratio of natural silicate liquids equilibrated in air. Contrib. Mineral. Petrol., v. 83, p. 136–140.

Mysen, B.O., Virgo, D., and Seifert, F.A., 1984. Redox equilibria of iron in alkaline earth silicate melts: Relationships between melt structure, oxygen fugacity, temperature and properties of iron-bearing silicate liquids. Am. Mineral., v. 69, p. 834–847.

Mysen, B.O., Virgo, D., Neuman, E.R., and Seifert, F.A., 1985. Redox equilibria and the structural states of ferric and ferrous iron in melts in the system $CaO-MgO-Al_2O_3-SiO_2-Fe-O$: Relationships between redox equilibria, melt structure and liquidus phase equilibria. Am. Mineral., v. 70, p. 317–331.

Sack, R.O., Carmichael, I.S.E., Rivers, M., and Ghiorso, M.S., 1980. Ferric-ferrous equilibria in natural silicate liquids at 1 bar. Contrib. Mineral. Petrol., v. 75, p. 369–376.

Virgo, D., and Mysen, B.O., 1985. The structural state of iron in oxidized vs. reduced glasses at 1 atm: A ^{57}Fe Mössbauer study. Phys. Chem. Miner., v. 12, p. 65–76.

Some Effects of Data-Base Variations on Numerical Simulations of Uranium Migration

C.L. Carnahan

Numerical simulators of migration of reactive chemicals in the subsurface generally rely upon thermodynamic data bases (in particular, values of equilibrium constants and their variations with temperature) for the chemical species to be included in the simulations. The work described here is an investigation of the sensitivity of computed uranium concentrations to variations of data bases used in numerical simulations of uranium transport. The calculations were made with the computer program THCC, a thermodynamically based simulator that incorporates homogeneous and heterogeneous chemical reactions, under the assumption of chemical equilibrium, into the solution of multicomponent solute-transport equations (Carnahan, 1987a,b). Uranium was chosen as the element of interest for several reasons. First, uranium is interesting chemically because of its possible existence in three principal oxidation states (IV, V, VI) and its ability to form complexes with ligands occurring in natural waters. Second, disagreement exists in the literature about the identities and formation constants of certain uranium species in aqueous solution. Third, practical interest in migration of uranium arises in investigations of formation of ore bodies and in performance assessments of geologic repositories for nuclear wastes.

SOME DIFFERENCES IN URANIUM DATA BASES

In the work summarized here, no attempt was made to create a comprehensive, critically evaluated data base. Instead, reliance was placed on existing compilations (Phillips et al., 1985; Langmuir, 1987; Schweingruber, 1981) of equilibrium constants for reactions of interest, supplemented by a selection of data from the recent literature. To keep the sensitivity analyses relatively uncomplicated, attention was focused on equilibria involving the aqueous species $U(OH)_4^0$, $U(OH)_5^-$, UO_2^+, $(UO_2)_2CO_3(OH)_3^-$, $UO_2(CO_3)_3^{5-}$, and $U(CO_3)_5^{6-}$.

The older literature contains formation constants for a series of hydrolysis products of U(IV) including $U(OH)_4^0$ and $U(OH)_5^-$. The validity of these constants, as well as the existence of $U(OH)_5^-$, has been questioned (Ryan and Rai, 1983). In addition, new data for the stability constant of $U(OH)_4^0$ have been reported (Bruno et al., 1986a,b) that do not support the older data.

The older literature provides data on UO_2^+ that indicate a significant field of stability for this species in the Eh-pH domain (Langmuir, 1978). However, Choppin (1983) has pointed out that UO_2^+ has a strong tendency to disproportionate. Thus UO_2^+

may not be an appropriate species for consideration in geologic environments. On the other hand, complexation may increase the stability of U(V).

New data have been reported for formation of the U(IV) species $U(CO_3)_5^{6-}$ (Ciavatta et al., 1983), the U(V) species $UO_2(CO_3)_3^{5-}$ (Ferri et al., 1983), and the binuclear U(VI) species $(UO_2)_2CO_3(OH)_3^-$ (Maya, 1982).

BASES OF THE SIMULATIONS

All simulations are based on the assumption that an influent fluid bearing dissolved uranium at a high Eh and moderate pH flowed into and mixed with an initial fluid containing no uranium at a low Eh and high pH. The composition of the initial fluid matched exactly the reported (Wikberg, 1986) composition of a Swedish deep groundwater. The composition of the influent fluid matched the major ion content and pH reported (Wikberg, 1986) for a different Swedish deep groundwater, but the Eh was assumed much higher than the reported value of −0.22 V, and the fluid was assumed to contain dissolved uranium at a total concentration of 4.31×10^{-5} M. This uranium concentration is about one order of magnitude smaller than the calculated solubility of $UO_2(OH)_2 \cdot H_2O(c)$ (schoepite), the uranium-containing solid that is most stable under the conditions assumed for the influent fluid. Detailed compositions of the two simulated fluids are shown in Table 1.

The initial fluid was contained within a one-dimensional spatial domain simulating a porous or fractured geologic medium. At time zero, the influent fluid began to penetrate this domain with a fluid velocity of 1×10^{-6} m/s. The domain had a dispersivity of 0.02 m and a diffusion coefficient of 1×10^{-10} m^2/s. The temperature of the system was assumed constant at 25°C. The corresponding equilibrium constants (expressed as log K values) for chemical reactions are shown in Table 2, where reactions forming aqueous complexes and dissolving solids are expressed in terms of a set of "basis species" consisting of UO_2^{2+}, CO_3^{2-}, $Si(OH)_4^0$, H^+, and e^-.

Three cases were simulated. In all cases the compositions of influent and initial fluids, the physical properties, and the equilibrium constants for ionization of H_2O and for formation of the complexes HCO_3^-, $H_2CO_3^0$, $UO_2CO_3^0$, $UO_2(CO_3)_2^{2-}$, and $UO_2(CO_3)_3^{4-}$ were the same. The possibility of precipitation of six solid phases was considered, and their solubility products were held constant for all simulations. The solid phases considered were $UO_2(OH)_2 \cdot H_2O(c)$ (schoepite), $UO_2(c)$ (uraninite), $USiO_4(c)$ (coffinite), $Ca(UO_2)_2(SiO_3OH)_2(c)$ (uranophane), $UO_2CO_3(c)$ (rutherfordine), and $CaUO_4(c)$ (calcium uranate). The simulations differed in the identities of certain aqueous species and in values of equilibrium constants for the formation of certain species.

Case 1: Older literature values of log K for formation of the species UO_2^+, $U(OH)_4^0$, $U(OH)_5^-$, and $(UO_2)_2CO_3(OH)_3^-$ were used.

Case 2: The same values of log K as in Case 1 were used for $(UO_2)_2CO_3(OH)_3^-$ and $U(OH)_4^0$, but UO_2^+ and $U(OH)_5^-$ were excluded form the simulation.

Case 3: Newer literature values of log K for formation of $(UO_2)_2CO_3(OH)_3^-$ and $U(OH)_4^0$ were used, UO_2^+ and $U(OH)_5^-$ were excluded, and the species $U(CO_3)_5^{6-}$ and $UO_2(CO_3)_3^{5-}$ were added to the chemical system.

Table 1. Compositions of initial and influent solutions.

Component	Initial	Influent
Na^+	1.30×10^{-2} *M*	1.60×10^{-3} *M*
Ca^{2+}	1.00×10^{-3} *M*	6.70×10^{-4} *M*
Cl^-	1.47×10^{-2} *M*	5.34×10^{-4} *M*
$Si(OH)_4^0$	1.10×10^{-4} *M*	1.10×10^{-4} *M*
Total carbonate	2.60×10^{-4} *M*	3.00×10^{-3} *M*
Total uranium	0.	4.31×10^{-5} *M*
Eh	−0.35 V	+0.30 V
pH	9.05	6.93

RESULTS AND DISCUSSION

At a simulated time of 1×10^6 s, profiles of Eh and concentrations of Ca^{2+}, $Si(OH)_4^0$, CO_3^{2-}, and H^+ did not differ significantly among the three cases. The total dissolved uranium concentrations are shown in Fig. 1. Here it is seen that, relative to Case 1, exclusion of $U(OH)_5^-$ from Case 2 (while retaining the same log K for formation of $U(OH)_4^0$) decreased total uranium concentrations in the region of precipitation of $USiO_4(c)$ by more than two orders of magnitude and extended this region by a factor of two. On the other hand, total uranium concentrations in equilibrium with $USiO_4(c)$ for Case 3 (with a different value of log K for formation of $U(OH)_4^0$) exceeded those for Case 1 by almost three orders, and they exceeded those for Case 2 by five orders of magnitude. Beyond the region of precipitation, total

Table 2. Chemical reactions and log K values used in the simulations.

Reaction	log K
Used in all cases	
$H_2O = H^+ + OH^-$	−13.99
$H^+ + CO_3^{2-} = HCO_3^-$	10.34
$2H^+ + CO_3^{2-} = H_2CO_3^0$	16.70
$UO_2^{2+} + CO_3^{2-} = UO_2CO_3^0$	10.09
$UO_2^{2+} + 2CO_3^{2-} = UO_2(CO_3)_2^{2-}$	17.13
$UO_2^{2+} + 3CO_3^{2-} = UO_2(CO_3)_3^{4-}$	20.64
$UO_2(OH)_2 \cdot H_2O(c) + 2H^+ = UO_2^{2+} + 3H_2O$	5.40
$Ca(UO_2)_2(SiO_3OH)_2(c) + 6H^+ = Ca^{2+} + 2UO_2^{2+} + 2Si(OH)_4^0$	17.21
$UO_2CO_3(c) = UO_2^{2+} + CO_3^{2-}$	−14.29
$CaUO_4(c) + 4H^+ = Ca^{2+} + UO_2^{2+} + 2H_2O$	15.00
$USiO_4(c) + 2H_2O = UO_2^{2+} + Si(OH)_4^0 + 2e^-$	−18.54
$UO_2(c) = UO_2^{2+} + 2e^-$	−13.19
Used in Case 1	
$2UO_2^{2+} + CO_3^{2-} + 3H_2O = (UO_2)_2CO_3(OH)_3^- + 3H^+$	−1.92
$UO_2^{2+} + e^- = UO_2^+$	−2.11
$UO_2^{2+} + 2e^- + 2H_2O = U(OH)_4^0$	−0.02
$UO_2^{2+} + 2e^- + 3H_2O = U(OH)_5^- + H^+$	−4.65
Used in Case 2	
$2UO_2^{2+} + CO_3^{2-} + 3H_2O = (UO_2)_2CO_3(OH)_3^- + 3H^+$	−1.92
$UO_2^{2+} + 2e^- + 2H_2O = U(OH)_4^0$	−0.02
Used in Case 3	
$2UO_2^{2+} + CO_3^{2-} + 3H_2O = (UO_2)_2CO_3(OH)_3^- + 3H^+$	−0.24
$UO_2^{2+} + 3CO_3^{2-} + e^- + UO_2(CO_3)_3^{5-}$	14.93
$UO_2^{2+} + 2e^- + 2H_2O = U(OH)_4^0$	4.40
$UO_2^{2+} + 5CO_3^{2-} + 4H^+ + 2e^- = U(CO_3)_5^{6-} + 2H_2O$	52.00

uranium concentrations for Case 3 exceeded those for Cases 1 and 2 by about two orders of magnitude.

It is noted that, of the six solid phases considered in the simulations, only $USiO_4(c)$ and $Ca(UO_4(c)$ were found to precipitate at any simulated time less than 2×10^6 s. Precipitation of $CaUO_4(c)$ was confined to the region of high Eh near the influent boundary in Cases 1 and 2 and did not occur anywhere in Case 3.

Among the individual uranium species, carbonato complexes of dioxouranium(VI) were dominant in the region of high Eh and showed only slight differences among the simulations. The concentration of $(UO_2)_2CO_3(OH)_3^-$ was slightly increased in

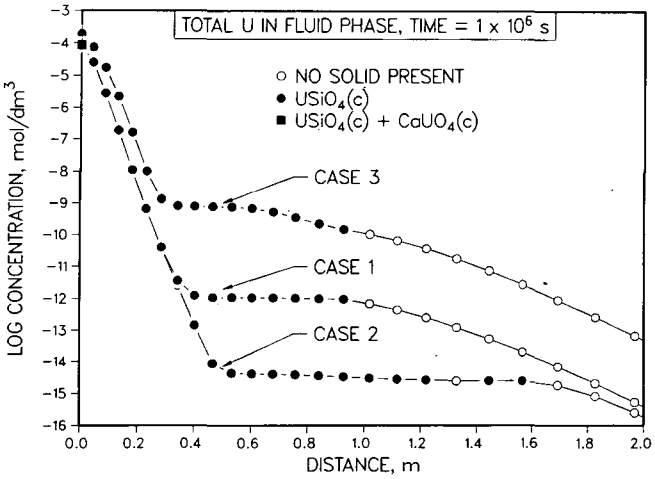

Figure 1. Total concentrations of uranium in fluid phases for Cases 1, 2, and 3 at time 1×10^6 s. Filled symbols denote presence of solid phases. [XBL 878-3729]

Case 3. In Case 1 UO_2^+ contributed negligibly, and the absence of this species from Cases 2 and 3 did not affect the computations. Similarly, the "new" species $UO_2(CO_3)_3^{5-}$ $U(CO_3)_5^{6-}$ contributed negligibly in Case 3. The major differences in the species' profiles occurred in the region of low Eh and are attributable to $U(OH)_4^0$ and $U(OH)_5^-$.

In summary, the results of the simulations indicated that "new" data (Case 3) for formation of $U(OH)_4^0$ predicted total migration of uranium significantly larger than that predicted by the older data. The difference between the data sets increased when $U(OH)_5^-$ was excluded from consideration (Case 2). These results indicate the need for a detailed, extensive review of thermodynamic data available for uranium solution species and solids with the aim of eliminating faulty data and producing a self-consistent data base for this important element. Such a review would lead also to the identification of new, critical experiments.

REFERENCES

Bruno, J., Ferri, D., Grenthe, I., and Salvatore, F., 1986a. Studies on metal carbonate equilibria. 13. On the solubility of uranium(IV) dioxide, $UO_2(s)$. Acta Chem. Scand., v. A40, p. 428–434.

Bruno, J., Grenthe, I., and Lagerman, B., 1986b. Redox processes and $UO_2(s)$ solubility: The determination of the UO_2^{2+}/U^{4+} redox potential at 25°C in $HClO_4$ media of different strength. *In* L.O. Werme (ed.), Scientific Basis for Nuclear Waste Management IX. Materials Research Society Symposia Proceedings (Vol. 50). Materials Research Society, Pittsburgh, Pennsylvania, p. 299–308.

Carnahan, C.L., 1987a. Simulation of chemically reactive solute transport under conditions of changing temperature. *In* C.F. Tsang (ed.), Coupled Processes Associated with Nuclear Waste Repositories. Academic Press, Orlando, Florida, p. 249–257.

Carnahan, C.L., 1987b. Simulation of uranium transport with variable temperature and oxidation potential: The computer program THCC. *In* J.K. Bates and W.B. Seefeldt (eds.), Scientific Basis for Nuclear Waste Management X, Materials Research Society Symposia Proceedings (Vol. 84). Materials Research Society, Pittsburgh, Pennsylvania, p. 713–721.

Choppin, G.R., 1983. Solution chemistry of the actinides. Radiochim. Acta, v. 32, p. 43–53.

Ciavatta, L., Ferri, D., Grenthe, I., Salvatore, F., and Spahiu, K., 1983. Studies on metal carbonate equilibria. 4. Reduction of the tris(carbonato)-dioxouranate(VI) ion, $UO_2(CO_3)_3^{4-}$, in hydrogen carbonate solutions. Inorg. Chem., v. 22, p. 2088–2092.

Ferri, D., Grenthe, I., and Salvatore, F., 1983. Studies on metal carbonate equilibria. 7. Reduction of the (carbonato)dioxouranate(VI) ion, $UO_3(CO_3)_3^{4-}$, in carbonate solutions. Inorg. Chem., v. 22, p. 3162–3165.

Langmuir, D., 1978. Uranium solution-mineral equilibria at low temperatures with applications to sedimentary ore deposits. Geochim. Cosmochim. Acta, v. 42, p. 547–569.

Maya, L., 1982. Hydrolysis and carbonate complexation of dioxouranium(VI) in the neutral-pH range at 25°C. Inorg. Chem., v. 21, p. 2895–2898.

Phillips, S.L., Phillips, C.A., and Skeen, J., 1985. Hydrolysis, formation and ionization constants at 25°C, and at high temperature-high ionic strength. Lawrence Berkeley Laboratory Report, LBL-14996.

Ryan, J.L., and Rai, D., 1983. The solubility of uranium(IV) hydrous oxide in sodium hydroxide solutions under reducing conditions. Polyhedron, v. 2, p. 947–952.

Schweingruber, M., Löslichkeits- und Speziationsberechnungen für U, Pu, Np und Th in natürlichen Grundwässern. Theorie, thermodynamische Dateien und erste Anwendungen. Technischer Bericht 81-13, NAGRA, Baden, Switzerland.

Wikberg, P., 1986. The assessment of reducing conditions at depth in granitic rock. *In* L. O. Werme (ed.), Scientific Basis for Nuclear Waste Management IX. Materials Research Society Symposia Proceedings (Vol. 50). Materials Research Society, Pittsburgh, Pennsylvania, p. 137–144.

Waste Dissolution with Diffusion, Advection, and Chemical Reaction

P.L. Chambré, C.H. Kang, W.W.-L. Lee, and T.H. Pigford

The prediction of dissolution rates is the starting point of safety assessments for nuclear waste disposal. The steady-state rate of dissolution is a function of the waste solid geometry, solid-liquid reaction rate, exterior flow field surrounding the waste-solid diffusion coefficient in the groundwater, and solubility of the dissolved constituent. Numerous leaching experiments have been conducted under laboratory conditions such that the chemical reaction rate is the rate-controlling mechanism. In previous analyses (Chambré et al., 1982; Pigford et al., 1983a; and Zavoshy et al., 1985) we have shown that diffusive-advective mass transfer in rock or other porous media surrounding the waste solid is expected to control the dissolution rate of low-solubility species in waste-solid sizes expected in a repository with low water flow. Hughes et al. (1983) have suggested qualitatively various flow regimes that could control mass loss rate in a repository, and they point out that at sufficiently high flow rates exterior-field mass transfer may no longer be the controlling mechanism. Here we introduce a new analytic theory that allows quantitative prediction of waste dissolution rates over a wide range of groundwater flow rates.

Our earlier analytic equations (Chambré et al., 1982, 1985) predict the rate at which low-solubility species in a waste solid dissolves in groundwater, under the conservative assumption that each dissolved species is at its saturation concentration in the liquid at the surface of the waste solid. We then considered the effect of a chemical-reaction-rate boundary condition (Zavoshy et al., 1985), using empirical rate data determined from laboratory glass leach tests, and provided a means of calculating the time-dependent concentration of dissolved species near the waste surface and the time-dependent diffusive mass transfer into the surrounding rock. Surface-liquid concentrations of low-solubility species from borosilicate glass waste and spent fuel are predicted to soon reach values close to saturation. The work summarized here extends the mass-transfer analysis to include the effect of advective transport in predicting the steady-state dissolution rate, with a chemical-reaction-rate boundary condition at the surface of a waste form of arbitrary shape. The solution has been obtained by three different approaches: an integral method, asymptotic expressions, and an interpolation formula (Chambré et al., 1987).

THEORETICAL RESULTS

In this article we consider as an example of the theory a spherical waste solid surrounded by water-saturated porous rock with a steady-state potential flow of groundwater. A chemical-reaction-rate boundary condition representing zero-order forward reaction of waste solid with water and a first-order backward reaction is assumed at the sphere surface:

$$-\epsilon D \frac{\partial C(r_0,t)}{\partial r} = j_0 \left[1 - \frac{C(r_0,t)}{C_s} \right], \quad t > 0 \quad (1)$$

where C is the concentration of the dissolved species in groundwater, r_0 is the radius of the waste sphere, ϵ is the porosity of the rock, D is the species diffusion coefficient in the liquid, j_0 is the reaction rate per unit area of waste solid at vanishing $C(r_0,t)$, and C_s is the saturation concentration of dissolving species.

The results relate the modified Sherwood number, Sh, and the Peclet number, Pe, with the square of the modified Thiele modulus, α, which is defined as the ratio of the reaction rate per unit area at r_0: to the steady-state diffusive mass-transfer rate per unit area at r_0:

$$Sh = \frac{kr_0}{\epsilon D}, \tag{2}$$

$$Pe = \frac{Ur_0}{D}, \tag{3}$$

$$\alpha = \frac{j_0 r_0}{\epsilon D C_s}. \tag{4}$$

Here U is the upstream pore velocity of groundwater, and k is the average mass-transfer coefficient for the spherical waste surface, such that the product kC_s gives the steady-state mass-transfer rate per unit area of sphere surface.

NUMERICAL ILLUSTRATIONS

Figure 1 shows the relative effects of Peclet numbers and α on concentration boundary layers of any solubility-limited constituent that obeys Eq. (1). The concentration boundary layers shown in Fig. 1 are isopleths estimated by the integral-method approximations for concentrations approaching zero. Material that is dissolving from the waste sphere at vanishing groundwater flow rate will form a spherical concentration boundary layer around the waste solid. As the groundwater flow increases, increasing the Peclet number, the flow sweeps past the waste solid, compressing the concentration boundary layer and forming it into a paraboloid-shaped wake. The concentration boundary layers shown in Fig. 1 are actually the edges of detectable concentration.

For a small Peclet number, e.g., $Pe = 0.1$, the boundary layers for $\alpha = 10$ and $\alpha = 1000$ are almost identical, because at low flow velocities molecular diffusion is more important than advection in species transport. At higher Peclet numbers, the downstream boundary layers differ somewhat for $\alpha = 10$ and $\alpha = 1000$, but the upstream boundary layer thickness remains almost the same.

Figure 2 shows the modified Sherwood number as a function of the Peclet number for various values of the square of the modified Thiele modulus α, obtained by the integral method and verified by the asymptotic expressions in the large Pe and small Pe ranges. In the range of $0.01 \leqslant Pe \leqslant 1$ it can be seen that the modified Sherwood number is almost constant for fixed values of α. In this same range of Peclet number a hundredfold increase in α, say from 10 to 1000, results in only a 10% increase in modified Sherwood number. At $Pe = 100$, increasing α from 10 to 1000 almost doubles the mass transfer rate. For $40 < Pe < 10^8$, well outside the range of Peclet numbers and flow speeds anticipated in geologic repositories, and for values of α of about 100 and greater, the modified Sherwood number is approximately proportional to the square root of the Peclet

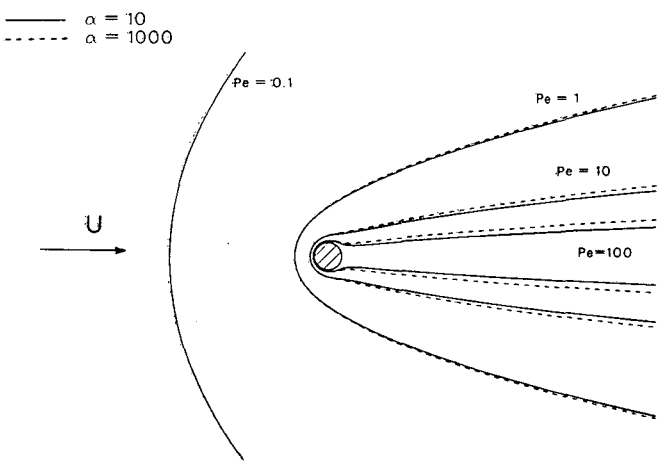

Figure 1. The concentration boundary layer about a sphere for various values of the Peclet number and the square of the modified Thiele modulus. [XBL 886-2148]

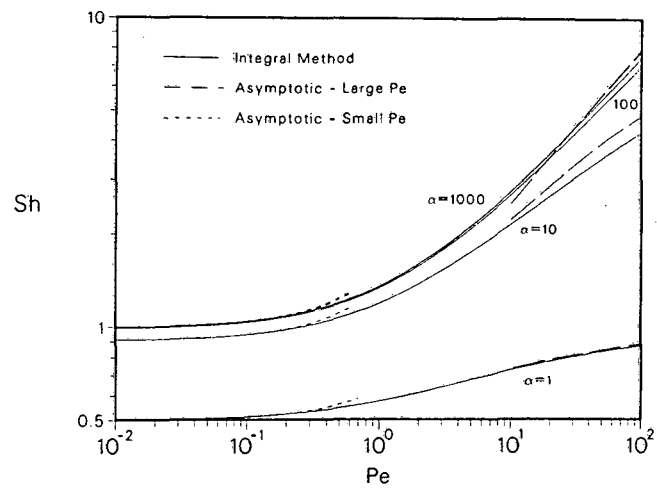

Figure 2. The Sherwood number as a function of the Peclet number, with the square of the modified Thiele modulus as a parameter. [XBL 886-2149]

number, showing that diffusive-advective mass transfer controls. At even larger Pe, well beyond the range of this figure, the curves level out when the exterior-field mass transfer is so intense that chemical reaction rate controls the dissolution rate. For $\alpha = 1$, which can obtain for small separated grains of a dissolving solid or for dissolution at very low temperature, chemical reaction rate reduces the influence on the modified Sherwood number over the entire range of Pe and causes the dissolution rate to be less affected by advective transport.

APPLICATION TO BOROSILICATE GLASS WASTE

To apply this theory to the simulation of repository conditions, we made calculations for a potential repository in basalt. Calculated temperatures at the emplacement hole wall (Pigford et al., 1983b) are listed in Table 1. For illustration we assume that at each instant the waste and rock are all at the listed temperature and that the steady-state mass-transfer theory applies. We assume a glass waste form with an equivalent spherical radius of 0.44 m. From the laboratory data for PNL 76-68 borosilicate glass (Pederson et al., 1983 and Westsik et al., 1983), we derive the temperature-dependent reaction rate values j_0, which are also listed in Table 1. Adopting earlier estimates of the effects of temperature on silica solubility and on the diffusion coefficient, we calculate the values of the square of the modified Thiele modulus shown in Table 1. Observe that α does not always increase as temperature increases, because it is also a function of other parameters such as C_s, D, and j_0, as shown in Eq. (4).

Figure 3 shows the steady-state mass-transfer rate from the surface of a glass waste in a basalt repository as a function of groundwater pore velocity with temperature as a parameter. The reaction rate j_0 at 250°C is about 260 times greater than that at the pre-emplacement repository temperature of 57°C, as shown in Table 1. However, Fig. 3 shows that the silica mass-transfer rate at $U = 0.01$ m/y at the maximum temperature is only about 40 times greater than it is at the pre-emplacement repository temperature. For $U = 100$ m/y at the maximum temperature, the mass-transfer rate is only 17 times greater than it is at the pre-emplacement temperature.

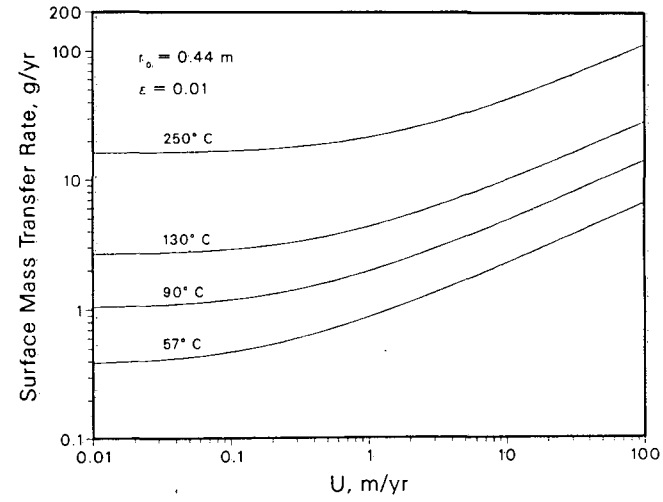

Figure 3. Surface mass transfer rate of a spherical borosilicate glass waste form. [XBL 886-2150]

CONCLUSIONS

This analysis provides a means for predicting steady-state dissolution as affected by chemical reaction rate, diffusion, and advection. For the groundwater velocities, waste dimensions, and temperatures expected in geologic repositories, the dissolution of borosilicate glass is predicted to be controlled by the mutual interplay of these three mechanisms. The groundwater velocities required for the chemical-reaction rate of borosilicate glass to control dissolution rate are far beyond those that can reasonably be expected in a repository. Chemical reaction rate and rate of diffusion from a borosilicate glass waste form can control the dissolution rate at temperatures much lower than are expected in a nuclear waste repository, i.e. when $\alpha \leq 1$.

Table 1. Calculated square of the modified Thiele modulus for a basalt repository.

Temperature (°C)	Time after emplacement (a)	C_s (g/cm^3)	D (cm^2/s)	j_0 (g/cm^2-s)	α
250	5	5.8×10^{-4}	1.6×10^{-4}	7.9×10^{-8}	3.7×10^{3}
130	100	2.3×10^{-4}	6.5×10^{-5}	1.5×10^{-8}	4.4×10^{3}
90	500	1.5×10^{-4}	3.9×10^{-5}	3.4×10^{-9}	2.5×10^{3}
57	> 5000	9.8×10^{-5}	2.2×10^{-5}	3.0×10^{-10}	6.0×10^{2}

REFERENCES

Chambré P.L., Pigford, T.H., Sato, Y., Fujita, A., Lung, H., Zavoshy, S.J., and Kobayashi, R., 1982. Analytical performance models. Lawrence Berkeley Laboratory Report LBL-14842.

Chambré P.L., Ahn, J., Kajiwara, L.S., Kim, C.L., Kimura, H., Lung, H., Williams, W.J., and Zavoshy, S.J., 1985. Mass transfer and transport in a geologic environment. Lawrence Berkeley Laboratory Report LBL-19430.

Chambré P.L., Kang, C.H., Lee, W.W.-L., and Pigford, T.H., 1987. The role of chemical reaction in waste-form performance. *In* M.J. Apted and R.E. Westerman (eds.), Scientific Basis for Nuclear Waste Management XI. Materials Research Society Symposia Proceedings (Vol. 84), p. 285–291.

Hughes, A.E., Marples, J.A.C., and Stoneham, A.M., 1983. The significance of leach rates in determining the release of radioactivity from vitrified nuclear waste. Nucl. Technol., v. 61, p. 496.

Pederson, L.R., Buckwalter, C.Q., and McVay, G.L., 1983. The effect of surface area to solution volume on waste glass leaching. Nucl. Technol., v. 62, p. 151.

Pigford, T.H., Blomeke, J.O., Brekke, T.L., Cowan, G.A., Falconer, W.E., Grant, N.J., Johnson, J.R., Matusek, J.M., Parizek, R.R., Pigford, R.L., and White, D.E., 1983a. A Study of the Isolation System for Geologic Disposal of Radioactive Wastes. National Academy Press, Washington.

Pigford, T.H., Chambré, P.L., and Zavoshy, S.J., 1983b. Effect of repository heating on dissolution of glass waste. Trans. Am. Nucl. Soc., v. 44 p. 115.

Westsik, J.H., Jr., Harvey, C.O., and Kuhn, W.L., 1983. High-temperature leaching of actinide-bearing, simulated high-level waste glass. Pacific Northwest Laboratory Report PNL-3172.

Zavoshy, S.J., Chambré, P.L., and Pigford, T.H., 1985. Mass transfer in a geologic environment. *In* C.M. Jantzen, J.A. Stone, and R.C. Ewing (eds.), Scientific Basis for Nuclear Waste Management VIII. Materials Research Society Symposia Proceedings (Vol. 44). Materials Research Society, Pittsburgh, Pennsylvania, p. 311–322.

Numerical Simulation of the Alteration of Sodium Bentonite by Diffusion of Ionic Groundwater Components

J.S. Jacobsen and C.L. Carnahan

Because of its ability to retard the movement of radionuclides, sodium bentonite is being considered as a packing and backfilling material in a number of nuclear waste isolation programs. Few studies, however, have considered how the chemical properties of the bentonite backfill will vary with distance from the canister and change in time as groundwater constituents diffuse through the bentonite. Of particular importance is the conversion of sodium bentonite to calcium bentonite by ion exchange, which will in turn affect the migration of cationic radionuclides, such as Cs^+ and Sr^{2+}, leaking from a waste canister. To address these questions, we have modified an existing transport code to include ion exchange and aqueous complexation reactions. The code is thus able to simulate the diffusion of major ionic groundwater components through bentonite and reactions between the bentonite and groundwater. Numerical simulations have been made to investigate the conversion of sodium bentonite to calcium bentonite for a reference groundwater characteristic of deep granitic formations.

DESCRIPTION OF TIP COMPUTER PROGRAM

The transport code that we have modified is based on the theory of the thermodynamics of irreversible processes (Carnahan, 1984) and is unique in its coupling of the velocity field with changes in fluid composition. The TIP code is able to simulate heat and mass transport under conditions of changing temperature, pressure, and composition. Previous versions of the code were used to study thermodynamically coupled processes in the near-field region of a nuclear waste repository (Carnahan, 1984;

Jacobsen and Carnahan, 1986, 1987). The current version of the program allows for more than one solute and calculates temperature and pressure as well as solute concentrations. In addition, aqueous complexation and ion-exchange reactions have been incorporated on the assumption of local chemical equilibrium. In the simulations summarized here, constant temperature and pressure distributions were assumed, and as a result thermodynamically coupled processes have been ignored, though the code still retains the flexibility described above.

The chemical reactions added were incorporated in such a way as to not increase the number of unknown variables. The reason for taking this approach is to reduce the size of the linear system associated with the n-dimensional Newton's method, which is used to advance the solution in time. Reducing the linear system that must be solved decreases the amount of computer memory and computation time used at each iterative step. The only disadvantage of this scheme is that the form of the Jacobian elements (required by the n-dimensional Newton's method) becomes more complicated. The tradeoff is well worth it, however. A timing analysis of the TIP code has shown that between 30 and 50% of the computation time is spent solving the linear systems resulting from the n-dimensional Newton's method.

INPUT DATA

Most of the input data for the simulations was taken or derived from a report by Wanner (1986). Wanner used data from experiments in which samples of sodium bentonite were allowed to interact with synthetic groundwater. Using these data, he calculated ion-exchange constants for Na^+, K^+, Mg^{2+}, and Ca^{2+}. In his calculations, Wanner assumed that the activity coefficient of a sorbed component is unity and thus that its activity is equal to its concentration. In the TIP program, the solid-phase activity of a species is approximated by its mole fraction. In addition, Wanner used a value of 0.2 as the B coefficient in the Davies equation; a value of 0.3 has been used in TIP (Stumm and Morgan, 1970). The results of recalculating the ion-exchange constants from the data that Wanner used and accounting for the adjustments noted above are given in Table 1, where the ion-exchange reactions have been written in terms of ion exchange with sorbed sodium.

Formation of the following aqueous complexes was considered: NaOH, KOH, $CaOH^+$, $MgOH^+$, $NaCO_3^-$, $CaCO_3$, $MgCO_3$, HCO_3^-, $NaHCO_3$, $CaHCO_3^+$, $MgHCO_3^+$, and H_2CO_3. The formation constants for these complexes were taken from a data base compiled by Benson and Teague (1980). All of the complexes listed above were considered in preliminary equilibrium calculations, but complexes with concentrations more than four orders of magnitude smaller than the concentrations of the bare ions forming them were not included in the simulations. The only complexes excluded from the simulations were NaOH, KOH, and $CaOH^+$.

Table 1. Ion-exchange coefficients.

Ion-exchange reaction	log K
$\overline{Na} + K^+ = \overline{K} + Na^+$	0.39
$2\overline{Na} + Mg^{2+} = \overline{Mg} + 2Na^+$	−0.20
$2\overline{Na} + Ca^{2+} = \overline{Ca} + 2Na^+$	0.54

The initial and boundary conditions for the system were taken from Wanner's report as well. The initial concentrations listed in Table 2 describe the speciation of pore water in equilibrium with a compacted sodium bentonite. Wanner calculated the values in column 1 using the MINEQL/EIR speciation code (Schweingruber, 1984) but did not consider sorption of Sr^{2+}. Column 2 gives the concentrations of the groundwater constituents diffusing into the bentonite.

Wanner's report also provides values of porosity (ϵ), bulk density (ρ_s), and cation-exchange capacity (CEC) for sodium bentonite MX-80, the same material used in the experiments to determine the ion-exchange coefficients. The values used in the simulations are $\epsilon = 0.38$; $\rho_s = 1.7 \times 10^3$ kg/m^3; CEC = 76.4 mequiv/100 g. The CEC is converted to

Table 2. Composition of equilibrated pore water and incoming groundwater (concentrations in moles/dm^3).

Ion	Pore water	Incoming GW
Na^+	2.33×10^{-1}	1.76×10^{-1}
K^+	3.63×10^{-4}	1.15×10^{-3}
Ca^{2+}	1.32×10^{-5}	2.16×10^{-2}
Mg^{2+}	2.03×10^{-5}	1.07×10^{-4}
Sr^{2+}	—	2.40×10^{-4}
CO_3^{2-}	2.64×10^{-3}	9.72×10^{-7}
pH	9.67	6.78

N_s, the concentration of exchangeable sites, by using $N_s = \rho_s$ (CEC) $\times 10^{-3}/\epsilon$. A value of 5×10^{-10} m^2/s was used for the diffusion coefficient (Hadermann, personal communication 1987).

NUMERICAL SIMULATIONS

The TIP code was used to simulate the radial diffusion of groundwater constituents into a compacted, saturated annulus of sodium bentonite. The inner radius of the bentonite packing is 0.315 m; the outer radius is 1.85 m. These values were chosen so that the geometry used in the simulations would approximate a series of nuclear waste canisters, 2 m in length, 1 m in diameter, separated, in the longitudinal direction, by a distance of 3 m and surrounded by a packing of bentonite. The bentonite is assumed to have been equilibrated with a groundwater characteristic of deep granitic formations. The chemical species included in the simulation were discussed in the previous section, and the initial concentrations and the composition of the incoming groundwater are given in Table 2. One shortcoming of the current version of TIP is that the concentrations of all species were held equal to their initial values at the inner boundary throughout the simulation. In future calculations this constant-concentration boundary condition will be replaced by a zero-flux boundary condition.

A constant temperature of 55°C was used. The log K values that Wanner calculated, and from which the log K values in Table 1 were determined, are based on experiments performed at 25°C. A lack of data (Wanner, 1986) made it impossible to correct the log K values in Table 1 for temperature.

Calculations of the changes in the fluid-phase and sorbed-phase concentrations were made for simulated times up to 1000 years. The results at a simulation time of 1000 years are shown in Fig. 1. The concentrations of both the bare ions (Fig. 1a) and the sorbed ions (Fig. 1b) have been plotted. With the exception of Na^+, the concentrations of the exchanging ions in the incoming groundwater are larger than their concentrations in the initial pore water. Therefore, the fluid-phase concentrations of all ions except Na^+ increase with time at the outer boundary.

In contrast, the solid-phase concentrations of K^+ and Mg^{2+} initially increase (not shown) and thereafter decrease (Figs. 1b). The solid-phase concentration of Na^+ monotonically decreases with time. The decrease in the sorbed-phase concentrations of ions other than Ca^{2+} is a result of competition with Ca^{2+}. The concentration of Ca^{2+} in the incoming groundwater is two orders of magnitude

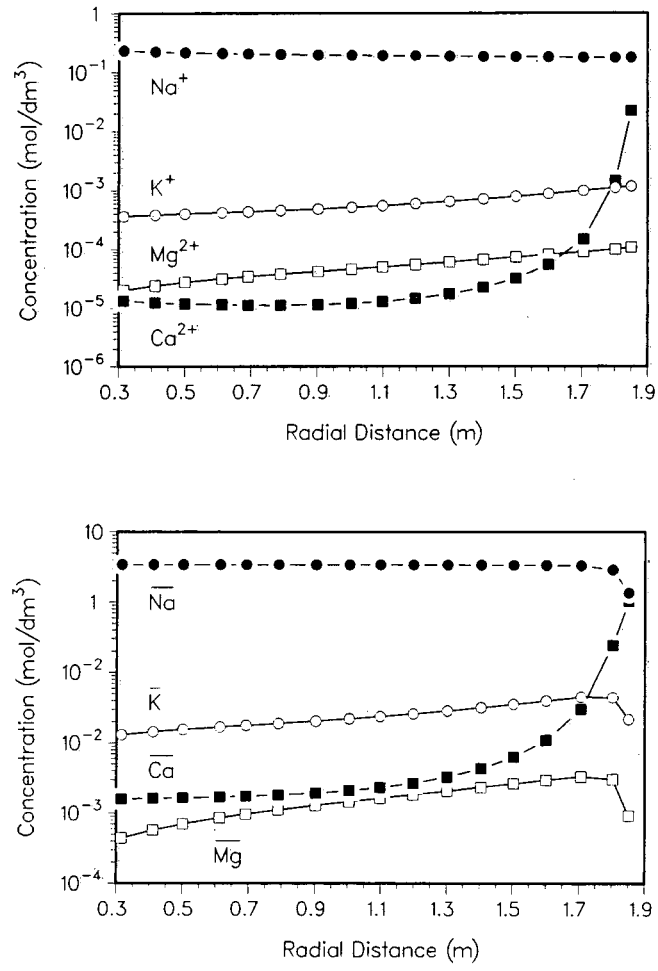

Figure 1. Concentrations of bare ions (**top**) and sorbed ions (**bottom**) at a simulation time of 1000 years. [Top, XBL 8711-4702; bottom, XBL 8711-4701]

larger than its concentration in the initial pore water. As the concentration of Ca^{2+} in the pore water near the outer boundary increases due to the inward diffusion of calcium, so does the competition for ion-exchange sites between Ca^{2+} and the other exchanging ions.

Table 2 shows that the concentration of Sr^{2+} in the incoming groundwater is greater than that of Mg^{2+}. Simulations were made in which Sr^{2+} was included in both the initial pore water and incoming groundwater. Including Sr^{2+} had a greater effect on Mg^{2+} than on any other ion, but at early times the sorption of all ions was affected. At a simulation time of 1000 years, the differences between the simulations with and without Sr^{2+} are much less evident: only the concentration of sorbed Mg^{2+} differs noticeably.

SUMMARY AND CONCLUSIONS

Chemical reactions of aqueous complexation and ion exchange have been incorporated into an existing transport code, unique in its coupling of fluid flow and changes in chemical composition. The new version of the program preserves the capability of the previous version for simulating the effects of thermodynamically coupled processes on heat and mass transport, though these effects were not included in the current simulations. The chemical reactions were included in such a way as to not increase the number of unknowns.

The code was used to simulate the effect of inwardly diffusing groundwater on the chemical properties of saturated sodium bentonite. Our results show that changes in the bentonite occur quite slowly. At a simulation time of 1000 years, the concentration of sorbed sodium has decreased by a factor of 2, but only in an annulus 0.5 m thick. The decrease of sorbed sodium is due to an increase of calcium in the pore water caused by the high concentration of calcium in the incoming groundwater. Though 1000 years was our longest simulation time, it is clear how the chemical properties of bentonite change for the chemical system considered. Including Sr^{2+} in the initial pore water and incoming groundwater did affect the sorption of the other ions considered. The sorbed concentrations of Mg^{2+} and Ca^{2+} are somewhat smaller than in the simulations in which Sr^{2+} was omitted, but at long simulation times the differences are quite small.

One important reaction not yet included in the TIP code is that of dissolution of calcite, which may significantly affect the concentration of Ca^{2+} in the pore water. The next version of TIP will, therefore, include precipitation/dissolution reactions. Once this modification has been completed, we will be able to investigate how the migration of cationic radionuclides, specifically Cs^{+} and Sr^{2+}, through bentonite will be affected by changes in the ion-exchange properties of bentonite.

REFERENCES

Benson, L.V., and Teague, L.S. 1980. A tabulation of thermodynamic data for reactions involving 58 elements common to radioactive waste package systems. Lawrence Berkeley Laboratory Report LBL-11448.

Carnahan, C.L., 1984. *In* G.L. McVay (ed.), Scientific Basis for Nuclear Waste Management VII. Materials Research Society Symposia Proceedings (Vol. 26). Elsevier, New York, p. 1023–1030.

Jacobsen, J.S., and Carnahan, C. L., 1986. Chemical osmosis and thermal osmosis near a heat source buried in a saturated, semi-permeable medium. Trans. Am. Geophys. Union, v. 67, p. 965.

Jacobsen, J.S., and Carnahan, C.L., 1987. Results from numerical simulations of thermodynamically coupled processes. *In* Earth Sciences Division Annual Report 1986. Lawrence Berkeley Laboratory Report LBL-22090, p. 143–146.

Schweingruber, M. 1984. User's guide for extended MINEQL (EIR version)—standard subroutine/data library package; EIR Internal Report TM-45-84-39, Würenlingen, Switzerland.

Stumm, W., and Morgan, J.J., 1970. Aquatic Chemistry (1st ed.). Wiley-Interscience, New York, p. 83.

Wanner, H., 1986. Modelling interaction of deep groundwaters with bentonite and radionuclide speciation. NAGRA Technical Report 86-21, Baden, Switzerland.

Mechanisms of Mobility Control with Foams

A.I. Jiménez, K.S. Udell, and C.J. Radke

Establishing mobility control is crucial in all enhanced oil-recovery schemes. A concerted effort is needed to find inexpensive, effective, and controllable mobility-control fluids. The objective of the work summarized here is to elucidate and quantify the microscopic mechanisms underlying foam flow in porous media for the purpose of establishing foam as a generic mobility-control fluid in all enhanced oil recovery.

One of the crucial issues is the stability of foam in porous media. Experimental studies of foam flow in two-dimensional water-wet porous media reveal the importance of the capillary pressure of the medium upon the existence of foam in a given

porous medium (Manlowe, 1988). Preformed foam injected into a dry medium simply cannot enter until the foam breaks and the released liquid is imbibed by the small pores. Only after a high enough liquid saturation is attained can foam flow into the porous medium. Additionally, studies of foam flow in partially liquid-saturated bead packs and sand packs reveal that breakage occurs if the gas superficial velocity is increased sufficiently (Khatib et al., 1986). For a porous medium with a given permeability and liquid saturation (and corresponding capillary pressure), there is a critical gas velocity above which lamellae rupture.

This article introduces a simple hydrodynamic theory that explains the foam-breakage phenomena described above by analyzing the stability of a single foam lamella flowing through a periodically constricted sinusoidal pore.

STABILITY OF A STATIC FOAM LAMELLA

To understand the effect of capillary pressure upon foam coalescence, consider a cylindrical foam lamella of thickness $2h_0$ (~1000 Å), and radius R (50–100 μm) subject to a capillary pressure, P_c, at the film meniscus or Plateau border. The liquid pressure at the film meniscus is $(P_g - P_c)$, where P_g is the gas pressure. The liquid pressure in the film is $(P_g - \Pi)$, where Π is the conjoining/disjoining pressure. For $P_c > \Pi$ the pressure difference, $P_c - \Pi$, drives liquid out of the lamella until a new state is reached. This new state, however, could be an equilibrium or an unstable state.

Figure 1 shows a typical conjoining/disjoining pressure curve in nondimensional form, $\hat{\Pi}(\hat{h})$, from the classical DLVO theory (Verwey and Overbeek, 1948). It is well known that the critical thickness limit for metastable films, $\hat{h}_{min}$, is given by the maximum of the $\hat{\Pi}$ curve, $\hat{\Pi}_{max}$, or equivalently when $\partial\hat{\Pi}/\partial\hat{h} = 0$ (Vrij, 1966). Unbounded films thinner than $\hat{h}_{min}$ are unstable to perturbations of long wavelength; films thicker than $\hat{h}_{min}$ are stable.

Consider now a relatively dry medium for which the corresponding capillary pressure in a dimensionless sense is greater than $\hat{\Pi}_{max}$, as shown in Fig. 1. Given sufficient time any foam lamella present in such a medium will thin down to a thickness less than $\hat{h}_{min}$ and rupture. On the other hand, for a relatively wet medium with $\hat{P}_c < \hat{\Pi}_{max}$ the lamella will thin or thicken, depending on its original thickness, to a new equilibrium stable state for which $\hat{\Pi} = \hat{P}_c$. This explains why foam cannot enter a completely dry porous medium. We expect that it is more difficult for a foam to exist in a low-permeability medium.

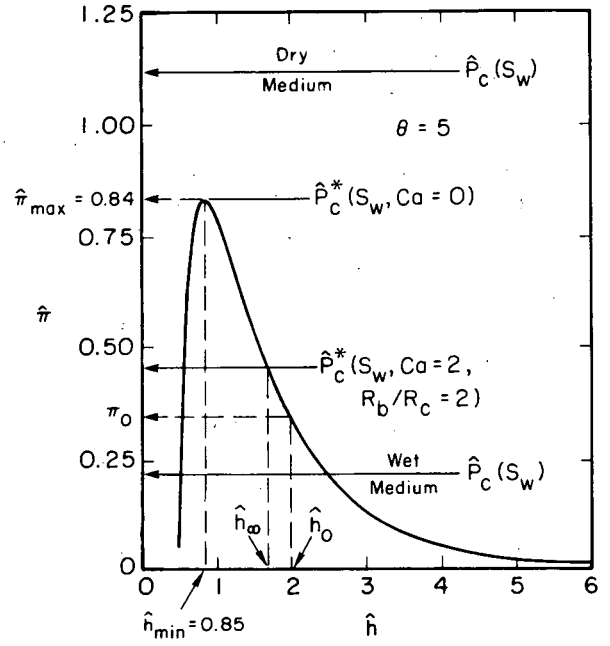

Figure 1. Dimensionless disjoining pressure isotherm for a constant surface potential. [XBL 886-2145]

STABILITY OF A MOVING LAMELLA

To explain dynamic foam coalescence in a porous medium, we consider a single lamella flowing through a periodically constricted sinusoidal pore, as shown in Fig. 2. The capillary pressure of the medium imposed on the lamella at the pore wall is assumed constant and is set by the local liquid saturation. Under an assumed constant volumetric flow, q, the lamella moves with interstitial velocity

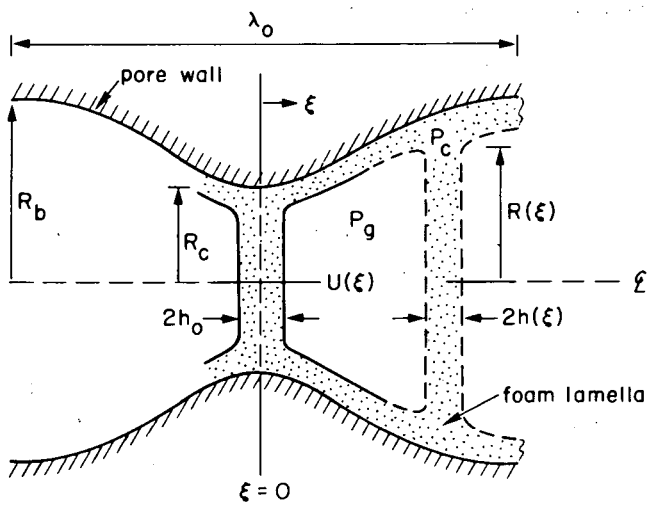

Figure 2. Lamella transport through a periodically constricted sinusoidal tube. [XBL 886-2146]

$U(\zeta)$, which varies according to the rate of change of the pore radius, given by the periodic function

$$R(\xi)/R_c = (1 + a) + a \cos[\pi(1 + 2\xi/\lambda_0)], \quad (1)$$

where ξ is the axial distance measured from the pore constriction; (1 + 2a) determines the ratio of pore body, R_b to pore constriction, R_c; and λ_0 is the wavelength of the periodic pore.

Upon moving from the pore constriction ($\xi = 0$) to the pore body ($\xi = \lambda_0/2$), the lamella is stretched as it is pulled by the wall. To achieve volume rearrangement a radial pressure differential is induced that thins the film but results in no net fluid efflux. The converse occurs when the film is squeezed upon moving from a pore body to a pore constriction.

In addition, as the lamella is thinned (thickened) by the stretching (squeezing) rate, the disjoining pressure changes accordingly, and, depending on the magnitude of the capillary pressure, there is a net flow of liquid out of or into the lamella. We adopt the simple Reynolds film model to describe this drainage (filling) flow (Ivanov and Dimitrov, 1974; Gumerman and Homsy, 1975).

The two phenomena of film-wall conformity and capillary-pressure-driven film flow can be combined linearly to yield an evolution equation that describes how the film thickness varies as the lamella percolates through the constricted pore (Jiménez, 1988).

For a finite nonzero velocity, as characterized by a dimensionless capillary number, Ca, both the stretching and the drainage rate play important roles. Thus, at a given capillary number there is a critical capillary pressure, $\hat{P}_c^*$, above which the local lamella thickness just thins to $\hat{h}_{\min}$ and breaks. For instance, in the case of a lamella of initial dimensionless thickness $\hat{h}_0 = 2.0$, $Ca = 2$, $a = 0.5$ (i.e., $R_b/R_c = 2.0$), and a disjoining pressure given by that in Fig. 1, $\hat{P}_c^*$ lies below $\hat{\Pi}_{\max}$ and above $\hat{\Pi}_0$. Under the influence of this particular critical capillary pressure, the film tends to drain to the thickness denoted by $\hat{h}_\infty$ in Fig. 1 but will vary in thickness from constriction to constriction with large enough amplitude as to become as thin as $\hat{h}_{\min}$ at the pore body. It is here that the film becomes unstable and ruptures.

Thus numerical solution of the evolution equation for various values of the parameters ($\hat{h}_0$, Ca, $\hat{P}_c$ and a) traces a locus of points corresponding to the critical capillary pressure of lamella stability versus the velocity of flow for a given initial foam texture and porous medium structure (Jiménez, 1988). Results are shown by the curve in Fig. 3. For a given value of Ca (i.e., a given superficial velocity) this curve provides the capillary pressure above

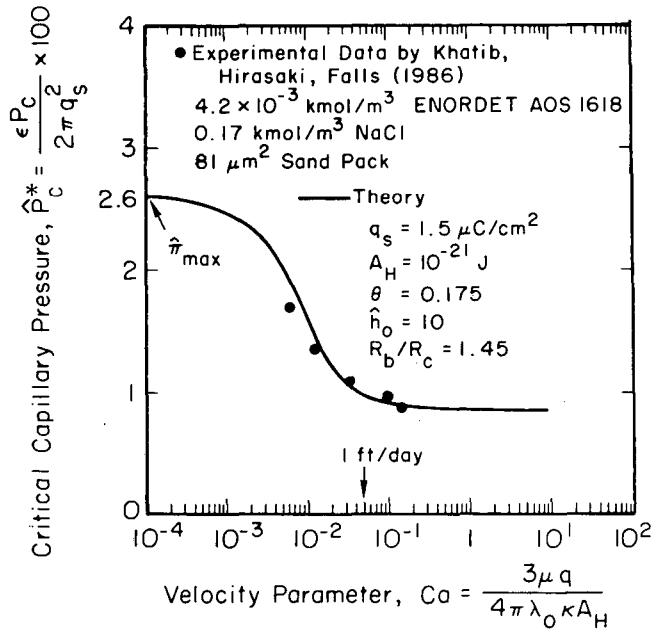

Figure 3. Comparison of theory with available experimental data. [XBL 886-2147]

which foam cannot exist. By choosing reasonable values for the surface charge density ($q_s = 1.5\ \mu C/cm^2$), the Hamaker constant ($A_H = 10^{-21}$ J), and setting $\hat{h}_0 = 10$ and $R_b/R_c = 2$, we achieve very good agreement with the experimental results of Khatib et al. (1986) for a solution of 4.2×10^{-3} kmole/m^3 ENORDET AOS 1618 surfactant and 0.17 kmole/m^3 NaCl in an 81 μm^2 sand pack.

CONCLUSIONS

The stability of foam lamellae has great significance in determining the fraction of gas present in the continuous phase as foam flows in porous media. By analyzing a single lamella as it percolates through a periodically constricted tube, we have developed a theory that explains the physical phenomena that govern foam coalescence in porous media. The conjoining/disjoining pressure curve proves to be the crucial physical property of the surfactant/water system. It determines the maximum capillary pressure that foam can sustain at rest in a porous medium. This critical capillary pressure can in turn be associated with a critical permeability or a critical liquid saturation for a given medium. For moving foam this critical capillary pressure is reduced as lamellae are thinned by the influence of both the capillary-pressure-driven flow and the wall-conforming flow. For a given gas superficial velocity foam cannot exist if the capillary pressure exceeds a critical value. The

theory introduced here proves to be in good agreement with available experimental data (Khatib et al., 1986).

REFERENCES

Gumerman, R.J., and Homsy, G.M., 1975. The stability of radially bounded thin films. Chem. Eng. Commun., v. 2, p. 27.

Ivanov, I.B., and Dimitrov, D.S., 1974. Hydrodynamics of thin liquid films. Colloid and Polymer Sci., v. 252, p. 982.

Jiménez, A.I., 1988. Stability of thin liquid films and its implications in foam flow in porous media (Ph.D. thesis). University of California, Berkeley, in progress.

Khatib, Z.I., Hirasaki, G.J., and Falls, A.H., 1986. Effects of capillary pressure on coalescence and phase mobilities in foams flowing through porous media. Paper SPE 15442 presented at the 1986 SPE Annual Technical Conference and Exhibition New Orleans, Louisiana, October 5–8, 1986.

Manlowe, D., 1988. Pore-level mechanisms of foam destabilization by oil in porous media (M.S. thesis). University of California, Berkeley.

Verwey, E.J.W. and Overbeek, J.T.G., 1948. The theory of stability of lyophobic colloids. Elsvier, Amsterdam, p. 106–133.

Vrij, A., 1966. Possible mechanism for the spontaneous rupture of thin free liquid films. Disc. Faraday Soc., v. 42, p. 23.

Time-Dependent Nuclide Transport through Backfill into a Fracture

C.H. Kang, P.L. Chambré, W.W.-L. Lee, and T.H. Pigford

Fractures (fissures) in the emplacement rock of a geologic repository for nuclear waste may intersect boreholes for waste packages and thus provide conductive pathways for hydrogeologic transport of radionuclides. Previous study (Neretnieks, 1986) of transport through backfill into a fissure considered only steady-state transport of a stable species. The U.S. regulatory framework (U.S. Environmental Protection Agency, 1985) for geologic disposal is for the first 10,000 years, perhaps before steady state is reached, thus requiring calculation of time-dependent radionuclide transport into fractures. We summarize here a transient analysis of radionuclide transport through backfill into a fissure.

As shown in Fig. 1, we consider a waste canister surrounded by backfill in a borehole intersected by a fracture in water-saturated rock. Radionuclides are released at a constant concentration C_s at the waste surface into the backfill. Groundwater flows in the fissure, but we assume no groundwater flow in the backfill, so that radionuclide transport through the backfill is controlled by molecular diffusion. The rock matrix is assumed to be completely impervious, so that mass transport in the rock takes place in only the fracture. The mass flux into the rock is given by the mass-transfer coefficient h times the average nuclide concentration $\overline{C}$ across the fissure mouth. For a small hole-to-canister radius ratio, cylindrical geometry can be simplified to planar geometry by unfolding the cylinder into a rectangular parallelepiped. This problem has been solved analytically, and we present a numerical illustration using planar geometry.

Figure 2 shows the dimensionless mass-transfer rate $M/2\pi r_2 bC_s h$ versus the Fourier modulus Dt/d^2, with the square of the modified Thiele modulus $\lambda d^2/D$ as a parameter. Here $D \equiv D_f/K$, where D_f is the species diffusion coefficient, K is the species retardation coefficient in backfill, λ is the decay constant, d is the backfill thickness, and t is time. The graph applies for an assumed value of the Sherwood number $(hd/\epsilon D_f)$ of unity, in which ϵ is the porosity, and represents a condition of mass-transfer-limited dissolution. At early time mass transfer into the backfill is large because of the steep concentration gradient near the waste surface. As time increases, nuclide concentration builds up in the backfill and the mass-transfer rate decreases and approaches steady state. Nuclide transfer into the fissure is zero at early times and increases as nuclides diffuse through the backfill until steady state is reached. For a stable nuclide ($\lambda d^2/D \equiv 0$) the mass-transfer rates into backfill and into the fissure become equal at steady state. For decaying radionuclides ($\lambda d^2/D \neq 0$) the general trend of mass transfer is the same as for a stable nuclide. Radioactive decay steepens concentration gradients near the waste surface and increases mass transfer into the

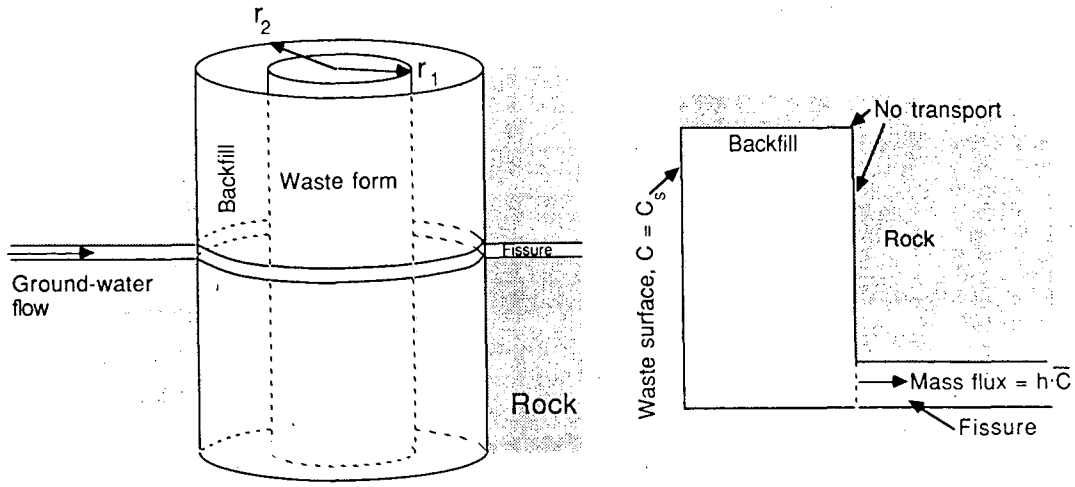

Figure 1. Waste package intersected by a fissure. [XBL 886-2143]

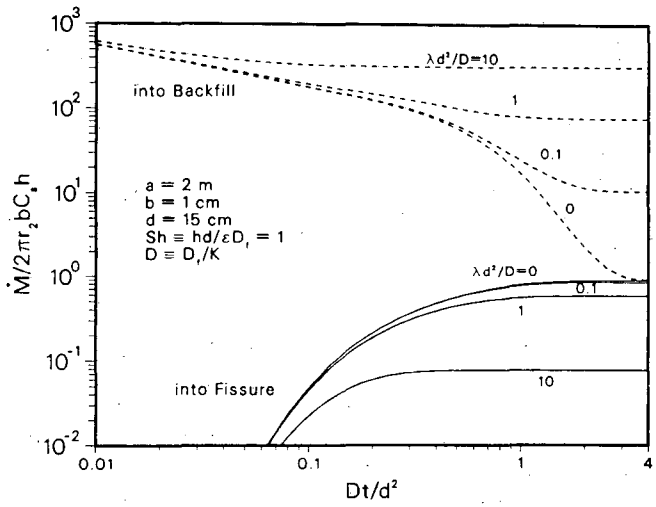

Figure 2. Mass-transfer rate into the backfill and into the fissure versus Fourier modulus with the modified Thiele modulus as a parameter. [XBL 886-2144]

backfill. The time to reach steady state is shorter for decaying radionuclides than for a stable nuclide.

This numerical illustration of a transient analysis of radionuclide transport through backfill into a fracture shows that time-dependent effects are significant. This contribution will aid the performance assessment of waste packages in nuclear waste repositories.

REFERENCES

Neretnieks, I., 1986. Stationary transport of dissolved species in the backfill surrounding a waste canister in fissured rock: Some simple analytical solutions. Nucl. Technol., v. 72, p. 194.

U.S. Environmental Protection Agency, 1985. Title 41, Code of Federal Regulations, Part 191.

Contaminant Transport from an Array of Sources

C.L. Kim, P.L. Chambré, W.W.-L. Lee, and T.H. Pigford

Nuclear waste in geologic repositories and hazardous materials in disposal sites will be emplaced in thousands of individual containers. In evaluating contaminant transport from such facilities, will it be necessary to consider each individual waste source? Here we compare the space-time-dependent concentration field predicted for an array of discrete sources with the concentration field predicted for an infinite-plane source. We develop solutions for an array source by superpositioning solutions for individual point sources.

ANALYTIC SOLUTIONS—SINGLE POINT SOURCES

For a single point source in an infinite porous medium, the dispersion of a contaminant is given by Eq. (1) (Box 1); X_1, X_2, X_3 are the Cartesian coordinates, c is the contaminant concentration, $\hat{D}_i$ is the dispersion coefficient in the ith direction, K is the retardation coefficient of the contaminant, and D_∞ is the unbounded space. Some solutions to this problem, without limit on the velocity field u_1, u_2, u_3, and for radioactive chains of arbitrary length, were obtained by Chambré et al. (1985).

The solution for a uniform flow along the X_1 axis with a pore velocity of u is given by Eq. (2) (Box 1); $\dot{M}(\tau)$ = contaminant input rate at time τ [M/T], D_i = normalized dispersion coefficient in the X_i direction, $D_i = \hat{D}_i/K$ [L^2/T], u = normalized groundwater pore velocity in the X_1 direction, $u = u_1/K$ [L/T], λ = decay constant [T^{-1}], ϵ = porosity, and $D = (D_1 D_2 D_3)^{1/3}$. The dispersion coefficients and the groundwater velocity have been normalized by dividing them by the retardation coefficient of the contaminant.

If the rate of contaminant input is temporally constant, the solution in (2) can be simplified by the substitution of a constant input rate $\dot{M}$ and integrated to give Eq. (3) (Box 1).

ANALYTIC SOLUTIONS—ARRAY SOURCES

For an array of $W \times Y \times Z$ point sources, the contaminant concentration field resulting from the array is given by Eq. (4) (Box 1); c^a = concentration from the array source. The location of the individual point sources in the array is given by

$$x_1^w = d_1\left(w - \frac{W+1}{2}\right), \quad w = 1,\ldots,W ,$$

$$x_2^y = d_2\left(y - \frac{Y+1}{2}\right), \quad y = 1,\ldots,Y ,$$

$$x_3^z = d_3\left(z - \frac{Z+1}{2}\right), \quad z = 1,\ldots,Z ,$$

where d_i are the separations or pitches along the ith coordinate.

NUMERICAL ILLUSTRATIONS

We present numerical illustrations from a 3×3 planar array of point sources, perpendicular to the flow of groundwater, as shown in Fig. 1.

In these calculations we make the following assumptions:

1. Each point source is of equal and time-invariant strength.
2. The center of the array is at the origin of the axes.
3. The constant source strength was derived from a separate model based on solubility-limited dissolution of the contaminant from the source. The details are given in Chambré et al. (1987).
4. Groundwater velocity is along X_1 only and is constant.
5. The dispersion coefficients are constant in space and time. This is not a requirement of the solutions. Actually, in the solutions as stated above, the dispersion coefficients can be functions of velocity but not of position.

The separations between sources have been chosen arbitrarily as d_2 = 3.7 m and d_3 = 36.7 m. The other parameter values used in the calculation are D_i = 50 m^2/y or 5 m^2/y, as stated, $\dot{M}$ = 0.48 g/y, K = 1, u = 1 m/y, λ = 0, and ϵ = 0.05.

Figure 2 shows a contaminant plume from the array source of Fig. 1 after *local steady state* has been reached. This is on the order of a thousand years after the start of contaminant dispersion. In this case the transverse dispersion coefficients are one-tenth the longitudinal dispersion coefficient. It can be seen that the plumes from all nine point sources have merged into an overall plume and that this plume has moved downstream.

The important question is when can simpler mathematical models of array sources give equally valid predictions? Figure 3 shows the comparison between two sets of predictions. The ordinate is the steady-state contaminant concentration along the X_1 axis predicted for the discrete array sources, normalized to the concentration predicted for an infinite-plane source of the same areal dissolution rate, and plotted as a function of a distance parameter $\theta = \sqrt{zD_{T/v}}$. When the ratio is unity the two models give identical predictions. For a value of the distance parameter of approximately 10 m, the ratio is above unity and the detailed array-source model should be used. Beyond this region the infinite-plane source model either gives identical predictions or overestimates conservatively. Where the concentration ratio becomes less than unity with increasing θ, the concentration field can be accurately predicted by replacing the discrete-source array by an equivalent finite-plane source.

We next compare the predictions of the detailed array-source model with those of a single point source at the origin. This single point source has the

Box 1. Equations

$$K\frac{\partial c}{\partial t} + u_1\frac{\partial c}{\partial X_1} + u_2\frac{\partial c}{\partial X_2} + u_3\frac{\partial c}{\partial X_3} = \frac{\partial}{\partial X_1}\hat{D}_1\left(\frac{\partial c}{\partial X_1}\right) + \frac{\partial}{\partial X_2}\hat{D}_2\left(\frac{\partial c}{\partial X_2}\right) + \frac{\partial}{\partial X_3}\hat{D}_3\left(\frac{\partial c}{\partial X_3}\right) - \lambda K c,$$

$$X_i \in D_\infty, \quad \mathrm{i} = 1,2,3, \qquad t > 0, \tag{1}$$

$$c(X_1, X_2, X_3, t) = \int_0^t \frac{\dot{M}(\tau)e^{-\lambda(t-\tau)}}{\epsilon K(4\pi D(t-\tau))^{3/2}} \exp\left\{\frac{-1}{4(t-\tau)}\left[\frac{x_1 - u(t-\tau)^2}{D_1} + \frac{x_2^2}{D_2} + \frac{x_3^2}{D_3}\right]\right\} d\tau \tag{2}$$

$$\begin{aligned} c(X_1, X_2, X_3, t) = {} & \frac{\dot{M}e^{x_1 u/2D_1}}{8\pi D^{3/2}[x_1^2/D_1 + x_2^2/D_2 + x_3^2/D_3]^{1/2}} \\ & \times \left[\exp - \sqrt{(x_1^2/D_1 + x_2^2/D_2 + x_3^2/D_3)\left(\lambda + \frac{u^2}{4D_1}\right)}\right. \\ & \times \left\{2 - \operatorname{erfc}\left(\sqrt{\left(\lambda + \frac{u^2}{4D_1}\right)t} - \sqrt{(x_1^2/D_1 + x_2^2/D_2 + x_3^2/D_3)\left(\frac{1}{4t}\right)}\right)\right\} \\ & + \exp\sqrt{(x_1^2/D_1 + x_2^2/D_2 + x_3^2/D_3)\left(\lambda + \frac{u^2}{4D_1}\right)} \\ & \left. \times \operatorname{erfc}\left(\sqrt{\left(\lambda + \frac{u^2}{4D_1}\right)t} + \sqrt{(x_1^2/D_1 + x_2^2/D_2 + x_3^2/D_3)\left(\frac{1}{4t}\right)}\right)\right] \end{aligned} \tag{3}$$

$$\begin{aligned} c^a(X_1, X_2, X_3, t) = {} & \frac{\dot{M}}{8\pi\epsilon K D^{3/2}} \sum_{w=1}^{W}\sum_{y=1}^{Y}\sum_{z=1}^{Z} \exp\{(x_1 - x_1^w)u/2D_1\}\left[\frac{(x_1 - x_1^w)^2}{D_1} + \frac{(x_2 - x_2^y)^2}{D_2} + \frac{(x_3 - x_3^z)^2}{D_3}\right]^{-1/2} \\ & \times \left[\exp - \sqrt{\left(\frac{(x_1 - x_1^w)^2}{D_1} + \frac{(x_2 - x_2^y)^2}{D_2} + \frac{(x_3 - x_3^z)^2}{D_3}\right)\left(\lambda + \frac{u^2}{4D_1}\right)}\right. \\ & \times \left\{2 - \operatorname{erfc}\left(\sqrt{\left(\lambda + \frac{u^2}{4D_1}\right)t} - \sqrt{\left(\frac{(x_1 - x_1^w)^2}{D_1} + \frac{(x_2 - x_2^y)^2}{D_2} + \frac{(x_3 - x_3^z)^2}{D_3}\right)\left(\frac{1}{4t}\right)}\right)\right\} \\ & + \exp\sqrt{\left(\frac{(x_1 - x_1^w)^2}{D_1} + \frac{(x_2 - x_2^y)^2}{D_2} + \frac{(x_3 - x_3^z)^2}{D_3}\right)\left(\lambda + \frac{u^2}{4D_1}\right)} \\ & \left. \times \operatorname{erfc}\left(\sqrt{\left(\lambda + \frac{u^2}{4D_1}\right)t} + \sqrt{\left(\frac{(x_1 - x_1^w)^2}{D_1} + \frac{(x_2 - x_2^y)^2}{D_2} + \frac{(x_3 - x_3^z)^2}{D_3}\right)\left(\frac{1}{4t}\right)}\right)\right] \end{aligned} \tag{4}$$

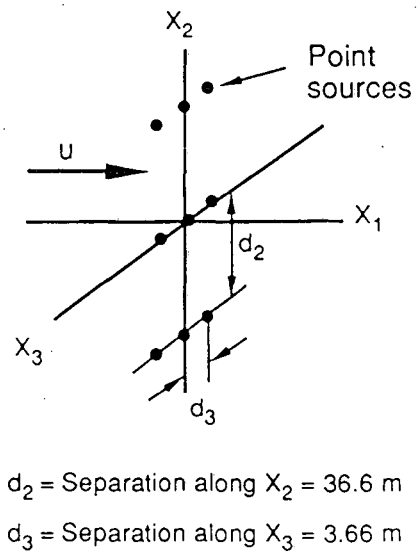

Figure 1. Array of point sources in porous media. [XBL 886-2287]

strength of all the point sources in the array combined. The results are shown in Fig. 4. Close to the center of the array plane and thus near the single equivalent point source, the strength of the single point source overwhelms the predictions for the array of sources. At a distance parameter of about 100 m and greater, transverse dispersion has reduced

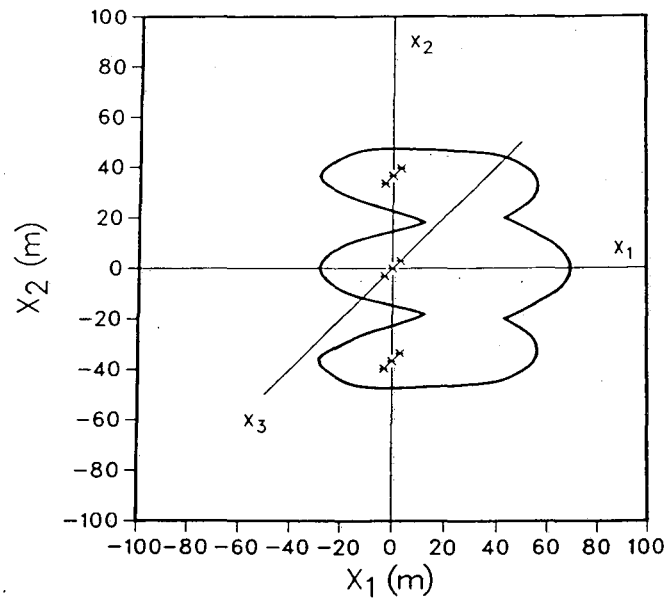

Figure 2. Isopleth of a contaminant at concentration 0.01 g/m^3 for local steady-state anisotropic dispersion for the 3 × 3 array of point sources (*) in Fig. 1. Source strength = 0.45 g/y; groundwater velocity = 1 m/y; no sorption; porosity = 0.05; longitudinal dispersion = 50 m^2/y; transverse dispersion = 5 m^2/y. [XBL 886-2288]

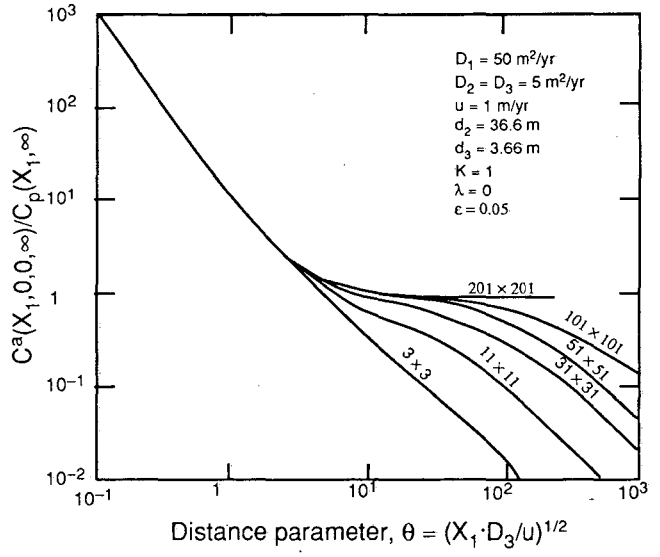

Figure 3. Comparison of concentration from array model with concentration from infinite-plane model (at steady state, along X_1 axis, anisotropic dispersion). [XBL 886-2289]

the prediction for the single equivalent point source to that for the array of sources. For the values of velocity and dispersion coefficients used, a distance parameter of 100 corresponds to a downstream distance of 10,000 m. Thus, for predicting contaminant concentrations at large distances, a single point source can replace the array of sources.

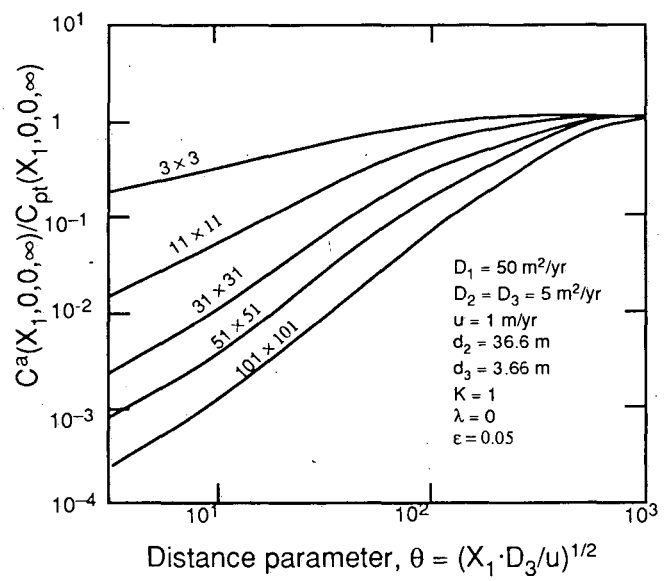

Figure 4. Comparison of concentration from array model with concentration from a single equivalent point source (at steady state, along X_1 axis). [XBL 886-2290]

CONCLUSION

Analytic solutions for contaminant dispersion in groundwater from an array of point sources in a porous medium are given and illustrated. The numerical illustrations indicate that for distances tens of meters downstream from the sources, simpler plane-source models might give equally satisfactory predictions.

REFERENCES

Chambré, P.L., Pigford, T.H., Lee, W.W.-L., Ahn, J., Kajiwara, S., Kim, C.L., Kimura, H., Lung, H., Williams, W.J., and Zavoshy, S.J., 1985. Mass transfer and transport in a geologic environment. Lawrence Berkeley Laboratory Report LBL-19430.

Chambré, P.L., Kim, C.L., Lee, W.W.-L., and Pigford, T.H., 1987. Anisotropic radionuclide dispersion from an array of point sources. In preparation.

Transmission Electron Microscope Studies on Aspects of Stress-Related Heterogeneous Dissolution

A. Meike

The effects of pressure and fluids on rocks are more extreme than the effects of either pressure or fluids alone. Combined effects are presently recognized phenomenologically and represent a group of undefined mechanisms. Premature rock failure that is observed to be associated with fluids is called stress corrosion cracking (SCC). Heterogeneous diffusive mass transfer that can be associated with a stress gradient is called "pressure solution." Our present inability to predict the response of rocks to the combined effects of fluids and stress concerns many areas that are critical to the safe disposal of radioactive waste, which include seismicity, fracture propagation, and intrafracture fluid flow.

Local deformation, caused by stress concentrations, is thought to be responsible for SCC and heterogeneous diffusive mass transfer. Stress concentrations occur at the tips of propagating fractures and, on a smaller scale, at grain contacts. However, investigations are usually not conducted on the appropriate scale to determine whether the deformation was elastic or permanent. The transmission electron microscope (TEM) can yield that information. TEM investigations of stress-related dissolution features in natural limestones (Meike, 1983; Meike and Wenk, 1988) and experiments on radially stressed single-crystal cylinders of calcite (Meike, 1984,1988b) have suggested that dislocations play a substantial role in the mechanism responsible for solution cleavage. To date, attempts to integrate permanent deformation into thermodynamic models of pressure solution (e.g., Wintsch and Dunning, 1985; Tada et al., 1987) have limited utility as predictive tools. Clearly, we need to clarify the mechanisms of "pressure solution" before theoretical models can be pursued. Unmeasured parameters, including dislocation-activation stresses (DAS), are necessary to describe and predict deformation mechanisms based on heterogeneous or discontinuous mechanisms, including stress-related heterogeneous dissolution.

DAS is specific to a mineral slip system. The closest approximation, critical resolved shear stress (CRSS), is usually measured by bulk methods. CRSS measurements are accurate enough to predict textures and other homogeneous deformation phenomena but are known to exceed the associated DAS. The three studies described below are steps toward the development of a predictive approach to stress-related dissolution. First, a natural case of stress-related dissolution, solution cleavage in cherts, was investigated. Second, two types of experiments were developed to measure DAS in minerals: dynamic in situ deformation of two mica minerals, muscovite and biotite (Meike, 1988), and more feasible but less direct measurements of dislocation density gradients in calcite.

A NATURAL CASE OF STRESS-RELATED DISSOLUTION IN DEFORMED CHERTS

The present transmission and high-resolution electron microscope investigation of a chert fold from the Marin headlands that contains solution-

cleavage seams was an extension of the previous limestone study, but not a repetition. This natural case of stress-related dissolution in a low-temperature SiO_2 system was intended as a companion study to the experimental investigation of radially stressed slotted cylinders of quartz (Apps, 1986). The diagenetic sequence of cherts offers the opportunity to examine the solution-cleavage mechanism from a different perspective. The potential of observing microstructures associated with heterogeneous diffusive mass transfer in a partially amorphous or microcrystalline material provided an opportunity to review the role of dislocations, which require crystalline material to exist. The purpose of this study was to identify the phases and their distribution with respect to the solution-cleavage surface and to characterize the grain boundaries.

Experimental Design

Thin sections were selected from areas and orientations that represent these fold features in three dimensions (Fig. 1). Copper grids were epoxied to key areas, excised from the rest of the thin section (Fig. 2), and ion milled to approximately 300 Å. Hand specimen, thin sections, and TEM foils have been mapped in detail, permitting identification of areas that represent the heterogeneous diffusive mass transfer process using high-voltage and high-resolution transmission electron microscopy.

Thicker parts of the specimen are visible at higher accelerating voltage. Transmission electron microscopy was conducted with a 1.5-MeV Kratos

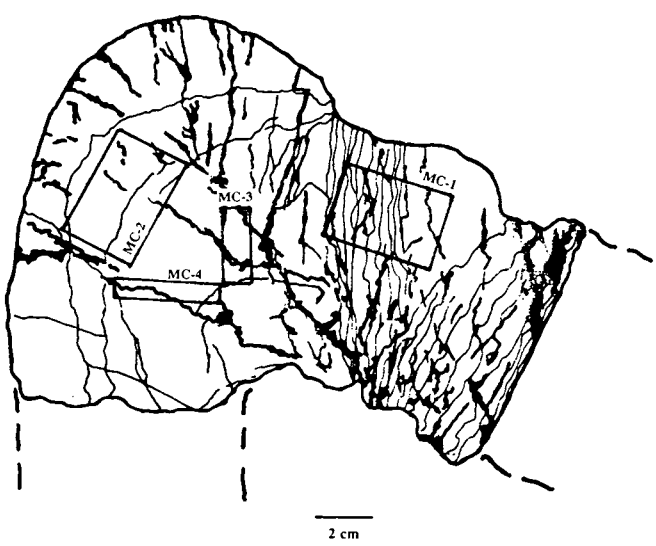

Figure 1. Diagram of the chert fold, showing the locations from which thin sections were selected. [XBL 881-187]

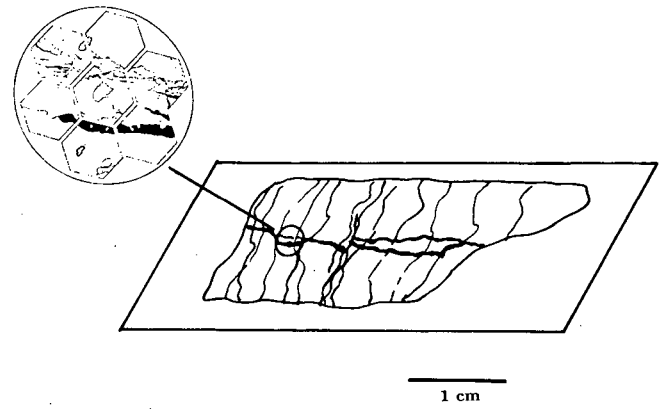

Figure 2. Diagram of a thin section and the TEM foil taken from it. The specimen is mapped at each step in order to retain contextual information from one scale to the next. [XBL 881-189]

high-voltage electron microscope (HVEM) at the National Center for Electron Microscopy (NCEM), Lawrence Berkeley Laboratory, which permitted greater flexibility in the choice of site and orientation in the specimen analyses. High-resolution and dark-field techniques were used extensively to determine the presence of second phases and perturbations of the crystal structures along grain boundaries.

High-resolution electron microscopy is not a substitute for standard electron microscopy. High-resolution lattice imaging involves the use of special procedures and often involves dedicated microscopes (in this case a 100-kV Siemens 102 high-resolution electron microscope (HREM) at the NCEM) that maximize resolution, at the expense of contrast (e.g., Gronsky, 1983). An analysis of grain boundaries is further complicated by the necessity of observing the lattices of more than one grain. Lattice images of crystals are obtained only at certain orientations. The lattices of more than one grain are observable only in a specimen orientation suitable to lattice images in all grains.

Results

The noncylindroidal fold collected from the Marin headlands exhibits soft-sediment deformation, bedding-parallel mineral segregation, two distinct phases of brittle fracture with secondary quartz filling, and cleavage perpendicular to bedding. The complexity of deformation survives to the submicroscopic scale. Representative microstructures from deformed quartz veins, bedding-parallel opaque layers, and the chert matrix have been documented (Fig. 3). The TEM photomicrographs (Fig. 4a,b,c and Fig. 5a) correspond to areas D, B, C, and A in Fig. 3, respectively.

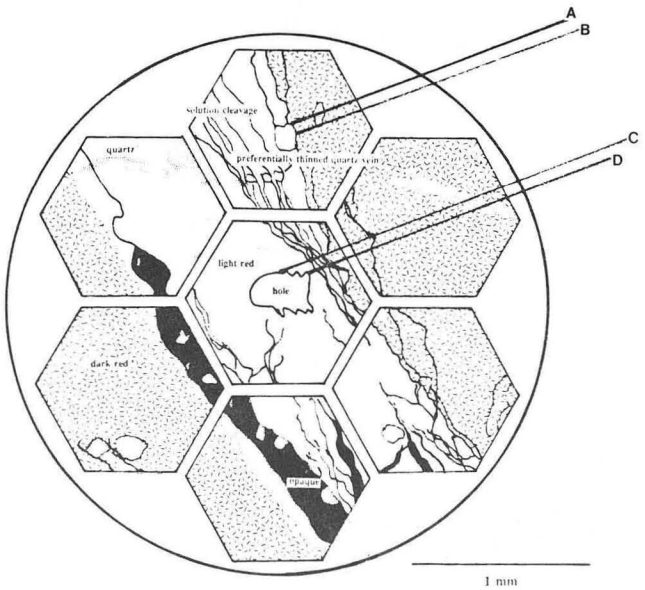

Figure 3. Diagram of a TEM foil, illustrating representative areas in which microstructures were characterized: deformed quartz vein, bedding-parallel opaque layer, and chert matrix. A, B, C, and D refer to locations of the TEM photomicrographs (Fig. 5, Fig. 4b, c, a, respectively). [XBL 881-190]

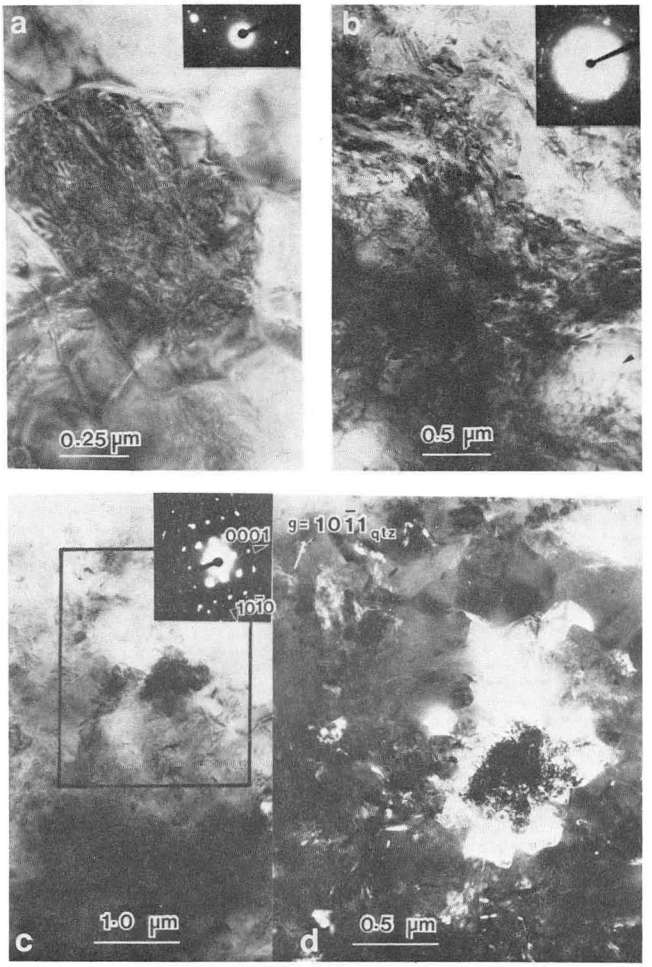

Figure 4. (**a**) Bright-field image of dislocation microstructures in the large-grained secondary vein-filling quartz. Note the uneven distribution of the microstructures. (**b**) Bright-field image of a phyllosilicate seam that trends from the upper left to the middle right. The seam also bears magnetic minerals. The arrowed quartz microstructure is probably of biogenic origin, the preserved features of a radiolarian test. (**c, d**) Bright-field/dark-field pair of chert matrix and adjacent phyllosilicate layer. The chert matrix consists of fine-grained interlocking grains of quartz that are more easily seen in the dark-field micrograph (g = 10$\bar{1}$1). [XBB 881-168]

The presence of dislocation microstructures in the large secondary vein-filling quartz (Fig. 4a) supports thin-section evidence of a subsequent episode of deformation. The heterogeneous distribution of dislocations within and between the crystals suggests that the secondary quartz was deformed under conditions between brittle and ductile styles of deformation. In contrast, the quartz microstructure (Fig. 4b) is probably biogenic, the preserved features of a radiolarian test. The bedding-parallel opaque layer consists primarily of fine-grained phyllosilicates. Large equant phyllosilicate plates can be observed in addition to the lath-shaped cross sections. Magnetic minerals are distributed irregularly through the rock, primarily with the phyllosilicates. Their heterogeneous distribution has been indicated by variable electron beam stability and has caused astigmatism in some of the images. The bright-field/dark-field pair (Fig. 4c,d) is typical of the chert matrix adjacent to the phyllosilicate-bearing opaque layer. It consists of fine-grained interlocking grains of quartz and chalcedony. The individual grains are more easily seen in the dark-field micrograph (g = 10$\bar{1}$1) (Fig. 4d), which highlights the quartz grains oriented with {10$\bar{1}$1} parallel to the beam.

Pods of quartz, often portions of quartz-replaced radiolarian or foraminifera tests (arrows), within the anastomosing phyllosilicate layers are standard examples of "pressure solution" (Fig. 5a). The large phyllosilicate lattice fringes are parallel to its tetrahedral silicate layers. The quartz crystals within the foraminifera indent each other in another common "pressure solution" configuration. In a high-resolution image, quartz lattice fringes (Table 1) from a similar quartz pod (Fig. 5b) terminate at a sharply defined, high-angle grain boundary. In another high-resolution image of quartz grains that

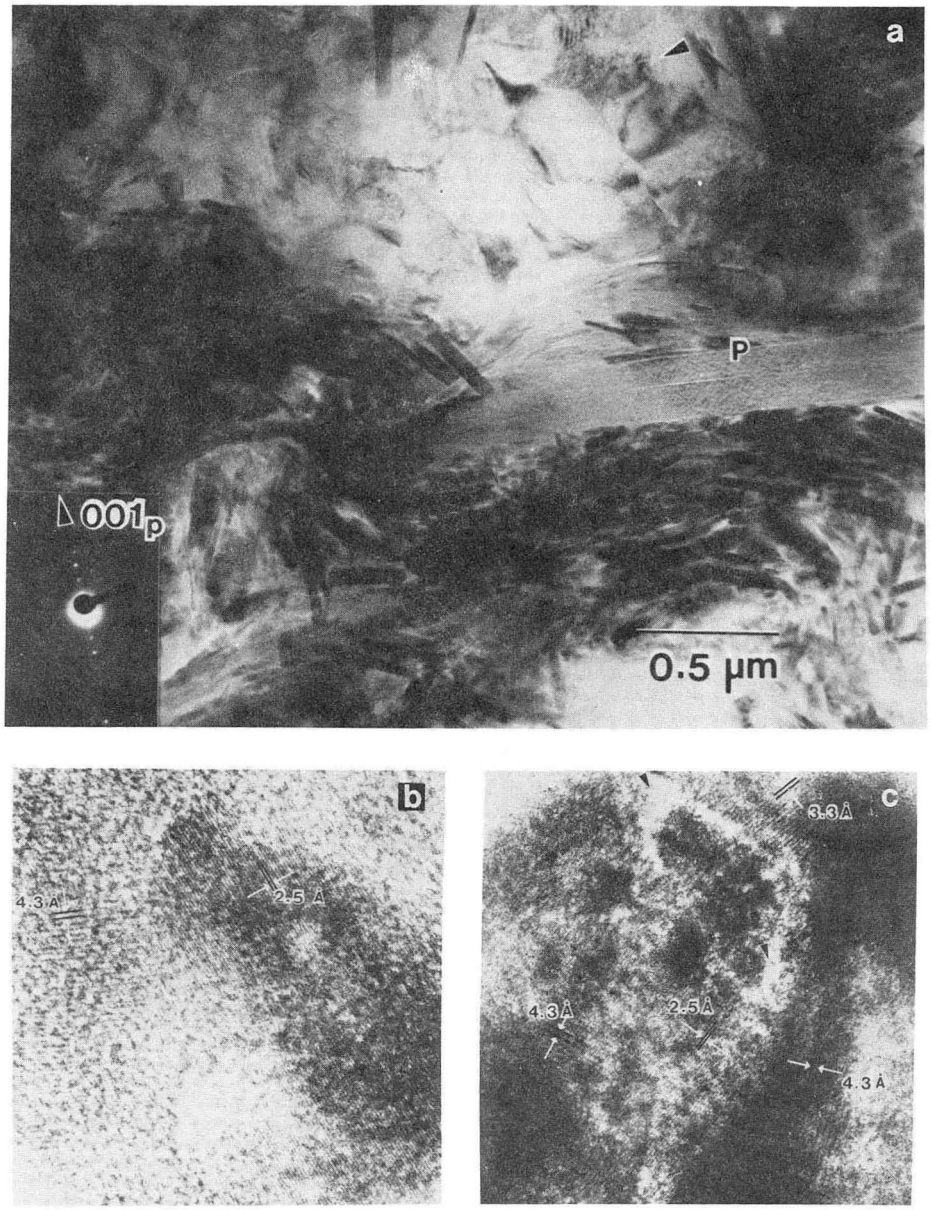

Figure 5. (**a**) Bright-field photomicrograph of quartz pods, often portions of radiolarian or quartz-replaced foraminifera tests (arrowed), within anastomosing phyllosilicate layers. The lattice fringes of the large phyllosilicate are parallel to the (001) silicate sheets. Note the indentation of the crystals in the quartz pod. (**b**) High-resolution image of quartz lattice fringes (Table 1) from indented quartz crystals similar to those represented in (a). The lattice fringes terminate at a sharply defined, high-angle grain boundary. (**c**) High-resolution image of quartz lattice fringes from grains that surround a pore. A small grain (lattice spacing 2.5 Å) indents a larger grain (lattice spacing 4.3 Å) at an abrupt high-angle boundary. [Part a, XBB 881-170; parts b and c, XBB 881-169]

surround a pore, a small grain (lattice spacing 2.3 Å) also indents a larger grain (lattice spacing 4.4 Å) at an abrupt high-angle boundary (Fig. 5c). To date no evidence of an amorphous or second phase has been observed along either the tightly interlocked or the more open type of grain boundary. Previous work on carbonates (Meike and Wenk, 1988) has demonstrated that the evidence for the mechanism of heterogeneous diffusive mass transfer can be confined to a very restricted area. Therefore, more high-resolution and standard electron microscopy is required.

Table 1. Selected lattice spacings for quartz.

(hkil)	Lattice spacing (Å)
(1000)	4.26
$(1\bar{0}11)$	3.34
$(1\bar{1}20)$	2.46
$(1\bar{0}12)$	2.28

DIRECT MEASUREMENTS OF DISLOCATION-ACTIVATION STRESSES FROM HVEM IN SITU EXPERIMENTS

The purpose of this section is to describe a technique for straining two mica minerals, muscovite ($KAl_2(Si_3Al)O_{10}(OH,F)_2$) and biotite ($K(Mg_{0.6-1.8}Fe_{2.4-1.2})(Si_3Al)O_{10}(OH,F)_2$) in situ using the HVEM. These sheet silicates were chosen for some characteristics that facilitate preparation and for others that hamper preparation but are common in rock-forming minerals. Muscovite and biotite are weak at room temperature, elastic, relatively easy to prepare, and translucent in thick section, but are brittle and cleave easily in thin fragments. Successful experiments will be used to calculate muscovite and biotite (001) DAS (e.g., Messerschmidt and Appel, 1979).

Experimental Design

Thin layers (30–60 μm) of mica were peeled along (001) cleavage planes and narrow strips ($\approx$ 2 mm $\times$ 5 mm) cut with a razor blade. One of the slip directions, determined with crossed polarizing filters and percussion figures, was aligned with the long axis of the strip. Specimens were attached to pieces of a sliding beryllium-copper alloy cage.

In previous experiments the ends of each specimen were attached to a preassembled sliding cage that transmitted tensile stress directly to the specimen. The standard tensile straining configuration was modified to a simple shear geometry to optimize conditions for (001) slip in the direction aligned with the long axis of the specimen (Meike, 1988a). The mica specimen was placed between the two cage pieces to permit an attachment method that modifies the stress geometry (Fig. 6). An atom-milled perforation in the middle of the specimen was the focus of the search for dislocation activation. The straining experiments were videotaped. The HVEM permitted the use of thick specimens, which reduce the tendency to fracture, and the surface control of deformation mechanisms.

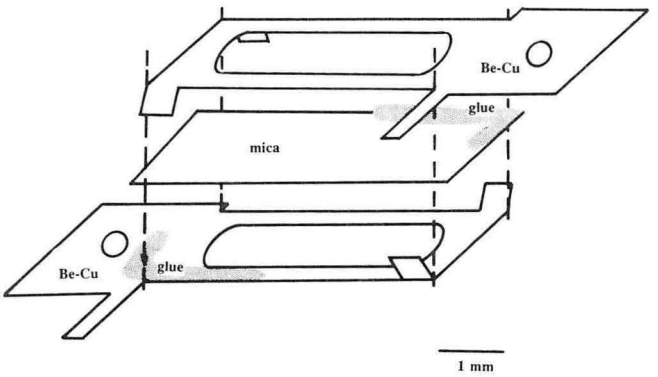

Fig. 2b Expanded diagram of modified specimen-cage attachment.

Figure 6. Diagram of the specimen cage assembly for shearing micas in situ at the high-voltage electron microscope. [XBL 8711-4849]

Results

Most dislocations observed to date originated during sample preparation. In muscovite, dislocation segments between pinpoints (>20 μm) (Fig. 7) were long and difficult to activate within the limits of the strain stage, even near the atom-milled stress raiser. However, (010) and (001) dislocations were easily activated in recent experiments on biotite. The apparent difference between biotite (001) DAS and muscovite (001) DAS can be explained in terms of chemical variation in the octahedral layer (Meike, 1988c) and is consistent with other observed distinctions in deformation microstructures (e.g., Bell and Wilson, 1981).

The intermediary cage used to modify the straining geometry between a specimen and the tensile straining stage makes possible the use of both the most widely available tensile apparatus and the

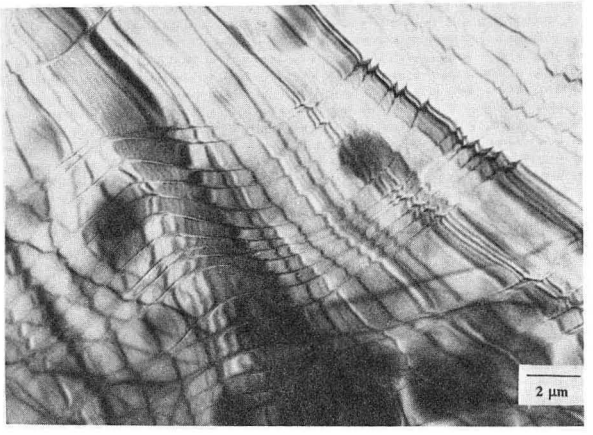

Figure 7. Bright-field photomicrograph of extended dislocations in muscovite. [XBB 881-315]

soundest orientation for the mineral specimen. The option introduces more flexibility for specimen preparation and should reduce barriers to in situ strain experiments on a variety of rock-forming minerals under more difficult, high-temperature conditions. The simple shear geometry offers a preparation alternative to other investigations of deformation, including shear-induced phase transformations and twinning.

ESTIMATES OF DISLOCATION-ACTIVATION STRESSES FROM STRESS GRADIENTS IN CALCITE

The purpose of these experiments was to create a predictable stress gradient in single crystals of calcite in order to extrapolate DAS from a gradient in dislocation density.

Experimental Design

Cones (9.25° half-angle) were cut from large crystals of calcite (var. iceland spar) parallel to [0001] and one end ground parallel to (0001). Sample breakage during preparation made it impossible to replicate the dimensions exactly. But although the end dimensions varied, the cone half-angle was consistent for all specimens. The cones were fitted with cylindrical indium jackets that had conical interiors (9.25° half-angle), placed in cylindrical silver jackets, and sealed with tungsten carbide disks (Fig. 8).

All experiments were conducted in a 10-kbar triaxial gas apparatus built by S. Kirby for the USGS Rock Mechanics Laboratory at Menlo Park, California. The calcite cones were heated to experimental temperature (50°, 100°, or 150°C) measured by two platinum-platinum 10% rhodium (type S) thermocouples that touched the tungsten carbide disks at either end of the sample. The gradient across a specimen at 600°C is known to be less than 10° and is assumed to be much lower at these experimental conditions. The confining medium, argon gas, was raised to 1 kbar before the uniaxial load was applied parallel to [0001]. The actual strain rate differs from the nominal rate (10^{-5}) by only a few percent for strong specimens and therefore must have differed very little for a weak calcite specimen at the low experimental stresses. The specimens were unloaded immediately after the strain gauge measured an initial permanent deformation.

Deformed cones were sectioned vertically through the center. TEM mounts (3-mm dia.) were taken along the cone axis of each thin section (Fig. 9) and thinned. Observation with the HVEM permitted the use of thicker parts of the specimen for more accurate dislocation-density estimates. Multiple orientations of the sample were used to determine Burgers vectors for dislocations and to avoid the systematic omission of low-contrast dislocations.

Results

A strain gradient was achieved in preliminary experiments. The smaller end of the cones deformed permanently, but the larger end retained its original shape (Fig. 10). Two of the three samples exhibit fractures that resulted from a strain rate too great for the crystal at the given confining conditions and from rapid unloading. The intruded indium in KP-110 suggests that the fractures opened during unload-

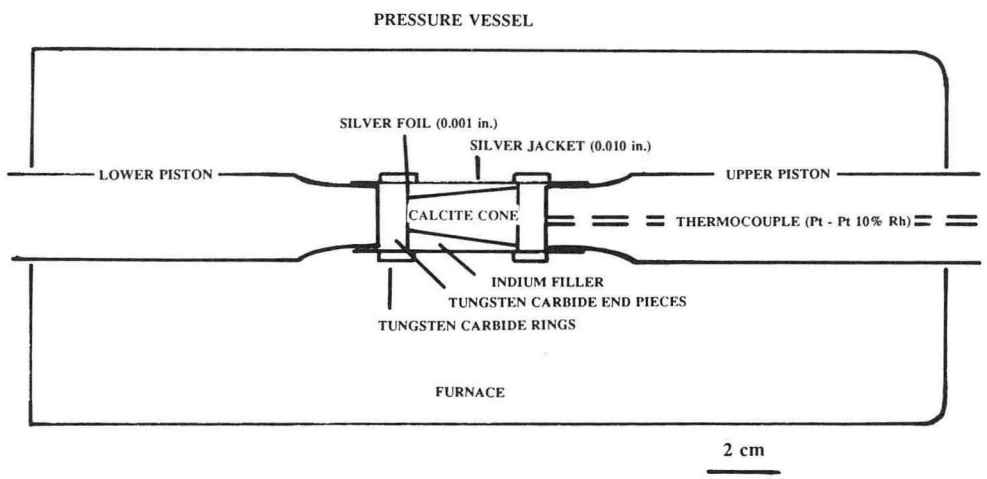

Figure 8. Diagram of triaxial deformation apparatus that includes the jacketed calcite cone assembly. [XBL 882-584]

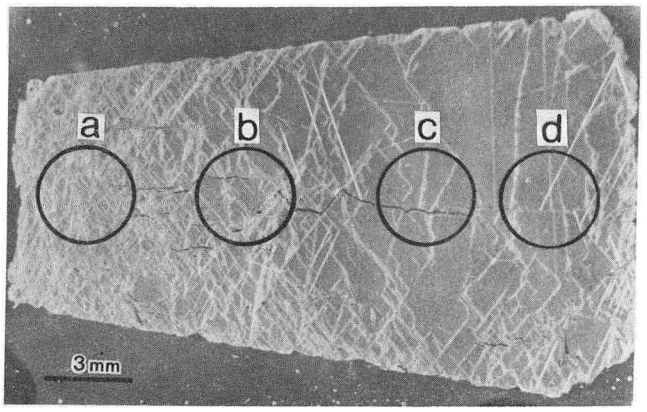

Figure 9. Thin section photomicrograph represents the locations along the axis from which TEM mounts were taken. Although the smaller end of the cone deformed permanently, the large end retained its original shape. [XBB 882-1387]

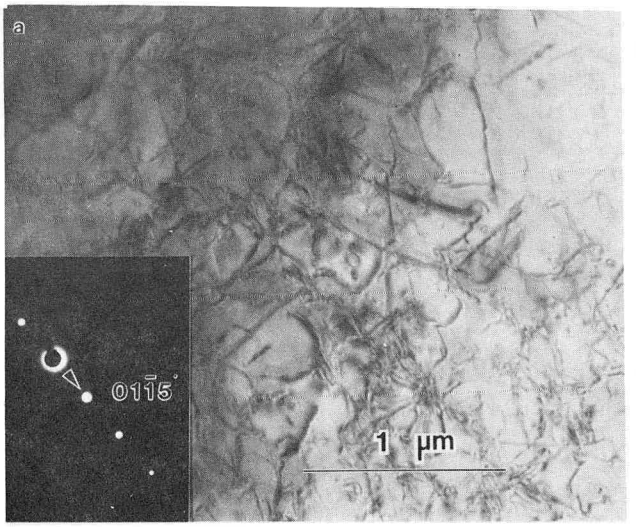

Figure 10. Bright-field photomicrograph of dense dislocations ($\approx 10^{10}/cm^2$) observed in foils taken from the smaller end of the cone. [XBB 886-6150]

ing. Dense concentrations of dislocations ($\approx 10^{10}$ cm^{-2}) have been observed at the small end of the cones (Fig. 10). In general, the dislocation density decreases in proportion to the maximum shear-stress magnitude calculated from an isotropic approximation (Table 2). The presence of very densely spaced dislocations support the observation

Table 2. Estimated values of shear-stress maxima[a] and observed dislocation densities.

100° cone			150° cone		
Location (see Fig. 9)	τ_{max} (bars)	Dislocation density cm/cm^3	Location (see Fig. 9)	τ_{max} (bars)	Dislocation density cm/cm^3
a	276	10^{10}	a	218	10^{10}
a	195	2×10^9	a	126	1×10^9
a			a	130	2×10^{10}
b	126	5×10^9	b	52	3×10^8
b	74	1.2×10^9	b	−21	10^7
b			b	−60	10^9
c	−56	2×10^8	c	−104	8×10^7
c	−56	2×10^7	c	−104	8×10^7
c	−76	2×10^8	c	−150	2×10^8
c			c	−174	8×10^8
c			c	−174	7×10^8
d	−124	2×10^8	d	−231	5×10^8
d	−152	5×10^8	d	−231	5×10^8
d	−152	4×10^8	d	−231	2×10^8
d	−124	2×10^8	d	−231	2×10^8
d	−124	4×10^8	d		

[a]Isotropic approximation.

that a strain gauge offers only a very crude approximation of microscopic deformation.

The next series of experiments will be conducted at a higher confining pressure, at a lower strain rate, and with a slower release of load in an attempt to minimize fracturing at the small end of the specimen. An estimate of DAS will be extrapolated from the dislocation-density gradient along a stress gradient in a single cone. Cones deformed at different temperatures will be compared to distinguish the roles of dislocation glide and dislocation climb in the character of the microstructural gradient.

ACKNOWLEDGMENTS

The cone experiments were conceived by H. Heard. After his death in 1987, the experiments continued thanks to R. Coe, S. Kirby, J. Pinkston, T. Teague, and K. Yi. Special thanks for the in situ experiments are due to D. Ackland, L. Callup, M. Moore, W. Smith, D. Howitt, T. Marela, W. Quan, S. Schaffer, and J. Tanger IV. Use of the HVEM and the Siemens 102 HREM at the NCEM for all investigations is gratefully acknowledged. This work was supported under U.S. Department of Energy Contract No. DE-AC03-76SF00098 and was supervised by J. Apps.

REFERENCES

Apps, J.A., 1987. Pressure-solution geochemistry. *In* Earth Sciences Division Annual Report 1986, Lawrence Berkeley Laboratory LBL-22090, p. 129–133.

Bell, I.A., and Wilson, C.J., 1981. Deformation of biotite and muscovite: TEM microstructure and deformation model. Tectonophysics, v. 78, p. 201–228.

Gronsky, R., 1983. High-resolution electron microscopy. *In* Treatise on Materials Science and Technology (Vol. 19B), Academic Press, New York, p. 225–257.

Meike, A., 1983. Microstructure of stylolites in limestone. Geol. Soc. Am. Abstr. Programs, v. 15, no. 6, p. 642.

Meike, A., 1984. Microstructural interpretation of low temperature and pressure strain-dissolution experiments on calcite. EOS: Trans. Am. Geophys. Union, v. 65, no. 5, p. 1098.

Meike, A., 1988a. Specimen cage modification for TEM *in situ* shearing. *In* J. Bravman et al. (eds.), Specimen Preparation for Transmission Electron Microscopy of Materials. Materials Research Society Proceedings (Vol. 115), p. 211–216.

Meike, A., 1988b. Heterogeneous strain resulting from stress gradients in calcite single crystals. Phys. Chem. Min., in press.

Meike, A., 1988c. Deformation of micas in situ at the high voltage electron microscope. Presented at the 1988 AGU Spring Meeting, Baltimore, Maryland, May 16–20, 1988.

Meike, A., and Wenk, H.R., 1988. A TEM study of microstructures associated with solution cleavage in limestone. Tectonophysics, in press.

Messerschmidt, U., and Appel, F., 1979. Method of evaluating geometrical-statistical parameters of the interaction between dislocations and point obstacles from electron micrographs. Kristall und Technik, v. 14, no. 11, p. 1331–1337.

Tada, R., Maliva, R., and Siever, R., 1987. A new mechanism for pressure solution in quartzose sandstone. Geochim. Cosmochim. Acta, v. 51, p. 2295–2301.

Wintsch, R.P., and Dunning, J., 1985. The effect of dislocation density on the aqueous solubility of quartz and some geologic implications: A theoretical approach. J. Geophys. Res., v. 90, p. 3649–3657.

Carbonate Complexation of Americium(III) in Aqueous Solution

H. Nitsche, E.M. Standifer, and R.J. Silva

In connection with the Nevada Nuclear Waste Storage Investigations (NNWSI) project, we are studying the chemical properties of americium in aqueous solution. Although data exist in the literature on proposed carbonate, bicarbonate, and hydroxycarbonate solution species of americium, they are internally inconsistent. Lundqvist (1982) reports $\log \beta_1 = 5.81 \pm 0.04$ (I = 1 M) for the formation constant of $AmCO_3^+$. Bernkopf and Kim (1984) obtain $\log \beta_1 = 5.08 \pm 0.92$ (I = 0.1 M) for the same reaction. Bidoglio (1982) claims that $AmHCO_3^{2+}$ forms instead of $AmCO_3^+$; his forma-

tion constant for this complex is log β_1 = 4.71 ± 0.08 (I = 0.2 M).

If, indeed, americium were to form the bicarbonate complex, $AmHCO_3^{2+}$, instead of the carbonate complex, $AmCO_3^+$, in carbonate solutions, then it would form much weaker complexes in near-neutral carbonaceous groundwaters, and carbonate complexation would become less important for geochemical modeling. To clarify these discrepancies, we studied the americium carbonate system in aqueous solutions at near-neutral pH. We used remote fiber-optic spectrophotometry to determine the thermodynamic formation constant of the complexation reaction. Spectrophotometry determines the americium solution species directly, whereas the other previously used methods make indirect determinations.

EXPERIMENTAL PROCEDURES

The spectrophotometer that we used (Guided Wave Inc., model 200) is portable, computer-controlled, and has fiber-optic sensing. The portability and the fiber optics make the instrument especially suitable for research on actinide elements and other highly radioactive materials: the instrument can be brought to the sample, instead of bringing the sample to the instrument. The spectrophotometer was adjacent to the inert-atmosphere glove box that we used to exclude air-CO_2 from the experiment. Two jacketed fiber-optic cables directed the light from the spectrophotometer into the box to the sample and back out to the instrument; their wavelength range was from about 400 to 1000 nm. A special holder positioned the 1-cm cuvette in the light beam. The spectrophotometer used a 63-μm exit slit and a germanium detector that gave 0.25-nm wavelength resolution. The single-beam instrument requires a separate reference scan before the test scan. The reference solutions were chemically identical to the test solutions, but without americium (same pH, carbonate concentration, and ionic strength). The computer subtracts the reference spectrum from the test scan automatically and displays the difference spectrum. All spectra were recorded digitally, which simplified further data treatment.

We prepared the ^{243}Am stock solution from AmO_2 powder and purified it through cation-exchange chromatography. It was fumed to near dryness with $HClO_4$. The final americium stock solution was 7.7×10^{-3} M in 0.05 M $HClO_4$. The carbonate solutions were made by dissolving weighed amounts of $NaHCO_3$ and $NaClO_4$ in double-distilled water. In order to compensate for the additional acidity from the Am stock solution, the pH of the carbonate solution was adjusted with a few microliters of 0.1 M carbonate-free NaOH to a pH value slightly higher than the desired pH. Then a microliter amount of americium stock was added to make the solution 1×10^{-5} M. A second, final adjustment of the pH was made with $HClO_4$ and/or carbonate-free NaOH solutions. The solutions were tightly sealed at all times to avoid loss of carbonate. The ionic strength for all solutions was 0.1 M.

The pH was measured with a micro-combination electrode (Beckman Instr. Inc., model 39522) and a digital pH meter (Orion Research Inc., model 231). A 4 M NaCl solution was used as bridge electrolyte. The electrodes were frequently standardized with NBS-traceable pH buffers of pH 7 and pH 4 (EM Science). The temperature was 22.5 ± 1.5°C.

Americium concentrations were determined by nuclear counting of acidified solution aliquots. We counted the 74.67 keV γ-line of ^{243}Am with an intrinsic germanium detector. The maximum calculated error in concentration was below 2.5% (2σ).

RESULTS AND DISCUSSION

Americium in 0.1 M $HClO_4$ shows strong light absorption at λ_{max} = 502.8 nm; the molar absorptivity for this band is ϵ = 380 M^{-1} cm^{-1} (Shiloh et al., 1969). The formation of americium carbonate complexes shifts this peak gradually to 509 nm and also broadens it. At sufficiently small carbonate concentrations, the shifted absorption peak actually consists of two absorption bands: one from the uncomplexed americium and (at least) one from the complexed americium (Bernkopf and Kim, 1984). These peaks overlap and appear as a single peak with an absorption maximum different from the maximum of the uncomplexed americium. We have studied the peak shift as a function of carbonate concentration and determined a formation constant for the americium carbonate complex through the determination of complexed and uncomplexed americium using peak-fitting techniques.

First, we determined the molar absorptivity for Am^{3+} in 0.1 M $HClO_4$ at four different americium concentrations from 5.1×10^{-5} to 1.4×10^{-4} M. The peaks were fitted with Gauss-Lorentzian functions, and the molar absorptivity was determined through a Lambert-Beer plot as ϵ = 1840 ± 112 M^{-1} cm^{-1} (λ_{max} = 502.8 nm). The molar absorptivity is given here as the area under the peak.

Second, we needed to determine the influence of americium hydrolysis on the absorption band, because this process may interfere at near-neutral pH. The increase to near-neutral pH values is necessary to reach sufficiently high concentrations of CO_3^{2-}. We increased the pH of the Am^{3+} solution

stepwise from 0 to 7.5 (while the ionic strength was held constant at 0.1 M) and monitored the absorption band at 502.8 nm. The spectra recorded at pH values above 0 were fitted with the spectrum of Am^{3+} in 0.1 M $HClO_4$. Up to pH 7.0 the spectra had the same shape and area as the spectrum of Am^{3+} at pH 0. This experiment confirmed that we could measure the Am^{3+} spectrum up to pH 7 without having any hydrolytic species influence the spectrum.

Third, we measured the shift of the absorption peak as function of carbonate concentration in the pH range 4.37–6.40, where the Am^{3+} is not hydrolyzed. The CO_3^{2-} concentration was calculated from the carbonate equilibrium using $pK_1 = 6.12$ and $pK_2 = 9.86$ (Phillips et al., 1985). The range was for $[CO_3^{2-}] = 3.4 \times 10^{-9}$ to 1.35×10^{-6} M. At the highest carbonate concentration, the peak was shifted to 505.3 nm, and we initially assumed that the absorption band was solely due to $AmCO_3^+$. This peak was also fitted with a Gauss-Lorentzian function.

Then the intermediate shifted spectra (between 502.8 and 505.3 nm) were fitted with both Gauss-Lorentzian functions (Am^{3+} uncomplexed and $AmCO_3^+$), and the contributions of each feature to the composite peaks were determined. Figures 1a and 1b show the spectrum and the fitted functions for Am^{3+} and $AmCO_3^+$, respectively. Figure 2 shows the spectra of the uncomplexed Am^{3+} and three intermediate shifted peaks. The isosbestic point indicates clearly the change of one species to only one other (Am^{3+} to $AmCO_3^+$).

The formation constant Q_{1n} for the equilibrium

$$Am^{3+} + n\ CO_3^{2-} = Am(CO_3)_n^{\ 3-2n} \qquad (1)$$

is

$$Q_{1n} = \frac{[Am(CO_3)_n^{\ 3-2n}]}{[Am^{3+}]\,[CO_3^{2-}]^n} \qquad (2)$$

or

$$\log \frac{[Am(CO_3)_n^{\ 3-2n}]}{[Am^{3+}]} = \log Q_{1n} + n \log [CO_3^{2-}]\,. \qquad (3)$$

From the plot of $\log\{[Am(CO_3)_n^{\ 3-2n}]/[Am^{3+}]\}$ against $\log [CO_3^{2-}]$, shown in Fig. 3, we obtain the equilibrium constant Q_{1n} as the intercept and the stoichiometry of the complex as the slope. The slope of $n = 0.88 \pm 0.15$ indicates that the complex

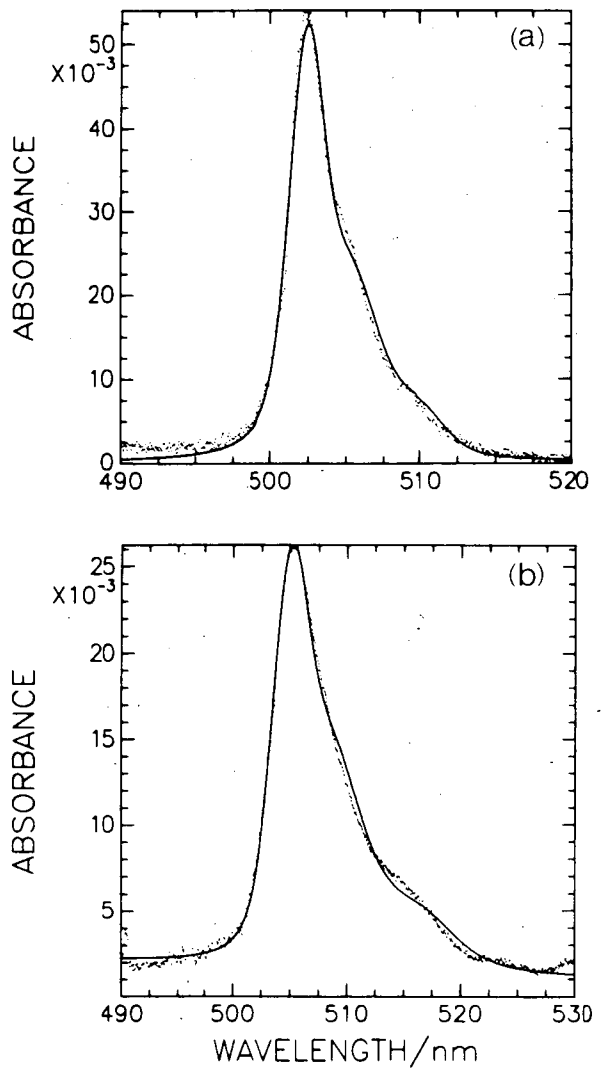

Figure 1. Gauss-Lorentzian nonlinear least-squares fit (solid line) of the absorption spectra (points) for (**a**) Am^{3+} in 0.1 M $HClO_4$, and (**b**) $AmCO_3^+$. [XBL 886-2127]

formed is $AmCO_3^+$. Setting the slope to $n = 1$ gives $\log Q_{11} = 6.69 \pm 0.15$ (I = 0.1 M).

From this formation constant and other values available in the literature, which were determined at different ionic strengths, we corrected to infinite dilution using the Brønsted-Scatchard-Guggenheim specific ion interaction theory (SIT) (Biedermann et al., 1982). Applying this theory to the equilibrium

$$Am^{3+} + CO_3^{2-} = AmCO_3^+ \qquad (4)$$

and introducing β^o and $\beta(I)$ as the overall formation constants at ionic strengths of 0 and I, respectively, gives

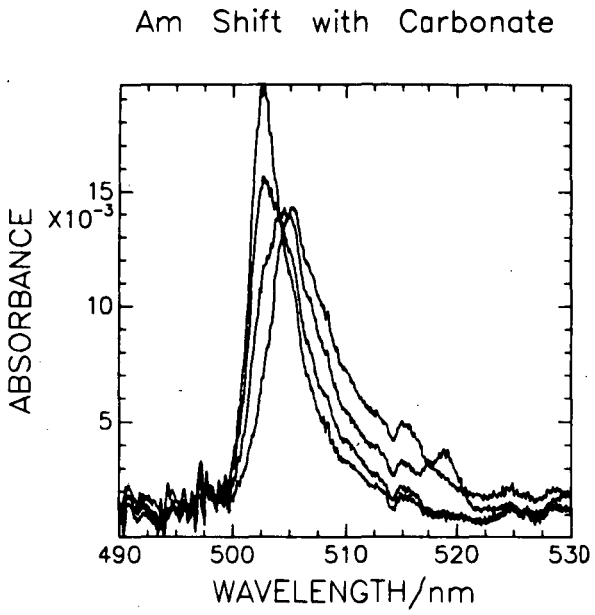

Figure 2. Shift of the americium spectra toward higher wavelength with increasing carbonate concentration; the isosbestic point indicates the change from one species to only one other (Am^{3+} to $AmCO_3^+$). [XBL 878-3640]

$$\log \beta(\mathrm{I}) + \Delta z^2 D = \log \beta^o + \Delta\epsilon m \qquad (5)$$

with

$$\Delta \epsilon = -\epsilon(AmCO_3^+,ClO_4^-) + \epsilon(Am^{3+},ClO_4^-) + \epsilon(Na^+,CO_3^{2-}) \qquad (6)$$

and

$$\Delta z^2 = -z^2_{AmCO_3^+} + z^2_{Am^{3+}} + z^2_{CO_3^{2-}} = 12\,, \qquad (7)$$

where z is the charge, D the Debye-Hückel term at 25°C, ϵ the interaction coefficients, and m the molality. From the plot of $\log \beta(\mathrm{I}) + 12\mathrm{D}$ against the ionic strength m (mole/kg), we obtain the formation constant β^o at infinite dilution as the intercept and $\Delta\epsilon$ as the slope. Figure 4 shows this plot. We have also included in this plot recent results of Robouch and Vitorge (personal communication, 1988). From solubility studies of $Am_2(CO_3)_3$ in 3 M $NaClO_4$, they obtained $\log \beta_1 = 5.45 \pm 0.12$. The uncertainties shown in Fig. 4 are 1σ, as given by the researchers. Lundqvist's uncertainty lies within the symbol. We

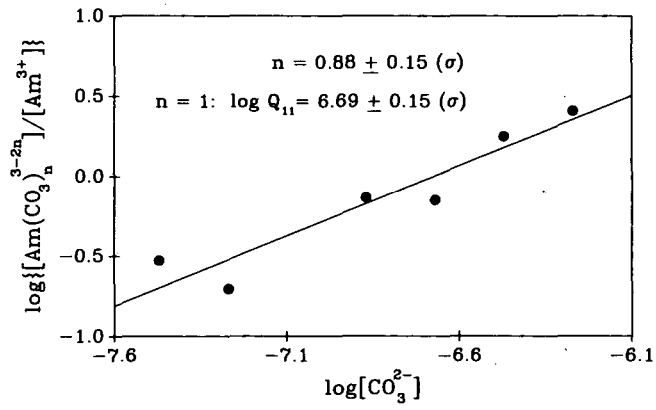

Figure 3. Linear least-squares regression for $\log \{[Am(CO_3)_n{}^{3-2n}]/[Am^{3+}]\} = \log Q_{1n} + n \log [CO_3^{2-}]$. [XBL 885-1631]

multiplied the uncertainties by 1.96 and calculated a $1/\sigma^2$ weighted least-squares regression. The results are $\log \beta^o = 8.16 \pm 0.10$ and $\Delta\epsilon = 0.11 \pm 0.07$. Using literature values for $\epsilon(Na^+,CO_3^{2-}) = -0.08 \pm 0.02$ (Ferri et al., 1983) and

$$\epsilon(Am^{3+},ClO_4^-) \approx \epsilon(Y^{3+},ClO_4^-) \approx \epsilon(La^{3+},ClO_4^-) = 0.49 \pm 0.04$$

(Robouch and Vitorge, personal communication, 1988; Ciavatta et al., 1981), we can solve Eq. (6) and obtain $\epsilon(AmCO_3^+, ClO_4^-) = 0.30 \pm 0.08$ ($\pm 1.96\sigma$).

The fourth and last task of our investigation was to determine whether americium bicarbonate complexes, $AmHCO_3^{2+}$, as postulated by Bidoglio

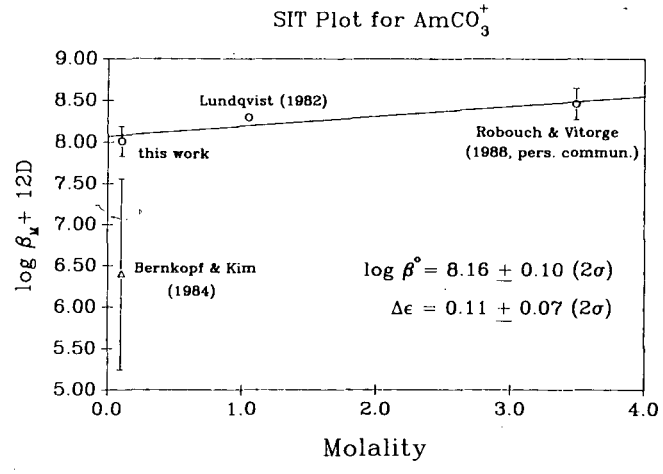

Figure 4. Linear least-squares regression for the specific ion interaction theory (SIT) of $\log \beta(\mathrm{I}) + 12\mathrm{D} = \log \beta^o + \Delta\epsilon m$; data for this plot were taken from this work and literature data. [XBL 884-1273]

(1982), do exist. The answer to this question lies in the pH dependence of the carbonate equilibria:

$$[HCO_3^-] = \frac{K_1}{[H^+]} K_H \cdot p_{CO_2} \quad (8)$$

and

$$[CO_3^{2-}] = \frac{K_1 K_2}{[H^+]^2} K_H \cdot p_{CO_2} . \quad (9)$$

Equations (8) and (9) show that a change of p_{CO_2} from 1 to 0.1 atm requires an increase of one pH unit to obtain the same $[HCO_3^-]$, whereas an increase of only one half pH unit is necessary to have the same $[CO_3^{2-}]$ present. Figure 5 shows two species distribution plots at (a) 1 and (b) 0.1 atm p_{CO_2}.

The species distributions were calculated from data of Bidoglio (1982). Assuming that $AmHCO_3^{2+}$ produces an absorption spectrum at a wavelength range similar to $AmCO_3^+$, one should observe this spectrum at pH values of about 3.3 and 4.4 when p_{CO_2} is lowered from 1 atm to 0.1 atm. We did not, however, observe any shift in the 502.8 nm peak at either pH. But we did obtain the same shifted carbonate spectra (505.3 nm) at pH values of 5.9 and 6.4 for p_{CO_2} of 1 and 0.1 atm, respectively. This result is consistent with the formation of $AmCO_3^+$ and not $AmHCO_3^{2+}$.

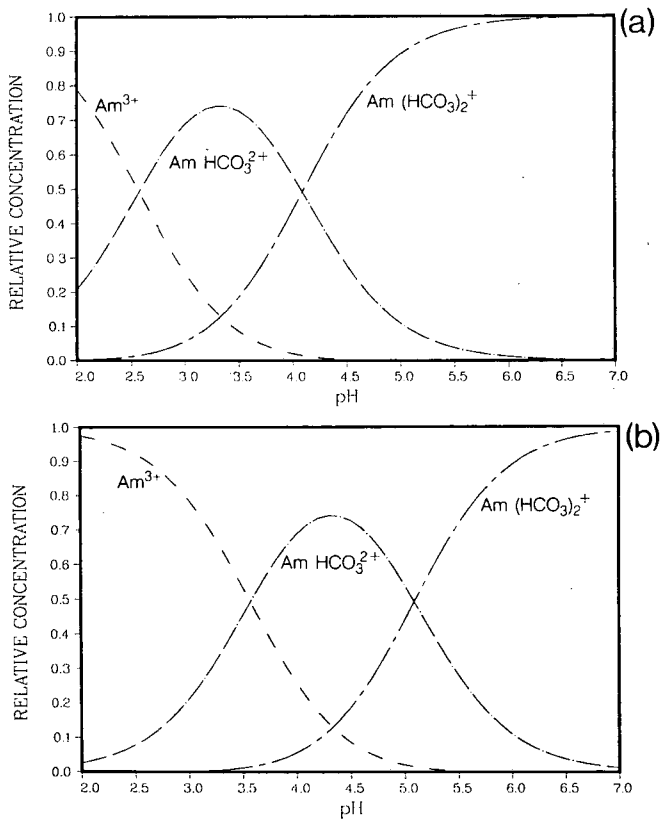

Figure 5. Species-distribution plot at a pH range from 2 to 7 using hydrolysis data from Kerrisk and Silva (1986) and bicarbonate complexation data from Bidoglio (1982) at (**a**) 1 atm, and (**b**) 0.1 atm p_{CO_2}. [XBL 885-1630]

REFERENCES

Bernkopf, M.F., and Kim, J.I., 1984. Hydrolyse-Reaktionen und Karbonat Komplexierung von Dreiwertigem Americium im Natürlichen Aquatischen System. Report RCM-02884, Technical University Munich, FRG.

Bidoglio, G., 1982. Characterization of Am(III) complexes with bicarbonate and carbonate ions at groundwater concentration levels. Radiochem. Radioanal. Lett., v. 53, no. 1, p. 45.

Biedermann, G., Bruno, J., Ferri, D., Grenthe, I., Salvatore, F., and Spahiu, K., 1982. Modelling of the migration of lanthanoids and actinoids in ground water; the medium dependence of equilibrium constants. *In* W. Lutze (ed.), Scientific Basis for Nuclear Waste Management, V. Materials Research Society Symposia Proceedings, Elvesier, New York, p. 791–800.

Ciavatta, L., Ferri, D., Grenthe, I., Salvatore, F., and Spahiu, K., 1981. Studies on metal carbonate equilibria. 3. The lanthanum(III) carbonate complexes in aqueous perchlorate media. Acta Chem. Scand., v. A35, p. 403.

Ferri, D., Grenthe, I., Hietanen, S., and Salvatore, F., 1983. Studies on metal carbonate equilibria. 5. The cerium(III) carbonate complexes in aqueous perchlorate media. Acta Chem. Scand., v. A37, p. 359.

Kerrisk, J.F., and Silva, R.J., 1986. A consistent set of thermodynamic constants for americium(III) species with hydroxyl and carbonate. *In* Proceedings, Workshop on Geochemistry Modeling, Fallen Leaf Lake, California, September 14–17, 1986.

Lundqvist, R., 1982. Hydrophilic complexes of the actinides. I. Carbonates of trivalent americium and europium. Acta Chem. Scand, v. A36, p. 741.

Phillips, S.L., Phillips, C.A., and Skeen, J., 1985. Hydrolysis, formation and ionization constants at 25°C, and at high temperature-high ionic strength. Lawrence Berkeley Report LBL-14496.

Shiloh, M., Givon, M., and Marcus, Y., 1969. A spectrophotometric study of trivalent actinide complexes in solutions: III. Americium with bromide, iodide, nitrate and carbonate ligands. J. Inorg. Nucl. Chem. v. 31, p. 1807.

Solubility Studies for the Potential High-Level Nuclear Waste Repository at Yucca Mountain, Nevada

H. Nitsche, S.C. Lee, R.C. Gatti, D.B. Tucker, and E.M. Standifer

The Nevada Nuclear Waste Storage Investigations (NNWSI) Project is characterizing a tuff formation at Yucca Mountain in southern Nevada to determine its suitability as a potential site for a high-level nuclear waste repository.

A possible worst-case scenario is the intrusion of groundwater into the underground storage vault. Groundwater would corrode the storage canisters, and the waste packages would release radionuclides into the groundwater. The contaminated groundwater would then become the principal mechanism for the transport of radionuclides from the disposal site to the accessible environment. The radioactive elements can react with the groundwater. The formation of solution species and solubility-controlling solid phases would define their maximum concentrations and migration characteristics. The nature of the compounds and solution species formed would depend on the oxidation state of the radioelement, the nature and concentrations of the complexing ligands and precipitating ions, the temperature, the pH, and the redox properties of the groundwater.

To meet the regulations and requirements of the Environmental Protection Agency and the Nuclear Regulatory Commission for site characterization, it is necessary to determine experimentally the radionuclide solubility in groundwaters from the potential disposal site. Such a study must include the characterization of the solubility-controlling solids and the speciation of the solution complexes.

This article summarizes results obtained during the second year of our long-term effort at the Lawrence Berkeley Laboratory to provide knowledge on the solubilities and the nature of compounds and solution species of waste radionuclides that form in natural waters found at or near Yucca Mountain. The waste elements to be studied are nickel, zirconium, tin, radium, thorium, uranium, neptunium, plutonium, and americium.

During fiscal 1987 we have studied the solubilities of neptunium, plutonium, and americium in J-13 groundwater from Yucca Mountain (Nevada) at two temperatures (60 and 90°C) and three hydrogen ion concentrations (pH 5.9, 7.0, and 8.5). The water from Well J-13 was chosen by NNWSI as a reference groundwater; characteristic of water compositions expected to be found in the unsaturated zone near the repository, the J-13 water is neutral, oxidizing, carbonaceous, and low in ionic strength (pH = 7, Eh = 700 mV, CO_3 total = 2.86 mequiv/L, I = 3.56 $\times 10^{-3}$ M). The pH range for the tests was chosen to cover the possibility that shifts from the natural pH of the water might occur (possibly induced by α radiation) and to provide a better understanding of the influence of pH on the solubility. The temperature span between 25 and 90°C covers the range from pre-emplacement temperatures to a maximum temperature with liquid water present. The maximum temperature at which solubility is important is expected to be limited by the boiling point of water at Yucca Mountain (95°C).

We studied the solubilities from oversaturation, which allows the determination of an upper solubility limit. The nuclides were added at the beginning of each experiment as $^{237}NpO_2^+$, $^{239}Pu^{4+}$, and $^{243}Am^{3+}$. Because the solubilities are highly sensitive to pH and temperature changes, we controlled those parameters closely. We designed a computer-operated control system (pH-stat) to maintain the aqueous actinide solutions at constant temperatures and pH values for the solubility experiments (Tucker et al., 1987). The pH-stat records and adjusts the pH values of the test solutions at the target values, with standard deviations not exceeding 0.1 pH unit. It uses small amounts (usually between 5 and 50 μL) of dilute (0.05–0.1 M) $HClO_4$ or NaOH solution for the pH adjustments. Temperatures from 25 to 90°C can be controlled within less than 1°C. The well water used in the tests was maintained at its nominal carbonate concentration when its temperature and pH value was adjusted to conditions differing from its natural state.

After efficient phase separation by ultrafiltration (Standifer et al., 1987), we counted periodic samples of the aqueous phase for nuclide concentration to determine steady-state conditions. The solubility tests typically lasted between 35 and 150 days. At steady state we separated the solid from the solution and characterized each phase individually. The oxidation states of the supernatant solutions were determined to see if the steady-state oxidation state differed from the one at the beginning of the test. For neptunium we used absorption spectrophotometry, but for plutonium, which was present in low concen-

Table 1. Results for solubility experiments on neptunium in J-13 groundwater at 60° and 90°C for three pH values.

	Steady-state concentration (M)	
	60°C	90°C
5.9	$(6.4 \pm 0.3) \times 10^{-3}$	$(1.2 \pm 0.1) \times 10^{-3}$
7.0	$(9.8 \pm 1.0) \times 10^{-4}$	$(1.5 \pm 0.5) \times 10^{-4}$
8.5	$(1.0 \pm 0.1) \times 10^{-4}$	$(8.9 \pm 0.4) \times 10^{-5}$

trations, we had to use an indirect method that involves several solvent extractions and coprecipitations (Nitsche et al., 1987).

The solid compounds were analyzed by x-ray powder diffraction measurements. When the measurements produced no pattern, or when the pattern could not be assigned to any known compound, Fourier-transform infrared spectroscopy (FTIR), neutron activation analysis (NAA), and chemical methods were applied to get additional information on the nature of the unidentified precipitates.

RESULTS

Steady-state solubility concentrations are given in Tables 1 and 2 for neptunium and plutonium, respectively. The neptunium solubility decreased with increasing temperature and with increasing pH. The soluble neptunium did not change oxidation state at steady state. For both temperatures the pentavalent neptunium was increasingly complexed by carbonate with increasing pH. The solid formed at 90°C and pH 5.9 was crystalline Np_2O_5. All other neptunium solids were crystalline and contained carbonate. We are currently further characterizing these solids.

The plutonium concentrations decreased with increasing temperature and showed no trend in pH. The steady-state solids were mostly amorphous,

Table 2. Results for solubility experiments on plutonium in J-13 groundwater at 60° and 90°C for three pH values.

	Steady-state concentration (M)	
	60°C	90°C
5.9	$(2.7 \pm 1.7) \times 10^{-8}$	$(6.2 \pm 1.9) \times 10^{-9}$
7.0	$(3.8 \pm 0.8) \times 10^{-8}$	$(8.8 \pm 0.8) \times 10^{-9}$
8.5	$(1.2 \pm 0.1) \times 10^{-7}$	$(7.3 \pm 0.4) \times 10^{-9}$

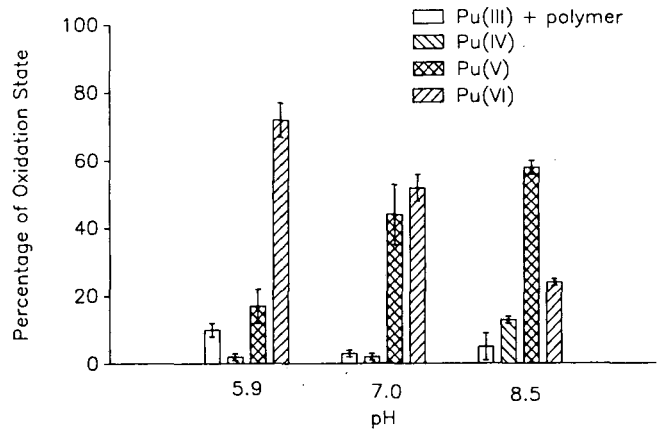

Figure 1. Plutonium oxidation-state distribution versus pH in J-13 groundwater at 60°C. [XBL 886-2128]

although some contained a crystalline component. They consisted of Pu(IV) polymer and unknown carbonates. Figures 1 and 2 show the oxidation states determined for the supernatant solutions at 60 and 90°C, respectively. Although the plutonium was tetravalent when first added, Pu(V) and Pu(VI) were the dominant oxidation states in solution. For the 60°C test the amount of Pu(V) increased with pH but Pu(VI) decreased. At 90°C Pu(V) predominated at pH 5.9 and 8.5. The results for pH 7.0 are ambiguous, because we have indications that the filter used for the phase separation leaked. Such leakage would introduce more Pu(IV) polymer and change the relative distribution of oxidation states. It is noteworthy, however, that PuO_2^+, which is very unstable in acid solutions, was stabilized in all J-13 groundwater solutions.

We could not determine steady-state concentrations for the 60°C americium solutions within the 168 days of the test. We have evidence that the α

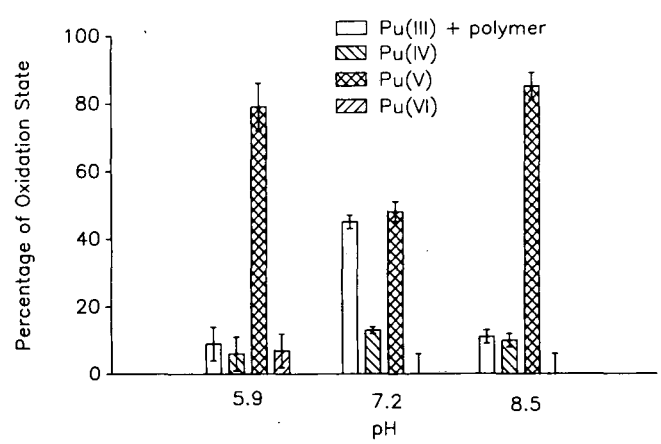

Figure 2. Plutonium oxidation-state distribution versus pH in J-13 groundwater at 90°C. [XB 886-2129]

radiation dislodged small particles from the test vessel, which served as adsorption sites for dissolved americium species, thus forming pseudocolloids. The irreproducible behavior of americium pseudocolloids in aqueous solution (Starik and Ginzberg, 1961) may be responsible for the observed sporadic changes in concentration. We are now performing the 90°C tests with neodymium as a substitute for americium. Because of the similarity between the two elements (ionic radii, valency), the results for neodymium also apply to americium. We spiked the neodymium with ^{241}Am tracer, which reduces the α-radiation level to about 10% of the level we used in the 60°C solubility experiment. The test container should better withstand this lower α-radiation level, thus avoiding pseudocolloid formation. We have analyzed the americium precipitates formed at 60°C despite the fact that no steady state was reached. The solids formed at pH 7.0 and 8.5 are orthorhombic $AmOHCO_3$, whereas the solid formed at pH 5.9 is hexagonal $AmOHCO_3$. Hexagonal $AmOHCO_3$ is isostructural with its neodymium analog and was not previously reported (Standifer and Nitsche, 1988).

REFERENCES

Nitsche, H., Lee, S.C., and Gatti, R.C., 1987. Determination of plutonium oxidation states of trace levels pertinent to nuclear waste disposal. J. Radioanal. Nucl. Chem., in press.

Standifer, E.M., Lee, S.C., and Nitsche, H., 1987. Separation of soluble transuranium species from particulates in groundwater by ultrafiltration. Presented at the 193rd American Chemical Society Meeting, Denver, Colorado, April 5–10, 1987. Lawrence Berkeley Laboratory Report LBL-23378.

Standifer, E.M., and Nitsche, H., 1988. First evidence for hexagonal $AmOHCO_3$. Lanthanide Actinide Res., in press.

Starik, I.Y., and Ginzberg, G.L., 1961. The colloidal behavior of americium. Sov. Radiochem., v. 3, p. 179.

Tucker, D.B., Standifer, E.M., Silva, R.J., and Nitsche, H., 1987. Data acquisition and feedback control system for solubility studies of the nuclear waste elements neptunium and plutonium. Lanthanide Actinide Res., in press.

Reaction of Uranium Chloride with Zirconium Alloy: A Chemical Model System for Spent-Fuel/Cladding Reactions

D.L. Perry and K.M. Ogle

The adsorption reactions of the uranyl ion (UO_2^{2+}) from aqueous solutions are of considerable interest. The uranyl ion is the most stable and common U(VI) species in an oxidizing environment and is the predominant form of uranium present in high-level nuclear waste that has undergone solution oxidation. Considerations involving the adsorption and desorption reactions of the uranyl ion and other spent-fuel nuclides with natural substrates play an important role in decisions about where nuclear waste repositories should be located. Further, the adsorption of uranyl ion from chloride media onto solid material is of especial interest to the nuclear industry as a method for extracting uranium from sea water.

Uranyl adsorption has been investigated on a variety of substrates, including organics, clays, glasses, numerous oxides, carbonates, and phosphates. The general consensus is that the adsorbed uranyl phase, regardless of the sorption material, is a surface complex of uranyl hydroxides and/or carbonates and that the equilibrium surface concentration maximizes at high pH values (> 7.0), increases with increasing temperature, and adsorbs most extensively on amorphous materials. Direct spectroscopic characterization of the adsorbed state has been attempted in only a few cases. Several workers, for example, have used Raman spectroscopy to characterize the adsorbed uranyl on hydrous titania, zirconia, and silica gels. Their results indicate that the adsorbed state is free of carbonate, in contrast to several models proposed prior to their work.

It is of interest to observe the changes in oxidation state that occur when the uranyl ion is adsorbed onto a metallic substrate. The x-ray photoelectron spectroscopy of synthetic and natural uranium compounds has been extensively studied in recent years. A survey of the literature reveals no papers describing the x-ray photoelectron spectroscopic characterization of the uranyl ion products formed via adsorp-

tion from solution. This article summarizes our investigation of the adsorption and precipitation of the uranyl ion onto the surface of Zircaloy-4, a zirconium alloy used as a cladding material for nuclear fuel packages. X-ray photoelectron and Auger spectroscopy, sensitive to chemical changes on reacted surfaces, have been used to characterize the thin uranium films and bulk precipitates formed by these reactions.

Figure 1 shows the uranium $4f_{7/2,5/2}$ transitions measured for a standard uranium(VI) hydrated oxide (Perry et al., 1984) and for zirconium substrates with which uranium has been reacted. In Fig. 1a, the well-documented uranium(VI) hydrolysis product, $UO_3 \cdot 2H_2O$, is shown with a binding energy typical of uranium(VI). Figure 1b, however, shows the photoelectron spectrum of unhydrolyzed $UO_2Cl_2 \cdot 3H_2O$ that has been reacted with Zircaloy-4 at low pH. The uranium(VI) line is quite evident; however, a reduced uranium(IV) line is also quite apparent. The intensity of the uranium(IV) line is greater than that of the uranium(VI) line, thus showing the tetravalent uranium to be the predominant species. Because of this mixture of the two lines, any subsequent model of the dissolution of the surface layer would have to account for these mixed uranium species. When the $UO_2Cl_2 \cdot 3H_2O$ is reacted with reagent ZrO_2 (chemically similar to the passivation layer on the Zircaloy-4 surface), no reaction occurs (Fig. 1c). Since the zirconium(IV) oxide passivation layer is not a reducing agent, the first step of the uranium reduction must be the dissolution (or alteration) of the oxide, followed by reductive chemisorption of the uranium(VI).

Studies of this type serve to verify chemical reactions, species, and mechanisms by which solutions containing spent fuel products interact with canister and cladding materials. This is important for the verification of models that are used to predict nuclear waste migration and transport processes. For example, it should be possible to confirm chemical species postulated for a corrosion or dissolution/alteration mechanism of a solid substrate.

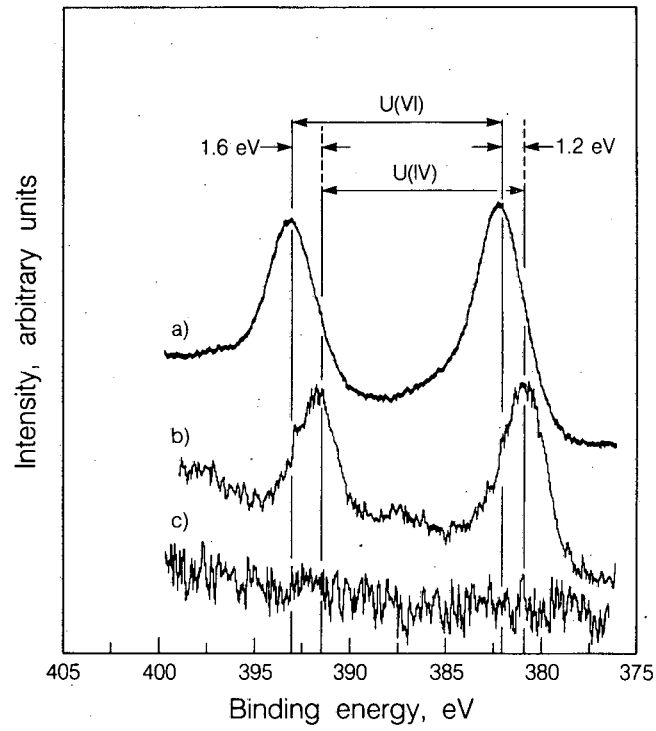

Figure 1. Uranium $4f_{7/2,5/2}$ x-ray photoelectron spectra for a representative uranyl hydrolysis product and zirconium substrates reacted with uranium. **(a)** $UO_3 \cdot 2H_2O$, formed by base hydrolysis of $UO_2Cl_2 \cdot 3H_2O$. **(b)** Zircaloy-4 foil reacted with $UO_2Cl_2 \cdot 3H_2O$ (0.01 M, pH = 1.8) at 100°C for 24 hours. **(c)** Reagent ZrO_2 reacted with $UO_2Cl_2 \cdot 3H_2O$ (0.01 M, pH = 1.8) at 100°C for 24 h. [XBL 877-10257]

REFERENCES

Perry, D.L., Tsao, L., and Brittain, H.G., 1984. Photophysical studies of uranyl complexes. 4. X-ray photoelectron and luminescence studies of hydrolyzed uranyl salts. Inorg. Chem., v. 23, p. 1232–1237.

Reactions of Chalcopyrite in Acidic Aqueous Media

D.L. Perry and K.M. Ogle

Over the last several years, many new techniques have been developed for studying surface reactions that occur on the faces of geologic materials. Such techniques are especially useful for studying chemical processes that are important to the processing of mineral ores and their mixtures in froth flotation effected in aqueous reaction systems. Alternatively, these surface techniques can also be applied to the study of the chemical mechanisms involved in the leaching of metal ions from spent ores for the purpose of recovering additional metal and determining how the pertinent metal ion complexes involved in the process migrate through soil, rock, and other material in the ground.

One surface technique that has found widespread applications to these studies is x-ray photoelectron spectroscopy (XPS), also sometimes referred to as electron spectroscopy for chemical analysis (ESCA). This technique yields a considerable amount of chemical information involving reactions, including the oxidation state of an element, the chemical species of the element involved in the reaction, and the changes that these chemical species undergo during the course of a particular reaction sequence (Perry, 1986). Materials that are particularly amenable to study by this technique are metal sulfide ores such as galena (Perry et al., 1984a), sphalerite (Perry et al., 1984b), and covellite (Perry and Taylor, 1986); in the case of covellite, for example, one can detect oxidation of the copper(I) ion to copper(II) as well as the possible oxidation of the sulfide (S^{2-}) anion to the sulfate (SO_4^{2-}) during its aqueous reaction chemistry.

This article summarizes the results from our study of the reaction of chalcopyrite, $CuFeS_2$, with aqueous solutions of H_2SO_4. The reaction was studied in two phases: (1) the simple reaction of the chalcopyrite with a solution of H_2SO_4 at pH = 2.00 and (2) the reaction of the chalcopyrite with the same H_2SO_4 under an electrochemical potential to simulate groundwater leaching conditions. In Fig. 1, for example, one can see the copper $2p_{3/2,1/2}$ photoelectron spectrum of the sputter-cleaned, unreacted sample (Fig. 1a). After exposure to air for 30 min (Fig. 1b), there is no perceptible change in the spectrum; the intense line on the right side of the spectrum (the $2p_{3/2}$ line) is still quite symmetric and narrow, indicative of the diamagnetic copper(I) species inherent in the mineral. This is confirmed by the lack of any satellite structure to the high-binding-energy side of the $2p_{3/2}$ line. This situation persists in the spectrum (Fig. 1c) of the sample that has been exposed to the H_2SO_4 solution, reflecting the lack of oxidation of the chalcopyrite copper in the solution or, alternatively (possibly), the dissolution of any oxidized copper species that might have formed.

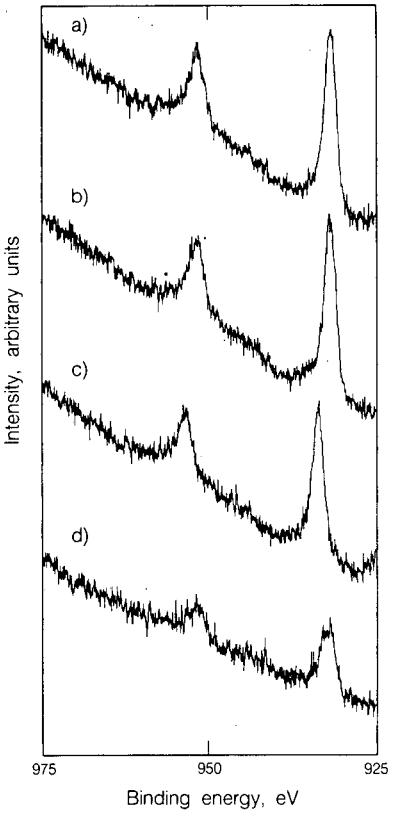

Figure 1. X-ray photoelectron spectrum of the copper $2p_{3/2,1/2}$ region of a chalcopyrite sample that has undergone different chemical treatment histories. **(a)** After 120 s of argon ion sputtering to remove natural contaminants. **(b)** After exposure of sample (a) to air for 30 min. **(c)** After exposure of sample (b) to to H_2SO_4 (pH = 2.00) for 60 s. **(d)** After exposure of sample (c) to H_2SO_4 (pH = 2.00) at a potential of E = 0.540 V versus Ag/AgCl for 12 hours. [XBL 878-10302]

In Fig. 1d, however, a different situation is observed. After reacting the chalcopyrite sample under an applied potential for 12 hours, the copper $2p_{3/2}$ photoelectron line broadens considerably, and a decided amount of satellite structure begins to form to the high-binding-energy side of the main line.

This satellite structure results from paramagnetic effects due to the formation of the copper(II) ion upon oxidation of the copper(I) ion. Moreover, this broadening is possibly due to the formation of another copper(I) sulfur phase; the initial sulfide attributable to the $CuFeS_2$ has disappeared in the sulfur $2p_{3/2,1/2}$ spectrum of this sample. All of these data point to a heterogeneous reaction surface with several chemical species present.

The changes in the sulfur $2p_{3/2,1/2}$ spectra for the samples are even more dramatic. In Fig. 2a,b, the binding energy for the sulfur $2p_{3/2,1/2}$ lines of the chalcopyrite have the same value, 161.2 eV (the two lines are separated by only 1.2 eV, and, unlike the $2p_{3/2,1/2}$ lines of copper, appear as a broadened singlet, hence only one binding energy is often given—for the more intense $2p_{3/2}$ line). In Fig. 2c, however, the binding energy has remained at 161.2 eV, indicating the presence of the original sulfide; this value is about 0.5 eV lower than that for elemental sulfur but indicates the approach of an oxidation product. Finally, in Fig. 2d, two forms of sulfur are observed. The first one, at a binding energy of 163.4 eV, is indicative of elemental sulfur; the second peak, however, at a binding energy of 168.0 eV, can be unequivocally attributed to the sulfate species. Thus one sees that the sulfur form and the sulfate ion are in equilibrium with one another on the electrochemically treated surface. These data are in agreement with the coexistence of the two chemical forms of sulfur on other sulfide minerals, such as galena (Perry et al., 1984a).

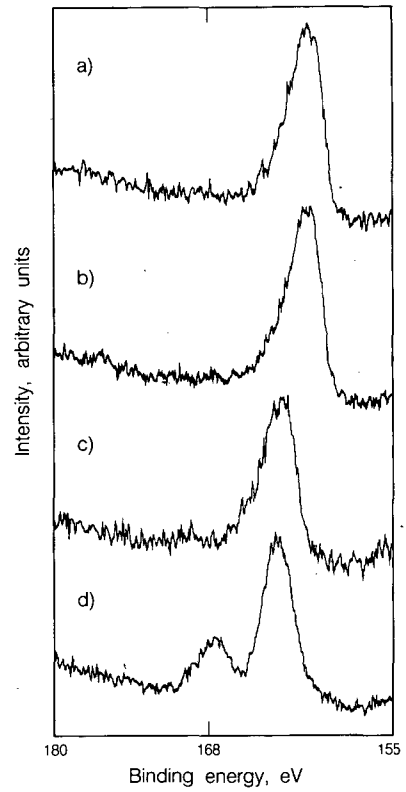

Figure 2. X-ray photoelectron spectrum of the sulfur $2p_{3/2,1/2}$ region of a chalcopyrite sample that has undergone different chemical treatment histories. **(a)** After 120 s of argon ion sputtering to remove natural contaminants. **(b)** After exposure of sample (a) to air for 30 min. **(c)** After exposure of sample (b) to H_2SO_4 (pH = 2.00) for 60 s. **(d)** After exposure of sample (c) to H_2SO_4 (pH = 2.00) at a potential of E = 0.540 V versus Ag/AgCl for 12 hours. [XBL 878-10303]

REFERENCES

Perry, D.L., 1986. Applications of surface techniques to chemical bonding studies of minerals (Chapter 18). *In* J.A. Davis and K.F. Hayes (eds.), Geochemical Processes at Mineral Surfaces (ACS Symposium Series No. 323). American Chemical Society, Washington, D.C., p. 389–402.

Perry, D.L., Tsao, L., and Taylor, J.A., 1984a. The calena/dichromate solution interaction and the nature of the resulting chromium(III) species. Inorg. Chim. Acta, v. 85, p. L57–L59.

Perry, D.L., Tsao, L., and Taylor, J.A., 1984b. Surface studies of the interaction of copper ions with metal sulfide minerals. *In* Proceedings, International Symposium on Electrochemistry in Mineral and Metal Processing (Vol. 84–10), p. 169–184.

Perry, D.L., and Taylor, J.A., 1986. X-ray photoelectron and Auger studies of Cu_2 and CuS. J. Mater. Sci. Lett., v. 5, p. 384–386.

Potentiostatic Measurement of the Diffusion Coefficient of UO_2^{2+} in Carbonate Media

D.L. Perry, S.L. Phillips, and J.D. Chung

For more than three decades a national program has been in progress to develop the necessary geochemical and other research for disposal of wastes from nuclear energy used in electric power production, in defense, and in energy research and development. An important aspect of this research is to understand the chemistry of actinides and other waste radionuclides in natural waters. The information is needed in order to calculate the amount of radioactivity that might be released from a subsurface disposal site at a distance of 5 km over a period of 10,000 years or more. The Environmental Protection Agency has promulgated final rules governing the release of radionuclides. One waste element of interest is uranium. Although a great deal more information is needed, the work summarized here was limited to the measurement of the diffusion coefficient of UO_2^{2+} in carbonate media. Besides the value of the diffusion coefficient, information was also obtained on the kinetics of the U(VI)-carbonate system in alkaline solution (Phillips et al., 1985).

Potentiometry, in which the faradaic current is monitored as a function of time under conditions of constant applied potential, was used to measure the diffusion coefficient in deaerated carbonate/bicarbonate solutions. A three-electrode system was used in which a potential of -1.300 V was maintained between a stationary mercury-drop working electrode and a saturated calomel reference electrode in an unstirred solution. Under these conditions the electroreduction of UO_2^{2+} is diffusion controlled when kinetic complications such as coupled chemical reactions or irreversibility in the electron transfer step are absent. Plots of the faradaic current versus $t^{-1/2}$ are linear, and the diffusion coefficient is calculated from the slope.

THEORY

The model used to measure the diffusion coefficient of UO_2^{2+} is based on an electrode reaction that is limited by the rate at which an electroactive substance diffuses to the electrode surface. The electrode reaction is formulated as a substance O being reduced by electron transfer at a conductive electrode surface, such as mercury, according to Eq. (1):

$$O + ne = R \,, \tag{1}$$

where n = number of electrons (e) and R is the reduced form of O. At a spherical electrode, e.g., a drop of mercury, the equation for Fick's law is written in the form of Eq. (2):

$$\frac{\partial C}{\partial t} = D\left[\frac{\partial^2 C}{\partial r^2} + \frac{2}{r}\frac{\partial C}{\partial r}\right], \tag{2}$$

Where C = concentration of substance O (moles/L), D = diffusion, t = time (s), and r = radial distance from the mercury drop surface (cm).

Initially, the concentration of substance O (UO_2^{2+}, in this work) is equal to that added to the solution, so that

$$t = 0, r_o < r < \infty : C = C^\circ \,, \tag{3}$$

where r_o is the mercury-drop electrode radius (cm) and C° is the concentration of electroactive substance (moles/L). On beginning the experiment, Eq. (1) takes place, and the following boundary conditions apply for semi-infinite radial diffusion:

$$t > 0, r \rightarrow \infty : C = C^\circ \,, \tag{4}$$

$$t > 0, r = r_o : C = 0 \,, \tag{5}$$

$$t > 0, r = r_o : \frac{D\partial C}{\partial r} = \frac{i}{nFA} \,. \tag{6}$$

In Eq. (6), i is the faradaic current (μA), F is the faraday (96,585.31 coul/mole), and A is the electrode surface area. Equation (4) assumes semi-infinite radial diffusion, Eq. (5) specifies that the electrode reaction take place under conditions in which the applied potential is in the limiting current region, and Eq. (6) equates the material flux at the electrode surface to the faradaic current i. When there are coupled kinetic reactions, an additional term, such as kC, is added to Eq. (2). In the absence of coupled homogeneous chemical reactions, the solution to Eq. (2) that takes into account the initial and boundary conditions is

$$i = \frac{nFACD^{1/2}}{(\pi t)^{1/2}} + \frac{nFACD}{r} \,. \tag{7}$$

According to Eq. (7), a plot of i versus $t^{-1/2}$ yields a straight line with a slope of $(nFACD^{1/2})/\pi^{1/2}$ and an intercept at $t^{-1/2} = 0$ of $(nFACD)/r$. The diffusion coefficient is then calculated from the slope or, less accurately, the intercept.

EXPERIMENTAL PROCEDURES

All chemicals were of analytical reagent grade and were used without further purification. The solutions were prepared by dissolving uranyl acetate $UO_2(C_2H_3O_2)_2 \cdot 2H_2O$, sodium carbonate, and sodium bicarbonate in deionized water that had been distilled from an all-quartz container. Before measurements were made all solutions were deaerated by bubbling water-saturated nitrogen into the solution through a fine glass frit for 10 min. The equipment used was a Princeton Applied Research Model 173 Potentiostat/Galvanostat coupled with a PAR Model 276 interface. The Model 276 interface was bussed to a Hewlett-Packard Model 85 microcomputer, which controlled the experiment and also stored the data. These data were digitized current-time or current-potential curves. Cyclic current-potential data were obtained by using the PAR Model 173/276 electrochemical system. These cyclic curves were important in obtaining qualitative information about the UO_2^{2+} system, such as adsorption or other complicated behavior. Besides computer storage, analog recordings were made on a Moseley Model 2D-2 X-Y recorder.

The electrochemical cell consisted of three electrodes: a three-drop mercury (Hg) hanging working electrode, a platinum-wire counter electrode, and a saturated calomel reference electrode (SCE). The SCE was connected to the cell via a salt bridge containing supporting electrolyte. This bridge served to prevent KCl in the SCE from entering the cell. The potential was maintained automatically between the working and reference electrodes by the potentiostat. The cell assembly was immersed in a water bath maintained at 25.0°C by a Fisher Model 173 Circulator. Triply distilled mercury was collected from a dropping-mercury electrode onto a Teflon spoon and hung on the stationary electrode. During experiments nitrogen gas was passed over the solution in the cell by raising the nitrogen bubbler out of the solution. Replicate results were obtained by using a fresh mercury electrode of constant surface area (0.07936 cm^2). The electrode area was calculated from the weight of 20 drops of mercury and the density of mercury.

A constant potential was applied by stepping from 0 to -1.300 V for 30 s, during which current-time curves were recorded. Blank $i-t$ curves were obtained to correct for background. A typical plot is shown in Fig. 1. The diffusion coefficient of UO_2^{2+} in carbonate media was calculated from plots like those shown in Fig. 2 and found to be 0.3×10^{-5} cm/s, in 0.1 M CO_3^{2-} and 0.1 M HCO_3^- buffer, pH = 9.8 at 25 ± 0.2°C.

Cyclic stationary-electrode polarograms indicate that the electroreduction of UO_2^{2+} in carbonate media is a complicated process in which sorption of a carbonate species can occur. Moreover, preliminary results indicate that the electrode reaction is complicated by a coupled homogeneous chemical reaction in which UO_2^{2+} reacts with carbonate to form the electroactive species prior to the electron-transfer step. Only one electrode reaction occurs: reduction of the U(VI)-carbonate species to a U(V) species (1). The stationary-electrode polarograms also show that the U(VI)/U(V) couple is either non-Nernstian (irreversible electron transfer) or complicated by a coupled, homogeneous chemical reaction that precedes the heterogeneous-electrode reaction.

ELECTROCHEMISTRY OF THE URANYL ION IN CARBONATE SOLUTION

Both cyclic current-potential and potentiostatic current-time curves were obtained for millimolar solutions of UO_2^{2+} in carbonate solutions (0.01–1.0 M) in order to study the effect of increasing carbonate concentration. Cyclic stationary electrode polarograms obtained at the two lowest concentra-

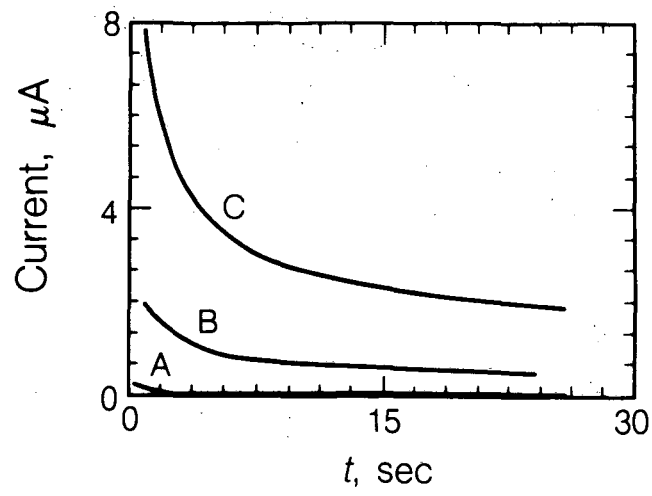

Figure 1. Faradaic current versus time for electroreduction of U(VI) to U(V) in 0.1 M $NaHCO_3$ and 0.1 M Na_2CO_3 solution; pH 9.8; Hg drop electrode (0.0794 cm^2 area). **(A).** 0.1 M $NaHCO_3$ and 0.1 M Na_2CO_3 solution; pH = 9.8. **(B)** 0.0004995 M U(VI). **(C)** 0.002001 M U(VI). [XBL 881-10013]

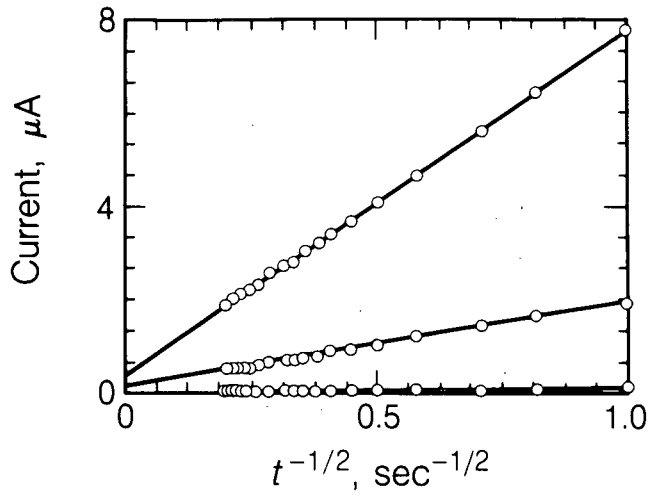

Figure 2. Plots of faradaic current versus $t^{-1/2}$ using data shown in Fig. 1. [XBL 881-10012]

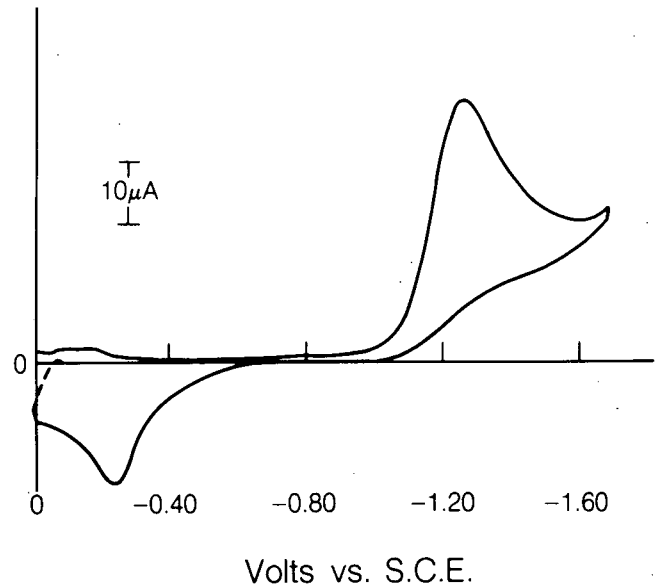

Figure 3. Cyclic stationary electrode polarogram for 0.00200 M U(VI) in buffer of 0.1 M $NaHCO_3$, 0.1 M Na_2CO_3, pH 9.8. Scan rate is 340 mV/s. [XBL 881-10011]

tions of carbonate, 0.01 and 0.02 M, showed a complex set of peaks at about −0.50 and −0.70 V versus SCE. These peaks appear to be typical of adsorption prewaves; however, they could also be small concentrations of electroreducible uranyl carbonates. These small peaks are followed by a larger irreversible peak, just prior to hydrogen evolution. The peaks disappear with increasing carbonate concentration, and the larger, drawn-out peak shifts to more positive potentials. The pH changed from 10.6 to 11.0 on addition of CO_3^{2-} (Table 1). The data are tentatively interpreted in terms of an aquo U(VI) species that complexes with one or more CO_3^{2-} ligands (Perry et al., 1984) to produce one or more complexes that are more easily reduced than the U(VI) species present in OH^- solutions. However, reduction of the carbonate species is still kinetically complicated because the anodic peak is far too positive for a Nernstian reaction (Fig. 3). Similar behavior was observed by Wester and Sullivan (1980). We conclude that U(VI)-carbonate in alkaline media is a stable species that is probably not easily reduced to a lower oxidation state in natural waters.

Table 1. Effect of increasing carbonate concentration on peak potentials and currents for 0.00100 M U(VI).

Concentration	pH	$E_p(c)$	$E_p(a)$	$i_p(c)$	$i_p(a)$
0.01	10.6	−1.7	−0.21	16.5	4.6
0.02	10.9	−1.60	−0.19	19.4	4.0
0.05	11.0	−1.43	−0.19	18.8	4.1
0.1	11.1	−1.33	−0.16	19.2	10.5
0.2	11.1	−1.26	−0.23	23.7	12.0
0.5	11.1	−1.17	−0.27	18.6	8.3
1.0	11.0	−1.12	−0.26	17.3	9.3

REFERENCES

Phillips, S.L., Perry, D.L., and Chung, J.D., 1985. Symposium for the Geochemistry of the Actinide Elements: Basic Chemical Studies in Support of Waste Disposal. Proceedings, 189th National Meeting of the American Chemical Society, Miami Beach, Florida.

Perry, D.L., Tsao, L., and Brittain, H.G., 1984. High resolution luminescence studies of $K_4UO_2(CO_3)_3$. J. Lumin., v. 29, p. 285–294.

Wester, D.W., and Sullivan, J.C., 1980. Electrochemical and spectroscopic studies of uranium(IV), -(V), and -(VI) in carbonate-bicarbonate buffers. Inorg. Chem., v. 198, p. 2838.

Prediction of Mineral Solubilities in Aqueous Mixed Electrolytes to Temperatures up to 300°C

K.S. Pitzer and R.T. Pabalan

Equilibrium considerations based on experimental data and thermodynamic calculations provide an important basis for understanding rock-fluid interactions in natural systems. The problems associated with experimental work, particularly in complex and concentrated electrolyte mixtures, underscore the need for a predictive model for calculating mineral-solution equilibria in brine systems. Applications for such a model include studies of (1) seawater and evaporite systems; (2) the origin and evolution of brines in sedimentary basins, rift zones, and geothermal systems; and (3) desalination.

This article summarizes a paper (Pabalan and Pitzer, 1987) that applies the ion-interaction model for aqueous electrolyte solutions (developed by Pitzer, 1973, 1979) to solubility calculations. Solubilities in binary and ternary electrolyte mixtures in the system Na–K–Mg–Cl–SO_4–OH–H_2O were calculated to high temperatures using available thermodynamic properties of the solids and of aqueous electrolyte solutions and were compared with experimentally determined values. Although a few parameters were adjusted to fit ternary mixtures, no additional parameters are needed by the model to describe electrolyte properties in more complex mixtures; consequently, the solubility calculations can be extended to compositions relevant to natural fluids.

THEORY AND EQUATIONS

Mineral solubilities in concentrated electrolyte solutions can be calculated from thermodynamic considerations provided that equilibrium constants are known and activity coefficients can be obtained. For a hydrated solid, $M_{\nu_M}X_{\nu_X}\cdot\nu_0H_2O$, having ν_M positive ions (M) of charge z_M, and ν_X negative ions (X) of charge z_X, and ν_0 molecules of water, the equilibrium constant at a fixed temperature and pressure for the dissolution reaction

$$M_{\nu_M}X_{\nu_X}\cdot\nu_0H_2O = \nu_M M^{+z_M} + \nu_X X^{-z_X} + \nu_0 H_2O \quad (1)$$

is given by

$$\ln K = -(\nu_M\mu_M^\circ + \nu_X\mu_X^\circ + \nu_0\mu_{H_2O}^\circ)/RT + \mu_s^\circ/RT\,, \quad (2)$$

where the μ_i°'s represent the chemical potential of the solid, of water, or of the aqueous ion in a defined standard state.

The equilibrium constant can be calculated provided that the chemical potential values are available at the temperature and pressure of interest. At constant pressure, the temperature dependence of the standard state chemical potential of component i is given by

$$\mu_{i,T_f}^\circ - \mu_{i,T_r}^\circ = -S_{i,T_r}^\circ(T_f - T_r)\,, + \int_{T_r}^{T_f} C_{p_i}^\circ\, dT - T\int_{T_r}^{T_f}(C_{p_i}^\circ/T)dt\,, \quad (3)$$

where S_i° represents the standard entropy of component i, $C_{p_i}^\circ$ is the standard-state heat capacity (at constant pressure), which itself is a function of temperature, and T_r and T_f are the reference temperature and temperature of interest, respectively.

In the case of water, the chemical potential at T and P can be conveniently calculated from the equation of state of Haar et al. (1984). The data base for the solids, although it includes some inaccuracies and lacks some data for high temperatures, is well organized and given in the compilations of Kelley (1960), Stull and Prophet (1971), Robie et al. (1978), and Wagman et al. (1982). The reference values at 25°C of the chemical potentials, enthalpies, and entropies for water, the aqueous ions, and the solids considered in this study, plus the temperature functions for the heat capacities of the aqueous electrolytes and the solids, are given in Pabalan and Pitzer (1987).

In terms of activities or molalities, the equilibrium constant for the solubility reaction is given by

$$\ln K = \nu_M\ln(m_M\gamma_M) + \nu_X\ln(m_X\gamma_X) + \nu_0\ln(a_{H_2O})\,, \quad (4)$$

where m_i and γ_i represent the molality and activity coefficient of the aqueous ions, respectively.

The activity of water is related to the osmotic coefficient, ϕ, by

$$\ln a_i = -\phi(M_w/1000)\sum_i m_i\,, \quad (5)$$

where M_w is the molecular mass of water and the sum covers all solute species.

The activity and osmotic coefficients are calculated from the ion-interaction model of Pitzer (1973, 1979). Equation (6) shows the expression for the osmotic coefficient, and Eq. (7) gives the activity coefficient of cation M, with an analogous expression for anion X,

$$(\phi-1) = -\frac{\partial G^{ex}/\partial n_w}{RT\sum_i m_i}$$

$$= (2/\sum_i m_i)\Big[-A_\phi I^{3/2}/(1+bI^{1/2})$$

$$+ \sum_c\sum_a m_c m_a (B^\phi_{ca} + ZC_{ca})$$

$$+ \sum_{c<c'}\sum m_c m_{c'}(\Phi^\phi_{cc'} + \sum_a m_a \psi_{cc'a})$$

$$+ \sum_{a<a'}\sum m_a m_{a'}(\Phi^\phi_{aa'} + \sum_c m_c\, \psi_{caa'})\Big] \quad (6)$$

and

$$\ln \gamma_M = \frac{1}{RT}\frac{\partial G^{ex}}{\partial m_M}$$

$$= z_M^2 F + \sum_a m_a(2B_{Ma} + ZC_{Ma})$$

$$+ \sum_c m_c(2\Phi_{Mc} + \sum_a m_a \psi_{Mca})$$

$$+ \sum_{a<a'}\sum m_a m_{a'}\psi_{Maa'} + |z_M| \sum_c\sum_a m_c m_a\, C_{ca}\,, \quad (7)$$

where c and c' are cations, a and a' are anions, z_M is the charge on cation M, and b is a universal constant with the value 1.2 $kg^{1/2}/mol^{1/2}$. The B_{ij} and C_{ij} terms can be evaluated empirically from data on binary systems, whereas the terms Φ_{ij} and ψ_{ijk} arise only for mixed solutions and can best be determined from common ion mixtures. Provided that the temperature and pressure dependencies of these parameters are known, solubilities in binary, ternary, and more complex mixtures can be calculated at various temperatures and pressures.

CHOICE OF INTERACTION PARAMETERS AND CALCULATED SOLUBILITIES IN BINARY AND TERNARY ELECTROLYTE MIXTURES

Ion-interaction coefficients necessary to calculate osmotic and activity coefficients at 25°C are available for a wide variety of binary mixtures (Pitzer, 1973; Pitzer and Mayorga, 1973). Recent experimental measurements of the thermodynamic properties of electrolyte solutions have extended our knowledge of these parameters to higher temperatures. An example of solubility calculations for a 1:1 electrolyte is shown in Fig. 1 for NaCl. In this case there is an extensive array of thermodynamic data for NaCl(aq) as reported by Pitzer et al. (1984). Their evaluation of these data yielded a complete set of parameters valid in the region 0–300°C and saturation pressure to 1 kbar. As Fig. 1 shows, there is excellent agreement between calculated and experimental solubilities, with a maximum deviation of 1.5% at 275°C.

An example of solubility calculations for a 2:2

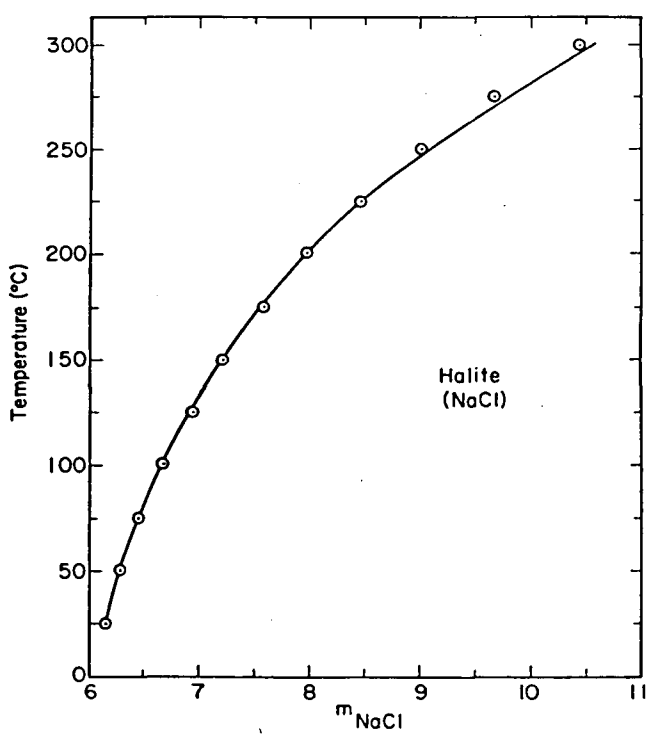

Figure 1. Calculated halite (NaCl) solubilities in the binary NaCl–H_2O system compared with experiment. The solubility data for 75–300°C are from Liu and Lindsay (1972); those for 75°C and below are from Linke and Seidell (1965). [XBL 886–2120]

electrolyte is shown in Fig. 2 for $MgSO_4$; data were obtained by using the ion-interaction parameters evaluated by Phutela and Pitzer (1986) from heat capacity, enthalpy, and osmotic coefficient data. Figure 2 shows that calculated solubilities are in good agreement with experimental data to 200°C.

For ternary mixtures, the mixing terms Φ_{ij} and ψ_{ijk} required for calculating osmotic and activity coefficients are available at 25°C for a large number of systems and have been reported by various investigators (Pitzer and Kim, 1974; Pitzer, 1975; Downes and Pitzer, 1976; Harvie and Weare, 1980; Harvie et al., 1984). Both these quantities undoubtedly vary with temperature, but they are both small and we found that it was an adequate approximation to hold Φ_{ij} at its 25°C value and to assume a simple temperature dependence for ψ_{ijk}. In most cases the form was: $\psi_{ijk} = A/T + B$, with examples illustrated in Figs. 3 and 4. Values of A and B for various mixtures are given in Pabalan and Pitzer (1987). Figure 3 shows that calculated solubilities in the system $NaCl-NaOH-H_2O$ are in good agreement with experimental values from 0–180°C; Fig. 4 shows that agreement is good to 200°C for the system $NaCl-MgCl_2-H_2O$.

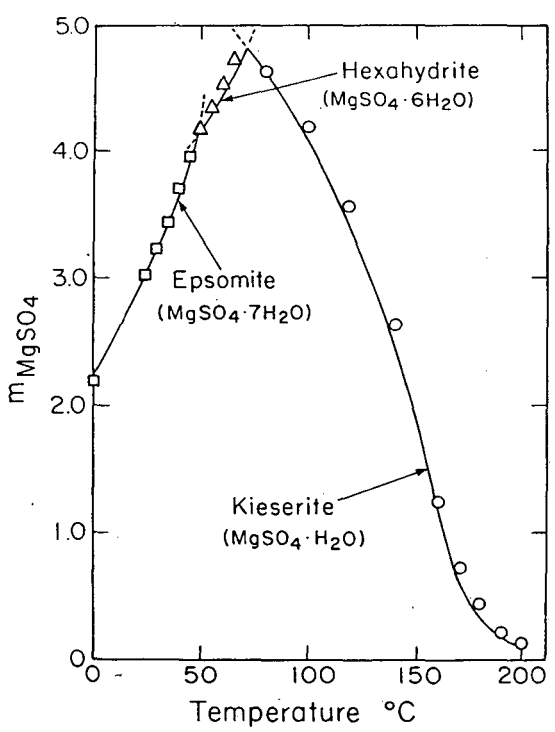

Figure 2. Calculated solubilities in the system $MgSO_4-H_2O$ compared with experimental data from Linke and Seidell (1965). [XBL 886-2121]

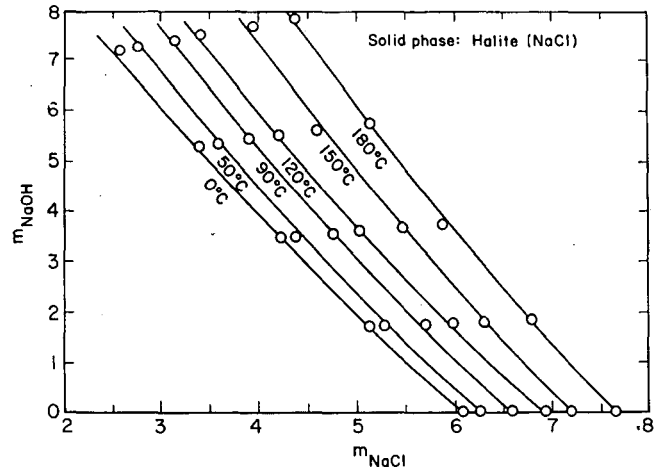

Figure 3. Calculated and experimental solubilities in the ternary system $NaCl-NaOH-H_2O$. The experimental data were taken from Linke and Seidell (1965) and were used to adjust $\psi_{Cl,OH,Na}$ above 25°C. [XBL 886-2122]

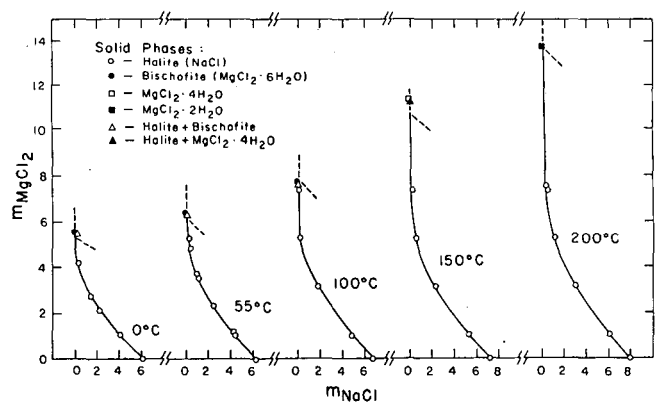

Figure 4. Calculated and experimental solubilities in the $NaCl-MgCl_2-H_2O$ system. Experimental data for 100°C and below are from Linke and Seidell (1965); those for 100°C and above are from Akhumov and Vasilev (1932). [XBL 886-2123]

In a few cases it was sufficient to use constant values of ψ_{ijk}. Examples are shown in Figs. 5 and 6 for the system $NaCl-Na_2SO_4-H_2O$ and $KCl-K_2SO_4-H_2O$, respectively.

DISCUSSION

Most measurements of the thermodynamic properties of binary electrolyte systems were made on solutions well below the saturation molalities. Thus solubility calculations mostly represent extrapolations of the molality dependence of the Pitzer equations to concentrations outside the fitted range. The results of this study indicate that in most cases, such extrapolations give a very good prediction of the

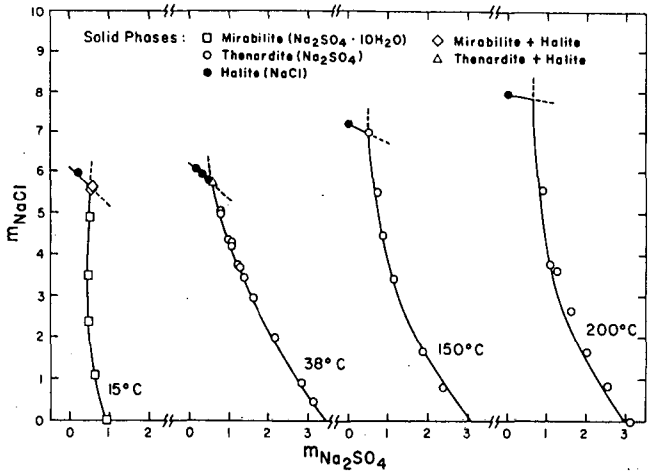

Figure 5. Calculated solubilities in the $NaCl-Na_2SO_4-H_2O$ system compared with experimental data from Linke and Seidell (1965) to 100°C and from Schroeder et al. (1935) to 150°C and above. [XBL 886-2124]

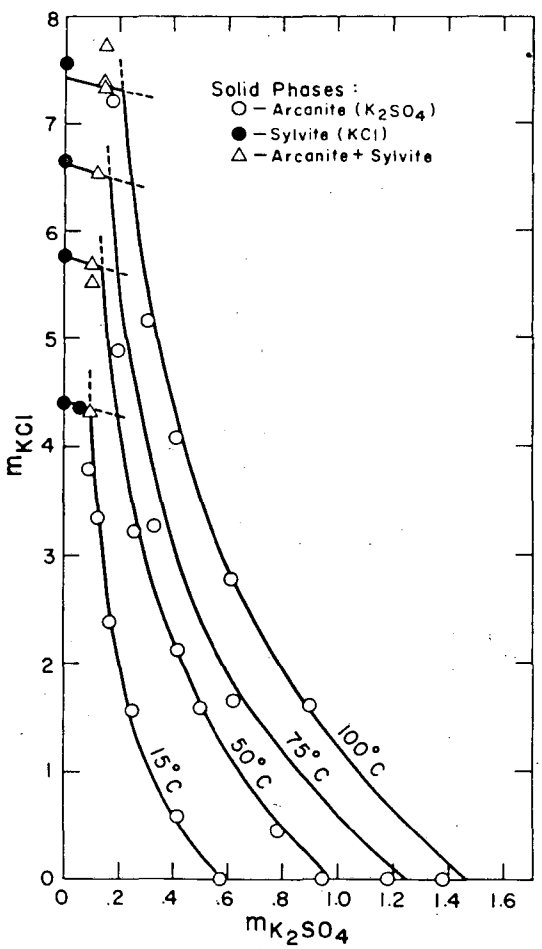

Figure 6. Calculated and experimental solubilities in the $KCl-K_2SO_4-H_2O$ system. The solubility values are from Linke and Seidell (1965). [XBL 886-2125]

activity and osmotic coefficients at saturation concentrations, particularly where the triple-ion interaction term, C^{ϕ}_{MX}, which essentially determines the molality dependence of the equations at high concentration, is well defined by data in solutions of moderate concentration. The results for binary and ternary systems involving the 2-2 electrolyte $MgSO_4$ are particularly encouraging because they indicate that the ion-interaction model can successfully predict activity and osmotic coefficients in concentrated electrolyte mixtures to high temperatures without the complication of an explicit accounting for ambiguous populations of ion pairs.

To the extent that the mixing terms Φ_{ij} and ψ_{ijk} were evaluated from solubility data, the calculations in the ternary systems can be considered as fitting exercises. However, the model is still valuable, since it permits interpolation between—and, in many cases, extrapolation beyond—the experimental solubility data for ternary systems. More importantly, since no additional parameters are needed for quaternary and more complex systems, the calculations can be extended to compositions relevant to natural fluids. As an initial test of the model and of our derived parameters, we calculated the solubility equilibria in the quaternary system $NaCl-KCl-MgCl_2-H_2O$. Figure 7 compares the predicted solubilities of halite, sylvite, or both, at 20, 55, and 90°C and at various molalities of $MgCl_2$ with experimental data given by Kayser (1923); Table 1 compares the predicted solution compositions up to 105°C at the quaternary invariant point halite+sylvite+carnallite

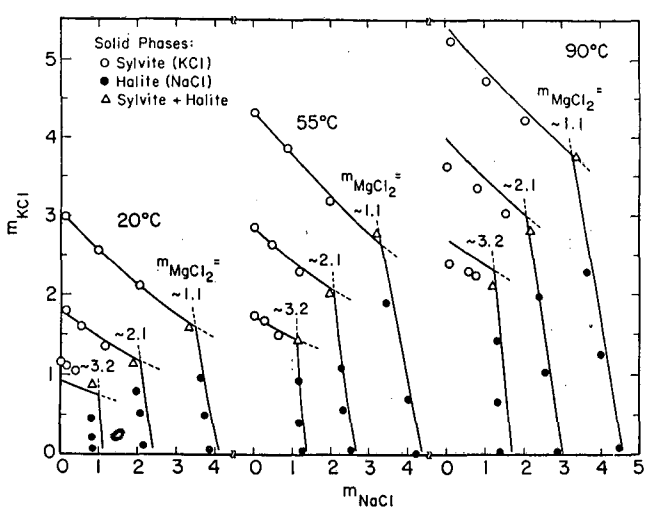

Figure 7. Predicted and experimental solubilities of halite and/or sylvite in the quaternary system $NaCl-KCl-MgCl_2-H_2O$ at 20, 55, and 90°C and at $MgCl_2$ molalities of approximately 1.1, 2.1, and 3.2. Experimental data are from Kayser (1923). [XBL 886-2126]

Table 1. Experimental and predicted compositions of solutions in the quaternary system NaCl–KCl–$MgCl_2$–H_2O at various temperatures in equilibrium with halite+sylvite+carnallite. Experimental values are from Serowy (1923).

	Experimental			Calculated		
T (°C)	m_{NaCl}	m_{KCl}	m_{MgCl_2}	m_{NaCl}	m_{KCl}	m_{MgCl_2}
0	0.50	0.35	3.77	0.50	0.31	3.83
10	0.46	0.45	3.84	0.50	0.40	3.89
15	0.45	0.49	3.88	0.51	0.45	3.92
20	0.44	0.54	3.92	0.51	0.50	3.95
25	0.43	0.59	3.97	0.51	0.56	3.98
30	0.42	0.64	4.02	0.52	0.61	4.02
40	0.40	0.73	4.13	0.52	0.73	4.09
50	0.39	0.83	4.26	0.51	0.85	4.18
55	0.39	0.88	4.34	0.51	0.91	4.23
60	0.38	0.93	4.41	0.50	0.98	4.29
70	0.39	1.03	4.58	0.49	1.10	4.42
80	0.39	1.13	4.72	0.47	1.21	4.57
83	0.41	1.15	4.78	0.46	1.24	4.63
90	0.46	1.22	4.90	0.44	1.31	4.76
95	0.49	1.27	4.99	0.43	1.35	4.87
100	0.55	1.32	5.10	0.41	1.39	4.99
105	0.60	1.37	5.20	0.39	1.43	5.12

+saturated solution with the experimental values of Serowy (1923). The agreement between predicted and experimental values is quite acceptable considering the uncertainties in the $MgCl_2$ ion-interaction parameters and in the thermodynamic properties of carnallite.

REFERENCES

Akhumov, E.I., and Vasilev, B.B., 1932. A study of aqueous solutions at elevated temperatures. II. Zh. Obs. Khimii, v. 2, p. 282-289 (in Russian).

Downes, C.J., and Pitzer, K.S., 1976. Thermodynamics of electrolytes. Binary mixtures formed from aqueous NaCl, Na_2SO_4, $CuCl_2$, and $CuSO_4$ at 25°C. J. Soln. Chem, v. 5, p. 389–398.

Haar, L., Gallagher, J.S., and Kell, G.S., 1984. NBS/NRC Steam Tables: Thermodynamic and Transport Properties and Computer Programs for Vapor and Liquid States of Water in SI Units. Hemisphere Publishing, 318 p.

Harvie, C.E., and Weare, J.H., 1980. The prediction of mineral solubilities in natural waters: The Na–K–Mg–Ca–Cl–SO_4–H_2O system from zero to high concentration at 25°C. Geochim. Cosmochim. Acta, v. 44, p. 981–997.

Harvie, C.E., Eugster, H.P., and Weare, J.H., 1982. Mineral equilibria in the six-component seawater system, Na–K–Mg–Ca–SO_4–Cl–H_2O at 25°C. II. Compositions of the saturated solutions. Geochim. Cosmochim. Acta, v. 46, p. 1603–1618.

Harvie, C.E., Møller, N., and Weare, J.H., 1984. The prediction of mineral solubilities in natural waters: The Na–K–Mg–Ca–H–Cl–SO_4–OH–HCO_3–CO_3–CO_2–H_2O system to high ionic strengths at 25°C. Geochim. Cosmochim. Acta, v. 48, p. 723–751.

Kayser, E., 1923. Die ersatzzahlen inkonstanter Lösungen über Kaliumchlorid und Natriumchlorid. Kali, v. 17, p. 1–9.

Kelley, K.K., 1960. Contributions to the data on theoretical metallurgy. XIII. High-temperature heat-content, heat-capacity, and entropy data for the elements and inorganic compounds. U.S. Bur. Mines Bull. 584, 232 p.

Linke, W.F., and Seidell, A., 1965. Solubilities of Inorganic and Metal Organic Compounds (4th ed.). American Chemical Society, Washington, D.C.; Vols 1 and 2.

Liu, C., and Lindsay, W.T., Jr., 1972. Thermodynamics of sodium chloride solutions at high temperatures. J. Soln. Chem., v. 1, p. 45–69.

Pabalan, R.T., and Pitzer, K.S., 1987. Thermodynamics of concentrated electrolyte mixtures and the prediction of mineral solubilities to high temperatures for mixtures in the system Na–K–Mg–Cl–SO_4–OH–H_2O. Geochim. Cosmochim. Acta, v. 51, p. 2429–2443.

Phutela, R.C., and Pitzer, K.S., 1986. Heat capacity and other thermodynamic properties of aqueous magnesium sulfate to 473 K. J. Phys. Chem., v. 90, p. 895–901.

Pitzer, K.S., 1973. Thermodynamics of electrolytes. I. Theoretical basis and general equations. J. Phys. Chem., v. 77, p. 268–277.

Pitzer, K.S., 1979. Theory: Ion interaction approach. *In* R. Pytkowitzc (ed.), Activity Coefficients in Electrolyte Solutions (Vol. 1). CRC Press, Cleveland, Ohio, p. 175–208.

Pitzer, K.S., and Kim, J.J., 1974. Thermodynamics of electrolytes. IV. Activity and osmotic coefficients for mixed electrolytes. J. Am. Chem. Soc., v. 96, p. 5701–5707.

Pitzer, K.S., and Mayorga, G., 1973. Thermodynamics of electrolytes: 2. Activity and osmotic coefficients for strong electrolytes with one or both ions univalent. J. Phys. Chem., v. 77, p. 2300–2308.

Pitzer, K.S., Peiper, J.C., and Busey, R.H., 1984. Thermodynamic properties of aqueous sodium chloride solutions. J. Phys. Chem. Ref. Data, v. 13, p. 1–102.

Robie, R.A., Hemingway, B.S., and Fischer, J.R., 1978. Thermodynamic properties of minerals and related substances at 298.15 K and 1 bar pressure and at higher temperatures. U.S. Geol. Survey Bull. 1452, 456 p.

Schroeder, W.C., Gabriel, A., and Partridge, E.P., 1935. Solubility equilibria of sodium sulfate at temperatures 150 to 350°C. I. Effect of sodium hydroxide and sodium chloride. J. Am. Chem. Soc., v. 57, p. 1539–1546.

Serowy, 1923. Die Polythermen der Viersalzpunkte des Chlorkaliumfeldes im quinären System ozeanischer Salzablagerungen; ihre teilweise Nachprüfung und Vervollständigung bis zu Temperaturen über 100°. Kali, v. 17, p. 345–350.

Stull, D.R., and Prophet, H., 1971. JANAF Thermochemical Tables (2nd ed.). Natl. Stand. Ref. Data Ser., U.S. Natl. Bur. Stand. (Vol. 37), 1141 p.

Wagman, D.D., Evans, W.H., Parker, V.B., Schumm, R.H., Halow, I., Bailey, S.M., Churney, K.L., and Nutall, R.L., 1982. The NBS tables of chemical thermodynamic properties. Selected values for inorganic and C_1 and C_2 organic substances in SI units. J. Phys. Chem. Ref. Data, v. 11, Suppl. 2, 392 p.

Geochemical Investigations of Fractured Heated Rock

H.A. Wollenberg and S. Flexser

In the near field of a nuclear waste canister, high temperatures will affect the local geochemical-hydrological regime. It is important that these hydrogeochemical processes be understood if the transport of radionuclides away from a breached canister is to be modeled and predicted. Thus the objective of these investigations is to develop an understanding of the interaction under elevated temperatures of radionuclides in the fracture-fluid system with the material lining the fractures. To accomplish this, samples of core from holes that have penetrated high-temperature zones are examined petrologically and geochemically. Emphasis to date has been on core samples of quartz monzonite, obtained by drilling back into rock previously subjected to a year-long heater experiment simulating high-level radioactive waste, conducted at Stripa, Sweden (Chan et al., 1980; Flexser et al., 1982). Recently, work has begun on core from a hole penetrating a fractured hydrothermal system in rhyolitic tuff (Wollenberg et al., 1987). In both cases, properties of rock in elevated temperature zones are compared with those of zones of lower and near-ambient temperature. In this article we describe radioelement investigations of core from the Stripa heater experiment.

RADIOELEMENT INVESTIGATIONS

The large-scale distribution of uranium, its daughter products and thorium in the Stripa quartz monzonite and its fracture-controlled groundwater system has been described by Wollenberg and Flexser (1985). At Stripa, U and Th, each at 30–40 ppm, are concentrated considerably higher than in most granitic rocks, and, contrary to their relative abundance in most granitics, they are present in nearly equal amounts. Uranium is strongly associated with fracture-filling material, predominantly chlorite, but in some cases epidote and sphene, enhancing the availability of U to the groundwater. Uranium is in relatively high concentrations (up to 20 ppb) in groundwater in the upper portion of the quartz monzonite, where Eh is also high (200–500 mV), whereas considerably lower concentrations (~ 1–5 ppb) occur at lower Eh (0–200 mV) at depths below 400 m (Andrews et al., 1982). Whole-rock gamma spectrometric measurements of U and Th in the heater drillback core (Wollenberg and Flexser, 1985) show U concentrations of ~ 40 ppm within ~ 1 m of the heater axis, decreasing to 33–36 ppm in core more distant from the heater. There is no corresponding change in Th over the same span. Initial alpha-track radiography suggested that U was added to fracture-lining material in rock near the heater. This, together with the whole-rock data, suggested mobility of U in response to fracturing and fluid movement in the near field of the heater.

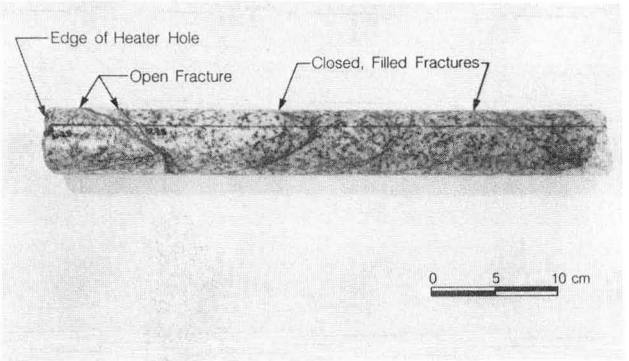

Figure 1. Core from Stripa drillback hole, showing locations of fractures examined for uranium. [CBB 809-10887A]

Subsequently, detailed alpha- and fission-track radiographic examinations have been made in core within 1 m of the heater, where distributions of radioelements in and adjacent to filled and open fractures have been measured. The zone of core investigated is shown in Fig. 1, with the prominent open fracture located 5–7 cm from the edge of the heater hole. The position of the open fracture near the edge of the heater hole, in comparison with closed fractures farther away from the heater, suggests that the fracture opened in response to heating (several kilograms of rock spalled from the wall of the heater hole, 0.3 m in diameter, 2.6 m long, during heating). Nelson et al. (1981) reported that water flowed readily into the hole in the early stages of heating. Flow into monitoring holes within several decimeters of the heater hole continued, but lessened throughout the experiment.

Both alpha- and fission-track densities were measured, because alpha tracks are from members of both the U and Th decay series, whereas fission tracks are essentially from ^{235}U. Fission tracks are generated by bombarding rock thin sections, covered with track detectors, by a flux of thermal neutrons that cause essentially only ^{235}U to fission. The resulting fission fragments impinge on the detectors, and their subsequent etching reveals the damage pits or "tracks" that show the distribution and abundance of U. Exposure of standards along with the thin sections permits determination of U concentration.

By comparing alpha- and fission-track patterns and track densities, we differentiate between contributions from the U and the Th decay series, because U fission-track densities are directly quantifiable into U concentrations (Table 1). In Fig. 2 alpha-track densities and U concentrations in fracture-lining minerals are plotted with distance from the edge of the open fracture. Alpha track densities and U concentrations decrease in similar patterns away from the sides of the fracture. The similarity in the profiles and the relatively high U concentrations (~ 0.2–1.6%) of the lining material, compared with 0.1–0.2% in filled fractures away from the heater and 0.003% in the rock, indicate that in this case U is the principal contributor to the alpha tracks. The pattern of decreasing U and alpha tracks away from the open fracture was not observed in a nearby fracture completely filled with similar minerals, where track

Table 1. Track densities and uranium concentrations of fracture-filling material and material lining an open fracture.

Distance from edge of heater hole (m)		Alpha-track density (T/mm^2)	Fission-track density (T/mm^2)	Uranium (%)
0.05[a]	Open fracture	Mean 1560 (range 550 to 2250)	Mean 1449 (range 254 to 2807)	Mean 0.88 (range 0.15 to 1.71)
0.15	Filling of closed fractures	438 ± 36[b]	273 ± 33	0.17 ± 0.02
0.39		574 ± 16		0.22[c]
1.40		562 ± 20		0.22
1.68		501 ± 20		0.19

[a]This population illustrated in Fig. 2.
[b]The ± values represent counting statistics.
[c]Estimated by applying the observed-to-calculated alpha-track ratio of 1.7, based on the 0.15 m position data.

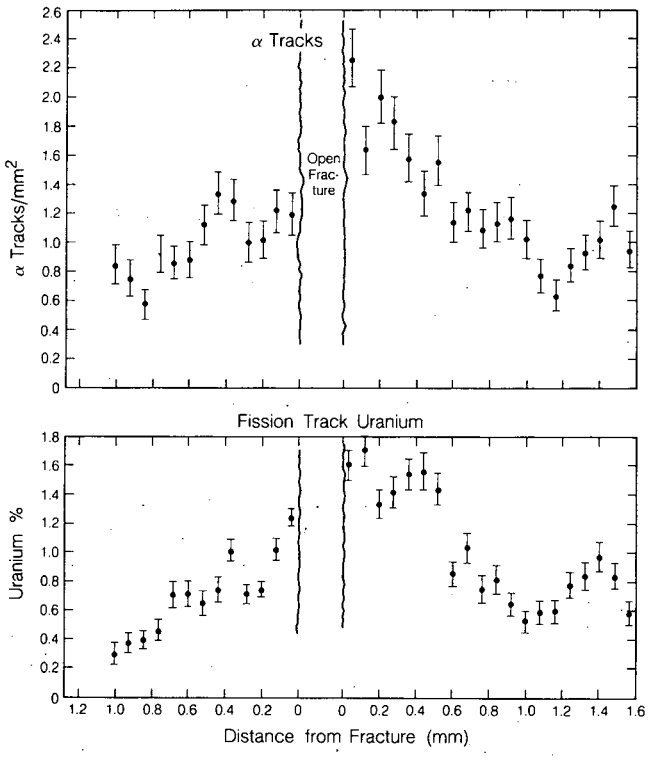

Figure 2. Alpha-track densities and U concentrations (by fission tracks) in filling material lining an open fracture in drillback core near the heater hole, Stripa experiment. Error bars reflect counting statistics. [XBL 8710-10411]

densities are uniform and U concentrations ~ 0.2%.

The measured track densities and U concentration patterns associated with the open fracture lead to consideration of evidence for mobility of U in response to prolonged heating of the rock. The U distribution pattern and evidence for disequilibrium in the U decay series are examined in this respect. The relatively high concentrations of U adjacent to the open fracture and its gradient in the lining material over the adjacent 1.2 mm, in contrast to lower concentrations and no apparent gradients in filled fractures of similar mineralogy, suggest that U was deposited from fluid moving through the fracture. Complicating factors, however, are the higher concentrations of U on the right side of the fracture (Fig. 2) and the approximate linear decrease of U away from the sides of the fracture. One might expect that recent addition of U to the lining material would result in relatively equal high concentrations on both sides.

Evidence for disequilibrium in the U decay series was examined by calculating the alpha-track densities that would result from the U concentrations (based on track densities of a U standard) observed from fission tracks and comparing those calculated track densities with observed alpha-track densities. This is illustrated in Fig. 3, where the ratio of observed to calculated track densities is plotted with distance from the fracture's edge. A ratio of 1 represents secular equilibrium and a ratio less than 1 represents the absence of some alpha-emitting daughters of the U decay series (disequilibrium). Uncertainties in spatial resolution of alpha and fission-track populations, abundances of U in standards, and track counting statistics cause uncertainties in the determination of the ratios, perhaps by 10–20%. However, there is still a strong indication of disequilibrium in that several values are less than 0.8. These could represent the recent addition of U to the fracture-lining material or the removal of one or more U daughter elements. The excess of alpha tracks at sites of relatively low U concentration, where the ratios are well above 1, might be due to the presence of thorium and its daughters in significant abundance. This may also be the case in the filled fracture ~ 15-cm from the heater hole, where U (by fission tracks) averages 0.17% and the ratio of observed to calculated alpha tracks is 1.7. As shown in Table 1, alpha track densities associated with filled-fracture material farther from the heater are somewhat greater than at the 15-cm position. If the ratio 1.7 holds for these populations, their U concentrations are also on the order of 0.2%.

Independent evidence of the preponderance of U in the zone within ~ 2 mm of the fracture was provided by secondary-ion mass spectrometric (SIMS) measurements. Even though the resolution of SIMS is not high enough for direct comparison with the

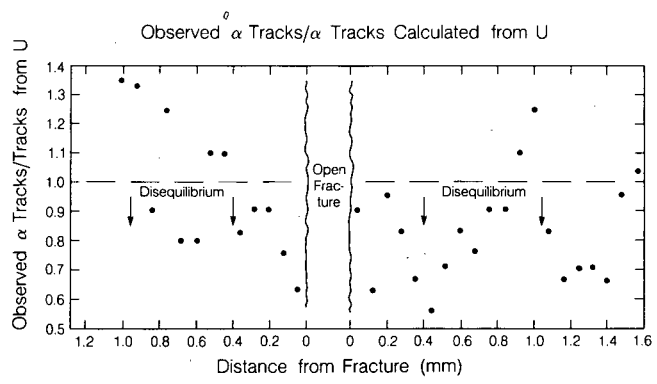

Figure 3. Ratios of observed alpha track densities to those calculated from concentrations, in filling material lining an open fracture in drillback core near the heater hole, Stripa experiment. Ratios less than 1 suggest disequilibrium in the U decay series. [XBL 8710-10412]

submillimeter resolution of the track-radiographic methods, SIMS is capable of determining element ratios over relatively small zones. The concentration ratio U/Th by this method is ~ 3, in contrast with approximate parity of U and Th in the rock matrix.

At this juncture the pattern of uranium distribution and the evidence of disequilibrium in the U-decay series suggest that U was mobilized and deposited along the open fracture. This implies that in a repository environment close to the waste canisters, fractures that had been mineral-filled might reopen in response to the thermally induced stress caused by the introduction and long-term presence of the waste. The open fractures would permit a vapor-dominated near-field thermal system to mobilize uranium leaking from a canister, but, depending on fracture-lining mineralogy, a significant portion of the uranium could be deposited on material lining the fractures in the near field of the canister.

When instrumentation becomes available in the new Center for Isotope Geosciences, micron-scale analytical methods will be used independently to determine U concentrations, U-series isotope ratios, and oxygen-isotope ratios to provide the detail necessary for more definitive examination of U mobility.

REFERENCES

Andrews, J.N., Giles, I.S., Kay, R.L.F., Lee, D.J., Osmond, J.K., Cowart, J.B., Fritz, P., Parker, J.F., and Gale, J., 1982. Radioelements, radiogenic helium and age relationships for groundwaters from the granites at Stripa, Sweden. Geochim. Cosmochim. Acta, v. 46, p. 1533–1543.

Chan, T., Littlestone, N., and Wan, O., 1980. Thermomechanical modeling and data analysis for heating experiments at Stripa, Sweden. *In* Proceedings, 21st Rock Mechanics Symposium, Rolla, Missouri, May 28–30, 1980.

Flexser, S., Wollenberg, H., and Wedge, D., 1982. Petrologic changes and damage in the Stripa quartz monzonite in response to heater tests. Lawrence Berkeley Laboratory Report LBL-14929.

Nelson, P., Rachiele, R., Remer, J., and Carlsson, H., 1981. Water inflow into boreholes during the Stripa heater experiments. Lawrence Berkeley Laboratory Report LBL-12574.

Wollenberg, H., and Flexser, S., 1985. The distribution of uranium and thorium in the Stripa quartz monzonite, Sweden. Uranium, v. 2, p. 155–167.

Wollenberg, H., Sorey, M., Farrar, C., White, A., Flexser, S., and Bartel, L., 1987. A core hole in the southwestern moat of the Long Valley caldera: early results. EOS: Trans. Am. Geophys. Union, v. 68, no. 20, p. 529–534.

GEOMECHANICS

The principal thrust of research in the Geomechanics group is to develop a fundamental understanding of the mechanical and hydrologic properties and behavior of rocks under conditions of temperature and pressure pertaining to engineered or natural phenomena in the upper crust. The properties of rocks and their behavior depend upon both the mechanical structure of the rock (pores, microcracks, joints, fractures, and faults) and the physical and chemical interactions between fluids and mineral surfaces.

Our research is both theoretical and experimental. Current theoretical studies involve applying the principles of linear elastic fracture mechanics to evaluate the effects of microcracks and asperities of contact on the deformation of intact and fractured rock. The effective elastic moduli of rocks containing any populations of cracks and fractures can readily be calculated. By accounting for the initiation, growth, and interaction of cracks, complete stress-strain curves can be derived that exhibit strain hardening, strain softening or slip weakening, dilation, and intrinsic instability under differential compressive stress. With this theoretical basis, practical problems such as borehole breakout and formation of fractures and spalling around underground excavations can be addressed. Faulting and earthquake rupture can be studied based on an understanding of the effects of asperities in contact on fracture deformation.

The growth of microcracks and their coalescence to form fractures is being studied experimentally using Wood's metal porosimetry. Wood's metal is molten above 90°C, when it resembles mercury, but at room temperature it is solid. By solidifying Wood's metal in rock specimens deformed to prescribed strains it is possible to preserve the deformed crack and fracture geometry in great detail for microscopic study after sectioning.

The interaction of the microstructure and composition of rock with the permeating fluid can have significant effects on properties such as permeability. Tests on shale have demonstrated significant differences in behavior as a function of temperature, depending upon the type and quantity of clay in the rock.

Important discoveries have been made relating to the geophysical and hydraulic properties of natural fractures. The flow of fluid through natural fractures is much more complex than previously thought, comprising a high-stress component that is very insensitive to the stress across the fracture and a low-stress component that is much more sensitive to stress than indicated by the well-accepted cubic law. Work is underway to model the mechanical deformation leading to this behavior.

Seismically, fractures can be represented by an elastic-displacement discontinuity. The resulting theoretical model predicts frequency-dependent coefficients for the reflection, transmission, and time delay of seismic waves propagating across a fracture and the existence of an interface wave that travels along the fracture.

Hollow-Cylinder Tests for Studying Fractures around Underground Openings

R.T. Ewy, N.G.W. Cook, and L.R. Myer

For decades, laboratory tests on rocks have sought to achieve a homogeneous state of stress on a sample of rock, and to increase these stresses until the entire sample fails. The aim of this procedure is to define the strength of the rock as a function of the stress invariants and also to obtain a constitutive law describing the pre-failure and post-failure stress-strain behavior. The results of these measurements have often been applied to the design of underground openings to determine, with varying degrees of success, the zones of rock subject to failure and the resulting deformations. In many cases the predictions do not match the observations, and the actual mechanism of failure is often different than expected.

This is not surprising when one compares the geometry and loading conditions around an underground opening to those in a laboratory core test. The rock next to an excavation is generally under polyaxial stress in a plane-strain condition but with only one free surface. It is subject to stress and strain gradients and is loaded by adjacent rock rather than by a testing machine.

The stress path imposed on the rock during excavation may be quite different than in a typical laboratory test. It is important to determine what effects these differences have on the strength, deformations, and failure mechanisms of the rock, and whether failure in this situation is controlled solely by the stress state. It is important also to determine whether stress-strain behaviors and macroscopic failure mechanisms observed in core tests are inherent material properties or if they are influenced by features such as core geometry, loading geometry, and stress path.

We are investigating these questions through experiments on thick-walled hollow cylinders of rock. These experiments incorporate several unique features: plane-strain loading, the ability to impose different stress paths on the rock, and "freezing" of the fracture geometry under load using a metal-injection technique.

EXPERIMENTAL TECHNIQUE

The rock samples are cored as coaxial hollow cylinders with an inner diameter of 1 inch, an outer diameter of 3.5 inches, and a length of 5.75–6 inches. Both the surface of the hole and the outer diameter are lined with rubber sleeves to seal the sample, and it is assembled into a test cell (Fig. 1). The sample is constrained to zero axial deformation, as would usually occur underground. In this way the effects of the plane-strain loading condition and of the intermediate stress on the strength and failure process can be examined.

Uniform fluid pressure is applied to the outer diameter using a servo-controlled testing machine, and a separate pressure is applied in the hole using a manually operated screw pump capable of measuring precise volume changes. These two independent pressures allow the imposition of various stress paths on the inner surface, and the tangential stress can be tensile or compressive. In this way one can explore the effect of stress path on the strength and failure process.

The apparatus has been designed to provide fluid access directly to the rock, and this is used to fill the pores and any stress-induced fractures with a liquid metal alloy at a constant pressure of about 5 MPa

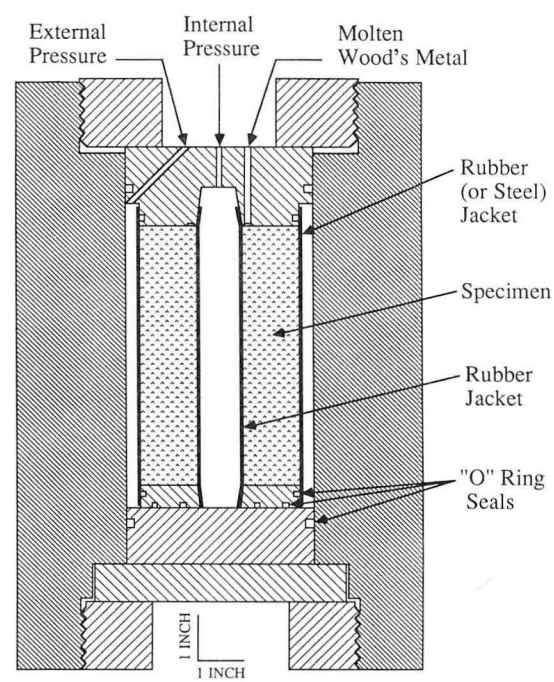

Figure 1. Simplified scale drawing of testing apparatus. [XBL 886-2270]

during the experiment. The experiment is performed at 90°C, at which temperature the alloy, commonly called Wood's metal, is liquid and resembles mercury. After the failure load is reached the sample is cooled while keeping the stresses constant, thus "freezing" the stress-induced fractures in the state they exist under load. In this way one can carefully study the processes of fracture formation and progression around the hole. Because of the scale of the sample, the resulting fractures can also provide insight into the transition from microscale fractures to macroscale fractures.

Observations that can be made from these tests include the elastic and inelastic deformations of the opening, stress level at which yield and rupture occur, types of fractures formed, extent of fractured zone, and stable shape achieved.

RESULTS

Preliminary tests have been performed on Berea sandstone, chosen because it is a well-documented clastic rock, considered to be nearly isotropic. Further tests will be performed shortly on Indiana limestone and possibly other rock types.

The final load state in all experiments was 75 MPa effective pressure on the external boundary and zero effective pressure in the hole. In one loading case the external pressure was increased with constant zero pressure in the hole, and in other cases the internal pressure was reduced to zero with constant external pressure. In all cases the ultimate failure zone consisted of two diametrically opposite regions, always oriented in the same direction (Fig. 2). The loading is axisymmetric, but the failure is not, as has been noted by other researchers using assumed isotropic materials (Daemen and Fairhurst, 1971; Gay, 1973; Bandis et al., 1987). The preferred failure direction is probably determined by slight anisotropy of the rock.

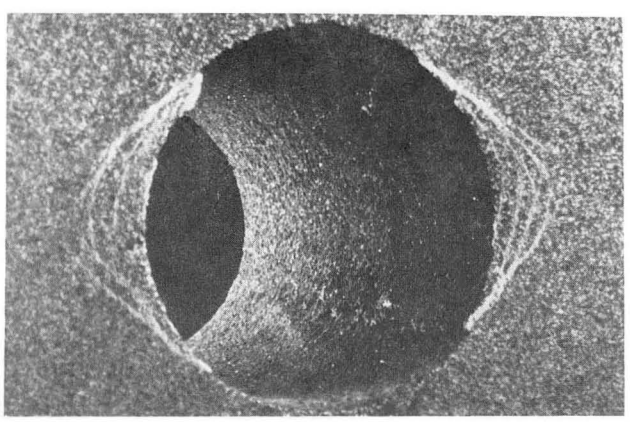

Figure 2. Failure resulting from slowly decreasing internal pressure with constant external pressure. Sample was saturated with Wood's metal prior to failing, then cooled under load. [XBB 870-9167]

The failure process itself appears to be one of progressive spalling, in which intact slabs of fairly uniform thickness are successively separated from the surrounding rock by fractures oriented roughly parallel to the free surface. The exact process of fracture growth and coalescence is not yet clear. It is interesting that brittle spalling behavior occurs in a porous clastic rock such as Berea sandstone. In fact, spalling appears to be a dominant mode of failure in underground openings subject to high stress conditions (Hoek and Brown, 1980; Maury, 1987). The discrete nature of the fractures and the preferred orientation under axisymmetric load raise doubts about the applicability of continuum theories describing the formation of a strain-softened or plastic zone.

Failure began at loads of about 63 MPa external pressure with constant zero pressure in the hole, and 3.5 MPa in the hole with constant 75-MPa external pressure. These loads would cause a tangential stress on the boundary of the hole equal to at least twice the uniaxial strength of this rock. This high strength of the hole wall agrees with the experimental results of Mastin (1984), Haimson and Herrick (1985), Santarelli and Brown (1987), and many others, as documented by Guenot (1987). It may be due to size effect, intermediate (axial) stress, or the geometry and stress and strain gradients.

The loading case of increasing external pressure resulted in triangular failure zones with distinct pointed tips. When the internal pressure was reduced to cause failure, it was reduced in one case slowly (Fig. 2) and in another instantaneously. These latter stress paths are similar to the excavation of an underground opening. Compared to the case of increasing external pressure, these failure zones encompassed a greater portion of the hole wall but were not as deep. Under microscopic observation the sample unloaded slowly revealed pointed tips in the failure zones, but the sample unloaded instantaneously did not. The failure zones of least depth resulted from the instantaneous pressure drop, possibly indicating an increase in strength with higher strain rate, as has been observed in other laboratory tests.

It thus appears that geometry, stress path, and perhaps strain rate or time do affect the strength, deformation, and failure processes of rock. Further research should yield qualitative and quantitative information directly relevant to the design of underground openings. Additional items of importance

include the effect of the axial stress magnitude, the influence of pre-existing discontinuities, and possible boundary effects due to the proximity of the outer diameter of the hollow cylinder. This latter issue will be investigated shortly by using steel jackets of appropriate stiffness to ensure that the external pressure acts exactly like a far-field stress.

REFERENCES

Bandis, S.C., Lindman, J., and Barton, N., 1987. Three-dimensional stress state and fracturing around cavities in overstressed weak rock. *In* Proceedings, Sixth International Congress on Rock Mechanics, Montreal, Canada, v. 2, p. 769–776.

Daemen, J.J.K., and Fairhurst C., 1971. Influence of failed rock properties on tunnel stability. *In* Proceedings, 12th U.S. Symposium on Rock Mechanics, New York, AIME, p. 855–875.

Gay, N.C., 1973. Fracture growth around openings in thick-walled cylinders of rock subjected to hydrostatic compression. Int. J. Rock Mech. Min. Sci., v. 10, p. 209–233.

Guenot, A., 1987. Stress and rupture conditions around oil wellbores (in French). *In* Proceedings, Sixth International Congress on Rock Mechanics, Montreal, Canada, v. 1, p. 109–118.

Haimson, B.C., and Herrick, C.G., 1985. In situ stress evaluation from borehole breakouts, experimental studies. *In* Proceedings, 26th U.S. Symposium on Rock Mechanics, Rotterdam, Netherlands, A.A. Balkema, p. 1207–1218.

Hoek, E., and Brown, E.T., 1980. Underground excavations in rock. Institute of Mining and Metallurgy, London, United Kingdom.

Mastin, L., 1984. The development of borehole breakouts in sandstone, (M.S. thesis). Stanford University.

Maury, V., 1987. Observations, researches and recent results about failure mechanisms around single galleries. *In* Proceedings, Sixth International Congress on Rock Mechanics, Montreal, Canada, v. 2, p. 1119–1128.

Santarelli, F.J., and Brown, E.T., 1987. Performance of deep wellbores in rock with a confining pressure-dependent elastic modulus. *In* Proceedings, Sixth International Congress on Rock Mechanics, Montreal, Canada, v. 2, p. 1217–1222.

Fracture Stiffness and Aperture As a Function of Applied Stress

D.L. Hopkins, N.G.W. Cook, and L.R. Myer

Understanding how single fractures deform under stress has important applications in a number of fields, including geophysics and hydrogeology. Most laboratory experiments provide information about the average response of a fracture, for example, average displacement as a function of stress. However, to understand phenomena such as fluid flow and seismic-wave transmission through fractured rock requires more detailed information about such attributes as contact area and aperture and knowledge of how they change under load. To that end, an analytical model has been developed and implemented numerically to study the deformation of a single fracture subjected to a normal stress. The model has been used to calculate aperture profiles and specific stiffness for specified fracture geometries.

THE MODEL

A typical rock fracture can be envisioned as a number of areas of contact surrounded by voids. A common approach to modeling the mechanical deformation of fractures has been to represent the fracture surfaces as parallel planes separated by asperities of varying height (Greenwood and Williamson, 1966; Gangi, 1978; Brown and Scholz, 1985). Implicit in these models is the assumption that the contacts are sufficiently far apart so that they do not interact mechanically. The closure of the fracture is based solely on the deformation of the asperities between the opposing fracture surfaces.

The model developed for the studies discussed here is also an asperity model, but the asperities are not assumed to be mechanically independent.

Rather, the force carried by each asperity depends on its height and the heights and proximity of neighboring asperities. Further, the model accounts for the deformation of the half-spaces defining the fracture in addition to the deformation of the asperities. The deformation of the half-spaces is calculated using the Boussinesq solution for displacement beneath a loaded circle assuming a constant-stress boundary condition. The deformation at any point on the half-planes is assumed to be a linear combination of the displacements caused by the forces acting on all asperities in the region.

CHANGES IN FRACTURE APERTURE WITH STRESS

An important area of research in recent years has been the investigation of the conditions under which flow through a fracture can be described by the cubic law for laminar flow; i.e., flow is proportional to the cube of the fracture aperture. If the adjacent sides of a fracture are not in contact, experiments indicate that the cubic relationship holds (e.g., Snow, 1965; Iwai, 1976). In reality, rock fractures are not usually open; rather, they are better described as two rough surfaces in contact at a number of asperities.

Deviations from the cubic law have been observed by a number of researchers who have analyzed data from laboratory experiments using both induced and natural fractures (e.g., Iwai, 1976; Witherspoon et al., 1980; Engelder and Scholz, 1981; Raven and Gale, 1985; Gale, 1987). For natural fractures, departures from the cubic law are seen even at relatively low stress levels, on the order of 10 MPa. The divergence increases with increasing stress.

A possible explanation for the divergence from the cubic law is the change in fracture topography that occurs with increasing stress. The change in aperture geometry can be illustrated in two dimensions. Figure 1a shows a two-dimensional slice through an idealized fracture, with the dotted lines representing reference planes. If only the deformation of the asperities is considered, and a normal stress is applied, the reference lines remain parallel and come together by an amount that depends on the deformation of the contacts. For the case of a simple interpenetration model, the surfaces come together in a manner equivalent to allowing the top and bottom fracture surfaces to overlap, as illustrated in Fig. 1b. The dimensions of the asperities themselves are important, but their spatial location on the fracture surface is not.

For comparison, the model described herein was used to calculate the displacement across the same

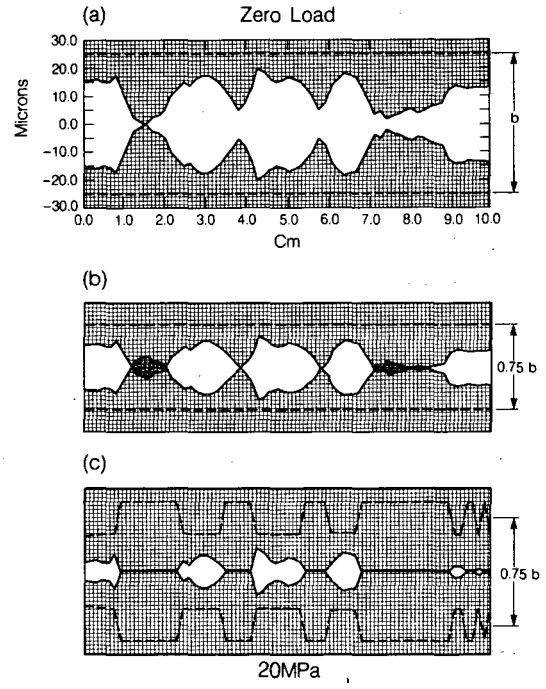

Figure 1. Comparison of fracture closure for two deformation models: **(a)** fracture cross section under zero load; **(b)** interpenetration model; and **(c)** model including deformation of the half-planes defining the fracture. |XBL 886-10288|

idealized fracture pictured in Fig. 1a. When a normal force is applied, the reference lines no longer remain parallel, because the asperities indent the half-spaces defining the fracture (Fig. 1c). The resulting reduction in void area of 80% is approximately double the reduction obtained from the interpenetration model. Although the average displacements across the fracture are similar, the difference in fracture void geometry resulting from the two models is quite significant.

This change in geometry has important implications for fluid flow through the fracture. The asperities have the effect of propping the fracture open while more-than-average closure occurs in open areas. To illustrate, consider the idealized case of a single circular asperity between two parallel fracture surfaces, as pictured in cross section in Fig. 2 (top). Under zero load, the fracture aperture b is everywhere equal and fluid flow is proportional to b^3 (Snow, 1965). As the load is increased, the fracture surfaces deform as illustrated in Fig. 2 (bottom). The aperture at the asperity is $b - \delta$, where δ is the deformation of the asperity. The high-aperture pockets formed around the asperity are everywhere surrounded by a region of smaller aperture (a). Under stress, the large voids formed around asperities will

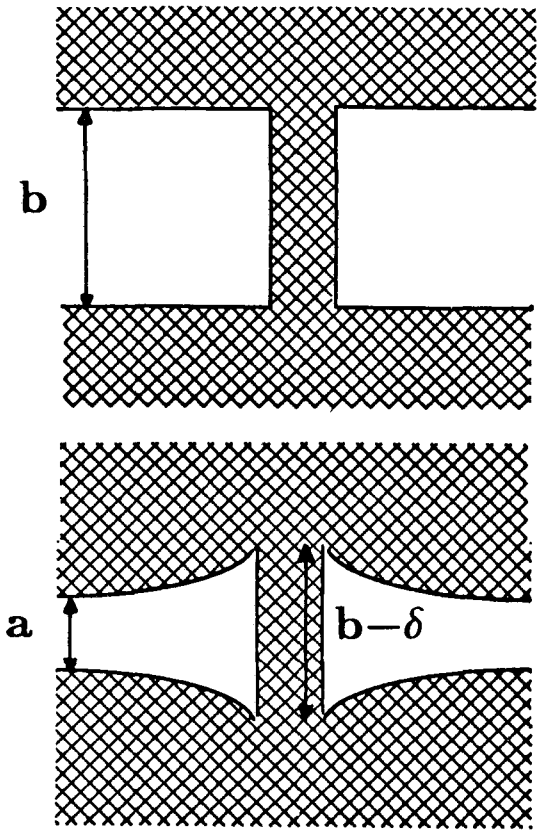

Figure 2. Cross section of aperture for a single asperity between parallel plates under zero load **(top)** and after a load is applied **(bottom)**. [XBL 886-2273]

affect the storativity of the fracture, whereas the permeability will be largely controlled by the smaller-aperture regions adjacent to the voids.

SPECIFIC STIFFNESS

Specific stiffness is a property that defines the relationship between applied stress and fracture deformation. To begin to understand which properties of the fracture surface are important in determining specific stiffness, the model described previously was used to perform a parameter-sensitivity study. In particular, the effect of the asperity height distribution was studied. It is the distribution of heights that determines the rate at which asperities come into contact with increasing stress. The values of specific stiffness calculated using the model were compared with laboratory measurements.

Curves of specific stiffness were generated using 100 disks of equal diameter (1 mm) distributed randomly across a planar surface, as shown in Fig. 3.

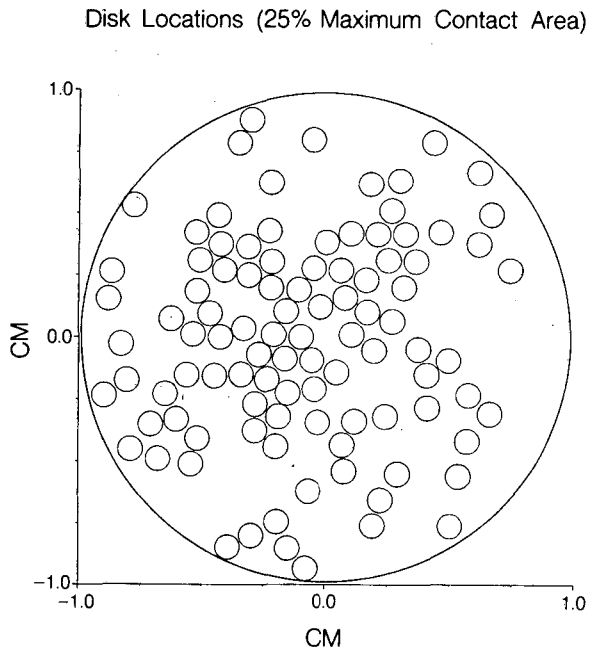

Figure 3. Spatial orientation of disks used to generate the curves of stress versus specific stiffness plotted in Fig. 4. Disk diameter is 1 mm. [XBL 886-2272]

The maximum contact area in this case is 25% when all disks are in contact. Using this spatial distribution, specific stiffness as a function of applied stress was calculated for a variety of height distributions. The resulting curves, and histograms of the height densities, are plotted in Fig. 4. The results show that for a fixed spatial geometry, a wide range of behavior can be obtained by varying the distribution of heights of the asperities. In all cases, the stiffness curve rises sharply as increasing numbers of asperities come into contact and then begins to level off as the rate at which asperities come into contact diminishes. Eventually, the curve reaches a horizontal asymptote when there is no increase in contact area with increasing stress.

For comparison, the specific stiffnesses calculated using the model are compared to a curve obtained by L. Pyrak-Nolte et al. (1987) in the laboratory for a granite core sample with a fracture oriented perpendicular to the axis of the core. In making the model calculations, a Young's Modulus of 50.0 GPa and a Poisson's ratio of 0.2 were used to coincide with the values of the granite used in the laboratory experiment. For the laboratory data, specific stiffness was calculated by taking the inverse of the tangent slope to the stress-versus-displacement curve. The curve obtained from the laboratory data is plotted in Fig. 4 as the bold line. As can be seen

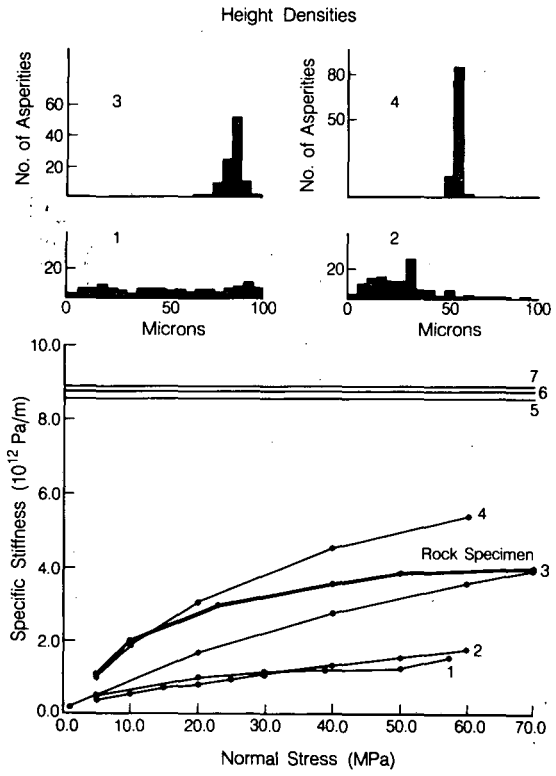

Figure 4. Curves (1–4) of stress versus specific stiffness for the spatial geometry shown in Fig. 3 and different height distributions (plotted as histograms). The bold line is a curve obtained from laboratory data for a granite core specimen containing a single fracture. Lines 5–7 are the values of a stiffness calculated assuming the asperities to be of equal height (heights of 80, 50, and 30 μm, respectively). [XBL 886-10289]

from the figure, the curves obtained using the model, assuming a maximum contact area of 25% and asperity heights distributed between zero and 100 μm, bracket the results obtained in the laboratory for this particular specimen. The best matches are with curves 3 and 4, which have height distributions that are more tightly clustered than those used to generate curves 1 and 2.

The horizontal lines in Fig. 4 show the maximum stiffness that can be achieved using the particular spatial configuration shown in Fig. 3. The curves represent the limiting case that occurs when all asperities are of equal height. Curves 5, 6, and 7 correspond to asperity heights of 80, 50, and 30 μm, respectively. The differences between the lines are due to the differences in the compressibility of the asperities; the shorter asperities are less compressible and thus create a stiffer interface. The small differences between the lines indicate that the absolute asperity height is not as important as the distribution of heights.

CONCLUSIONS

In modeling the behavior of a single fracture with an asperity model, it has been shown that accounting for the deformation of the half-spaces defining the fracture leads to greater reductions in aperture than would be calculated if only the deformation of the asperities were considered. In addition, the spatial geometry of the asperities becomes important, leading to differential deformation of the fracture surfaces that can result in significant changes in void geometry. This change in aperture geometry with stress has particularly important implications for fluid-flow calculations.

Previous work demonstrated that the spatial geometry of the asperities and their dimensions are important parameters in determining fracture stiffness (Hopkins et al., 1987). For a constant contact area, small, dispersed contact points form a stiffer interface than large or clustered contact areas. Results discussed here show that the distribution of asperity heights affects both the shape and magnitude of the stress-stiffness curve. The more nearly equal the heights, the stiffer the fracture. The distribution of heights is found to be more important than the absolute height.

REFERENCES

Brown, S.R., and Scholz, C.H., 1985. Closure of random elastic surfaces in contact. J. Geophys. Res., v. 90, p. 5531–5545.

Engelder, T., and Scholz, C.H., 1981. Fluid flow along very smooth joints at effective pressures up to 200 megapascals. *In* Mechanical Behavior of Crustal Rocks. Am. Geophys. Union Monogr. 24, p. 147–152.

Gale, J.E., 1987. Comparison of coupled fracture deformation and fluid flow models with direct measurements of fracture pore structure and stress-flow properties. *In* I.W. Farmer et al. (eds.), Proceedings, 28th U.S. Symposium on Rock Mechanics. A.A. Balkema, Rotterdam, Netherlands, p. 251–261.

Gangi, Anthony F., 1978. Variation of whole and fractured porous rock permeability with confining pressure. Int. J. Rock Mech. Min. Sci., v. 15, p. 249–257.

Greenwood, J.A., and Williamson, J.H., 1966. Contact of nominally flat surfaces. Proc. R. Soc. London, Ser. A., v. 295, p. 300–319.

Hopkins, D.L., Cook, N.G.W., and Myer, L.R., 1987. Fracture stiffness and aperture as a function of applied stress and contact geometry. *In* I.W. Farmer et al. (eds.), Proceedings, 28th U.S. Symposium on Rock Mechanics. A.A. Balkema, Rotterdam, Netherlands, p. 251–261.

Iwai, K., 1976. Fundamental studies of fluid flow through a single fracture (Ph.D. thesis). University of California, Berkeley.

Pyrak-Nolte, L.J., Myer, L.R., Cook, N.G.W., and Witherspoon P.A., 1987. Hydraulic and mechanical properties of natural fractures in low permeability rock. *In* G. Herget and S. Vongpaisal (eds.), Proceedings, Sixth International Congress on Rock Mechanics. A.A. Balkema, Rotterdam, Netherlands, p. 225–231.

Raven, K.B., and Gale J.E., 1985. Water flow in a natural rock fracture as a function of stress and sample size. Int. J. Rock Mech. Min. Sci. Geomech. Abstr., v. 22, p. 251–261.

Snow, D.T., 1965. A parallel plate model of fractured permeable media (Ph.D. thesis). University of California, Berkeley.

Witherspoon, P.A., Wang, J.S.Y., Iwai, K., and Gale, J.E., 1980. Validity of cubic law for fluid flow in a deformable rock fracture. Water Resour. Res., v. 16, p. 1016–1024.

Fracture Mechanics Applied to Faulting and Earthquake Rupture

J.M. Kemeny and N.G.W. Cook

There has been a growing interest in recent years in the geometry and properties of the earthquake source. In the brittle seismogenic region (less than 20 km depth), the earthquake source is often characterized by a growing, cracklike rupture or the progressive failure of individual asperities or barriers (Das and Aki, 1977). The models usually assume that slip occurs along a planar region, which has been shown to be a fairly accurate description for shallow strike-slip earthquakes (Kagan and Knopoff, 1985). One way to characterize the earthquake source is through static earthquake-source parameters. These include the seismic moment, stress drop, and strain-energy release associated with an unstable rupture. Relationships between these parameters were originally derived for simple source geometries by Knopoff (1958) and Keilis Borok (1959). More recently, Madariaga (1979), Rudnicki and Kanamori (1981), Rudnicki et al. (1984), and others have looked at relationships between the source parameters for more complicated source geometries. These papers show that the seismic moment can be overestimated and the stress drop can be underestimated, due to the interaction of neighboring slip zones. All of the above results are based on the change in compliance of an elastic body due to the addition of cracks, and they show a linear relationship between stress drop and moment and also show that the strain energy release is proportional to the stress drop squared. These analyses do not address criteria for the starting and stopping of earthquake rupture, and implicit in these results is the fact that the far-field stress is being held constant.

Also related to the earthquake source is the phenomena of slip weakening. Slip weakening describes the stress-displacement relationship for a fault undergoing shear, and, in conjunction with the applied boundary conditions, slip weakening gives criteria for the starting and stopping of earthquake rupture and aseismic slip (Kemeny and Cook, 1987). In particular, slip weakening describes a decreasing strength with increasing displacement, with instability occurring when the slope of the slip-weakening curves becomes less than the unloading stiffness of the surrounding ground, and aseismic slip occurring when the opposite is true (Rice, 1983; Li, 1986). The two limits for the unloading stiffness are horizontal for stress-controlled boundary conditions and nearly vertical for displacement-controlled boundary conditions, with the actual stiffness for field conditions falling somewhere between. For instance, assuming that the ground surrounding the fault responds as a Maxwell viscoelastic solid, Li and Rice (1983) derive relationships for the unloading stiffness. A method of measuring the stiffness for field conditions was proposed by Stuart (1981). Laboratory measurements of slip weakening by testing precut surfaces in shear under a constant normal stress have been conducted by Jaeger and Cook (1979), Cook (1981), Dieterich (1981), Okubo and Dieterich (1984), and others. Two important parameters with regard to slip weakening are the displacement over which slip

weakening occurs, referred to as the critical slip-weakening distance, and the stress drop that occurs from the start of slip weakening to the stress value at which uniform sliding occurs across the sample. Recent laboratory studies have revealed important relationships between the critical slip-weakening distance, stress drop, and the roughness of the fault surface (Okubo and Dieterich, 1984) and also relationships with the applied normal stress (Wong, 1986).

Up until now a direct correlation between the static earthquake-source parameters and slip weakening has not been made. Slip weakening predicts nonlinear stress-displacement relationships for faulting, while the assumptions in the standard stress-moment relations assume a linear stress-strain relationship. It has usually been assumed that slip weakening is a result of nonlinear processes occurring at the tips of sharp cracks, due to the singularity in the elastic solution for a sharp crack (Palmer and Rice, 1973). However, it has recently been shown by Kemeny and Cook (1987) that slip weakening can be the result of the propagation of a cracklike rupture, or the progressive failure of asperities, without regard for the nonlinear processes at the tips of the cracks. Of course, nonlinear processes may be operating at the tips of cracks or the edges of asperities, but the consequences of these nonlinear processes will be of lower order when larger-scale changes in geometry are occurring, such as the failure of asperities. This difference is important, because the breaking of asperities or the rupture in a cracklike mode is also associated with the occurrence of a moment, stress drop, and energy release, as described above. Thus the moment and stress drop due to an unstable rupture occur by the same mechanism as that causing slip weakening, and this sharing of the mechanism constrains relationships between the moment, stress drop, and strain-energy release due to unstable rupture.

The constraints on the source parameters takes several forms. First of all, the relationship between the moment and stress drop will not be linear as usually assumed, but rather, the stress and moment will depend on each other in a nonlinear fashion and also depend on parameters such as the fracture energy G_c. In addition, the relationships between the source parameters will depend strongly on the boundary conditions, in particular the unloading stiffness of the ground surrounding the fault. This makes it possible to have a large release of energy with almost no seismic moment. These constraints may help to explain some discrepances between the source parameters, as noted by McGarr et al. (1979) and others.

Theoretical and numerical models have been developed for the mechanical behavior of a fault plane containing asperities, and these models are used to predict relationships between the static source parameters. The asperities are modeled with collinear distributions of cracks in an elastic matrix, where the asperity is the object between cracks. The stress distributions in the asperities, and the criteria for the progressive failure of the asperities, are calculated using the theory of elastic-brittle fracture mechanics (e.g., Rice, 1968). We consider very simple source geometries, such as the propagation of a single crack or the breaking of a single asperity. These simple formulas allow insight, and the results are derived in closed form. For example, the nonlinear stress-moment relation for a source consisting of a single growing crack is given by

$$M_o = \frac{G_c{}^2 E^2}{\tau^3 \pi (1 - \nu^2)(1 + \nu)} ,$$

where M_o is the seismic moment, G_c is the fracture energy, E is Young's modulus, τ is the effective shear stress, and ν is Poisson's ratio.

The results of more complicated configurations of asperities, and statistical distributions such as a factual distribution of asperities, have also been calculated. Our models take into account the propagation of the cracks or progressive failure of the asperities, and this results in both slip weakening and nonlinear relationships between the source parameters. A meaningful way of presenting the results of these models is on a plot of stress drop versus moment. The traditional relationships between the source parameters plot as a straight line on a stress-moment diagram, and thus the use of these diagrams in seismology has not afforded any additional insight. However, in our analysis, the relationship between stress drop and moment is nonlinear, and, in conjunction with the applied boundary conditions, the nonlinear stress-moment diagram gives information on the starting and stopping of unstable rupture and regions of aseismic slip and also the moment, stress drop, and energy release due to an unstable rupture. These stress-moment diagrams are similar in many respects to the stress-displacement or stress-strain diagrams used in rock mechanics (Jaeger and Cook, 1979). An example of a nonlinear stress-moment diagram for the breaking of a single asperity is shown in Fig. 1, which shows that during an instability, the stress drop and the seismic moment are related by the linear relationship

$$\tau = k_m M_o ,$$

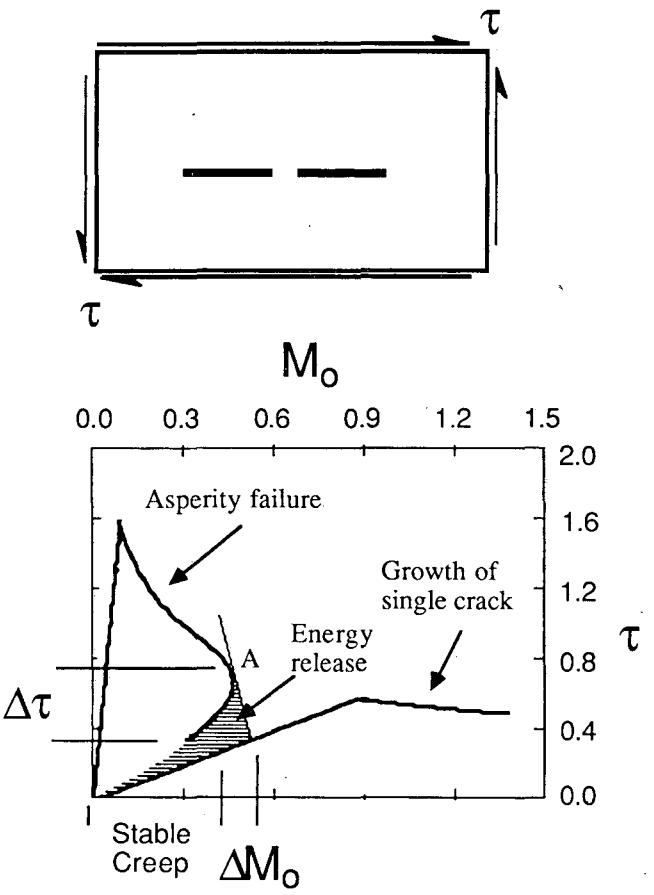

Figure 1. Normalized shear-stress/seismic-moment diagram for a single asperity represented by the region between two equal-sized cracks. Instability occurs when the slope of the stress-moment diagram becomes less than the unloading stiffness of the surrounding ground (point A in the figure). The stress drop, change in moment, and energy release for the instability are shown. [XBL 886-221]

where k_m is related to the unloading stiffness of the surrounding ground. Values for the unloading stiffness of the ground surrounding the San Andreas fault have been estimated to be about 0.25 bar/mm.

REFERENCES

Cook, N.G.W., 1981. Stiff testing machines, stick slip sliding, and the stability of rock deformation. *In* The Mechanical Behavior of Crustal Rocks, Am. Geophys. Union, Monogr. 24.

Das, S., and Aki, K., 1977. Fault plane with barriers: a versatile earthquake model. J. Geophys. Res., v. 82, p. 658–5670.

Dieterich, J. H., 1981. Constitutive properties of faults with simulated gouge. *In* N.L. Carter et al. (eds.), The Mechanical Behavior of Crustal Rocks. Am. Geophys. Union, Monogr. 24, p. 103–120.

Jaeger, J.C., and Cook, N. G. W., 1979. Fundamentals of Rock Mechanics, Chapman and Hall, London, United Kingdom.

Kagan, Y.Y., and Knopoff, L., 1985. The two point correlation function of the seismic moment tensor. Geophys. J.R. Astr. Soc., v. 83, p. 637–656.

Keilis Borok, V., 1959. On estimation of the displacement in an earthquake source and of source dimensions. Ann. Geofis. (Rome), v. 12, p. 205–214.

Kemeny, J.M., and Cook, N.G.W., 1987. Crack models for the failure of rock in compression. *In* C.S. Desai et al. (eds.), Constitutive Laws for Engineering Materials: Theory and Applications (Vol. II), Proceedings, Second International Conference on Constitutive Laws for Engineering Materials, Tucson, Arizona, January 5–8, p. 879–887.

Knopoff, L., 1958. Energy release in earthquakes. Geophys. J., v. 1, p. 44–52.

Li, V.C., 1987. Mechanics of shear rupture applied to earthquake zones. *In* B. Atkinson (ed.), Rock Fracture Mechanics, Academic Press, New York, p. 351–428.

Li, V.C., and Rice, J.R., 1983. Preseismic rupture progression and great earthquake instabilities at plate boundaries. J. Geophys. Res., v. 88, p. 4231–4246.

Madariaga, R., 1979. On the relation between seismic moment and stress drop in the presence of stress and strength heterogeneity. J. Geophys. Res., v. 84, p. 2243–2250.

McGarr, A., Spottiswoode, M., Gay, N.C., and Ortlepp, W.D., 1979. Observations relevant to seismic driving stress, stress drop, and efficiency. J. Geophys. Res., v. 84, p. 2251–2261.

Okubo, P.G., and Dieterich, J.H., 1984. Effects of physical fault properties on frictional instabilities produced on simulated faults. J. Geophys. Res., v. 89, p. 5817–5827.

Palmer, A.C., and Rice, J.R., 1973. The growth of slip surfaces in the progressive failure of overconsolidated clay. Proc. R. Soc. London, Ser. A, v. 332, p. 527–548.

Rice, J.R., 1968. Mathematical analysis in the mechanics of fracture. *In* H. Liebowitz (ed.), Fracture: An Advanced Treatise (Vol. 2). Academic Press, New York, p. 191–311.

Rice, J.R., 1983. Constitutive relations for fault slip and earthquake instabilities. Pure Appl. Geophys., v. 121, p. 443–475.

Rudnicki, J.W., Hirashima, K., and Achenbach, J.D.,

1984. Amplification of moment and strain energy release due to interaction of different size fault slip zones. J. Geophys. Res., v. 89, p. 5828–5834.

Rudnicki, J.W., and Kanamori, H., 1981. Effects of fault interaction on moment, stress drop, and strain energy release. J. Geophys. Res., v. 86, p. 1785–1793.

Stuart, W.D., 1981. Stiffness method for anticipating earthquakes. Bull. Seis. Soc. Am., v. 71, p. 363–370.

Wong, T.-F., 1986. On the normal stress dependence on the shear fracture energy. *In* Earthquake Source Mechanics, Am. Geophys. Union, Monogr. 37.

Permeability of Shale At Elevated Temperatures and Pressures

L.R. Myer and T.L. Christian

A laboratory test program is in progress to measure rock-matrix permeabilities as a function of temperature and pressure for different shale rocks. These measurements provide baseline data for studies of shale as potential media for siting of a nuclear-waste repository. To perform the measurements, an apparatus was constructed with the capability of measuring permeabilities as low as 6×10^{-24} m^2 at effective pressures up to 14 MPa and temperatures up to 150°C. The measurement technique is based on the transient-pulse decay method as first described by Brace et al. (1968). The apparatus design was modified to permit measurements at elevated temperatures.

Permeability measurements were completed on samples of the Green River Formation and an eastern Devonian shale (Rhinestreet Formation). Dry samples were obtained.

TEST PROCEDURES

In the transient-pulse decay method, the sample and two fluid volumes, referred to as "upstream and downstream reservoirs," are brought to an equilibrium pore pressure. An instantaneous pressure pulse is then imposed on one reservoir, increasing the pressure at that end of the sample. The pore fluid system is then isolated from external pressure sources, and the subsequent decay of the pressure pulse as a function of time is related to the sample hydraulic conductivity by the following expression:

$$\Delta P/PP = \exp\left[\frac{KAt}{l}\left(\frac{1}{S_d}+\frac{1}{S_u}\right)\right],$$

where $K = k\gamma_w/\mu$ is the hydraulic conductivity of the sample, μ is the viscosity of the fluid, k is intrinsic permeability, γ_w is the specific weight of the fluid, t is time, l is the sample length, ΔP is the differential pressure between reservoirs, PP is the magnitude of the pressure pulse, S_u and S_d are the compressive storage of the upstream and downstream reservoirs, respectively. From this expression it is seen that the hydraulic conductivity can be obtained from the slope of a semilog plot of the dimensionless differential pressure versus time. The terms S_d and S_u, the compressive storage of the reservoirs, are specific parameters of the test apparatus and are measured independently.

To perform a test, the sample is first saturated with pore fluid using a vacuum saturation process. After placement of the samples in the test vessel, the confining pressure is slowly brought up to 20.7 MPa. As the confining pressure is increased, the pore pressure is raised by a hand pump. A 3.4-MPa differential between the two fluid systems is maintained until the desired pressures are achieved.

The temperature inside the vessel is slowly raised at approximately 0.5°C/min to the required setting (pressure increases due to temperature are relieved in both systems). The system is allowed to equilibrate for approximately 24 hours under the elevated temperature and pressure conditions. Once pore-pressure equilibrium is achieved, a pressure pulse is applied to the upstream reservoir by a hand pump, or, as in the case for very-low-permeability rocks such as the Green River Formation, a pressure decrement is applied to the downstream reservoir. The decay of the pressure pulse with time is monitored until either it has decayed completely or 100 hours of test time have passed. After completion of one test on the sample, the upstream and downstream reservoirs are allowed to communicate with each other and with the external pressure source, and

the pore pressure and/or temperature are increased or changed to the appropriate settings. The test procedure is then repeated at the new conditions.

GREEN RIVER FORMATION TEST RESULTS AND DISCUSSION

The Green River Formation is a finely laminated dolomitic marlstone containing yellowish gray and brown organic and inorganic material. Hydraulic conductivity measurements were performed on three samples of the Green River Formation: one with bedding oriented perpendicular to the fluid-flow direction and two with bedding oriented parallel to flow. Tests were performed at an effective stress (confining pressure minus pore pressure) of approximately 10 MPa and at temperatures of about 24°C, 75°C, 132°C, and 144°C. Deionized water was used as the pore fluid.

Testing was first conducted on the samples with bedding oriented parallel to the fluid-flow direction. One sample was tested at 24°C, 75°C, and 132°C. As the temperature was being raised to 144°C, the sample holder developed a leak, causing the core to be flooded with silicon oil. Thus, the second core (same orientation) was tested at 144°C and 24°C.

Results in Fig. 1 show that at 10 MPa effective stress, increasing the temperature by about 120°C over ambient resulted in an increase in permeability by about an order of magnitude. The increase is nonlinear, as shown in Fig. 1, with a greater increase at higher temperatures than at lower temperatures. These results are quite contrary to observed temperature effects upon permeability of sandstones (Weinbrandt et al., 1975) but are in accordance with the increase in permeability noted with increase in temperature for crystalline rocks (Summers et al., 1978).

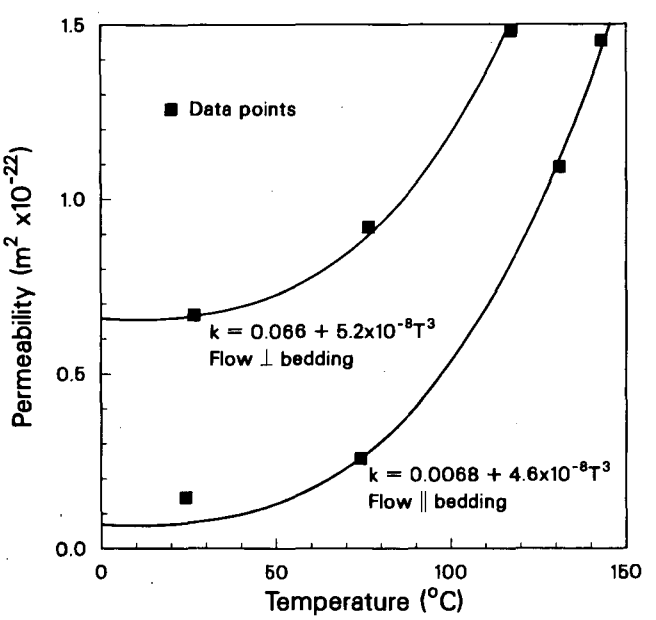

Figure 1. Permeability versus temperature of Green River Formation for flow directions parallel and perpendicular to bedding. Tests performed at 10 MPa effective stress. [XCG 8710-11416]

The results also show some similarity with observed hydraulic characteristics of single fractures. As shown in Fig. 1 the data are well fit by a curve that corresponds to permeability proportional to the cube of temperature. As noted by Gale (1982) and others, the permeability of a fracture is proportional to the fracture aperture cubed. If it is assumed that this change in apertures of the microfractures is directly proportional to temperature, then a relationship between permeability and the cube of temperature might be expected.

Though little data on the effect of temperature on the permeability of low-porosity rocks are available, there are considerable data on the effect of temperature on thermomechanical properties. A nonlinear decrease in thermal conductivity of Green River Shale with increased temperature has been observed by Prats and O'Brien (1975). They were able to fit the decrease to a second-order polynomial of temperature. Nonlinear decreases in moduli and increases in thermal expansion with increasing temperature have been observed, for example, by Richter and Simmons (1974), Heard and Page (1982), and Myer (1985). The explanation for these changes in mechanical properties with temperatures has been attributed to microcrack growth and an increase in microcrack density as a result of heating. Even though heating rates are low, microcrack growth can occur due to differential thermal expansion of the mineral grains.

Results of a test to evaluate hysteresis due to heating-induced microcrack growth showed that the permeability measured after the sample had been cycled to elevated temperature was equivalent to that measured before heating. These results suggest that additional cracking did not occur as a result of heating and that cracks opened or closed reversibly in response to changes in temperature.

As can be seen in Fig. 1, the permeabilities measured with with flow perpendicular to bedding are greater than the permeability measured with flow parallel to bedding. However, the same nonlinear (cubic) relationship was observed. A higher permeability perpendicular to bedding was not expected but indicated that the interconnectivity of the microstructure is not influenced by the bedding directions.

EASTERN DEVONIAN SHALE RESULTS AND DISCUSSION

The Rhinestreet Formation is a black, fairly fissile, silicious shale. Bedding was approximately at 80° from centerline of the core. Permeability measurements were conducted on one sample oriented with bedding approximately 80° to the direction of fluid flow. A suite of tests at 10.0 MPa, 11.4 MPa, 13.8 MPa, and 17.2 MPa effective stress and temperatures of 22°C, 75°C, and 135°C was conducted.

Before testing, the core was vacuum saturated to 76 μm of mercury with deionized water. During the saturation process the core appeared to swell, with separations forming along bedding planes and at the locations of incipient fractures. The sample remained intact, however, with no visible indication that any of the separations extended completely across the sample.

The test sequence began with measurements at the lowest effective stress level (10 MPa). While holding this effective stress constant, measurements were made at the various elevated temperatures. The effective stress was again held constant while the sample was cooled to ambient temperature. To evaluate hysteresis in the measurements, permeability tests were also performed during the cooling cycle. After completion of a temperature cycle at one effective stress state, the effective stress was raised to the next level and the temperature cycle repeated. It was decided to follow a test sequence involving cycling of temperature at a constant effective stress rather than cycling effective stress at a constant temperature because test results on the Green River Formation had indicated some nonreversible effect of effective pressure cycling but no such effect of temperature cycling.

Results of the tests are plotted in Fig. 2. The numbers on the data points indicate the sequence in which testing progressed from one pressure/temperature state to another. One general trend in the data is that the permeability decreased as the effective stress increased. However, there appears to be a coupled effect of temperature. At any one effective stress state, the response of the permeability during the temperature cycle was complex, with both increases and decreases occurring. However, at each effective stress state the permeability at ambient before the temperature excursion was always higher than the permeability at ambient after completion of the temperature cycle. Thus, the net result of performing a temperature excursion is, at all effective stress levels, a decrease in permeability. Currently, testing is under way to establish if the permeability loss due to changing effective stress states and thermal cycling is recoverable.

In comparing the results from the Green River Formation tests (Fig. 1) and eastern Devonian shale tests (Fig. 2), very different behavior is seen for the two types of materials. First of all, the permeability of the eastern Devonian shale was one to two orders of magnitude higher than that of the Green River Formation. More importantly, however, the effect of temperature on the two types of shale was completely different. For the Green River Formation, permeability increased in proportion to the temperature cubed, and this trend was reversible. However, the net result of a temperature cycle on the eastern Devonian shale was a decrease in permeability. Also, throughout the temperature cycle the percentage change in permeability from the ambient value was much less for the eastern Devonian shale than for the Green River Formation sample. It is believed that the presence of illite clay in the eastern Devonian shale sample may be responsible for different behavior, but the mechanisms controlling the behavior are not yet understood.

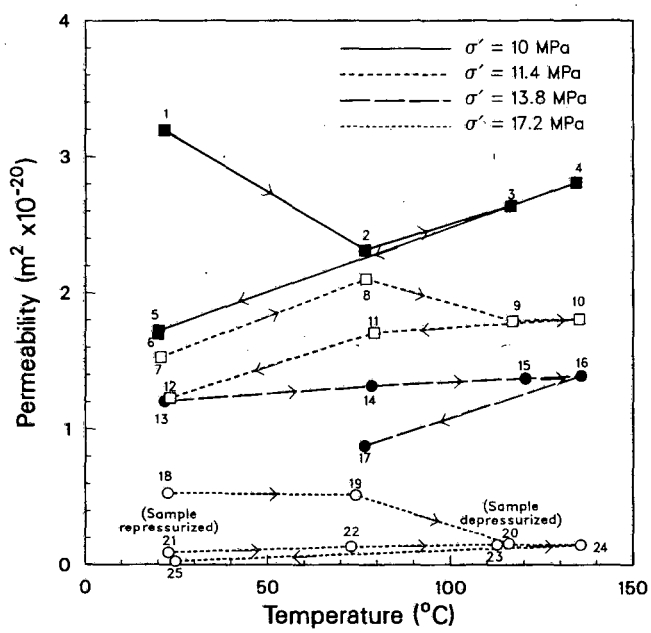

Figure 2. Permeability of eastern Devonian Shale as a function of temperature at different effective stress states (σ'). Tests number chronologically, with arrows indicating test sequence. [XCG 8710-11417]

REFERENCES

Brace, W.F., Walsh, J.B., and Brangos, W.T., 1968. Permeability of granite under high pressure. J. Geophys. Res., v. 73, p. 2225–2236.

Gale, J.E., 1982. Assessing the permeability characteristics of fractured rock. Geol. Soc. Am., Special Paper 189, p. 163–181.

Heard, H.C., and Page, L., 1982. Elastic moduli, thermal expansion, and inferred permeability of two granites to 350 C and 55 megapascals. J. Geophys. Res., v. 86, no. B11, p. 9340–9348.

Myer, L.R., 1985. Electro-servo control systems for thermomechanical properties testing. Geotech. Testing J., v. 8, no. 4, p. 171–178.

Prats, M., and O'Brien, S.M., 1975. The thermal conductivity and diffusivity of Green River oil shales. J. Pet. Tech., v. 27, p. 97–106.

Richter, D., and Simmons, G., 1974. Thermal expansion behavior of igneous rocks. Int. J. Rock Mech. Min. Sci. Geomech. Abstr., v. 11, p. 403–411.

Summers, R., Winkler, K., and Byerlee, J., 1978. Permeability changes during the flow of water through westerly granite at temperatures of 100–400 C. J. Geophys. Res., v. 85, p. 7059–7071.

Weinbrandt, R.M., Barney, H.J., and Casse, F.J., 1975. The effect of temperature on relative and absolute permeability of sandstones. Soc. Pet. Eng. J., p. 376–381.

Elastic Interface Waves Along a Fracture

L.J. Pyrak-Nolte and N.G.W. Cook

The reflection and refraction of seismic waves by welded interfaces between lithologies, across which both stresses and displacements in the wave are continuous, are understood well and are used extensively. Under conditions of low and even moderate effective stress, which may prevail to crustal depths of several kilometers, contacts between lithologies may not be welded. Furthermore, discontinuities in the form of joints, fractures, and faults are important crustal features. These discontinuities within the same lithology also may behave as nonwelded contacts at low and moderate values of effective stress. There is considerable interest in locating and characterizing both natural discontinuities in rock masses and induced discontinuities such as hydrofractures.

In this article, we develop the theory for a seismic interface wave that can propagate along a fracture. This theory is based on the seismic properties of a nonwelded interface or a displacement discontinuity. We have determined that the seismic response of a single fracture is modeled well by representing the fracture as a boundary between two elastic half-spaces subject to the following set of boundary conditions: continuous stress, but discontinuous displacements (Schoenberg, 1980). The discontinuity in displacement is defined to be inversely proportional to the specific stiffness of the fracture. We applied this set of boundary conditions to a generalized Rayleigh wave and derived the dispersion relationship of elastic interface waves that can travel along a fracture. These waves are not Stoneley waves (Stoneley, 1924; Sezawa and Kanai, 1939), because the material properties of the half-spaces on either side of the fracture can be the same. When the material properties are the same, two waves exist: a "slow" wave, which exists at all frequencies and all fracture stiffnesses, and a "fast" wave, which exists only for certain excitation frequencies.

EXISTENCE OF ELASTIC INTERFACE WAVES

An interface wave between two media separated by a nonwelded contact (or fracture) can be derived by finding the displacements at the surfaces of the media, subject to coupling through the fracture stiffness. The half space for $z > 0$ is medium 1, while medium 2 is the half-space for $z < 0$. The fracture consists of the xy plane and has components of specific stiffness κ_x, κ_y, and κ_z in the x, y, and z directions, respectively. The solution for the elastic interface wave can be derived using a solution for a generalized surface wave and displacement discontinuity boundary conditions (Eqs. 1–6):

$$u_{z1} - u_{z2} = \tau_{zz1}/\kappa_z \ , \qquad (1)$$

$$\tau_{zz1} = \tau_{zz2}\,, \tag{2}$$

$$u_{x1} - u_{x2} = \tau_{zx1}/\kappa_x\,, \tag{3}$$

$$\tau_{zx1} = \tau_{zx2}\,, \tag{4}$$

$$u_{y1} - u_{y2} = \tau_{zy1}/\kappa_y\,, \tag{5}$$

$$\tau_{zy1} = \tau_{zy2}\,, \tag{6}$$

where

$$\tau_{zz} = \lambda\,\{\partial u_x/\partial x\} + (\lambda + 2\mu)\,\{\partial u_z/\partial z\}$$

$$\tau_{zx} = \mu\,\{\partial u_z/\partial x + \partial u_x/\partial z\}$$

$$\tau_{zy} = \mu\,\{\partial u_z/\partial y + \partial u_y/\partial z\}.$$

These boundary conditions describe continuous stress across the interface (Eqs. 2,4,6), but discontinuous displacements (Eqs. 1,3,5). The discontinuity in displacement is inversely proportional to the specific stiffness of the fracture κ.

For a wave to exist, the velocity of this interface wave must be real. The wave velocities were found numerically for the case where the properties of the elastic half-spaces are equal, namely $\alpha_1 = \alpha_2 = 5800$ m/s, $\beta_1 = \beta_2 = 3800$ m/s, $\rho_1 = \rho_2 = 2600$ kg/m^3, for both $\kappa_x = \kappa_z$ and $\kappa_x \neq \kappa_z$. At most, two solutions to the resulting determinant are found, corresponding to two distinct interface waves. For sufficiently low frequencies, however, only one wave is found to exist. Figure 1 displays the wave velocity versus frequency for the two waves (referred to as the "fast" wave and the "slow" wave) that exist at a nonwelded contact for the specific case where $\kappa_x = \kappa_z = 10^9$ Pa/m. At high frequency or low stiffness, both waves approach an asymptote defined by the Rayleigh wave velocity. At low frequencies or high stiffness, the slow wave approaches an asymptote defined by the shear wave velocity, while the fast wave approaches the shear velocity with a finite slope and ceases to exist below a threshold frequency. Both wave velocities are functions of frequency and stiffness, and therefore these waves are weakly dispersive.

The particle motion of the waves is depicted in Fig. 2. From direct calculation of the normal modes,

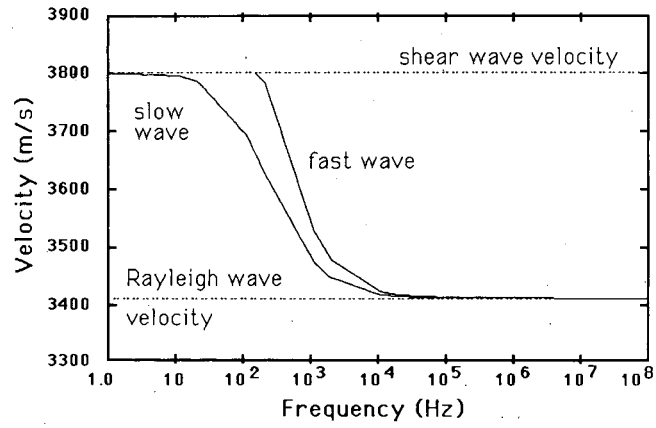

Figure 1. A graph of slow-wave and fast-wave velocity as a function of frequency. Upper asymptote is the shear-wave velocity, and the lower asymptote is the Rayleigh-wave velocity. $\alpha_1 = \alpha_2 = 5800$ m/s, $\beta_1 = \beta_2 = 3800$ m/s, $\rho_1 = \rho_2 = 2600$ kg/m^3, $\kappa_x = \kappa_z = 1.0 \times 10^9$ Pa/m. [XBL 886-2274]

it was determined that the x components of displacement are in phase in the fast wave, and therefore the fast-wave velocity is insensitive to κ_x. For the slow wave, the z components of the wave are in phase, and therefore the slow-wave velocity is insensitive to κ_z. Together, the waves can be thought of as coupled Rayleigh waves. In the limit of low stiffness or high frequency, the fracture behaves as two free surfaces each of which supports a Rayleigh wave. As stiffness is increased, the coupling increases between the two Rayleigh waves, providing two new waves that contain different combinations of the original Rayleigh wave particle motions.

Figure 3 shows the regions of existence for the waves as a function of frequency and of the specific stiffness in the x direction along the fracture. It was found that the slow wave exists for all frequencies

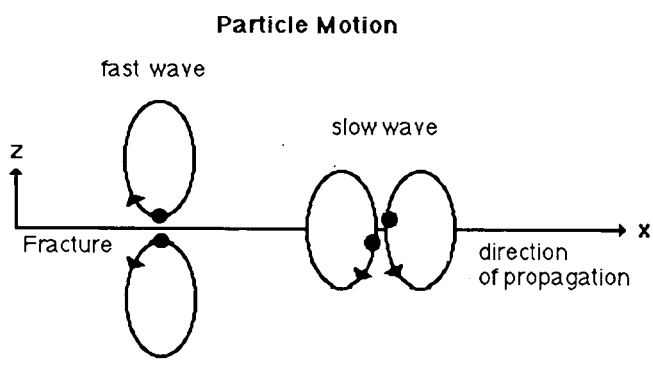

Figure 2. Particle motion of the fast and slow interface waves. [XBL 886-2275]

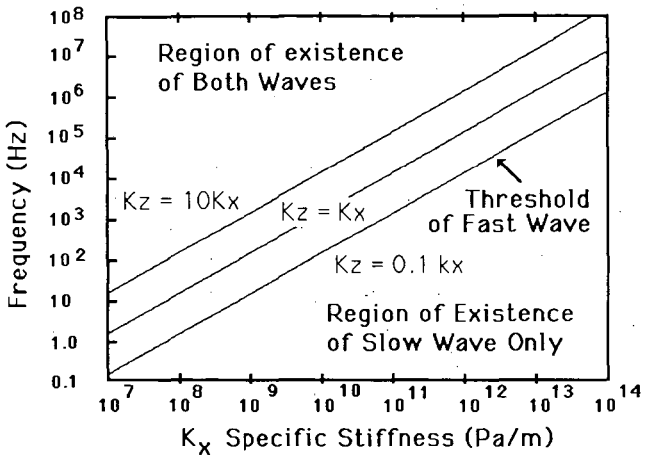

Figure 3. A graph showing the regions of existence of slow and fast interface waves in terms of frequency and specific stiffness in the x direction, and the ratio of κ_z/κ_x, the specific stiffness in the x and z directions. The slow wave always exists. $\alpha_1 = \alpha_2 =$ 5800 m/s, $\beta_1 = \beta_2 =$ 3800 m/s, $\rho_1 = \rho_2 =$ 2600 kg/m^3. [XBL 886-2276]

and all stiffnesses. However, the region of existence of the fast wave depends on frequency and the relationship between κ_x and κ_z. In Fig. 3, threshold curves are drawn for the cases where $\kappa_x = \kappa_z$, $\kappa_x = 0.1\kappa_z$, and $\kappa_x = 10\kappa_z$. As κ_z/κ_x increases, the threshold of existence for the fast waves moves to higher frequencies.

CONCLUSIONS

Elastic interface waves can exist along a nonwelded contact between two media having the same material properties. The "slow" wave always exists, while the "fast" wave has a threshold of existence that depends on the excitation frequency and the relationship between components of the specific stiffness parallel and perpendicular to the fracture. Both waves are weakly dispersive.

ACKNOWLEDGEMENTS

The authors gratefully acknowledge useful discussions with D.D. Nolte and the careful reading of the original manuscript by Lane Johnson.

REFERENCES

Schoenberg, M., 1980. Elastic wave behavior across linear slip interfaces. J. Acoust. Soc. Am., v. 68, no. 5, p. 1516–1521.

Sezawa, K., and Kanai, K., 1939. The range of possible existence of Stonely waves and some related problems. Bull. Earthquake Res. Inst. (Tokyo), v. 17, p. 1–8.

Stoneley, R., 1924. Elastic waves at the surface of separation of two solids. Proc. R. Soc. London, Ser. A., v. 106, p. 416–428.

Direct Three-Dimensional Observations of Microfracturing in Indiana Limestone

Z. Zheng, F.M. Doyle, L.R. Myer, and N.G.W. Cook

A useful technique for examining the stress-induced microstructure of rocks in three dimensions has been developed. Laboratory specimens of many rocks tested in axisymmetric, differential compression show a complicated relationship between stress and strain. With increasing compression, the deformation progresses from initial consolidation through nearly linear, elastic deformation to strain hardening and finally, strain softening. Axial strain hardening and softening are usually accompanied by radial dilatation. At zero or low confining stress, the dilatation is so pronounced that it must be a result of the generation and opening of voids within the rock, and, the initial mode of rock fracture is observed to be by axial extensile splitting or spalling, parallel to the direction of the maximum (compressive) stress (Fairhurst and Cook, 1966; Wawersick and Fairhurst, 1970), particularly near free surfaces.

Most endeavors to explain the phenomenon of extensile splitting are based on the sliding-crack model (Fairhurst and Cook, 1966; Horii and Nemat-Nasser, 1985; Kemeney and Cook, 1987). In this model, sliding occurs between pre-existing microcrack surfaces inclined in the direction of the maximum principal stress when the shear stress across them exceeds the frictional resistance to sliding. Sliding produces high tensile stresses near the crack tips and a local tension that results in extensile wing

cracks that propagate in the direction of the maximum compressive stress. These cracks are stabilized by the negative crack driving force that results from the minimum principal stress normal to their direction of propagation.

Although these models are examples of physically realizable processes that could produce extensile crack propagation in rock subjected to compressive stresses, it is highly improbable that the pervasive phenomenon of extensile crack growth in compression results only from the growth of two-dimensional sliding cracks, as is assumed in most theoretical analyses. Nevertheless, the basic concept embodied in these models is very powerful.

We have sought to develop a technique for preserving the population of microcracks as they exist in deformed rock at the values of stress and strain of interest. Wood's metal is an alloy that is liquid above 90°C and is solid at room temperature. Wood's metal can be used as a pore fluid at elevated temperatures and solidified in place, thereby preserving the pore geometry in great detail (Yadev et al., 1984). Recently Pyrak-Nolte et al. (1987) have used this technique to make precise castings of the void spaces between the surfaces of natural fractures in rock subjected to different effective stresses, to study how contact areas, void apertures, and interconnectivity change with stress.

EXPERIMENTAL PROCEDURE

Cerrosafe®, an alloy similar to Wood's metal, was used as the pore fluid in triaxial compression tests on Indiana limestone specimens. The alloy has a surface tension of 400 mN/m; at a pore fluid pressure of 10 MPa, the alloy should penetrate tube-like pores with diameters exceeding 0.16 μm, and planar voids with apertures exceeding 0.08 μm.

Specimens of Indiana limestone 71 mm in length by 24.5 mm in diameter, with the axis orthogonal to the original bedding planes, were used. To obtain stable extensile fractures, we developed a technique that subjects the ends of the specimens to a confining stress, leaving the central portion in uniaxial compression. Pretensioned stainless steel wires were wound from each end of the specimen to 11 mm from the center, using a pitch slightly greater than the diameter of the wire. Because extensile splitting is greatly inhibited by confining stresses normal to the direction of propagation, one would expect extensile fractures to start from the central, unconfined part of the specimen and be suppressed and arrested as they grow into the confined portions. Thus, collapse of the whole specimen under uniaxial compression can be avoided, and the complex stress distribution between the specimen and the testing machine has no effect on fracture.

The specimens were loaded in a stiff, servo-controlled testing machine, to points on the stress-strain curve corresponding to: (i) apparent elastic deformation only, (ii) stable strain hardening near their peak stress or strength, and (iii) strain softening beyond this peak. The samples were deformed at a temperature of 92°C, which is just above the melting point of the alloy, while a 10 MPa pressure was maintained in the liquid alloy permeating the specimen. At the values of effective stress and strain of interest, the specimen was cooled to room temperature, to solidify the alloy in place, preserving the deformed microcrack geometry.

Each test specimen was sectioned along the central longitudinal and transverse planes and polished to obtain smooth surfaces. To reveal the three-dimensional microstructure, the sectioned surfaces of the specimens were treated with 0.2 M HCl for 30 minutes, mounted and carbon sputtered, and then examined by scanning electron microscopy (SEM). This acid concentration gives rapid dissolution of the calcite in the limestone while corroding the alloy only very slowly. Thus, preferential dissolution of the rock matrix leaves casts of the pores, voids, and microcracks.

RESULTS

Figure 1 is a plot of axial stress versus axial strain, and axial stress versus radial strain, for one of the limestone specimens, strained to just past the peak stress, then cooled. The figure shows how the

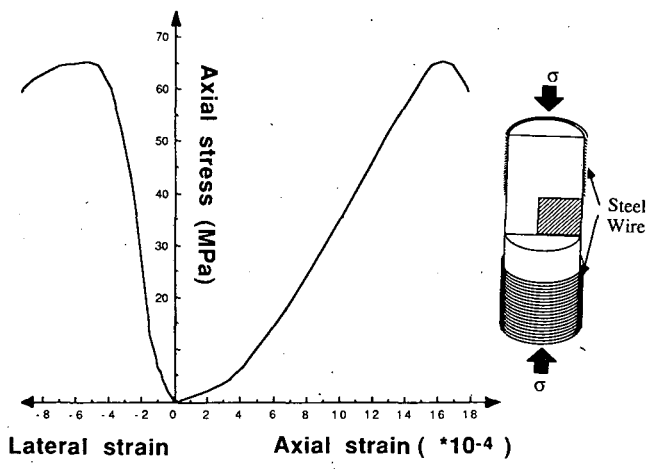

Figure 1. Axial and radial stress-strain curves for Indiana Limestone specimen **(left)**. Isometric sketch showing axial and radial stresses as well as the section photographed in the SEM **(right)**. [XBL 879-3887]

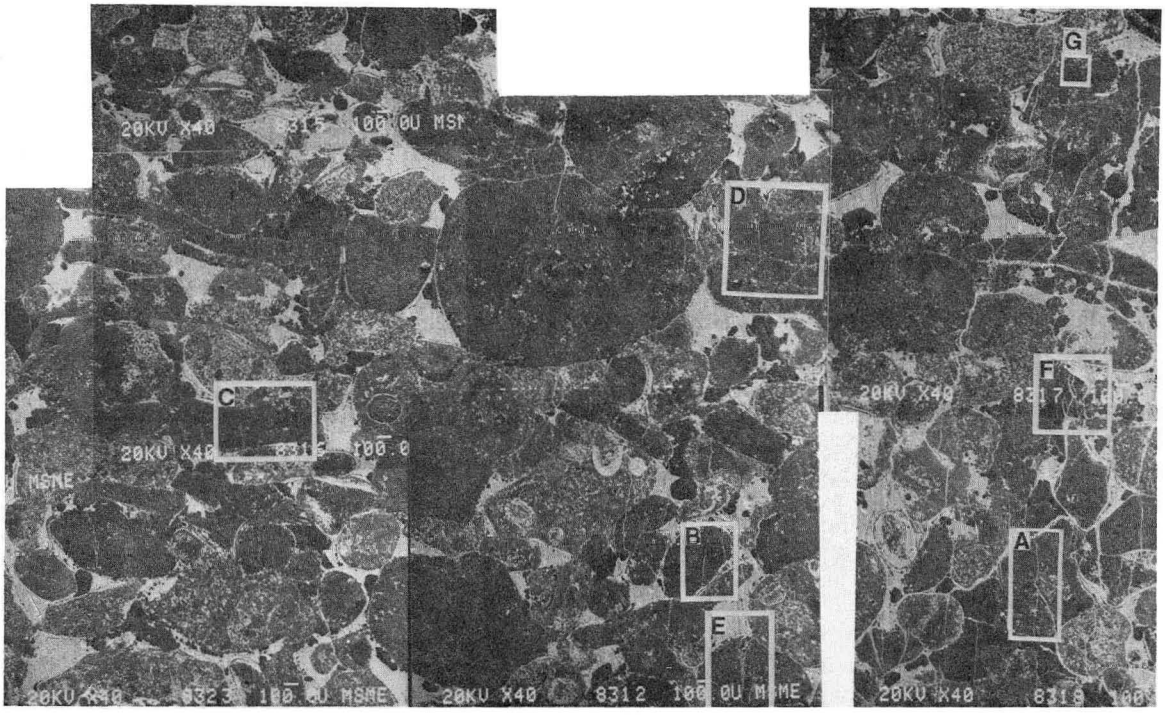

Figure 2. Lightly etched section of Indiana Limestone (as indicated in Fig. 1), showing intergranular porosity and stress-induced intragranular microcracks oriented parallel to compressive stress (light areas are alloy casts). [XBB 878-6962A]

stresses were applied. Figure 2 shows the lightly etched (2 seconds) section of the specimen identified by shading in Fig. 1. The light areas are the alloy and correspond to voids or fractures, while the dark areas are the original limestone matrix. Figure 2 shows pronounced, stress-induced vertical extensile fractures in the direction of axial loading. Although all of the unwired portion of the sample is initially under uniform uniaxial stress, cracking is observed to be most pronounced near the free surface. Various modes of microfracture are evident in Fig. 2. At location A, extensile cracks grew from a classic, intragranular sliding crack. At B, fractures have initiated at the grain boundary and grown into the grain. A long, narrow grain at C, with its long axis perpendicular to the loading direction, has fractured in bending. At D, fractures have changed their direction of propagation on crossing a grain boundary. At G, an alloy-filled microcrack observed under a magnification of over 3000× was found to have a thickness of only 0.1 μm.

Figure 3 shows the detail at location E in Fig. 2, after prolonged etching. The central fracture has grown in the direction of the compressive stress. It is clear from the stereo pair that the left side of the fracture lies below the right side; this orientation is parallel to the free cylindrical surface of the specimen. The small voids through the fracture cast correspond to points of contact between fracture surfaces.

Figure 4 is a stereo pair taken at F in Fig. 2. The fractures seen here are predominantly parallel to the

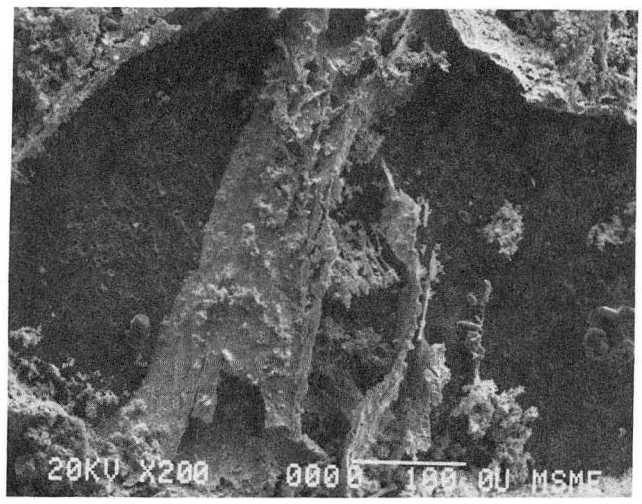

Figure 3. Fractured grain (location E in Fig. 2) after prolonged etching of limestone matrix. Fracture is in the direction of compressive stress and parallel to the free surface. [XBB 878-6988]

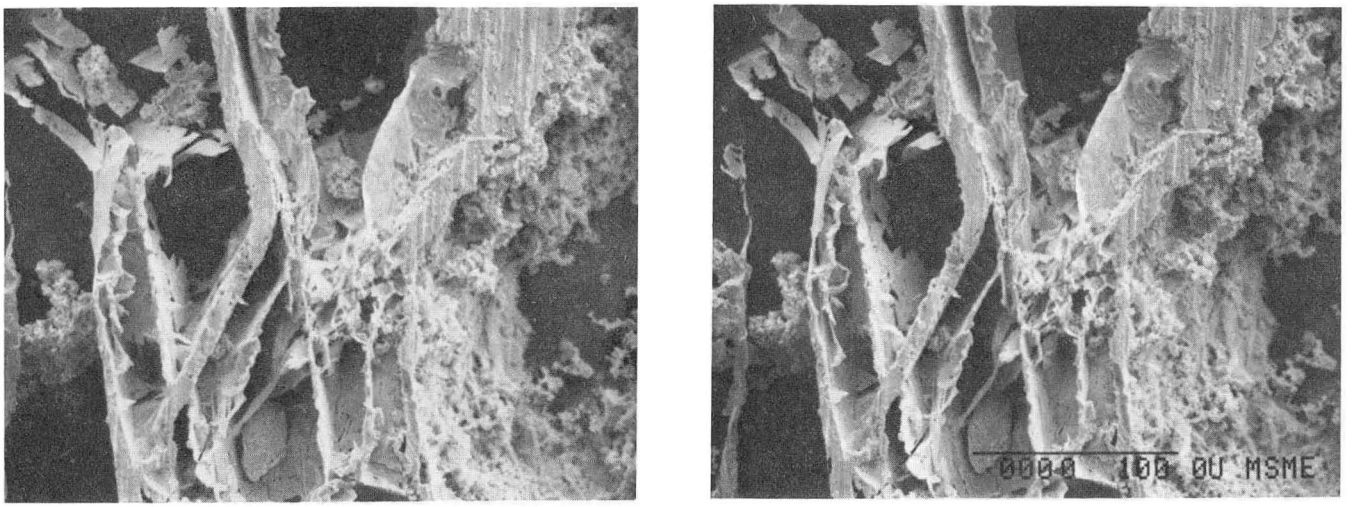

Figure 4. Stereo pair showing fractures (at left) and grain boundary (at right) at point F in Fig. 2 after prolonged etching. [XBB 878-6989; XBB 878-6990]

direction of loading, and the fracture planes are roughly parallel to the free surface. A grain boundary is visible at the far right of these figures; there is substantial, small-scale porosity associated with this boundary, giving a cast morphology quite distinct from that of the fracture, which is clean.

CONCLUSIONS

The above results demonstrate that the alloy-injection technique, followed by deep etching, enables us (i) to preserve and examine the geometry of fine (0.1 μm) microfractures as they existed under stressed conditions, and (ii) to obtain three-dimensional images of the microstructure. The results suggest that a variety of microscopic mechanisms—sliding, point loading, and bending—produce extensile cracking parallel to the direction of maximum compression. The cracking is more dense and more extensive adjacent to the stress-free surfaces of the specimen than it is at the center, and the cracks tend to be parallel to these surfaces.

REFERENCES

Fairhurst, C., and Cook, N.G.W., 1966. The phenomenon of rock splitting parallel to a free surface under compressive stress. *In* Proceedings, 1st. Cong. I.S.R.M., Lisbon, Portugal, 1966, v. 1, p. 687.

Horii, H., and Nemat-Nasser, S., 1985. Compression-induced microcrack growth in brittle solids: Axial splitting and shear failure. J. Geophys. Res. v. 90, no. 4, p. 3105.

Kemeney, J.M., and Cook, N.G.W., 1987. Crack models for the failure of rocks in compression. *In* Proceedings, Second International Conference on Constitutive Laws for Engineering Materials: Theory and Applications, Tucson, Arizona, January 5–8, 1987, p. 879–887.

Pyrak-Nolte, L.J., Myer, L.R., Cook, N.G.W., and Witherspoon, P.A., 1987. Natural fractures in low permeability rock. *In* Proceedings, 6th Cong. I.S.R.M., Montreal, Canada, v. 6, p. 225.

Yadev, G.D., Dullien, F.A.L., Chatzis, I., and Macdonald, I.F., 1984. Microscopic distribution of wetting and non-wetting phases in sandstone during immiscible displacements. Paper SPE 13212 presented at the 1984 SPE Annual Technical Conference and Exhibition, Dallas, Texas.

Wawersick, W.R., and Fairhurst, C., 1970. A study of brittle rock fracture in laboratory compression experiments. Int. J. Rock Mech. Min. Sci., v. 7, p. 561.

GEOPHYSICS

The research program of the Geophysics group is strongly oriented toward detecting and monitoring natural and man-made processes in the subsurface. These efforts serve the DOE Nuclear Waste Management, Geothermal, and Basic Energy Sciences programs. Coupled to efforts in reservoir engineering and hydrogeology, many of the projects have been designed to investigate the movement of fluid in rocks of the earth's crust and have employed geophysical methods to delineate magma distribution and movement, to detect the mixing of waters of different conductivities, and to locate and characterize natural fractures and hydrofractures. Major emphasis is given to cross-hole tomography and vertical seismic profiling methods for mapping seismic-wave attenuation, velocity, and shear-wave anisotropy. Borehole and surface-based electromagnetic methods are being developed for a number of applications.

In addition to numerical modeling techniques and field experimentation, the program has also emphasized the development of improved field instruments. During 1987 a high-speed system was completed for monitoring high-frequency (up to 100 kHz) seismicity associated with grout and fluid injection. A novel borehole vibrating seismic source is under development. We have also studied the feasibility of using a transportable magnetohydrodynamic (MHD) generator as a current source for electromagnetic soundings.

The Center for Computational Seismology offers full seismic-reflection-processing software (SierraSEIS plus in-house additions), various synthetic seismograms and ray-tracing modeling programs, and an archive of the Global Digital Seismological Network data. Field capabilities managed through the Geophysical Measurements Facility include a digitally telemetered microearthquake network, *P*- and *S*-wave vibrators, two fully outfitted logging trucks, electrical and electromagnetic sounding equipment, and much associated hardware.

Division geophysicists are involved actively in several national programs, such as the Continental Scientific Drilling Program, CALCRUST, IRIS, and the Earthquake Prediction Program. Participation of graduate and undergraduate students and faculty from several departments, postdoctoral fellows, and visiting scientists creates a rich scientific environment for a wide range of geophysical research.

A Three-Dimensional Structural Model for the Long Valley Caldera, California

S.F. Carle and N.E. Goldstein

The Long Valley caldera in east-central California lies near the topographic margin of the Sierra Nevada batholith and the Basin and Range geomorphic province (Fig. 1). Scattered andesitic volcanism in the area began in the Pliocene and culminated in a major silicic ash-flow eruption about 0.73 Ma when over 600 km^3 of magma was expelled from a zoned chamber to produce the Bishop Tuff (Bailey et al., 1976; Bailey, 1987). Collapse of the roof rocks over the evacuated magma chamber, followed by volcanic resurgence and Basin and Range deformation, has resulted in an elliptical caldera measuring 32 km east-west by 17 km north-south. Episodic volcanism has continued up to the present; the youngest lava domes of the 45-km-long Inyo-Mono chain in the western part of the caldera are dated at 600–700 years and may be a consequence of active bimodal volcanism.

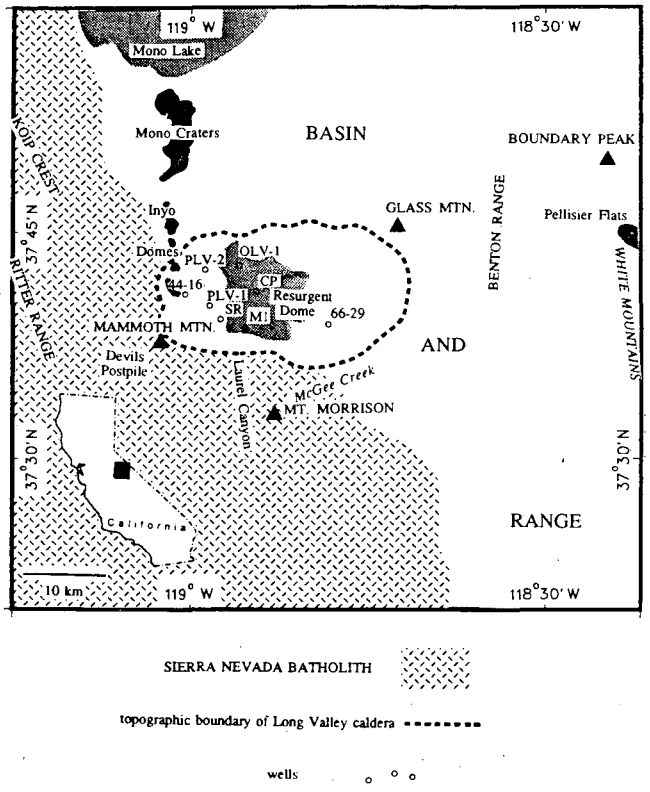

Figure 1. Location map of the Long Valley caldera showing some of the principal exploration and hydrogeologic test holes. [XBL 887-2570]

The Long Valley caldera is among the candidate areas selected for thermal-regimes scientific drilling by the U.S. Department of Energy (DOE) Office of Basic Energy Sciences. Because there is evidence that melt occurs at drillable depths, the caldera has also been selected by the DOE Geothermal Technology Division for the drilling of a deep hole under the Magma Energy Program. The arguments for a crustal magma body have been based mainly on seismic and deformation studies. In the study discussed here, we find supportive evidence for a crustal melt on the basis of a detailed 3-D analysis of gravity data.

GRAVITY INVERSION

The gravity set used for the 3-D modeling consists of 2026 station readings obtained from the U.S. Geological Survey (USGS), and another 473 station readings that were made available to us by Unocal Geothermal. The resulting residual isostatic anomaly (Fig. 2) was obtained after a regional correction to the data was made by applying the "best-fitting" Airy-Heiskanen isostatic model to the Bouguer gravity (Carle, 1987). Because crustal and mantle densities are not likely to be uniform and the crust may not be entirely compensated, the isostatic correction is at best a good first approximation for the regional effect.

Similar to the gravity anomalies observed over other Holocene ash-flow calderas, Long Valley exhibits a gravity low whose margin closely matches the topographic boundary shown as the dashed line in Fig. 2. The low of up to −48 mGal is attributed to the lower densities of the caldera-filling volcanics and sediments. Kane et al. (1976) and Abers (1985) modeled a less complete gravity-data set by means of 1-D and 2-D methods, respectively, and attributed the gravity changes entirely to variations in the thickness of the caldera fill. The shape of the caldera they obtained was in rough agreement with seismic-refraction profiles (Hill et al., 1985).

Because of the structural and lithologic complexities, the isostatic residual gravity data were modeled three dimensionally. To do this the earth was represented as a grid of square vertical prisms, each measuring 1.4 km on a side and extending from the mean surface elevation to a reference depth. Each

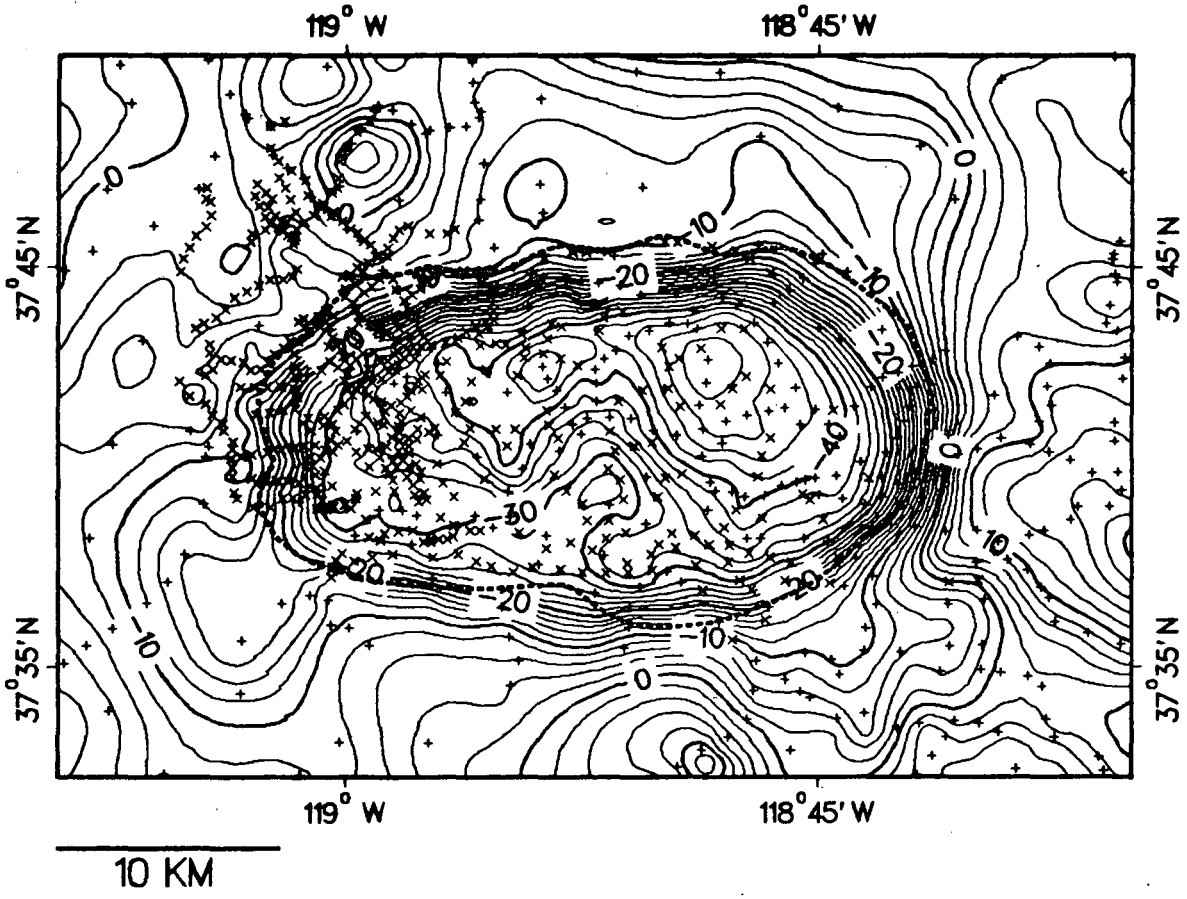

Figure 2. Residual Bouguer gravity map used in the 3-D inversion. The contour interval is 2 mGal. The +'s and x's denote USGS and Unocal Geothermal gravity stations, respectively. The dashed line is the topographic margin of the caldera. [XBL 887-2571]

prism is composed of a number of lithologic units based on known geology (Bailey and Koeppen, 1977). Each unit is assigned a constant density based on published bulk densities determined either from direct measurements on outcrop and core samples or indirectly from well logs (Abers, 1985). To be determined are the thicknesses $t_{i,j,k}$ of unit k at all grid rectangles i,j (Fig. 3). The lateral extent of unit k is described by nonzero values of a 2-D array of the parameter $t_{i,j,k}$, and a file for each unit was created on the basis of drill-hole lithologies and the surface geology (Bailey and Koeppen, 1977). Lithologic information for all the holes shown in Fig. 1, except OLV-1, provided constraints for both the lateral extent of some units and the thicknesses of specific units within the grid blocks where the holes are located. The grid size of 1.4 km, which is the lateral resolution of the model, is too coarse to resolve small features. However, grid size is a reasonable compromise between resolution, accuracy, and computer time. The grid size is large enough so that at least one gravity station lies within most rectangles, yet small enough to resolve major caldera features.

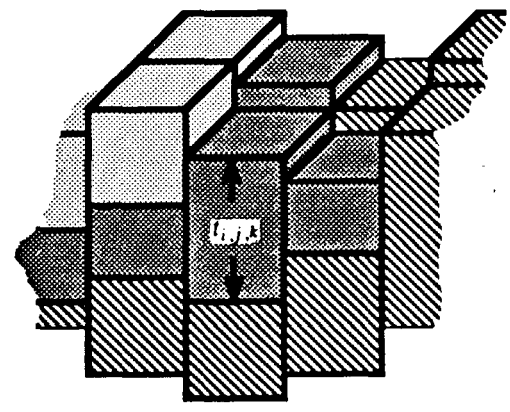

Figure 3. Simplified diagram of model geometry. [XBL 887-2575]

The vertical gravitational field on the surface at the center of each prism is calculated by summing the contributions from every element in the model. To reduce the computational expense by at least a factor of six while maintaining a level of computational accuracy well within the limits of uncertainty of model parameters, the prismatic elements are approximated by cylindrical elements (Kane, 1962). Edge-approximation calculations are needed to account for mass variations outside the grid boundaries. Units that abut the outer grid boundary are assumed to extend to infinity with the same thickness as in the boundary elements of the model. A line-mass approximation was used to calculate these effects, and it was effective in repressing instabilities at the edge of the modeled area. The edge approximation contributes less than 1 mGal at points within the caldera.

Determination of the unit thicknesses was done following an iterative approach introduced by Cordell and Henderson (1968), but modified to account for multiple density units and edge effects. After an initial model is created, based as much as possible on known geology, the gravity field g_{calcij} is calculated at each grid point. Because the calculated and observed values will not agree, the next step is to adjust unit thicknesses to force a convergence. For a single density unit, Cordell and Henderson (1968) proposed that a new unit thickness be found as follows:

$$t'_{ij} = t_{ij} \frac{g_{obsij}}{g_{calcij}} ,$$

where g_{obsij} and g_{calcij} are the observed and calculated values at grid point ij. After this calculation is made at all grid points, the gravitational effect is recalculated and the whole process repeated. After 3–10 of these iterations, convergence is obtained to better than 1 mGal at every grid point. In the case of multiple units, the process is modified so that two or more unit thicknesses may be adjusted at each iteration. Usually only a few units are iterated at a time, and we normally begin the iteration process by choosing the "key" units: those that have a large density contrast and/or are expected to be thick. After each cycle of the iteration process, we stop to display unit thicknesses and to make sure they are geologically plausible before proceeding.

CALDERA STRUCTURE

Most of the isostatic residual anomaly can be accounted for by the Bishop Tuff, early rhyolite flows and tuffs associated with resurgent volcanism 0.6 Ma, and lake sediments. The other pre-collapse and post-collapse units within the caldera are thin or not extensive. The total thickness of supra-basement rocks is shown in Fig. 4. There is a strong asymmetry in the caldera floor. Caldera fill in the north and east moat areas is up to 2.8 km. This feature has been recognized for some time, and explanations have been proposed: (1) there was a more complete evacuation of the magma chamber beneath the east moat (Lachenbruch et al., 1976), and (2) the east moat was a topographically lower area at the time of the Bishop Tuff eruption (Bailey, 1987).

The trench-like thickening of caldera fill lies 3–4 km inboard of the caldera margin and is difficult to explain. Carle (1987) speculated that the feature may be structural (i.e., a ring graben) or may be caused by highly fractured and lower-density rocks extending into basement and associated with an inner ring-fracture zone.

On the basis of geologic data such as the results of the Unocal 44-16 hole (Suemnicht and Varga, 1987) and the DOE Inyo 4 corehole (Eichelberger et al., 1988) in the west moat area, as well as the location of known faults (Fig. 4), the concept of a graben seems reasonable for the west moat. Whether a complete ring graben formed, similar to the one associated with the Mount Suswa volcano in the East African Rift Valley (Johnson, 1969), is still not established, but it seems possible in view of the gravity results (Fig. 5). On the basis of the stratigraphic correlations between holes 44-16 and Inyo 4 (Eichelberger et al., 1988), the ring graben seems to have formed before eruption of the early rhyolite sequence was complete (~ 0.6 Ma).

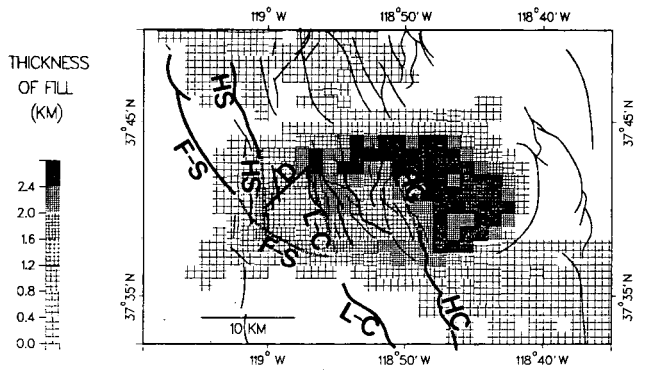

Figure 4. Thickness of all caldera fill, including pre-caldera volcanics, and the major recognized faults from Bailey and Koeppen (1977). The heaviest solid lines are the major northwest-trending Sierran faults, dashed where extended into the caldera. HS is the Hartley Spring fault, HC is the Hilton Creek fault, L-C is the Laurel-Convict fault. [XBL 887-2572]

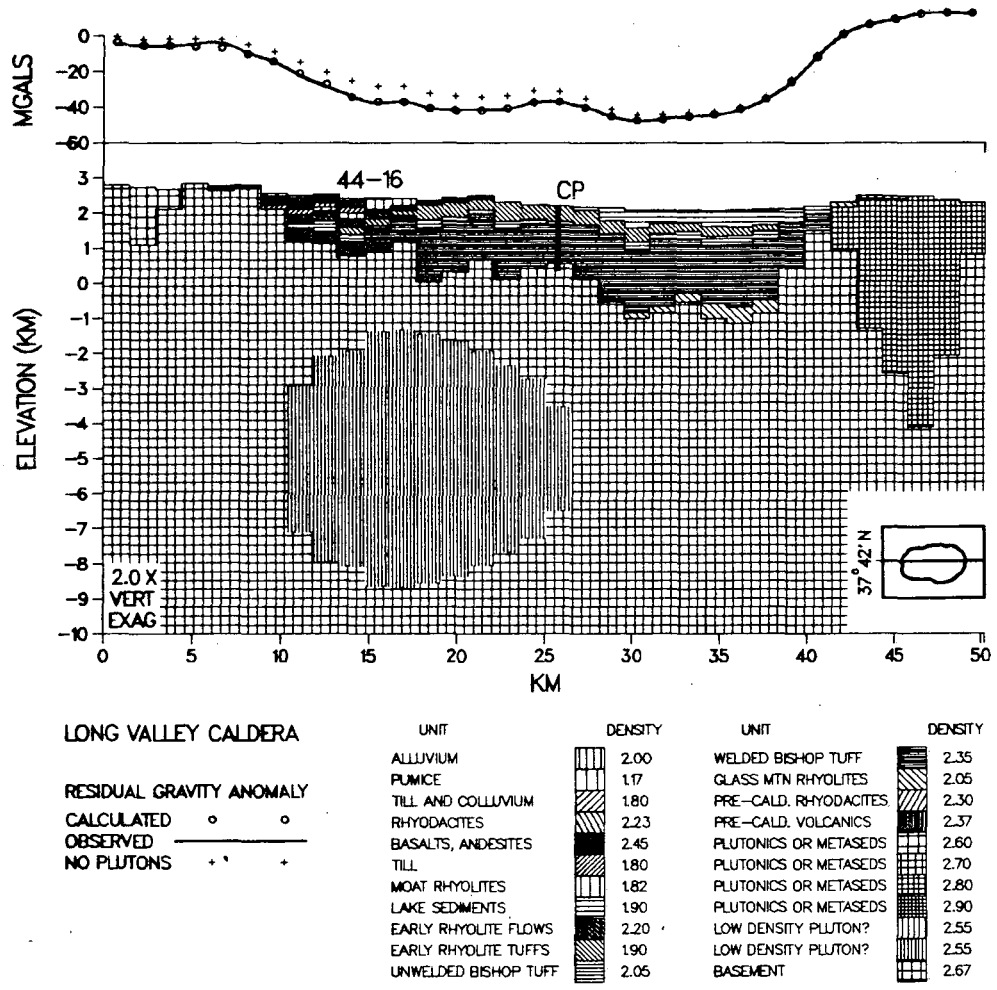

Figure 5. An east-west geologic model based on the gravity through the south moat and drill hole 44-16. See insert for location of the cross section. [XBL 887-2573]

CRUSTAL LOW-DENSITY ZONES

There remained a persistent long-wavelength difference in the calculated and observed isostatic gravity anomalies after the caldera structure and caldera-filling lithologies were fitted to the data. The difference was centered near the west side of the caldera and extended well into the Sierran block. For this reason we could exclude errors in the caldera-fill model as the cause of the misfit. Several causes were considered (Carle, 1987), but only a large low-density zone within the crust seems to satisfy the data. The 3-D inversion routine was run several more times to determine the geometry and density of the low-density crustal zone. Rather than finding a single zone, the inversion process identified two zones (Fig. 5). The larger one, centered at a depth of 10 km beneath the western part of the caldera, suggests an equidimensional subvolcanic pluton with an average density of 2.50 g/cm^3 Neither the shape nor the density of this zone is well constrained by the gravity data. However, because the zone corresponds very closely to a *P*-wave delay anomaly with roughly the same size and location (Dawson et al., 1987), there is an independent confirmation for the gravity model. It is also interesting that the average density for the zone strongly indicates that a large fraction of a silicic melt must be present. The second and smaller low-density zone in the crust underlies the area of the Devil's Postpile (Fig. 5) and is centered at a depth of 8 km below the the surface. This too may be associated with a subvolcanic pluton, but because of the unusually low density (only 2.40 g/cm^3) for this zone and the absence of corroborating geophysical evidence, it is difficult relate the gravity model to geology. The gravity study certainly could have benefited from more data points west of the caldera.

ACKNOWLEDGMENTS

The authors would like to thank Roy Bailey and Bob Jachens of the USGS for many fruitful discussions and Carle Otte and Dick Dondanville of Unocal Geothermal for making the Unocal gravity data available.

REFERENCES

Abers, G., 1985. The subsurface structure of Long Valley caldera, Mono County, California. J. Geophys. Res., v. 90, p. 3527–3638.

Bailey, R.A., Dalrymple, G.B., and Lanphere, M.A., 1976. Volcanism, structure, and geochronology of Long Valley caldera, Mono County, California. J. Geophys. Res., v. 81, p. 725–744.

Bailey, R.A., and Koeppen, R.P., 1977. Preliminary Geologic map of Long Valley caldera. U.S. Geol. Survey Open-File Map 77–468.

Bailey, R.A., 1987. Relationship between basement geology, faults and volcanic vents, Long Valley caldera, eastern California. *In* N.E. Goldstein (ed.), Proceedings, Symposium on the Long Valley Caldera: A Pre-Drilling Data Review. Lawrence Berkeley Laboratory Report LBL-23940, p. 1–7.

Carle, S.F., 1987. Three-dimensional gravity modeling of the geologic structure of Long Valley caldera (M.S. thesis). University of California, Berkeley. Lawrence Berkeley Laboratory Report LBL-23538.

Cordell, L., and Henderson, R.G., 1968. Iterative three-dimensional solution of gravity anomaly data using a digital computer. Geophysics, v. 33, p. 596–601.

Dawson, P.B., Iyer, H.M., and Evans, J.R., 1987. Structure of crust and upper mantle in the Long Valley, California region as determined from teleseismic travel-time residuals. *In* N.E. Goldstein (ed.), Proceedings, Symposium on the Long Valley Caldera: A Pre-Drilling Data Review. Lawrence Berkeley Laboratory Report LBL-23940, p. 54–62.

Eichelberger, J.C., Younker, L.W., Vogel, T.A., and Miller, C.D., 1988. Structure and stratigraphy beneath a young phreatic vent; South Inyo Crater, Long Valley caldera, California. J. Geophys. Res. (in press).

Hill, D.P., Kissling, E., Luetgert, J.H., and Kradolfer, N., 1985. Constraints on the upper crustal structure of the Long Valley–Mono Craters volcanic complex, eastern California from seismic refraction measurements. J. Geophys. Res., v. 90, p. 11135–11150.

Johnson, R.W., 1969. Volcanic geology of Mount Suswa, Kenya. Philos. Trans. R. Soc. London, v. 265, p. 383–412.

Kane, M.F., 1962. A comprehensive system of terrain corrections using a digital computer. Geophysics, v. 27, no. 4, p. 455–462.

Kane, M.F., Mabrey, D.R,. and Brace, R., 1976. A gravity and magnetic investigation of the Long Valley caldera, Mono County, California. J. Geophys. Res., v. 81, p. 754–762.

Lachenbruch, A.H., Sass, J.H., Munroe, R.J., and Moses, Jr., T.H., 1976. Geothermal setting and simple heat conduction models for the Long Valley caldera. J. Geophys. Res., v. 81, p. 769–784.

Suemnicht, G.A., and Varga, R.J., 1987. Constraints on models of structures and hydrothermal circulation in Long Valley, California. *In* N.E. Goldstein (ed.), Proceedings, Symposium on the Long Valley Caldera: A Pre-Drilling Data Review. Lawrence Berkeley Laboratory Report LBL-23940, p. 32–38.

Multicomponent VSPs at Cajon Pass and the Salton Sea

T.M. Daley, T.V. McEvilly, and E.L. Majer

The Vertical Seismic Profile (VSP) is a proven tool for studying the seismic-wave properties near a well and detailing subsurface structure (Hardage, 1985; Oristaglio, 1985). The usefulness of the VSP method has been increased by the acquisition of multicomponent data using a three-component borehole geophone in conjunction with both *P*-wave and *S*-wave seismic sources. The three-component geophone allows recording of the entire wavefield, and the *S*-wave source (usually a seismic vibrator truck) allows control of the shear-wave polarization. Among the possible uses of these data are fracture

detection and characterization via seismic anisotropy measurements (Crampin, 1985; Majer et al., 1988). The application of multicomponent VSP data is seen in two surveys conducted by Lawrence Berkeley Laboratory (LBL) and analyzed at LBL's Center for Computational Seismology (CCS). First was the Salton Sea VSP (SSVSP), acquired at the Salton Sea scientific well in southern California's Imperial Valley; the other was the Cajon Pass VSP (CJVSP) at the Cajon Pass scientific well near the San Andreas fault in southern California. Both surveys made use of LBL's seismic shear-wave vibrators to obtain shear-wave surveys along with the more standard *P*-wave surveys. Use of a three-component geophone, along with careful rotation of the recorded data traces into a wavefront-based coordinate system, allowed analysis of many aspects of the seismic-wave propagation properties around the wells.

At the Salton Sea well, located near the Salton Sea geothermal field, standard VSP analysis techniques were used to identify reflecting horizons both within the survey interval (from 457 to 1737 m) and deeper in the well (Fig. 1). The reflection at 2100 m in Fig. 1 is associated with a fractured reservoir, and event C is interpreted as a scattered wave from a fracture zone near the well at a depth of 900 m. One goal of the SSVSP was location of fracture zones that are associated with the geothermal process. Seismic-velocity anisotropy and the associated shear-wave splitting are indicators of fracturing utilized in the SSVSP analysis. Travel-time differences observed between orthogonal polarizations of the shear-wave source, labeled *SV* and *SH*, show a variation in anisotropy with depth. The *SV* source motion is polarized in the radial direction toward the well, and the *SH* source motion is polarized transverse to the radial. In an isotropic material, these polarizations will generate the standard *SV*- and *SH*-type shear waves. Since the travel time is measured on a component with the same polarization as the source, travel-time difference is a measurement of shear-wave velocity anisotropy.

Three-component particle-motion analysis of shear-wave arrivals was found to be an effective method for characterizing the subtleties in the *S*-wave splitting throughout the various zones in the well. Although the travel-time measurements show anisotropy of only around 1%, the particle-motion analysis showed clear definition of changes in the *S*-wave propagation characteristics. Figure 2 shows the particle motion at 580 m, where the data are in the rotated, wavefront-based coordinate system of radial, *SH*, and *SV* components and plotted as three 2-dimensional cross sections on the faces of a cube

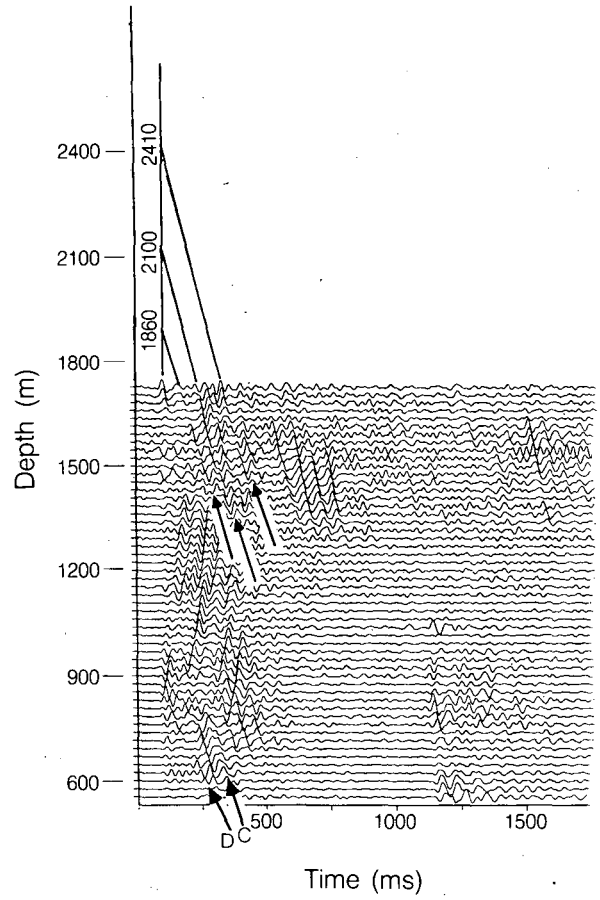

Figure 1. Reflector depth estimation for far-offset *P*-source, vertical component. Section is time-shifted to align first arrivals and dip-filtered to attenuate downgoing energy. Three deep events are identified with generation depths estimated at 1860, 2100, and 2410 m. Event D is a *P*-wave reflection from 850 m. Event C is a vertically scattered *P*-wave event. The different moveout of events D and C indicate different modes of generation. [XBL 884-10168]

(Daley, 1987; Majer et al., 1988). This linear motion is typical of that expected for isotropic propagation. Changes in particle motion associated with propagation in anisotropic material are easily seen on this type of three-component hodograph.

In the CJVSP survey, the shear-wave vibrator occupied one offset position for three runs of the borehole geophone, allowing three different *S*-wave polarizations to be obtained. These polarizations were radial and transverse to a line from the well, and the intermediate orientation, and were called *SV*, *SH*, and *S*45, respectively. Complete data sets were obtained for the *SV* and *SH* polarizations (from surface to 1800 m, with 10-m spacing), but the third run was not finished, giving coverage with the *S*45

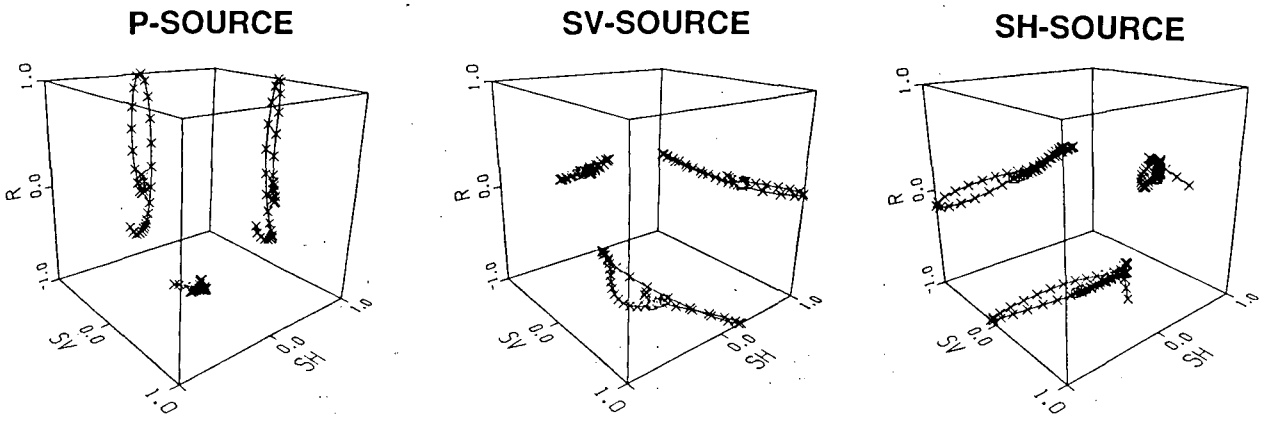

Figure 2. Three-component particle-motion hodographs for all three far-offset sources at 580 m recording depth. Plotted points are 2 ms apart. Each axis of the cube displays one component of motion, giving three 2-D projections. Purely isotropic *S*-wave propagation would produce linear trajectories in the *SV*-*SH* plane shown on the cube's bottom. [XBL 877-3164A]

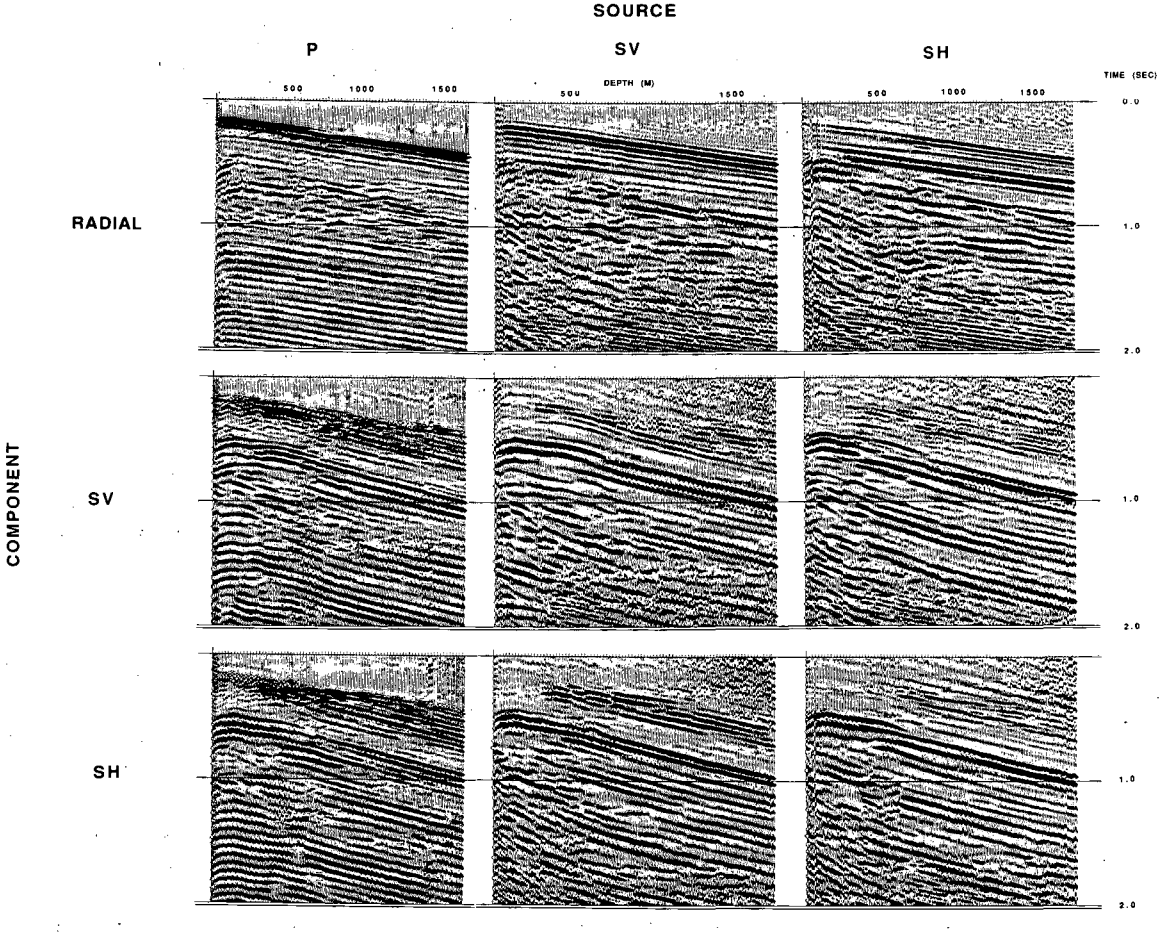

Figure 3. Nine-component display of Cajon Pass VSP data. Each section is a depth versus time display of the data from one source type (*P*, *SH*, or *SV*) recorded on one geophone component (radial, *SH*, or *SV*). The data have been rotated into radial, *SH*, and *SV* components from the original, randomly rotated geophone recordings using the first *P*-wave arrival. [XBL 8710-4019]

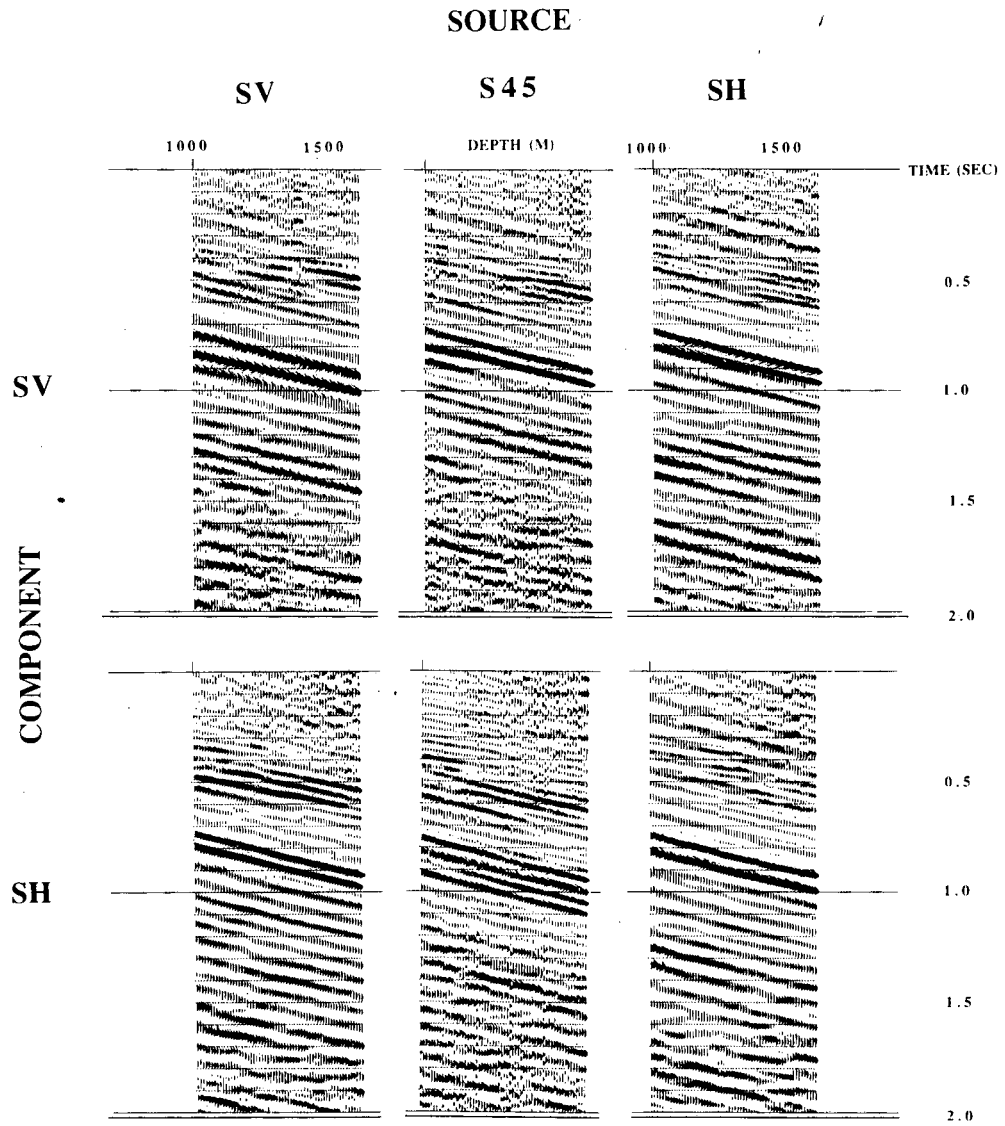

Figure 4. Shear-wave data from Cajon Pass VSP. The *SV*, *SH*, and *S*45 sources are three polarizations of a shear-wave vibrator. The borehole geophone data have been rotated into *SH* and *SV* components. The variation in observed arrivals between sources can be used to study seismic anisotropy. [XBL 8712-5118]

source from 1040 to 1630 m. By rotating the data from the *P*, *SV*, and *SH* sources into the radial, *SH*, and *SV* components, a nine-component display could be produced for the CJVSP (Fig. 3). The variation of events seen on each of these nine components shows the details that multicomponent VSPs produce compared to standard VSPs, which have one source and one receiver component (such as the *P*-source, radial-component data shown in Fig. 3). In the CJVSP there is a significant interface near 500 m between the Punchbowl sedimentary formation and the granitic basement rock. The effect of this contact is seen in the breakup of the first shear-wave arrival near 0.5 s on the *SV* and *SH* components of the *SV* and *SH* sources. The contact is also delineated by the mode-converted shear waves seen on the *SV* and *SH* components of the *P* and *SV* sources at 0.25 s.

The three shear-wave data sets are shown in Fig. 4 for the *SH* and *SV* component data. Anisotropic effects are clearly seen on the *SH* components, where the *S*45-generated arrival between 0.7 and 1.1 s has a split waveform and a less coherent arrival. The affect of this anisotropy is seen on two-component particle-motion plots in Fig. 5. The nearby San Andreas fault is expected to cause

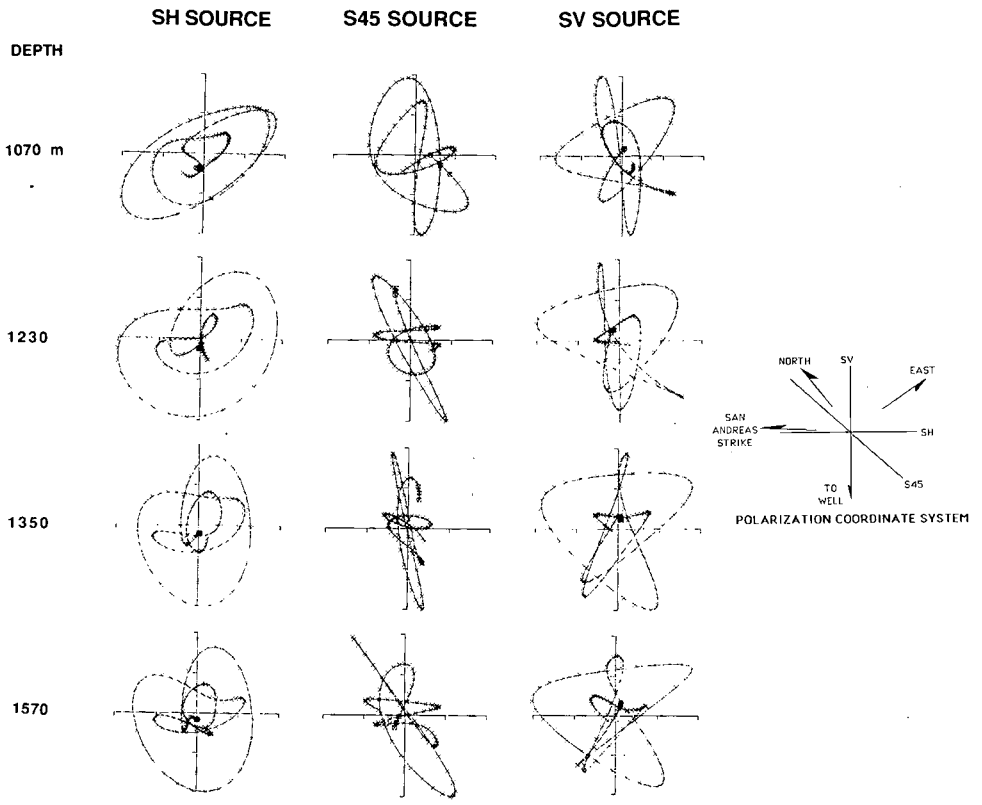

Figure 5. Two-component particle motion of shear-wave arrivals at depths from 1070 to 570 m for three polarizations of the shear source. The vertical axis of each plot is motion on the *SV* component, and the horizontal axis is motion on the *SH* component. Each data point is 2 ms apart in time, and the first three points are circled to identify first motion. The side plot shows the orientation of each source and axis with respect to north, and with respect to the strike direction of the San Andreas fault. [XBL 8712-5272]

microfracturing, which will affect the orientation of the shear-wave particle motion. In Fig. 5, the *S*45- and *SV*-generated arrivals have a component of motion in the fault direction, but the *SH*-generated arrival, which is aligned with the fault, does not stay linear as we would expect. This type of particle-motion analysis of the CJVSP data shows that factors other than the San Andreas fault are affecting the seismic anisotropy.

REFERENCES

Crampin, S., 1985. Evaluation of anisotropy by shear-wave splitting. Geophysics, v. 50, no. 1, p. 142–152.

Daley, T.M., 1987. Analysis of *P*- and *S*-wave VSP data from the Salton Sea geothermal field (M.S. thesis). University of California, Berkeley. Lawrence Berkeley Laboratory Report LBL-24661.

Hardage, B.A., 1985. Vertical Seismic Profiling—Part A: Principles. Geophysical Press Limited, London, p. 337–340.

Majer, E.L., McEvilly, T.V., Eastwood, F., and Myer, L., 1988. Fracture detection using *P*- and *S*-wave VSPs at the geysers geothermal field. Geophysics, v. 53, no. 1, p. 76–84.

Oristaglio, M.L., 1985. A Guide to the current uses of vertical seismic profiles. Geophysics, v. 50, no. 12, p. 2473.

The Development of Seismological Techniques for the Real-Time Mapping of Grout Injections

E.L. Majer and R.J. Haught

During the last several years LBL has been involved in a program to map the path of grout as it is injected into the ground. This work has been funded by the U.S. Army Corps of Engineers Waterways Experimental Station and by the Civilian Nuclear Waste Program of DOE. In both programs the work has been directed toward determining the seismic signature of the grout as it is being injected into the ground. In the U.S. Army application, the final goal was also to build an in-field monitoring system that could be used in a routine fashion. In the DOE application, the work was directed toward monitoring grout injections in tight rock for shaft sealing in the nuclear waste repository.

ARMY GROUT-MONITORING SYSTEM

Shown in Fig. 1 is the experimental field setup that was used to determine the seismic signals generated by the pumping of grout into the ground. This work was carried out at the U.S. Army Corps of Engineers McNary dam near Umatilla, Oregon. The rock type in this area is a fractured basalt. Complete hydrologic testing of the holes was carried out prior to the injection of grout. A 3-D array of piezoelectric sensors was placed around a potential grout zone. The distance of the sensors away from the grout injection hole ranged from a few meters to tens of meters. Once the arrays were in place, several grout injections were monitored. The rate, pressure, and viscosity of the grouting were varied. Two distinct types of signals were observed, the discrete acoustic emission (AE) signals and the harmonic-tremor signals. The observed frequency range of these signals varied from 1 to 10 kHz. These signals were observable at distances up to 10 m away at pressures of 50 psig and flow rates of 2–4 L/min.

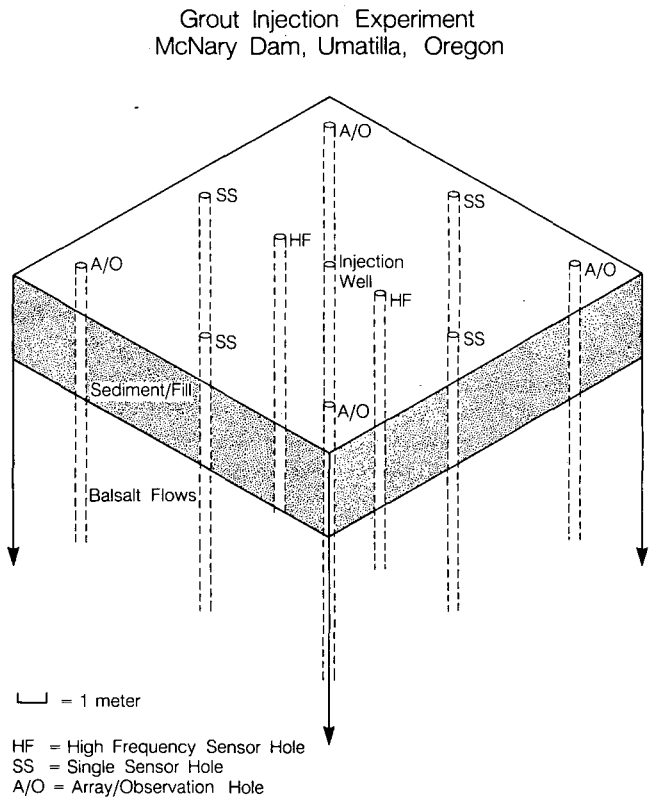

Figure 1. Perspective view of survey layout used in the Army Grouting Project, showing the locations of the monitor boreholes and injection holes. [XBL 868-10957]

From the field experiments it is clear that there are basically two types of useful seismic signals:

1. The discrete seismic activity associated with the grout as it is pumped into the rock. During the grout injections monitored, shear and tensile failure discrete events have been detected, i.e., acoustic emissions. The frequency range of these events at the distances used, 5–10 m, varies from 5000 to 15,000 Hz. Potentially this is the most straightforward technique to use. The acoustic emission/microseismic (AE/MS) activity will be the most useful when the grout is extending fractures. Techniques have already been developed by us as well as by others to map this AE/MS activity.
2. If there is not a sufficient amount of discrete seismic activity associated with the propagation of the grout, it may be possible to use the signals generated by the resonance of the grout or the waves guided along it to characterize the extent of the grout invasion. The frequency content of these signals ranges from 1000 to 5000 Hz.

Field System

The field tests indicated that it was possible to design and build at a reasonable cost a PC-based system that will collect and analyze the data in times that, while not real time, will be useful to the field engineer, i.e., within a few minutes. The approximate

target cost of the system, including software, was $30,000. A diagram of the system is shown in Fig. 2. The field data have shown that the bandwidth of the signals is less than 25 kHz. Also, the tests to date indicate that the seismic energy of interest occurs in discrete times of less than 100 ms at a time. Using these parameters as general guidelines, the system in Fig. 2 was selected and built.

The system is designed to collect up to 16 channels of data, at up to 100,000 samples/s at 12-bit resolution on each channel. Amplification of 1 to 1024 is provided in steps of powers of 2. We have observed in the tests to date that, depending on the surface noise, signal conditioning may be necessary. There is a fast front end to the system (DSP Inc.) that senses an event, digitizes up to one million samples, and then passes the data to an IBM/AT or IBM/AT-compatible device for further processing. The speed of this processing is a function of how many PCs are networked together to perform the higher-level processing. The higher-level processing includes event association and timing, event location, and graphical display in cross section and in plan view of the grout location. To aid in the computing, an array processor is included in the PC selected for event association and timing. The goal was to have a flexible system with the capability to process the two different types of data that we have encountered to date, as well as to provide the capability to view and process other data types not yet encountered. This is part of the reason we selected an IBM PC-based system. It also provides a development environment that takes advantage of many second-vendor hardware and software products.

Shown in Fig. 2 is the present hardware status of the system. The front end is a DSP Inc. product that is CAMAC-compatible. This includes the trigger module, amplifiers, 12-bit digitizers, a control module, memory, and the general-purpose interface board (GPIB). It is expandable to more channels and higher data rates if one desires. DSP also provides IBM-compatible software, both source and executable versions. There are two PCs for the processing. The hardware included in each is shown in Fig. 2. The user interacts with the system through a monitor and keyboard. The final system is menu-driven, with the user supplying the location of the seismic sensors and any known rock-property information. The system is really an in-field processing system for time-series data. It will provide the capability to locate and display not only AE data but also any high-frequency time-series data. In addition, beam forming is carried out to locate the grout if there are no discrete events and only coherent noise.

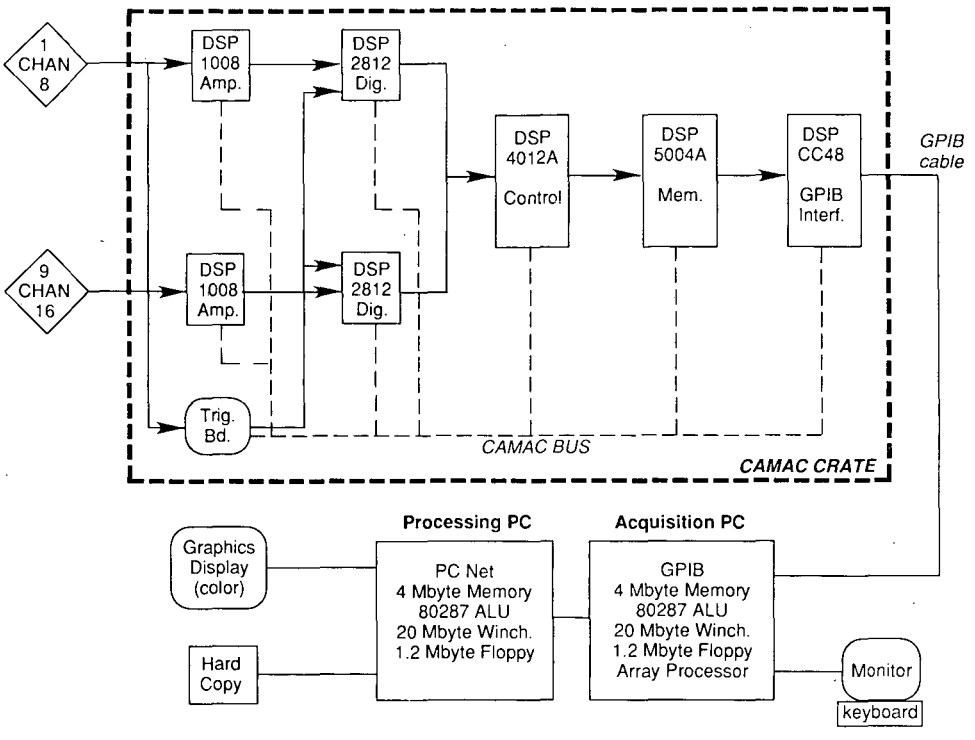

Figure 2. Diagram of the grout-monitoring field system. [XCG 887-6722]

URL GROUT EXPERIMENT

To address questions regarding the applicability of using seismic techniques for grout monitoring in tight rock, a series of grout trials was set up at the Underground Research Laboratory (URL) site in Canada. Past seismic experiments monitoring hydrofractures and grout injections at crystalline rock sites as well as at the URL (Majer, 1988) indicated a good possibility of using high-frequency monitoring for mapping the grout path. Although the permeabilities were small compared to most grouting work, the in situ stress values indicated that AE activity could be expected during the grouting injections. During the grouting-trials phase of the project, the primary objectives were to (1) determine the rate and level of seismic activity during the grouting; (2) correlate the AE activity to pressure, flow rate, and viscosity; and (3) if possible, locate the seismic activity and use the spatial distribution of events to infer the grout path. Although these three objectives have been obtained at other sites, each site is different, and the nature of seismic activity at the URL site was not known.

The approach taken is similar to that taken in developing grout-monitoring techniques at shallow depths (10–30 m) for the U.S. Army Corps of Engineers. In the Army project two distinct types of signals have been observed, the discrete AE-type signals and the harmonic tremor signals.

Field Experiment

To accomplish the goal of mapping the grout path at the URL, we used a wide-band monitoring system that records signals from 1 to 30 kHz. This is the same system we have used in past lab and small-scale field experiments. Basically, an array of sensors was placed around the grout zone. The location of the seismic sensors is shown in Fig. 3 in plan view. For the first of the three grout injections, only six sensors in two holes (holes HC-24 and and HC-25) were used. Hole HC-24 is inclined, and hole HC-25 is vertical; thus, in the plan view in Fig. 3, the sensor separation is not seen in HC-25. Three sensors were placed in each hole. The sensors were spaced 5 m apart in each hole, with the center sensor placed as close as possible to the middle of Fracture Zone 2. Because these were not cased holes, the sensors were emplaced in packed off-zones to maintain the pressure in Fracture Zone 2. For the last two grout trials, three more sensors were placed in GH-1, 5 m apart, also centered on Fracture Zone 2.

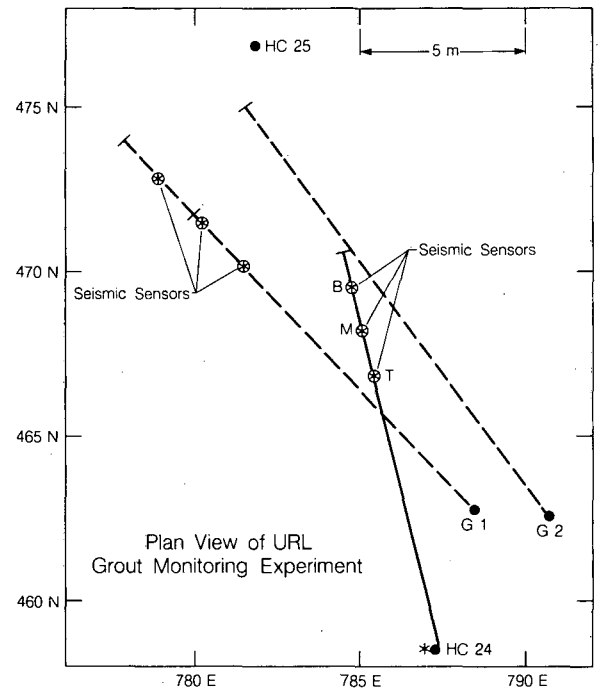

Figure 3. Plan view of the URL experiment. [XBL 877-10270]

Results

Figures 4 and 5 show the rates of AE activity as a function of time for grout trials 1 and 2. At this time accurate pressure records are not yet available. However, there are significant differences between the two trials. In the first trial the activity built up to a peak and died down as pumping stopped. In the second trial activity was at a maximum at the beginning of pumping and decreased during pumping but increased significantly after pumping decreased. In trial 1 recording stopped when the pumping stopped. However, the behavior during pumping appears different between trials 1 and 2. Until there is further correlation between the flow rates and pressures, it is not fruitful to speculate on the cause of this difference.

With respect to location of the events, it is easiest to explain the results if the trial 2 results are explained first. Trial 2 was the only job in which there were operational sensors in all three holes. Although activity was detected at all three holes, there was only a brief period—after pumping had ceased—during which simultaneous activity occurred in all three holes. Only during this period were the events strong enough to be seen in all three holes, thus providing adequate data for source location.

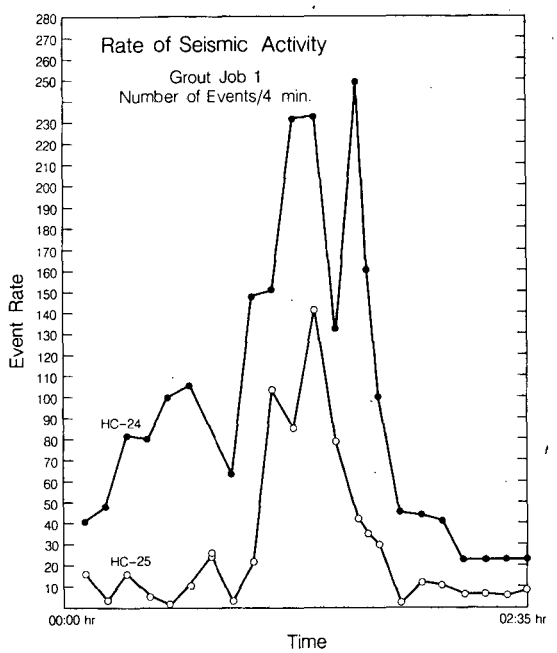

Figure 4. Rate of AE activity for the first grout trial as a function of time. [XBL 887-2545]

All events recorded during this were located within a few meters of each other. The cloud of events is located asymmetrically around GH-2, extending to GH-1 (Fig. 6). The cloud of events includes 50–60 "quality" locations. The term quality is used loosely here. At most only five sensors had good data, and usually only four. The depth of the events was calculated to be between 30 and 35 m. Only five sensors provided adequate arrival data; thus there is uncertainty of at least 0.5 m in the *xy* coordinate and 2–3 m in the vertical coordinate. In the locations shown in Fig. 6, it was necessary to constrain the depth at 33 m to obtain a sufficient amount of events to form a cloud. If more sensors had been operational, then it would have been possible to locate the events more accurately. For trial 1 there were few if any events detected at both boreholes. The location of the cloud was based on relative event occurrence rather than event triangulation.

Even though the data are only fair in quality, some conclusions can be reached:

1. There is AE activity at the pressure and injection rates used.
2. AE activity was detected at all operational sensors, but it was very localized. This result leads to the conclusion that much of the activity was due to pore-pressure increase in the formation over a much larger volume than the grout may have penetrated.

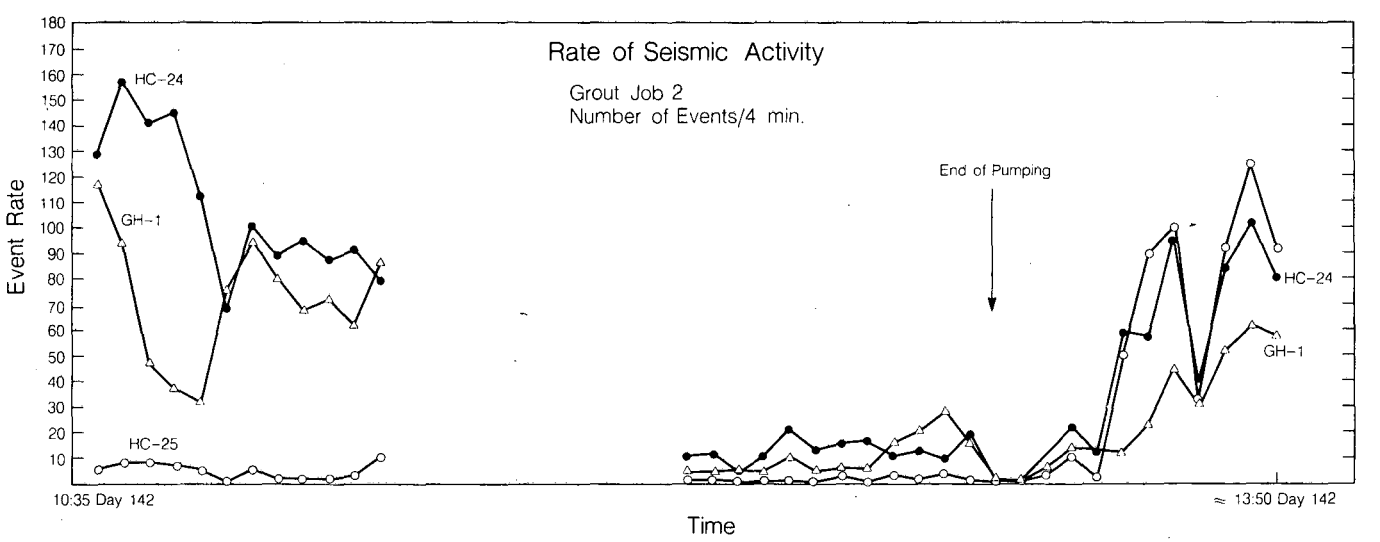

Figure 5. Rate of AE activity for the second grout trial as a function of time. [XBL 877-10268]

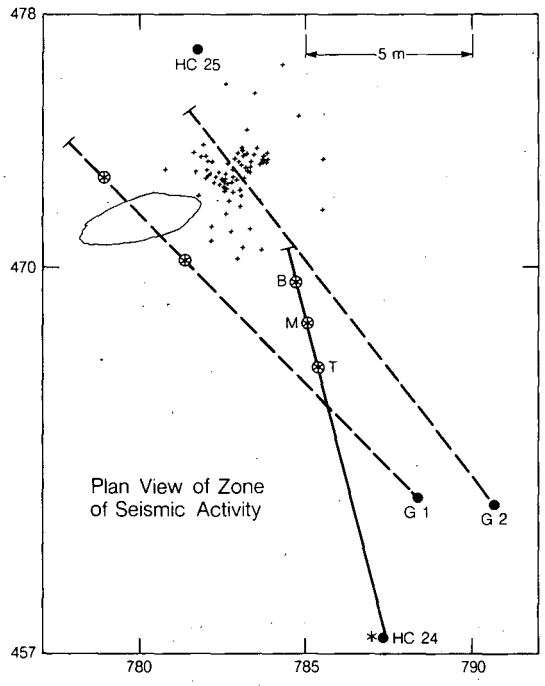

Figure 6. Plan view of the approximate locations of the seismic activity associated with the grout penetration at GH-1 and GH-2. [XBL 877-10269]

3. The largest events occurred after pumping had ceased and after pressure was taken off the injection well. These were the only locatable events, and they were located relatively close to the injection well. This result seems to indicate that there was a slow inflation of the rock during pumping locally around the injection well. Upon the release of pressure, there was a more rapid deflation of the rock, thus releasing the stored energy in larger events.

In conclusion, the experiment was useful as a trial. It provided information on rate and strength of seismic activity to be expected during any future grouting. Detailed correlation with pressure and flow rates should provide information on grout-penetration rate and thus dispel some ambiguities in the data.

REFERENCES

Majer, E.L., 1988. The application of high frequency seismic monitoring methods for the mapping of fluid injections. Int. J. Min. Sci. and Rock Mech. (in press).

CCS: Center for Computational Seismology

E.L. Majer, T.V. McEvilly, and L.R. Johnson

The Center for Computational Seismology (CCS) has now been in existence for five years. It has expanded from a several-user facility occupying 10–25 percent of a VAX/780 to a 20–30 member user community. For this reason CCS has upgraded its facilities to accommodate the load. The purpose of CCS has been to provide a facility with a wide range of computational tools to serve Department of Energy (DOE) programs in the basic energy sciences and other areas of energy research. Research over the entire spectrum of seismology is carried out at CCS, from basic studies in earthquake source mechanisms to the applied work of reflection seismology. The software base is made up of five years of our own efforts in coding internal-analysis routines, in addition to processing tools of DISCO (Digicon Inc.®), SierraSEIS (Sierra Geophysics®), INGRES (Relational Technology®), and the Geoquest Inc. AIMS package.

During the last quarter of 1987, the CONVEX C-1/XP computer was installed and tested at CCS. The CONVEX is a UNIX (Bell Labs®) based machine that runs 4.2 BSD. It is a 64-bit vector machine. Benchmarks to date indicate that in straight scalar mode it is 6–8 times faster than our previous system, a VAX 11/780; and if the calculations vectorize, we have observed speed increases of up to 20 times. For some very specialized uses, i.e., FFTs, the speed is the same as that of a Cray-1. In addition to the new hardware installed, CCS will be running the SierraSEIS seismic-reflection processing package. This package, like DISCO, is a complete processing package that replaces the DISCO package. The graphics system will be the NCAR package running on top of the ATC GKS package. The present configuration of CCS and networking is shown in Fig. 1.

We now have the ability to address research

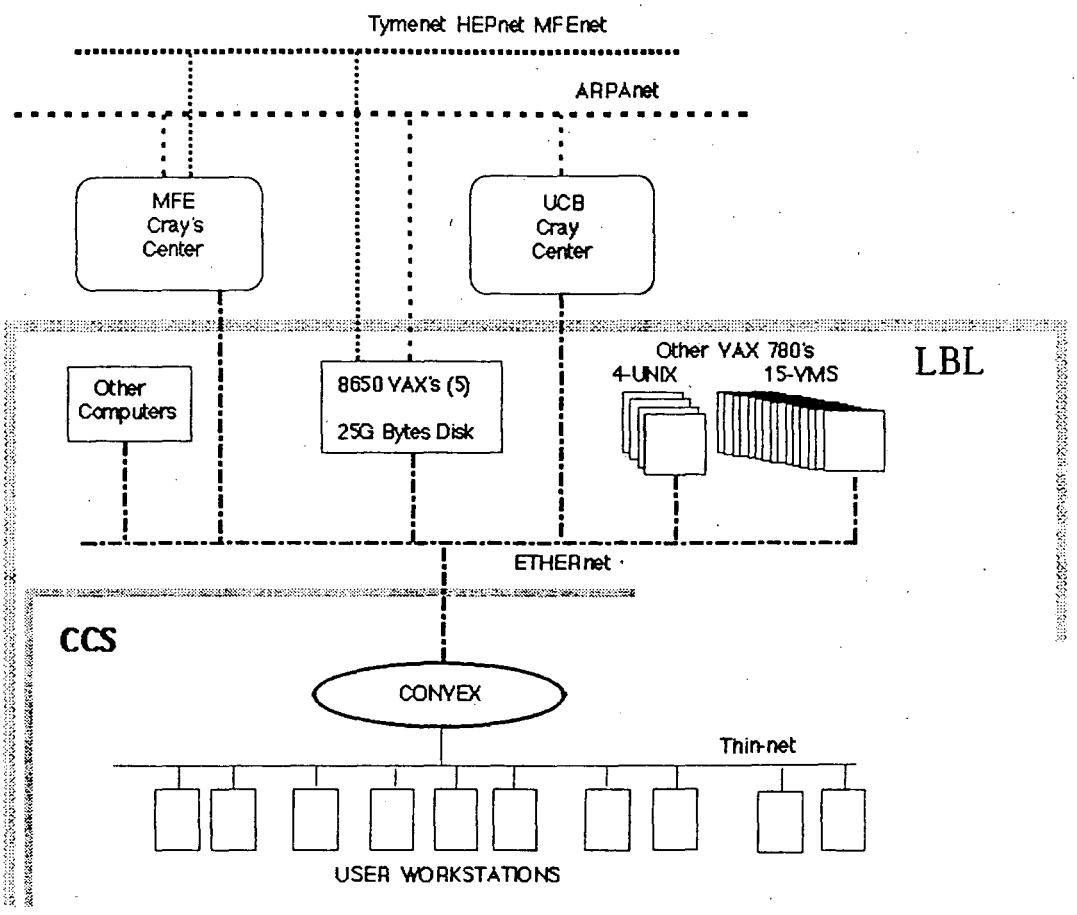

Figure 1. CCS configuration. [XBL 886-2291]

topics that we were previously not capable of embarking upon. The principal areas of research are, of course, various programs in the DOE involving seismic projects relating to basic and applied research. During the past year this has involved work for the Office of Basic Energy Sciences in the Salton Sea project and the Long Valley data synthesis. Another area of work has been for geothermal programs. Vertical seismic profiling (VSP) for fracture detection and microearthquake studies for reservoir management are two examples. We are also carrying out work for the DOE nuclear waste program. This involves relating the seismic response of fractured media to the hydrologic response. This program will soon involve field work, but the main thrust of the present study is to develop 2-D and 3-D models for ray-tracing *P*-, *SV*-, and *SH*-waves through fractured rock. The goal is to use seismic tomography for mapping fracture density, spacing, and orientation. We hope that sufficient resolution can be achieved to aid the hydrologist/reservoir engineer in predicting fluid flow. Last but not least we are still carrying out work related to mapping fluid flow in natural and induced (hydrofracture) fractures.

Overall, CCS has grown into a mature research unit carrying out a broad range of research topics. We have grown to the point where we will soon have to expand our facilities. During the next year we hope to implement a hardware upgrade that will greatly enhance our computational capabilities. At the present time we are leaning toward a semidistributed workstation system. We feel that to stay on the leading edge of the research projects we are involved in, we must also have modern facilities.

Controlled Seismic Cross-Hole Experiments for Fracture Characterization

E.L. Majer, J.E. Peterson, and J.C.S. Long

During 1987 work was started at the Grimsel Rock Laboratory in Switzerland as part of a joint DOE/NAGRA research program. NAGRA is the Swiss agency responsible for the disposal of nuclear waste in Switzerland. The Grimsel Rock Laboratory is located in the Swiss Alps in a granitic rock. It is a series of tunnels that have been excavated into the side of a mountain using a 3.5-m-diameter tunnel-boring machine (TBM). The tunnels extend 1.5 kilometers into the side of the mountain. The maximum overburden above the tunnels is approximately 450 m. A series of experiments in hydrology, geophysics, and rock mechanics is being carried out at the site.

The work described here that is being carried out at the Grimsel Rock Laboratory is designed to answer questions regarding the fundamental nature of seismic-wave propagation in fractured rock and to aid in the development of seismic-imaging methods for defining fracture characteristics (density, orientation, spacing). To address these goals field work at the Grimsel Rock Laboratory was undertaken at two controlled cross-hole sites at the laboratory. At the first site, testing was done on the FRI zone (Fig.1). As can be seen in Fig.1, there are two parallel boreholes 10 m apart. The holes extend between two tunnels. This configuration allowed access to all four sides of the rock mass. The fractures in this zone were the target of the investigations. The goal is to image the area tomographically using three-component sources and receivers. A core was also taken from the FRI zone so that it could be tested seismically in the lab. These results would then be compared to the results of the field measurements.

At the second site, testing was done in the BK zone (Fig. 2). At this site there is a slightly different granite, with less anisotropy but more fracturing, and a considerable amount of hydrologic data has been collected there. The experiment in the BK zone was conducted with receivers down borehole 85–008 and source down borehole 85–010. Both 45-m-deep boreholes dip 35° from the horizontal and are azimuthally 45° apart. The holes are 1 m apart at the surface, diverging toward the ends of the holes. (Figure 2 shows a plan view from above.) Both boreholes were filled with water flowing from them onto the tunnel floor. The data were collected with the source initially at 28 m down borehole 85–010

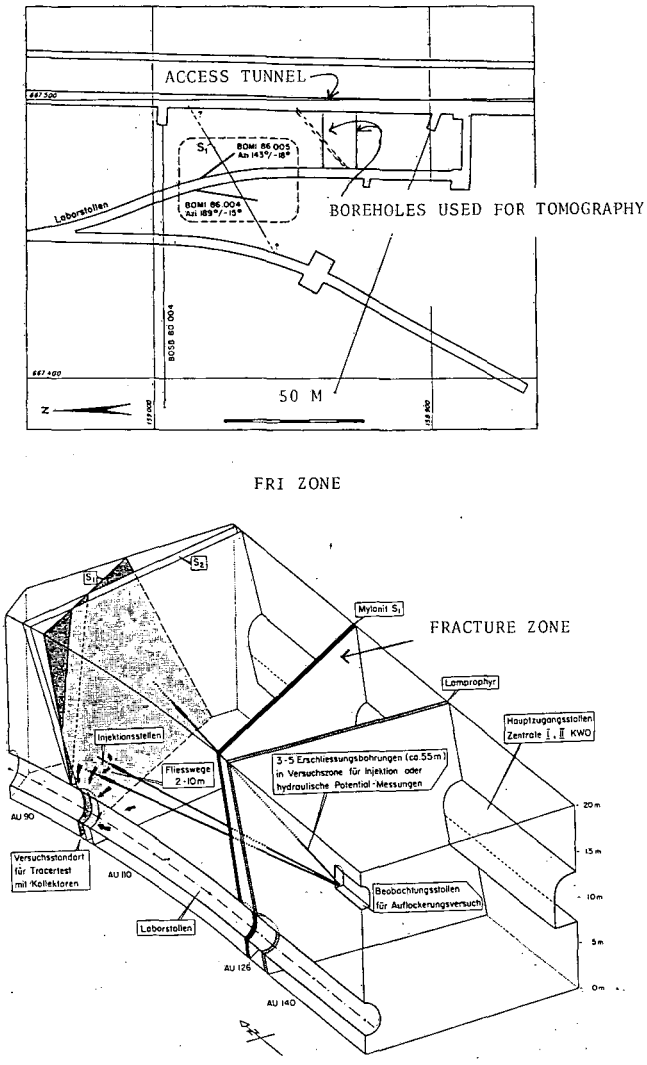

Figure 1. Experimental layout of the FRI zone. Shown are the two boreholes that the seismic measurements were taken in and the two tunnels that surrounded the area of interest. Also shown is the fracture zone that was the subject of the investigation. The zone is shown in plan view and in 3-D. [XBL 886-2278]

and moved up at 1-m increments for a distance of 5 m. We were able to place the receiver at a depth of 39 m in borehole 85–008. The receiver was moved up the borehole in 1-m increments for each source point for a distance of 5 m. In both areas the data were recorded on an in-field PC-based acquisition system. Nearly 30,000 ray paths (*P*-, *SV*-, and

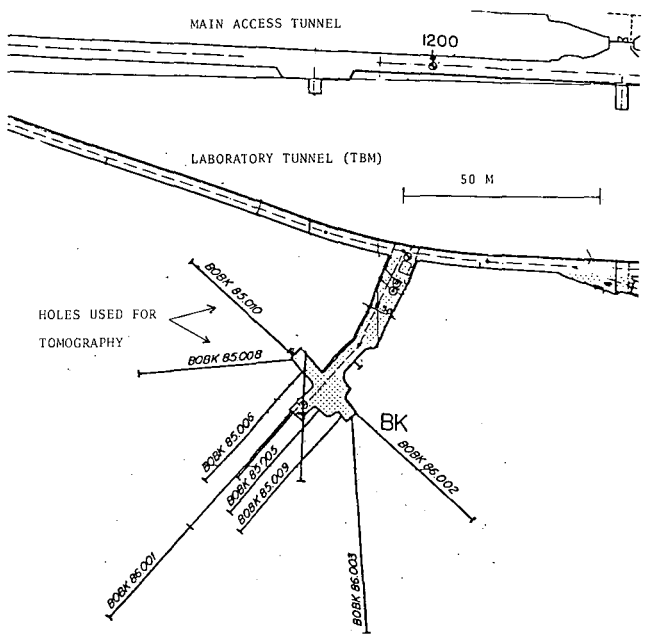

Figure 2. Experimental layout of the BK zone. Shown are the two boreholes in which the seismic cross-hole measurements were taken. [XBL 886-2279]

SH-wave) were collected in the FRI zone, and 1500 were collected in the BK zone, with travel-path distances ranging from 0.5 m to nearly 40 m.

RESULTS

After the data were recorded, they were brought back to LBL for processing. Two approaches were tried, inversion of the data using travel times and using amplitudes. Travel times were picked on the source sections with an interactive picking routine developed at LBL (TRACE2). Each section of traces displayed for picking consisted of 35 seismograms displayed 10 at a time in order for a clear correlation between traces for accurate picking of *P* arrivals. The repeatability of the picks is about 0.08 ms. The errors amount to a 3% total reading error over an average travel time of about 6.0 ms. Various methods can be used to pick amplitudes. We have taken the Fourier transform of the first 90 samples (1.8 ms) after the *P*-energy onset. These values are squared at each frequency, then summed over all frequencies to determine the total *P*-wave energy. It is not necessary to take the gain or the instrumentation into account, because the natural logarithm of the relative amplitude is used in the inversion.

To date, processing has been completed on the BK zone, and only preliminary results are available for the FRI zone. The zone mapped between the boreholes in the FRI zone exhibited significant anisotropy and complexity in fracture structure and content. The most useful data were derived from the borehole-to-borehole travel paths. The drift-to-borehole travel paths in the FRI zone were significantly affected by the damage zone near the walls. We also found that coupling was increased with a water-filled hole, which was expected; but for consistency all future work if possible should be done in water-filled holes if ray travel paths are involved. The shear waves were most significantly affected by the fractures. Shear-wave arrival would be quickly damped out in areas of fractures. Although the piezoelectric source was designed to generate *S*-waves as well as *P*-waves, it is obvious that the *S*-waves being generated by the present source should be much stronger to penetrate the same distance as the *P*-waves. The results of the field work to date indicate that the original premise of using *P*- and *S*-waves for mapping fracture content is valid. Future work should focus on using improved shear-wave data for improving the resolution of the technique and for defining such parameters as fracture density and spacing.

In the BK area several interesting results were obtained. The most obvious was the higher Q, or lower attenuation, of the rock type there versus the rock in the FRI area. The geometry of this experiment using source-receiver distances of 1 m produces a sampling of a 70 × 70 array of pixels. Previous tests have shown the pixel sampling to correspond quite well to the resolution matrix of the least-squares problem, with greater sampling corresponding to resolvability of features. The algebraic reconstruction technique is being used to perform the inversions. The 70 × 70 pixel array results in square 0.5 × 0.5 m pixels.

The travel-time inversion produces little slowness (or velocity) contrast [see Fig. 3; the shading range is from 4.8 km/s (dark) to 5.1 km/s (light)]. The dominant feature of the velocity reconstruction is a large low-velocity zone below 30 m. Unfortunately, borehole 85–010 was sampled only to 28 m, which means that the extensive low-velocity feature can be produced by a single fracture spanning the boreholes. The geometry prevents any sort of resolution of the zone. Another low-velocity zone appears at the 20–21 m level midway between boreholes.

Energy for the attenuation inversion was calculated over the entire spectrum (0–20 kHz) and over bandwidths of 1.0 kHz from 0.0 to 10.0 kHz to improve the resolution of the attenuation features.

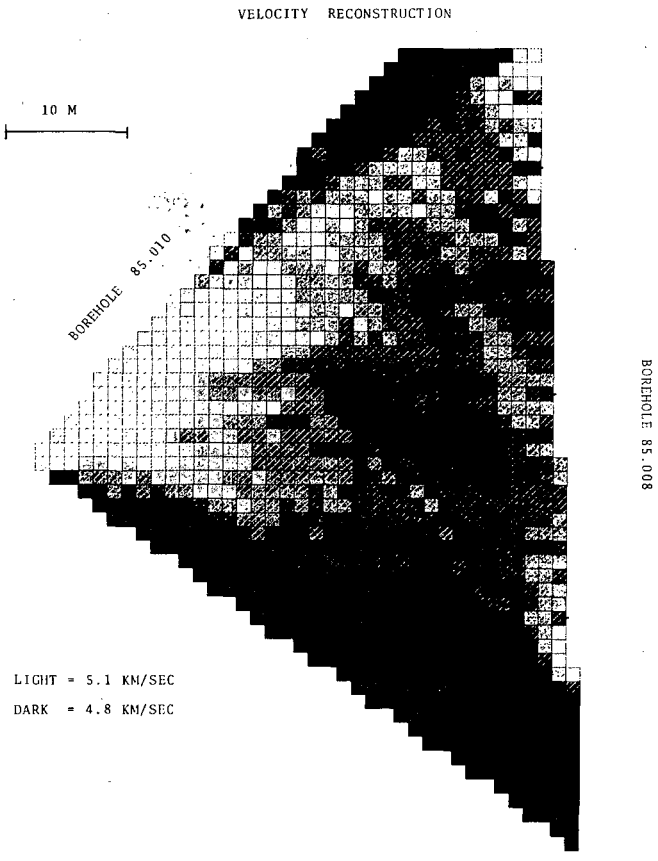

Figure 3. The results of the travel-time inversions for the BK zone. [XBL 886-2280]

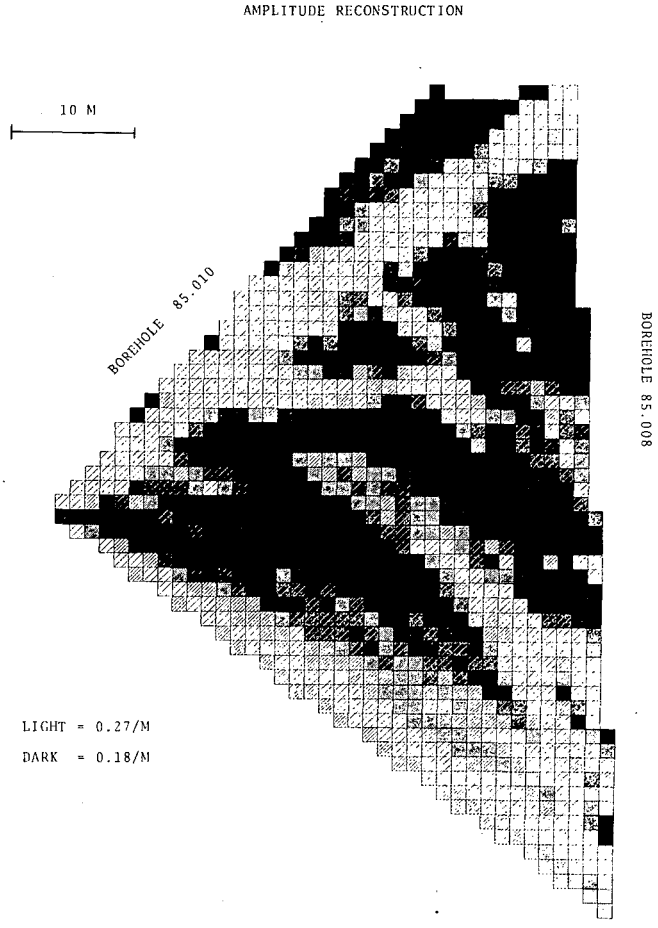

Figure 4. The results of the amplitude inversions for the BK zone. [XBL 886-2281]

The inversion equation is

$$\ln\frac{A_k}{A_0} = -\int_{R_k}\alpha(x,y)ds \ ,$$

where A_k is the received energy, A_0 is the source energy, and $\alpha(x,y)$ is the attenuation field. In practice A_0 must be estimated to be some reasonable value greater than the maximum energy at any receiver. The values were corrected for geometric spreading by multiplication with the ray length.

The energy data show much greater contrasts than the travel-time data [see Fig. 4; the shading range is from 0.18/m (dark: high attenuation) to 0.27/m (light: low attenuation)]. The low-velocity zones of Fig. 4 are better resolved in the attenuation-field reconstructions. This agrees with fracture theory, where the time delay due to a fracture decreases at higher frequencies while the corresponding attenuation increases. A strong attenuation zone that extends halfway across the field is shown at 28 m down borehole 85–010. The 21-m zone is much more distinct and indicative of a fracture zone. It extends from borehole 85–008 to a few meters from borehole 85–010. A similar zone at 15 m is also resolved, as well as a few minor features along the holes.

Moderate smearing decreases the resolution of the amplitude reconstruction. Tube-wave energy produces much of this smearing by increasing the energy when the tube waves are close enough to the primary to be included in the window. Tube-wave spectra are similar to those of the primary arrival, eliminating the possibility of easily reducing their effect. Energy is calculated from incremental frequency bandwidths of 1.0 kHz. The resulting attenuation inversion shows that most information is acquired in the 3–5 kHz and 7–8 kHz ranges. The remaining frequencies show that higher attenuation occurs when the fracture intersects the boreholes or in areas of borehole damage, and in fact, these areas are the dominant features of the reconstructed image. The presence of these fractures leads to the most common error of interpretation; the smearing

of these features between boreholes gives the impression of a fracture zone where none may exist.

The geometry is such that the area along the source borehole below 30 m is poorly resolved due to the inability of the receiver to progress farther than 28 m down borehole 85–010. This prohibits the resolution of the lamphrophere that intersects the boreholes in these areas. The lamphrophere is a zone with the same acoustic characteristics as the surrounding granite, but one that is intruded with several intertwining fractures. It shows up as the extensive low-velocity/high-attenuation area below 29 m. A tube wave is also generated from this area at 32.5 m down borehole 85–010. According to the core drawings this corresponds to a mylonite zone within the lamphrophere. The reconstructed attenuation shows the feature extending from borehole 85–010 halfway to borehole 85–008. The borehole data suggest that it extends all the way to borehole 85–008, but the poor sampling and smearing destroy the resolution.

The next zone of interest occurs at 20 to 21 m. The velocity reconstruction shows it as a small, circular low-velocity area between the boreholes with a low-velocity contrast. The attenuation field shows a thin, strong attenuating zone extending from 85–008 to a few meters from 85–010. A large tube wave is generated from the zone in borehole 85–008 having comparable amplitude as the *P*-wave. Another, smaller tube wave is generated from the same level in borehole 85–010. This area corresponds to a known fracture zone, as inferred from the core logs. The core logs show a small fracture zone here, and the hydrological evidence is in the form of increased flow in the hydrologic tests.

In general we were very encouraged with the results from the BK zone. The results indicate that features such as significant fracture zones and changes in rock type are very distinguishable by using *P*-wave seismic tomography. Amplitudes are much more sensitive to these changes than velocities. The next phase of the work is to start processing the FRI data. The data have been transferred from the field computer to the lab computer. The next step will be to sort and pick the arrival times for tomographic processing.

Summary of CALCRUST Program

T.V. McEvilly and D.A. Okaya

Current CALCRUST activities are focused on the greater Mojave Desert block and its transitions to adjacent provinces. This region contains numerous geologic elements central to the Mesozoic and Cenozoic tectonic evolution of the southwestern continental margin. To explore the crustal structure associated with some of the first-order features, CALCRUST has begun work along three primary transects or corridors (see C-I, C-II, and C-III in Fig. 1).

Corridor I will explore the transition from the Colorado Plateau to the Salton Trough, as well as the deep structure of the Peninsular Ranges. Early work (1985) along this corridor has dealt with the detachment fault terrane in the vicinity of the Whipple Mountains. No new profiling was carried out in 1986; however, the region is targeted for appreciable new data acquisition in 1987.

Corridor II will address the question of "flake tectonics" associated with the Transverse Ranges and the San Andreas fault. It will ultimately tie to the COCORP Mojave line near Randsburg. DOSECC's Cajon Pass Deep Scientific Borehole is also located within this corridor, and CALCRUST is acquiring seismic-reflection data in support of this project and is also participating in the interpretation of VSP data. In 1986, a 30-km line was run north from the northern flank of the San Bernardino Mountains through Apple Valley. Two roughly orthogonal, approximately 4-km-long lines were also run at Cajon Pass. An extended-offset experiment was also carried out in conjunction with the Apple Valley line.

Finally, corridor III is investigating the crustal structure in the Mojave "wedge" between the Garlock and San Andreas faults, and the structures beneath the adjacent central Transverse Ranges and southernmost Sierra Nevada (Tehachapi Mountains). During 1986, a 35-km line was run between the White Wolf fault in the southern San Joaquin Valley and the Garlock fault. Primary targets were structures associated with these major east-west trending features, including the Rand thrust (north branch of the Garlock fault?) and the Rand/Pelona schist. A

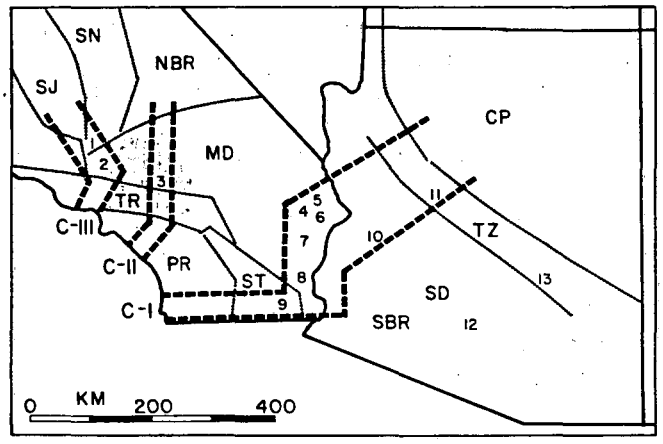

Figure 1. Map of southwestern United States. Corridors I, II, and III are designated C-I, C-II, and C-III, respectively. Tectonic provinces: SJ—San Joaquin Valley; SN—Sierra Nevada; NBR—Northern Basin and Range; MD—Mojave Desert; TR—Transverse Range; PR—Peninsular Range; ST—Salton Trough; CP—Colorado Plateau; TZ—Transition Zone; SD—Sonoran Desert; SBR—Southern Basin and Range. Numbers refer to localities mentioned in text. [XBL 886-2282]

115-km-long refraction survey using USGS instruments was run in conjunction with the reflection work; the reflection profile was coincident with the center of the refraction spread.

CALCRUST SAN JOAQUIN VALLEY–TEHACHAPI MOUNTAINS SEISMIC-REFLECTION SURVEY

In November 1986, CALCRUST acquired deep seismic-reflection data linking the southern San Joaquin Valley basin and underlying basement with the Tehachapi Mountains (locality 1 in Fig. 1; also see Fig. 2). The data were obtained using Western Geophysical's MDS-16 fiber-optic system. Thanks to the cooperative efforts of USC and the USGS, seismic-refraction and gravity surveys were run in conjunction with the seismic-reflection profile.

The Vibroseis survey began just northwest of the enigmatic White Wolf fault in the 12-km-deep Maricopa sub-basin, then crossed the Tejon Embayment southeastward along Comanche Point. The line continued up El Paso Canyon along basement rocks, ending just north of the Garlock fault. These new data and field observations of rock units imaged in the subsurface are being integrated with existing seismic and subsurface data and geologic maps.

Cretaceous crystalline rocks comprising the western Tehachapi Mountains probably represent the deepest-exposed levels of the Sierra Nevada. These rocks have been uplifted and rotated clockwise in Cenozoic time, though the structures that facilitated this deformation have not been identified. Tertiary marine and nonmarine terrigenous clastic rocks and a Miocene (22 Ma) volcanic unit crop out along the narrow rim of the Tejon Embayment and abut these basement rocks.

Preliminary results are based on an unedited brute stack section that reveals several prominent reflections despite substantial noise. The past few months have been spent editing and muting these data for more detailed processing. A north-dipping Moho reflection rises above 8 s (approximately 25 km) beneath the Tehachapi Mountains. A 17-km-long, north-dipping mid-crustal reflection apparently terminates updip underneath crystalline basement rocks (Fig. 3). This reflection may represent the Pelona/Rand schist lying below the offset equivalent to the Rand thrust (north branch of the Garlock fault). An alternative hypothesis is that this reflection is truncated by a large, south-dipping reverse fault that may be the buried, eastern equivalent to the Plieto thrust system.

Interpretation of the shallow section is enhanced by seismic stratigraphy. For example, by combining well and seismic data, the basin/basement contact can be traced north from its surface exposure into the subsurface beneath the Tejon Embayment. The upper basement and younger sedimentary and volcanic rocks are broken by a series of unmapped reverse and thrust faults along the margin of the embayment. Basinward of the margin, the structural style changes dramatically, as indicated by industry seismic data. Extension during Miocene time is indicated by a wide, northwest-trending graben system. Indeed, the Tejon Embayment is dominated by high-angle normal faults and volcanics. Pliocene to Recent faults associated with contraction partially overlap these normal faults. This transition of structural style is perhaps due to convergent strike-slip along the present strand of the San Andreas fault.

In addition to continued processing and interpretation, CALCRUST plans to conduct geologic field work in the southern San Joaquin and northwestern Tehachapi Mountains. CALCRUST has obtained well cores from the Tejon Embayment and is currently examining petrographic and diagenetic features of Oligocene sandstones. This study may help constrain the burial history of the region immediately south of the oblique-slip White Wolf fault. Future seismic reflection profiling will extend this line southward into the Mojave block and tie to the COCORP (1982) Mojave profiles.

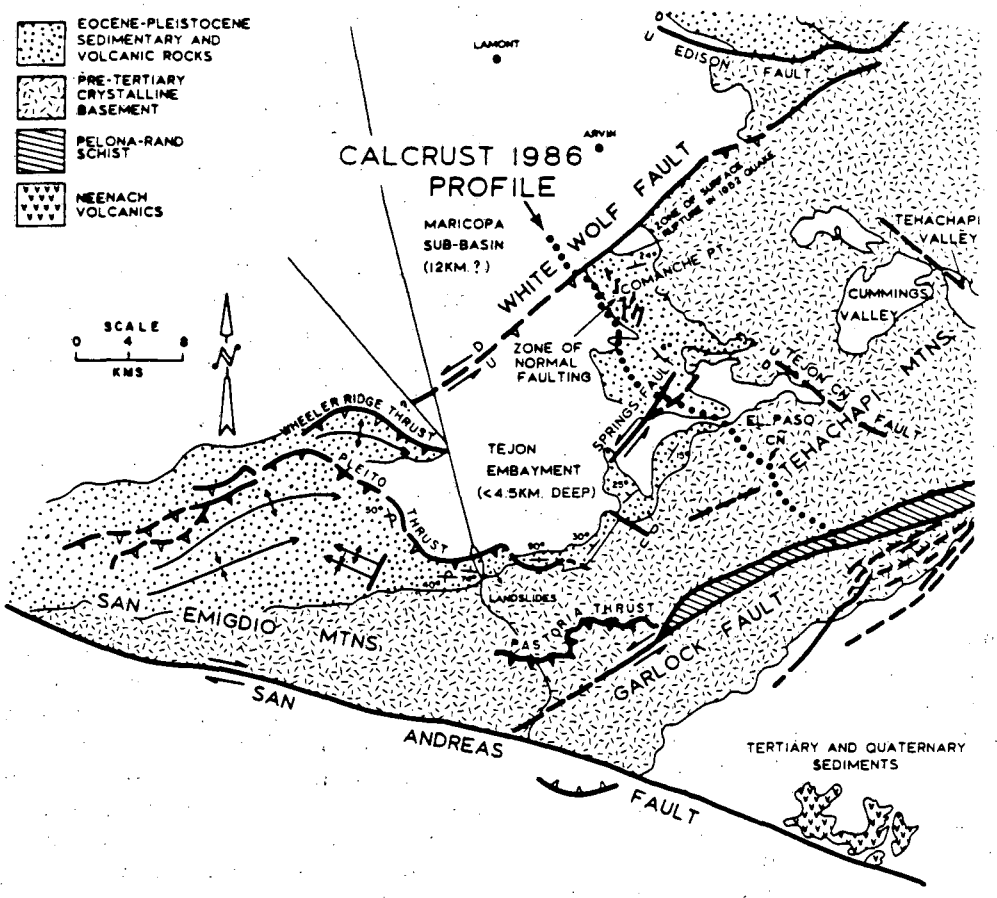

Figure 2. Index map of the Tejon area showing the generalized surface geology and the location of the 1986 CALCRUST survey. The profile was designed to join the San Joaquin Valley to the Mojave Desert as well as to study the White Wolf and Garlock faults. [XBL 886-2283]

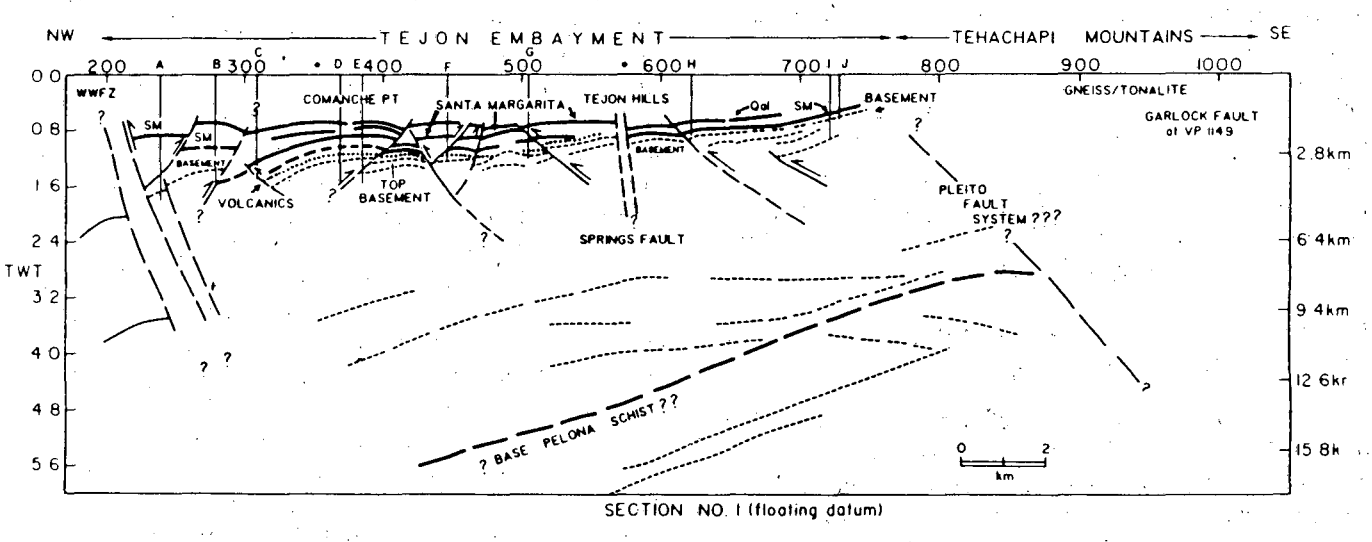

Figure 3. Integrated section between the San Joaquin Valley and Mojave Desert based on a portion of the CALCRUST Tehachapi Mountains profile. Basement reflectors are shown by the dashed lines as judged from preliminary processing of the data. Wells are shown by letters "A" through "J." [XBL 886-2284]

CALCRUST / USGS TEHACHAPI SEISMIC-REFRACTION SURVEY

A 115-km-long seismic-refraction line was collected across the Tehachapi Mountains in conjunction with the CALCRUST seismic-reflection survey (locality 1 on map). The reflection and refraction lines coincided for the center third of the refraction profile. The refraction line was oriented northwest-southeast, crossing the following important regional geotectonic features: (1) the southern end of the Maricopa sub-basin (Great Valley), a thickly sedimented basin; (2) the White Wolf fault, site of the 1952 M = 7.7 Kern County earthquake, and a major target of the reflection survey; (3) the mafic Tehachapi Mountains, the southern, uplifted portion of the Sierra Nevada batholith; (4) the Garlock fault; and (5) the topographically elevated Antelope Valley, part of the predominantly granitic Mojave block. Receivers used were 120 USGS portable vertical-component seismometers, deployed at approximately 1-km intervals; the sources were dynamite explosions. Preliminary interpretation of the data shows the following features observable on a reduced time section: (1) low velocities in the Maricopa sub-basin, corresponding to large thicknesses of sedimentary rocks; (2) an abrupt decrease in travel time south of the White Wolf fault, corresponding to the abrupt decrease in sedimentary-rock thickness across the fault as inferred from well-log information; (3) a further decrease in travel time over the Tehachapi Mountains, probably correlated with the presence there of high-velocity material; and (4) travel times increasing south of the Garlock fault and into the Antelope Valley. Observations (3) and (4) are particularly significant, as they confirm geologic and geophysical data in the region which indicate that uplifted, formerly deep-level granulite facies (high-velocity) rocks north of the Garlock fault are juxtaposed with relatively shallow, granitic rocks to the south. Initial results of the data analysis were presented at the April meeting of the Seismological Society of America and at the Cordilleran section meeting of the Geological Society of America.

NORTHERN SAN BERNARDINO MOUNTAINS SEISMIC SURVEY

CALCRUST collected a reflection seismic profile during December 1986 in order to investigate the crustal transition between the Mojave Desert and the eastern Transverse Ranges, with special emphasis on structures related to the evolution of the San Bernardino Mountain block. Geologic mapping in this area suggests that opposing thrusts bound the San Bernardino Mountains and may root in a regional decollement along a southward dipping microseismic zone at mid-crustal depths.

Data were collected using six 55,000-lb vibrators shooting into an 8-km spread with 33-m group intervals and a minimum of 30-fold CDP coverage. The line extended 30 km, 10 km within the basement outcrop of the northern flank of the San Bernardino Mountains and 20 km northward over the Quaternary(?)-filled sediments of Apple Valley (locality 3 in Fig. 1).

Brute stacks of the data from areas with favorable geometry and minimum statics show a sub-valley crust of variable reflection characteristics. Basin sediments approach a thickness of no more than 1000 m and appear relatively underformed. Beneath the northernmost San Bernardino Mountains under Arrastre Canyon exists a shallow reflection event rising to the range-front that can be interpreted as an underlying North Frontal thrust fault. A mid-crustal reflection zone across the profile dips toward the San Bernardino Mountains at less than 10 degrees; this zone may correlate with the base of the zone of microseismicity. Reflections below this zone are more numerous and are stronger in amplitude than reflections above the zone (upper crust). Shot gathers suggest the presence of a 10-s Moho with a probable southward dip.

CAJON PASS EXPANDED NOISE STUDY

A compact stationary-spread CDP survey (240 55′ groups E-W; 120 55′ groups N-S) was run at the Cajon Pass deep drilling site near the San Andreas fault in southern California (locality 3 in Fig. 1). The survey was designed to provide structural constraints on the crystalline basement into which the Cajon Pass well is being drilled. Because of lateral structural and near-surface heterogeneity, crooked-line geometry, and abundant surface noise, appreciable specialized data processing is being undertaken. Based on brute stacks, we report the following results: (1) the basement-sedimentary interface dips steeply to the north; (2) the basement may well be bounded to the east of the drill site by a steep contact manifested at the surface as the Squaw Peak fault; and (3) a reflector at depth (1-s travel time; about 6000 ft in depth) appears in the CDP section; it is possible this is a major discontinuity in the basement or an overthrust sedimentary horizon. It appears certain that detailed subsurface structure below 2 s will require VSP in the deep drill hole.

CALCRUST WHIPPLE MOUNTAINS REFLECTION SURVEY

CALCRUST collected 110 km of high-resolution crustal seismic-reflection profiles in the Whipple Mountains region in 1985 (locality 6 in Fig. 1; also see Fig. 4). These profiles were collected in an attempt to image low-angle detachment faults that are exposed in the Whipple Mountains and to look for subsurface expressions of Mesozoic compressional features. The crustal profiles revealed a highly reflective crust from shallow to deepest crustal levels.

Working with CGG, CALCRUST designed a field survey that collected multichannel seismic data with the following field parameters. A Sercel-348 recording system was used to record 192 channels. These channels were deployed in a symmetrical split-spread array at 25- and 33-m intervals. Vibroseis sources were placed every three receiver intervals; each VP consisted of six to eight sweeps. The 8–36 Hz sweeps were 31 s in length, and a 12-s listen time was used. Subsequent processing created 32-fold stacks. Currently, five manuscripts based on these data either have been submitted to journals or are in internal review. Additional manuscripts are in preparation.

In addition to vertical-incidence multichannel profiling, CALCRUST deployed additional passive multichannel arrays to record the Vibroseis sources. These "piggyback" recordings provide intermediate-offset (10–30 km) arrivals for refraction analysis and longer-offset reflection processing.

Detachment Faults

The combination of the CALCRUST profiles with three industry profiles by CGG allows for an examination of detachment-fault geometry. The uppermost detachment fault in the Chemehuevi Mountains is imaged in a seismic profile to the west in Chemehuevi Valley. A CALCRUST profile at the foothills images portions of the Whipple detachment fault. Continuation of the Whipple detachment fault to the west is difficult to see on adjacent profiles; the fault appears not to reflect. Geological reasons for this include (1) the detachment fault zone is too thin,

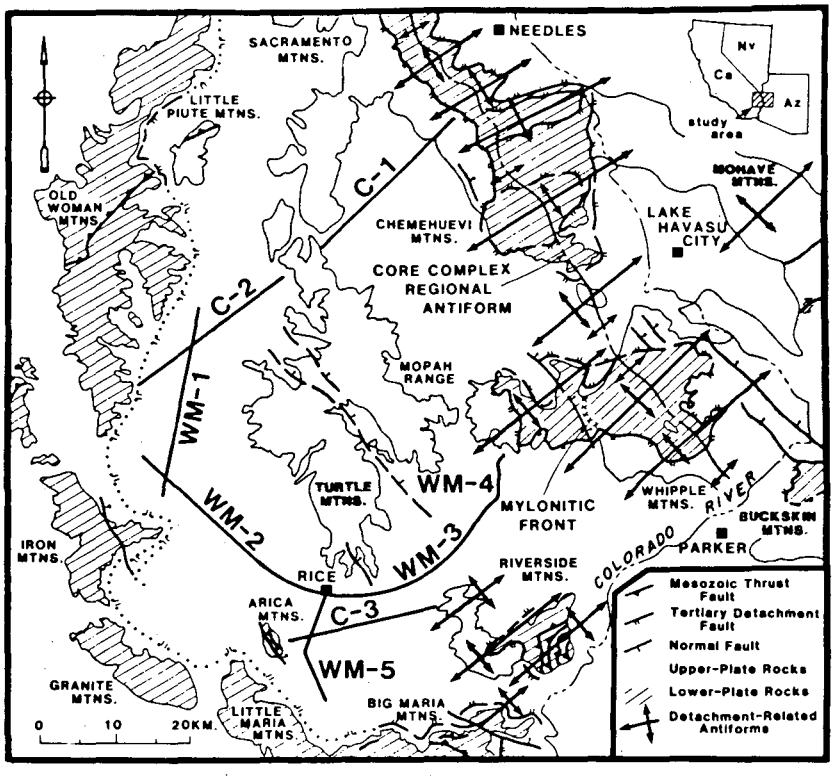

Figure 4. Regional tectonic map showing the location of CALCRUST lines WM-1 through WM-5 and industry lines C-1, C-2, and C-3 in the Whipple Mountains region of southern California. Major detachment faults are shown in the areas as is the mylonitic front (small x's) in the SW Whipple Mountains. Lines to be shot during the 1987–1988 field season will further refine our knowledge of this extensional terrane and continue southward toward the San Andreas and the Salton Trough. [XBL 886-2285]

and/or (2) the rock velocities above and below the fault zone are too similar to produce significant acoustic-impedance contrasts.

Interpretation of Mylonitic Reflections

The mid- to lower-crustal portions of the five CALCRUST seismic profiles are highly reflective (see Fig. 5). Subhorizontal, discontinuous reflections appear between 3 and 9 s. A higher density of reflections exists between 3 and 7 s; in certain profiles, these reflections constitute packets that exhibit significant lens-shaped structures. At 7–9 s, the reflection pattern is different from those at shallower depths; the base of the crust is interpreted to be the basal termination of reflection density.

The pattern and location of the reflections allow for an interpretational projection of these high-density reflections toward the Whipple Mountains. Specifically, a boundary ("mylonitic front") between nonmylonitic crystalline and mylonitized crystalline rocks is exposed in the western Whipple Mountains. The structural relationship as is exhibited in the mountain range is consistent with the nonreflective shallow-most crust (1–3 s) and the onset of the highly reflective middle crust (3–7 s). While this seismic pattern is most pronounced on CALCRUST line WM-3, the seismic line closest to the mylonitic front, WM-4, does not image these reflections well. Line WM-4 was collected on a crooked jeep trail and has required crooked-line processing. Secondary reprocessing of this profile is currently under way in an attempt to remove source-related noise and more accurately account for the crooked geometry.

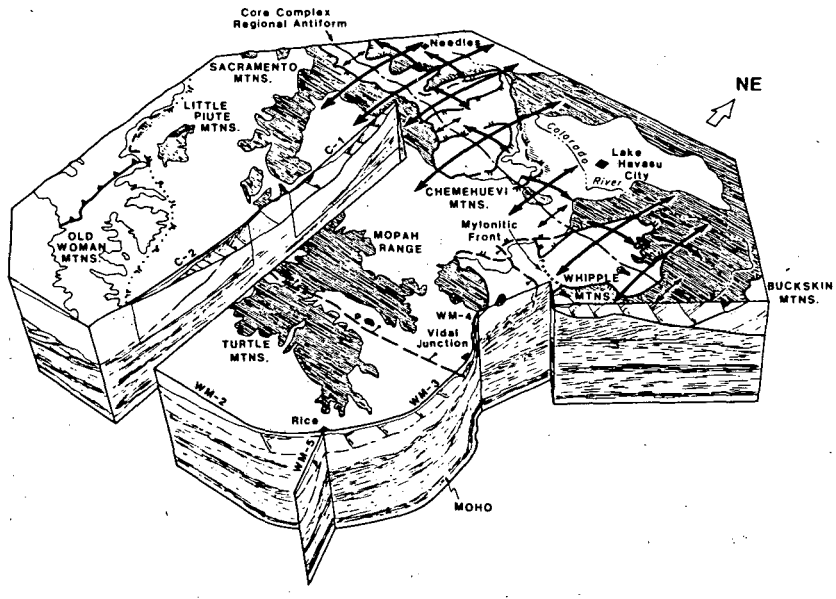

Figure 5. Block diagram combining a portion of the regional map (Fig. 4) with the crustal structure imaged on seismic lines WM-2, WM-3, WM-4, WM-5, and industry lines C-1 and C-2. A strongly reflective crust dips gently to the southwest away from its apparent exposure as a structural window in the Whipple, Chemehuevi, and Buckskin Mountains. [XBL 886-2286]

Transfer-Function Estimation for Natural Electromagnetic Fields

H.F. Morrison and E.A. Nichols

Magnetometer-array experiments using baseline lengths of 3 km and 120 km were completed in Grass Valley, Nevada (1984), and Long Valley, California (1985), to study the natural background field variations. Three techniques were developed for calculating the transfer function between fields meas-

ured at one site with fields measured at another site, or with different fields measured at the same site. These techniques were applied to determine the minimum magnetic signals that could be resolved at the different separations. The techniques are (1) linear point-to-point time-domain estimation (LPP); (2) frequency-domain transfer-function estimation (FD); and (3) multichannel Weiner estimation in the time domain (WE).

These methods have been applied to a high-precision SQUID magnetometer array data using fields in the frequency band 10^{-4} to 1.0 Hz. To monitor the "signal" introduced by motion of the sensors in the Earth's large static field, high-sensitivity cryogenic tiltmeters were used in each magnetometer. These methods have accounted for more than 70 dB of the signals received at one site using fields measured at another site. The removal of the motion-induced magnetic signals provides as much as 30 dB further reduction in the residual signal compared with using solely electromagnetic fields.

As the depth of exploration for electromagnetic methods increases, the natural electromagnetic fields become the limiting factor in measurement accuracy. Increasing measurement-averaging time or increasing source moment become impractical for efficient exploration programs. One solution is to develop schemes for removing or cancelling the background "noise" at the measurement site using fields measured at a remote site. To do this accurately we must account for the electromagnetic signals and their interaction with the earth's conductivity structure. Figure 1 illustrates two sites on the earth's surface, one that is over an anomalous conducting body and will consequently have its electromagnetic fields perturbed by the buried structure. The efficiency of the transfer functions relating the fields at the two sites determines how well the background field variations can be described at each point on the surface, which will determine the minimum local electromagnetic signal one could expect to detect. This local signal could be produced by a local transmitter as in CSAMT, IP, or other geophysical exploration techniques, or it could be the result of a local changing magnetic field, as would be produced by the injection of a hydrofracture with magnetite or the movement of a nearby magnetic body (e.g., a ship). We demonstrate three methods to calculate these transfer functions applied to multicomponent array data acquired in surveys in Grass Valley, Nevada, and Long Valley, California.

In these experiments, we simultaneously recorded signals from four magnetometers buried in

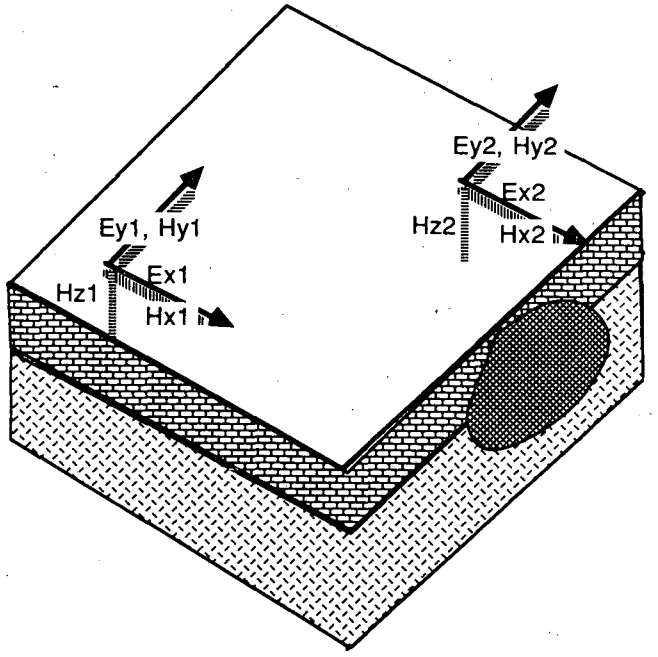

Figure 1. Transfer function geometry. [XBL 882-430]

insulated vaults and mounted on granite slabs. Two were located at the base vault on a single granite slab, and two others were located at the ends of an L-shaped array (Nichols et al., 1988). Three independent 18-bit data-acquisition systems were used to acquire the array data for the Long Valley experiment, which used station separations of 3, 10, 30, and 120 km.

DATA ANALYSIS

For uniform incident fields the observed fields will be related by point-to-point linear transfer functions determined solely by the conductivity of the ground. For bands of frequency where the transfer functions have very small imaginary components (i.e., little phase shift between the input and output) this process can be simplified to solve for real coefficients relating the input and output time series. A least-squares minimization procedure (LPP) solves for these coefficients directly in the time domain. These coefficients account for orientation and sensitivity differences and make a first-order correction for the motion of the magnetometers. For a 3-km reference site, the residual signal is progressively reduced by 30, 50, and 59 dB (residual standard deviations of 0.319, 0.031, and 0.0106 nT) using the parallel magnetic component (LPP1), all three components (LPP3), and three components plus tiltmeter outputs from each site (LPP tilt), respectively. The observed and signal residual spectra are presented in

Fig. 2. The observed magnetic fields are generally reduced 40–60 dB by this method.

The LPP method does not allow frequency dependence of the transfer functions and consequently works much more poorly for the secondary fields (E_x,E_y, and H_z) at sites where the conductivity structure is different. FD transfer-function estimation is obtained by inverting the crosspower matrix calculated at each of the constant Q-frequency windows of the Fourier-transformed data. The frequency-dependence formulation yields a better physical description of the electromagnetic-field behavior than the LPP method and yields more-robust solutions. Figure 3 illustrates the higher efficiency of the FD technique applied to the data of Fig. 2. Using the FD method we obtained 36, 54, and 77 dB (FD1, FD3, and DF tilt) of reduction of the background field (residual standard deviations of 0.153, 0.02, and 0.001 nT).

Multichannel Weiner estimation (WE) theory was implemented in the time domain as well. In this case, we assumed a moving-average (MA) process and parameterized the transfer-function estimation task. Weiner estimation hypothesizes second-order stationarity and is not suited for strictly random source phenomena. We obtained results comparable to the LPP transfer-function estimation process. The main limitation in our implementation was the error introduced in the residual signals by the startup time for the models. The WE models had residual standard deviations of 0.318, 0.0302, and 0.0103 nT (30, 50, and 59 dB), which are essentially the same values as obtained with the LPP method.

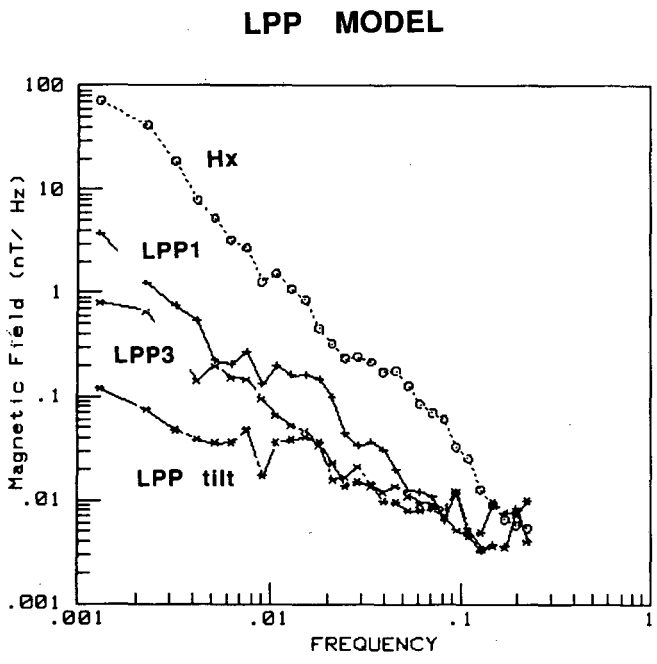

Figure 2. Observed and residual LPP spectra using one component (LPP1), three components (LPP3), and three components plus tilt (LPP tilt). [XBL 882-438]

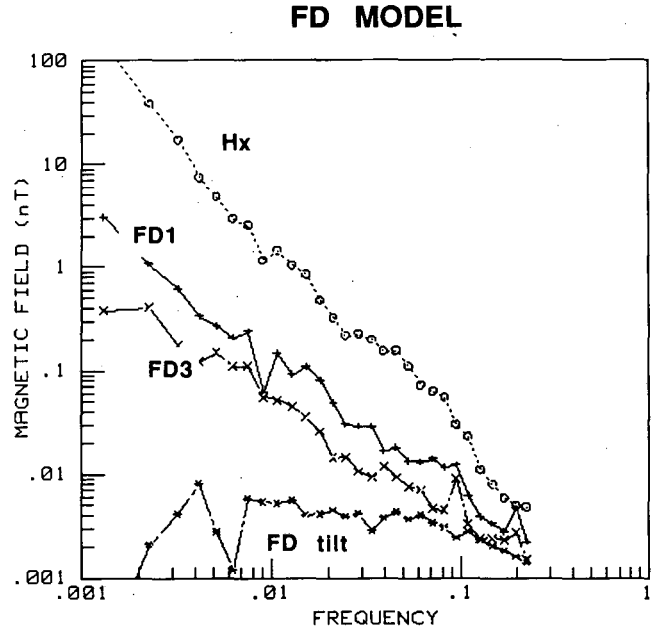

Figure 3. Observed and residual FD spectra using one component (FD1), three components (FD3), and three components plus tilt (FD tilt). [XBL 882-439]

All three techniques were used to estimate the magnetic field at a site from the local electric fields (admittance transfer function). This method of estimation would be useful when nonelectromagnetic magnetic anomalies (such as those caused by a passing ship) must be detected in real time without recourse to telemetry to another remote site. Figure 4 shows the LPP and FD estimated and residual signals for the same data set. These models had residual standard deviations of 1.88 and 0.58 nT, which correspond to cancellation of the background fields by 14 and 45 dB, respectively. Figure 5 illustrates the residual spectra for these models.

There was only minor reduction of the model prediction efficiency as the station separation increased to 120 km. The WE models gave residual standard deviations of 0.014 and 0.007 nT (33 and 39 dB) for the 1-m and 120-km separations, respectively, whereas the FD models had much lower deviations of 0.004 and 0.002 nT for 45 and 52 dB, respectively.

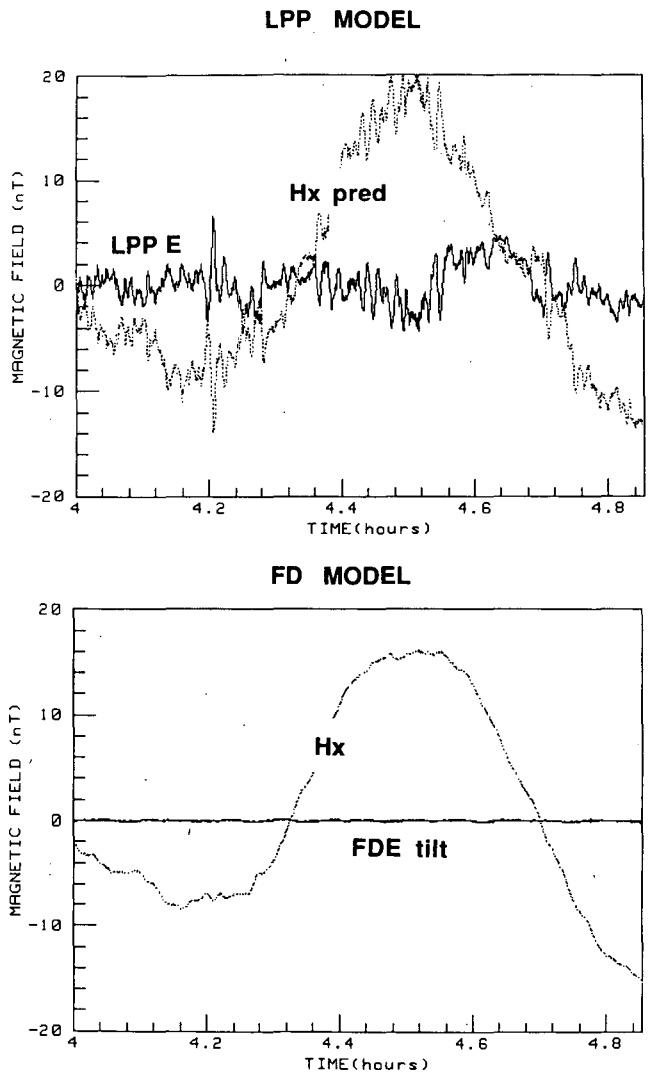

Figure 4. (**Top**) Admittance transfer function from electric fields and tilt: LPP E model. (**Bottom**) Admittance transfer function from electric fields and tilt: FDE model. [XBL 882-440]

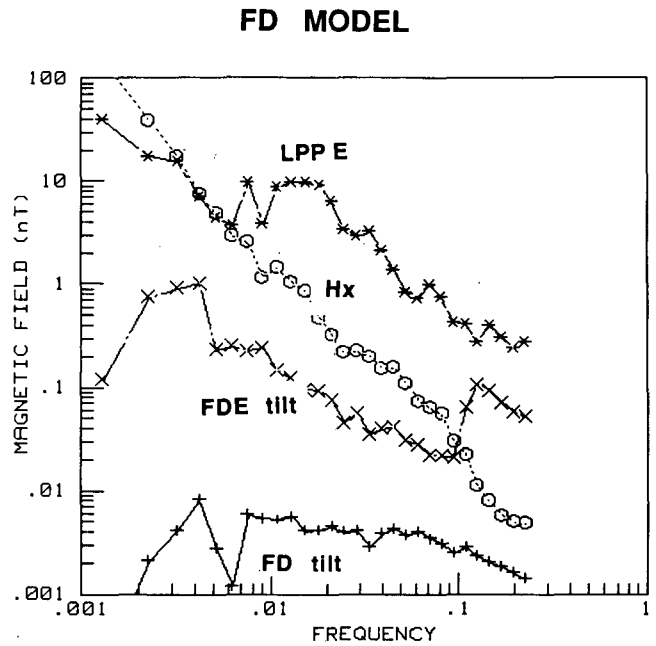

Figure 5. Comparison of observed H_x spectra and residual spectra for models LPP E, FDE, and FD tilt. [XBL 882-437]

REFERENCES

Nichols, E.A., Morrison, H.F., and Clarke, J., 1988. Signals and noise in measurements of low frequency geomagnetic fields. J. Geophys. Res., in press.

Three-Dimensional Interpretation of Magnetotelluric Data in Long Valley, California

S.K. Park, C. Torres-Verdin, and H.F. Morrison*

The volcanic complex at Long Valley has been the subject of intensive study, as summarized by Hermance (1983) and Hill et al. (1985). It is a silicic system that has exhibited recent activity, although the last major eruption was 0.73 Ma (Bailey et al., 1976). Long Valley is of great interest for several reasons, including (1) the possibility of damaging earthquakes and volcanic eruption and (2) a source region of thermal and electrical energy from both magma and hydrothermal systems.

Recent deformation was reported for the period 1975–1982, and a spherical magma chamber at a

depth of 10 km was inferred as the cause of the deformation (Savage and Clark, 1982). Intense seismic activity, including swarms of earthquakes in 1980 and 1982, accompanied this deformation (Ryall and Ryall, 1980, 1983). Long Valley has been monitored with a dense array of seismometers since then, and data from this array have been used to construct a three-dimensional seismic-wave attenuation model of the caldera (Ryall and Ryall, 1983; Sanders, 1984). Sanders (1984) found regions at depths of 4–13 km that are attenuating both compressional and shear waves. He suggests these regions may be composed of magma.

Several types of geophysical data have been cited in support of shallow magma beneath Long Valley (Rundle et al., 1986), but the evidence from electrical surveys has been inconclusive. Most of the electrical surveys have been concentrated on shallow targets. Hermance et al. (1984) measured telluric fields and examined deeper structure. They concluded that their measurements were insensitive to the presence or absence of magma. However, Long Valley is the site of rich geothermal resources regardless of the existence of magma at depth.

Many geophysical surveys have been made of the geothermal resources in Long Valley. Lachenbruch et al. (1976) developed thermal models for the distribution of heat in Long Valley caldera. Hydrological investigations of the caldera provide lithological logs of many wells (Farrar et al., 1985). Stanley et al. (1976) conducted an extensive resistivity and electromagnetic survey that delineated several conductive anomalies. Chevron Resources Company and Unocal both have detailed studies of Long Valley, which have been proprietary until recently. In 1986, Chevron and Unocal released magnetotelluric (MT) data from 77 Long Valley stations to us for the purpose of a 3-D interpretation.

Our goals were to develop interpretive methods in a complex volcanic environment and to confirm or deny the earlier assertion that the telluric data were insensitive to the presence of magma (Hermance et al., 1984). We worked with many more MT sites (77 versus 23) than did Hermance et al. (1984) and used a 3-D modeling program (Park, 1985). All possible pertinent geophysical information was incorporated into our electrical model.

The MT response at frequencies from 0.001 to 100 Hz is controlled almost completely by shallow structure in the caldera. The complex electrical structure in the first kilometer, coupled with a good conductor at a depth of 1.5 km, effectively screens any deeper structure beneath the caldera.

Our interpretation is based principally on phase spectra of the complex impedances. Static offsets of the amplitude spectra are so severe that they were useful only in constraining the shallow structure. The phase was particularly sensitive to the presence or absence of the conductor at 1.5 km.

CONSTRAINTS ON THE MODEL

An interpretation of MT data is often impractical without independent, external constraints on the resistivity distribution. The electrical survey of Stanley et al. (1976) provided resistivities for the interval between the surface and a depth of 1.0 km. These results were supplemented by 1-D inversions of the MT responses at the higher frequencies for each station. The range of frequencies used at each site was variable and depended on the onset of significant anisotropy in the sounding curves. We used electrical logs for three deep (1.6 km or more) wells in the caldera to establish the resistivity of several volcanic formations. In addition, lithologic logs (Farrar et al., 1985), seismic data, and isopach/structural maps based on gravity (Carle, 1987) were incorporated into our resistivity model.

The synthesized resisting mode is shown in Fig. 1. The structure for the uppermost 1.0 km is based on the above constraints, with minor adjustments to the model to fit the data. The structure from 1.0 to 1.5 km is also based on the above constraints but required greater modification to fit the observed phases. The main modification consisted of placing the good conductor (1 ohm-m) where it was needed.

We attribute the high conductivity of the depth interval from 1.5 to 1.7 km to metasediments and to fractured zones. The conductor is observed at a depth of 1.5 to 1.7 km in the m-1 well approximately 5 km east of Mammoth Lakes. This unit is a remnant of a Paleozoic roof pendant in the Sierra Nevada batholith and consists of metamorphosed sediments containing graphite (Goldstein, personal communication, 1986). Measured resistivities from logs for this unit range from below 1 ohm-m to over 100 ohm-m, with approximately 80% of the unit below 1 ohm-m.

The location of the conductor is consistent with the hypothesis that the metasediments were simply part of the down-dropped cauldron block that was covered by the Bishop Tuff and later volcanic units. These metasediments crop out to the north and south of the caldera, and the conductor matches nicely with these outcrops. However, the conductor

*Institute of Geophysics and Planetary Physics, University of California, Riverside, CA 92521.

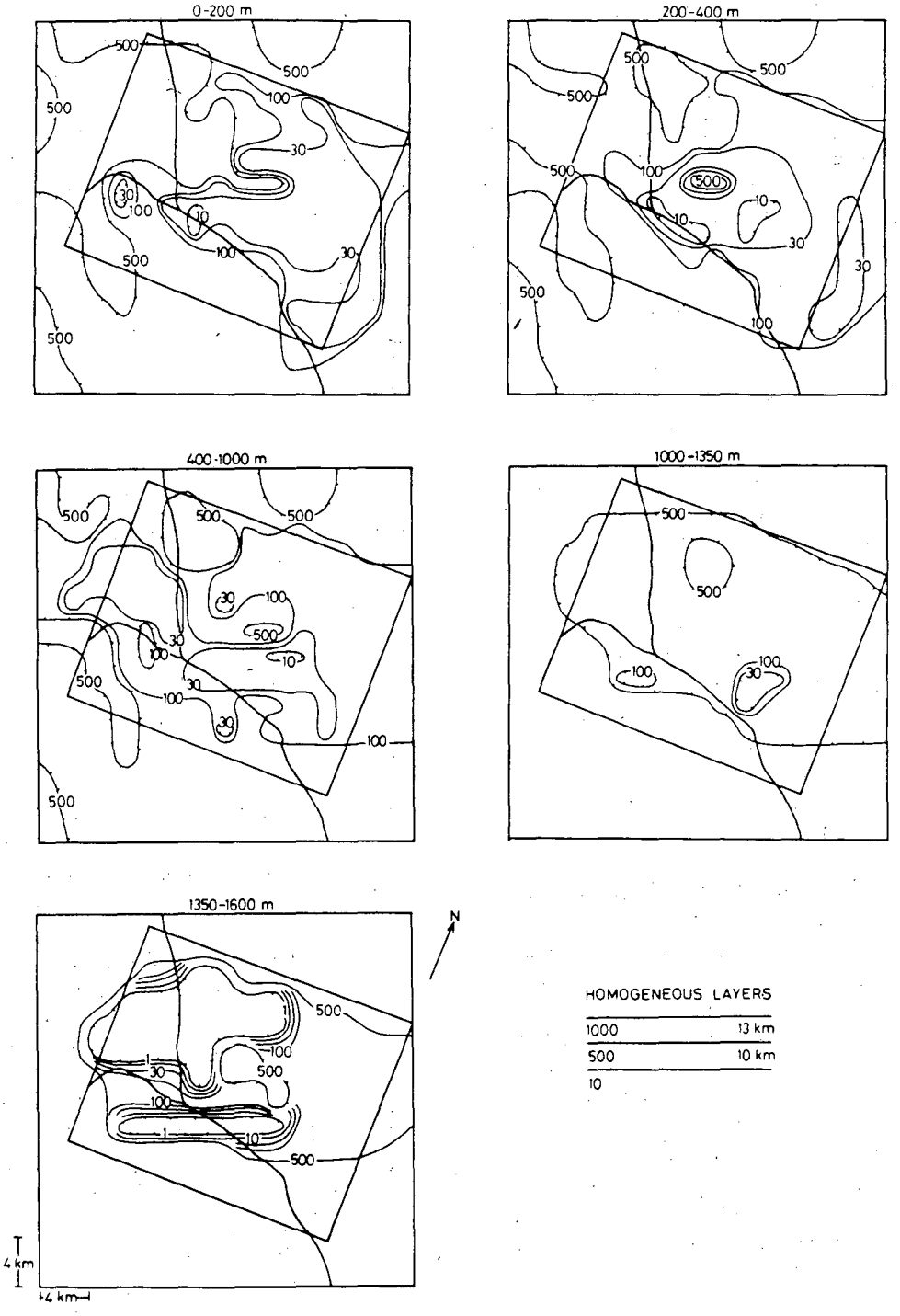

Figure 1. Plots of electrical resistivity (ohm-m) in Long Valley. The 3-D interpretation shows that the phase spectra can be satisfied by five inhomogeneous layers to a depth of 1.6 km underlain by three homogeneous layers. [XBL 887-2574]

is also close to numerous intracaldera faults, and the conductor may be enhanced by hydrothermal alteration and fluid circulation along permeable zones associated with the faults.

COMPARISON DATA

Chevron Resources Company released of MT data from 54 stations to us in 1986, and Unocal released data from 23 of their stations to us in Janu-

ary 1987. Hence much of the interpretation is based on Chevron's data, with Unocal's data used as an additional control.

We found that several patterns emerged on careful examination of the phases at the 54 Chevron sites. Many sites were close to one another and exhibited similar phase spectra in spite of severe distortions in the amplitude spectra caused by local inhomogeneities at the surface. We clustered sites with similar spectra and averaged their data. This procedure was necessary because of the poor quality of the data and because of the complex, shallow structure. The data from Chevron were collected without a remote reference, so the quality of the soundings is variable. The later data from Unocal were collected with a remote reference, and the quality of these soundings is much better. However, those data exhibit phases that do not match the Chevron phase spectra or the phases for any reasonable model. We therefore conclude that the Unocal data lack a proper phase calibration.

Nearly all predicted phases decrease to below 45° near 1 Hz. The quality of the data precluded a more detailed model than is shown in Fig. 1. Note that no structure deeper than 1.6 km is needed to provide a fit to the data. The decrease in phase below 45° near 1 Hz is associated with the absence of the good conductor at 1.5 km. A phase in the northeast quadrant of the caldera never dips below 45° and is almost monotonically decreasing with increasing frequency. This behavior could be predicted only if a conductor is present beneath this region.

An extremely important finding from this study is that phase is not insensitive to lateral heterogeneity, but merely less sensitive to it than amplitude. The differences in the phases of the maximum and minimum apparent resistivities (referred to hereafter as anisotropy in the phases) persist to frequencies at which the sounding is responsive to the electrical mantle (0.1 Hz and lower). This anisotropy in phases is caused wholly by shallow (depth < 1600 m) structure. We conclude from our work that there is simply no substitute for 3-D modeling in this complex environment.

SENSITIVITY TO A CRUSTAL MELT ZONE

The analysis of the MT data provides no unequivocal answer regarding the presence or absence of melt beneath the caldera. On the basis of the data at hand and our modeling studies, we are prepared, however, to place bounds on magma chamber size and depth. (1) The presence of a large, well-connected magma chamber, approximated by a 5-ohm-m spherical conductor, radius 4 km, and centered at a depth of 10 km, is not likely. The response of such a conductor is several times larger than the mismatch between our model and the observed sounding curves. (2) Small, isolated bodies of melt may be present, but these cannot be resolved using the data available. A small 5-ohm-m body (e.g., 2 km $\times$ 2 km $\times$ 0.5 km) at a depth of 4 km or more would affect only those stations directly above it. Small changes in the amplitude/phase spectra would also occur at neighboring stations, but these would be too small to be resolved from the effects of small shallow heterogeneities.

CONCLUSIONS

We have shown by this study that an interpretation based principally on phase spectra is useful in complex volcanic environments. Although the problem of static offsets of sounding curves is alleviated by using these data, the effects of shallow heterogeneity are still seen in the phases. There is no substitute for 3-D modeling of the structure, and this requires a high density of MT stations as well as independent data or the distribution of shallow or near-surface resistivities.

REFERENCES

Bailey, R.A., Dalrymple, G.B., and Lanphere, M.A., 1976. Volcanism, structure, and geochronology of Long Valley caldera, Mono County, California. J. Geophys. Res., v. 81, no. B5, p. 725–744.

Carle, S.F., 1987. Three-dimensional gravity modeling of the geologic structure of Long Valley caldera, California (M.S. thesis). University of California, Berkeley, Lawrence Berkeley Laboratory Report LBL-23376.

Farrar, C.D., Storey, M.L., Rojstaczer, S.A., Janik, C.J., Mariner, R.H., and Winnett, T.L., 1985. Hydrologic and geochemical monitoring in Long Valley caldera, Mono County, California. USGS Water-Resources Investigation Report 85–4183.

Hill, D.P., Bailey, R.A., and Ryall, A.S., 1985. Active tectonic and magmatic processes beneath Long Valley caldera, eastern California: An Overview. J. Geophys. Res., v. 90, p. 11111–11120.

Hermance, J.F., 1983. The Long Valley/Mono basin volcanic complex in eastern California. Status of present knowledge and future research needs. Rev. Geophys. Space Phys., v. 21, p. 1545–1565.

Hermance, J.F., Slocum, W.M., and Neumann, G.A., 1984. Long Valley/Mono basin volcanic complex: A preliminary magnetotelluric and mag-

netic variation interpretation. J. Geophys. Res., v. 89, p. 8325–8337.
Lachenbruch, A.H., Munroe, R.J., and Moses, T.H. Jr., 1976. Geothermal setting and simple heat conduction models for Long Valley caldera. J. Geophys. Res., v. 81, p. 769–784.
Park, S.K., 1985. Distortions of magnetotelluric sounding curves by three-dimensional structure. Geophysics, v. 50, p. 785–787.
Rundle, J.B., Carrigan, C.R., Hardee, H.C., and Luth, W.C., 1986. Deep drilling to the magmatic environment in Long Valley caldera. EOS, v. 67, p. 490–491.
Ryall, F., and Ryall, A., 1980. Spatial-temporal variations in seismicity preceding the May, 1980 Mammoth Lakes, California earthquakes. Spec. Rept. Calif. Div. Mines Geol., v. 150, p. 27–39.
Ryall, F., and Ryall, A., 1983. Attenuation of *P* and *S* waves in a magma chamber in Long Valley caldera, California. Geophys. Res. Lett., v. 8, p. 557–560.
Sanders, C.O., 1984. Location and configuration of determined by anomalous earthquake signals. J. Geophys. Res., v. 89, p. 8287–8302.
Savage, J.C., and Clark, M.M., 1982. Magmatic resurgence in Long Valley caldera, eastern California. Science, v. 219, p. 1432–1433.
Stanley, W.D., Jackson, D.B., and Zohdy, A.A.R., 1976. Deep electrical investigations in the Long Valley geothermal area, California. J. Geophys. Res., v. 81, p. 810–820.

Self-Potential Anomalies Due to Contaminated Aquifers

M.J. Wilt

The self-potential (SP) method consists of measurement and interpretation of naturally occurring dc electrical potentials. Potentials may arise from a variety of sources, including electrokinetic or streaming potentials that are due to fluid flow, thermoelectric potentials that are due to heat flow, and Eh or oxidation-reduction potentials that can arise near sulfide ore bodies. The SP method has been successfully used in mineral and geothermal exploration (Corwin and Hoover, 1979; Sato and Mooney, 1960), engineering and groundwater studies (Olgilvy et al., 1973), and in steam-flooding and coal-burning experiments (Corwin and Hoover, 1979).

Sizable self-potential anomalies are associated with many fluid-flow processes. The potentials arise from the interaction between moving pore fluid and the Helmholtz double layer at the surface of the pores. The double layer is a separation in charge between the ionic pore fluid and induced charges in the pore walls. The separation results in a "zeta" potential that is a function of the fluid and the rock. Interaction between the moving pore fluid and the double layer produces a streaming current that is returned galvanically to form a closed cell. The size and shape of the SP anomaly depends on the fluid pressure or velocity, the electrical cross-coupling between rock and pore fluid, and the electrical conductivity of the rock. Anomalies of the order of several volts have been reported in areas of fast-moving subsurface water and resistive rock, although typical electrokinetic anomalies are of the order of tens to hundreds of millivolts (Corwin and Hoover, 1979).

SELF-POTENTIAL MODELS OF GROUNDWATER CONTAMINATION SITES

Groundwater pollution arising from disposal of industrial and agricultural waste products has become a major problem, particularly in urban areas. The self-potential method may provide a simple, low-cost means of detecting the leakage of pollutants from surface dump sites and monitoring the movement of liquid waste through aquifers.

Several factors suggest that significant SP anomalies may be associated with contaminated groundwater, although no known field results are available to confirm any correlation. If contaminated groundwater is different in pH, salinity, or concentration of metallic ions from the native groundwater, then a significant change in zeta potential may result (Adamson, 1982).

In general, the addition of contaminants to groundwater results in a decrease in the electrical cross-coupling coefficient (Ishido and Mizutani, 1981). If the contaminants change the pH or salinity of the groundwater, then the change in coupling coef-

ficient may be of the same magnitude as the change in electrical resistivity. In some cases, however, a change in cross-coupling coefficient may not be accompanied by a change in resistivity.

NUMERICAL MODELING

For simple problems, analytic solutions to SP fluid-flow problems are available, but most problems require some sort of numerical modeling (Sill, 1983). For this study a two-dimensional computer code was used that computes the induced current sources by finite differences and calculates the potentials using a transmission-surface analogy (Sill, 1982). The program requires a fluid velocity function; a model for the velocity coupling coefficients, which relate the fluid flow to the induced current; and a two-dimensional resistivity distribution. The program then provides electrical potentials at all points in the model.

Figure 1 schematically shows a two-dimensional model of a contaminant site that could produce an SP anomaly. The model parameters are adjusted to reflect the change in SP anomaly due to changes in width, depth of burial, and electrical resistivity of the contaminant body. The parameters of the model were chosen to correspond to actual field conditions. The model features a horizontal aquifer 3 m thick at a depth of 25 m. Water is moving horizontally at the rate of 100 m/y. The background resistivity at the site is 10 Ω-m. The coupling coefficient changes from 80 C/m in the unaffected region to 30 C/m in the contaminated region.

Figure 2 gives the surface voltage profiles for contaminant bodies having three different widths. Each profile shows a dipolar anomaly with the peaks located somewhat inwards from the boundaries of the contaminant body. The magnitude of the anomaly increases with increasing width of the anomalous zone. This is because the induced charges are separated further for wider bodies and therefore interfere less with each other.

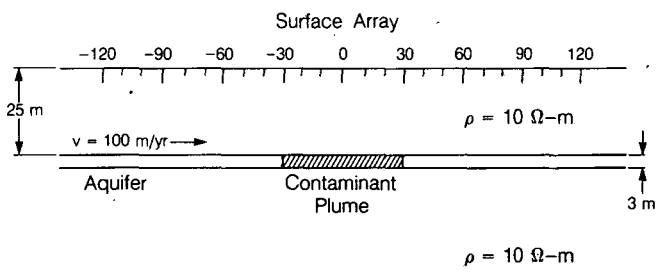

Figure 1. Schematic diagram of a two-dimensional contaminant site. [XBL 873-9976]

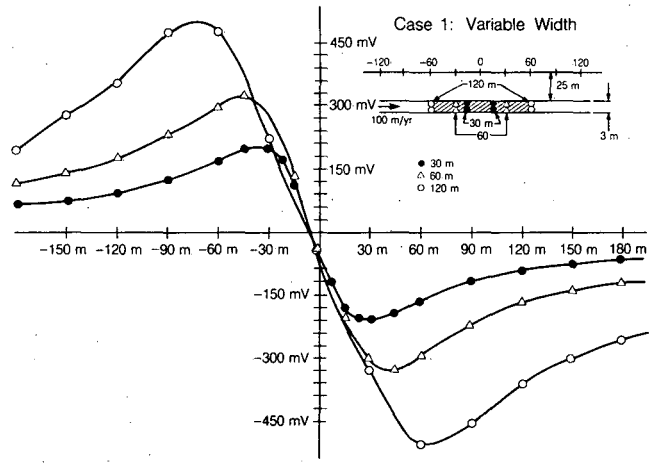

Figure 2. Surface SP voltage profiles over contaminant bodies of three different widths. [XBL 873-9977]

In Fig. 3 the depth to the contaminant plume is varied from 10 to 50 m. In this case the voltage anomaly is smoother and broader and has a lower amplitude at greater depths of burial. At a depth of 10 m, the positions of the dipolar peaks correspond well to the boundaries of the subsurface plume; at greater depths this correlation is less clear, and the peaks are broader.

In Fig. 4 the resistivity of the contaminant is changed from 10 to 30 Ω-m (curve a) and 3 Ω-m (curve b). The curves show that the effect of resistivity change is much less than changes in coupling coefficient. Changing the resistivity by a factor of 10 results in a maximum voltage difference of only about 10%.

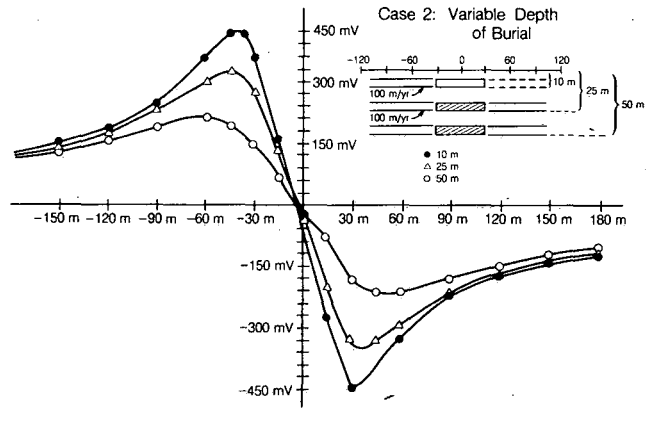

Figure 3. Surface SP voltage profiles over contaminant bodies at three different depths. [XBL 887-10329]

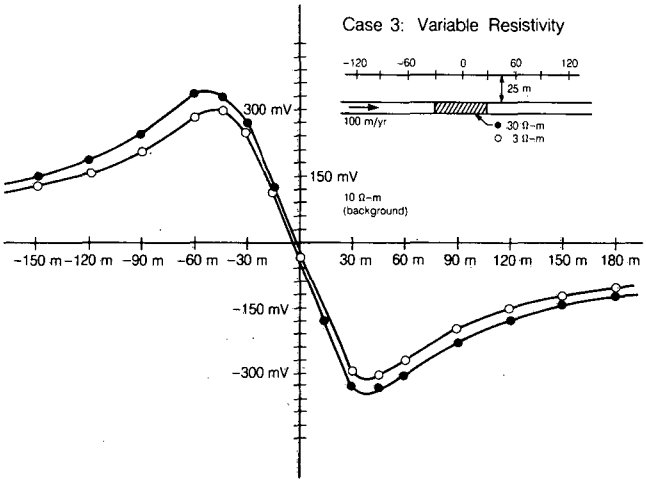

Figure 4. Surface SP voltage profiles over a contaminant body illustrating the effect of changing the resistivity of the body. [XBL 873-9978]

DISCUSSION AND SUGGESTED RESEARCH

The above models show that distinctive SP anomalies can be associated with contaminant plumes in areas of high subsurface flow. Since the SP anomaly is due to current sources induced at the contaminant boundary, it should be possible to locate the boundaries from surface measurements if enough other information is known. The problem may therefore be reduced to the downhole-surface resistivity problem, which already has been studied (Morrison et al., 1986).

Since only two-dimensional cases were considered, the anomalies are probably substantially larger than in the three-dimensional cases that can be more reasonably associated with subsurface contaminants. However, even if anomalies only 20% as large as those shown above are associated with contaminant sites, they should be sufficiently large to indicate plume boundaries except in very noisy areas.

Because contaminant sites are often located near urban areas, the background noise levels are probably much higher than the 5–10 mV reported in the literature (Corwin and Hoover, 1979). The effects of power-line transients, grounded fences, and rusting metal can add tremendously to noise levels. To combat this background-noise problem, SP surveys should be measured from arrays where data are taken simultaneously rather than sequentially. Simultaneous measurements should reduce the effect of transients by common-mode rejection and also allow for signal stacking and low-pass filtering to further reduce noise levels. Under these conditions it should be possible to acquire usable data even in noisy areas.

The area where further research is most needed is in laboratory studies of the effect of various contaminant species on the SP coupling coefficient. Because of the nature of some of these chemicals, the effect may be significant even at small concentrations.

REFERENCES

Adamson, A.W., 1982. Physical Chemistry of Surfaces. John Wiley and Sons Inc.

Corwin, R.F., and Hoover, D.B., 1979. The self potential method in geothermal exploration. Geophysics, v. 44, no. 2.

Ishido, T., and Mizutani, H., 1981. Experimental and theoretical basis of electrokinetic phenomena in rock-water systems and its application to geophysics. J. Geophys. Res., v. 86, no. B3.

Morrison, H.F., Asch, T., Wilt, M.J., Pouch, G.W., Tsang, C.F., and Javandel, I., 1986. Resistivity monitoring of subsurface contaminants. Proposal to the Regional Groundwater Quality Control Board, Alameda County, California.

Olgilvy, A.A., Ayed, M.A., and Bogoslovsky, V.A., 1973. Geophysical studies of water leakages from reservoirs. Geophys. Prosp., v. 22, no. 1.

Sato, M., and Mooney, H.M., 1960. The electrochemical mechanism of sulfide self potentials. Geophysics, v. 25, no. 1.

Sill, W.R., 1982. Self-potential effects due to hydrothermal convection — velocity cross coupling. University of Utah, Department of Geology and Geophysics, DOE ID 12079-68.

Sill, W.R., 1983. Self potential modeling from primary flows. Geophysics, v. 48, no. 1.

Fracture Detection Using Low-Frequency Cross-Hole Electromagnetic Techniques

Q. Zhou, A. Becker, N.E. Goldstein, H.F. Morrison, and K.H. Lee

A practical problem in waste-repository or geothermal-reservoir evaluation is the detection of a major fracture zone close to, but missed by, drill holes. These holes provide the opportunity to use subsurface electromagnetic techniques for detecting any nearby fracture. A number of geophysical techniques have been used to address the fracture-detection problem, and each has its own advantages and limitations. To date, however, most of the work has centered on the use of conventional geophysical borehole logs to detect and characterize fractures intersected by the drill (Nelson et al., 1980; Jones et al., 1985). Because most holes are drilled close to vertical, conventional logging techniques are sensitive mainly to the flat-dipping shear or fracture discontinuities. To determine the possible presence of a major, steeply dipping shear or fracture zone that is not intersected by a borehole, workers have recently looked at advanced geophysical techniques. Among these is cross-hole seismic/acoustic tomography to map velocity and attenuation anomalies (Peterson, 1986). Electromagnetic techniques have also been studied in this regard, because a clay-rich shear zone or water-filled fracture zone in crystalline rock has a much lower resistivity than the host medium (Green and Mair, 1983). Deadrick et al. (1982) and Ramirez and Lytle (1983) used cross-hole radar-frequency geotomography to map fractures. Lytle et al. (1979) studied cross-borehole electromagnetic probing to locate high-contrast anomalies, and Chang et al. (1984) developed a downhole VHF radar apparatus with directional source and receiver antennas. Because of the high attenuation at radar frequencies, lower frequencies may be more suitable for fracture detection between widely spaced holes or where the host rock is more conductive than a low-permeability granite.

We have investigated the applicability of a downhole grounded vertical electric-dipole (GVED) source (Zhou et al., 1987). The implied assumptions always are that the fracture is a good scatterer of electromagnetic waves and that it is embedded in a less-conductive but otherwise homogeneous region. The GVED source has its unique advantages under these conditions. It has deep penetration and evokes a large response because it can be operated at relatively low frequencies, e.g., below 30 kHz. Of course, if the host rock is very resistive, the GVED source may fail because little current can be produced in the host rock.

FORMULATION OF THE PROBLEM

The fracture is represented by a rectangular thin-sheet conductor of arbitrary orientation in a half-space of conductivity σ (Fig. 1). It strikes 90° and it dips at an angle β with respect to the coordinate axes. The coordinates of the center of the top edge of the sheet are $(X_0, 0, H)$, where H is the depth to the horizontal top of the sheet from the surface. The conductance of the sheet conductor is τ, and its dimensions are denoted by a and b. The source is a grounded vertical electric dipole, harmonic in time ($e^{i\omega t}$), at a depth of H_{tx}. In all calculations we use a unit dipole moment ($P = I\delta l = 1$ A·m). The depth of the receiver is represented by H_{rx}.

The displacement current is neglected, and the magnetic permeability is assumed to have the free space value μ_0 of $4\pi \times 10^{-7}$ (H/m). The boreholes, whose diameters are assumed to be nil, are considered to be vertical, and the effects of water in the hole are not taken into account in the calculations. The separation between transmitting and receiving holes is X_{dh}.

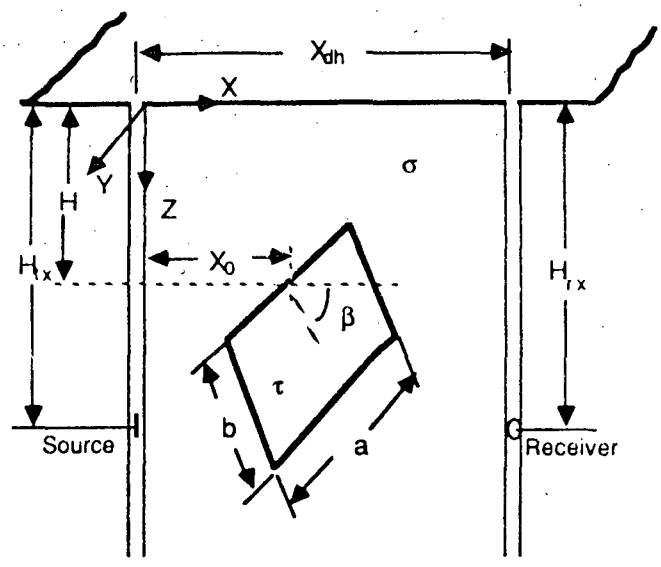

Figure 1. Schematic model. [XBL 866-2261]

The approach used to calculate the frequency-domain magnetic-field responses is based on the algorithm developed by Weidelt (1981), who calculated the magnetic-field anomaly due to a sheet conductor for a magnetic-dipole source and receiver in the air. In the modified version of the code, the GVED source is placed in the conductive medium. The following is a brief summary of the algorithm.

Beginning with Maxwell's equations,

$$\nabla \times \mathbf{E} = -i\omega\mu\mathbf{H}, \tag{1}$$

$$\nabla \times \mathbf{H} = (\sigma + i\omega\epsilon)\mathbf{E} + \mathbf{J}, \tag{2}$$

the following two integral equations are derived by using the thin-sheet approximation (Price, 1949):

$$\mathbf{E}_s(\mathbf{r}_0) = \mathbf{E}_{ns}(\mathbf{r}_0) - i\omega\mu_0\int_s \tau(\mathbf{r})g_s(\mathbf{r}_0/\mathbf{r})\cdot\mathbf{E}_s(\mathbf{r})ds, \tag{3}$$

$$\mathbf{H}(\mathbf{r}_0) = \mathbf{H}_n(\mathbf{r}_0) + \int_s \tau(\mathbf{r})\mathbf{E}_s(\mathbf{r})\cdot\nabla_0 \times g(\mathbf{r}/\mathbf{r}_0)ds. \tag{4}$$

Here the integration is carried out on the sheet surface s. $\mathbf{E}_s$ is the total tangential electric field on the sheet, and $\mathbf{E}_{ns}$ is the incident tangential electric field on the sheet. Likewise, $\mathbf{H}$ is the total magnetic field, and $\mathbf{H}_n$ is the incident magnetic field at the point of observation. The terms $g_s(\mathbf{r}_0/\mathbf{r})$ and $g(\mathbf{r}_0/\mathbf{r})$ are the Green's dyadic functions relating the tangential current distribution on the sheet to the electric fields everywhere. The conductance $\tau(\mathbf{r})$ is the sheet conductivity-thickness product and is be assumed to be a constant.

Both the incident fields $\mathbf{E}_{ns}$ and $\mathbf{H}_n$ and the Green's dyadic function g and g_s are related to the dipole fields in the layered medium and are easy to evaluate. After these are calculated, Eq. (3) is solved for $\mathbf{E}_s$, which is then used in Eq. (4) to obtain $\mathbf{H}$ at the receiver sites.

NUMERICAL RESULTS AND ANALYSIS

A few numerical results are shown to demonstrate the properties of the anomalous (secondary) magnetic fields due to GVED excitation. A more complete set of cases was presented by Zhou et al. (1987). The model parameters used are given in Fig. 2 and are maintained unless otherwise specified. In particular, we consider the case with operating frequency to be 1 kHz. The conductive target, which has a size of 150 m × 100 m, is vertical and has a conductance of 1 S, while the host rock has a conductivity of 10 mS/m. The magnetic-field anomalies

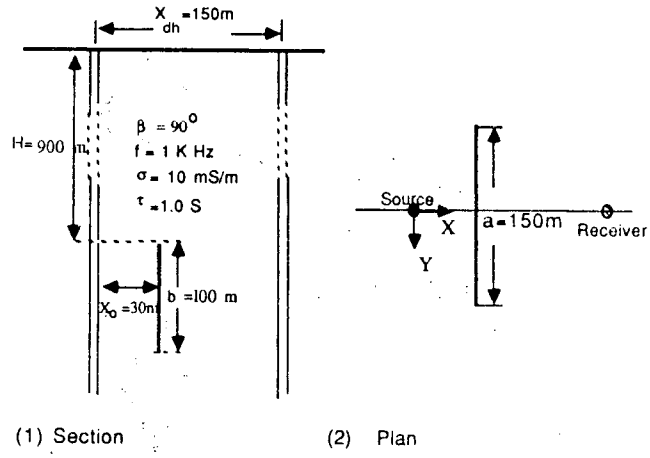

Figure 2. Model geometry. [XBL 866-2262]

are expressed in SI units (A/m). Because the sheet conductor is placed far below the surface, the observed response will be basically the same as that for a conductor in a homogeneous conductive space. It should be pointed out, however, that the code can handle the more general and realistic problem of a target close to the ground surface or to a layered interface such as an overburden layer. Because of the symmetry of the model in Fig. 2, only the H_y component is nonzero for the source-receiver configurations used. The zero values of H_z and H_x are easily explained, because the net effect of the current distribution on the sheet conductor is equivalent to that of an electric dipole in the profile plane defined by the drill holes. Therefore, only the secondary magnetic fields perpendicular to that plane can occur. In a more realistic case, all three components of the magnetic field will be observed. From a practical standpoint, we note that a three-component borehole sensor has already been designed (Cull and Cobcroft, 1986) and could be used to make the necessary measurements.

Cross Hole, Moving Source, and Receiver

In this configuration, the receiver and the source are at the same elevation ($H_{tx} = H_{rx}$) and move in vertical unison past the sheet conductor. The primary field is constant in this case.

Figure 3 shows the response profiles at various frequencies. At low frequency, the imaginary part of the magnetic field is almost zero because the conduction current dominates. The real part of the secondary field is similar to the dc response. As the frequency increases, the real part decreases and finally reverses sign. The imaginary part, on the other hand, increases with frequency, peaks at around

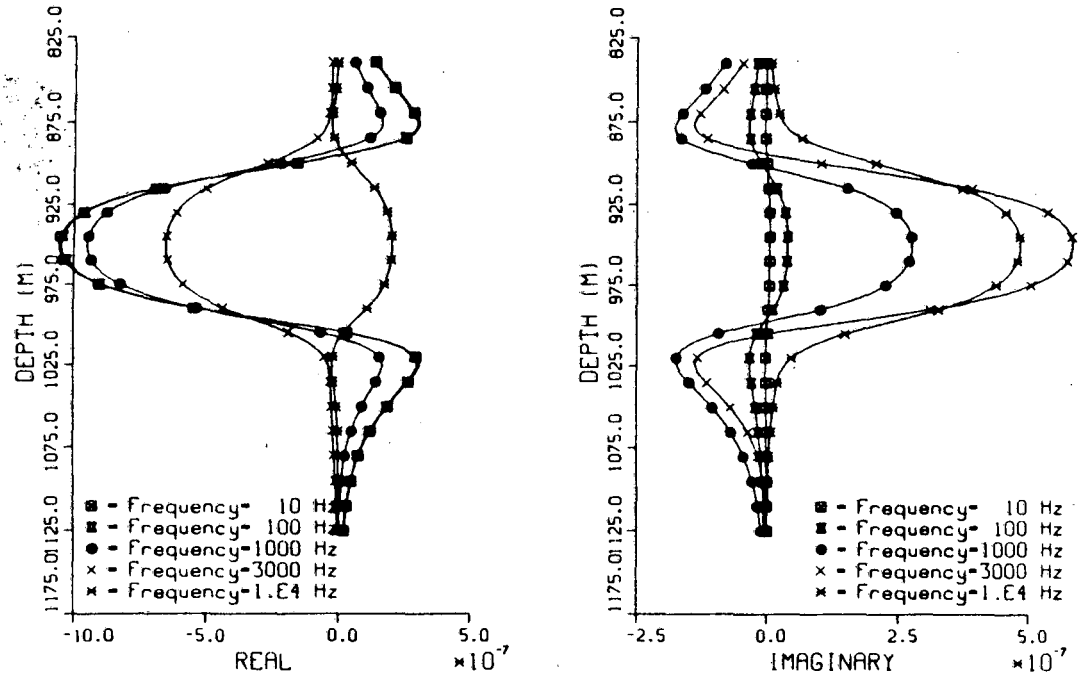

Figure 3. Response as a function of frequency for a moving source. [XBL 866-2263]

3 kHz, and then decreases. The anomaly widths measured between the half-amplitude points give a good measure of conductor extent.

The effects of horizontal separation (X_0) between the vertical fracture and the source are shown in Fig. 4. As expected, both real and imaginary ampli-

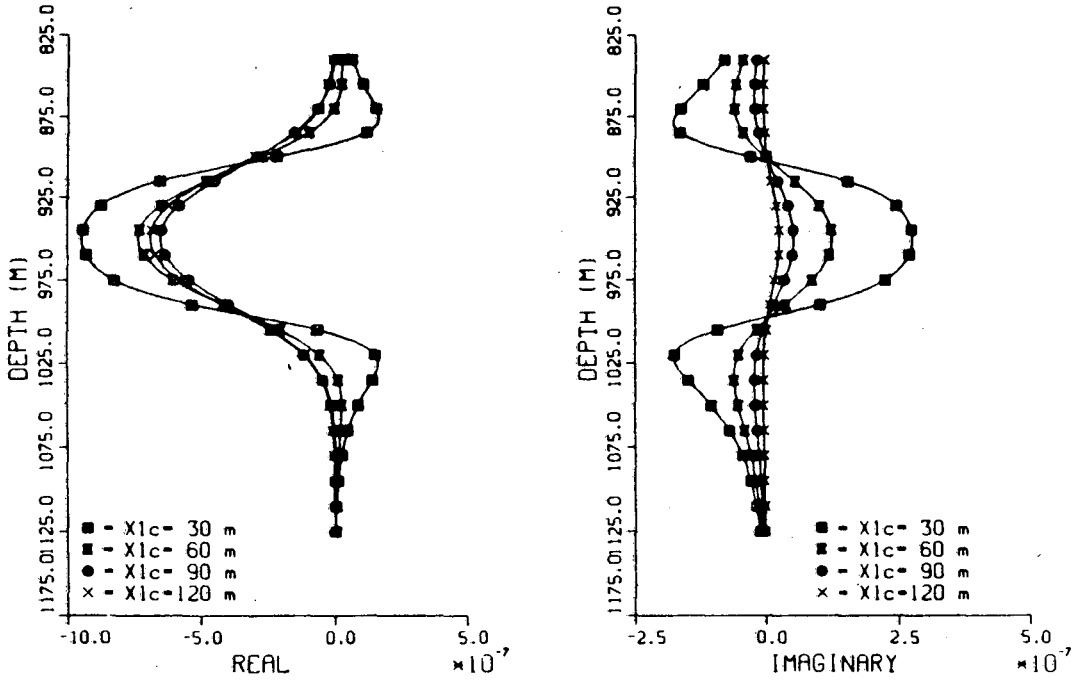

Figure 4. Response as a function of source-target separation for a moving source. [XBL 866-2264]

tudes decrease with distance of the fracture from the source, and this effect is more pronounced for the imaginary component. In fact, the real component begins to increase slightly as the target-receiver distance becomes smaller. We also note that the anomaly exhibits side lobes only at small source-sheet separations. This feature offers a crude way of estimating the proximity to the fracture zone.

The variation of target response as a function of fracture conductance and source-sheet separation can be summarized in the series of Argand diagrams shown in Fig. 5. These are computed at 1 kHz for the mobile cross-hole array and a vertical fracture with a strike length/width ratio (a/b) of 1.5. The fracture is normal to the plane defined by the drill-hole axes. The calculations were done in parametric form so that in addition to the usual geometric factors the anomaly amplitude (i.e., shoulder value–central value) is plotted as a function of the dimensionless parameters

$$r_1 = \tau b / \sigma X_{dh}^2$$

and

$$r_2 = X_0 / X_{dh}$$

for $X_{dh}/\delta = 0.77$, 1.33, and 2.30, where the skin depth δ is equal to $503/(\sigma f)^{1/2}$; τ is the target conductance, σ is the half-space conductivity, X_{dh} is the borehole separation, and b is the sheet dip length. The solid lines indicate a positive imaginary component, whereas the dashed lines are for a negative imaginary component. The real component of the secondary field is always negative. Both the real and imaginary components of the secondary field are normalized by the value of the primary field at the receiver position. In general, the anomaly strength increases with target conductance and decreases with the source-target separation. Surprisingly, an increase in host-rock conductivity results in an enhancement of the anomaly, which for large source-target distances becomes independent of the source-target separation.

Finally, we examine the effects of dip angle (β) at constant frequency 1 kHz (Fig. 6). The symmetric response for vertical dip (β = 90°) becomes distorted as the conductor assumes a progressively shallower dip. One can roughly estimate the dip angle β from the anomaly shape. When the sheet conductor is horizontal there is minimum coupling between the conductor and the source, and both the real and imaginary parts are nearly zero.

DISCUSSION

The cross-hole moving GVED source and magnetic receiver provide better resolution of the frac-

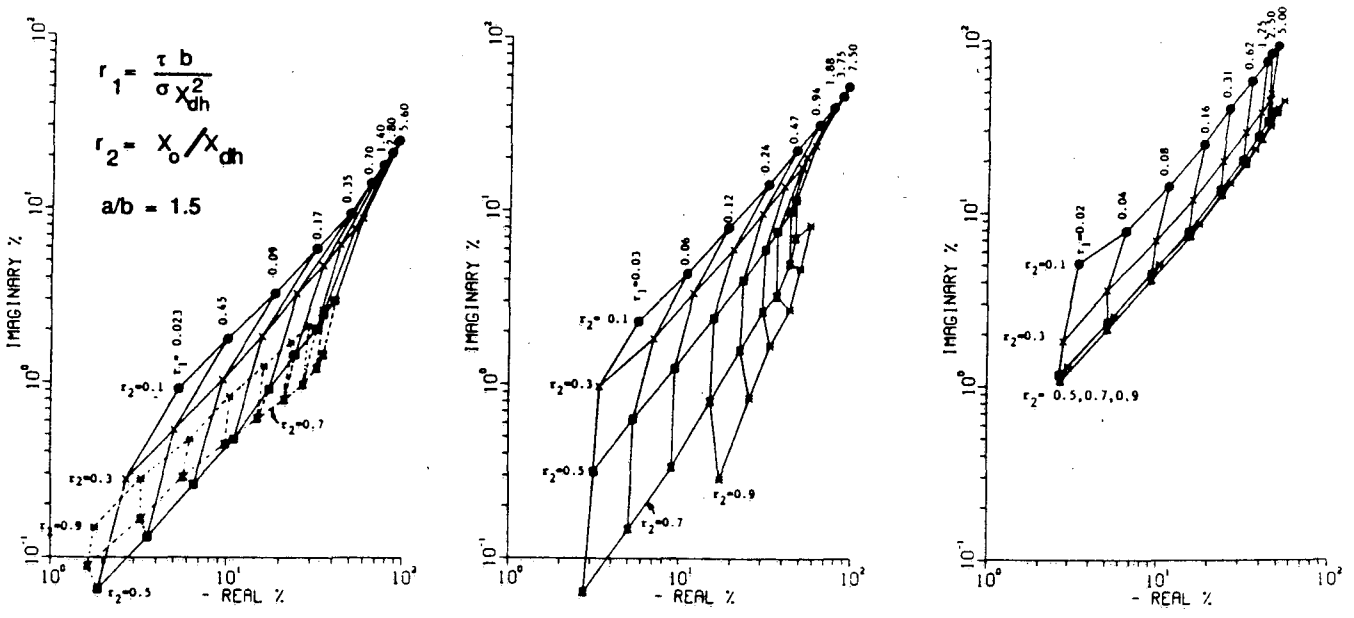

a) $X_{dh}/\delta = 0.77$ b) $X_{dh}/\delta = 1.33$ c) $X_{dh}/\delta = 2.30$

Figure 5. System response for a cross-hole moving source and receiver. [XBL 866-2265]

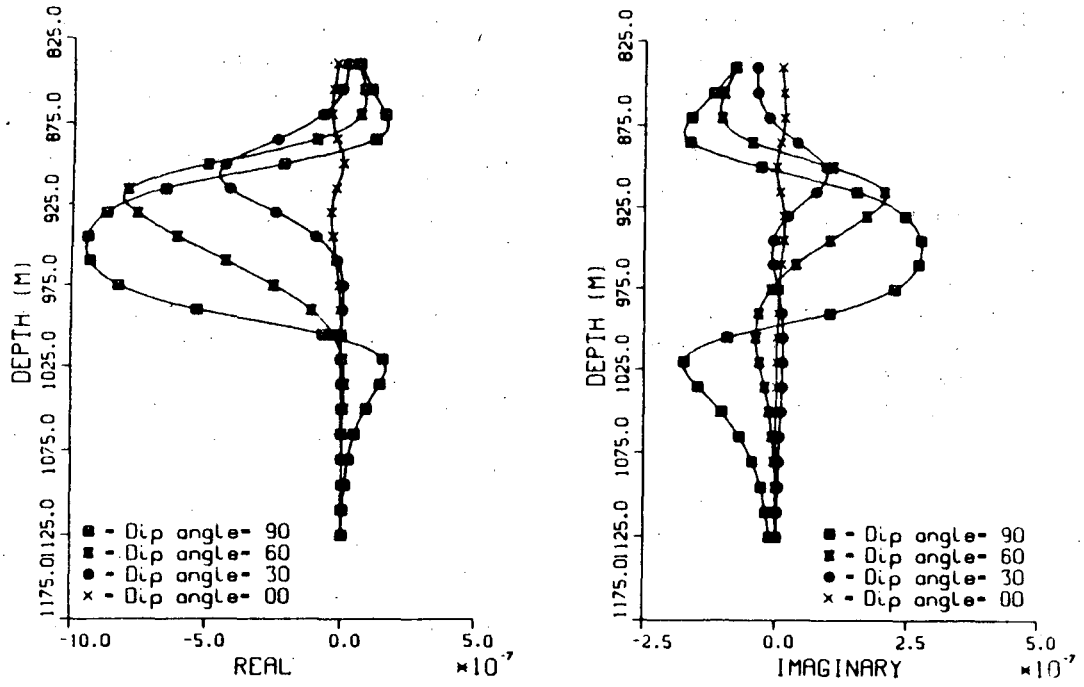

Figure 6. Response as a function of dip angle for moving source. [XBL 866-2266]

ture parameters than the cross-hole fixed-source configuration (the latter not discussed here). The moving source-receiver configuration also allows for easier data interpretation because the primary field is constant, as long as the target is located well below the surface. A unique advantage of the single-hole configuration, however, is that there is no primary field at the receiver site. If any signal is detected, it must be caused by a lateral inhomogeneity.

A major advantage of a GVED source is in its simplicity and thus in the ease with which this type of transmitter can be constructed. The obvious disadvantage is that it cannot be used in the steel-cased portion of a hole, which may eliminate its use in some practical applications. A second disadvantage, but one that may actually work to an advantage in some cases, is its insensitivity to horizontal and flat-dipping conductors. Because such features can be identified by means of conventional well-logging methods, it may turn out that the GVED's lack of response to these features may eliminate a common source of geologic noise and improve our ability to detect steeply dipping conductors.

REFERENCES

Chang, H.-T., Suhler, S.A., and Owen T.E., 1984. Evaluation of bore hole electromagnetic and seismic detection of fractures. Sandia National Laboratories Report SAND 84-7109, 75 p.

Cull, J.P., and Cobcroft, R., 1986. Omni-directional downhole EM probes. Geophys. Prospect., v. 34, p. 569–579.

Deadrick, F.J., Ramirez, A.L., and Lytle, R.J., 1982. In-situ fracture mapping using geotomography and brine tracers. IEEE Trans. Nucl. Sci., v. NS-29, no. 1.

Green, A.G., and Mair, J.A., 1983. Sub-horizontal fractures in a granitic pluton: Their detection and implications for radioactive waste disposal. Geophysics, v. 48, p. 1428–1449.

Jones, J.W., Simpson, E.S., Neuman, S.P., and Keys, W.S., 1985. Field and theoretical investigations of fractured crystalline rock near Oraele, Arizona. Department of Hydrology and Water Resources, University of Arizona, NUREG/CR-3736, p. 104.

Lytle, R.J., Laine, E.F., Lager, D.L., and Davis, D.T., 1979. Cross-borehole electromagnetic probing to locate high-contrast anomalies. Geophysics, v. 44, no. 10.

Nelson, P.H., Magnusson, K.A., and Rachiele, R., 1980. Application of bore hole geophysics at an experimental waste storage site. Lawrence Berkeley Laboratory Report LBL-11982/SAC-3a, 50 p.

Peterson, J.E., Jr., 1986. The application of algebraic reconstruction techniques to geophysical problems (Ph.D. thesis). University of California, Berkeley. Lawrence Berkeley Laboratory Report LBL-21498, 188 p.

Price, A.T., 1949. The induction of electric currents in nonuniform thin sheets and shells. Q. J. Mech. Appl. Math., v. 2, p. 283–310.

Ramirez, A.L., and Lytle, R.J., 1983. Alternant geophysical tomography: IGRASS, v. 2, Paper FA 2-9.

Weidelt, P., 1981. Report on dipole induction by a thin plate in a conductive half-space with an overburden. Federal Institute for Earth Science and Raw Materials, Hannover, West Germany.

Zhou, Q., Becker, A., Morrison, H.F., Goldstein, N.E., and Lee, K.H., 1987. Fracture detection using subsurface electromagnetic techniques. *In* I.W. Farmer et al., (eds.), Proceedings, 28th U.S. Symposium on Rock Mechanics, Tucson, Arizona, June 29–July 1, 1987. A.A. Balkema, Rotterdam, Netherlands, p. 5–17.

RESERVOIR ENGINEERING AND HYDROGEOLOGY

The scientists and engineers in the Reservoir Engineering and Hydrogeology group are primarily concerned with several different approaches to the fundamental problem of the movement of mass and energy through rocks. For a number of years, we have been striving to understand geothermal systems and to unravel the complex physics that controls such systems. This has required the perfection of mathematical models and their application to rather large and complicated field projects. Several articles in this section present the results of recent developments and serve to illustrate the level of sophistication that has been attained in modeling geothermal reservoirs.

Several years ago we began to investigate the phenomenon of flow in fractured rocks, and this has now become a major effort. The importance of fractures in fluid flow arose in connection with our work on geothermal systems and has become a central theme in our investigations of problems related to the isolation of radioactive and toxic wastes. One of these problems is to be able to characterize the fracture system of a rock mass; several articles discuss the difficulties in the evaluation of field data and the use of well tests. Another problem is to develop models that are appropriate to use in evaluating the factors that control fluid movement in fractures; different approaches are being pursued in this area, which address a vast range of spatial scales, from small (cored) sections of individual rough-walled fractures to three-dimensional fracture networks in the field. Single- and multiphase flow as well as chemical transport in fractures are being studied.

High-level radioactive waste generates substantial amounts of heat, and once the waste is placed underground the dissipation of this thermal energy and its effects on the rock mass must be understood. Our previous work on geothermal systems has provided us with an excellent background for confronting this problem; the results of several investigations are included here. Another problem of great practical importance concerns the migration of chemical species in groundwater systems. We are developing numerical methods for handling organic as well as inorganic contaminants.

Expert Systems As Tools for the Nuclear Repository Program

D. Billaux, M. Uszynski, and S.M. Benson

An expert system is a computer program that applies substantial knowledge of specific areas of expertise to the problem-solving process (Bobrow et al., 1986). It is characterized by narrow specialization and competence and differs from a classical computer program mainly in that it uses technology for the explicit representation of knowledge. In fact, these programs are often called knowledge-based systems.

An expert system has three main parts (Denning, 1986): (1) a data base for storing axioms and rules of inference called the knowledge base; (2) an algorithm for constructing proofs, called the inference engine; and (3) a user interface. This new kind of software can be of help in many areas of the nuclear waste storage program. This article investigates what help they can bring. A prototype expert system, WES (Well-test analysis Expert System), has been designed and built. WES is intended as an example of what can be achieved using expert systems in some crucial areas of the nuclear waste storage program.

APPLICATIONS TO NUCLEAR WASTE STORAGE

Expert systems can be of help during the preliminary study of a site, during the detailed study of a site, or during the operation of the transport, conditioning, and burying activities.

During preliminary studies, the site identification is typically a case-by-case study in which the expertise involved varies from site to site. Expert systems are not efficient at this type of task. For a given site, the predesign of the repository may be helped by a design-support expert system, and the preliminary characterization studies may be optimized by a planning expert system.

During the detailed study of a site, expert systems can be helpful on many different topics. First, they can be of help in the planning of field investigations. Second, they can be used for interpretation of field data: geochemistry, hydrology, geophysics. Third, they can be very helpful for risk-assessment studies. For example, scenario generation and analysis of consequences are two areas in which expert systems can help. During scenario generation, an expert system can be used to discard unwanted scenarios efficiently as early as possible. Also, generating scenarios requires the generation of many interrelated parameters. Checking the consistency of the whole set of parameters together with the soundness of the scenario can be done by a design-type expert system.

During the operation of the storage plant, expert systems can be of help in industrial management, in the management of individual waste canisters from power plant to burial, and in the management of monitoring and warning systems.

WES, THE WELL-TEST-ANALYSIS EXPERT SYSTEM

This program is by no means a complete system. It has the potential for solving a much broader set of problems than the one it is now being used to solve. However, this prototype provides a good insight into the complexity of the expert-system building task and into the versatility of the tools that are now available for this purpose.

General Description

The output of one run of WES consists of both a conceptual model of the underground flow system and the values of the parameters needed to properly characterize this particular type of flow system. Contrary to classical curve-fitting softwares, WES achieves its goal not by using sophisticated numerical algorithms but by trying to mimic the behavior of an expert well-test interpreter. The input data are principally the results of pumping tests, which consist of data points representing the variations of water pressure versus time.

In its present state the system can accommodate only a single testing well and a drawdown phase (a constant flow rate following a zero-flow period), but it will be extended to handle a buildup phase or, more generally, a multiple-flow-rate pumping phase as well as situations in which there is a pumping well and possibly more than one observation well. The system has knowledge only about a limited set of conceptual models: two general types of reservoir (homogeneous and double-porosity); a wellbore-storage effect or a fractured-well effect, both of which may distort the response in the early part of the data set; and three boundary configurations (infinite system with no boundary, closed system with no flow boundary, or pressure-maintenance boundary). Certain assumptions are also implicitly made, such as a constant flow rate and a constant atmospheric pressure.

The analysis is conducted using both the classical semilog and log-log representations of this input data and the newer pressure-derivative method (Bourdet et al., 1984). The advantage of the latter method is that the signature of different types of geologic formations are more readily discerned than with conventional analysis methods. One disadvantage is that pressure-derivative plots usually appear to have more random noise than the original data.

The system is written in ART (Automated Reasoning Tool from Inference Corp.), which provides an easy interface to Lisp; hence, part of the system is written in Lisp.

Data Structure and Organization

The system uses a frame-oriented approach to structure its data and any conclusion or intermediate result reached during execution. The basic object architecture refers to wells and characteristics of wells, but objects are also used for graphics to represent windows opened on the screen, curves, mouse-sensitive icons, etc.

Before execution of the program, only generic objects are defined, along with the attributes used to characterize those objects. At execution time, in order to study a specific well test, WES creates "instances" of these generic objects. Relations connecting these specific objects allow the program to link various bits of information relative to a specific well. Each time a new well test is considered for analysis, new objects are created, and information about any specific well is kept distinct from that about the other wells. Information is stored as instances of five generic objects: well, well semilog, well log-log, well derivative, and well model.

During the analysis, the human expert is likely to follow several alternative interpretations until he or she is eventually convinced that one is more likely than the others. WES models this kind of behavior by generating hypotheses about the actual model. These hypotheses are kept in separate "worlds." Each of these hypothetical worlds is the state of the data base resulting from one hypothesis, or one group of compatible hypotheses. The program maintains these worlds simultaneously, and rules of inference can be activated independently in each of them, depending on whether the left-hand-side conditions of the rules are met or not in the particular state of the data base. Compatible hypotheses can be grouped together. The rules generating hypotheses are fairly weak, and as soon as there is a slight chance for a particular model to be true, the corresponding hypothesis is generated.

The basic data architecture is common to all the subsequent hypothetical worlds generated by the system. Typically, attributes in an instance of the object **well-model** will have different values in different hypothetical worlds. This concept of hypothetical worlds is achieved by making use of the more general concept of *viewpoints* available in ART.

Rule Architecture and Run-time Behavior

The rules do not refer to a specific well; instead, they can be executed "simultaneously" for more than one well so that many wells can be analyzed in parallel. In the long term, this feature will be useful for performing the analysis of multiple-well tests, i.e., tests in which water is pumped in or from a single well and several other wells are used for observation. This is possible because of the use of objects to represent the data. Data concerning distinct wells are simply stored in distinct objects.

The sequence of steps used in the analysis of a single well is shown below:

Data extraction from a disc file

↓

Window and initial curve drawing

↓

Data filtering

↓

Computation of pressure derivatives and checking validity

↓

Extraction of characteristics on semilog, log-log, and derivative plots

↓

Generation of hypotheses

↓

Selection of one or several models

The initial data are read from a file. These data consist of readings of pressure at different times. For each well, a window is used for curve drawing and for interactions between the user and the system. This window contains five mouse-clickable icons: **initial, filtered, semilog, log-log, and derivative**. The reasoning process on a well is started by clicking on the **filtered** icon with the left button. Once the process is started, clicking any icon displays the corresponding curve inside the window. The system first filters the initial data set and selects a specified number of data points evenly spaced on a log-time scale.

A human expert conducts an analysis by looking at global characteristics of curves. Conceptual models can be inferred from unique signatures on the derivative, log-log, and semilog plots. These signatures are combinations of straight lines, up or down humps, or slope values. In order to mimic the expert's behavior, WES looks for such characteristics on the three different plots. Partial models are generated from the descriptions of curves in terms of straight lines and humps. Rules represent the decision criteria used by the experts. An example of such a rule is: "if there is a hill hump followed by a horizontal straight line on the derivative plot, then generate the hypothesis of a homogeneous and infinite system." A rule generates a hypothesis based on only a part of the time scale, for example, "wellbore storage" based on early time data. When they are compatible, partial hypotheses can then be grouped to form a complete model, accounting for the response at all times. In the present state of the program, all possible complete models are simply printed on the screen. In some cases, for some data sets, no models are proposed. This means either that the expertise present in the system is not sufficient to analyze this particular case or that this data set has some abnormal shape due to some external event.

Possible Extensions

So far, the system has limited notions of simple models, such as homogeneous or simple double-porosity transition and certain boundary configurations. More models need to be inserted, and a more complete description is needed of the existing ones.

In the same respect, little hydrogeologic expertise is used in the extraction of curve characteristics. This part of the processing is presently performed as a purely numerical procedure. However, early findings often lead the expert in the search for other significant shapes on the curve. The fact that the shape-identification procedures are controlled by rules will make it relatively easy to reproduce this kind of expertise.

In the present state of the system, only single wells with a constant flow rate and a drawdown phase are analyzed. The next step would be to allow a buildup phase and more generally a multiple-rate pumping phase. The system should be able to reason about these different phases, compare results between them, decide which phase is more informative than the others, and so on. Another step in the development of the system will be to allow more than one observation well for a single pumping well.

REFERENCES

Bobrow, D.G., Mittal, S., and Stefik, M.J., 1986. Expert systems: Perils and promise. Commun. ACM, v. 29 no. 9, p. 880–894.

Bourdet, D., Ayoub, J.A., and Pirard , Y.M., 1984. Use of pressure derivative in well test interpretation. Paper SPE 12777 presented at the 1984 SPE California Regional Meeting. Long Beach, April 11–13, 1984.

Denning, P.J., 1986. Towards a science of expert systems. IEEE expert, no. 1, p. 80–83.

A Casting Technique for Determining the Geometry of Voids in a Fracture

*D. Billaux, L. van Vliet, and S. Gentier**

Laboratory studies of rock fractures are aimed at understanding the mechanical and hydrologic behavior of fractures. Both kinds of behavior are controlled by the geometry of the voids of the fracture, as defined by its two sides and their relative position. The mechanical response will be strongly dependent on the contact area; the shear response is also dependent on the inclination of the sides of the fracture relative to its main plane. The hydrologic response will be governed by the connectivity, the size of the voids, and the roughness of the sides. This shows that the laboratory determination of the geometry of the voids of a fracture is necessary to understand its properties.

It is extremely difficult to achieve a full description of the fracture-void geometry. Techniques used previously include measuring profiles of each side of the fracture with a profilometer (Gentier, 1986) or injecting a low-melting-point metal into the fracture (Pyrak-Nolte et al., 1987). The profile-measurement technique gives cross sections of the geometry of each side of the fracture. Several cross sections from

a given side can generally be well fitted with each other. But fitting the cross sections from the two sides with each other is a major difficulty. Similarly, when the two sides of the fracture are taken apart after a metal cast has been made, the metal breaks, and some metal adheres to each side. The pictures from the two sides then need to be superimposed, which may lead to serious inaccuracies. Moreover, this technique yields a map of the voids but does not give void heights.

A new casting technique has been developed jointly by Lawrence Berkeley Laboratory (LBL) and the Bureau de Recherches Gélogiques et Minières (BRGM). It gives precise reproductions of the sides and void space of a fracture and is reasonably easy to implement. A photograph of a translucent cast yields a map of the void heights, which can then be digitized and processed using an image analyzer.

The material used for casting is a room-temperature vulcanizing silicone polymer resin named RTV 1556, manufactured by Rhône-Poulenc. The casting can be performed in various ways. The cast may be taken while the sample is subjected to a normal stress. Several casts at various stress levels then reproduce the variation of the geometry of the fracture with stress. The resin can be injected from a hole in the center of the rock sample or from its side or simply poured on one side of the fracture before fitting the other side to it. This resin can be dyed or left transparent. Since local inhibition of the cure of the material may be caused by the presence of some chemical elements on the side of the fracture, a thin film of acrylic resin is sprayed on both sides before casting. This also facilitates removal of the polymer after cure. In order to obtain a satisfactory cast, the RTV needs to be thoroughly homogenized after the base, the active agent, and (if needed) the dye have been mixed. Curing of the material is facilitated by heating at about 100°C. In fact, heating is a requirement when dealing with thin casts.

Until now, the authors have used the simple procedure shown in Fig. 1 to assess the technical feasibility of the method. The procedure consists of pouring the RTV onto one side of the fracture, fitting the other side to it, and then allowing the RTV to cure under no load other than the weight of the sample. Because the liquid RTV is allowed to wet the whole surface of both sides before they are put in contact, the size of the voids in the fracture may be slightly overestimated A variant of this procedure is to fit the two sides together, pour the RTV around the sample, and then drive the RTV into the fracture by

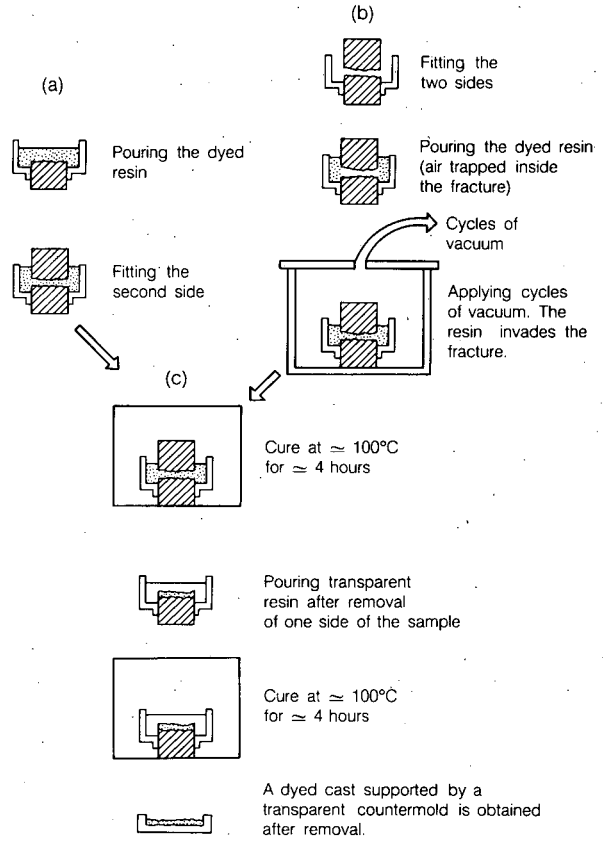

Figure 1. Summary of the casting procedure. **(a)** "Pouring-fitting" method. **(b)** "Fitting-pouring-vacuum" method. **(c)** Curing and casting of a transparent countermold. [XBL 8712-10501]

putting the whole sample in a vacuum jar and submitting it to cycles of vacuum. This technique may yield an underestimate of the size of the voids in the fracture. Once the material is cured, it is removed from the rock sample. If the fracture is thin, the resulting thin film of RTV may be deformed, and consequently the mean plane of the fracture may not be well reproduced. Thin RTV films may also tear during removal from the rock sample. To avoid these problems, when one of the sides of the rock sample has been removed, another thicker batch of RTV can be cast onto the film. The two batches adhere and can be removed from the rock sample easily. One way to proceed is to dye the first batch (fracture voids) and not the second batch (fracture side). This allows the two batches to be easily distinguished.

Once a cast has been obtained, a photograph is taken from above while the cast is illuminated from below by a homogeneous light source. The photograph in Fig. 2 shows the variations in thickness of the fracture in shades of gray for the cast obtained by

*Bureau de Recherches Géologiques et Minières, Orléans, France

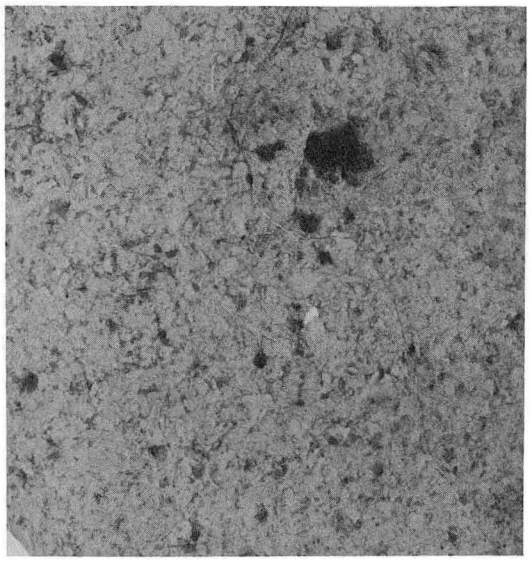

Figure 2. Photograph of the cast of a fracture in a granite under no stress. [XBB 8711-9792A]

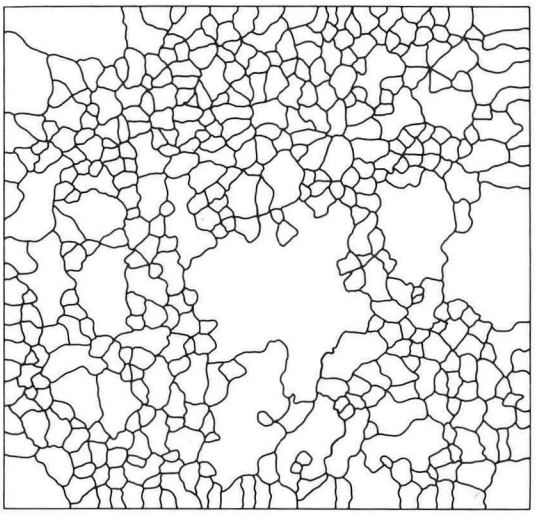

Figure 4. Main flow paths of the above fracture; connectivity map of the image in Fig. 3. [XBL 881-10001]

pouring and then fitting (Fig. 1b). The darker gray corresponds to the larger fracture voids. This photograph can then be digitized into a pixel map of the void space and processed using an image analyzer. Each time a cast is produced, another cast must be made with the same dye lot of a mold with varying known thicknesses, so that the gray levels can be calibrated in terms of fracture apertures.

Simple image processing includes getting the histogram of void heights, the contact area, and the average size of the contacts. More sophisticated processing can yield the connectivity of the voids or the contacts. Figures 3 and 4 show an attempt at obtaining the connectivity of the voids with a height above a given threshold for the fracture cast shown in Fig. 2, using algorithms from mathematical morphology, such as erosion, dilation, opening, and skeletonization (Serra, 1982). To obtain the image shown in Fig. 3 from that in Fig. 2, the picture is captured in an image analyzer, resulting in a 512-by-512 pixel map of the voids of the fracture. Then all the pixels lighter than the threshold are set to white. From the intermediate stage in Fig. 3, all nonwhites are set to black, resulting in a black-and-white (or binary) pixel map. The black patches are then "thinned" to a width of one pixel, without cutting any connection but discarding dead ends in the process. In this way, a map of the connectivity of voids higher than the chosen threshold is obtained (Fig. 4). This is an example of how the map of apertures can be filtered to reveal its most important features, either for flow or for mechanical response.

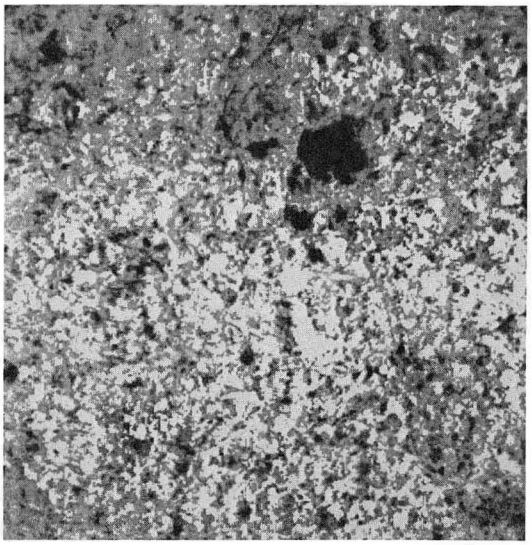

Figure 3. Digitized and filtered map of the fracture in Fig. 2. [XBB 8711-9792B]

Future work at both BRGM and LBL will include a thorough study of the resolution and precision of the method and the development of systematic procedures for image analysis.

REFERENCES

Gentier, S., 1986. Morphologie et comportement hydromecanique d'une fracture naturelle dans un granite sous contrainte normale (doctoral thesis) Université d' Orléans, Orléans, France, 640 pp.

Pyrak-Nolte, L.J., Myer, L.R., Cook, N.G.W., and Witherspoon, P.A., 1987. Hydraulic and mechanical properties of natural fractures in low permeability rock. *In* Proceedings, Sixth International Congress on Rock Mechanics, Montreal, Quebec, Canada, August 30–September 3, 1987, p. 225–231

Serra, J., 1982. Image analysis and mathematical morphology. Academic Press, New York, 610 p.

CHANGE: A Numerical Model for Three-Dimensional Modeling of Channelized Flow in Rock

D. Billaux and J.C.S. Long

Two-dimensional and three-dimensional stochastic models of fracture flow have been built at Lawrence Berkeley Laboratory (LBL) during the last 5 years. These models are based on the assumption that the flow in a given fracture can be approximated by parallel-plate flow (Long, 1983; Gilmour et al., 1986). However, there is now evidence that the voids in fractures often form channels (Billaux, 1986; Neretnieks et al., 1987). In fact, deriving the characteristics of the channel system from the morphology of fracture voids obtained using a new casting technique is a current research topic of one of the authors (Billaux et al., 1988). These channels can be considered as a network of quasi-one-dimensional channels. Building upon our previous experience with two- and three-dimensional fracture networks, we have designed and coded a new program, CHANGE (CHANnel GEnerator), which generates random channels on a given network of discs and produces a three-dimensional finite-element grid of line elements. This code is then used to generate an input for the transient flow and transport code TRINET.

CHANNEL GENERATION AND BOUNDARY CONDITIONS

Input to the program consists of the parameters necessary to specify a three-dimensional network of discs, the statistical properties needed for the channel network on the discs, and boundary conditions. The disc network is obtained by using the program FMG3D developed at LBL (Gilmour et al., 1986). The channels in each fracture disc can be generated independently with random distributions of length, conductivity, and orientation in the fracture plane.

Complex distributions of channel characteristics can be obtained by superposing several channel sets on each fracture disc. If the fracture discs have been generated in several sets, then the characteristics of the channels can be controlled in each fracture set independently. In this way, different fracture morphologies can be reproduced in the same rock mass. Figure 1 shows part of a three-dimensional network of disc-shaped fractures with subnetworks of channels in the fractures. Figure 2 shows just the network of channels for the whole cubic region.

We currently generate channels over the whole area of each fracture disc, except when the discs lie

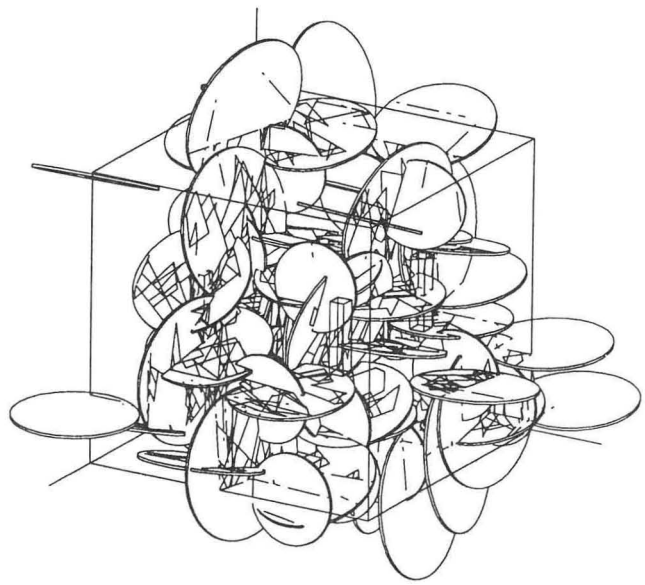

Figure 1. Part of a mesh of channels on discs. The broken lines are intersections with discs not shown. [XBL 881-324]

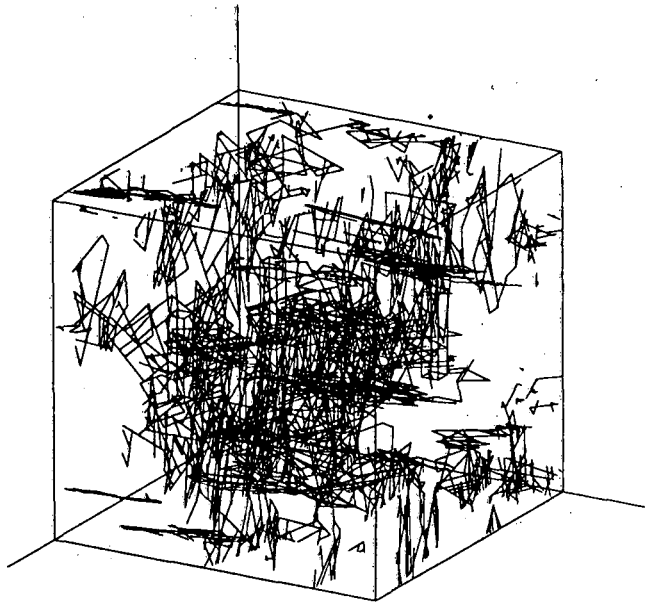

Figure 2. Plot of the channels alone from the mesh in Fig. 1. [XBL 881-325]

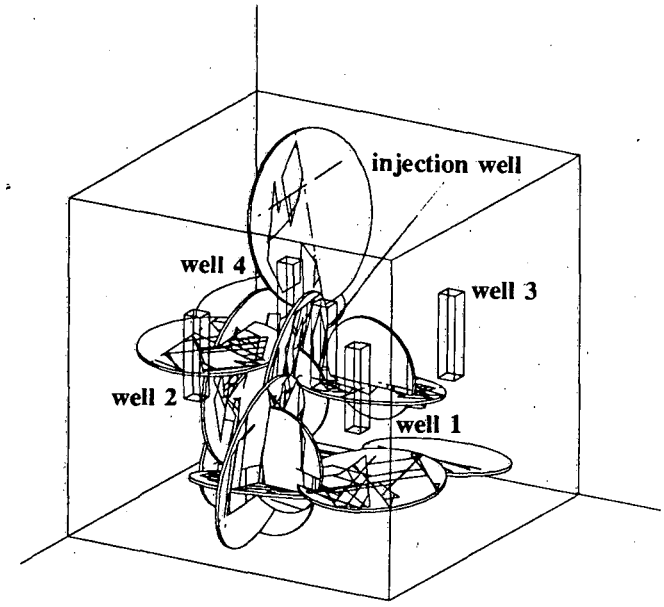

Figure 3. Modeling boreholes. [XBL 881-326]

partly outside the "flow region," i.e., outside of the total system in which flow occurs. However, the generation of channels within a fracture disc could be confined to any subarea of the disc. This would effectively eliminate the constraint of having disc-shaped fractures. In fact, the disc shape is only necessary in locating intersections between fractures.

The total flow region must be a rectangle parallelepiped with any orientation in space. In addition, any number of rectangular-shaped "holes" can be specified within the region in order to simulate sections of drifts or boreholes. Five such boreholes are present in the network shown in Figs. 1 and 2. In Fig. 3, most of the fractures have been removed to reveal the locations of the "holes" used to simulate the open sections of boreholes.

FLOW MESH

The intersections between fracture discs are treated as a separate class of conductors in this model. As such, they can be characterized separately. Currently, the disc intersections are treated in the model as high-conductivity channels. This seems to be geologically most reasonable. However, these intersections can be treated otherwise, if that is desirable. The union of the generated channels and the fracture-disc intersections makes up the flow mesh; we use the generic term "pipe" for both kinds of conductors.

Before the mesh can be used to compute flow, the program must determine which channels are in the flow region and which ones are truncated at the boundaries of the flow region. The boundary conditions will be applied to the endpoints of truncated channels. Once the mesh within the flow region has been identified, intersections between pipes must be found. This is done from the boundaries inward, determining all the intersections between boundary pipes and any other pipes, then intersections between these pipes and other ones, and so on. In this way, pipes not connected to a boundary are never included. A special option can disable this feature and effectively produce a mesh containing all the pipes in the flow region; this option is of use in pipe-matrix flow studies, for example. If a pipe is a channel within a fracture disc, only other pipes in the same disc can intersect it. If a pipe is a fracture-disc intersection, it lies on two different discs, and the pipes on either disc forming the intersection must be searched for intersections with that particular pipe.

All the computations for truncating channels and finding intersections between pipes are performed in a local coordinate system defined by the plane of the relevant fracture. This saves both computer memory and processing time. Once all intersections have been found, the program can identify and eliminate simple dead ends, i.e., pipe endpoints or pipes showing only one intersection with the rest of the mesh. This option can be overridden for transient-flow

computations. The program produces a mesh with pipe segments as line elements and pipe intersections as nodes and with specifications of head or flux imposed at the boundary nodes.

COMPUTING FLOW

The mesh is processed by program RENUM, which optimizes the finite-element network by merging nodes, removing complex dead ends, and then renumbering the nodes. The short-circuit effect of wells is taken into account by shrinking all the boundary nodes on a given imposed flux "hole" into one node. This is equivalent to assuming that the well has an infinite transmissivity. Nodes very close to each other are also merged. The program optionally removes complex dead ends (Billaux and Fuller, 1988). The nodes are finally renumbered using an algorithm published by Cuthil and McKee (1969) to minimize the bandwidth of the corresponding linear system of equations.

Program TRINET (Karasaki, 1987) can then compute flow and transport in the network. TRINET incorporates the Lagrangian and Eulerian schemes with adaptive gridding to solve the advection-dispersion equation. The model avoids numerical dispersion by creating new Eulerian grid points to preserve the exact shape of the front instead of interpolating the advected profile back to the original Eulerian grid. The head distribution in the network is solved using the usual Galerkin finite-element method with linear shape functions. The flow can be either steady state or transient, where the time derivative is treated in a finite-difference manner.

CONCLUSION

The newly completed chain of programs FMG3D, CHANGE, RENUM, and TRINET is now a unique tool for the modeling of flow and transport in complex channel geometries. Such a tool can give us more insight into the relationship between the three-dimensional geometry of fractured rocks and their flow properties. Getting the right parameters to put into the numerical model is the emphasis in the next stage of this research, which involves studying the morphology of the voids of fractures under stress in the laboratory and in the field.

REFERENCES

Billaux, D., and Fuller, P., 1988. An algorithm for mesh simplification applied to fracture hydrology. J. Int. Assoc. Math. Geol. (in press).

Billaux, D., van Vliet, L., and Gentier, S., 1988. A casting technique for determining the geometry of voids in a fracture. *In* this Annual Report.

Cuthil, E., and McKee, J., 1969. Reducing the bandwidth of sparse symmetric matrices. *In* Proceedings, 24th National Conference of the Association for Computing Machinery. ACM Publications, New York, 69 p.

Gentier, S., 1986. Morphologie et comportement hydromecanique d'une fracture naturelle dans un granite sous contrainte normale (doctoral thesis). Université, d'Orléans, Orléans, France, 640 p.

Gilmour, P., Billaux, D., and Long, J.C. S., 1986. Models for calculating fluid flow in randomly generated three-dimensional networks of disc-shaped fractures—theory and design of FMG3D, DISCEL, and DIMES. Lawrence Berkeley Laboratory Report LBL-19515, 143 p.

Karasaki, K., 1987. A new advection-dispersion code for calculating transport in fracture networks. *In* Earth Science Division Annual Report 1986. Lawrence Berkeley Laboratory Report LBL-22090, p. 55–57.

Long, J.C.S., 1983. Investigation of equivalent porous medium permeability in networks of discontinuous fractures, (Ph.D. thesis). University of California, Berkeley, 277 p.

Neretnieks, I., Abelin, H., and Birgersson, L., 1987. Some recent observations of channeling in fractured Rocks—Its potential impact on radionuclide migration. *In* Proceedings, DOE/AECL 1987 Conference on Geostatistical, Sensitivity, and Uncertainty Methods for Ground-Water Flow and Radionuclide Transport Modeling, San Francisco, 23 p.

A Multi-Feedzone Wellbore Simulator

G. Bjornsson and G.S. Bodvarsson*

Most geothermal reservoirs are located in fractured rocks, with fluids entering the wells in discrete zones (feedzones). These feedzones frequently have different pressure potentials, so that internal flow occurs in the well when the well is in a static condition and in some wells during discharge or injection. Examples in the literature include wells in Iceland (Stefansson and Steingrimsson, 1980), Kenya (Haukwa, 1984), and New Zealand (Grant et al., 1982, 1983). Currently there are few tools available for the design of multi-feedzone wells or for analyzing their behavior during discharge.

We have developed a multi-feedzone wellbore simulator that can handle an arbitrary number of feedzones. The simulator is quite general as it allows for calculations of downhole conditions during both fluid discharge and injection. It also has the capability of computing the conditions within the well either from wellhead to wellbottom, or from wellbottom to wellhead, depending upon whether wellhead or downhole thermodynamic conditions are known. For example, it is useful to start the computations at the bottom of the well and proceed upwards when the wellbore simulator is coupled with a reservoir model that provides reservoir conditions at specific depths (grid blocks).

The multi-feedzone wellbore simulator has many potential applications, including

1. designing multi-feedzone wells;
2. matching flowing temperature and pressure profiles in order to determine flow rates and enthalpies of individual feedzones;
3. investigating internal flows in wells and optimizing the operating wellhead conditions of the well to maximize productivity;
4. investigating the effects of multi-feedzones on pressure transient data during well tests; and
5. coupling with a reservoir simulator to determine well productivity or injectivity changes with time.

In this article the multi-feedzone simulator is briefly described in terms of its mathematical formulation and solution procedures. The model is then validated using flowing pressure profiles from wells with single feedzones. Finally, the simulator is used to interpret pressure and temperature profiles of two-phase wells in Iceland and Kenya. The interpretation yields estimates of the flow rate and enthalpies of individual feedzones.

*National Energy Authority of Iceland, Grensasvegi 9, Reykjavik, Iceland.

THE WELLBORE SIMULATOR HOLA

The governing equations for two-phase flow are highly nonlinear and must be solved numerically. Mixed analytical and empirical formulations do exist for various types of flow (Orkiszewski, 1967; Wallis, 1969; Chisholm, 1983). These have been used by several authors in their development of wellbore models for numerically predicting downhole pressures, given the well design and either wellhead or bottomhole flow conditions (Gould, 1974; Juprasert and Sanyal, 1977; Upadhyay et al., 1977; Goyal et al., 1980; Miller, 1980; Miller et al., 1981; Barelli et al., 1982; Parlaktuna, 1985). The predictions usually compare fairly well with measured data. All of the present available codes assume that fluid enters only at the bottom of the well.

The wellbore simulator HOLA (the Icelandic word for "well") solves numerically the differential equations that describe mass, momentum, and energy flow in a vertical pipeline. A detailed description of the code and its application is given by Bjornsson (1987). The mass flow is assumed to be steady state. Calculations start either at the wellhead and continue downwards in a finite difference grid, or at the wellbottom and proceed upwards. The nonlinear governing equations are solved using the Newton-Raphson iteration procedure. Frictional pressure-drop and phase-velocity calculations in two-phase flow are based on empirical relations given by Chisholm (1983). Pure water is the flowing fluid, but it can flow under either single- or two-phase conditions. All physical properties are assumed uniform at any given depth within the well. The program HOLA allows for multiple feedzones, variable grid spacing, pipe roughness, and well radius. Heat exchange with the surrounding rocks is computed analytically.

Feedzones are assumed to occur at single grid points in the well, which is a reasonable assumption for wells in fractured, geothermal reservoirs. Two-phase mixtures are always assumed to flow upwards, whereas single-phase fluid can flow either up or down. Thus, internal downflow and upflow can be computed between feedzones.

The wellbore simulator computes mass, energy, and momentum balances explicitly, assuming steady-state mass flow. In the portions of the well between feedzones, the thermodynamic conditions in the next grid node can be readily computed based upon the known conditions in the last known grid node and the constant mass flow between the adjacent nodes. At nodes containing a feedzone, mass- and energy-balance calculations are performed using the specified mass rate and enthalpy of the feedzone in question. This allows for the determination of mass and energy flow to be used as inlet conditions for the next interzonal section of the well. This procedure can be followed using either the known wellhead conditions and computing down the well or known bottomhole conditions for calculations up the well to the wellhead.

FEEDZONE CONTRIBUTIONS

One of the most practical applications of a multi-feedzone wellbore simulator is to use it for estimating flow rates and enthalpies of the different feedzones in a well. This information is often difficult to gain by other methods. A possible alternative is to measure the wellbore flow rate by flow meters, also called spinners (see, for example, Solbau et al., 1983), but this is difficult in high-temperature geothermal wells.

The wellbore simulator HOLA can be used to estimate internal flow rates in geothermal wells, given the measured downhole pressure and/or temperature profiles. Simulation begins at the wellhead, where all the flow parameters are known. Downhole profiles are then calculated down to the first feedzone encountered. The interpretation begins at that point by specifying the feedzone flow rate and enthalpy. Calculations then proceed to the next feedzone, where new feedzone parameters are specified. This continues down to the lowest feedzone, for which parameters need not be specified, since they can be computed from the specified wellhead conditions and the flow rate and enthalpies of all of the other feedzones. The flow values and enthalpies of the individual feedzones are then varied in a trial-and-error fashion until the calculated downhole temperature and pressure profiles match the measured ones.

As an example, Fig. 1 shows calculated and measured downhole profiles for well NJ-7 in the Nesjavellir Field, Iceland. The data were provided by B. Steingrimsson (personal communication, 1987). During the measurements the well discharged 23 kg/s of steam/liquid mixture, with a total fluid

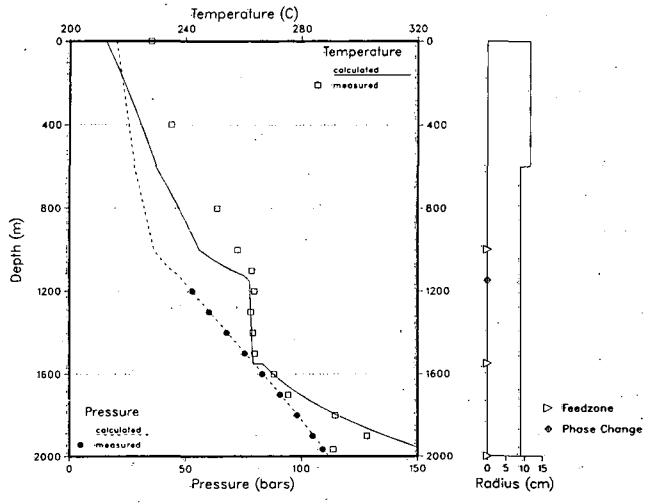

Nesjavellir, well NJ-7
Pressure and enthalpy during discharge
6-feb-1986

Wellhead pressure (bar abs.)	:	20.00
Wellhead temperature (C)	:	212.37
Wellhead dryness	:	0.239
Wellhead enthalpy (kJ/kg)	:	1360.00
Wellhead total flow (kg/s)	:	23.00

Feedzone no:	Depth (m)	Flow (kg/s)	Enthalpy (kJ/kg)
1	1000.0	14.50	1500.0
2	1550.0	8.40	1150.6
3	2000.0	0.10	1526.2

Figure 1. Calculated and measured downhole profiles in well NJ-7, Nesjavellir, Iceland. [XBL 874-1958]

enthalpy of 1360 kJ/kg. Feedzones are located at depths of 1000, 1550, and 2000 m.

The constant 260°C temperature at the depth interval 1100–1600 m in well NJ-7 indicates flow of single-phase liquid with an enthalpy of approximately 1150 kJ/kg. This enthalpy is substantially lower than that measured at the wellhead and requires discharge of high-enthalpy fluid from the feedzone at 1000 m depth. It also indicates that the liquid water at 1100–1600 m depth is flowing upwards in the well from the feedzone at 1550 m depth. Below 1550 m the temperature increases rapidly, which is most likely due to small upward flow from the deepest feed, resulting in a near-static water column in thermal equilibrium with the surrounding rocks.

The initial reservoir pressure and temperature at 1000 m depth in well NJ-7 are approximately 80 bars and 260°C, respectively (Stefansson, 1985). Liquid water at these thermodynamic conditions has an enthalpy of 1100 kJ/kg. In order to match the data, a higher enthalpy is required, suggesting two-phase conditions in the reservoir at that depth.

The calculated pressure and temperature profiles shown in Fig. 1 are obtained by assuming an enthalpy of 1500 kJ/kg for the feedzone at 1000 m

depth. The calculated results show that most of the produced fluids are flowing from the feedzone at 1000 m. The remaining 30% come from the feedzone at 1600 m, with negligible flow from below (2000 m feedzone).

The assumed 1500 kJ/kg fluid enthalpy at 1000 m depth is uncertain; it is only necessary that this enthalpy must be higher than the wellhead enthalpy, since colder fluid is flowing from below and mixing with the discharge from the uppermost feedzone. This makes the estimated feedzone parameters shown in Fig. 1 nonunique. Independent information, such as geochemical data, may help in determining relative contribution of feedzones, hence making the parameter determination more distinct.

CONCLUSIONS

A multi-feedzone wellbore simulator has been developed. The simulator allows for calculations of downhole pressure, temperature, and vapor-saturation conditions in wells with an arbitrary number of feedzones. It can simulate well conditions during both discharge and injection. The computer code can be applied to various problems, including the design of multi-feedzone wells, evaluation of internal flow, and relative contributions of feedzones and studies of productivities and injectivities of wells.

The simulator was validated by comparing computed pressures and temperatures to actual data from three wells, each one with a single dominant feedzone. Most of the measured data were matched reasonably well.

The simulator was also used to match flowing profiles in two wells that show effects of two or more feedzones. Flow rates and enthalpies of individual feedzones were estimated, thus giving important information on the characteristics of each well feedzone.

ACKNOWLEDGMENTS

The authors would like to thank Benedikt Steingrimsson and his colleagues at the Icelandic National Energy Authority for providing data used in this report and for cooperation during this work. Technical and editorial review by M. J. Lippmann and M. G. Bodvarsson is appreciated.

REFERENCES

Barelli, A., Corsi, R., Del Pizzo, G., and Scali, C., 1982. A two-phase flow model for geothermal wells in the presence of non-condensible gas. Geothermics, v. 11, no. 3, p. 175–191.

Bjornsson, G., 1987. A multi-feedzone geothermal wellbore simulator (M.S. thesis). University of California, Berkeley.

Chisholm, D., 1983. Two-phase flow in pipelines and heat exchangers. George Godwin, London and New York.

Gould, T.L., 1974. Vertical two-phase steam-water flow in geothermal wells. J. Pet. Technol., v. 26, p. 833–842.

Goyal, K.P., Miller, C.W., and Lippmann, M.J., 1980. Effects of wellhead parameters and well scaling on the computed downhole conditions in Cerro Prieto wells. *In* Proceedings, Sixth Workshop Geothermal Engineering, Stanford University, Stanford, California, SGP-TR-50, p. 130–138.

Grant, M.A., Donaldsson, I.G., and Bixley, P.F., 1982. Geothermal reservoir engineering. Academic Press, Orlando, Florida.

Grant, M.A., Bixley, P.F., and Donaldsson, I.G., 1983. Internal flow in geothermal wells: Their identification and effect on the wellbore temperature and pressure profiles. Soc. Pet. Eng. J., v. 23, p. 168–176.

Haukwa, C.B., 1984. Recent measurements within Olkaria east and west fields. Paper for Kenya Power Company, Scientific and Technical Review Meeting, November, 1984, The Kenya Power Company Ltd.

Juprasert, S., and Sanyal, S.K., 1977. A numerical simulator for flow in geothermal wellbores. Geoth. Resour. Counc. Trans., v. 1, p. 159–161.

Miller, C.W., 1980. Wellbore user's manual. Lawrence Berkeley Laboratory Report LBL-10910, p. 48.

Miller, C.W., Benson, S.M., O'Sullivan, M.J., and Pruess, K., 1981. Well-bore effects in the analysis of two-phase geothermal well tests. Presented at the Society of Petroleum Engineers California Regional Meeting, Bakersfield, California, March 25–27, 1981.

Orkiszewski, J., 1967. Predicting two-phase pressure drop in vertical pipe. J. Pet. Technol., v. 19, p. 829–838.

Parlaktuna, M., 1985. Two-phase wellbore simulator and analysis of reinjection data from Svartsengi, Iceland. The UNU Geothermal Training Programme, Iceland, Report No. 1985–7.

Solbau, R.D., Goranson C.B., and Benson, S.M., 1983. The development and use of a high temperature downhole flow meter for geothermal well logging. *In* Proceedings, Ninth Workshop, Geothermal Engineering, Stanford University, Stanford, California, SGP-TR-74, p. 205–210.

Stefansson, V., 1985. The Nesjavellir high-temperature geothermal field in Iceland. *In* Proceedings, Tenth Workshop, Geothermal Reservoir Engineering, Stanford University, Stanford, California, SGP-TR-84, p. 23–30.

Stefansson, V., and Steingrimsson, B., 1980. Production characteristics of wells tapping two-phase reservoirs at Krafla and Namafjall. *In* Proceedings, Sixth Workshop, Geothermal Engineering, Stanford University, Stanford, California, SGP-TR-50, p. 49–59.

Upadhyay, R.N., Hartz, J.D., Tomkoria, B.N., and Gulati, M.S., 1977. Comparison of calculated and observed pressure drops in geothermal wells producing steam-water mixtures. *In* Proceedings, 52nd Annual Fall Technical Conference and Exhibition of the Society of Petroleum Engineers of AIME, Denver, Colorado, Paper SPE-6766.

Wallis, G.B., 1969. One-dimensional two-phase flow. McGraw-Hill, New York.

Preliminary Calculations of the Effects of Air and Liquid-Water Drilling on Moisture Conditions in Unsaturated Rocks

G.S. Bodvarsson, A. Niemi, A. Spencer, and M.P. Attanayake

At the request of the United States Geological Survey (USGS), the Earth Sciences Division of Lawrence Berkeley Laboratory (LBL) has conducted limited numerical studies of the effects of air and liquid-water drilling on moisture conditions in unsaturated rocks. Decisions must be made on which drilling fluid should be used in the drilling of boreholes associated with the exploratory shaft at Yucca Mountain and if dry or wet mining should be used in the excavation of underground chambers. It is of interest to use simplified models to obtain order-of-magnitude estimates of the disturbance to in situ moisture conditions when gas or liquid water are used as drilling fluids.

Montazer et al. (1987a) discuss the effects of dry versus wet mining on the hydrological conditions near underground chambers. They argue that minimally perturbed conditions are required if meaningful results are to be obtained from the infiltration and bulk-permeability tests. They stress the importance of these tests for obtaining combined characteristic curves for the fracture-porous rocks. They conclude that dry-mining techniques should be used in the mining of the infiltration and bulk-permeability test rooms. Previous numerical studies addressing the effects of wet mining and drilling with water are reported by Peters and Gauthier (1986) and Kwicklis and Hoxie (1987).

In the present work a coarse model is used to investigate the effects of gas and liquid-water drilling on fracture and matrix hydrological conditions. Lateral water migration during drilling and the effects of various mobility weighting schemes (harmonic, arithmetic, and upstream weighting) at grid-block interfaces are briefly investigated. A fracture-matrix model similar to that used by Kwicklis and Hoxie (1987) is employed in the studies. It should be noted that very coarse spatial discretization is used; hence, the results obtained are only rough approximations.

PROBLEM SPECIFICATION

The basic model used is shown in Fig. 1. It consists of vertical fractures surrounding a matrix block on all sides. In the horizontal plane the matrix is discretized using the MINC method developed by Pruess (1983). A logarithmic grid spacing is used in the matrix with a 1-mm element adjacent to the fracture, increasing to 27 cm for the innermost element.

The fracture spacing was assumed to be 0.6 m based upon reported fracture densities of about 8–40 fractures per cubic meter for the Topopah Springs welded unit (Montazer and Wilson, 1984). A very coarse vertical grid spacing is used, with a 1.5-m element at the top of the system, increasing in size to a 15-m element at the bottom of the system; altogether a 50-m-thick block is modeled. Limited sensitivity studies were conducted on the effects of the vertical gridding.

The parameter values used in the simulations are described in detail by Bodvarsson et al. (1988). Two sets of characteristic curves were used, referred to as USGS curves (Rulon et al., 1986) and the so-called

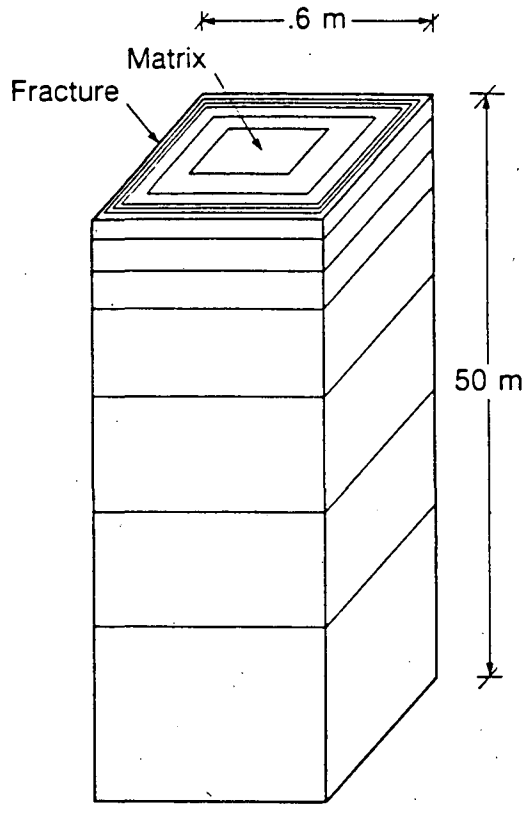

Horizontal discretization (m)
.0001 (fracture), .001,.005,.01,.05,.1,.134

Vertical discretization (m)
1.5, 2.5, 4.0, 7.0, 10.0, 10.0, 15.0

Figure 1. Discretized flow region used in the simulations. [XBL 887-2514]

Sandia curves (Klavetter and Peters, 1986). In general, for a given liquid saturation the USGS curves yield smaller absolute values of capillary pressure and higher liquid relative permeability than the Sandia curves. This holds true for both the fracture and matrix characteristic curves.

Stable initial conditions were established by infiltrating a flux equivalent to 0.1 mm per year of liquid water through the system. This liquid flux was turned off during drilling but re-established during the recovery period after drilling. During drilling a water head equivalent to 20 m (2.0 bars) was imposed at the top of the system. In most cases drilling was assumed to last 12.25 minutes, after which the redistribution of moisture was computed for one year.

In the case involving gas drilling, a 2-bar air pressure was maintained at the top of the system. Air movement was also computed for the liquid-water drilling cases and was found to have practically no effect for the system modeled. In all cases the lower boundary was far enough downwards so that the specified constant-pressure boundary condition did not affect the solution significantly. The simulations were carried out using the numerical code TOUGH (Pruess, 1987).

RESULTS

USGS Characteristic Curves

In the first set of simulations, the USGS characteristic curves were used. Figures 2 through 5 show some of the results obtained. Figures 2 and 3 show the liquid-saturation profiles for the fracture and the rock matrix (0.5 mm from the fracture), respectively, after 12.25 minutes of drilling and for selected times during the subsequent recovery. At the end of drilling, the matrix is near saturation in the top 7.5 m; below that the liquid saturation decreases monotonically to the initial value of 0.69 at 20 m depth. In the fracture large increases in liquid saturation have occurred to about 7.5 m depth at the end of drilling (Fig. 2). Below this depth the liquid saturation increased significantly to a depth of about 11.5 m, although the scale used in Fig. 3 is too coarse for this to be seen. The liquid saturation in this region has increased by more than an order of magnitude (from 1.6×10^{-4} to $> 10^{-3}$), thus decreasing the magnitude of capillary pressure greatly. Hence, fluids flowed into the rock matrix, causing the observed increase in liquid saturation there.

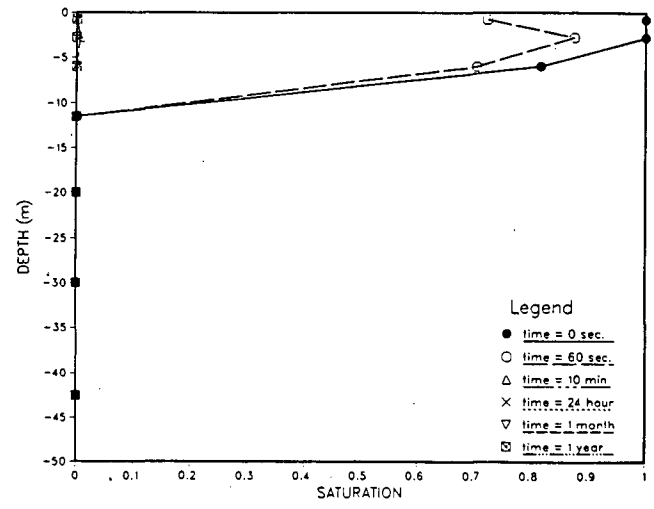

Figure 2. USGS characteristic curves: liquid saturation in the fracture for various recovery times. [XBL 887-2515]

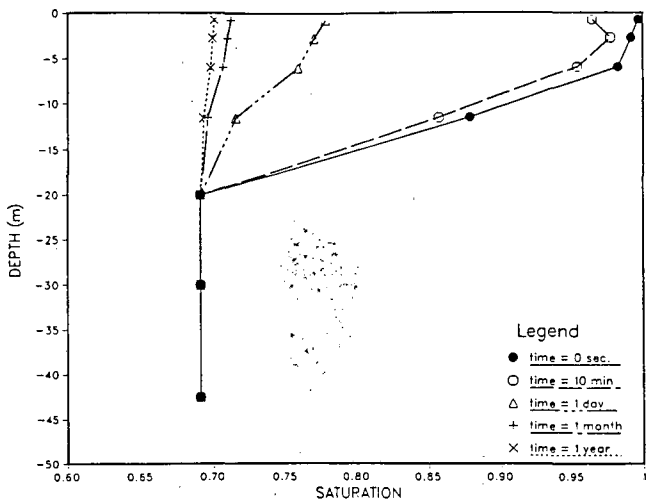

Figure 3. USGS characteristic curves: liquid saturation in the matrix (0.5 mm from the fracture) for various recovery times. [XBL 887-2516]

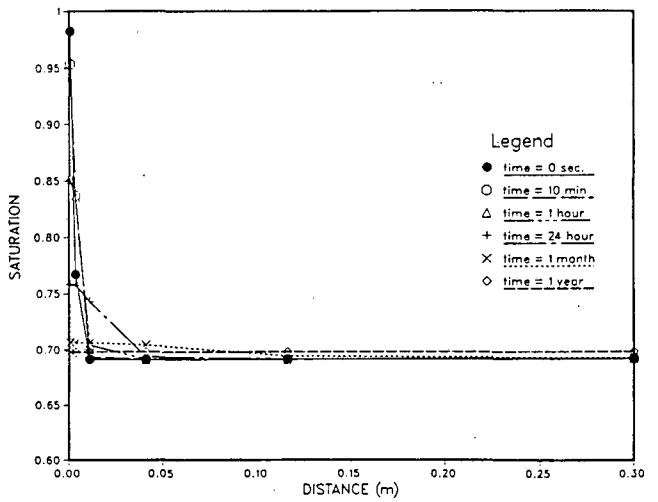

Figure 5. USGS characteristic curves: liquid saturation in the matrix at a depth of 6 m for various recovery times. [XBL 887-2518]

After drilling stopped the fracture recovered to close to its initial moisture content in a time frame of hours (Fig. 4). Most of the fluids within the fracture are sucked into the matrix by capillary forces, so that the front does not advance significantly farther along the fracture after the constant-head boundary condition is removed. This behavior was also observed by Kwicklis and Hoxie (1987) in their numerical calculations. The moisture redistribution in the rock matrix takes much longer than that for the fracture because of the low permeability of the rock matrix (microdarcies). Figure 3 shows that rapid moisture redistribution occurs during the first month of recovery, with the liquid saturation recovering to within two percentage points of the initial liquid saturation.

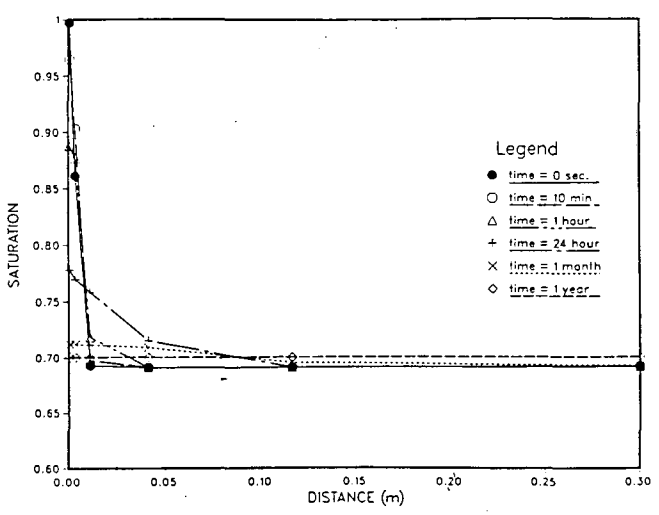

Figure 4. USGS characteristic curves: liquid saturation in the matrix at a depth of 0.75 m for various recovery times. [XBL 887-2517]

Figures 3 through 5 show that the main mechanism of moisture redistribution is continued capillary suction into the rest of the matrix block until a quasi-equilibrium in capillary pressure is achieved. After one month of recovery the liquid saturation differs by up to two percentage points from the initial value, which corresponds to a 23% change in the liquid relative permeability. After one year of recovery the maximum difference is about one percentage point, which corresponds to a maximum increase of 10% in the liquid relative permeability.

Sandia Characteristic Curves

The same problem was investigated using the Sandia characteristic curves, as reported by Klavetter and Peters (1986). For a 0.1-mm/year flux, these characteristic curves yield a liquid saturation of about 80% in the matrix. The results using the Sandia curves are very similar to those obtained using the USGS curves, with a maximum of 1.9 percentage points difference in saturation between the initial value (80%) and that obtained after a recovery of 1 month, depending upon the depth of observation within the matrix. This corresponds to a maximum of about 20% difference in the relative permeability of the liquid phase.

Hysteretic Capillary-Pressure/Liquid-Saturation Relationship

A brief sensitivity study was conducted on the effects of hysteresis in the matrix capillary-pressure/liquid-saturation relation on the moisture migration and redistribution. We only considered hysteresis for the matrix; the fracture characteristic curves were assumed nonhysteretic.

Since no actual hysteresis measurements for the welded units at Yucca Mountain are presently available, a theoretically derived hysteresis model was used. The model, which we have modified from the dependent domain model of Mualem (1984) and programmed into the numerical simulator TOUGH, computes the hysteretic scanning paths when the equations of the main wetting and main drying curves are known. Details of the model are given in Niemi et al. (1987).

Comparison of the results shows that the fracture liquid saturations at the end of drilling are somewhat higher in the hysteretic case than in the nonhysteretic case. This is a result of the lower matrix capillary suction in the hysteretic case. (When a system wets along a first-order wetting curve instead of the main drying curve, the same liquid saturation corresponds to a lower capillary pressure.)

A more significant difference was observed during the recovery period. Due to the lower matrix capillary suctions in the interior of the matrix, the recovery is somewhat slower for the hysteretic case. At the end of the one-year recovery period, the capillary pressure in each matrix layer is uniform and in equilibrium with conditions within the adjacent fracture element. However, because of hysteresis, the liquid saturations were not uniform horizontally in the upper layers. This nonuniformity was most pronounced in the top matrix layer.

At the end of the recovery, the matrix liquid saturations were everywhere within 2.6 percentage point of the initial liquid saturation, in comparison to the 1 percentage point for the nonhysteretic case. This corresponds to a maximum increase of 29% in the matrix relative permeability, in comparison to the 10% for the nonhysteretic case.

Grid Effects

A limited-sensitivity study was conducted on the effects of grid spacing on the moisture migration and distribution within the fracture and the rock matrix. The "coarse" grid spacing was identical to that used in the previously described simulations (Fig. 1). The "fine" grid was constructed by refining the coarse grid by a factor of 3 in the vertical direction, i.e., allowing three equally spaced elements for each element of the coarse grid. The horizontal gridding in the rock matrix remained the same.

The limited-sensitivity study suggests that the grid effects mainly affect the shape of the moisture front but do not significantly affect the moisture redistribution and liquid saturations during the recovery period. As the long-term residual effects in the liquid saturations of the fracture and the matrix are of most importance in testing following drilling, the results suggest that the grid effects are secondary in importance.

Effects of Weighting Schemes

In numerical modeling of fluid, heat, and chemical transport where spatial variations are present in fluid or rock parameters, one must choose a rationale for averaging the parameters between grid blocks. For example, in problems involving unsaturated fluid flow, the effective permeability to both phases (liquid and gas) will vary spatially with the liquid saturation. In each grid block the liquid saturation is known, an consequently the effective permeability associated with the grid block is known. However, the effective permeabilities for the two phases are needed at the interfaces between grid blocks in order to compute flow of gas and liquid between the two grid blocks. Various weighting schemes have been devised for estimating the interface values, including those referred to as harmonic-mean, upstream-weighting, and arithmetic-mean weighting. The results obtained using the arithmetic-mean weighting scheme were very similar to those observed earlier using upstream weighting.

The results obtained using the harmonic-mean weighting scheme were considerably different, as the front moves only about 3 m down the fracture and the adjacent rock matrix after 31 days of drilling. The reason for this is the relatively low mobility obtained at interfaces when the harmonic-mean weighting is used. Unlike the other two weighting schemes, the harmonic-mean weighting scheme puts most weight upon the downstream permeabilities, which are low due to the lower liquid saturations. Thus, in fact the moisture front cannot move down to the next grid block until after the grid block at the edge of the front becomes fully saturated. The low fluid mobility of the harmonic-mean weighting scheme allows very little liquid water to enter the fracture from the constant head boundary in comparison to the other weighting schemes.

Air Drilling

A brief study was conducted on the effects of air drilling on moisture conditions in nearby fractures and rock-matrix blocks. In this case, a 2-bar air-pressure condition was specified at the top of the system. The relative permeability to air, k_{rg}, was assumed to be $1-k_{rl}$ for all saturations. The liquid-saturation transients observed suggest that only small changes in liquid saturation will occur as a result of air drilling. The maximum decrease in liquid saturation in the matrix is about 0.005 in a matrix element adjacent to the fracture. After one day of recovery, the liquid saturations have practically recovered in both the fracture and the rock matrix. In the interior of the rock matrix, no significant changes in the liquid saturation are observed.

SUMMARY

In summary, our studies suggest that, as a result of water drilling, the wetting front will advance tens of meters down the fractures. The moisture redistribution in the fracture following liquid-water drilling occurs in minutes or hours, with the water being sucked into the matrix and with very little further advancement of the moisture front. The moisture redistribution within the matrix takes much longer, on the order of years. After one year of recovery, the matrix saturation is fairly uniform at a given depth and up to one to two percentage points higher than the initial liquid saturation. For the characteristic curves used, this corresponds to about 10 to 20% difference in the relative permeability of the liquid phase. When hysteresis in the capillary-pressure/liquid-saturation relationship for the matrix is considered, the recovery may be considerably slower and result locally in considerably larger differences between the values for liquid saturations in the matrix and the values obtained after one year of recovery. For the nonhysteretic case, the USGS and Sandia characteristic curves gave similar results for the problem solved. Limited-sensitivity studies of grid effects suggested that they are secondary in importance, as similar results were obtained with two grids with different element sizes.

The results for the case involving air drilling suggest that much less disturbance in the moisture conditions of nearby fractures and rock-matrix blocks will occur. Slight changes in liquid saturations occurred in the fractures and the adjacent rock-matrix elements, with rapid recovery within a time frame of hours or days after drilling ceased.

REFERENCES

Bodvarsson, G.S., Niemi, A., Spencer, A., and Attanayake, M.P., 1988. Preliminary calculations of the effects of air and liquid-water drilling on moisture conditions in unsaturated rocks. Lawrence Berkeley Laboratory Report LBL-25073 (in preparation).

Klavetter, E.A., and Peters, R.R., 1986. Fluid flow in a fractured rock mass. Sandia National Laboratory Report SAND85-0855, Albuquerque, N.M., 55 p.

Kwicklis, E., and Hoxie, D., 1987. An estimation of the influence of drilling-induced moisture perturbations in an hypothetical infiltration test. Draft report. U.S. Geological Survey, Denver, CO.

Montazer, P., Harrold, P.E., Snow, D. T., and Trautz, R. C., 1987a. Effects of dry versus wet mining in portions of the main test horizons of the exploratory shaft at Yucca Mountain. Draft Report. U.S. Geological Survey, Denver, CO.

Montazer, P., and Wilson, W.E., 1984. Conceptual hydrologic model of flow in the unsaturated zone, Yucca Mountain, Nevada. U.S. Geological Survey Water Resources Investigation Report 84-4345, 55 p.

Mualem, Y., 1984. A modified dependent domain theory of hysteresis. Soil Science, v. 137, no. 5, p. 283–291.

Niemi, A., Bodvarsson, G.S., and Montazer, P., 1987. Preliminary capillary hysteresis simulations for fractured rocks. Lawrence Berkeley Laboratory Report LBL-23593, 80 p.

Peters, R.R., and Gauthier, J.H., 1986. NNWSI Hydrologic Analysis No. 8.

Pruess, K., 1983. GMINC—A mesh generator for flow simulations in fractured reservoirs. Lawrence Berkeley Laboratory Report LBL-15227, 64 p.

Pruess, K., 1987. TOUGH users guide. Lawrence Berkeley Laboratory Report LBL-20700, 84 p.

Rulon, J., Bodvarsson, G.S., and Montazer, P., 1986. Preliminary numerical simulations of groundwater flow in the unsaturated zone, Yucca Mountain, Nevada. Lawrence Berkeley Laboratory Report LBL-20553, 88 p.

Equivalent Permeability of Statistically Simulated Single Fractures

K. Coakley, K. Muralidhar, J.C.S. Long, and L.R. Myer

We have modeled single-fracture void-space and contact-area geometry and then solved the equations of flow within the defined space. We simulate void-space geometries that are statistically similar to an observed void-space geometry as observed in the plane of the fracture. We solve for flow and determine equivalent permeability with Darcy's law, as well as the Navier-Stokes equations. We compare equivalent permeabilities computed in each flow model to determine the relative advantage of solving the fundamental but computationally intensive Navier-Stokes equations rather than solving the computationally fast but empirical Darcy's law. We also study how the variability of permeability and anisotropy depend on scale, using Darcy's law. We present a lower bound for the variability of equivalent permeability, using Darcy's law, based on the Power Average Model (Journel et al., 1986). The bound is for fractures with contact areas of zero aperture and void spaces of constant aperture. The bound incorporates knowledge of contact area, scale, and correlation. We then extend the bound to the case of variable void-space aperture distributions using a critical-path analysis (Katz and Thompson, 1986; Charlaix et al., 1987).

GEOMETRY

We have developed a statistical model of fracture void-space geometry based on an observed pattern of voids in the plane of a fracture void space taken from a metal-injection experiment (Pyrak-Nolte et al., 1987). We compute the two-point correlation function of the void space and simulate statistically similar void spaces such that they have the same two-point correlation function. The two-point correlation function (Berryman and Blair, 1986), S_2 (**r**), gives the probability that two points, separated by **r**, both lie in the void space. In our model, we assume an isotropic two-point correlation function.

DATA

Our data come from a metal-injection experiment (Pyrak-Nolte et al., 1987) performed on a cylindrical core sample of quartz monzonite from the Stripa mine in Sweden. The sample (diameter 4.55 in., height 7.26 in.) contained a single natural fracture orthogonal to the long axis of the core. Hot molten Wood's metal was injected into the voids of the fracture, which was under a 10-MPa stress. After the metal solidified, the fracture was taken apart and both the upper and lower fracture surfaces were photographed. Because the metal sticks to either the upper or lower fracture surface, we superimposed two images to get our composite void-space geometry. We used a Zeiss image analysis system to digitize the images of bright metal on darker rock. The fracture was discretized into pixels with side lengths of 0.21 mm. We classified each pixel as void space or contact area depending on whether the pixel's grey-level intensity was above or below a chosen threshold. Sources of error include nonuniform illumination of the fracture; rotation, tilt, and translation of each fracture surface before superimposition; subjective choice of threshold; and classification errors due to void spaces having shapes different from our square pixels.

We took the inner section of the fracture, 128 pixels by 128 pixels, as our data set. The observed void-space geometry, shown in Fig. 1, has 18.3% contact area.

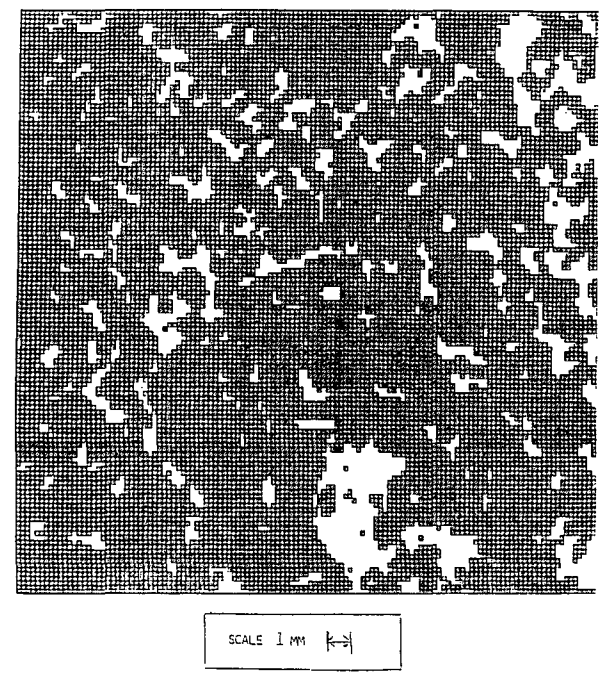

Figure 1. Observed void-space geometry. 128 by 128 pixels. Scale: 1 pixel length is 0.21 mm. Contact area = 18.3%. Voids are black pixels. Data from metal-injection experiment. [XBL 878-3490]

SIMULATION

In our simulation, we first assign an independent Gaussian random variable to each pixel. We then convolve this "white noise" process with a radially symmetric filter that has exponentially decaying weights. Hence, a moving average filter assigns the (i,j)th pixel a new Gaussian random variable that is the weighted average of all the independent Gaussians previously assigned to pixels within a circular neighborhood of the (i,j)th pixel. We then clip our correlated Gaussian process such that pixels with random variables above a chosen cutoff are void and the remaining are contact.

To get a variable-aperture distribution, we transform the random variables assigned to the void pixels. In our example, we chose the exponential transform so as to get a correlated log-normal void-space aperture distribution. We chose this transformation for convenience and as a first step. The next step will be to obtain data on the void-space aperture histogram and spatial correlation function. These will dictate which transformation to use. However, casts of single fractures made by Gale (1987) do suggest a lognormal distribution for void-space apertures.

FLOW

We try to model both the details of void-space geometry and the details of flow. We solve for flow using the Navier-Stokes equations (Muralidhar and Long, 1987), rather than just Darcy's law. This is an improvement because the Navier-Stokes equations are based on Newton's second law for fluids (Schlichting, 1979), whereas Darcy's law is empirical in nature.

We also derive a set of reduced Navier-Stokes equations by ignoring some tortuosity terms in the Navier-Stokes equations. By ignoring even more tortuosity terms, we show how to get a Darcy's-law flow model from the reduced Navier Stokes equations.

We then compare the different flow models—Navier-Stokes, reduced Navier-Stokes, and Darcy's—by solving for flow and equivalent permeability for the same four-constriction geometry. We varied the pinch, i.e., minimum aperture, and found that the flow models disagree more as minimum aperture decreases and tortuosity in the vertical plane becomes more important (Fig. 2).

We also solved for flow, using the reduced Navier-Stokes equations and Darcy's law, for the simulated variable void-space geometry (Fig. 3). We used the reduced Navier-Stokes equations because we could not solve the Navier-Stokes equation due

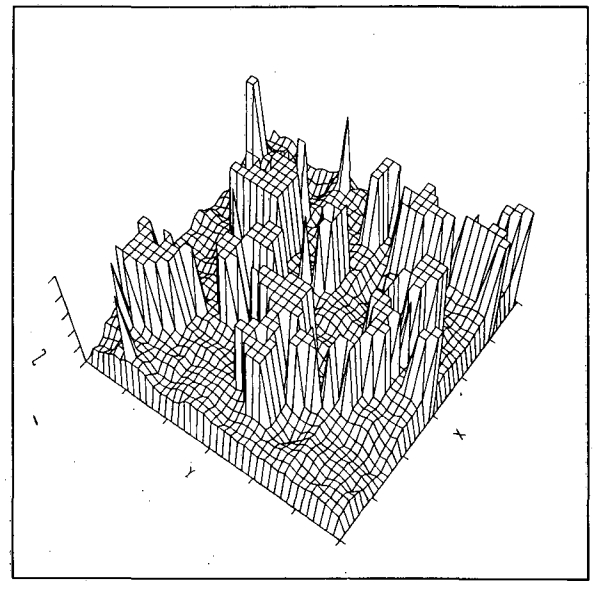

Figure 2. Plot of simulated void-space geometry with variable-aperture distribution. Data set is not tapered near boundaries. Fracture geometry is 41 by 41 pixels; length = 6. Contact areas appear as plateaus. Void-space apertures range from 0.64 to 1.0. [XBL 878-3498]

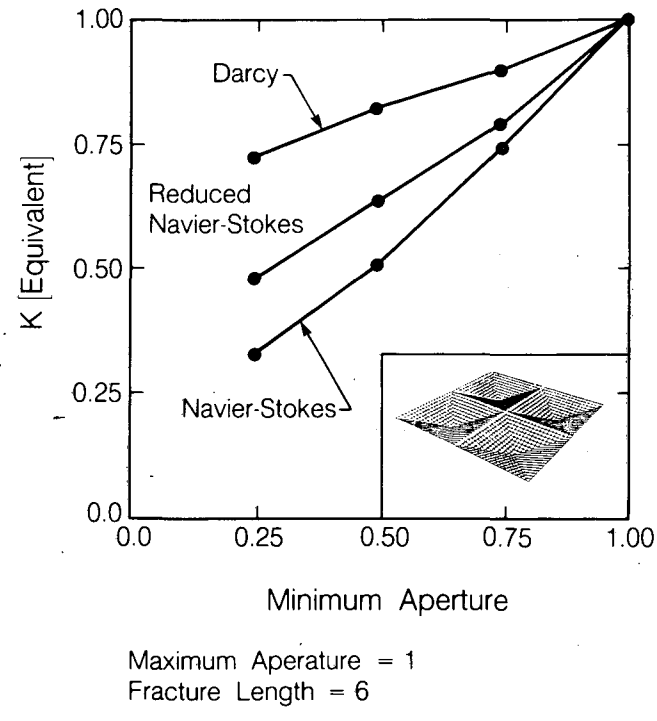

Figure 3. Plot of equivalent permeability as a function of minimum aperture for four-constriction geometry. Comparison of three flow models—Navier-Stokes, reduced Navier-Stokes, and Darcy's law. [XBL 887-10343]

to computer-time constraints. We found that the equivalent permeabilities determined by the two flow models, Darcy's law and reduced Navier-Stokes equations, were close.

SCALE

We study how the variability of equivalent permeability of simulated fracture void-space geometries with given contact-area percentage depends on scale. Voids have unit apertures, and contact areas have zero-valued apertures. For each selected geometry, we solved for two equivalent permeabilities, one corresponding to an east/west pressure drop and the other to a north/south pressure drop. We took the magnitude of the difference between the two equivalent permeabilities as our anisotropy statistic. Our scale study shows that both the variability of equivalent permeability and anisotropy of equivalent permeability decrease as fracture size increases.

Lower Bound for Variability of Equivalent Permeability

We present a lower bound for the variability of equivalent permeability, using Darcy's law, for the single fracture based on the power-average model (Journel et al., 1986). We first consider voids that have constant aperture and then extend our results to the variable-aperture case using a critical-path analysis (Katz and Thompson, 1986; Charlaix et al., 1987). If we assign contact areas in the plane of the fracture zero conductances and void spaces in the plane of the fracture unit apertures and assume the validity of the power-average model, we get

$$<K_{eq}> = p^{1/w} , \tag{1}$$

where p is the fraction of void spaces.

Assuming that the two-point correlation function has an exponential form

$$S_2(\mathbf{r}) = p^2 + p(1-p)e^{-\lambda|\mathbf{r}|} , \tag{2}$$

we derive

$$\frac{\sigma_{K_{eq}}}{<K_{eq}>} \geqslant \left|\frac{1}{wp}\right| \times \sqrt{1 + 2\pi e^{-\lambda}\left(\frac{1}{\lambda^2} + \frac{1}{\lambda}\right)} \frac{\sqrt{p(1-p)}}{N} \tag{3}$$

for an N-pixel by N-pixel fracture.

Lower Bound for the Variable-Aperture Case

We can extend our lower-bound result to the variable-aperture void-space distribution. For broad variable-aperture distributions, the smallest apertures may control the flow. Following the ideas of Shante (1977), Kirkpatrick (1979), Katz and Thompson (1986), and Charlaix et al. (1987), we identify a cut-off apertures, b_c, that controls the flow. We set all conductances less than b_c to zero, and all above b_c to b_c.

Because of this assignment, this method gives a lower bound for equivalent permeability. Hence, we choose the b_c that gives the largest lowest bound for equivalent permeability.

Critical-path analysis for the power-average model gives

$$\hat{K}_{eq} = b^{*3}\, p^{*1/w} , \tag{4}$$

$$\frac{\sigma_{K_{eq}}}{<\hat{K}_{eq}>} \geqslant \frac{1}{wp^*} \times \sqrt{1+2\pi e^{-\lambda}\left(\frac{1}{\lambda^2} + \frac{1}{\lambda}\right)} \frac{\sqrt{p^*(1-p^*)}}{N} , \tag{5}$$

where p^* is the fraction of apertures above b^{*2} and

$$b^* = \frac{3wp^*}{f(b^*)} ,$$

where $f(b)$ is the probability density function for the apertures.

Critical-path analysis for the percolation model gives (Kirkpatrick, 1973)

$$\hat{K}_{eq} = K_o\, b^{*3} (p^* - p_{crit})^t , \tag{6}$$

$$\frac{\sigma_{K_{eq}}}{<K_{eq}>} \geqslant \frac{t}{N} \times \sqrt{\frac{p^*(1-p^*)}{(p^*-p_{crit})^2}\left\{1+2\pi e^{-\lambda}\left(\frac{1}{\lambda^2} + \frac{1}{\lambda}\right)\right\}} , \tag{7}$$

where p_{crit} is the percolation threshold and

$$b^* = \frac{3(p^*-p_{crit})}{tf(b^*)} .$$

DISCUSSION

This work shows the importance of specifying fracture void-space geometry accurately and identifying the relevant physics to select a practical flow model. Darcy's law always gives the largest equivalent permeability, and the Navier-Stokes equations give the smallest equivalent permeability. The reduced Navier-Stokes equations give an intermediate value. For tracer studies, this means that Darcy's law overestimates velocity. We can rescale the equivalent permeability computed using Darcy's law to get the equivalent permeability computed using the Navier-Stokes equations as long as flow remains linearly related to gradient of pressure.

The three flow models gave significantly different equivalent permeabilities for the four different constriction geometries. For our more complex variable-aperture geometry, Darcy's law and the reduced Navier-Stokes equations gave nearly the same equivalent permeabilities. The full Navier-Stokes solution could not be obtained for this case.

We identified two sources of variability of equivalent permeability. In our scale study, we showed how, at fixed contact area, percentage equivalent permeability varies about some average equivalent permeability. In our lower-bound study, we related fluctuations in contact-area percentage, at varying scales, to fluctuations in average equivalent permeability.

Since real fracture void spaces will have variable aperture distributions, we need more sophisticated procedures than assigning each void a constant aperture and then computing flow. A critical-path analysis combined with the power average or percolation model offer such promise to estimate the variability of equivalent permeability analytically.

REFERENCES

Berryman, J.G., and Blair, S.C., 1986. Use of a digital image analysis to estimate fluid permeability of porous materials. Application of two-point correlation functions. J. Appl. Phys., v. 60, p. 1930–1938.

Charlaix, E., Guyon, E., and Roux, S., 1987. Permeability of a random array of fractures of widely varying apertures. Transport in Porous Media, v. 2, no. 1, p. 31–43.

Gale, J.E., 1987. Comparison of coupled fracture deformation and fluid flow models with direct measurements of fracture pore structure and stress flow properties. *In* I.W. Farmer, et al. (eds.), 28th U.S. Symposium on Rock Mechanics, Tucson, Arizona, June 29–July 1, 1987. A. A. Balkema, Rotterdam, Netherlands, p. 213–222.

Journel, A.G., Deutsch, C.D., and Desberats, A.J., 1986. Power averaging for block effective permeability. Paper SPE 15128 presented at the 56th California Regional Meeting of the SPE, Oakland, California, April 2–4, 1986.

Katz, A.J., and Thompson, A.H., 1986. A quantitative prediction of permeability in porous rock. Phys. Rev. B, v. 34, no. 11, p. 8179–8181.

Kirkpatrick, S., 1973. Percolation and conduction. Rev. Modern Phys., v. 45, no. 4, p. 574–588.

Kirkpatrick, S., 1979. Course 5. Models of disordered materials. *In* R. Balian, R. Maynard, and G.T. Toulouse (eds.), Ill-Condensed Matter, North-Holland, Amsterdam.

Muralidhar, K., and Long, J.C.S., 1987. A scheme for calculating flow in fractures using numerical grid generation in three-dimensional domains of complex shapes. Lawrence Berkeley Laboratory Report LBL-24453.

Pyrak-Nolte, L.J., Myer, L.R., Cook, N.G.W., and Witherspoon, P.A., 1987. Hydraulic and mechanical properties of natural fractures in low permeability rock. Presented at Sixth International Conference on Rock Mechanics, Montreal, Canada, August 30, 1987.

Schlichting, H., 1979. Boundary-Layer Theory. McGraw Hill, New York.

Shante, V.K.S., 1977. Hopping conduction in quasi-one-dimensional disordered compound. Phys. Rev. B, v. 16, p. 2597.

Analysis of Pressure, Enthalpy, and CO_2 Transients in Well BR21, Ohaaki, New Zealand

S.W. Gaulke and G.S. Bodvarsson

Interpretation of data from wells completed in two-phase fractured geothermal reservoirs is difficult because methods available for analysis of such data are limited. In most cases methods developed for single-phase porous-media reservoirs are modified to take into account enthalpy variations and relative-permeability effects. It is well known that the application of these methods may yield very unreliable results for important reservoir parameters.

Interpretation of two-phase well data using numerical techniques may yield more reliable results because more of the true reservoir complexities can be introduced into the analysis. In addition to the multiphase effects on such data, we can also model the fractured nature of the reservoir and the effects of noncondensible gases and dissolved solids, if those are considered important. Actually, it may be beneficial to consider multicomponent effects, because these may constrain the results, giving a better representation of the true system.

Data are available for Ohaaki geothermal field, New Zealand, well BR21 that will allow for the interpretation of the near-well reservoir parameters. For a two-week period, the well was opened to a constant throttle while the transient changes in downhole pressure, discharge enthalpy, and flowing mass fraction of CO_2 were monitored. The flow rate during this period was about 25 kg/s.

The data are typical of two-phase systems showing large variations in enthalpy and flowing mass fraction of CO_2 (see Fig. 1). In addition, there is an extended transient period before the enthalpy and mass fraction of CO_2 stabilize, suggesting that the well response is dominated by the fracture-matrix effects rather than behaving as a porous medium. (Grant and Glover, 1984).

Results from numerical simulations are shown to aid in the interpretation of the data from well BR21. A match with the pressure, enthalpy, and mass fraction of CO_2 provides insight into the reservoir conditions in situ. The analysis of CO_2 transients is shown to be valuable in the interpretation of reservoir parameters affecting the performance of two-phase wells.

RESERVOIR AND WELL DESCRIPTION

Ohaaki is currently under development for 110-MW electrical power production. The field is a "hot-water" system containing between 2 and 4 percent CO_2 by weight (Grant, 1977; Sutton and McNabb, 1977; Grant and Glover, 1984).

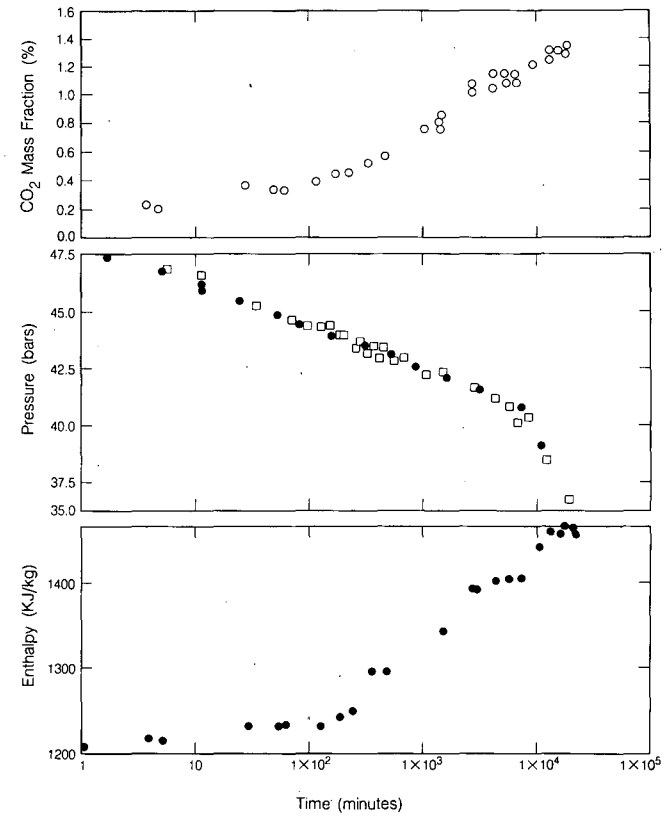

Figure 1. Changes in the downhole pressure, flowing mass fraction of CO_2, and flowing enthalpy for well BR21, Broadlands, New Zealand. [XBL 876-10202]

Well BR21 was drilled in 1970 to a depth of 1120 m; the casing extended to 425 m. In 1971, during the initial discharge period, the BR21 fluid contained 4.8% gas by weight. Later, however, during a flow test in 1975, the gas content was down to 1.9% by weight. BR21 is a two-phase well producing fluids with enthalpy in excess of that for a saturated liquid under reservoir conditions. The primary permeable zone is at 500-m depth in a pumiceous lapilli tuff that is locally water-laid and contains a low quartz content (Ministry of Works and Development, 1977). This formation has an injectivity of 15 kg/bar·s and a productivity of 1.5 kg/bar·s. The temperature of this zone is about 255°C. The formations directly above and below are largely impermeable.

PREVIOUS ANALYSIS

Grant and Glover (1984) carried out an extensive analysis of BR21 data using analytical techniques developed by Grant (1979). They noted that the enthalpy took several weeks to stabilize while the pressure transients lasted only for minutes or even seconds. Assuming reasonable reservoir parameters, they determined that the enthalpy transient period should be on the order of minutes for a porous medium. From this analysis, Grant and Glover concluded that a fractured medium was required to explain the enthalpy transients. A fracture model with impermeable matrix blocks was used to match the pressure and enthalpy transients. Analysis of the chemical transients was determined to be too complex to include in their study (Grant and Glover, 1984).

PRESENT ANALYSIS

Numerical studies were undertaken to determine the characteristics of the reservoir near well BR21, using the simulator MULKOM (Pruess, 1983) with an equation of state for H_2O-CO_2 mixtures developed by O'Sullivan et al. (1985). The primary feed zone in the well was assumed to provide all of the fluid during production and, hence, a single-layer radially infinite model was used. The MINC method (Pruess and Narasimhan, 1982) was used to approximate the fractured nature of the reservoir, with the matrix being discretised into five nested elements. The effective thickness of the reservoir was assumed to be 100 m, the approximate thickness of the Waiora Formation in the vicinity of well BR21. The reservoir initially had 50 bars total pressure at the primary feed zone, and the well produced at a constant rate of 25 kg/s. Other rock and fluid parameters used in the simulations are given in Table 1.

The "best" match with the BR21 pressure, enthalpy, and mass fraction of CO_2 transient data is shown in Fig. 2. We found that a composite reservoir model is necessary to match the data (Fig. 3). The early transients are dominated by the properties of the fracture system. The rapid decline in pressure

Table 1. Model reservoir parameters.

Parameter	Reservoir value(s)
Reservoir thickness	100 m
Wellbore radius	0.12 m
Flow rate	25 kg/s
Fracture spacing	30 m
Fracture porosity	0.1%
Matrix porosity	18%
Fracture transmissivity	10.0 Dm from well to 125 m
	1.0 Dm beyond 125 m
Matrix permeability	0.3 md
Thermal conductivity	2.2 W/m°C
Rock heat capacity	1000 J/kg°C
Rock density	2650 kg/m^3
Fracture relative permeability	X-curves
	S_{rl} = 0.0 S_{rg} = 0.0
Matrix relative permeability	X-curves
	S_{rl} = 0.05 S_{rg} = 0.40
Initial total pressure	50 bars
Initial gas saturation	6% in fracture to 70 m
	15% in fracture beyond 70 m
	33% in matrix
Initial partial pressure of CO_2	2.0 bars
Initial temperature	≈ 260°C
Diffusion coefficient	1.38×10^{-5} m^2
Tortuosity	0.25 m/m

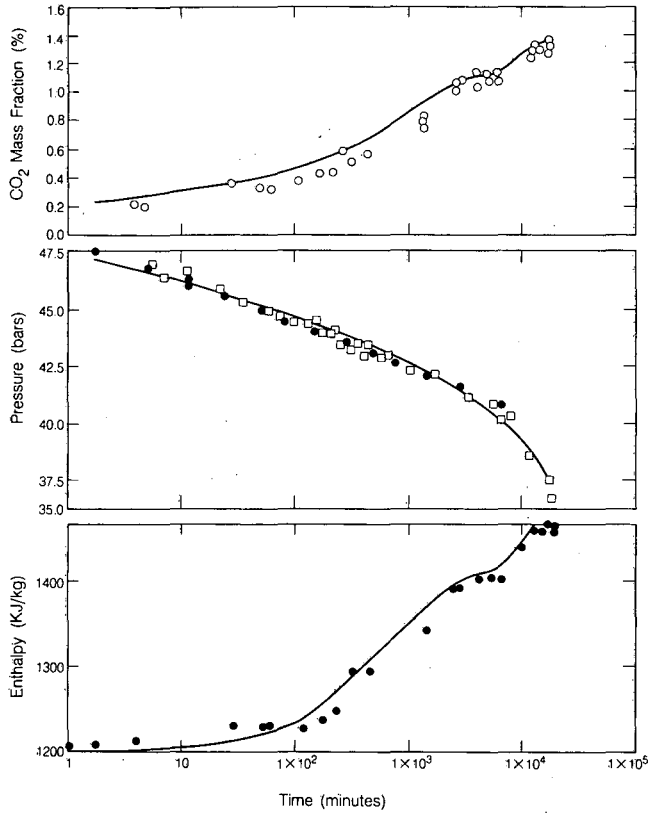

Figure 2. Comparison of best-fit model (curves) with measured results (points) of changes in downhole pressure, flowing mass fraction of CO_2, and flowing enthalpy with time. [XBL 876-10203]

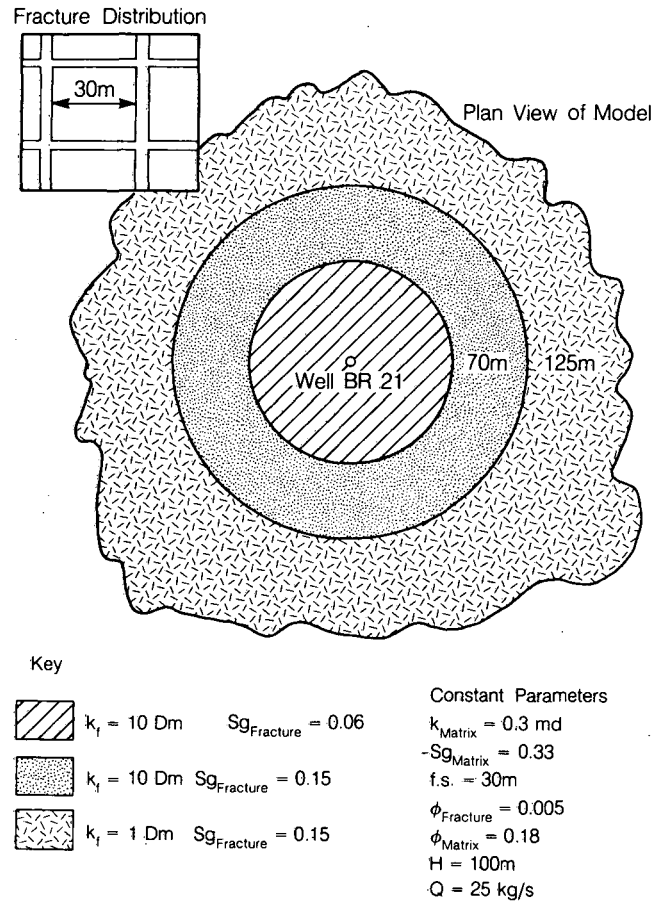

Figure 3. Diagram of best-fit model including important reservoir and fluid parameters. [XBL 8612-12791]

without a concurrent rise in enthalpy (see Fig. 2) indicates that the fracture storage is small and that the fractures are fairly permeable. For the 100-m-thick reservoir, we found that a fracture porosity of 0.5% was needed to provide the appropriate short-term storage effects. Here, fracture porosity is defined as the total volume occupied by the fractures in a unit volume of rock. Typical fracture porosities range from 0.1–1.0%, so that the value of 0.5% deduced from the modeling appears reasonable. Near the well a fracture transmissivity of 10 Dm provides a reasonable match with tBe pressure-transient data. The steeper decline at later time (after 5×10^5 s) necessitates smaller transmissivities away from the well. The best match was obtained when an outer region with a 1-Dm transmissivity was used 125 m away from the well (see Fig. 3).

The initial gas saturation assumed in the fractures near the well is 6%, so that the computed initial flowing enthalpy matches the observed one (1190 kJ/kg). A 2-bar initial partial pressure of CO_2 was used, which, along with an initial gas saturation of 6%, gives the observed early time mass fraction of CO_2 of 0.28% (see Fig. 2). Different values for the initial gas saturation and the partial pressure of CO_2 not only will result in incorrect initial enthalpy and mass fraction of CO_2, but also will result in a pressure decline that will not match the observed one.

The stabilized values of both the enthalpy and the flowing CO_2 mass fraction at about 7000 min help to determine two other parameters, matrix gas saturation and porosity. The enthalpy of approximately 1400 kJ/kg is representative of the equilibrium fluid enthalpy between the fractures and the matrix. Therefore, this value helps establish the required gas saturation in the matrix, which was determined to be about 33%. The matrix porosity has been shown to have strong effects on the rise in the flowing mass fraction of CO_2 without significantly affecting the enthalpy (Gaulke, 1986). An assumed matrix porosity of 18% provided sufficient CO_2 to cause an increase in the CO_2 mass fraction to 1.1% as observed. This matrix porosity would seem rather high except that the rock is pumiceous, suggesting a large void volume.

The fracture spacing is proportional to the surface area between the fractures and the matrix and, hence, will control the rate at which equilibrium flow of heat and mass is established between the fracture and matrix. In addition, the matrix permeability controls the amount of fluids recharging the fractures from the matrix. Using a simple trial-and-error method, it is easily established that the fracture spacing needed to cause the time delay before the rise in enthalpy and CO_2 content is about 30 m. The matrix permeability that provides fluid at a rate necessary to enhance the enthalpy and flowing CO_2 mass fraction is 0.3 md. Actually, the matrix-fracture interaction is proportional to k_m/D^2, where k_m is the matrix permeability and D^2 is the square of the fracture spacing (Bodvarsson and Witherspoon, 1985). Thus, different values for k_m and D^2 are possible as long as the ratio k_m/D^2 is about 3×10^{-19}. However, the values for D of 30 m and k_m of 0.3 md seem reasonable.

The final consideration here is the moderate rise in both the flowing enthalpy and the flowing mass fraction of CO_2 accompanying the steep pressure drop at late times (after about five days). If only the enthalpy and the pressure are considered, this response would be characteristic of boundary effects. However, since the flowing CO_2 mass fraction also rises, boundary effects are not sufficient by themselves to explain the changes (Bodvarsson, 1984). Therefore, a combination of changes in the gas saturation and fracture permeability are required to accurately match these data. The pressure pulse travels along the fracture more rapidly than the hydrodynamic front. This indicates that changes in gas saturation are needed closer to the well than changes in fracture permeability in order to match transient conditions. Thus the gas saturation in the fracture is increased to 15% from 6% at 70 m, while the fracture transmissivity decreases from 10 Dm to 1 Dm, at about 125 m. This allows the increase in the pressure decline to be felt at the well at the same time as the changes in the fluid composition and thermodynamic conditions.

CONCLUSIONS

A model of well BR21 has been developed that adequately matches observed pressure, enthalpy, and flowing CO_2 mass-fraction data. This model is the result of trial-and-error numerical-simulation studies. From the available data it was possible to estimate various reservoir parameters that seem reasonable given the field conditions at Ohaaki. It should be noted that these values are dependent on the assumed relative-permeability curves. However, the values obtained for important reservoir parameters indicate the value of multicomponent modeling of well test data. Modeling of multicomponent changes give additional constraints on modeling results.

REFERENCES

Bodvarsson, G.S., 1984. Numerical studies of enthalpy and CO_2 transients in two-phase wells. Geoth. Resour. Counc. Trans., v. 8, p. 289–294.

Bodvarsson, G.S., and Witherspoon, P.A., 1985. Flow rate decline of steam wells in fractured geothermal reservoirs. *In* Proceedings, Tenth Workshop on Geothermal Reservoir Engineering, Stanford, California, January 22–24, 1985.

Gaulke, S.W., 1986. The effect of CO_2 on reservoir behavior of geothermal systems (M.S. thesis). University of California, Berkeley.

Grant, M.A., 1977. Broadlands—a gas-dominated geothermal field. Geothermics, v. 6, p. 9–29.

Grant, M.A., 1979. Quasi-analytic solutions for two-phase flow near a discharging well. Tech. Rep. 86, Appl. Math Div., Dept. of Sci. and Ind. Res., Wellington, New Zealand.

Grant, M., and Glover, R., 1984. Two-phase heat and mass transfer experiment at well BR21 Broadlands. Geothermics, v. 13, no. 3, p. 193–213.

Ministry of Works and Development, 1977. Broadlands Geothermal Investigation Report. Ministry of Works and Development, Wellington, New Zealand.

O'Sullivan, M.J., Bodvarsson, G.S., Pruess, K., and Blakeley, M.R., 1985. Fluid and heat flow in gas-rich geothermal reservoirs. Soc. Pet. Eng. J., v. 25, no. 2, p. 215–226.

Pruess, K., 1983. Development of the general purpose simulator MULKOM. *In* Earth Sciences Division Annual Report 1982. Lawrence Berkeley Laboratory Report LBL-15500, p. 133–134.

Pruess, K., and Narasimhan, T.N., 1982. On fluid reserves and the production of superheated steam from fractured, vapor-dominated geothermal reservoirs. J. Geophys. Res., v. 87, no. B11, p. 9329–9339.

Sutton, F.M., and McNabb, A., 1977. Boiling curves at Broadlands Geothermal Field, New Zealand. New Zealand Journal of Science, v. 20, p. 333–337.

Statistical Modeling of a Three-Dimensional Fracture Network

K. Hestir, D. Billaux, J.-P. Chiles, and J.C.S. Long

One step in the modeling of groundwater flow through systems of fractured rock is the construction of numerical simulations of fracture systems or networks. We briefly describe the construction of such a simulation: The interested reader can refer to Hestir et al. (1987) for more detail.

The model we have used represents fractures as thin discs in three-dimensional space. The location of a disc is defined as the location of its center. The placement of fracture centers is determined by a stochastic process called the parent-daughter point process. Diameter and aperture of discs are assumed to be independent random variables. Orientation of fractures is taken to be a stationary random field.

Two numerical simulations of fracture meshes using this model have been made. We have also started a study of the flow properties of these simulations. The model and simulations are based on drift-wall mapping data collected at the uranium mine of Fanay-Augères, in Limousin, France. The fractures at Fanay have been divided into five sets. A separate model and simulation is constructed for each set. Finally, the simulations are superimposed to form a simulation of the complete fracture system.

The data were taken from drifts 1 and 2 (S1 and S2) at Fanay. We have made two simulations, one based on data from S1 and one based on data from S2. An important difference between S1 and S2 is that S1 is wet and S2 is dry. We show below how an analysis of the connectivity of the two simulations seems to reflect this difference.

PARAMETER INFERENCE: FITTING THE MODEL

The fracture-network model is specified by the values of several parameters. These parameters describe the probability distributions of the three-dimensional characteristics of the network. The biggest problem in fitting the model to the data is using two-dimensional information to draw inferences about these parameters. Several statistical tools had to be developed for this purpose. The modeling is done set by set, so parameter values are needed for each set in S1 and S2. In particular, we need to specify parameters that describe:

1. The stochastic process of fracture orientation.
2. Average and standard deviation for the lognormal diameter distribution.
3. The parent-daughter process of fracture locations in space.

Once all of these quantities are specified for each set, the simulation can be constructed. In this section we discuss the determination of each of these model parameters.

Parameters for Orientation Distribution

The orientation of a fracture can be represented by a unit vector orthogonal to its plane, called its pole. The mean orientation of a set of fractures is defined to be a unit vector parallel to the sum of the poles in that set. The actual calculation of mean orientation is a bit more complicated than this; for details see Hestir et al. (1988).

The idea behind modeling the orientation is to envision the deviation of the fracture from the mean orientation as a random field in three-dimensional space. This random field can be characterized by a few parameters that can be determined from the drift-wall mappings. After these parameters are found, simulation of the random field is a standard procedure.

Determination of the Disc-Diameter Distribution

Assuming fracture diameters are lognormally distributed, a Monte Carlo procedure can be used to find the parameters of this distribution.

Calculation of the Trace-Density Semivariogram from the Data

We have chosen to model the random placement of fractures in space with a point process called the parent-daughter point process. This point process will produce a a higher degree of clustering than the usual Poisson point process. This clustering is typical of fracture patterns. Mathematically, the parent-daughter point process can be described as a Poisson process with a discontinuous random intensity. A particular parent-daughter point process is determined by several parameters that describe the average density of points, degree of clustering, and size of clusters. For a complete description see Hestir et al. (1988).

To find the parameters of the parent-daughter

process of fracture placement we have used a statistic, $\gamma(h)$, called the trace-density semivariogram. The idea is to calculate this semivariogram from data and compare it to one calculated from theory assuming certain values for parameters. Parameter values are then chosen that give a match between the data and theoretical semivariograms. Below we describe how these semivariograms are calculated from the data and theory.

Data Trace-Density Semivariogram

The drift mappings are in vertical planes measuring 100 m × 2 m and 80 m × 2 m. Length is in the x direction and height in the y direction. Hence, $0 \leqslant x \leqslant 100$ or 80 and $0 \leqslant y \leqslant 2$. To calculate the experimental trace-density semivariogram, we count the number of traces in a window that measures 5 m × 2 m and is centered at the point $\vec{x}$, then multiply this number by a correction factor (the orientation-correction factor) that adjusts for the fact that the fractures are not perpendicular to the sampling plane.

Let $E_{\vec{x}}$ denote the resulting (adjusted for orientation) number of traces in our window centered at $\vec{x}$. We slide the window centered on $\vec{x} = (x,y)$ across the length of the drift, fixing $y=1$ and letting x range from 2.5 to 97.5 (or 77.5 for S2), using increments of size 1. The semivariogram, $\gamma(h)$, is estimated by calculating

$$\gamma(h) \approx \frac{1}{2}\frac{1}{n_h}\left\{ \sum_{\{(\vec{z},\vec{w}):\,|\vec{z}-\vec{w}|\,=\,h\}} (E_{\vec{z}} - E_{\vec{w}})^2 \right\},$$

where n_h is the number of terms in the sum.

To describe the orientation-correction factor, let θ denote the angle between a fracture pole and the sampling plane measured in degrees, $0 \leqslant \theta < 90$. If a fracture with angle θ is placed randomly in space, the probability that the fracture intersects the sam-

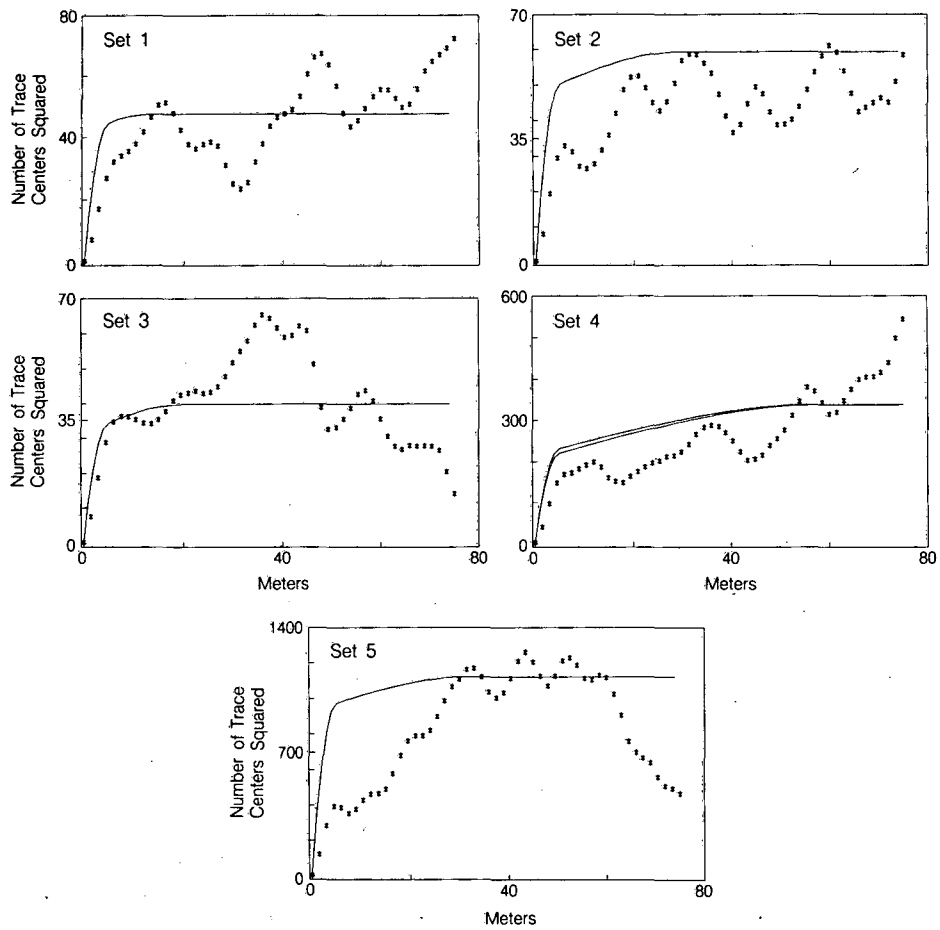

Figure 1. Plane-density semivariogram and theoretical semivariogram for five sets in S1. [XBL 886-10280]

pling plane is proportional to cos θ. This result can be used to show that the orientation-correction factor for a particular window should be

$$\frac{1}{\overline{\cos(\theta)}},$$

where $\overline{\cos(\theta)}$ is the average of the list of $\cos(\theta)$'s for all fractures in the window.

Theoretical Trace-Density Semivariogram for the Parent-Daughter Model and Comparison with the Data

The parameters of the parent-daughter model determine a specific form for the trace-density semivariogram (Deverly, 1984). A sample comparison between theory and data is given in Fig. 1 for the five sets in S1. It turns out that there are several combinations of parameter values that will give a good fit between theory and data. Two such theoretical curves illustrating this are shown for set 4 in Fig. 1. Possible ways to deal with this nonuniqueness include development of more statistics to give similar comparisons between data and theory. Some preliminary results in this direction are discussed in Hestir et al. (1988).

CONNECTIVITY STUDY

One major point of this study is to compare S1 and S2. A measure of connectivity, developed by the second author, D. Billaux, has been developed for this purpose.

Recall that S1 is a wet section of the drift and S2 a dry section. We have taken data from each of these drift sections and created simulations. The data were analyzed and parameters determined in exactly the same way for each section. The connectivity measure, when applied to each simulation, shows that the wet section tends to be more connected. The connectivity measure was also applied to simulations based on a simple Poisson model for fracture placement with the same results.

This measure of connectivity is obtained as follows. The first step is to place an artificial fracture somewhere in the center of our simulation. This is the starting point, which is called the level 0 fracture.

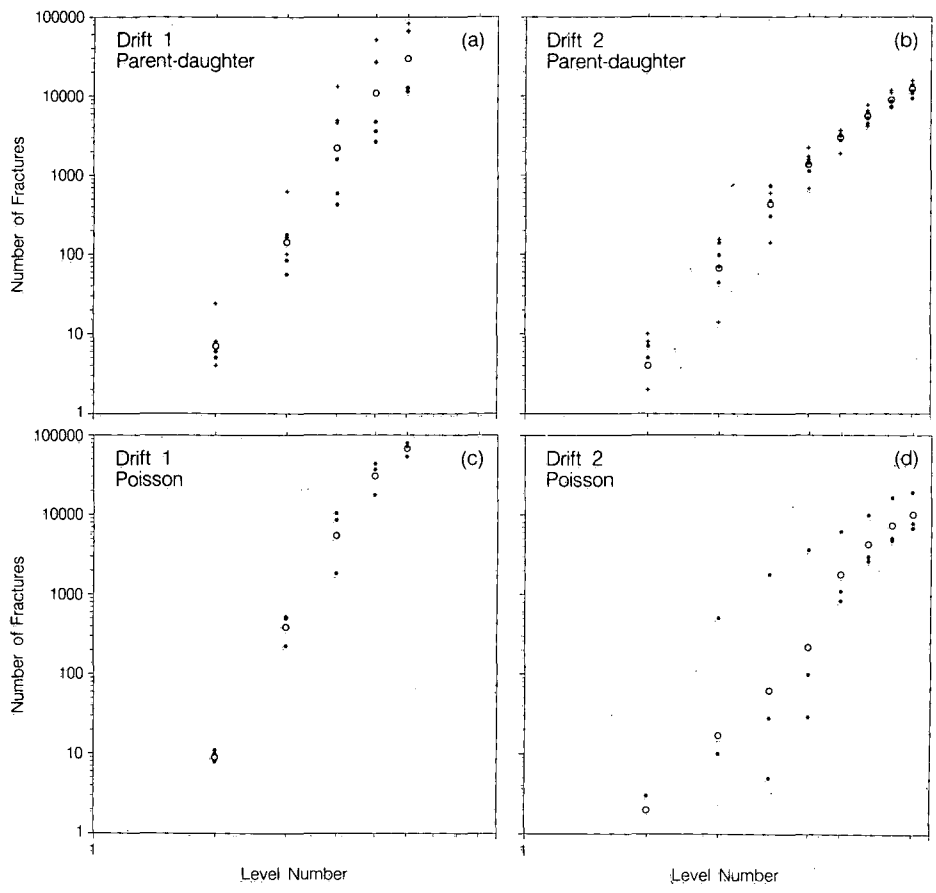

Figure 2. Example of connectivity measure in S1 and S2. [XBL 886-10286]

Level 1 fractures are defined to be all fractures that intersect the level 0 fracture. In general, level k fractures are defined to be all fractures that intersect a level $k-1$ fracture and have not been previously assigned to a level. The number of fractures in each level is our measure of connectivity. Of course, this measure depends on where the level 0 fracture is placed. The process is therefore repeated for several different level 0 fractures and the variations recorded. One way to view this measure of connectivity is as a simple summary of the size of path through which water can flow if injected into the level 0 fracture. A few results of this measure are displayed in Fig. 2. One can see in the figure that the level numbers for the wet section increase much faster than the level numbers for the dry section.

A practical limitation of this idea is that the number of fractures that can be examined to find level sizes is limited by computing faculties. Also, of course, this is a method that is suited to examination of simulations and not to "real life" fracture meshes. Its relevance is therefore dependent on the relevance of the simulation. This dependence may not be severe in situations like this one, where a comparison is being made.

CONCLUSION

We have described the simulation of a fracture mesh based on data from a fracture system in France. The simulation reproduces the spatial variability of fracture density and orientation. To accomplish this we have developed a stochastic model that incorporates this spatial variation. Finally, we have introduced a measure of connectivity for fracture-mesh simulations.

REFERENCES

Deverly, F., 1984. Echantillonnage et Géostatistique, these, Ecole Nationale Superieure des Mines de Paris.

Hestir, K., Chiles, J.P., Long, J., and Billaux, D., 1987. Three dimensional modeling of fractures in rock: From data to a regionalized parent daughter model. *In* Flow and transport through unsaturated fractured rock. AGU Geophysical Monograph 42, American Geophysical Union, Washington, D.C.

Hestir, K., Chiles, J.-P., Long, J., and Billaux, D., 1988. Stochastic modeling of a 3-dimensional fracture network at Fanay-Augères. *In* Proceedings, 1987 DOE/AECL Conference on Geostatistical Sensitivity and Uncertainty Methods for Ground-Water Flow and Radionuclide Transport Modeling, in press.

Warburton, P.A., 1980. A stereological interpretation of joint trace data. Int. J. Rock Mech. Min. Sci. Geomech. Abstr., v. 17, p. 181–190.

Fracture Modeling at the Nevada Test Site

K. Hestir, K. Karasaki, and K. Grossenbacher

The fractured volcanic tuff at Yucca Mountain in Nevada is being investigated as one of the potential host rocks for a high-level nuclear-waste repository. The U.S. Geological Survey (USGS) has been conducting a number of tests and measurements at the Yucca Mountain area. LBL has been assisting the USGS in an effort to characterize the hydrologic behavior in the region. One of the subtasks of LBL is to model the fracture system near the UE-25 C holes. Preliminary tests conducted in these holes indicate that fractures are the main conduits of groundwater and that the porous-medium approximation may not be valid at the scale of well tests. We have developed a methodology to construct a three-dimensional strata-bound fracture model based on the observations in boreholes. This article briefly describes the model and its application to field data.

BULLFROG MEMBER

Three boreholes, designated UE-25 C#1, C#2, and C#3, have been drilled through stratified ash-flow tuff. Borehole geophysical logs, hydraulic tests, and intraborehole flow surveys have been conducted by the USGS. Preliminary interpretation of these data indicate that water-transmitting fractures typically occur at these wells in moderately to densely welded tuff of the Bullfrog Member of the Crater Flat Tuff (Devin Galloway, USGS, personal communication, 1986). Many fractures do not transmit

measurable quantities of water. Fracture strike, dip, and location among the boreholes were estimated from geophysical logs (Richard Spengler, USGS, personal communication, 1986). Other fracture characteristics, such as fracture size and aperture, are not known.

Surface geologic investigations supplemented by limited borehole data have provided a qualitative description of relations between fracture patterns and stratigraphy (Scott et al., 1983). Fractures tend to be strata-bound, with more fractures occurring in welded tuff near the middle of the cooling units. Fewer fractures have been observed near the relatively nonwelded margins of the cooling units. Fractures rarely cross formation and member boundaries. As a first approximation, we have assumed that fractures in the vicinity of wells UE-25 C#1, C#2, and C#3 are bounded by bedded tuffs that separate the Bullfrog Member from overlying and underlying strata. Accordingly, our model is a three-dimensional mesh of fractures bounded by two horizontal planes. The distance between the planes is 600 ft. We use fracture mappings from boreholes C#1, C#2, and C#3 to construct our model.

THE MODEL

We have modeled fractures as thin subvertical rectangular sheets lying between two large bounding planes. We call these the upper and lower bounding planes. They represent the boundaries of the Bullfrog Member (Fig. 1).

To specify locations in space, we use the standard xyz Cartesian coordinate system. The z-axis is taken to be vertical and the xy-plane to lie halfway between the upper and lower bounding planes.

The placement of fractures, their shape, and orientation are all taken to be random quantities. To specify the model we need to specify the probability distributions of these quantities and their relationships to each other. The distributions are summarized in Table 1 and discussed in the following paragraphs.

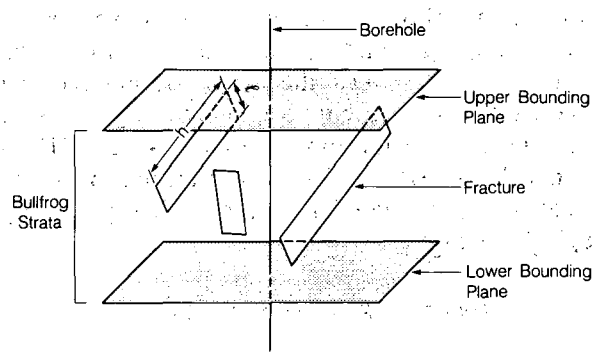

Figure 1. Sketch of conceptual strata-bound fracture model. [XBL 882-10079]

Fracture Location

The location of a fracture is specified by the location of its center. The x and y coordinates of the fracture centers are determined by a Poisson process with rate λ_A in the xy-plane. In the future, with more data, this could be changed to a variable-rate Poisson process or a doubly stochastic Poisson process; i.e., λ_A is variable or λ_A is a stochastic process.

The z-coordinates of fracture centers are assumed to follow a normal distribution with mean μ_z and standard deviation σ_z. If $|z|$ is large for a particular fracture and the fracture falls partly outside the strata, we only consider that part of the fracture that lies between the bounding planes. If a fracture is completely outside the strata, it is ignored. The reason for choosing the normal distribution with this truncation is that we want to have some degree of control of the vertical placement of fractures. For example, if it is found that most fractures occur near the upper bounding plane or intersect it, then this can be modeled with an appropriate choice of μ_z and σ_z.

Fracture Shape

Each fracture has a height h and a length l, as shown in Fig. 1. We assume that h has a lognormal density with mean μ_h standard deviation σ_h and that l has a lognormal distribution with mean μ_l and standard deviation σ_l.

Table 1. Distributions of fracture model parameters.

Parameter	Distribution	Distribution parameters
Location		
x,y	Planar Poisson process	λ_A
z	Normal	μ_z , σ_z
Shape		
h	Lognormal	μ_h , σ_h
l	Lognormal	μ_l , σ_l
Orientation		
θ	Discrete bootstrap	—
ϕ	Polynomial	p

Fracture Orientation

The first assumption we make about the orientation distribution is that strike and dip are independent. Although this assumption is not standard, it is convenient, and we see little evidence against it in scatter plots of orientation.

The strike distribution is modeled as a discrete distribution with probability mass $1/N$ at each data point of observed strike, where N is the number of data points. In statistics this method of modeling is known as bootstrapping and is valid in this context if the sample of strikes from the borehole is unbiased and strikes are independently and identically distributed among fractures.

The dip distribution cannot be modeled with a bootstrap because there is a bias in the dips observed in the borehole. This bias results from the fact that fractures with a dip of 0° are more likely to intersect the borehole than fractures with a dip near 90°. Based on preliminary data analysis, we have chosen a probability density function for dips $f(\phi)$ that has the simple polynomial form

$$f(\phi) = \frac{p}{90°}\left[\frac{\phi}{90°}\right]^{p-1} \qquad 0° \leq \phi \leq 90° .$$

Joint Distribution of Fracture Parameters

We make the simplest possible assumption about the joint distribution of fracture parameters, which is that they are all statistically independent. In particular, for each fracture and among fractures we take the x,y coordinates, the z coordinate, the height, length, strike, and dip to be independent random variables. This assumption can be modified in many ways if new data so indicate.

PARAMETER ESTIMATES AND MODEL FITTING

We have chosen a model that has a small number of parameters and at the same time has some degree of plausibility. Unfortunately we find that it is impossible to infer the value of several parameters from the available data. At best the orientation can be recovered in a satisfactory way, but the remaining parameters λ_A, μ_c, σ_c, μ_h, σ_h, μ_l, and σ_l can only be guessed at. However, a wide variety of these values can be chosen and the resulting models studied. We discuss the parameter estimation problems below.

Fracture Frequency in the Borehole

We can derive a formula for the frequency of fractures in a borehole in terms of the model parameters. This is the main relationship used to infer parameter values.

Recall that we characterize a fracture by the quantities (x,y,z,h,l,ϕ,θ), where x,y,z are the three-space coordinates of the fracture center, h is the fracture height, l is the fracture length, ϕ is the dip, and θ is the strike. To describe the formula for borehole-fracture frequency, assume the strata has thickness 1 so that the upper bounding plane has equation $z = 1/2$ and the lower bounding plane has equation $z = 1/2$. Let

$$T = \min\left(\frac{t}{2}, z + \frac{h}{2}\sin\phi\right) ,$$

$$B = \max\left(\frac{-t}{2}, z - \frac{h}{2}\sin\phi\right) ,$$

$$I_{(a,b)}(x) = \begin{cases} 0 \text{ if } x \notin (a,b) \\ 1 \text{ if } x \in (a,b) \end{cases}$$

for any open interval (a,b). Then one can show that the number of fractures intersecting the borehole is a Poisson process with rate

$$\lambda_A \bar{A} ,$$

where

$$\bar{A} = ml \int\int\int (T - B)\cos\phi I_{(-\frac{1}{2},\infty)}(T) I_{(-\infty,\frac{1}{2})}(B)$$

$$\times\, gz(znot)gh(hnot)f(\phi)dzdldhd\phi . \qquad (1)$$

In practice this formula can be used to determine some of the parameter values given others. For example, if we choose a combination of values for μ_c, σ_c, μ_h, σ_h, μ_l, and σ_l, we can determine the value of λ_A that makes the model reproduce the observed fracture frequency on the average. To fit the orientation distribution, one can use Eq. (1) to show that the density of observed fracture dips in the borehole, $h(\phi)$, is related to the overall dip density through the relation

$$h(\phi) = k\, \mu_l \cot\phi\, A(\phi) f(\phi) ,$$

where

$$A(\phi) = \int\int (T - B)\, I_{(-\frac{1}{2},\infty)}(T)\, I_{(-\infty,\frac{1}{2})}(B)$$

$$\times\, g_z(z_0) g_h(h_0) dz_0 dh_0$$

and k is a constant. Basically $A(\phi)$ is a factor that accounts for the truncation effects of fractures intersecting the upper and lower bounding planes. What we find is that $h(\phi)$ is relatively insensitive to choices of mz , sz , mh , and sh, as shown in Fig. 2.

Parameter Fitting

For a given set of parameter values, the model will predict the observations in the boreholes. A set of parameter values that makes the model correspond to the given data is called a parameter solution. In some modeling settings there is only one set of parameter values that is consistent with the data, so there is a unique parameter solution. In our model, with the given borehole data, the parameter solution is nonunique. This is typical when there is a three-dimensional model whose parameters are being inferred from one- or two-dimensional data (O'Sullivan, 1986). We deal with the nonuniqueness problem in the following steps:

1. Use heuristic judgment to determine what range of parameter settings are reasonable. This judgment can be based on a physical understanding of the formation of the fractures being modeled. We can also get some information about model parameters from surface outcrops of the strata bounding the fractures.

2. Use the statistical relationships between the parameters and data to eliminate parameter settings.

3. Once the range of possible parameter values is determined, construct a series of models corresponding to parameter values that cover this range. We can then examine flow and transport for each model in the series.

The biggest problem with this method is that the number of models required to cover the range of possible parameter values may be prohibitive since there is a large effort required to model flow and transport in each model. We can partially alleviate this problem by chosing a simple and efficient way to characterize the flow and transport of a model. This characterization is described in the next section.

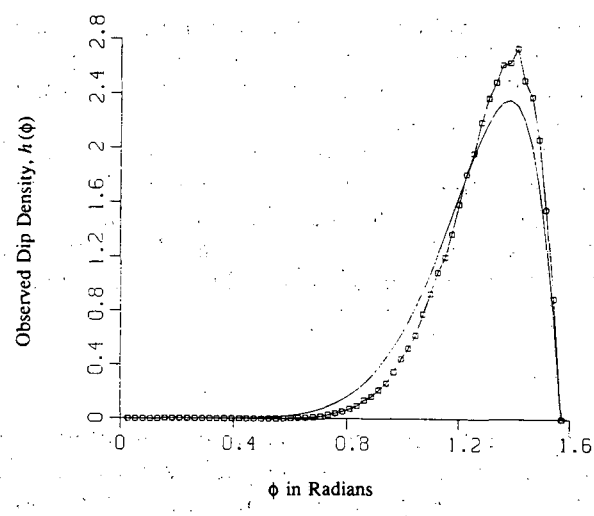

Figure 2. Two possible density curves for dips observed in the borehole. For each curve the parameter settings are the same except for μ_z , σ_z , μ_h, and σ_h. This shows how differing truncation can affect the dip density. [XBL 882-548]

AVERAGE NUMBER OF INTERSECTIONS PER FRACTURE

Since we have to examine a wide range of possible parameter values for the model and their effect on flow and transport, it is desirable to have an easily calculated measure of a system that summarizes the system's important properties. We believe that the average number of intersections per fracture is such a quantity.

To define the average number of intersections per fracture, visualize a realization of the model. Chose one fracture at random from this realization and count the number of fractures intersecting the chosen fracture. Let Y denote this random quantity. The average number of intersections per fracture, ζ, is defined as the average of Y, $\zeta = E(Y)$.

In recent unpublished work, Long and Hestir have shown how to find the permeability of a two-dimensional system of random lines as a function of ζ. This method seems to work for a wide range of ζ, although some difficulty is encountered near the percolation threshold, as one would expect.

Let

$$\vec{F}_i = (z_i, h_i, \phi_i, \theta_i) \quad i = 1,2$$

denote vectors formed from two different settings of fracture parameters. Let $f(\vec{F})$ be the probability density of $\vec{F}$. One can define a function, $\alpha(\vec{F}_1, \vec{F}_2)$, which gives a formula for ζ,

$$\zeta = \lambda_A \int\int \alpha(\vec{F}_1, \vec{F}_2) f(\vec{F}_1)\, f(\vec{F}_2) d\vec{F}_1 d\vec{F}_2 .$$

For a given parameter setting, ζ is easily calculated using a Monte Carlo algorithm that randomly chooses $\vec{F}_1$ and $\vec{F}_2$.

We can now calculate ζ for different parameter settings and use it as a summary of the flow and transport properties of the model. Exact ways of relating ζ to flow and transport in the model are under development.

CONCLUSION

We have developed a three-dimensional model for strata-bound fractures that incorporates data, from boreholes. Since the parameters of the model are hard to infer from the data, we have proposed a simple method of characterizing the response of the model for a range of parameter settings. This could help us to find the range of possible flow and transport properties of the system.

REFERENCES

Hestir, K., Chiles, J.-P., Long, J., and Billaux, D., 1987. Three dimensional modeling of fractures in rock: From data to a regionalized parent daughter model. *In* Flow and Transport through Unsaturated Fractured Rock. AGU Geophysical Monograph 42, American Geophysical Union, Washington D.C.

Long, J.C.S., and Billaux, D., 1987. From field data to fracture network modeling—An example incorporating spatial structure. Water Resour. Res., v. 23, no. 7, p. 1201–1216.

O'Sullivan, F., 1986. A statistical perspective on ill-posed inverse problems. Statistical Science, v. 1, no. 4, p. 502–527.

Scott, R.B., Spengler, R.W., Diehl, S., Lappin, A.R., and Chornack, M.P., 1983. Geologic character of tuffs in the unsaturated zone at Yucca Mountain, Southern Nevada. *In* J.W. Mercer (ed.), Role of the Unsaturated Zone in Radioactive and Hazardous Waste Disposal. Ann Arbor Science Pubs.

Dissolution and Transport of Slightly Water-Soluble Gasoline Components in Groundwater

H.-Y.N. Holman and I. Javandel

An important aspect of the pollution of an aquifer by gasoline leakage is the transfer of slightly water-soluble components (SWSC) such as benzene, toluene, and xylene from the gasoline to the groundwater. This transfer process involves three steps: (1) diffusion of these compounds in the gasoline phase toward the contact between water and gasoline, (2) dissolution of them at the interface, and (3) transport of dissolved organic compounds by groundwater. The overall rate of this heterogeneous process is governed by the slowest step.

Two mathematical models are available to study this transfer process when the capillary fringe of porous medium is saturated with gasoline: the multiphase model of Abriola and Pinder (1985a,b) and the single-point-source model of Hoffmann (1969, 1970). The multiphase model is a complex numerical model with many good features. However, the researchers treated each spatial element in their numerical model as a "homogeneous reactor" within which there exists a local equilibrium between phases. This leads to an unrealistically high dissolution rate. The single-point-source model, on the other hand, is a simple analytical model. It idealized the oil body as a constant point source whose strength is independent of the flow velocity and time. Although this analytical solution was constructed to evaluate the impact of infiltrated gasoline on groundwater quality, the actual driving forces behind the mass-exchange process at the gasoline-water interface were not considered.

Currently, we have developed an analytical solution that enhances our understanding of the mass-exchange process across the interface of gasoline and groundwater and predicts the spatial and temporal distribution of the slightly soluble compounds of gasoline in the groundwater.

THEORY

Consider a significant volume of gasoline being released from an underground storage facility. Although some gasoline is trapped in the vadose zone by capillary forces, most of it reaches the groundwater capillary fringe zone and spreads horizontally to form a lens resting upon the water table, where dissolution occurs (see Fig. 1). A mathematical model has been developed to study the dissolu-

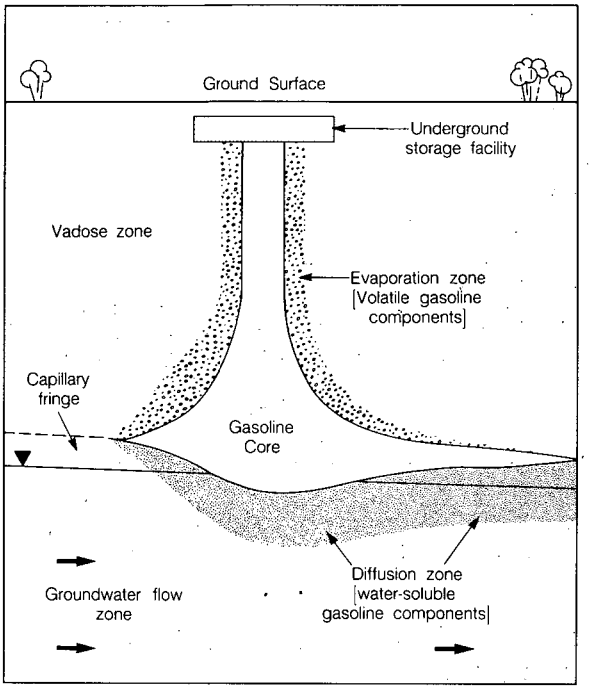

Figure 1. A schematic cross section of gasoline leakage from an underground storage facility. [XBL 878-10324]

tion process when the temperature and pressure remain constant. The following assumptions have been used in this development:

1. The aquifer is unconfined, homogeneous, isotropic, and infinite in areal extent with uniform groundwater velocity.
2. The water-table fluctuation is negligible.
3. The water content within the gasoline lens is equal to, or less than, the residual saturation.
4. Dissolution of SWSC is the only mass-transfer process. (Although biodegradation of hydrocarbons is an important process in the fate of gasoline in the subsurface environment, it has not been considered at this stage of the study.)
5. The homogeneous dissolution reaction at the interface depends on the thermodynamic equilibrium distribution of SWSC between the gasoline and the water phase.
6. The hydraulic head of the gasoline lens remains unchanged.
7. Because most of the underground storage facilities underlie a paved ground surface, rainwater infiltration and the additional contamination that would have leached from gasoline trapped in the vadose zone above the lens are negligible.

The conceptual model used is two dimensional and is divided into three regions (Fig. 2). Region 1 represents a rectangular gasoline lens overlying the

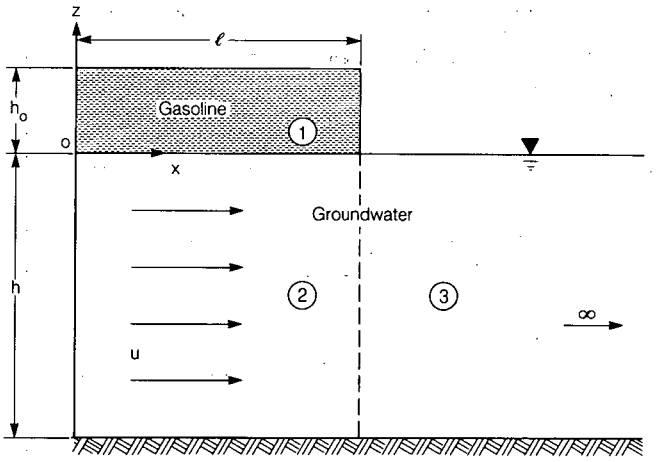

Figure 2. A schematic diagram of the modeling region. [XBL 878-10327]

groundwater. The only mode of transport within the lens is molecular diffusion, by which the SWSC are transferred to the gasoline-water interface, where dissolution occurs. The aquifer is hypothetically divided into two separate regions in order to handle nonuniform boundary conditions along the water table. Region 2 receives a vertical flux of the dissolved organic compound from Region 1. The solute transport in Regions 2 and 3 is controlled by advection and hydrodynamic dispersion.

A system of governing equations with the appropriate initial and boundary conditions within each region has been developed for this model. Because of the uncertainties associated with the type of upstream boundary conditions in transport models, analytical solutions were derived for three types of conditions: the Dirichlet condition with zero concentration, the Neumann condition with zero concentration gradient, and the Cauchy condition with zero net flux.

RESULTS

Following are some results from the analytical solution using the Neumann upstream boundary condition. A layer of highly contaminated groundwater is found directly under the gasoline body (Fig. 3). Note that, although the solubility of pure benzene in water is about 1780 mg/l, the maximum concentration calculated in the aquifer immediately beneath the gasoline lens is only 62 mg/l, which is the local equilibrium concentration. The reason for such a low concentration is the presence of other hydrocarbons within the gasoline. Similar patterns are found for toluene and xylene.

The time variations of SWSC fluxes across the

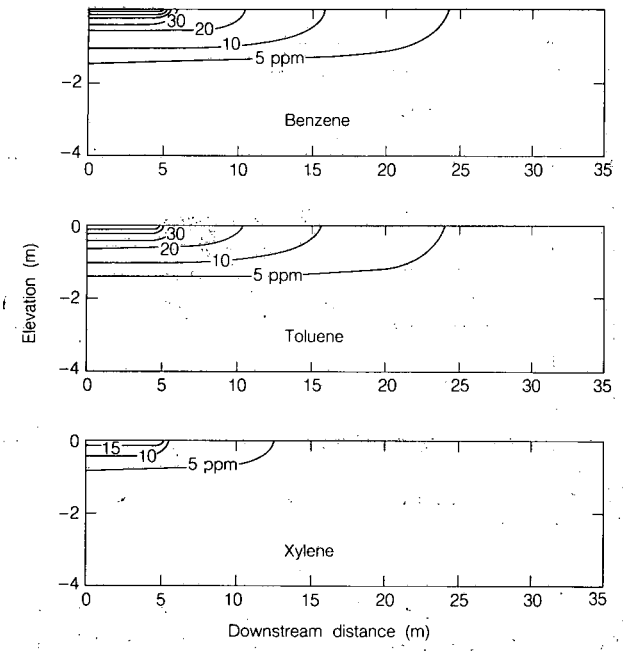

Figure 3. Distribution of various SWSC in groundwater after one year (groundwater velocity $u = 4\times10^{-7}$ m/s, longitudinal dispersivity $\alpha_x = 0.25$ m, transverse dispersivity $\alpha_z = 0.01$ m, gasoline lens length $l = 5$ m). [XBL 878-10323]

gasoline-groundwater interface are controlled by many environmental parameters. The benzene flux, for example, increases with regional groundwater velocity and decreases with time (Fig. 4).

The flux also varies with gasoline type due to differing compositions and thermodynamic properties. The benzene flux shown in Fig. 5, for instance, varies with gasolines of different thermodynamic properties (or partition coefficient).

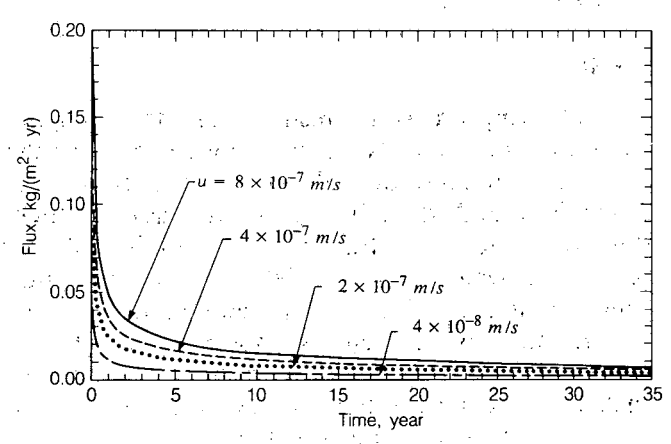

Figure 4. Flux of benzene for various groundwater velocities (longitudinal dispersivity $\alpha_x = 0.25$ m, transverse dispersivity $\alpha_z = 0.01$ m). [XBL 878-10326]

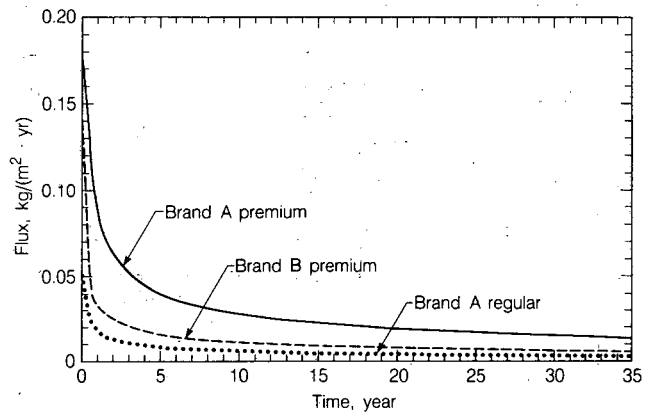

Figure 5. Flux of benzene for various types of gasoline (groundwater velocity $u = 8\times10^{-7}$ m/s, longitudinal dispersivity $\alpha_x = 0.25$ m, transverse dispersivity $\alpha_z = 0.01$ m). [XBL 878-10325]

CONCLUSIONS AND SIGNIFICANCE OF FINDINGS

Results from the analytical solution show that at constant pressure and temperature, the dissolution rate of SWSC is time dependent and strongly controlled by the regional groundwater velocity, the gasoline-water contact area, and the composition and thermodynamic properties of gasoline and groundwater. Although this study is constrained by several assumptions such as constant aquifer properties and absence of adsorption and biodegradation processes, it is a major step toward understanding the mass-exchange process across the gasoline-water interface. Results from this theoretical work can be extended to predict the mass-exchange process across the interface between the nonaqueous-phase liquid and water, to form guidelines for designing appropriate laboratory experiments and to verify numerical codes. These results can also be used to interpret and to understand, in a less rigorous sense, the existing field data.

REFERENCES

Abriola, L.M., and Pinder, G.F., 1985a. A multiphase approach to the modeling of porous media contamination by organic compounds. 1. Equation development. Water Resour. Res., v. 21, no. 1, p. 11–18.

Abriola, L.M., and Pinder, G.F., 1985b. A multiphase approach to the modeling of porous media contamination by organic compounds. 2. Numerical simulation. Water Resour. Res., v. 21, no. 1, p. 19–26.

Hoffmann, B., 1970. Dispersion of soluble hydrocarbons in groundwater stream. *In* Advances in Water Pollution Research. Proceedings, 5th International Conference 1970, Pergamon, New York, 1971. p. HA1-7.

Hoffmann, B., 1969. Uber die Ausbreitung geloster Kohlenwasserstoffe im Grundwasserleiter. Mitt. Inst. fur Wasserwirtschaft und Landwirtsch. Wasserbau, Techn. Univ. Hannover (D). H 16, 197 p.

Modification to TRINET: A Three-Dimensional Advection-Dispersion Code for Fracture Networks

K. Karasaki

This article summarizes the status of the advection-dispersion code TRINET, which is being developed to study flow and solute-transport phenomena in fracture networks. The code is a hybrid of the Lagrangian and Eulerian schemes. The concentration front is tracked by a moving grid. TRINET is now capable of simulating flow and transport in a three-dimensionally interconnected line network.

Various field and laboratory observations support the idea that flow in a fracture is not the same as flow between two smooth parallel plates. Fractures generally have contact areas, where no flow occurs, and the fracture walls are not always smooth. Because of these irregularities, the velocity profile may not be that of Poiseuille, and preferred fluid paths or channels may exist in fractures. Therefore, it is believed that the flow in a network of fractures can be better approximated by three-dimensionally interconnected line networks. TRINET, initially developed for two-dimensional line networks (Karasaki, 1987), has been modified and is now capable of running three-dimensional problems. TRINET uses the input mesh generated by a three-dimensional channel-network model, CHANGE (Billaux, 1988) through the interface program, INTER. INTER provides program control parameters pertinent to transient and solute-transport problems. The control parameters, node catalog, and element catalog are read into TRINET from separate input files to reduce the size of a single input file and, thus, to provide more flexibility for manual modification of the input. The output from TRINET is plotted by a three-dimensional plotting routine, FPLT, which represents the solute concentration in each element by the thickness of a line.

Figure 1 shows an example of output from TRINET plotted by FPLT. The mesh is a regular three-dimensional lattice and is represented by the dotted lines. The top left corner is held at unit head, and the bottom right corner is held at zero head. Thus, a steady flow field is established, and a solute of unit concentration is injected at the top left corner. The figure shows the three-dimensional image of the concentration front.

The mixing law at fracture intersections is not well known. Some laboratory observations suggest complete mixing at intersections and others indicate no mixing at all. Long and Shimo (1986) investigated this problem, but a more complete study is needed. Both laboratory and numerical experiments are required. TRINET currently assumes complete mixing. The program should be modified to include the nonmixing condition as well. TRINET could then be used to study the two extreme conditions, which should bracket the range of results. Future work on the code also will include switching to a more-efficient solution scheme. Currently, TRINET uses a banded matrix solver. Through use of a sparse matrix solver, the storage requirement can be significantly reduced. Also, the code must be further optimized for vector machines to take advantage of their vectorization scheme.

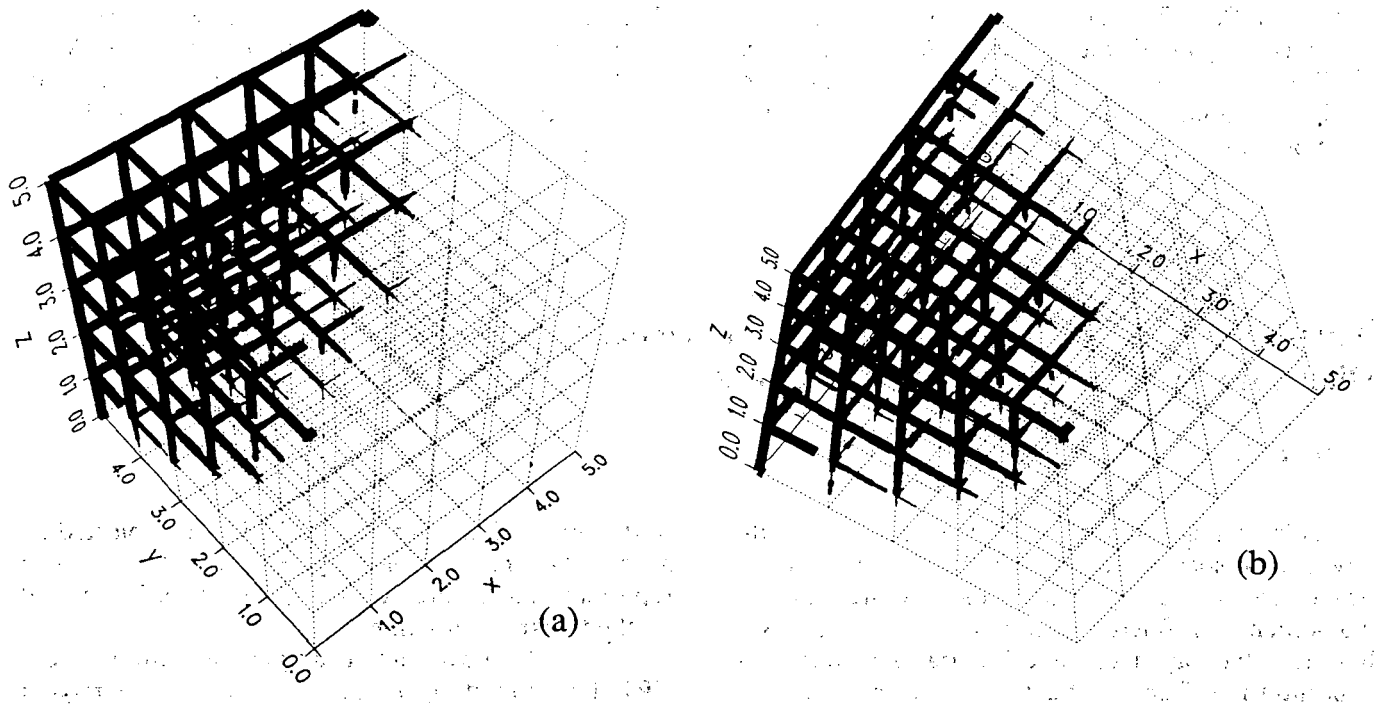

Figure 1. Concentration profile in a 3-D lattice network: (a) top view and (b) bottom view. [XBL 887-2519]

REFERENCES

Billaux, D., 1988. CHANGE: A numerical model for three-dimensional modeling of channelized flow in rock. Theory and design. Lawrence Berkeley Laboratory Report LBL-24910.

Karasaki, K., 1987. A new advection-dispersion code for calculating transport in fracture networks. *In* Earth Sciences Division Annual Report 1986. Lawrence Berkeley Laboratory Report LBL-22090, p. 55–57.

Long, J.C.S., and Shimo, M., 1985. The control of fracture aperture on transport properties of fracture networks. Lawrence Berkeley Laboratory Annual Report LBL-20450.

Studies of Hierarchically Fractured Media

K. Karasaki, J.M. Polek, and J.C.S. Long

Discontinuities or fractures exist at all scales. There are faults that may be on the order of several kilometers long on one end of the spectrum, and on the other end there are thin, small microcracks at rock-grain level. It is known that most reservoir rocks are fractured. The degree of fracturing and its significance to reservoir performance vary from one reservoir to another. In many cases accurate evaluation of the effects of fractures on fluid flow is essential to successful reservoir management. However, analysis of fluid flow behavior in fractured reservoirs is very difficult because the fracture geometry is generally unknown and complex. Therefore, various simplifying assumptions are being made about the geometry of fractures. Several authors (Gringarten and Witherspoon, 1972; Raghavan, 1977) used the single-vertical-fracture solution to analyze well tests in naturally fractured reservoirs. They assumed that the behavior of a naturally fractured system can be approximated by that of a single vertical fracture in a

porous medium. The underlying assumptions of the double-porosity models originated by Barenblatt, et al. (1960) and extended by many others (Warren and Root, 1963; Odeh, 1965; Kazemi and Seth, 1969; Streltsova, 1983) include the assumptions that (1) the fracture system behaves as an equivalent continuum and (2) the permeability of the porous matrix is very small compared to that of the fracture system so through-flow can be neglected in the porous matrix.

It may be very difficult to know, a priori, whether these assumptions are appropriate for a given system. In fact, whether the criteria for these assumptions are valid may depend on the conditions to which the system is subjected and the phenomena of interest. For example, the criterion for equivalent porous-medium behavior for transport phenomena is more restrictive than that for permeability (Long and Witherspoon, 1985; Endo, 1984). Also, where gradients are changing rapidly, erratic behavior will result from heterogeneities that cannot be accounted for by an equivalent continuum.

In this study the effect of small fractures on the overall permeability of a hierarchically fractured rock is investigated using a two-dimensional fracture-network model. The feasibility of replacing these small fractures by a porous-medium block is also investigated.

NUMERICAL STUDY

In our model the fracture-length distribution $f(l)$ was assumed to be negative exponential: $f(l) = e^{-0.5l}$. This distribution was divided into eight sets, and each set has a range of fracture lengths. By dividing fracture lengths into sets, the smaller fractures could be deleted by sets from the generated mesh, and the effect on permeability could be studied. The range of each set is shown in Table 1 with the fracture density calculated from the negative-exponential function. Within each set the fracture length is uniformly distributed between the set boundaries. Figure 1 shows the negative-exponential function and the length distribution of the generated fractures. All eight sets of fractures were used in the first generated fracture mesh, and the principal permeabilities were recorded. The first set of fractures with the shortest length distribution was deleted from the next mesh, and each additional mesh was created with one less set, until the eighth mesh, which had only the large fractures (Fig. 2). The square root of the product of the principal permeabilities was calculated for each run. These permeability values were plotted against the upper boundary value of each fracture-length set (Fig. 3). The curve shows that the permeability is not dependent on the small fractures because the permeability is approximately constant for the first six runs.

Table 1. Fracture length and density distribution.

Range of fracture length (m)	Fracture density
0.0 – 0.1	4.9%
0.1 – 0.2	4.6%
0.2 – 0.4	8.6%
0.4 – 0.8	14.8%
0.8 – 1.6	22.1%
1.6 – 3.2	24.7%
3.2 – 6.4	16.1%
6.4 – 12.8	3.9%

The fracture length, however, was not the only parameter that could effect the permeability. The aperture of the fractures directly effects the overall permeability, so the study was repeated with various aperture distributions to see if this changed the earlier result that the smaller fractures are unimportant. Three aperture distributions were used. The first of these was a constant aperture of 5×10^{-5}m for all fractures. The second type was distributed apertures, which had a negative exponential distribution for each set of fractures: $f(b) = \exp(-2 \times 10^4 b)$. The third type was again the same negative-exponential distribution of apertures, but in this case aperture was correlated to fracture length; i.e., fractures with small lengths had small apertures and ones with large lengths, large apertures. There were at least three realizations generated for each one of these aperture distributions. For constant apertures the permeability of each run was approximately the same no

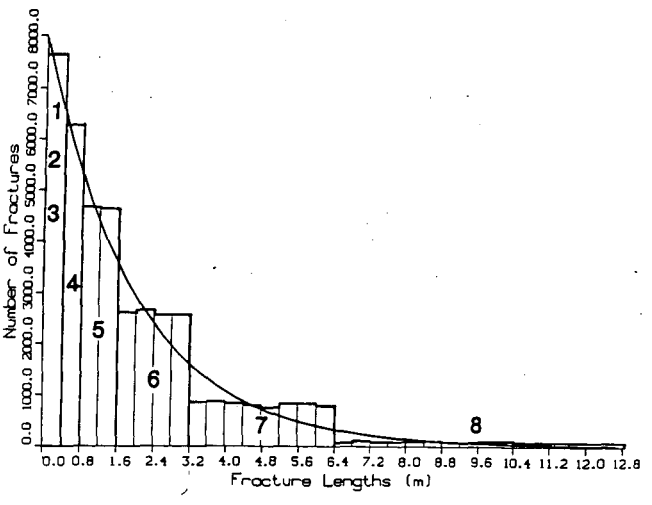

Figure 1. Negative exponential distribution and the eight generated fracture sets. [XBL 888-2739]

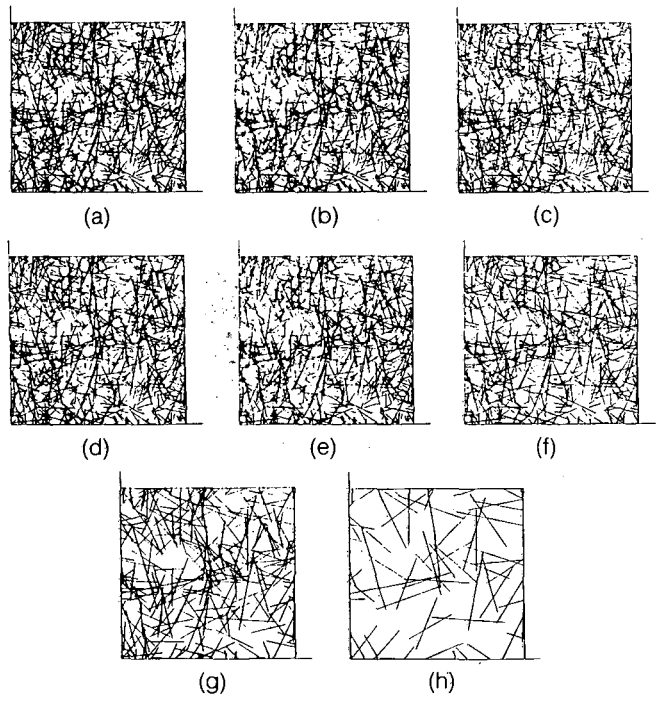

Figure 2. Fracture meshes with decreasing number of sets from **(a)** through **(h)**. [XBL 887-10359]

matter how many times the meshes were generated. The other two distributions had a range of permeabilities over the series of runs. The permeability values, however, for the correlated apertures were greater than the constant or distributed apertures by more than a factor of ten. This fact supports the assumption that the smaller fractures are unimportant to the permeability. The large increase in permeability must be due to the large fractures and their larger apertures from the correlated distribution. The shape of the curve of the fracture length versus permeability was similar for all aperture distributions (Fig. 3). The curves are flat with a sudden drop off at higher fracture lengths, 3.2 m to 12.8 m. This flatness at lower fracture lengths means that at least 80%

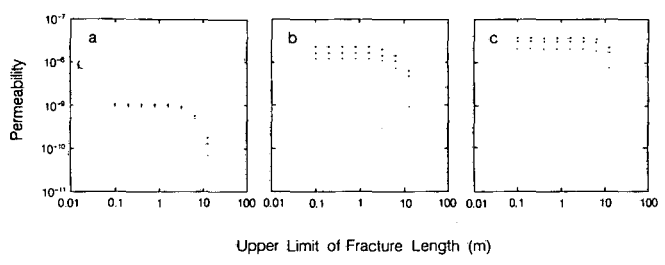

Figure 3. Permeability vs. upper boundary value of each fracture length set with **(a)** constant aperture, **(b)** distributed aperture, and **(c)** correlated aperture. [XBL 887-10362]

of the fractures can be neglected in the case studied. The sharpness of the drop off in the permeability curve was greatest with constant aperture and was the most flat with correlated apertures.

Next, using the same mesh, the feasibility of replacing the small fractures with porous-medium blocks was investigated. Figure 4 shows the meshes used in this study. By replacing the small fractures by porous-medium blocks, the number of nodal points can be substantially reduced. The fracture/porous-medium mesh was constructed using the fracture matrix mesh generator (FMMG) (Karasaki, 1986). The FMMG discretizes the rock-matrix portion of the fracture mesh generated by the fracture mesh generator (FMG) (Long et al., 1982). Only the fracture set with the longest length distribution (6.4 m to 12.8 m) was kept in the fracture/porous-medium mesh. The rest of the fractures were replaced by porous-medium blocks of constant permeability. The permeability of these blocks was

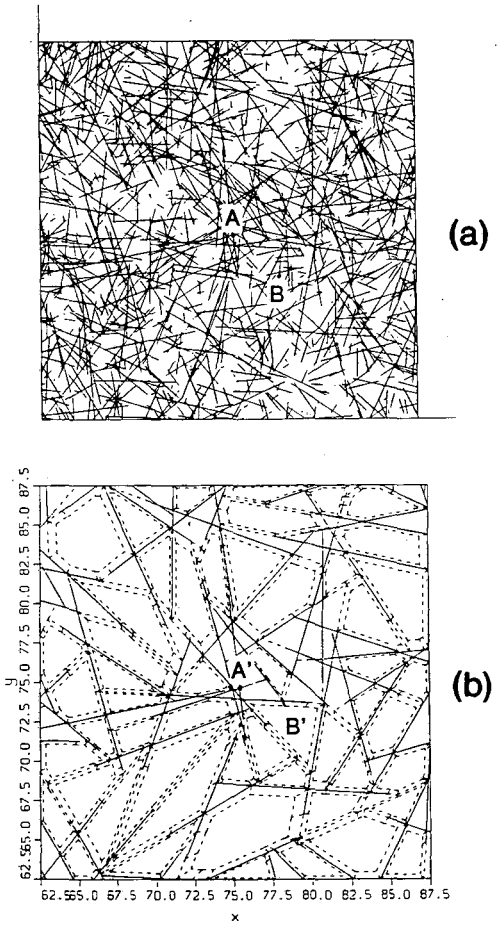

Figure 4. **(a)** Mesh with all the fractures. **(b)** Mesh with small fractures replaced by porous medium blocks. [XBL 888-2740]

determined so that the overall permeability of the mesh is the same as that of the original fracture mesh under one-dimensional steady-state flow condition. The porosity of these blocks was determined to match that of the fracture mesh.

One-dimensional transient-flow behavior between the fracture-only mesh and the fracture/porous-medium mesh was then compared. The transient flow in the former mesh was solved using the finite element flow and transport simulator TRINET (Karasaki, 1987). The transient flow in the latter was solved using the integrated finite difference simulator, PT (Bodvarsson, 1982). Figure 5 shows the time-vs.-pressure curves at the same locations in each mesh. The first location was chosen so that the pressure behavior of the same fracture in the two meshes can be compared. The other location was chosen to compare the pressure behavior of a fracture node and a porous-medium node at the same relative location in the two meshes. From these figures it can be concluded that a substantial saving in nodal points can be made by replacing the small fractures with porous-medium blocks, with little loss of accuracy.

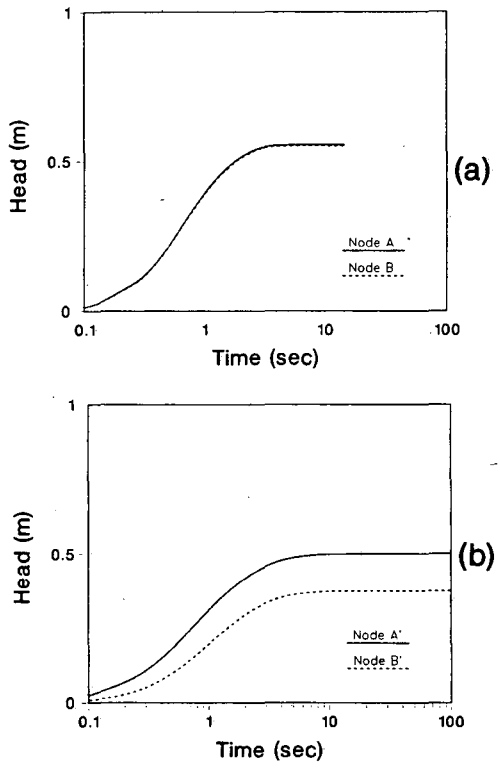

Figure 5. Transient pressure responses at **(a)** node A and B in the fracture-only mesh in Fig. 5a and **(b)** node A' and B' in the fracture/porous-medium mesh in Fig. 5b. [XBL 888-2741]

CONCLUSION

In the case studied it was found that small fractures are relatively unimportant. However, the above conclusion is only pertinent to the case examined in this study. If this conclusion holds some generality, it would be very useful for field geologists who do fracture mapping of outcrops. They need to map only those fractures whose trace lengths are longer than some lower limit. It is also impractical to represent all the fractures explicitly in a numerical model. If a cluster of fractures could be represented by a porous-medium block, one could save substantial amount of computer memory. More study is needed to make a quantitative assessment. Sensitivity to various fracture parameters must be investigated. Other processes such as heat transport and mass transport should also be studied.

REFERENCES

Barenblatt, G.I., Zheltov, Iu.P., and Kochina, I.N., 1960. Basic concepts in the theory of seepage of homogeneous liquids in fissured rocks. J. Appl. Math. Mech., v. 24, no. 5, p. 1286–1303.

Bodvarsson, G.S., 1982. Mathematical modeling of the behavior of geothermal systems under exploitation. Ph.D. Thesis, University of California, Berkeley.

Endo, H.K., 1984. Mechanical transport in two-dimensional networks of fractures (Ph.D. thesis). University of California, Berkeley. Lawrence Berkeley Laboratory Report LBL-17491.

Gringarten, A.C., and Witherspoon, P.A., 1972. A method of analyzing pump test data from fractured aquifers. *In* Proceedings, Symposium on Percolation in Fissured Rock, v. 3, p. B1B9, Int. Soc. Rock Mech., Stuttgart.

Karasaki, K., 1986. Well test analysis in fractured media (Ph.D. thesis). University of California, Berkeley. Lawrence Berkeley Laboratory Report LBL-21442.

Karasaki, K., 1987. A new advection-dispersion code for calculating transport in fracture networks. *In* Earth Sciences Division Annual Report 1986. Lawrence Berkeley Laboratory Report LBL-22090, p. 55–58.

Karasaki, K., Long, J.C.S., and Witherspoon, P.A., 1988. An analytic model for fracture dominated reservoirs. SPE Formation Evaluation, v. 3, no. 1, p. 242–250.

Karasaki, K., Long, J.C.S., and Witherspoon, P.A., 1988. Analytical models of slug tests. Water Resour. Res., v. 24, no. 1, p. 115–126.

Kazemi, H., and Seth, M.S., 1969. Effect of anisot-

ropy and stratification on pressure transient analysis of wells with restricted flow entry. J. Pet. Tech., v. 21, no. 5, p. 639–647.
Long, J.C.S., Remer, J.S., Wilson, C.R., and Witherspoon, P.A., 1982. Porous media equivalents for network of discontinuous fractures. Water Resour. Res., v. 3, no. 18, p. 645–658.
Long, J.C.S., and Witherspoon, P.A., 1985. The relationship of the degree of interconnection to permeability in fracture networks. J. Geophys. Res., v. 90, no. B4, p. 3087–3098.
Odeh, A.S., 1965. Unsteady-state behavior of naturally fractured reservoirs. Soc. Pet. Eng. J., v. 234, p. 60–64.
Raghavan, R., 1977. Pressure behavior of wells intercepting fractures. *In* Proceedings, International Well-Testing Symposium, Berkeley, CA, Oct. 19–21, 1977.
Streltsova, T.D., 1983. Well pressure behavior of a naturally fractured reservoir. Soc. Pet. Eng. J., v. 23, p. 769–780.
Warren, J.F., and Root, P.J., 1963. The behavior of naturally fractured reservoirs. Soc. Pet. Eng. J., v. 228, p. 245–255.

The Genesis of Shear Fracture Zones in Brittle Rock

J.M. Kemeny, and J.C.S. Long

Fractures permeate brittle rocks such as granite on all scales and in various patterns and complexities. Of particular importance to the design of underground openings for waste storage are shear fracture zones in rock, which are locations where a substantial amount of shear displacement has occurred. A shear zone can be a well-defined, through-going fault, or a partially developed fault consisting of a high density of fractures. The fracture density in shear zones is usually much higher than in the surrounding rock, and thus the mechanical, hydrological, thermal, chemical, and electrical properties of the rock mass are altered in shear zones. Drill holes in shear zones at the Stripa underground laboratory in Sweden (Carlsten et al., 1985) indicate that shear zones are very heterogeneous, with fracture density, fracture morphology, and fluid properties that vary greatly with spatial direction. Understanding the variation in fracture density and fluid permeability with spatial direction is important in predicting the properties of shear zones at depth and in other regions that cannot be mapped or be penetrated by drill holes. The aim of the research presented here is to be able to model the genesis of fracture zones to gain further insight into their heterogeneity in morphology and properties. Also, we would like to understand the controlling parameters or "boundary conditions" for a particular field problem, i.e., those factors at a particular site that control the eventual pattern of fractures. These factors include local geologic conditions and the stresses and strains applied to the rock mass. For instance, at the underground test site at Grimsel, Switzerland, the occurrence of lamprophyre dikes is correlated with the occurrence of fracture zones and shear zones.

Our present knowledge of the mechanisms controlling the genesis of shear zones comes primarily from three types of information. First, from field studies, relationships between tectonic conditions and the evolution of joints and faults have been compiled, as described in reviews by Price (1966), Bles and Feuga (1986), Einstein and Connelly (1986), Tirn (1986), and others. The basic mechanisms of joint and fault development under compressive, shear, and tensile stresses, plus sequential combinations of these, are discussed in these reviews. Second, the behaviors of rock samples in the laboratory under compressive, shear, and tensile stresses have been used as analogies to the behaviors of rock on larger scales. These tests allow very controlled studies on joint and fault formation to be conducted, but the implications of the scale differences have not yet been fully assessed (Wong, 1982; Kemeny and Cook, 1987a). Third, theoretical and numerical studies have been conducted on modeling joint and fault development under various conditions. This third type of information is the least developed, yet it offers much hope in adding to the present understanding of fracture genesis, and it allows for scale effects to be understood quantitatively. The use of fracture mechanics has greatly improved these modeling efforts, as shown by recent works by Segall and Pollard (1980), Pollard et al., (1982), Segall and

Pollard (1983), Segall (1984), Horii and Nemat-Nasser (1985), Ashby and Hallam (1986), Sammis and Ashby (1986), Kemeny and Cook (1987b), and others. Another area of importance concerns factors that control the final fabric of rock in the shear zones. This includes the formation of gauge and cataclasite material and involves the mechanisms of crushing, sliding, and brecciation in addition to fracture propagation and coalescence. A few recent papers by Sibson (1986), Sammis et al., (1986), and others have dealt with this subject.

STRUCTURE OF SHEAR ZONES

When examined in detail, shear zones can be extremely complex; they often result from many independent tectonic events and are due to both brittle and ductile types of deformation. To simplify the analyses, here we consider conditions for the initial development of shear zones. This is very important in itself, since the geometry and properties of the final complex structure of a fault will depend a great deal on geometric features in the initial stages of the development of the fault, as discussed by Sibson (1986). Our knowledge of the initiation of shear zones comes from field examples of partially developed shear zones and from laboratory tests. A common feature of the initiation of shear zones is their discontinuous nature; they consist of straight segments that partially overlap and are separated by unfractured regions referred to as "rock bridges." When the straight segments are examined in detail, they, too, often consist of smaller straight segments separated by rock bridges. Thus a basic element of partially developed shear zones or faults is this discontinuous or segmented substructure. Deng and Zhang (1984) refer to the pattern of segments as "en echelon" when the angle of the individual segments relative to the angle of the fault is greater than 25 degrees and "pinnate" when the angle is less than 25 degrees. Another feature of the segments is the stepping of the segments relative to the direction of the far-field shear. Right- and left-stepping segments are defined by whether the overlapping segments step to the right or left, respectively, upon crossing the fault. The stepping of the fault segments relative to the direction of far-field shear indicates whether the rock between the segments is under compressional or tensile stresses. Segall and Pollard (1980) show that right steps under left-lateral faulting and left steps under right-lateral faulting produce tensile stresses in the rock bridges, where as right steps under right-lateral faulting and left steps under left-lateral faulting produce compressional stresses in the rock bridges. Sibson (1986) refers to the stepping-fault segments as fault jogs and defines conditions that result in compressive or tensile stresses in the rock bridges as antidilatational and dilatation fault jogs, respectively. Fault jogs are important for many reasons; for example, earthquake rupture is often terminated by dilatation fault jogs, but not by antidilatational fault jogs (Kerr, 1987). Also, because the rock in the neighborhood of fault jogs can be under either compressive or tensile stresses, microstructural fracturing can occur in the rock bridges, and the type of fracturing will depend on the nature of the fault jog, as well as on other features such as the spacing and angle between fault segments and material properties. Thus en-echelon or pinnate segmenting forms a very heterogeneous pattern of regions under compressive, tensile, and shear stresses, with microstructural patterns associated with each of these stress conditions. This will result in flow properties of the fault that depend on spatial location.

MECHANICS OF FRACTURE GENESIS

To model the genesis of complicated structures containing fractures such as shear zones, the ways in which fractures grow, interact, and coalesce under specific tectonic conditions must be understood. Linear elastic fracture mechanics (LEFM), originally developed for application in metals and ceramics, deals with the stress concentrations in structures containing cracks and the criteria for crack growth (e.g., Lawn and Wilshaw, 1975). The application of fracture mechanics to rocks, referred to here as rock-fracture mechanics, is now becoming a field of its own (Rice, 1980; Rudnicki, 1980) and differs in several respects from the traditional fracture mechanics developed for metals and ceramics. The three main differences are (1) in rocks, in-situ stress conditions are primarily compressive or shear rather than tensile; (2) in rocks, fractures grow long compared with their original length; and (3) rocks usually contain a high density of fractures, and thus interaction and coalescence of fractures are important concerns. One of the most important issues in rock-fracture mechanics concerns how cracks grow under compressive stress fields. Laboratory work by Wawersik and Brace (1971), Tapponier and Brace (1976), Evans and Wong (1985), and others has revealed that, under compressive stresses, fractures initiate as microcracks and grow in the direction of the maximum principal stress, in response to local regions of tension. Nemat-Nasser (1985) showed that the tensile crack growth is due to heterogeneous deformation in the rock, such as from sliding along pre-existing microcracks, stress concentrations around pores, and stress concentrations due to elastic

moduli contrasts. Many of the models for tensile crack growth under compressive stresses are based on the "sliding crack," as developed originally by Brace et al., (1966) and Fairhurst and Cook (1966). The sliding crack consists of an initial, planar microcrack under shear and normal stresses derived from the externally applied triaxial compressive stresses. Once the frictional forces along this initial crack have been exceeded, the crack faces will slide past one another, forming tensile stresses in the regions near the crack tips. Under continued loading, the tensile stresses will increase until two tensile "wing cracks" emerge symmetrically from both ends of the initial crack, and as the wing cracks propagate they orient themselves in the direction of the maximum principal stress. Fracture models based on the sliding crack include Horii and Nemat-Nasser (1985), Ashby and Hallam (1986), and Kemeny and Cook (1987b). The importance of the sliding-crack model is that the initial crack represents a "flaw" in the rock that serves as a stress concentrator for future crack growth to occur, and other types of flaws (material property boundaries, pores) will result in almost identical crack-growth patterns.

Another important consideration with regards to fracture genesis involves the issue of the stability of a system of growing and interacting cracks. As the cracks are growing and interacting, certain fractures may propagate or link up in an unstable manner. On the other hand, crack growth or crack interaction may increase the stability of the system, in which case the in-situ stresses must increase for cracks to continue to grow. The stability of crack growth is analyzed by calculating stress-strain relations associated with fracture genesis, as discussed by Kemeny and Cook (1987b). For instance, stress-strain curves associated with crack growth have been calculated for a body containing a single sliding crack, under tensile, compressive, or shear stresses. The cases under shear and tension show strain-softening behavior, whereas the case under compressive stresses exhibits strain-hardening behavior. A strain-hardening material is stable under all boundary conditions, whereas a material undergoing strain-softening can be unstable, depending on the slope of the strain-softening curve and the applied boundary conditions (Jaeger and Cook, 1979). Thus we get the important result that different regions within a shear zone may respond with either strain hardening or strain softening, with the appropriate differences in stability. Crack interaction can cause significant changes in the stability of crack growth, as analyzed by Kemeny and Cook (1987b). This explains why en-echelon fracture patterns initially grow very easily but require a much-larger amount of stress to combine into a through-going fault.

Finally, to model the genesis of fractures, stochastic processes that are operating must be understood. These processes control various parameters such as the distribution of joint spacing and joint terminations. It is important to distinguish between those properties that are stochastic and those that are deterministic. Fractures initiate at flaws in the rock, such as microcracks, pores, or grain contacts. In general, these features are randomly distributed and represent a stochastic process. On the other hand, once the initial distribution of microflaws is given, the growth, interaction, and coalescence of the fractures under prescribed boundary conditions can be considered a deterministic process, based on the principles of linear elastic fracture mechanics. It has been suggested by several authors (e.g., Nemat-Nasser et al., 1980; Kemeny and Cook, 1985) that the ultimate pattern of fractures under a given set of conditions is governed by energy principles; i.e., the final pattern of fractures in some way minimizes the strain energy of the fractured rock mass. If this is so, then we need to understand how the fractures in the rock mass achieve this state of minimum energy. This relates to the initial set of flaws, and thus the model must ensure that the distribution of flaws correctly represents the actual field conditions. This may require that a large population of flaws be used, and thus the model for fracture genesis should be capable of analyzing the growth of a large number of cracks, as discussed in the next section. It may be possible later to reduce the number of flaws in genesis calculations by using these energy principles.

INITIAL MODEL FOR THE GENESIS OF SHEAR FRACTURE ZONES

The initial model that we have developed for analyzing the genesis of shear zones is based on the work described in the previous section. The first step has been to develop a program capable of accurately calculating the stress-intensity factors for interacting cracks. Many numerical methods now exist for calculating stress-intensity factors for interacting cracks. In almost all of these methods, the cracks must be discretized, using at least 20 elements per crack. In a system containing, for example, 100 cracks, these methods would require the solution of a matrix with at least 4000 by 4000 elements. These large storage requirements limit the number of interacting cracks that can be analyzed in a given problem. As mentioned before, problems in rock fracture may require the solution of a large

number of interacting cracks, and therefore we have developed a program to avoid these large storage requirements. The method is based on the work of Kachanov (1987) and uses an approximation whereby each crack requires four elements of storage. Thus a system with 100 cracks requires the solution of only a 200-by-200 matrix, which can easily be calculated on a microcomputer.

The reason for the large reduction in storage requirements is that the "standard" solution at the heart of the method is that of a single crack. This is opposed to the "standard" solution of a point load, which is at the heart of most other crack programs and that must be integrated over a line to give the results of a single crack. Crack interaction is handled by breaking up the problem of a linear elastic solid with N cracks and known boundary conditions into the equivalent system of N problems, each problem containing only one crack but with unknown tractions (external loads) along the crack faces. The unknown tractions are found by the solution of the system matrix. The approximation in the method comes from some simplifying assumptions in the unknown tractions. In particular, it is assumed that the interacting crack has the impact of producing unknown but *uniform* tractions on all the other cracks. Further details of the method are given in Kachanov (1987). Even though the program uses this approximation, it is still very accurate for the calculation of stress-intensity factors for interacting cracks. In Fig. 1 we compare stress-intensity factors computed with our model with exact results, for a configuration consisting of a collinear row of cracks under tensile stress. For this configuration only the Mode I stress-intensity factor, K_I, is nonzero. The stress-intensity factors are normalized with the factor $\sigma\sqrt{(\pi a)}$, which is the Mode I stress-intensity factor for a single noninteracting crack of length $2a$ under a tensile stress σ. The normalized stress-intensity factor is plotted against the crack-interaction parameter, a/b, where b is the spacing between the centers of the cracks. Thus as a/b approaches zero, the cracks are noninteracting, and the normalized stress-intensity factor approaches 1, whereas for a/b approaching 1, the cracks coalesce, and the normalized stress-intensity factor approaches infinity. The exact solution is for a configuration containing an infinite number of cracks; however, in our numerical model, we have used a crack array containing nine cracks, and the stress intensity factor is computed from the center crack. Figure 1 shows that even for $a/b = 0.99$, which represents a crack spacing two orders of magnitude less than the crack length, the numerical model agrees within a few percent with the exact results.

Based on the stress-intensity factors at each of the crack tips for an initial configuration of cracks, the program then calculates crack growth. The direction of crack growth is determined by the direction from the crack tip that is along the maximum value of the Mode I stress-intensity factor. In general this will cause the crack to grow out of the plane of the original crack (referred to as mixed-mode fracture). An example of mixed-mode fracture is shown in Fig. 2 (two dimensions). Initially, there is a straight crack at an angle θ to the direction of an applied tensile stress. If θ is equal to 0 degrees, then crack growth occurs in the same direction as the original crack; for $\theta = 90$ degrees no crack growth will occur (the stress-intensity factors are equal to 0). For all other angles, the crack will grow out of plane as shown in Fig. 2, and as the crack grows it follows a

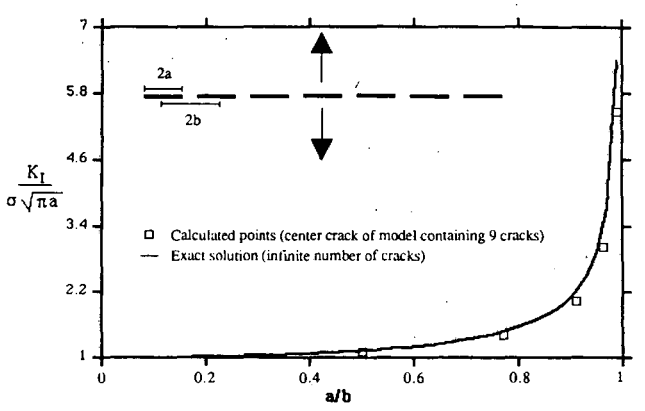

Figure 1. Normalized Mode I stress-intensity factor versus crack spacing for a collinear row of cracks under tension. Comparison of cracks under tension. Comparison of predictions from the model for a row of nine cracks (data from center crack) with the exact solution for an infinite row of cracks. [XBL 888-2975]

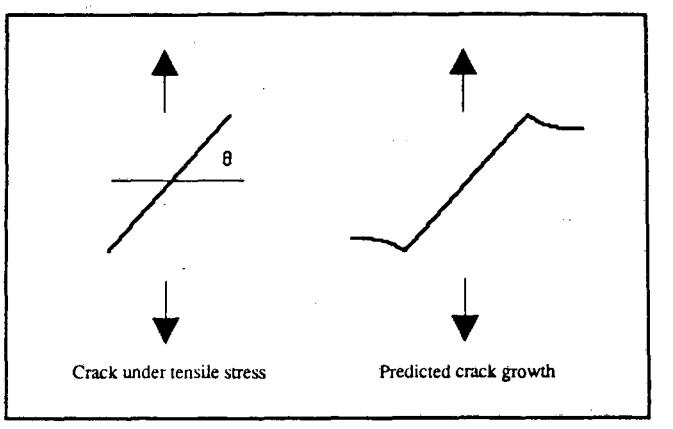

Figure 2. Predicted crack growth from the model for a single crack under tension. [XBL 888-2976]

curved path that eventually grows in the direction of the minimum principal stress (normal to the applied load in this case). This agrees with laboratory tests on rocks containing precut slits (Cotterell, 1972).

An example of a more-complicated crack-growth pattern is shown in Fig. 3. In this example, there are initially two parallel but offset cracks under a pure shear stress. For this direction of shear relative to the type of offset, the "rock bridge" between the two offset cracks is of the dilatational type, and thus, according to Segall and Pollard (1980), the crack tips closest to the offset should grow together. Figure 3 shows that these cracks do grow together, at angles that again are along the minimum principal stress direction. Figure 3 shows that the crack tips away from the rock bridge also extend, and, in this case, they grow apart. However, these tips only grow for a short distance and become stable. This agrees with fracture patterns in granodiorite within the central Sierra Nevada, as mapped by Martel (1987).

REFERENCES

Ashby, M.F., and Hallam, S.D., 1986. The failure of brittle solids containing small cracks under compressive stress states. Acta Metall., v. 34, p. 497–510.

Bles, J.L., and Feuga, B., 1986. The fracture of rocks. North Oxford Academic, London, United Kingdom.

Brace, W.F., Paulding, B.W., and Sholtz, C., 1966. Dilatancy in the fracture of crystalline rocks. J. Geophys. Res., v. 77, p. 3939.

Carlsten, S., Magnusson, K.-A., Olsson, O., 1985. Crosshole investigations—Description of the small scale site, SKB 85-05. Swedish Geological Co., Uppsala, Sweden.

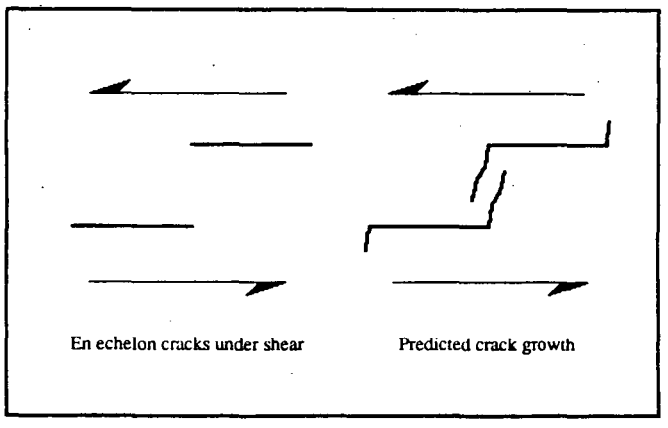

Figure 3. Predicted crack growth from the model for two en-echelon cracks under stress. [XBL 888-2977]

Cotterell, B., 1972. Brittle fracture in compression. Int. J. Fracture Mechanics, v. 8, p. 195–207.

Deng, Q., and Zhang, P., 1984. Research on the geometry of shear fracture zones. J. Geophys. Res. v. 89, p. 5699–5710.

Einstein, H.H., and Connelly, T.R., 1986. Literature review on rock joint genesis. Golder Assoc., Redmond, Washington.

Evans, B., and Wong, T.-F., 1985. Shear localization in rocks induced by tectonic deformation. *In* Z. Bazant (ed.), Mechanics of Geomaterials. John Wiley and Sons, New York.

Fairhurst, C., and Cook, N.G.W., 1966. The phenomenon of rock splitting parallel to a free surface under compressive stress. *In* Proceedings, First Congress, International Society for Rock Mechanics, Lisbon (Vol. 1), p. 687–692.

Horii, H., and Nemat-Nasser, S., 1985. Compression induced microcrack growth in brittle solids: Axial splitting and shear failure. J. Geophys. Res., v. 90, p. 3105–3125.

Jaeger, J.C., and Cook, N.G.W., 1979. Fundamentals of Rock Mechanics. Halsted Press, New York.

Kachanov, M., 1987. Elastic solids with many cracks: A simple method of analysis. Int. J. Solids Struct., v. 23, p. 23–43.

Kemeny, J.M., and Cook, N.G.W., 1985. Formation and stability of steeply dipping joint sets. *In* Proceedings, 26th U.S. Rock Mechanics Symposium (Vol. 1), p. 471–478.

Kemeny, J.M., and Cook, N.G.W., 1987a. Determination of rock fracture parameters from crack models for failure in compression. *In* Proceedings, 28th U.S. Symposium on Rock Mechanics, Tucson, Arizona, June 29–July 1, 1987. A.A. Balkema, Rotterdam, Netherlands, p. 367–374.

Kemeny, J.M., and Cook, N.G.W., 1987b. Crack models for the failure of rock under compression. *In* Proceedings, 2nd International Conference on Constitutive Laws for Engineering Materials, Tucson, Arizona, January 5–8, 1987, p. 879–887.

Kerr, R.A., 1987. Delving into faults and earthquake behavior. Science, v. 23, p. 165.

Kranz, R.L., 1983. Microcracks in rocks: A review. Tectonophysics. v. 100, p. 449–480.

Lawn, B.R., and Wilshaw, T.R., 1975. Fracture of Brittle Solids. Cambridge University Press, London, United Kingdom.

Martel, S.J., 1987. Development of strike-slip fault zones in granitic rock, Mount Abbot quadrangle, Sierra Nevada, California (Ph.D. thesis). Stanford University.

Nemat-Nasser, S., 1985., Discussion of "Geometric probability approach to the characterization and analysis of microcracking in rocks" by Teng-Fong Wong. Mech. Mater., v. 4, p. 277–281.
Nemat-Nasser, S., Sumi, Y., and Keer, L.M., 1980. Unstable growth of tension cracks in brittle solids: Stable and unstable bifurcations, snap through, and imperfection sensitivity. Int. J. Solids Struct., v. 16, p. 1017–1035.
Pollard, D.D., Segall, P., and Delaney, P.T., 1982. Formation and interpretation of dilatant en-echelon cracks. Geol. Soc. Am. Bull., v. 93, p. 1291–1303.
Price, N.J., 1966. Fault and Joint Development in Brittle and Semi-brittle Rock. Pergamon Press, New York.
Rice, J.R., 1980. The mechanics of earthquake rupture. *In* A.M. Dziewonski and E. Boschi (eds.), Physics of the Earth's Interior. Italian Physical Society, Bologna, Italy.
Rudnicki, J.W., 1980. Fracture mechanics applied to the earth's crust. Ann. Rev. Earth Planet., v. 8, p. 489–525.
Sammis, C.G., and Ashby, M.F., 1986. The failure of brittle porous solids under compressive stress states. Acta Metall., v. 34, p. 511–526.
Sammis, C.G., Osborne, R.H., Anderson, J.L., Banerdt, M., and White, P., 1986. Self similar cataclasis in the formation of fault gouge. Pure Appl. Geophys., v. 124, p. 53–78.
Segall, P., 1984. Formation and growth of extensional fracture sets. Geol. Soc. Am. Bull., v. 95, p. 454–462.
Segall, P., and Pollard, D.D., 1980. Mechanics of discontinuous faults. J. Geophys. Res., v. 85, p. 4337–4350.
Segall, P., and Pollard, D.D., 1983. Nucleation and growth of strike slip faults in granite. J. Geophys. Res., v. 88, p. 555–568.
Sibson, R.H., 1986. Brecciation processes in fault zones: Inferences from earthquake rupturing. Pure Appl. Geophys., v. 124, p. 159–175.
Tapponier, P., and Brace, W.F., 1976. Development of stress induced microcracks in Westerly granite. Int. J. Rock Mech. Min. Sci., v. 13, p. 103.
Tirn, S.A., 1986. Fractures and fracture zones: Structural elements, their character, and tectonic environment. SKB 86-16, Swedish Geological Company, Uppsala.
Wawersik, W.R., and Brace, W.F., 1971. Post-failure behavior of a granite and diabase. Rock Mech., v. 3, p. 61–85.
Wong, T.-F., 1982. Shear fracture energy of Westerly granite from post-failure behavior. J. Geophys. Res., v. 87, p. 990–1000.

The NAGRA-DOE Cooperative Research Program

J.C.S. Long, E.L. Majer, K. Karasaki, K. Pruess, C.L. Carnahan, J.S. Jacobsen, K. Hestir, D. Billaux, J. Peterson, L.R. Myer, and C.F. Tsang

In June of 1987, the U.S. Department of Energy signed an agreement with the Nationale Geonossenschaft für die Lagerung Radioacktiver Abfalle (NAGRA) of Switzerland for the purpose of pursuing joint research in the field of Flow and Transport in Fractured Media. The signing of this agreement began a three-year multidisciplinary cooperative research project at LBL and NAGRA aimed at improving the technology of nuclear-waste storage in geologic media.

The objectives of this research are to develop and augment performance-assessment tools and evaluate performance issues using the data and facilities available through the NAGRA program. The data and facilities include deep boreholes in crystalline rock in the northern part of Switzerland, extensive laboratory and theoretical studies on repository performance, and the Grimsel Rock Laboratory in the crystalline rock of central Switzerland.

The research to be carried out takes advantage of NAGRA's extensive experimental and data-collection efforts to augment and extend the research LBL has been doing for DOE's nuclear-waste storage program. All the areas of proposed research are or will be problems faced by DOE in pursuit of a repository in fractured rock.

The six tasks listed here and described below form the program of work specified in the DOE/NAGRA Cooperative Agreement of June 1987.

Task 1. Determination of Fracture Hydraulic Parameters by Means of Fluid-Logging in Boreholes—C.F. Tsang.

Task 2. Determination of Fracture Hydraulic Parameters by Means of Hydraulic Testing in Boreholes—K. Karasaki.

Task 3. Flow and Transport in Fracture Media—J.C.S. Long, K. Hestir, J.M. Kemeny, K. Karasaki.

Task 4. Investigation on the Influence of Gas Flow on Solute Transport in Fractured Media—K. Pruess.

Task 5. Design of Methodologies to Determine Relevant Host-Rock Hydraulic Parameters by Means of an Underground Rock Laboratory—E. Majer, J.C.S. Long, L.R. Myer, K. Karasaki, D. Billaux, K. Hestir.

Task 6. Coupling of Transport and Geochemistry—C.L. Carnahan, J.S. Jacobsen.

The work falls under two major categories: characterization of fractured rock and near-field repository effects. Tasks 1, 2, 3, and 5 are all concerned with characterization of fractured rock. Tasks 4 and 6 attack problems related to near-field repository effects. In the category of characterization of fractured rock, Tasks 1, 2, and 3 form a subgroup concerned with the analysis of data from deep boreholes. Such boreholes are expected to be the main source of data about repository host rock. Borehole data can be derived from the rock core recovered during drilling and from downhole testing. Tasks 1 to 3 are all concerned with finding techniques to characterize the repository rock with such data. The final product of these tasks will be an evaluation of these techniques as tools for repository-performance assessment.

In the category of near-field repository effects, Task 4 is concerned with the effects of gas production due to corrosion of the cannister, and Task 6 is concerned with transport of contaminants through the backfill. NAGRA has developed data related to each of these topics that cannot be obtained elsewhere. The results of Task 4 will help to resolve the issue of whether gas production is a serious problem in repository design. The results of Task 6 will be a tool capable of predicting the complex interactions between backfill, groundwater, and waste transport.

TASK 1

The purpose of this task is to develop well-test interpretation methods to determine key fracture-flow parameters by interpreting temperature and conductivity logs obtained in the borehole. In particular, methods to understand and analyze borehole-logging data will be developed and applied. The results will be important for the characterization of subsurface fractures and their flow properties, which are the necessary inputs for performance assessment of a potential nuclear-waste geologic repository. If successful, the interpretation will yield information about the distribution of permeability in the hole and is an inexpensive complement to packer testing.

Electric conductivity and temperature of borehole fluid along the depth of the well were measured in a deep borehole in northern Switzerland (Leuggern) by NAGRA in 1985. Fluid-conductivity and temperature logs are available as a function of depth and time. The data indicate the initiation and growth of conductivity and temperature peaks at fluid-input points corresponding to water-bearing fractures intersecting the wellbore. Fluid-inflow rates at these input points are very low and cannot be measured by conventional methods.

A new procedure is applied to this existing set of data, which shows the initiation and growth of nine conductivity peaks in a 900-m section of a 1690-m borehole. These peaks correspond to nine fractures that intersect the hole. We are able to determine the flow rates from these fractures. The methodology and results are described in Tsang (1987). The computer programs used are documented in Hale and Tsang (1988). Testing procedures to validate the methodology were prepared, based on which NAGRA performed a new, carefully controlled test in the Leuggern hole during the months of August and September of 1987.

TASK 2

Tasks 2 and 3 are actually a single effort aimed at characterizing the hydrologic properties of fracture zones. Fracture zones are common and usually the most hydrologically significant features in rock. However, such zones are highly heterogeneous. They may carry the majority of groundwater flow in rock, but parts of the zones may be highly impermeable. Task 2 is an attempt to develop a conceptual model for at least one zone and parameterize the model using core and well-test data.

Well-test design and interpretation is an integral part of site-characterization efforts for all potential repository sites. Although well testing is an established part of water-supply and petroleum-reservoir investigations in low-permeability fractured rock, conventional techniques and interpretations often fail. In order to overcome these problems, LBL has been working on a variety of well-test equipment, design, and interpretation techniques specifically for fractured rock. These include solutions for well tests that specifically include the geometry and boundary

conditions encountered in fracture systems and advanced well-testing equipment for low-permeability environments.

In FY 1987 we reviewed the well-test results from the deep hole at Leuggern. NAGRA has recently sent us several excerpts of the reports on the well tests and the data recorded on a magnetic tape. The analysis of the data reported thus far had assumed a radial, equivalent-porous-medium flow. It is anticipated that in some cases these assumptions are not appropriate and lead to misleading results. We will reinterpret the data and account for vagaries in the flow system, such as cases where the flow is nonradial and where the system is a composite medium or bounded. The analysis will help develop a conceptual model of the flow system at depth. A correct conceptual model will be the first step in planning the long-term pumping tests in the future as planned by NAGRA for the borehole at Leuggern.

TASK 3

NAGRA has data from a borehole intersecting major shear features in granite. Such features are likely to be the focus of many site investigations in that they provide a potential pathway for radionuclides to reach the biosphere. Characterization of these features will likely have to be done from the borehole with data similar to that available in Switzerland. We propose to attempt to build a conceptual model of such a shear zone and use the model to predict the flow and transport properties of the feature. Hydraulic and tracer tests in the zone could then be compared with model results. NAGRA is planning to perform a tracer test in the Leuggern borehole during FY 1988.

In building a conceptual model for the fracture zones, we will look at well-test results (Task 2, above), fracture genesis, and geology. As the data from the hole are very limited, we expect that this will require some amount of hypothesis. Secondly, we will try to use the fracture data themselves in a statistical analysis. This analysis will be used directly in Task 2 and in an attempt to develop a consistent description of the fracture zone.

TASK 4

Studies carried out in the Swiss program indicate that various processes (corrosion, radiolysis, microbial degradation of organic material) will cause substantial amounts of gas to be released in geologic nuclear-waste repositories situated in saturated geologic formations. This release is expected to take place for all forms of nuclear waste, regardless of whether they are high- or low-level. Gas release will cause pressurization of the environment, which may cause an uncontrolled release of contaminants in the near or intermediate field. The severity of the problem can be appreciated by noting that gas pressure in a closed repository would be expected to reach several hundred bars in a 100-year time frame until corrosion stops. Vented gas could substantially alter natural groundwater flows and solute travel times to the accessible environment. A quantitative understanding of groundwater flow in fractured rock as affected by gas release is needed so that a waste repository can be designed to meet required performance criteria. The issues raised by the problem of gas release have not been adequately addressed in U. S. studies relating to nuclear-waste isolation. Our cooperation with Swiss organizations in this area benefits greatly from their experience with gas release and its impacts. Utilizing data to be provided by NAGRA, we propose to investigate the following topics:

1. Buildup of repository pressure due to gas release.
2. Large-scale patterns of groundwater and gas flow in the vicinity of the repository.
3. Impact of gas release on the transport of dissolved species.
4. Laboratory experiments and design of field tests suitable for quantifying parameters that can strongly impact gas pressurization and flow.

Several approaches for modeling of multiphase flow in fractured rock will be investigated. An attempt will be made to identify the most crucial parameters affecting system behavior and to study the feasibility of laboratory and field tests that could quantify those parameters. At the present time virtually no empirical information on two-phase (liquid-gas) flow in fractures is available. We anticipate that laboratory experiments will be required to provide crucial data (relative-permeability and capillary-pressure curves) on such flows.

TASK 5

Task 5 is focused on work in the NAGRA Rock Laboratory at Grimsel. Grimsel provides a unique opportunity to confirm and expand much of the theories we have been developing for fractured rock under the Office of Civilian Radioactive Waste Management program. This is the largest task in the program and can be considered as a project within a project. In FY 1988, we will focus, in particular, on several experiments within this facility: the fracture-zone experiment (FRI site), the seismic

cross-hole experiment (US site), and the hydraulic cross-hole experiment (BK site). The BK experimental site is embedded in the US site, which provides the unique opportunity to include the vast amount of data from each experiment in a single description.

The fracture-zone experiment has been jointly designed by LBL and NAGRA as a new experiment at Grimsel. The site consists of a shear zone that can be seen intersecting two parallel drifts about 30 m apart. This fracture zone is intermediate in scale between a simple fracture and a complex fracture network. We will perform seismic tomography described below in Task 5.1. We will also collect core from the zone and study the seismic properties of the fractures in the core (Task 5.2). From this experiment we can see how the lab-scale measurements relate to the field values and how electromagnetic measurements compare with seismic measurements. Through geologic investigation and limited hydrologic tests we hope to relate these measurements to the hydrologic characterization of the fracture zone (Task 5.3).

The migration experiment is conducted in a zone similar to the one being used for the FRI experiment. Here extensive hydrologic and geochemical tests are being carried out. As the schedule permits we will repeat some of the above investigations at the MI site, where we expect to have better hydrologic and geochemical information for comparison.

In one section of Grimsel (BK), several shear zones intersect, forming a complex network of fractures. This site represents the next level of complication relative to the FRI site. Here we are analyzing seismic data from the underground seismic (US) site and will conduct further geophysical experiments (Task 5.1). Extensive hydrologic data are already available, and further tests are planned. This area will be the focus of the hydrological investigations (Task 5.3), where we will try to integrate the geophysical data, fracture statistics, geomechanics, and hydrologic data to form a hydrologic model of the fracture network.

TASK 6

The performance of nuclear-waste repositories is heavily influenced by the geochemical environment of both the near field and the geosphere. The purposes of this study are to develop and, as far as possible, to validate models for prediction of spatial and temporal evolution of the geochemical environment relevant to radionuclide mobility. In these studies the most relevant geochemical processes, hydrodynamic transport, and coupled processes will be considered. If successful, these studies will be important for performance assessment of nuclear-waste repositories.

NAGRA has collected a significant amount of data pertinent to transport of contaminants through the backfill. At LBL we have developed software that can account for transport in semipermeable media, such as clays. By combining this code with one that calculates chemical reactions, we will have a tool that is capable of predicting chemical changes that will occur in the backfill as the native groundwater infiltrates the repository. Next we will be able to calculate the transport of contaminants through the chemically altered backfill. These calculations will be possible using the data base that NAGRA has developed. The result will be a tool that can much better predict the source terms for radioactive-waste release into the groundwater system.

The objectives of Task 6 are to simulate the chemical interactions between backfill materials and major cationic components of infiltrating, ambient groundwater and to investigate the effects of these interactions on the sorption, retardation, and migration of radionuclides released from a waste form and migrating through the chemically altered backfill.

The modeling work on bentonite has simulated alteration of a sodium bentonite backfill toward a more calcic bentonite by reactions with inwardly diffusing groundwater components. Sensitivity calculations with radionuclides diffusing outward from a waste canister will provide data on performance of a backfill altered by reaction with ambient groundwater.

In summary, this project is an effort to use the data and facilities available through NAGRA to develop and evaluate characterization tools for performance assessment. An evaluation of the techniques used in this project will be part of the final reports for all of these tasks. In this way the project meets needs in DOE's OCRWM program as well as NAGRA's.

REFERENCES

Hale, F.V., and Tsang, C.F., 1988. A code to compute borehole fluid conductivity profiles with multiple feed points. Lawrence Berkeley Laboratory Report LBL-24928.

Tsang, C.F., 1987. A borehole conductivity logging method for the determination of fracture inflow parameters. Lawrence Berkeley Laboratory Report LBL-23096.

Hydrodynamics of a Vertical Hydraulic Fracture

T.N. Narasimhan

This research aims at improving our current ability to estimate in situ rock stresses through pressure-transient analysis of hydraulic-fracturing experiments. A numerical approach is used in which attention is focussed on the fluid-flow process, using assumptions based on elasticity theory to take into account rock deformation. Parametric studies have been carried out to gain insights into the sensitivity of the system to various controlling factors.

SYSTEM DESCRIPTION

A vertical fracture of constant height and rectangular shape in a homogeneous rock (Fig. 1) is considered. This fracture is created and propagated as energy is supplied at the injection pump and is transmitted to the fracture by the fracturing fluid, water. The process of fracture initiation and propagation is considered with respect to a fracture that has an elliptical cross section in mid section to a distance equal to fracture height, beyond which it has a parallel-plate configuration. An energy criterion based on Griffith's theory is used to model rock rupture. The Griffith's criterion is transformed to an equivalent criterion of *fracture overpressure* for purposes of modeling. Fracture propagation is a discrete process in time, accompanied by sudden releases of energy from a capacitor. In the present case, the capacitor is mainly the wellbore, with the fracture itself playing a subordinate role. As the energy is released, it is expended in many ways as work. The energy release is accompanied by a sudden drop in fluid pressure in the fracture and a small increase in the fracture aperture. Work is done by displacing the fracture walls against the least principal stress in situ, and work is done by creating a new fracture surface by overcoming rock cohesion. Energy is also consumed by way of seismic, acoustic, and other radiations. An important inference is that only a small portion of the energy supplied at the pump is actually expended in creating the new fracture surface.

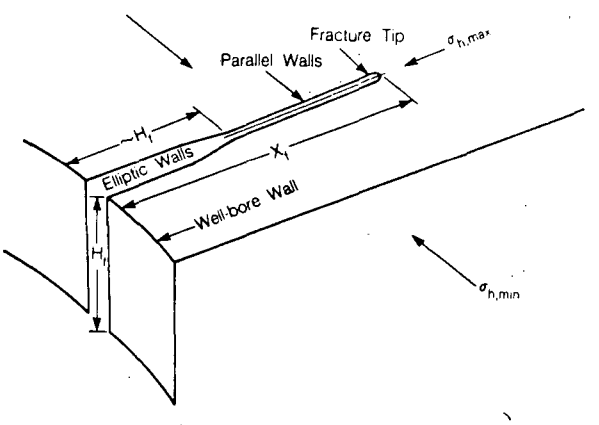

Figure 1. Schematic representation of a vertical fracture. [XBL 873-9981]

MODELING APPROACH

Based on the integral finite-difference method, a numerical model, HUBBERT, has been developed (Narasimhan, 1987). Using the criteria discussed above, this model simulates the initiation and propagation of a vertical hydraulic fracture of constant height. In addition to the usual information required for modeling fluid flow in rocks, the present model requires such additional data as depth to the fracture, breakdown pressure, fracture height, initial fracture aperture, wellbore dimensions, Young's modulus, crack-extension force, and so on. Injection history can be arbitrary and cyclic. Time steps are automatically controlled and account for sharp changes in the forcing function (injection history) and abrupt fracture extension.

RESULTS

A series of parametric studies conducted with the model HUBBERT has led to the following observations:

1. Using parameters relevant on a field scale, the model simulations yield results on fracture length, pressure magnitudes, and time scales that are compatible with field experience.
2. The pressure-transient pattern in the wellbore is characterized by instantaneous spikes accompanying sudden releases of energy (Fig. 2). This pattern as well as its time scale are compatible with acoustic-emission data from experimental hydraulic fractures.
3. As the fracture grows, more energy is needed to pressurize it, and it also stores more energy. As a consequence, the intervals between successive fracture events become longer as the fracture grows, and the magnitude of incremental fracture extension also increases. This phenomenon is consistent with the knowledge that on seismic faults, the longer the seismic gap, the larger the seismic event.

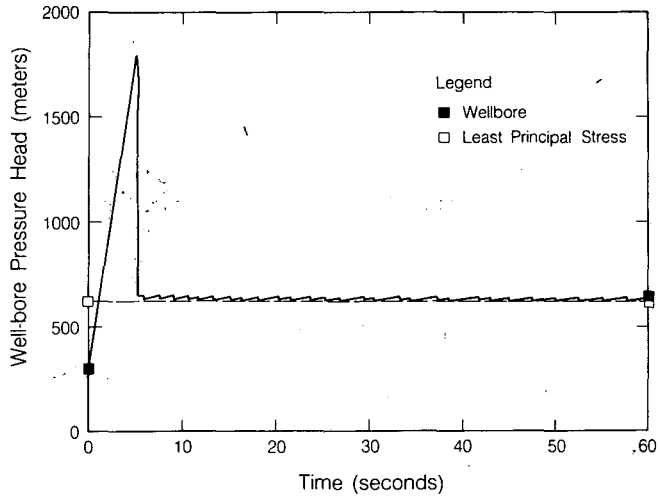

Figure 2. Case I-1: constant flow rate of 2 L/s. Wellbore pressure head as a function of time. [XBL 887-10352]

4. The pattern of fracture evolution is quite sensitive to several factors, such as efficiency (energy actually spent in extending the fracture as a ratio of the available energy in the water), rock permeability, wellbore capacity, aperture and stiffness of the incipient fracture, and pattern of fluid injection.

5. All but two of the cases studied dealt with controlled injection rates. In the two cases in which the injection pressure was maintained constant, fracture propagation tended to become unstable with fracture growth. There is reason to suspect that this pattern is relevant to the analysis of massive hydraulic fracturing, a topic that is beyond the scope of the present study.

6. Current techniques of pressure-transient analysis with reference to in situ stress measurement rely on identifying changes in slope on the pressure-transient curve to interpret for least principal stress. The present study shows that that approach can be successful, provided that the aperture and stiffness of the nascent fracture are relatively large. The pressure transients may show spikes and mask the identity of the least principal stress if the the newly created fracture is stiff and has a small aperture. All the analyses in the present study were carried out using simple arithmetic plots. No need was felt nor any special advantage perceived for resorting to the use of a logarithmic time scale. Indeed, in some situations a logarithmic time scale may actually suppress slope contrasts that are essential to identify least principal stress.

7. Step-rate injection tests could be useful in identifying least principal stress. However, some caution is in order. The use of step-rate tests stems from simple reasoning based on steady or quasi-steady flow behavior. However, the problem at hand is intrinsically a transient one. It appears that the best chance of identifying the least principal stress is likely when injection is carried out at low rates over a long period of time. The break in slope of the time transient manifests itself most markedly under low flow rates.

8. Two outstanding issues in the area of present research relate to (a) the identification of maximum stress in the horizontal plane and (b) the identification of the fracture-opening pressure. Both these issues require for their resolution a detailed handling of the stress field within few wellbore diameters. In the context of elastic theory, such a stress field can be effectively incorporated into the present model if the need arises.

9. The present model has shown that the features of pressure-transient curves of hydraulic-fracturing experiments can be simulated in terms of physically realistic processes. The next step is to apply the model to the wealth of data that is already available in the literature. Such an application should be motivated by a twofold iterative purpose: How best to get the most out of available field data? How best to minimize the gap between the mathematical model and the physical system it seeks to portray?

REFERENCE

Narasimhan, T.N., 1987. Hydrodynamics of a vertical hydraulic fracture. Lawrence Berkeley Laboratory Report LBL-23175.

DYNAMIX: A Multidimensional, Multiple-Species Chemical-Transport Model for Redox-Driven Transport in Geologic Media

T.N. Narasimhan and C.W. Liu

Chemical processes driven by oxidation and reduction reactions (redox reactions) have a significant influence on the chemical evolution of the earth. Among the spectrum of topics of scientific and engineering interest that are dictated by redox reactions, one may cite sedimentary diagenesis, ore deposition, migration of heavy metals in groundwater systems, genesis of petroleum, secondary beneficiation of metals from waste heaps, and corrosion of metals. It is therefore of considerable practical interest to earth scientists and reservoir engineers to have a workable tool of computation for quantitatively analyzing hydrogeochemical systems that are driven by redox reactions. We here briefly describe the computer program DYNAMIX (for redox-driven chemical transport involving multidimensional systems), which can handle realistic field systems involving several hundred grid blocks, more than a dozen chemical species, and several tens of mineral phases and complexes.

DYNAMIX

Program DYNAMIX, an acronym for DYNAmic MIXing, was originally developed as part of the UMTRA program (Uranium Mill Tailings Remedial Action program) of the U.S. Department of Energy and was successfully applied to model contamination around the abandoned uranium mill-tailings pile at Riverton, Wyoming (Narasimhan et al., 1986). The program was developed by extending the advective transport algorithm TRUMP, developed at the Lawrence Livermore National Laboratory (Edwards, 1972), and coupling it with a geochemical-speciation algorithm, PHREEQE, developed at the U.S. Geological Survey (Parkhurst et al., 1980). This first version of DYNAMIX primarily focused on titration-type aqueous-aqueous interactions and thus had limited utility. However, the developmental exercise clearly established the modeling approach as potentially viable for simulating realistic field systems that are of interest to many DOE missions.

We have now updated and extended DYNAMIX to handle a variety of redox-driven systems and have been able to verify the model not only against other independently developed computational algorithms but also against field data. This work is the subject matter of a doctoral dissertation currently approaching completion (Liu, 1988) and of a two-part manuscript under preparation (Liu and Narasimhan, 1988a,b).

Using the integral finite-difference method, DYNAMIX solves a set of equations that represent various reactions, such as advection, molecular diffusion, hydrodynamic dispersion, and source terms. Options are available for including decay as well as general nonlinear sorption, although we have not investigated these processes in the present study. Chemical reactions leading to precipitation and dissolution are explicitly coupled with the transport equation via the time-dependent source term.

For chemical reactions we use a partial-equilibrium approach. To provide redox drive, we simulate the transport of oxygen. Speciation, complexation, ion exchange, precipitation/dissolution, and related aspects are handled through equilibrium thermodynamic calculations of PHREEQE. We have embellished these with a mass-balance inventory for required number of mineral phases, a Gibbs free-energy minimization criterion for choosing the correct mineral assemblage, and a module for handling kinetic dissolution. We also provide for alternate ways of handling the redox reaction itself. The current version of DYNAMIX runs on VAX and Cray systems. The algorithm is yet to be efficiently vectorized.

Verification and Application

We have successfully matched the results of Walsh et al. (1984) on a four-component dissolution-front problem and the results of Carnahan (1986) in regard to uranium transport involving dissolution as well as precipitation. We have successfully simulated field observations pertaining to supergene enrichment of copper at Butte, Montana, as well as the attenuation of selenium in the shallow groundwater aquifer at the Kesterson Wildlife Refuge in California. All these problems were handled in a one-dimensional idealization.

In order to test the ability of the model to simulate realistic field systems economically, we recently set up a hypothetical problem involving 400 volume elements, 15 chemical species (Table 1), 26 mineral species, and over 75 complexes. The problem seeks to portray a contamination scenario that is likely to accompany the surface disposal of fly ash from coal-

Table 1. Initial aqueous chemical composition in the simulation of two-dimensional reactive-contaminant transport.

Chemical components	Concentration (mole/m^3) Tailing water	Groundwater	Rainwater
pH	3.5	7.6	6.0
pE	8.0	−4.0	8.0
Ca	1.0	1.5	5×10^{-3}
Mg	100.0	1.0	1×10^{-3}
Na	10.0	5.0	1×10^{-2}
K	1×10^{-2}	1.0	2×10^{-3}
Fe	5×10^{-2}	1×10^{-3}	1×10^{-4}
Mn	3.0	1×10^{-2}	1×10^{-5}
Al	4.0	1×10^{-3}	1×10^{-3}
Si	10.0	0.5	1×10^{-3}
Cl	6.0	2.5	1×10^{-2}
C	1.0	4.0	1×10^{-4}
S	200.0	2.0	1×10^{-3}
Se	2.78×10^{-3}	0.0	0.0
As	3.523×10^{-3}	0.0	0.0

burning power plants, leading to groundwater contamination by such metals as arsenic and selenium. The computations were carried out on the Cray-XMP computer at the campus of the University of California at Berkeley. Using approximately 200 explicit time steps, a 30-year hydrogeochemical evolution of the system was simulated. An example of the simulation results, portraying the disposition of the selenium plume at the end of 30 years, is shown in Fig. 1. For the particular combination of circumstances included in the hypothetical problem, the simulations suggested the occurrence of incongruent dissolution of dolomite, a phenomenon

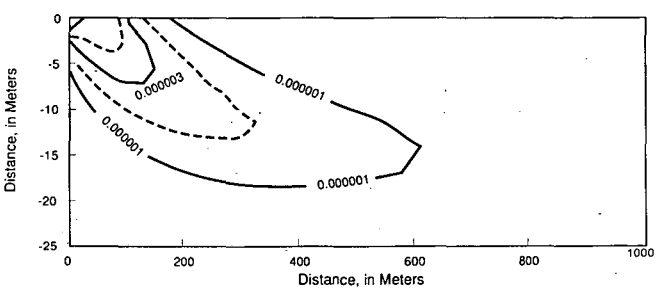

Figure 1. Two-dimensional reactive-chemical transport: contour of aqueous Se concentration (moles/m^3) at 30 years. [XBL 888-2932]

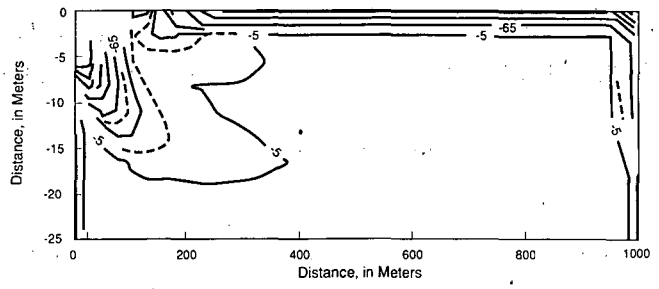

Figure 2. Two-dimensional reactive-chemical transport: precipitation contour of calcite solid (equivalent moles/m^3) at 30 years. [XBL 888-2933]

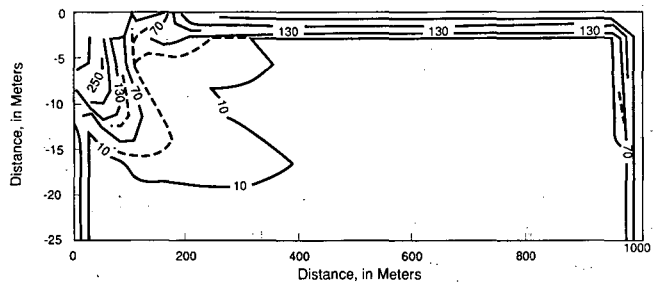

Figure 3. Two-dimensional reactive-chemical transport: dissolution contour of dolomite solid (equivalent moles/m^3) at 30 years. [XBL 888-2934]

that is controlled by sensitive redox and pH variations with time. The simulated dissolution pattern of dolomite and the corresponding precipitation pattern of calcite under incongruent dissolution are shown in Figs. 2 and 3.

REFERENCES

Carnahan, C.L., 1986. Simulation of uranium transport with variable temperature and oxidation potential: The computer program THCC. Lawrence Berkeley Laboratory Report LBL-21639.

Edwards, A.L., 1972. TRUMP: A computer program for transient and steady state temperature distributions in multidimensional systems. Lawrence Livermore National Laboratory Report UCRL-14754 Rev. 3.

Liu, C.W., 1988. Multiple species chemical transport involving oxidation/reduction reactions in geologic media (Ph.D. thesis). Department of Materials Science and Mineral Engineering, University of California, Berkeley, in preparation.

Liu, C.W., and Narasimhan, T.N., 1988a. Redox-driven multiple species reactive chemical transport in groundwater systems, Part 1: Model development. Submitted to Water Resour. Res.

Liu, C.W., and Narasimhan, T.N., 1988b. Redox-driven multiple species reactive chemical transport in groundwater systems, Part 2: Verification and application. Submitted to Water Resour. Res.

Narasimhan, T.N., White, A.F., and Tokunaga, T., 1986. Groundwater contamination from an inactive uranium mill tailings pile, Part 2. Application of a dynamic mixing model. Water Resour. Res., v. 22, no. 13, p. 1820–1834.

Parkhurst, D.L., Thorsterson, D.C., and Plummer, L.N., 1980. PHREEQE: A computer program for geochemical calculations. U.S. Geological Survey, Report of Investigation, P.B. 167801.

Walsh, M.P., Bryant, S.L., Schechter, S.R., and Lake, L.W., 1984. Precipitation and dissolution of solids attending flow through porous media. Am. Inst. Chem. Eng. J., v. 30, no. 2, p. 317–328.

Capillary Hysteresis Model Development and Application to Flow in Fractured Rocks

A. Niemi and G.S. Bodvarsson

As part of the code development and modeling work being carried out to characterize the flow in the unsaturated zone at Yucca Mountain, Nevada, capillary hysteresis models simulating the history dependence of the $\theta = \theta(h)$ relation have been developed.

The characteristic curves defining the transmission and storage properties of an unsaturated porous medium are $k_{rl} = k_{rl}(\theta)$ or $k_{rl} = k_{rl}(h)$ and one or the other of $\theta = \theta(h)$ and $C = C(h)$, where k_{rl} = relative permeability, θ = water content, h = pressure head, and $C = \partial\theta/\partial h$ = specific moisture capacity, exhibits hysteresis. The presence of hysteresis in the $\theta = \theta(h)$ relation, and consequently in the $C = C(h)$ relation, as well as in the $k_{rl} = k_{rl}(h)$ relation, is well established. The $k_{rl} = k_{rl}(\theta)$ relation, however, exhibits considerably less hysteresis and is often assumed to be nonhysteretic when modeling otherwise hysteretic flow (Pickens and Gillham, 1980; Scott et al., 1983; Banerjee and Watson, 1984; Curtis and Watson, 1984; and Jaynes, 1984). This article describes the hysteresis models developed and summarizes some numerical results obtained for hysteretic flow in fractured rocks. More detailed information is given by Niemi and Bodvarsson (1988 a,b) and Niemi et al. (1988).

MODELS

Numerical-modeling capabilities were developed for three different models. In these models different principles are used for determining the scanning paths: in model (1) the scanning paths are interpolated from tabulated first-order scanning curves; in model (2) empirical interpolation functions of Killough (1976) are used for scaling the scanning paths from the expressions of the main wetting and main drying curves; and in model (3) the scanning paths are determined from expressions derived on the basis of the dependent domain theory of hysteresis.

Of these approaches the third one is based on a theoretical representation of hysteresis. According to the domain theory, the total volume of pores in the soil can be divided into subvolumes (domains), each of which has a characteristic wetting and drying pore radius (or is characterized by a pair of capillary pressure intervals $\Delta\phi_d$ and $\Delta\phi_w$ at which the domain drains and rewets). The distribution of these domains, expressed in terms of distribution functions, determines the hysteretic behavior of the soil. Domain models can be divided into two groups: models treating the pores as independent of the neighboring pores are called independent-domain models, and models that attempt to take into account the influence of the neighboring pores are called dependent-domain models. The domain model used in our work is based on the modified dependent-domain model of Mualem (1984), which we extended to handle scanning curves higher than second-order. All three hysteresis models are presented in detail in Niemi and Bodvarsson (1988a,b).

APPLICATION

These models were interfaced with a numerical simulator (TOUGH) for unsaturated flow (Pruess,

1987; Niemi et al., 1988), and preliminary simulations were carried out. An idealized fracture-rock matrix system discretized with the MINC method (Pruess, 1983; Fig. 1), using material properties reported for the welded units at Yucca Mountain by Rulon et al. (1986; Table 1), was simulated under variable infiltration conditions. Pulse penetration in a similar system was studied earlier by Wang and Narasimhan (1986), neglecting the hysteresis effects. The width of the hysteresis envelope was estimated on the basis of experimental as well as theoretical results from soils literature by assigning a ratio of $\alpha_{\text{wetting}}/\alpha_{\text{drying}} = 2$, where α is the van Genuchten parameter (van Genuchten, 1980). Comparisons were made between the hysteretic cases and the nonhysteretic case that took place along the main drying curve alone. An intense rainfall was assumed to take place every 10 years for 3 months, during which a 40-mm/yr infiltration was assumed. This period was followed by a 9.75-yr drying period with the 0.1-mm/yr background infiltration. The following hysteretic effects were observed:

Table 1. Parameter values used in the simulations.[a]

Matrix	
Porosity	$\phi_m = 0.12$
Absolute permeability	$k_m = 3.9 \times 10^{-18}\ m^2$
Capillary pressure[b]	nonhysteretic: main drying curve hysteretic: main drying and main wetting curves
Relative permeability[b]	$k_{rl} = \left[\frac{S - S_{\min}}{S_{\max} - S_{\min}}\right]^{1/2} \left\{1 - \left[1 - \left(\frac{S - S_{\min}}{S_{\max} - S_{\min}}\right)^{1/m}\right]^m\right\}^2$
Initial Conditions[c]	
Capillary pressures	$\psi_m = -0.968$ bar
Liquid saturation	$S_l = 0.691$
Fracture	
Aperture[d]	$\delta_f = 0.1$ mm
Porosity	$\phi_f = 1.$
Spacing	$D = 0.60$ m
Absolute permeability per fracture[e]	$k_f = 8.33 \times 10^{-10}$ m^2
Relative permeability	$k_{rl} = S_l^{1.936}$
Capillary pressure	$\psi_f = 0.0134 \times S_l^{-0.491}$ bar
Initial Conditions	
Capillary pressure[f]	$\psi = -0.968$ bar
Liquid saturation	$S_l = 0.164 \times 10^{-3}$

[a]Source: Rulon et al. (1986), unless otherwise indicated.

[b]van Genuchten parameters $S_{\max} = 0.984$, $S_{\min} = 0.318$, $m = 0.671$, $n = 3.040$, $\alpha_{\text{drying}} = \alpha_{\text{nonhyst}} = 1.147$, $\alpha_{\text{wetting}} = 2.294$.

[c]Obtained with a large-scale composite fracture-matrix model.

[d]Fracture aperture approximately corresponds to the air-entry value = 0.0134 bar through the capillary rise equation (Wang and Narasimhan, 1986):

$$\text{aev} = \frac{2\gamma}{\delta_f \cdot \rho},$$

where $\gamma = 0.07$ kg/s^2, $\rho = 1000$ kg/m^3, and g = 9.81 m/s^2.

[e]Permeability determined from cubic law: $k_f = (\delta_f)^2/12$.

[f]Assume capillary pressure equilibrium between fracture and the matrix.

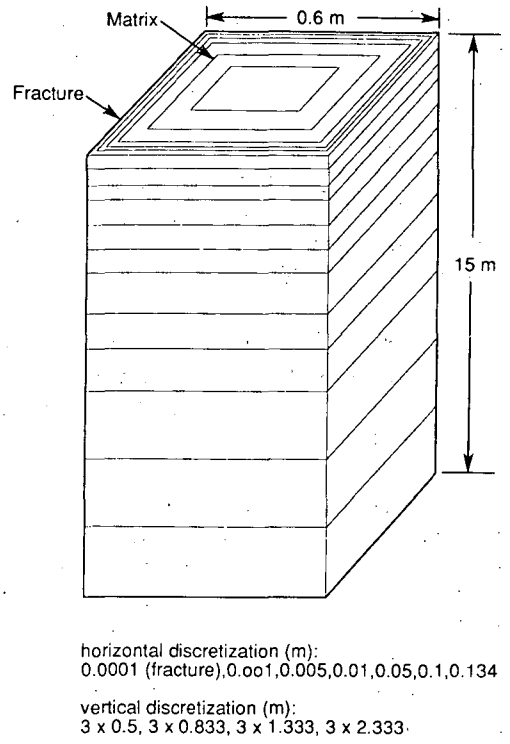

Figure 1. Discretized flow region modeled. [XBL 888-3017]

1. Due to the lower matrix capillary suction and lower matrix permeabilities, pulse in the fracture penetrated deeper in the hysteretic case than in the nonhysteretic case.

2. Due to the combined effect of lower matrix capillary suction and higher fracture flow, the matrix liquid saturation distribution had a more smeared shape in the hysteretic cases.

3. Strong hysteretic behavior (Fig. 2) was limited to the uppermost layers (0.25–0.75 m depth). In these layers nonuniform liquid-saturation distributions resulted even after capillary pressure equilibrium with the adjacent fracture was reached.

4. Using the theoretically derived hysteresis model, model (3), and assuming that the main wetting and drying curves converge toward the same maximum saturation (no air entrapment assumed during the wetting), the pulse in the fracture penetrated ≈1 m deeper in the hysteretic case. The

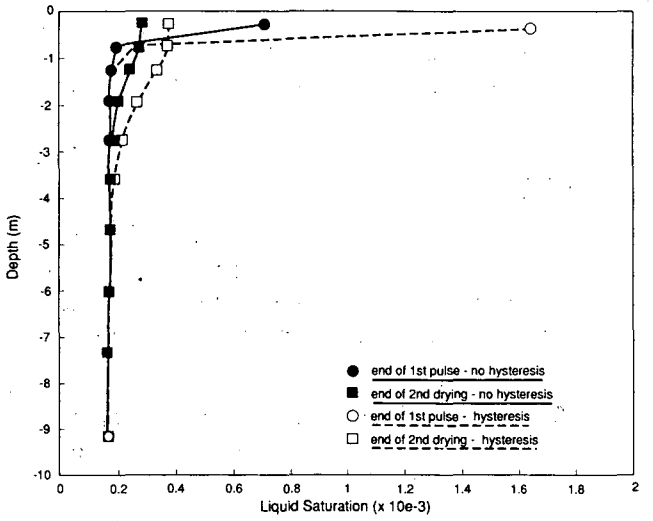

Figure 3. Simulated liquid saturations for the matrix cross section at 0.5 mm from the fracture. [XBL 888-3019]

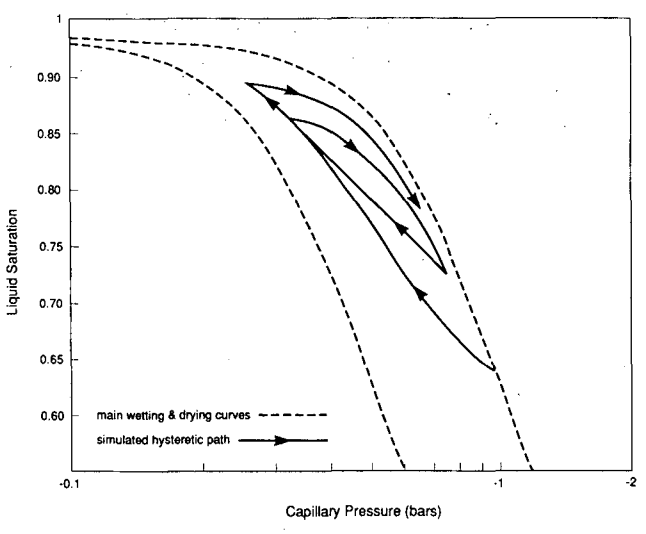

Figure 2. Simulated hysteretic flow path for a gridblock at 0.5 mm from the fracture, 0.25 m depth. [XBL 888-3018]

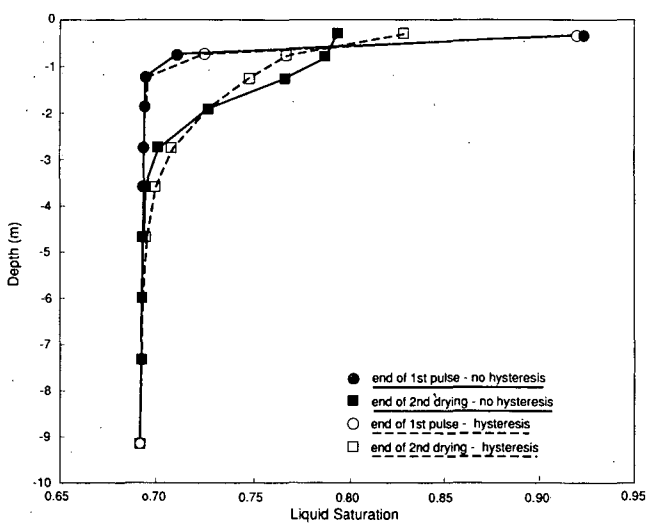

Figure 4. Simulated liquid saturations in the fracture. [XBL 888-3020]

biggest local difference in matrix liquid saturations between the hysteretic and the nonhysteretic cases at the end of the simulations was ≈ 4% (Figs. 3 and 4).

REFERENCES

Banerjee, M., and Watson, K.K., 1984. Numerical analysis of soil water movement under conditions of rapid intermittency of water application. Water Resour. Res., v. 20, no. 1, p. 119-125.

Curtis, A.A., and Watson, K.K., 1984. Hysteresis affected water movement in scale heterogeneous profiles. Water Resour. Res., v. 20, no. 6, p. 719–726.

Daily, W., Lin, W., and Buscheck, T., 1987. Hydrological properties of Topopah Springs Tuff—Laboratory measurements. Submitted for publication in J. Geophys. Res.

Jaynes, D.B., 1984. Comparison of soil water hysteresis models. J. Hydrol., v. 75, p. 287–299.

Killough, J.E., 1976. Reservoir simulation with history dependent saturation functions. Soc. Pet. Eng. J., v. 16, no. 1, p. 37–48.

Mualem, Y., 1984. A modified dependent domain theory of hysteresis. Soil Science, v. 137, no. 5, p. 283–291.

Niemi, A., and Bodvarsson, G.S., 1988a. Preliminary capillary hysteresis simulations for fractured rocks—Model development and results of simulations. Lawrence Berkeley Laboratory Report LBL-23593, 40 p.

Niemi, A., and Bodvarsson, G.S., 1988b. Capillary hysteresis model HYSTR—User's guide. Lawrence Berkeley Laboratory Report LBL-23591, 30 p.

Niemi, A., Bodvarsson, G.S., and Pruess, K., 1988. Incorporation of the hysteresis model HYSTR into the numerical code TOUGH. Lawrence Berkeley Laboratory Report LBL-23592, 10 p.

Pickens, J.F., and Gillham, R.W., 1980. Finite element analysis of solute transport under hysteretic unsaturated flow conditions. Water Resour. Res., v. 16, no. 6, p. 1071–1078.

Pruess, K., 1983. GMINC—A mesh generation for flow simulations in fractured reservoirs. Lawrence Berkeley Laboratory Report LBL-15227, 64 p.

Pruess, K., 1987. TOUGH users guide. Lawrence Berkeley Laboratory Report LBL-20700, 84 p.

Rulon, J., Bodvarsson, G.S., and Montazer, P., 1986. Preliminary numerical simulations of groundwater flow in the unsaturated zone, Yucca Mountain, Nevada. Lawrence Berkeley Laboratory Report LBL-20553, 88 p.

Scott, P.S., Faraquhar, G.J., and Kouwin, N., 1983. Hysteretic effects on net infiltration. *In* Proceedings of National Conference on Advances in Infiltration, Chicago, Illinois.

van Genuchten, M.T., 1980. A closed-form equation for predicting the hydraulic conductivity of unsaturated soils. Soil Sci. Soc. Am. J., v. 44, p. 892–898.

Wang, J.S.Y., and Narasimhan, T.N., 1986. Hydrologic mechanics governing partially saturated fluid flow in fractured welded units and porous non-welded units at Yucca Mountain. Sandia National Laboratory Report SAND85-7114, LBL-21022.

Unsaturated-Zone Thermal-Energy Storage: Model Development and Field Validation

A. Nir, C. Doughty, and C.F. Tsang*

Seasonal heat storage is an essential element in the utilization of alternative energy sources with low-temperature heat supplies in warm climates. Unsaturated-zone soils have been identified as the most suitable medium for this purpose (Nir et al., 1987). Since 1981, detailed theoretical development of such a storage system has been underway, in a cooperative effort between Lawrence Berkeley Laboratory (LBL) and Ben-Gurion University of the Negev. This year a field validation experiment of the concept has begun.

During the past year the following subjects have been investigated: (1) previously developed numerical models of unsaturated-zone thermal-energy storage (Doughty et al., 1983; Nir et al., 1986) have been applied to the specific conditions of the proposed experiment; (2) environmental information has been assembled (geology, meteorology), and local soil temperature- and moisture-depth profiles have been measured; (3) the results of (2) have been used to estimate thermal and hydraulic properties of the local soil; (4) an area has been assigned for the experimental wells; (5) engineering design for well construction, heat-exchanger placement, and system integration has been subcontracted; (6) cooperation with Technion researchers (Bear et al., 1987) has indicated the possibility of novel results in heat and mass transfer in the soil near the heat exchanger; and (7) the results of (6) indicate the need for laboratory validation experiments; these have been initiated, and preliminary measurements have been performed.

Items (1) and (3) are being addressed at LBL and are described below.

NUMERICAL MODELING

Prior to this year, numerical-modeling work has been applied to the full-scale storage system, consisting of a heat-exchanger duct in the form of a 12-m-long vertical helix, located 4 m below the ground surface in the unsaturated-zone soil. Energy is stored and produced on a seasonal basis. Results are presented in Doughty et al. (1983) and Nir et al. (1986). The current field experiment, called the module experiment, is being conducted on a reduced scale, with a 6-m-long duct, so that shorter time periods can be used. Figure 1 shows numerical model results for the heat-exchanger outlet temperature and flow rate as a function of time for the module and full-scale calculations. The same energy charge and discharge requirements, heat-exchanger inlet temperature, and material properties are used for both calculations. The product of the heat-exchanger flow rate and inlet/outlet temperature difference is proportional to the amount of energy deposited to or withdrawn from the storage medium. For the smaller module experiment, the storage is more quickly filled or depleted, causing less difference between inlet and outlet temperatures, thus requiring greater flow rates so that energy deposited or withdrawn meets the imposed energy charge or discharge requirement. The time at which the maximum practical flow rate is reached indicates the appropriate duration for the module experiment.

Because the value of thermal conductivity is not well known at the site, two module calculations

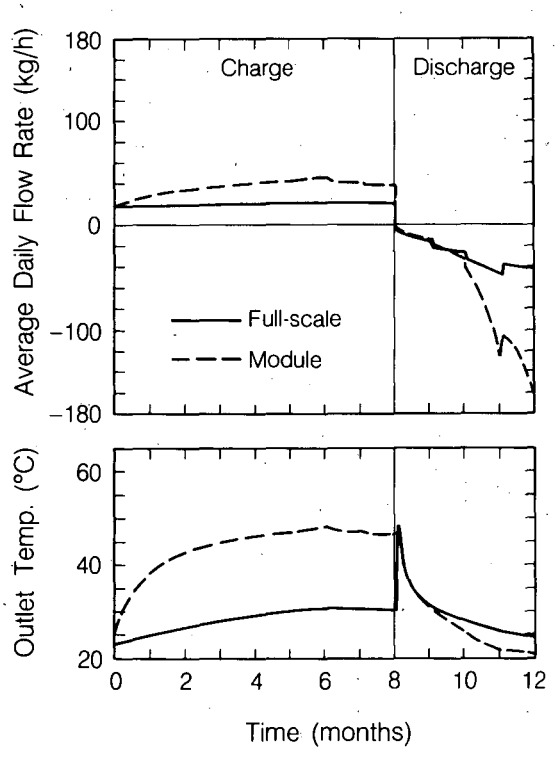

Figure 1. Heat-exchanger outlet temperature and flow rate for the full-scale experiment and the module experiment. [XBL 887-10353]

*Also at Institute of Desert Research, Ben-Gurion University of the Negev, Israel.

using alternative values have been done. The difference between the results for the two calculations is known as the delta model. The temperature field for the delta model, shown in Fig. 2, shows the regions most sensitive to the value of thermal conductivity, which identify the key locations for thermistor placement.

ESTIMATION OF SOIL THERMAL PROPERTIES

In order to obtain a better estimate of thermal conductivity, thermal profiles in the soil have been measured at a series of times. The observed data consist of weekly temperature measurements taken at 0.5-m intervals between 0.5 m and 7.0 m below the ground surface.

An analytical solution for the temperature distribution in the soil is used to infer the value of soil thermal conductivity, by matching the calculated temperature profiles to the observed ones. The analytical solution considers conduction through a semi-infinite homogeneous medium with a sinusoidal surface temperature. The equation for the temperature distribution is

$$T(z,t) = T_0 + T_1 e^{(-z/D)} \cos(\omega t - z/D + \phi),$$

where T is temperature; z is depth below the ground surface; t is time; T_0 is the annual average temperature; T_1 is the amplitude of the sinusoidal variation; $\omega = 2\pi/\tau$ where τ is the period of the variation, 365 days; D is the decay constant, given by $D = \sqrt{2\alpha/\omega}$, where α is the thermal diffusivity of the medium; and ϕ is the phase of the variation, given by $\phi = \omega t_0$

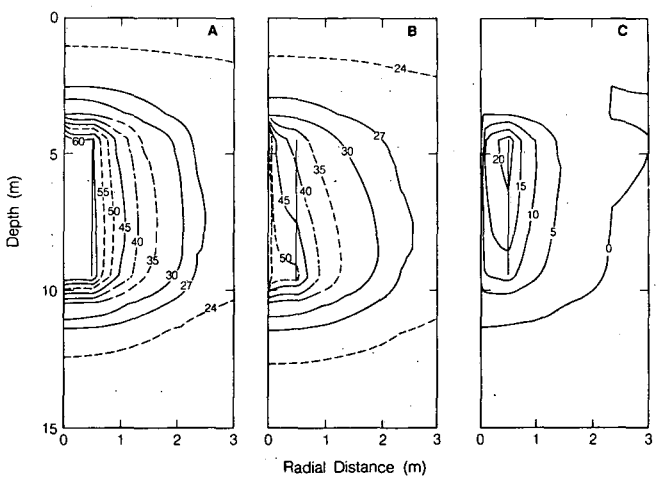

Figure 2. Temperature distribution after two months of charge for **(A)** thermal conductivity of 0.8 W/m°C; **(B)** 1.8 W/m°C, and **(C)** the delta model. [XBL 887-10351]

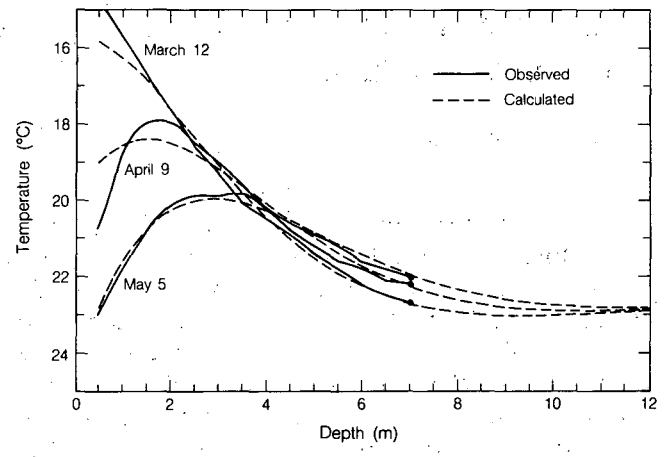

Figure 3. Observed and calculated temperature-depth profiles for the best match. [XBL 887-10354]

where t_0 is the time of the maximum temperature at the surface. Thermal diffusivity α is given by $\alpha = \lambda/C$, where λ and C are the thermal conductivity and volumetric heat capacity, respectively, of the medium.

Because daily and synoptic temperature variations are not considered, the upper 1.5 m of the temperature profile is not used in the matching procedure. Incomplete temperature records at the experimental site require that T_0, T_1, and t_0 be determined by the matching procedure, as well as D. Initial guesses for the parameters are $T_0 = 22.7$°C, $t_0 = 0$ days, $T_1 = 8.2$°C, $D = 2.76$ m^2/s. The resulting calculated temperature profiles show that $T_0 = 22.7$°C is reasonable. Each of the other three parameters has been varied over a range of values. The best match to the observed data, shown in Fig. 3, is given by the following values: $T_0 = 22.7$°C, $t_0 = -10$ days, $T_1 = 10.2$°C, and $D = 2.94$ m^2/s. Assuming a value of 2.1×10^6 W/m^3°C for C, the above value of D yields a thermal-conductivity value of $\lambda = 1.8$ W/m°C.

REFERENCES

Bear, J., Nir, A., and Bensabat, J., 1987. Heat and mass transfer in unsaturated porous media with application to thermal energy storage. *In* Proceedings, NATO Advanced Study Institute on Mechanics of Fluids in Porous Media, June, Lisbon, Portugal.

Doughty, C., Nir, A., Tsang, C.-F., and Bodvarsson, G.S., 1983. Heat storage in unsaturated soils: Initial theoretical analysis of storage design and operational methods. *In* Proceedings, International Conference on Subsurface Heat Storage in

Theory and Practice, June 6–8, Stockholm, p. 518–523.

Nir, A., Doughty, C., and Tsang, C.-F., 1986. Seasonal heat storage in unsaturated soils: Example of design study. *In* Proceedings, 21st Intersociety Energy Conversion Engineering Conference, August 25–29, San Diego, California, p. 669–675.

Nir, A., Doughty, C., and Tsang, C.-F., 1987. Unsaturated-zone thermal energy storage: Design considerations for warm climatic zones. *In* Earth Sciences Division Annual Report 1986. Lawrence Berkeley Laboratory Report LBL-22090, p. 68–72.

A Simple Weighted Nonlinear Least-Squares Method for Estimating Michaelis-Menten or Langmuir Isotherm Constants

P. Persoff

The Michaelis-Menten, or Monod, equation for microbial growth rate under conditions of substrate limitation and the Langmuir adsorption isotherm are both described by mathematically similar expressions, as shown in Table 1. For both these equations, the two constants (K_s and V_{max} in the case of the Michaelis-Menten equation; a and b for the Langmuir isotherm) are determined by fitting the curve to experimental data. This is usually done by transforming Eq. (1) or (2) of Table 1 into a linearized form, as shown in Table 1. The transformed data are plotted and fit by a least-squares straight line, and the values of the two constants are determined from the slope and the intercept. If the untransformed data points fit Eq. (1) or (2) exactly, then each of the linearizations gives the same pair of values for the two constants. Usually, however, the linearizations yield different values, because errors in measurement of q or V (the variables that are treated as dependent) are distorted by the transformation (Dowd and Riggs, 1965). The most accurate estimates of the constants are obtained by using non-

Table 1. Analogous linearizations of the Michaelis-Menten and Langmuir isotherm equations.

Michaelis-Menten	Eq. no.	Langmuir isotherm	Eq. no.	Linearization
$V = \frac{V_{max}S}{K_m + S}$	(1)	$q = \frac{abc}{1 + bc}$	(2)	(Untransformed)
$\frac{1}{V} = \frac{1}{V_{max}} + \left(\frac{K_m}{V_{max}}\right)\frac{1}{S}$	(1a)	$\frac{1}{q} = \frac{1}{a} + \left(\frac{1}{ab}\right)\frac{1}{c}$	(2a)	Lineweaver-Burk
$\frac{S}{V} = \frac{K_m}{V_{max}} + \left(\frac{1}{V_{max}}\right)S$	(1b)	$\frac{c}{q} = \frac{1}{ab} + \left(\frac{1}{a}\right)c$	(2b)	Hanes-Woolf
$V = V_{max} - \left(K_m\right)\frac{V}{S}$	(1c)	$q = a - \left(\frac{1}{b}\right)\frac{q}{c}$	(2c)	Eadie-Hofstee

Notes: V = microbial growth rate, S = substrate concentration, K_m = Michaelis constant. c = fluid-phase concentration of sorbate, q = sorbed concentration in equilibrium with c, a = adsorptive capacity of soil, b = affinity constant related to the energy of sorption.

linear least-squares fitting, weighting the points inversely proportionally to the squares of their respective errors (Colquhoun, 1969; Bevington, 1969). Although this has long been accepted, nonlinear least-squares fitting has not displaced linearization as the standard method for fitting Eqs. (1) and (2), presumably because of the inconvenience of the computations involved. This note presents a weighted nonlinear least-squares fitting method that is convenient to use and that provides better estimates than any linearization or unweighted nonlinear least-squares fitting method.

For simplicity of notation, the derivation is written for the Langmuir isotherm equation; the derivation for the Michaelis-Menten equation proceeds identically, substituting the analogous quantities as indicated in Table 1. Let c_i and q_i be the measured values, respectively of c and q. Let $\hat{q}_i$ be the value of q corresponding to c_i calculated by Eq. (2). Each calculated value $\hat{q}_i$ differs from the measured value q_i by some quantity e_i. The object is to find a and b such that the weighted residual sum of squares (RSS), $\sum_{i=1}^{n} w_i(e_i)^2$, is minimized, where w_i is the weight assigned to point i.

To find a and b that minimize the RSS, one first sets equal to zero the derivative of the RSS with respect to a; this yields an equation relating a and b. Then the procedure is repeated, this time differentiating with respect to b; this yields a second, independent, equation relating a and b. The required values of a and b are found by solving the two equations simultaneously. The results are:

$$0 = \sum \left\{ \frac{w_i}{(1 + bc_i)^2} \left[\frac{(1 + bc_i)q_i c_i - q_i b c_i^2}{a} \right] + \frac{w_i}{(1 + bc_i)^3} \left[(1 + bc_i)(2bc_i^2) - (2b^2c_i^3) \right] \right\}, \tag{3}$$

where

$$a = \frac{\sum \left(\dfrac{w_i b c_i q_i + w_i b^2 c_i^2 q_i}{(1 + bc_i)^2} \right)}{\sum \left(\dfrac{w_i b^2 c_i^2}{(1 + bc_i)^2} \right)}. \tag{4}$$

The analogous equations for the Michaelis-Menten equation are found by replacing c_i with S_i, q_i with V_i, a with V_{max}, and b with $(1/K_m)$ in Eqs. (3) and (4). Because Eq. (3) must be solved by trial and error, it is convenient to program it in BASIC, but if the number of data points is not large, a programmable calculator can be used. For the full derivation, a comparison with linearization methods, and a short BASIC program to calculate a and b, see Persoff and Thomas (1988).

The method is demonstrated by applying it to the data of Frankenberger and Phelan (1985) for biosynthesis of ethylene in Pico soil, using 1-aminocyclopropane-1-carboxylic acid as a substrate. The substrate concentrations and initial microbial growth rates for seven incubations are shown in Fig. 1, along with curves fit to the data using the three linearizations and unweighted nonlinear least-squares fitting. In this data set, the uncertainties of the individual measurements are not known, so nonlinear least-squares fitting is used with all points weighted equally. Figure 1 shows that unweighted nonlinear least-squares fitting fits the data better than any of the linearizations. Even better estimates of the constants could be made if the precisions of the individual determinations of V were known. This could be done by calculating the standard deviation of multiple determinations of V for each value the individual measurements are not known, so nonlinear least-squares fitting is used with all points weighted equally. Figure 1 shows that unweighted

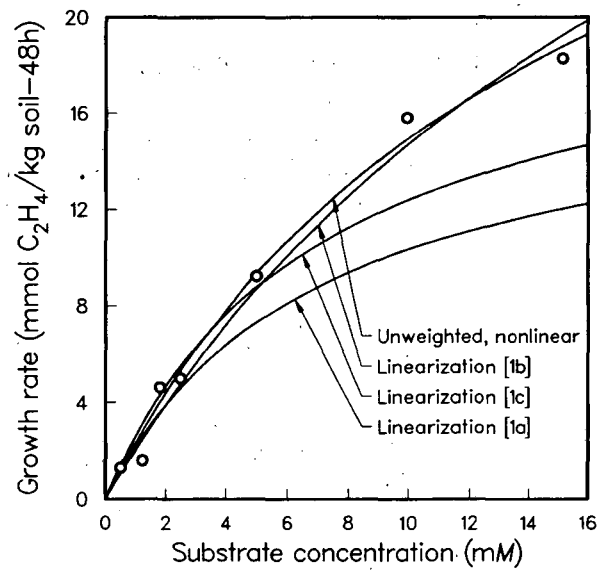

Figure 1. Data of Frankenberger and Phelan (1985), fitted by three linearizations and by unweighted nonlinear least squares. [XBL 881-331]

nonlinear least-squares fitting fits the data better than any of the linearizations. Even better estimates of the constants could be made if the precisions of the individual determinations of V were known. This could be done by calculating the standard deviation of multiple determinations of V for each value of S, and then weighting each point inversely to the square of its standard deviation.

REFERENCES

Bevington, P.R., 1969. Data reduction and error analysis for the physical sciences. McGraw-Hill Book Co., New York.

Colquhoun, D., 1969. A comparison of estimators for a two-parameter hyperbola. Appl. Stat. (J. Roy. Stat. Soc., Series C), v. 18, p. 130–140.

Dowd, J.E., and Riggs, D.S., 1965. A comparison of estimates of Michaelis-Menten kinetic constants from various linear transformation. J. Biol. Chem., v. 240, no. 2, p. 863–869.

Frankenberger, W.T., Jr., and Phelan, P.J., 1985. Ethylene biosynthesis in soil: I. Method of assay in conversion of 1-aminocyclopropane-1-carboxylic acid to ethylene. Soil Sci. Soc. Am. J., v. 49, p. 1416–1422.

Persoff, P., and Thomas, J.F., 1988. Estimating Michaelis-Menten or Langmuir isotherm constants by weighted nonlinear least squares. Soil Sci. Soc. Am. J., v. 52, no. 3, p. 886–889.

Groupings of Organic Waste Chemicals for Studies of Deep Subsurface Disposal

S.L. Phillips, F.V. Hale, and C.F. Tsang

Injection wells are used to isolate liquid wastes containing organic materials resulting from industrial processes by pumping the liquids into carefully selected subsurface geologic formations to depths of 7000 feet. This is an attractive method for disposal of hazardous liquid organic wastes because the injected material is efficiently removed from man's immediate environment. Although injection of hazardous wastes is not a widespread practice, questions have been raised about the possibility of these wastes entering sources of underground drinking water.

The intent of this work is to provide a compilation of physical and chemical data useful in predicting the fate of organic-waste chemicals injected into the subsurface environment. These include half-lives for hydrolysis and biotransformation reactions and equilibrium sorption values at the soil/water interface. Although the available data are largely at 25°C and atmospheric pressure, they can provide the basis for predicting the rates and equilibrium values in the deep subsurface, using appropriate mathematical equations. We found that there are numerous gaps in the tables, representing a lack of experimental values. An especially large gap is represented by rates of biological transformations. Where no data are available, sorption coefficients, biodegradation rates, or hydrolysis rates might be estimated using the model outlined below.

In this model, the fate of an organic substance injected into the deep subsurface depends mainly on the rate of reaction of the original material into an initial product. An example is hydrolysis of a bromoalkane to form an alcohol. This alcohol product may then undergo further reactions, but these subsequent reactions have not been considered in this work.

A report has been prepared that presents a compilation of about 300 organic chemicals and their properties (Phillips et al., 1988). The chemicals are grouped according to their properties, and available descriptive, physical, and chemical data are provided for each entry. In addition, a preliminary model is proposed to predict transformation rates in the deep subsurface, as shown in Fig. 1.

The following sections describe the approach used in compiling the data and estimating missing values for chemical reaction rates.

COMPILATION OF DATA

The organic substances in the tabulation have been selected because they are listed in the proposed listing of hazardous wastes (Rosengrant, 1984). The organic wastes are organized into the following major groupings: halogenated solvents, phthalates, halogenated pesticides, polynuclear aromatics, oxygenates, polymerizables, phenolics, nonhalogenated sol-

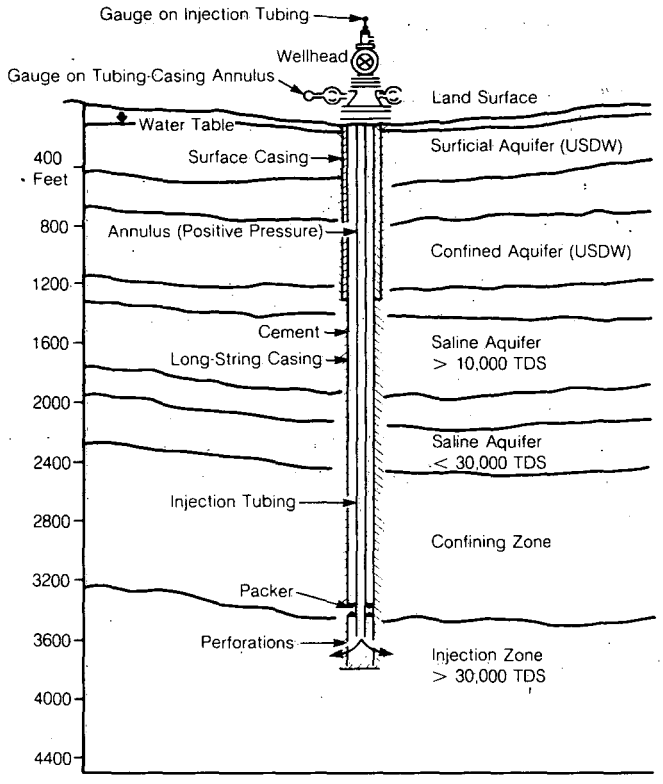

Figure 1. A model of the injection environment. At land surface: organic carbon (OC) is 0.06 to 2 wt% (assumed bound to minerals); bacteria amount to 10^6 to 10^7 per gram of soil; other microorganisms include 1,000,000 to 20,000,000 actinomycetes; 5000 to 900,000 fungi; 1000 to 100,000 yeasts; 1000 to 500,000 algae; and 1000 to 500,000 protozoa. Temperature is variable. In the deep subsurface environment, such as 4000 to 7000 feet, it can be assumed that organic carbon < 0.06%; microorganisms (principally bacterial) << 10^6 cells per gram; temperatures exceed about 35°C. [XBL 887-10355]

vents, reactive (noncyanide) nonhalogenated pesticides, organonitrogens, organosulfurs, halogenated N.O.S., pharmaceuticals, and dyes. The result is a tabulation of about 300 organic chemicals representing both liquid and solid forms of the pure chemicals. Figure 2 is a sample entry in this compilation.

SORPTION COEFFICIENT

Although sorption data are not always available, studies have shown a linear correlation between sorption of hydrophobic organic chemicals and the octanol/water partition coefficients (Chiou et al., 1983). Values of the octanol/water partition coefficient, K_{ow}, are obtained from laboratory measurements. Chiou et al. (1983) developed a correlation applicable to the partition equilibrium of nonionic organic compounds distributed between organic matter bound to soil and the water phase, log K_{om} = (0.904) log K_{ow} − 0.779, where K_{om} is the solute-partition coefficient between the soil organic phase and water. We have used this equation to calculate values of K_{om} for selected missing data in the compilation. It is suggested that this model be used to calculate the magnitude of K_{om} in the deep subsurface, after adding terms or otherwise modifying the equation to account for increased temperature, pressure, and salinity in the deep subsurface (e.g., 5000 ft).

BIODEGRADATION RATE

Bouwer and McCarty (1984) describe a model for the biotransformation of trace organics in subsurface groundwaters according to biofilm processes. An idealized biofilm is composed of a homogeneous matrix of bacteria and extracellular polymers that bind the bacteria together, and to the subsurface organic matter, which in turn is bound to the rock. Webster et al. (1985) found 10^6 to 10^7 cells per gram of subsurface soil, at depths from 2 to 9 m. The number of cells is undoubtedly far less in the deep subsurface, although recent studies show aerobic bacteria at 1000 feet (Phillips, 1988).

Bouwer and McCarty (1984) give an expression for the degradation half-life, $t_{1/2} = \ln 2/[(kX)/K_s]$, where k is the first-order reaction maximum rate constant (s^{-1}) of substrate utilization by bacteria and X is the average concentration of organisms such as bacteria capable of degrading the organic contaminant. The quantity K_s is the Monod half-maximum-rate concentration.

In the deep subsurface, the half-life of organic wastes might be estimated by assuming that $t_{1/2}$ can be divided by a factor of 10 for laboratory-measured aerobic biotransformations and by a factor of 100 for anaerobic. It might also be assumed that the microorganism concentration is 0.001 mg/L or less, so that laboratory data obtained at surface conditions could be divided by 10^5. In the absence of other information on the kinds of microorganisms down to 5000 feet, it might be assumed, as a first approximation, that data at 25°C can be used to estimate biotransformation rates in the deep subsurface under anaerobic conditions, although the rate slows as temperatures approach 0°C or 60°C, where microorganism activity is at a minimum (Phillips et al., 1988).

HYDROLYSIS RATE

Hydrolysis is a chemical process in which an organic hazardous-waste constituent reacts with water to form a different substance. The reaction rate

HALOGENATED SOLVENTS
bis(Chloromethyl) ether
April 1987

Other Names: sym-Dichloromethyl ether; Oxybis[chloromethane]; BCME; Chloro(chloromethoxy)methane; Chloromethyl ether; Dichlorodimethyl ether; alpha-alhpa'-Dichlorodimethyl ether; Monochloromethyl ether

CAS No.: 542-88-1
Hazardous Waste No.: P016
Industry/EPA Generic No.:
Formula: (CH2-Cl)2O; C2H4Cl2O

Description: Colorless liquid; suffocating odor; strong irritant to eyes, respiratory tract; listed as a carcinogen by the EPA (Ref. 2)

Physical properties:		Ref.
Molecular weight:	114.97	2
Melting point (C):		
Boiling point (C):	106.00	2
Density (g/cc, 20 C):	1.3150	2
Vapor pressure (torr, 25 C):		
Henry's law constant (atm m**3 mole**-1, 25 C):		
Solubility in water (mg/L, 25 C):		
Decomposed by water into HCl and formaldehyde		2

Retention properties:		Ref.
log (octanol/water) partition (25 C):	-0.38	3
Partition coefficient, soil/water:	0.75000E-01	17
Hydrolysis rate in water (t1/2, month**-1, 25 C):		
Very rapid, to form HCl and HCHO		3
Biodegradation rate in water (t1/2, month**-1):		
Not important		3

Figure 2. A sample entry from the compilation. [XBL 887-2587]

is a function of a number of parameters, such as pH, temperature, ionic strength, and concentration of metal ions that might catalyze the reaction. The enhanced hydrolysis rates due to temperature of the deep subsurface, e.g., 55°C, can be calculated from the equations given by Mabey and Mill (1987). Effects of increased pressure, catalytic effects, and differences in hydrolysis rates due to ionic strength are difficult to predict; these may be negligible compared with the larger effects of increased temperature, as a first approximation.

Hydrolysis half-life is estimated according to the usual expression $t_{1/2} = 0.693/k_h$. The relationship between k_h, the pseudo-first-order reaction-rate constant, and pH is $k_h = k_B[OH^-] + k_A[H^+] + k_N$, where $K_W = [OH^-][H^+]$, and k_B, k_A, and k_N are second-order rate constants for acid- and base-catalyzed and neutral processes, respectively. The constant K_W is the ion product of water. This is equal to −13.995 at 25°C and −13.275 at 50°C (Marshall and Franck, 1981).

SUMMARY

A compilation was made of the properties of about 300 hazardous waste chemicals, and a model has been proposed to depict the fate of organic-waste substances disposed of in a deep subsurface environment by injection, assuming that the principal reactions are sorption, biotransformation, and hydrolysis.

ACKNOWLEDGMENT

Thanks are given to Iraj Javandel and Richard H. Fish of Lawrence Berkeley Laboratory and David Morganwalp of EPA for their comments. Gene Collins, NIPER, Bartlesville, Oklahoma, reviewed this work. David Balkwill, Florida State University, Tallahassee, provided detailed comments on aerobic bacteria down to 1000 feet.

REFERENCES

Bouwer, E.J., and McCarty, P.L., 1984. Modeling of trace organics biotransformation in the subsurface. Ground Water, v. 22, p. 433.

Chiou, C.T., Porter, P.E., and Schmedding, D.W., 1983. Partition equilibria of nonionic organic compounds between soil organic matter and water. Environ. Sci. Technol., v. 17, p. 227.

Mabey, W., and Mill, T., 1978. Critical review of hydrolysis of organic compounds in water under environmental conditions. J. Phys. Chem. Ref. Data , v. 7, p. 383.

Marshall, W.L., and Franck, E.V., 1981. Ion product of water substance, 0–1000°C, 1–10,000 bars. New international formulation and its background. J. Phys. Chem. Ref. Data, v. 10, p. 295.

Phillips, S.L., 1988. Microbiology of subsurface environments. DOE/ER-0312, Office of Health and Environmental Research, U.S. Department of Energy, Washington, D.C. (Interim Results, Sept. 22–23, 1986 meeting). File memorandum, Lawrence Berkeley Laboratory.

Phillips, S.L., Hale, F.V., and Tsang, C.F., 1988. Groupings of organic waste chemicals based on sorption, biotransformation and hydrolysis at standard conditions for application to the deep subsurface environment. Lawrence Berkeley Laboratory Report LBL-23848.

Rosengrant, L.E., 1984. Proposed grouping of listed U and P waste codes. Title 40, Code of Federal Regulations, Part 261, p. 345.

Webster, J.J., Hampton, G.J., Wilson, J.T., Ghiorse, W.C., and Leach, F.R., 1985. Determination of microbial cell numbers in subsurface samples. Ground Water, v. 23, p. 17.

An Analytical Solution for Heat Transfer at a Moving Boiling Front

K. Pruess, C. Calore, R. Celati,* and Y.S. Wu*

A problem of current interest in geothermal reservoir engineering is the injection of cold water into a permeable medium containing superheated vapor. Such injection gives rise to complex phenomena of phase change and coupled fluid and heat flows. A realistic quantitative description of these highly nonlinear processes can only be achieved by numerical simulations, and it remains a difficult challenge. Some useful insight can be obtained from the consideration of simplified models that are amenable to analytical description. Moreover, analytical solutions provide important checks on the accuracy of complex simulators.

The present work investigates an approximate model in which all flow around the injection well is assumed to be horizontal with cylindrical symmetry. The major features of this process can be deduced from well-known results for the problem of cold-water injection into a hot-water reservoir (Bodvarsson, 1972) and from the symmetry properties of the governing flow equations (O'Sullivan, 1981). As shown in Fig. 1, the injection process will give rise to two fronts: a thermal front separates an inner region with water at injection temperature T_{inj} from a single-phase liquid region at a temperature intermediate between injection temperature and original reservoir temperature. This hot-liquid region is bounded by a moving boiling front, beyond which the reservoir is in single-phase vapor conditions at essentially unchanged temperature. It should be pointed out that, for a porous medium and neglecting heat-conduction effects, the fronts are mathematically sharp; they become diffuse when heat-conduction effects are taken into account, and they become very broad in fractured media.

O'Sullivan (1981) showed that the temporal and spatial evolution of this idealized injection system depends on time t and radial distance r only through the variable $x = r^2/t$. Based on this "similarity" property, it can be deduced that the boiling front occurs at a fixed value x_f of the similarity vari-

*Istituto Internazionale Per Le Ricerche Geotermiche, Pisa, Italy.

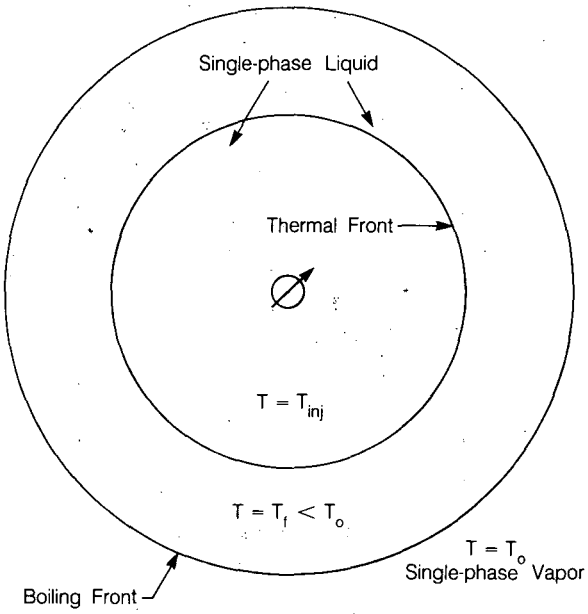

Figure 1. Schematic diagram of fronts for cold-water injection into a superheated vapor zone. [XBL 869-11015]

able x. Consequently, the temperature T_f at the boiling front, and the fraction b of injected liquid that is vaporizing, are constant, independent of time.

MATHEMATICAL TREATMENT

We consider temperature-driven flow of heat from the rock to the advancing liquid-injection plume, as well as pressure-driven flow of vapor away from the front. At the front, reservoir temperature drops from the transfer of heat from the rock to the liquid. From a heat balance over a small region swept by the advancing front, we find the following expression for the front temperature:

$$T_f = T_o - \frac{h_{vl}\,\phi\bar{\rho}_l}{(1-\phi)\,\rho_R C_R\,(q_l/q_{vf} - 1)}\,. \qquad (1)$$

Mathematical symbols are defined in Table 1. The heat transfer results in boiling with outflow of vapor and buildup of vapor-phase pressure ahead of the front. From a linearized approximation to the vapor-flow equation, we obtain for vapor pressure at the front:

$$p_f^2 = p_o^2 - \frac{ZRT_o\mu_v q_{vf}}{2\pi kHm} \times \exp\left(\frac{r_f^{\,2}}{4\alpha t}\right) \mathrm{Ei}\left(\frac{-r_f^{\,2}}{4\alpha t}\right). \qquad (2)$$

Adding the condition that pressure and temperature at the boiling front must be linked by the relationship for saturated vapor pressure,

$$p_f = p_{sat}(T_f)\,, \qquad (3)$$

we have three nonlinear coupled equations for the primary unknowns: front temperature T_f, front pressure p_f, and vaporization rate q_{vf}. All parameters appearing in Eqs. (1) and (2) can be expressed in terms of these unknowns.

Eqs. (1)–(3) were solved by computer, using a two-step iteration procedure. Starting from a fairly insensitive guess on boiling rate q_{vf}, we perform an inner Newton/Raphson iteration to obtain a solution for front temperature from Eq. (1), then use the temperature solution together with the condition Eq. (3) in an outer iteration to compute an updated value for q_{vf} from Eq. (2). Convergence usually requires

Table 1. Mathematical nomenclature.

Roman	
b	boiling fraction, $b = q_{vf}/q_l$
C	specific heat
Ei	exponential integral
h	specific enthalpy
H	formation thickness
k	absolute permeability
m	molecular weight of water
p	pressure
q	mass flow rate
r	radial distance from injection well
R	universal gas constant
t	time
T	temperature
x	similarity variable, $x = r^2/t$
Z	real-gas compressibility factor
Greek	
α	diffusivity parameter for vapor flow
μ	dynamic viscosity
ρ	density
$\bar{\rho}$	average density
ϕ	porosity
Subscripts	
o	initial value
f	relating to boiling front
l	liquid water
R	rock
sat	at saturation (vapor-liquid equilibrium)
v	vapor

4–6 iteration steps. All water properties used in the calculations are accurately represented by the steam-table equations as given by the International Formulation Committee (1967).

RESULTS

Using reservoir parameters representative of the upper depleted zones of the Larderello field (Calore et al., 1986), we have calculated solutions to Eqs. (1)–(3) for a range of "specific" injection rates and porosities. In Figs. 2 and 3 these are compared with results from numerical simulations of the injection process, which were obtained with the MULKOM code (Pruess, 1983). Agreement between the two is excellent. We observe that boiling fraction diminishes with increasing porosity and with increasing injection rate. Boiling-front temperature is lower for larger vaporization rate, as expected.

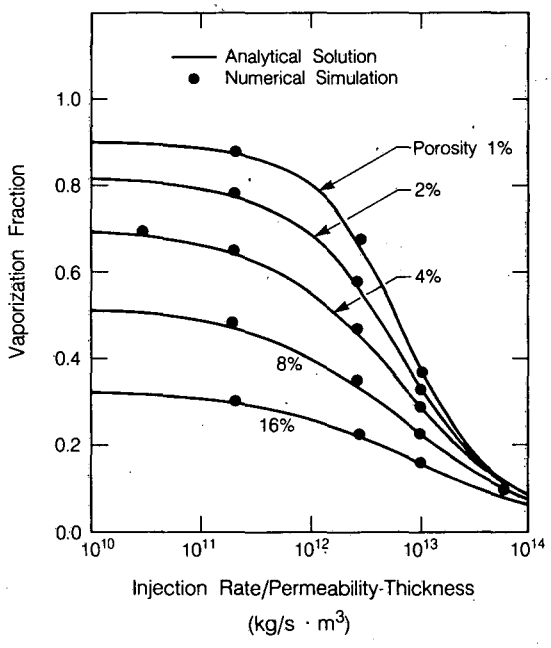

Figure 2. Fraction of injected fluid vaporizing. [XBL 869-11017]

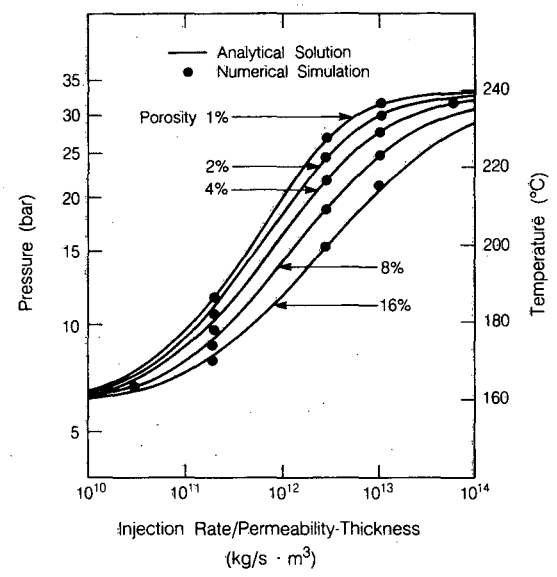

Figure 3. Pressure and temperature of moving boiling front. [XBL 869-11018]

REFERENCES

Bodvarsson, G., 1972. Thermal problems in the siting of reinjection wells. Geothermics, v. 1, no. 2, p. 63–66.

Calore, C., Pruess, K., and Celati, R., 1986. Modeling studies of cold water injection into fluid-depleted, vapor-dominated geothermal reservoirs. Proceedings, 11th Workshop, Geothermal Reservoir Engineering, Stanford University, Stanford, California. Stanford Geothermal Program Report SGP-TR-93, p. 161–168.

International Formulation Committee, 1967. A formulation of the thermodynamic properties of ordinary water substance. IFC Secretariat, Düsseldorf, Federal Republic of Germany.

O'Sullivan, M.J., 1981. A similarity method for geothermal well test analysis. Water Resour. Res., v. 17, no. 2, p. 390–398.

Pruess, K., 1983. Development of the general purpose simulator MULKOM. Earth Sciences Division Annual Report 1982. Lawrence Berkeley Laboratory Report LBL-15500

On Fluid and Heat Flow in Deep Zones of Vapor-Dominated Geothermal Reservoirs

K. Pruess, R. Celati, C. Calore,* and G. Cappetti†*

Vapor-dominated reservoirs are overlain by a caprock of low permeability, in which heat transfer occurs mainly by conduction. In the main vapor-dominated zone, vertical gradients of temperature and pressure are small, and the dominant mode of heat transfer is through a vapor-liquid counterflow process known as "heat pipe" (White et al., 1971; Pruess, 1985). Vapor originates at depth from boiling of liquid. It rises to shallower horizons where it condenses, depositing its large latent heat of vaporization. The condensate then returns to depth driven by gravity force.

THERMODYNAMIC DATA

Little is known about temperature and pressure conditions beneath the main permeable zones of vapor-dominated systems. Systematic long-term increases in production temperature observed in the Larderello reservoir suggested that fluids with very high enthalpy can be delivered from depth. In recent deep drilling, temperatures of 300–400°C have been encountered at Larderello (Cappetti et al., 1985). Temperatures in excess of 300°C have been observed at The Geysers. Figure 1 presents temperature-depth data obtained from three productive wells in the central area of Larderello. Temperatures are similar for the three wells. Down to approximately 500 m depth, there is a conductive gradient of 0.49°C/m, while in the underlying vapor zone there is a very small gradient of 0.015°C/m down to a depth of 2400 m. Substantially higher temperature gradients are encountered at greater depth.

HEAT-FLOW ANALYSIS

In the natural undisturbed state, heat flow in vapor-dominated systems is essentially vertical and close to steady-state conditions. It is well known that, for a given convective heat flux, a balanced liquid-vapor counterflow is possible in two distinct conditions, corresponding to vapor-dominated and liquid-dominated heat pipes, respectively (Martin, 1976; Pruess, 1985). The heat-pipe process requires a contrast in density and enthalpy between liquid and vapor phases; it therefore breaks down as temperatures approach the critical point (374.15°C for pure water). We have examined the temperature dependence of the heat-pipe process and have found that heat-transfer rates do not decline dramatically for temperatures up to 350°C (see Figs. 2 and 3).

The total vertical heat flux through a vapor-dominated system is rather accurately known from the observed conductive gradients in the caprock. From a mathematical analysis of the heat-pipe process, we have derived a relationship between total heat flux, vertical temperature trends, and effective vertical permeability to liquid and vapor phases. Applying this to the Larderello data (Fig. 1) results in the estimates for (absolute) vertical permeability plotted as circles in Fig. 4. These estimates are uncertain because reservoir conditions are likely to have been profoundly disturbed by several decades of production, so that applicability of a steady-state model is questionable. An alternative (upper) limit for vertical permeability, plotted as squares in Fig. 4, was obtained from a stabilized production model. Actual vertical permeability should be intermediate between the two estimates.

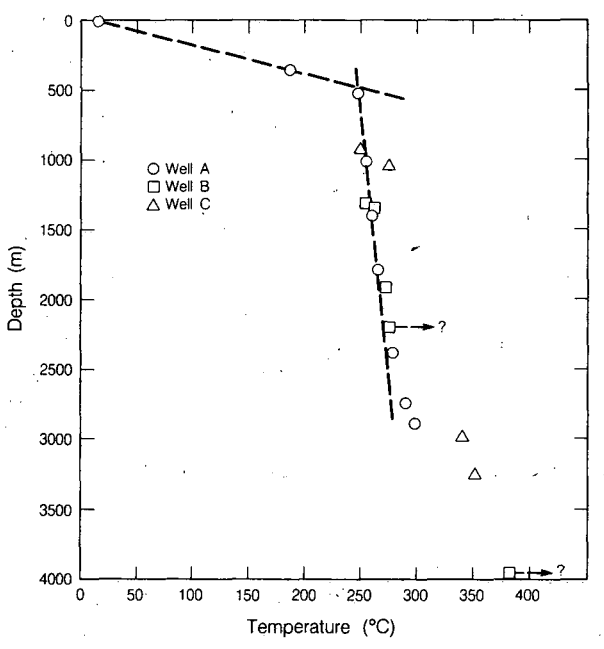

Figure 1. Measured temperatures for three deep wells in the central area of the Larderello field, Italy. [XBL 871-9817]

*Istituto Internazionale Per Le Ricerche Geotermiche, Pisa, Italy.
†ENEL, Unita Nazionale Geotermica, Pisa, Italy.

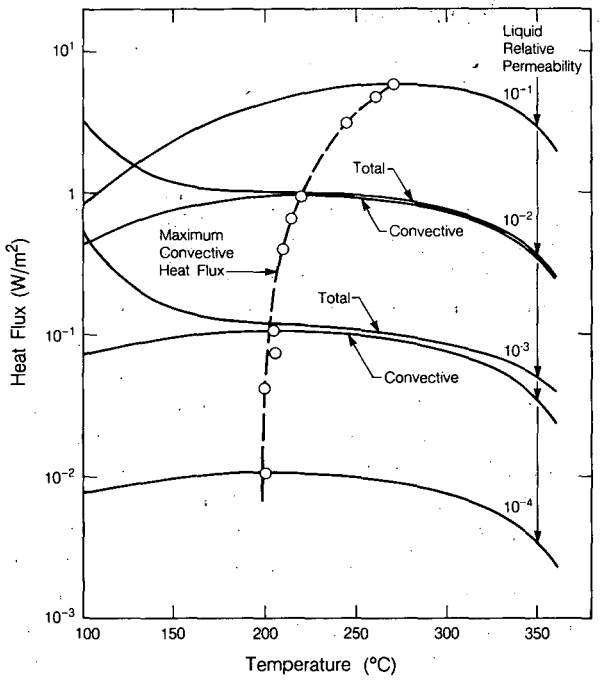

Figure 2. Heat flux in a balanced vapor-dominated heat pipe. [XBL 871-9815]

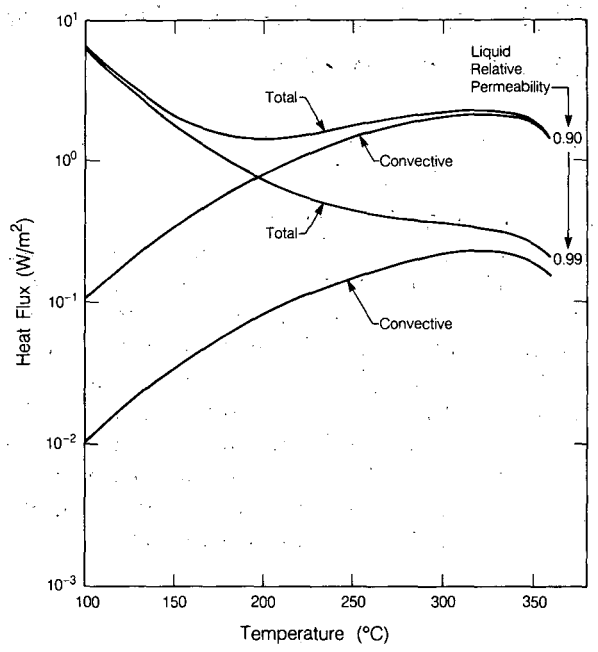

Figure 3. Heat flux in a balanced liquid-dominated heat pipe. [XBL 871-9814]

NUMERICAL SIMULATIONS

A more detailed evaluation of reservoir conditions should be possible from numerical simulations. The main constraints on a model are the following: (1) total vertical heat flux in the natural state is well known from the temperature profiles in the caprock; (2) well behavior is characterized by a rather rapid flow-rate decline by a factor of 3–5 in the first few years of production, followed by a stabilization of rates; and (3) there is a long-term rise in produced enthalpy, corresponding with a temperature increase at the reservoir top of approximately 1–1.5°C per year.

We have numerically simulated the response of vertical-column models to long-term production. Vertical-permeability structure was chosen in accordance with the results from the heat-flow analysis (see Fig. 4). Initial conditions were specified as a vapor-dominated heat pipe overlying a liquid-dominated heat pipe, as suggested from the temperature data (Fig. 1). Production causes a decline in reservoir pressures and flow rates, and an increase in vapor saturations and production enthalpies. Complex fluid and heat-flow processes are initiated when the production-induced disturbances propagate to greater depth, encountering the liquid-dominated heat pipe. Our simulations show that porous-medium models underpredict produced enthalpies and give rather low temperatures at the reservoir top. Models incorporating the fractured-porous nature of the reservoir formations give results consistent with field observations. They facilitate access to heat stored at depth, and they provide a mechanism for delivering high-enthalpy fluids from an interplay between two-phase flow and heat conduction in low-permeability rocks (Pruess and Narasimhan, 1982).

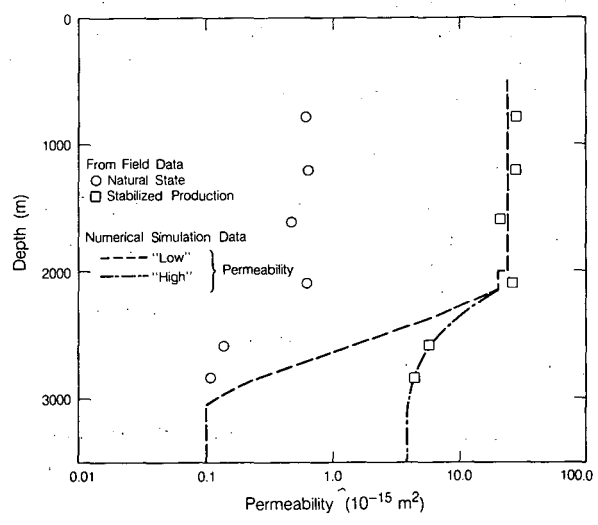

Figure 4. Derived vertical-permeability distribution in Larderello. [XBL 871-9818]

REFERENCES

Cappetti, G., Celati, R., Cigni, V., Squarci, P., Stefani, G., and Taffi, L., 1985. Development of deep exploration in the geothermal areas of Tuscany, Italy. 1985 International Symposium on Geothermal Energy, International Volume, Geothermal Resources Council, p. 303–309.

Martin, J.C., Wegner, R.E., and Kelsey, F.J., 1976. One-dimensional convective and conductive geothermal heat flow. Proceedings, Second Workshop on Geothermal Reservoir Engineering, Stanford University, p. 251–262.

Pruess, K., 1985. A quantitative model of vapor-dominated geothermal reservoirs as hat pipes in fractured porous rock. Trans., Geo. Res. Council, v. 9, Part II, p. 353–361.

Pruess, K., and Narasimhan, T.N., 1982. On fluid reserves and the production of superheated steam from fractured vapor-dominated geothermal reservoirs. J. Geophys. Res., v. 87, no. B11, p. 9329–9339.

White, D.E., Muffler, L.J.P., and Truesdell, A.H., 1971. Vapor-dominated hydrothermal systems compared with hot-water systems. Econ. Geol., v. 66, no. 1, p. 75–97.

On the Validity of an Effective-Continuum Approximation for Multiphase Fluid and Heat Flow in Fractured Porous Media

K. Pruess, J.S.Y. Wang, and Y.W. Tsang

The U.S. Department of Energy is currently performing detailed studies at several sites to determine their suitability as hosts for a geologic repository of high-level nuclear wastes. The thick tuff formations at Yucca Mountain, Nevada, are unique among the candidate sites in that the potential repository horizon is located above the water table in partially saturated rock. In hydrologic terms, we are dealing with a two-phase (liquid-gas) two-component (water-air) flow system in fractured rock with low matrix permeability. The fractures are believed to be well connected; however, because of capillary-suction and phase-adsorption effects, their large permeability is under undisturbed conditions only available to gas-phase flow, while the liquid phase is held in the tight matrix. Strong phase-transformation effects (boiling and condensation) are expected near the heat-generating wastes.

THE CONCEPT OF "EFFECTIVE CONTINUUM"

Evaluation of the suitability of the proposed Yucca Mountain site for nuclear-waste disposal requires a capability to quantitatively describe non-isothermal two-phase, two-component flow in a fractured porous medium. We have developed a numerical simulator, named TOUGH, that can handle most of the physical processes of importance in this problem (Pruess, 1987). However, the geometric complexity of the fractured porous setting is such as to preclude a "head-on" modeling approach. It is desirable to reduce the geometric complexity of flow in a fractured porous medium to manageable proportions by means of suitable averages over geometric detail. The effective-continuum approximation accomplishes such simplification.

The basic idea behind the effective-continuum approximation is the following. Suppose a fractured porous medium with well-connected fractures and a tight rock matrix is subjected to a hydrologic or thermal perturbation. It will then undergo a change in thermodynamic conditions that will tend to propagate rapidly through the fractures but will migrate only slowly into the tight unfractured rock. However, if the rate of change in thermodynamic conditions caused by the external perturbation is "sufficiently" slow, and the equilibration locally between fractures and rock matrix is "sufficiently" rapid, then fractures and rock matrix will remain in approximate thermodynamic equilibrium locally at all times. In this case, the description of thermohydrologic processes should simplify considerably, because it is not necessary to keep track of the changes in fracture and matrix conditions separately, the two being linked by local thermodynamic equilibrium.

QUANTITATIVE CONSIDERATIONS

Several important questions need to be answered so that one may develop a quantitative description of flow based on the ideas sketched above. What are

the equations governing flow in an effective continuum? How can the hydrologic properties of the effective continuum be expressed in terms of properties of rock matrix and fractures? What is the accuracy and range of applicability of an effective-continuum approximation?

We have performed numerical-simulation experiments to study thermohydrological conditions near high-level nuclear-waste packages emplaced in partially saturated fractured rock, as encountered in the Topopah Spring unit of the Yucca Mountain tuffs. A highly idealized flow geometry was used, with regularly spaced plane parallel fractures intersecting an infinite linear string of waste packages. Further neglecting gravity effects, this results in a sufficiently small symmetry element to permit a detailed resolution of fluid- and heat-flow phenomena at matrix-fracture interfaces (Pruess et al., 1985, 1988a; see Fig. 1). The numerical simulations reveal complex vaporization-, condensation-, and multiphase-flow effects. The fractures act as highly permeable pathways for gas-phase (air and vapor) flow. Strong capillary forces constrain liquid to flow essentially only in the rock matrix. Vapor-liquid counterflow processes ("heat pipes") play an important role in heat transfer and dominate the thermal and hydrologic conditions near the waste packages.

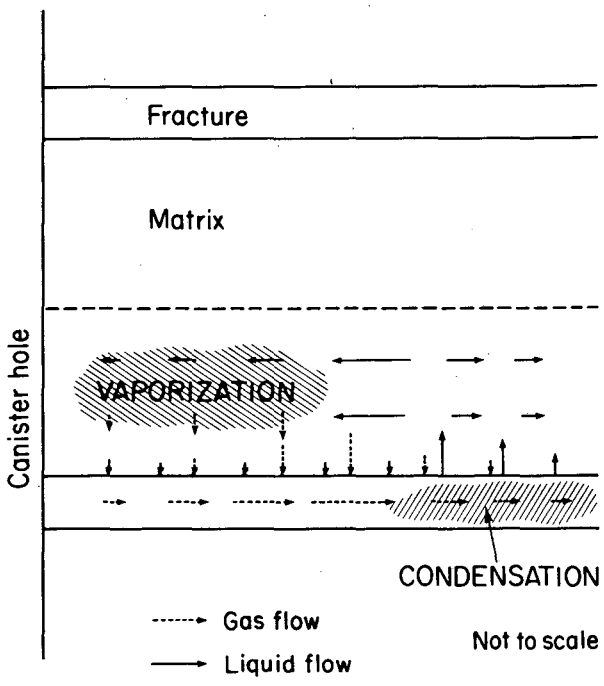

Figure 1. Idealized flow geometry and simulated thermohydrologic phenomena for a high-level nuclear-waste package emplaced in partially saturated fractured rock. [XBL 847-9830]

Based on the behavior observed in these simulations, we developed a mathematical model that provides quantitative relationships between the hydrologic and thermal parameters of the separate rock matrix and fracture domains on the one hand and those of an "equivalent" effective continuum on the other. The most characteristic feature of the effective continuum is its extremely nonlinear relative-permeability behavior, with order-of-magnitude changes in liquid and gas relative permeabilities occurring over small saturation intervals. The governing heat- and mass-balance equations formally resemble those of a (generally anisotropic) porous medium, albeit with highly nonlinear coefficients.

COMPETING DIFFUSIVE PROCESSES

Our numerical-simulation studies showed that, under certain conditions, the effective-continuum approximation can provide an accurate quantitative approximation to the fluid- and heat-flow conditions calculated from highly detailed models with explicit representation of fractures (Pruess et al., 1985, 1988b; see Fig. 2). In an attempt to develop a more general insight into the applicability of the effective-continuum approximation, we have considered competing diffusive processes in the direction of fracture planes as well as in the perpendicular direction into the rock matrix. The crucial concepts are a "radius of investigation,"

$$r_i = 2\sqrt{D_r t} \ , \qquad (1)$$

indicating the distance to which thermohydrologic

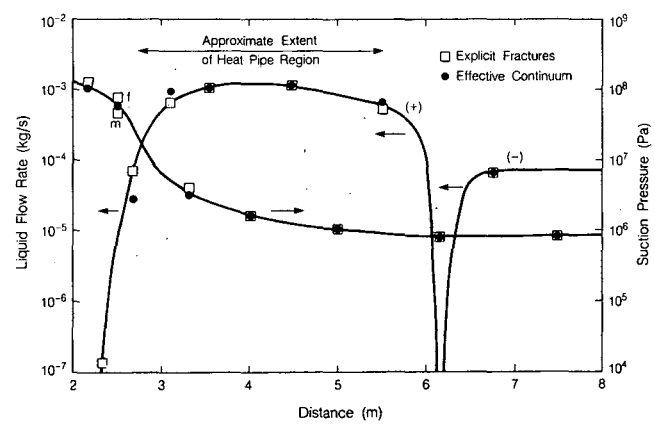

Figure 2. Patterns of liquid flow and suction pressures at 2016.5 days after waste emplacement. (The rates are given on a per-waste-package basis; points labeled "f" and "m" represent fractures and innermost matrix regions, respectively.) [XBL 8511-12624]

perturbations migrate away from the waste packages, and a "penetration depth,"

$$z = \sqrt{D_z t} \ , \tag{2}$$

to which perturbations invade the rock matrix perpendicular to fracture faces. In these definitions, t is the time, and D_r and D_z are the diffusivities in the radial direction and into the rock matrix, respectively. Noting that the z coordinate describes "local" interporosity flow between matrix and fractures, whereas the r coordinate describes global flow away from the source of perturbation, a general criterion for the validity of the effective-continuum approximation can be stated as follows: the time increment Δt required for a thermohydrologic perturbation at the surface of a matrix block to penetrate to the center must be "short" enough so that the advancement Δr of global flow during Δt is negligibly small. If this condition is met, approximate local thermodynamic equilibrium will be maintained, and an effective-continuum approximation is applicable. Quantitatively, the criterion for this can be stated in the time domain as follows:

$$t \gg L^2/D_z \ , \tag{3}$$

where L is the distance of matrix-block centers from the surface. An alternative criterion can be formulated for the space domain,

$$r_i \gg 2L\sqrt{D_r/D_z} \ . \tag{4}$$

As expected, favorable conditions for an effective-continuum approximation exist when matrix-block dimensions are small (small fracture spacing). Furthermore, regardless of applicable thermal and hydrologic parameters, an effective-continuum approximation will be valid for "sufficiently" large times or distances from the source of perturbation.

To apply these criteria it is necessary to identify and quantitatively evaluate the applicable diffusivities for fluid and heat flow. For the problem of a high-level nuclear-waste package in partially saturated rock, the appropriate radial diffusivity is that corresponding to heat conduction, whereas the appropriate diffusivities for matrix flow perpendicular to the fracture faces are those corresponding to single-phase gas- and capillary-driven liquid flow. Data appropriate for conditions as expected in the Topopah Spring unit of the Yucca Mountain tuffs are given in Table 1. The diffusivities for liquid and gas flow are of similar magnitude. They are larger than the thermal diffusivity when rock-matrix permeability is assumed a high 32.6 μd but are smaller

Table 1. Diffusivities for fluid- and heat-flow processes.

Process	Parameters	Diffusivity (m^2/s)
Heat conduction	K = 1.6 W/m°C ρ = 2550 kg/m^3 C_R = 768.8 J/kg°C	8.16×10^{-7}
Single-phase gas flow	$k_m = 32.6 \times 10^{-18}$ m^2 ϕ_m = 10.3 % $\beta \approx 1/P \approx 10^{-5}$ Pa^{-1} $\mu = 1.2 \times 10^{-5}$ Pa·s*	2.64×10^{-6}
Single-phase gas flow, tight matrix	$k_m = 1.94 \times 10^{-18}$ m^2	1.57×10^{-7}
Unsaturated liquid flow	$k_m = 32.6 \times 10^{-18}$ m^2 ϕ_m = 10.3 % $\beta \approx dS_l/dP_{cap} = 2.34 \times 10^{-7}$ Pa^{-1}† $\mu_l = 2.79 \times 10^{-4}$ Pa·s‡	4.85×10^{-6}
Unsaturated liquid flow, tight matrix	$k_m = 1.94 \times 10^{-18}$ m^2	2.89×10^{-7}

*Vapor at T = 100°C.

†At initial saturation S_l = 80%.

‡At T = 100°C.

when the matrix is assumed to be tight (1.94 μd). A quantitative evaluation from Eqs. (3) and (4) using these diffusivities results in the following time and space conditions for an effective-continuum approximation:

(a) large matrix permeability (32.6 μd)
$t >> 4583$ s
$r_i >> 0.122$ m;

(b) tight matrix (1.94 μd)
$t >> 7.71 \times 10^4$ s
$r_i >> 0.502$ m.

CONCLUDING REMARKS

From considerations of competing diffusive fluid- and-heat flow processes in a multiphase system, we have developed general quantitative criteria for the applicability of an effective-continuum approximation. Such an approximation is predicted to improve with increasing temporal or spatial distance from the source of perturbation in a fractured porous medium. These predictions were confirmed by numerical simulations.

An important practical conclusion for studies of fluid and heat flow in fractured media is that an effective-continuum approximation is valid whenever space or time resolution is chosen coarse enough to meet the criteria stated above. With coarser discretization one simply fails to resolve details on smaller scales on which deviations from the effective-continuum approximation could be seen.

With an effective-continuum approximation, the problem of coupled multiphase fluid and heat flow in fractured porous media is greatly simplified, so that numerical simulations over large space and time scales become feasible. An illustrative example of such large-scale modeling is provided by a recent study of thermally buoyant gas-phase flow near a high-level nuclear-waste repository in partially saturated fractured rock (Tsang and Pruess, 1987).

REFERENCES

Pruess, K., 1987. TOUGH User's Guide. U.S. Nuclear Regulatory Commission Report NUREG/CR-4645 (also Lawrence Berkeley Laboratory Report LBL-20700).

Pruess, K., Tsang, Y.W., and Wang, J.S.Y., 1985. Modeling of strongly heat driven flow in partially saturated fractured porous media. *In* International Association of Hydrogeologists (ed.), Memoires, v. XVII, p. 486–497.

Pruess, K., Wang, J.S.Y., and Tsang, Y.W., 1988a. On thermohydrological conditions near high-level nuclear wastes emplaced in partially saturated fractured tuff. Part 1. Simulation studies with explicit consideration of fracture effects. Lawrence Berkeley Laboratory Report LBL-24563. Submitted to Water Resour. Res.

Pruess, K., Wang, J.S.Y., and Tsang, Y.W., 1988b. On thermohydrological conditions near high-level nuclear wastes emplaced in partially saturated fractured tuff. Part 2. Effective continuum approximation. Lawrence Berkeley Laboratory Report LBL-24564. Submitted to Water Resour. Res.

Tsang, Y.W., and Pruess, K., 1987. A study of thermally induced convection near a high-level nuclear waste repository in partially saturated fractured tuff. Water Resour. Res., v. 23, no. 10, p. 1958–1966.

Geologic and Reservoir-Engineering Studies of The Geysers Geothermal Field

M. Ripperda, G.S. Bodvarsson, S. Gaulke, and S.E. Halfman

The Earth Sciences Division of Lawrence Berkeley Laboratory (LBL) is conducting a research project on The Geysers geothermal field for the California State Lands Commission (SLC). During the first year of the project (fiscal 1986), a comprehensive computerized data base was developed and some preliminary engineering studies were carried out. During fiscal 1987 various geologic and reservoir-engineering studies were conducted using the data base (Bodvarsson et al., 1987). The main purpose of this work was to obtain a better understanding of processes and reservoir parameters present at The Geysers in preparation for the development of a field-wide model.

GEOLOGY

Considerable effort was devoted to obtaining an understanding of the geologic features controlling steam migration. Two important factors affecting the location and orientation of steam entries are the large-scale faults and deep felsite intrusions. The primary faults were identified by analyzing surface-geology maps and more than 200 detailed lithology logs. The surface traces of the major faults are shown in Fig. 1. The faults all strike to the northeast, following the trend of the regional geology. Squaw Creek faults X, Y, and Z are normal faults that dip to the southwest. The vertical displacements along these faults are approximately 460 m for fault X, 1200 m for fault Y, and 670 m for fault Z. Fault K is a right-lateral strike-slip fault that predates the Squaw Creek faults. It merges with Squaw Creek fault X at approximately 200 m below sea level. Displacement along fault K introduced a unique 600-m-thick serpentinite unit into the center of The Geysers field. The base of this serpentinite unit is a thrust fault dipping to the northeast. The Sulphur Creek fault zone is located near the southwest margin of the field. Its displacement and orientation could not be determined because of the lack of subsurface data in this area.

The felsite intrusions are a probable source of heat and cause of fracturing throughout The Geysers reservoir (Walters et al., 1988). The felsite is found at depths ranging from 30 m below sea level in the southeast region of the field to over 240 m below sea level in the northwest Geysers area. The depth to the first reported steam entries follows the trend of the depth to the underlying felsite. This implies that warping and fracturing of the graywacke reservoir rock by the felsite intrusions have a significant effect on the system hydrology.

The fracturing caused by the felsite intrusions helps explain the fairly poor correlation between drilling direction and the number of reported steam entries (Fig. 2). Figure 2 represents the average for over 200 wells located throughout the field. A similar analysis was performed on a local basis. Only the wells in the immediate vicinity of the Squaw Creek faults appear to have a correlation between direction of wellbore deviation and the number of steam entries encountered during drilling.

RESERVOIR ENGINEERING

Pressures have declined by more than 250 psi (17 bars) in the central part of the reservoir, with smaller pressure declines toward the northwest,

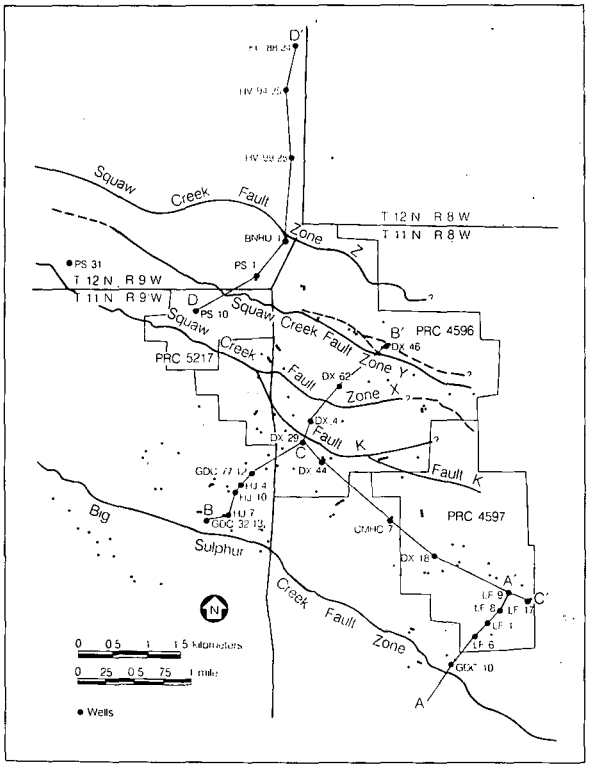

Figure 1. Fault-location map of The Geysers geothermal field (surface contacts of thrust faults beneath serpentinites are not shown). [XBL 8711-10457]

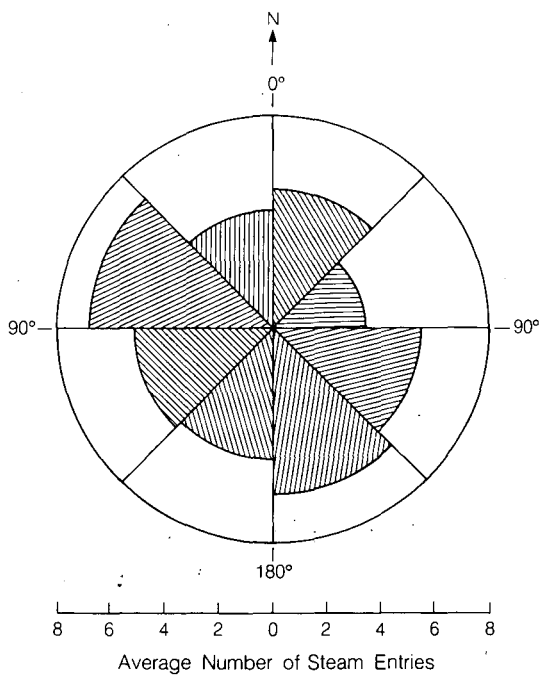

Figure 2. Average number of steam entries per well versus the direction of the wellbore displacement. [XBL 8611-12772]

northeast, and southeast. Analysis of the total fluid production and corresponding pressure decline suggests that over 50% of the fluid reserves have been depleted from the central areas of the field. Significant pressure declines in areas with little cumulative steam production show that most of the reservoir is well connected and that steam migration is an important phenomenon.

The decline in well flow rate at The Geysers is primarily controlled by the recharge factor, which depends upon matrix permeability and average fracture spacing. Other major factors affecting the flow-rate decline are liquid saturation, well spacing, and matrix porosity. The effects of these factors were quantified and the results compared for wells located in different regions of The Geysers. It was found that the recharge factor varies by two orders of magnitude throughout the field, probably because the effective fracture/fault spacing is highly variable.

Type-curve matching software was developed using the method proposed by Fetkovich (1980). The software allows rapid matching of flow-rate declines for Geysers wells and yields the decline factor and an estimate of transmissivity (kH) for the region near the well. This analysis was performed for all available Geysers wells having a significant production history (approximately 200 wells) and provided a transmissivity distribution for the field. It was found that the average transmissivity is around 45,000 md-ft (15 Dm), with values ranging from below 15,000 to over 100,000 md-ft (5 to 30 Dm).

Theoretical calculations of pressure-buildup tests for steam wells show that wellbore-storage effects control much of the pressure-buildup data. However, a unit slope is rarely observed because of changing wellbore-storage conditions caused by condensation in the wellbore. Conventional methods for analyzing pressure-buildup data for gas wells were found to be adequate for steam wells. However, the limited time allocated for pressure-buildup tests at The Geysers precludes the observation of long-term effects such as partial penetration.

Injection at The Geysers has shown beneficial results, but the effects are limited because only 25% of the mass produced is injected. A much higher fraction of the produced fluids must be injected to halt the pressure decline and to recover a significant amount of thermal energy from the reservoir rocks. However, the relatively low injection percentage has had a noticeable impact upon the reservoir. Flow-rate declines of production wells located close to injection wells have leveled off, as evidenced by comparison with Fetkovich's (1980) type curves. An analysis of injection effects has shown that decline rates of wells located near injection wells are approximately one-half the decline rates for wells farther away. No noticeable decline in the temperatures of the produced fluids has occurred in wells located near injection wells.

The various studies performed during fiscal 1987 have provided valuable insight into important geologic features, the characteristics of steam migration, and hydrologic parameters and their variation across the field. All of the results obtained are critical to the forthcoming modeling work.

REFERENCES

Bodvarsson, G.S., Gaulke, S., Halfman, S., and Ripperda, M., 1987. Geological and reservoir engineering studies of The Geysers geothermal field. LBID-1299.

Fetkovich, M.J., 1980. Decline curve analysis using type curves. J. Pet. Technol., v. 32 p. 1065–1077.

Walters, M.A., Sternfeld, J.N., Haizlip, J.R., Drenick, A.F., and Combs J., 1988. A vapor-dominated reservoir exceeding 600°F at The Geysers, Sonoma County, California. *In* Proceedings, Thirteenth Workshop on Geothermal Reservoir Engineering, Stanford University, Stanford, CA.

A Borehole Fluid-Conductivity Logging Method for the Determination of Fracture-Inflow Parameters

C.F. Tsang

In the study of the hydrology of fractured rocks, it is important to know the fracture properties. Surface observations may be useful, but more relevant observations are made at the depths of interest.

Such measurements are mainly carried out through boreholes or underground openings. In the case of boreholes, various methods of studying fracture properties have been used. For example, a downhole televiewer can be used to map the fracture traces on the borehole walls and determine their density and orientation. However, it is well known that these traces do not often correspond to locations of water-conducting fractures. Hence, there is a need to (1) identify the location and (2) measure directly the hydraulic or flow properties of an identified water-conducting fracture or group of fractures intersected by the borehole. The present paper describes a new method involving the use of a time sequence of electric-conductivity logs of borehole fluids.

FLUID-CONDUCTIVITY LOGGING PROCEDURE

Consider the uncased section of a wellbore that intersects a number of flowing fractures. In general, the flowing fractures contain fluids with different chemical compositions and ion contents, and hence with different electric conductivities.

Suppose the wellbore is first washed out with de-ionized water by passing a tube to the well bottom. There will be some residual ion content and associated electric conductivity. In the field data shown later in the article, the residual electric conductivity turns out to be about 60 $\mu S/cm$, corresponding to a residual salinity concentration of 0.03 kg/m^3. Now let us produce from the wellbore at a low flow rate Q. For three fractures we have a situation shown schematically in Fig. 1. Note that the flow rates at different parts of the wellbore are different, being equal to the sum of all upstream inflow rates. At each fracture-inflow point, the parameters characterizing the flow are t_{oi}, the time when the fracture fluid emerges at the wellbore; x_i, the location of the inflow point; q_i, the volumetric inflow rate; and $q_i C_{oi}$, the solute mass inflow rate, where C_{oi} is the concentration of ionic solutes in the fracture fluid.

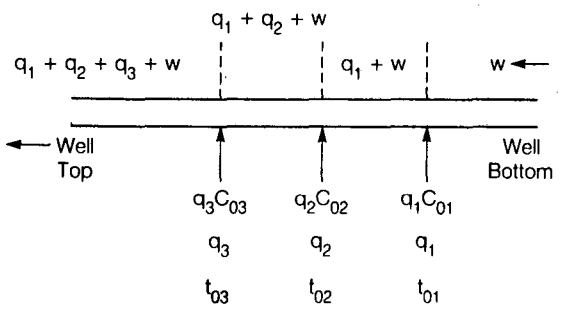

Figure 1. Schematic picture of a wellbore with three inflow points and a wellbore flow rate w from below. [XBL 873-9947]

With the well producing at the constant flow rate Q, a fluid-conductivity logging probe is run through the wellbore and electric-conductivity distribution recorded. This is done a number of times. Care should be taken not to disturb the wellbore fluid to induce large-scale disturbances. With the time sequence of fluid-conductivity logs, the inflow characteristics of the fractures can then be determined. For the field case described later in this article, the well is about 1690 m deep, with the section under survey ranging from 770 to 1637 m below the surface. Each logging run took about an hour, and five logs were taken at intervals of about 4 to 20 hours.

MATHEMATICAL APPROACH

For early times, the salinity concentration is still localized near the inflow points, so that we may consider each inflow point by itself. Further, if we assume that the overall wellbore flow velocity is relatively small and has little effect on the salinity curves at these early times, the problem is then equivalent to release of a chemical beginning at time $t = 0$ at a given point $x = 0$, say, in a linear pipe of stationary water, and an analytic solution is available. An important parameter here is D, the molecular-diffusion parameter associated with the spread of the chemical after it enters the pipe. If the mass-inflow rate is qC_o, where q is flow rate in m$^3/s$ and C_o is concentration of inflow fluid in kg/m^3, and d is wellbore diameter in meters, the solution is given by (see, e.g., Fischer et al., 1979):

$$C(x,t) = \frac{qC_o}{\sqrt{4\pi D}} \cdot \frac{4}{\pi d^2} \cdot \int_0^t \frac{1}{\sqrt{t-\tau}} \times \exp\left[-\frac{x^2}{4D(t-\tau)}\right] d\tau . \qquad (1)$$

Several interesting properties of this expression that will be useful later may be pointed out here. First, at the inflow point, $x = 0$, we find the following expression for peak height:

$$C(0,t) = \frac{qC_o}{\sqrt{\pi D}} \cdot \frac{4}{\pi d^2}$$

so that

$$[C(0,t)]^2 = \frac{(qC_o)^2}{\pi D} \cdot \frac{16}{\pi^2 d^4} \cdot t \,. \qquad (2)$$

This shows that $[C(0,t)]^2$ is linearly dependent on t for early times, and the slope of $[C(0,t)]^2$ versus t is $S_c = 16(qC_o)^2/\pi^3 D d^4$. Furthermore, if we calculate the area under the salinity curves at these early times, we obtain

$$\int C(x,t)dx = (qC_o)\,, \qquad (3)$$

as one would intuitively expect. Now a plot of $\int C(x,t)dx$ versus t will give a slope of $S_A = 4qC_o/\pi d^2$. Then, the ratio S_A^2/S_c is just πD, a constant. The validity of the early-time data can be checked by comparing this ratio for a number of inflow points in the same wellbore. Thus, by these simple considerations, one can obtain from early-time curves both t_o and (qC_o). These are then used as initial guesses for a numerical code to fit the measured data in order to obtain the basic parameters t_o, q_o and C_o.

A numerical code was written for a general problem of multiple inflow points, overlapping salinity curves, and variable dispersion coefficient K. It solves the linear advective-dispersive equation by a finite-difference solution scheme with upstream weighting and can accommodate various boundary conditions. It has been verified against a number of analytic solutions and other numerical codes.

FIELD EXPERIMENT AND DATA ANALYSIS

The method described above was applied to data from the Leuggern borehole, which is one of six boreholes drilled by Nationale Genossenschaft für die Lagerung Radioaktiver Abfälle (NAGRA) as part of a regional investigation program in northern Switzerland. The borehole is located near the confluence of the Rhine and Aare Rivers in the Tableland south of the Black Forest Massif. Drilling of the borehole began in June 1984 and was completed in February 1985, at a total apparent depth along the borehole of 1688.9 m. The borehole deviates slightly from vertical, and thus, the true terminal depth of the borehole below the ground surface is 1631.6 m. In this article, depth is measured along the borehole.

The geology intersected by the borehole is described in Fig. 2. A thin layer of unconsolidated Quaternary deposits is underlain by consolidated Triassic sediments consisting of the Muschelkalk and Buntsandstein. The base of the Buntsandstein group lies unconformably on crystalline rock consisting of biotite gneiss to a depth of 1387.3 m and biotite granite from 1387.3 m to 1688.9 m.

A suite of investigations was conducted in the borehole, including core logs, geophysical logs, hydraulic-packer testing, and hydrochemical sampling. Thury and Gautscchi (1986) provide a brief overview and results of the standard testing program in the NAGRA deep boreholes in northern Switzerland.

Fluid-logging experiments were carried out by NAGRA. Only the section between 770 m and 1637 m below the ground surface was studied by the fluid-log measurements. First the borehole water was replaced by de-ionized water through a downhole tubing, and the fluid conductivity was measured at the outflow at welltop to be 60 μS/cm. Then the tubing was pulled out of the well and the water level in the well was kept at zero by pouring de-ionized water into it. A pump was placed at 210 m, and the background-temperature and electric-

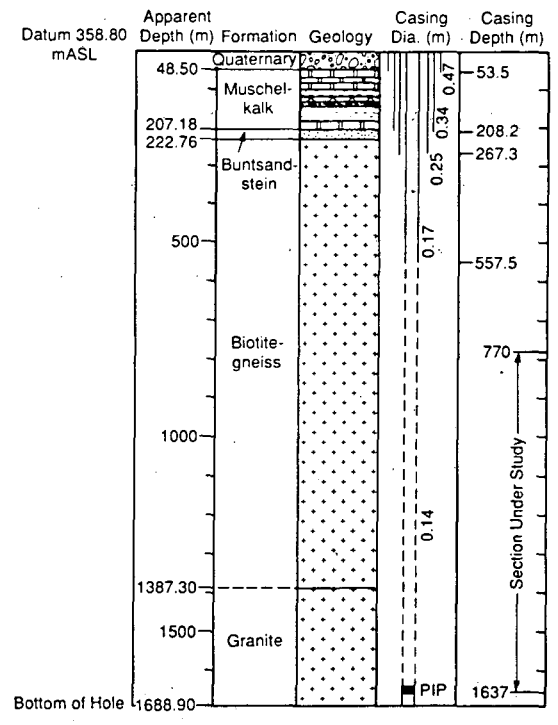

Figure 2. Geologic formations intersected by the Leuggern borehole and various borehole characteristics. [XBL 881-10028]

conductivity logs were obtained. Then, with pumping maintained at about 20 L/min, a series of five complete electric-conductivity logs was taken over two days. After that a temperature log was again taken. The fluid electric conductivity σ depends on temperature. The measured values are normalized conductivity values at a uniform temperature T_n of 20°C. The normalized electric conductivity log is shown in Fig. 3. Now we proceed to study and match the nine peaks in this figure.

The positions of the nine peaks range from the deepest one (peak 1) at x = 1440 m to the shallowest one (peak 9) at x = 843 m. We have selected an arbitrary starting time of pumping as a reference. Peaks 8 and 9 have data at 13.03 hours relative to this reference time. All peaks have data at 27.12, 31.28, 38.41, and 57.24 hours. We consider the starting times of these inflows to be unknown and possibly different from each other. First these peaks were treated independently and the results applied from Eqs. (1)–(3), where we have converted the concentration C to conductivity values σ.

Having made the analysis for obtaining initial-guess parameters, we proceed to apply the numerical code described in the last section to match all nine peaks, and we attempt to obtain the parameters t_{oi}, q_i, and C_{oi}.

The parameter q_i is the value of the flow rate for each inflow point. These values are found by successive guesses, under the constraint that

$$\Sigma q_i = Q,$$

if Q can be measured independently. A few attempts at fitting the data show us that it is impossible to match the data with the assumed value of 20 L /min for Q. By adjusting Q, we found that we can match the data if $Q \approx 2$ L/min, ten times less than the number we used originally. We then sent a request to the NAGRA Staff (1987), who went back to the field data and found that the value of the flow rate from the field experiment may be dominated by flow from a wellbore section above the section under study. The value of Q may indeed be only 3.3 $\times 10^{-5}$ m^3/s, or 2 L/min. This value is used for all later calculations.

After a number of these sensitivity studies, the parameters for each peak were varied to obtain a best fit to observed data. The best fit was obtained by visually comparing calculated and observed curves. The results for the time = 57.24 hours are shown in Fig. 4, with the final matching parameters listed in Table 1.

CONCLUSIONS

In this article we first discussed the procedure and physical processes associated with a time series of fluid-conductivity logs in a borehole intersected by a number of flowing fractures. Simple formulas to evaluate some of the relevant parameters are described and their uses demonstrated. Then numerical matching of the data to obtain the remaining parameters is shown. The results are not sensitive to borehole radius variations, and the method may be able to measure small inflow rates. From Table 1, it appears that flow rates as low as 0.2 $\times 10^{-6}$m^3/s, or 0.01 L/min, can be measured. This may prove to be a useful technique and may complement existing flow-meter or temperature-log methods.

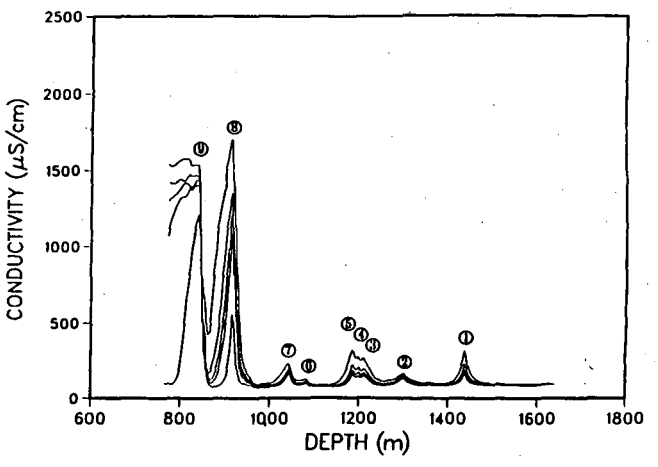

Figure 3. Normalized fluid-conductivity log data. [XBL 888-2812]

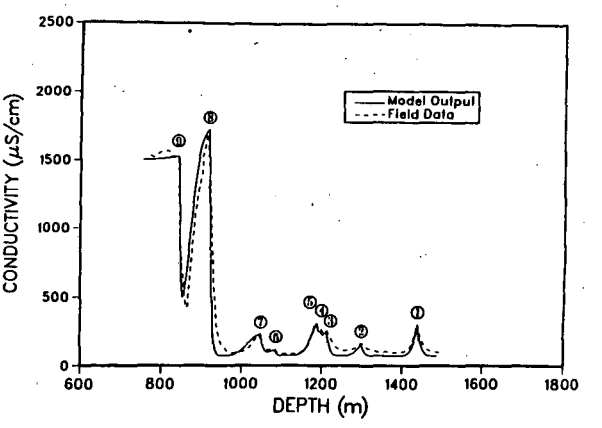

Figure 4. Comparison of field data (broken lines) and final-matched calculated results (solid lines). Only results at 57.24 hours are shown. [XBL 888-2814]

Table 1. Parameters used in final match of field data.

Peak no.	x (m)	t_{oi} (hr)	$q_i C_{oi}$ (10^{-6}kg/s)	q_i (10^{-6}m^3/s)	C_{oi} (kg/m^3)
1	1440	18	0.23	0.65	0.35
2	1300	18	0.09	0.46	0.20
3	1215	18	0.23	0.50	0.45
4	1200	18	0.09	0.21	0.45
5	1188	18	0.24	0.54	0.45
6	1085	18	0.06	0.18	0.35
7	1048	2	0.27	0.53	0.50
8	918	9	4.2	1.5	2.80
9	843	−24	25.	28.	0.90

Note: $K = 5.0 \times 10^{-4}$ m^2/s; $Q = 3.3 \times 10^{-5}$ m^3/s.

ACKNOWLEDGEMENTS

Discussions and cooperation with NAGRA personnel, especially P. Hufschmied, M. Thury, A. Zingg, and P. Zuidema, are much appreciated. Assistance in computation and graphing from C. Doughty and F. Hale is gratefully acknowledged. Thanks are also due C. Doughty, N. Goldstein, and I. Javandel for reviewing and commenting on the manuscript. The work is jointly supported by the Nationale Genossenschaft für die Lagerung Radioaktiver Abfälle, Switzerland and by the U.S. Department of Energy (Office of Basic Energy Sciences, Engineering and Geology Division; Repository Technology Division, Office of Civilian Radioactive Waste Management).

REFERENCES

Fischer, H.B., List, E.J., Koh, R.C.Y., Imberger, J., and Brooks, N.H., 1979. Mixing in Inland and Coastal Wates. Academic Press, New York.

Thury, M., and Gautschi, A., 1986. Testing programme in deep boreholes drilled in sediment-covered crystalline rocks in northern Switzerland. *In* Proceedings, 2nd International Conference on Radioactive Waste Management, Winnipeg, Manitoba, Canada, September 7–11, 1986.

Channeling Characteristics of Flow and Solute Transport through a Rough-Surfaced Fracture

Y.W. Tsang, C.F. Tsang, F.V. Hale, L. Moreno,† and I. Neretnieks†

There is experimental evidence (from both laboratory and field work) that fluid flow in a single fracture does not occur evenly in a fracture plane, but that the majority of the flow takes place along a limited number of preferred paths. We present our investigation of flow in two dimensions, corresponding to the physical situation of flow in single fractures. By solving for flow using the Laplace equation in two dimensions, we try to understand flow characteristics in single fractures and to identify the key parameters that control the channeling flow pattern, thus offering a way to interpret single-fracture field and laboratory experiments that exhibit channeling behavior.

†Department of Chemical Engineering, Royal Institute Of Technology, S-100 44 Stockholm, Sweden.

METHOD AND RESULTS

Here we outline the numerical model used to calculate fluid flow and solute transport through a single fracture with apertures of differing sizes. The fracture plane is partitioned by grids, with different aperture sizes assigned to each square enclosed by grid lines. The spatially varying apertures in the single fractures are generated using a geostatistical method based on a given aperture-density distribution and a specified spatial correlation length. Figure 1 shows two realizations of statistically generated apertures with identical mean and variance of their log-normal aperture-density distribution. Figure 1a differs from Fig. 1b only in the spatial correlation length of the apertures. The correlation length is expressed in terms of a fraction of the linear extent

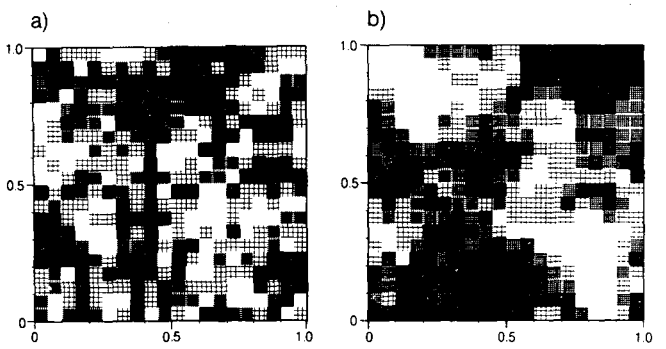

Figure 1. (a) Statistically generated apertures with a spatial correlation length of 0.1 in the plane of a single fracture of linear dimension 1.0. **(b)** Statistically generated apertures with a spatial correlation length of 0.4 in the plane of a single fracture of linear dimension 1.0. [XBL 888-10390]

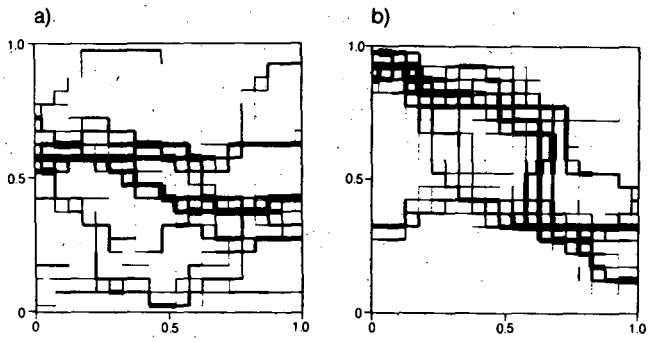

Figure 2. (a) Fluid-flow rates for the fracture with aperture variation as shown in Fig. 1a. The thickness of the lines is proportional to the square root of the flow rate. **(b)** Fluid-flow rates for the fracture with aperture variation as shown in Fig. 1b. The thickness of the lines is proportional to the square root of the flow rate. [XBL 888-10391]

of the square region; it is 0.1 in Fig. 1a and 0.4 in Fig. 1b. The variation in aperture size is represented by the different shadings of the mesh: the darker the shading, the smaller the aperture. A square region of unit area in Fig. 1 therefore represents a single fracture with spatially correlated variable-sized apertures as a flow region. Constant-head boundary conditions were assumed for the left and right boundaries, and no-flow conditions were assumed for the other two boundaries. The local resistance to fluid flow was assumed to vary inversely as the cube of the local aperture. The fluid potential at each mesh intersection was computed, and the steady-state flow rates between all adjacent nodes were obtained.

The flow rates between the nodes varied over several orders of magnitude. To display the large variation in the large range of flow rates over the entire fracture, the volumetric flow rates are plotted in Fig. 2, where the thickness of the lines joining nodes varies as the square root of the flow rate. We have carried out this kind of simulation for many realizations of the aperture variation (Tsang et al., 1987; Moreno et al., 1988). We found (1) that the flow patterns always display the preferred paths of large volumetric flow rates that are formed because of the variation of the apertures within the single fracture plane and (2) that there is a tendency for all the flow paths with large flow rates to coalesce into a "channel" on the order of one spatial correlation length in width, and the spacing between these large flow-rate "channels" is also on the order of the spatial correlation length of the fracture apertures.

Solute-transport phenomena are investigated by tracking the particles advected through the fracture. Particles enter at the left-hand (higher constant-head) boundary in Fig. 1 and are collected at the right-hand (lower constant-head) boundary. A plot of the number of particles collected at all the outlets on the right-hand boundary at different arrival times constitutes the breakthrough curve. In general, the breakthrough curves of tracer transport in two dimensions through these variable-aperture fractures have a fast initial rise, since most particles take the fast flow paths; then there is a long tail in the breakthrough curve due to the small fraction of particles that meander through the fracture, including in their flowpaths many sections with extremely small volumetric flow rates. Our results show that the dispersion displayed by these breakthrough curves does not vary significantly either with different statistical realizations of apertures or with different correlation lengths. This result follows from the fact that these breakthrough curves include the residence times of all possible flow paths that originate from the injection line on the left boundary and terminate on the exit line of the right boundary, and both boundaries cover several correlation lengths. So the information contained in the breakthrough curves is an average over several correlation lengths, hence the insensitivity to it.

On the other hand, the spatial pattern of the tracer breakthrough seems to depend strongly on the spatial correlation length of the aperture variation in the single fracture. The tracer-breakthrough characteristics as a function of space are shown in the contour plot of the number of particles in Figs. 3 and 4. The x axis represents the spatial axis of the left-hand boundary in Fig. 1, which is the inlet boundary. The y axis represents the spatial axis of the right-hand boundary, which is the outlet boundary. In experimental measurements, information on the position of the outgoing tracer is represented by the y coordi-

nate of the tracer concentration in Figs. 3 and 4. The position from which the outgoing tracer originates is contained in the x coordinates. This information can be obtained experimentally only when different tracers (e.g., different dyes) are introduced at different locations at the input boundary. The contours denote the number of particles that enter or exit the single fracture. These figures show that the fast flow paths for tracer transport tend to coalesce into "channels" with width and spacing on the order of one spatial correlation length. A comparison of Fig. 3 with Fig. 4 shows the difference in flow pattern between the cases with correlations 0.1 and 0.4. This kind of plot of measurable data may be a means to estimate the spatial correlation lengths of the system.

CONCLUSION

The variable-aperture character of a fracture causes its fluid-flow and tracer-transport properties to be quite different from those derived from the parallel-plate model of the fracture. To understand the character of fracture flow and transport requires new measurement and analysis methods. In this report, the channeling of fluid flow and tracer transport in a single fracture has been demonstrated.

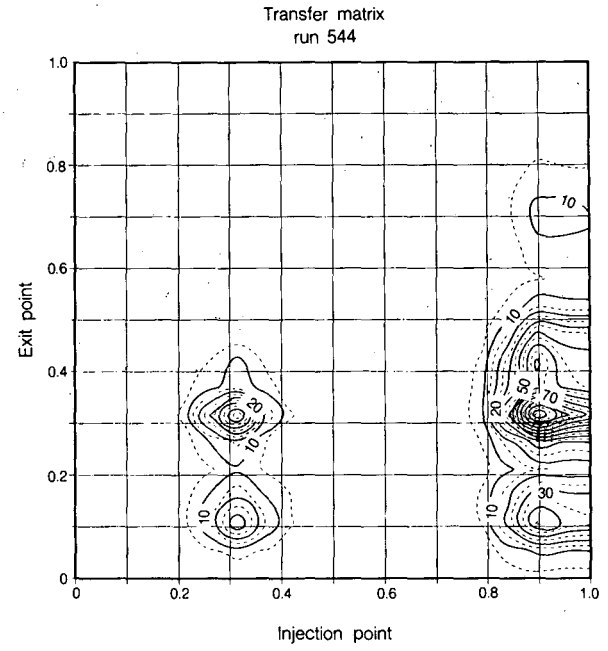

Figure 4. Contours of particle number as a function of tracer entrance location and collection location for a fracture with aperture variation as shown in Fig. 1b. [XBL 875-9680]

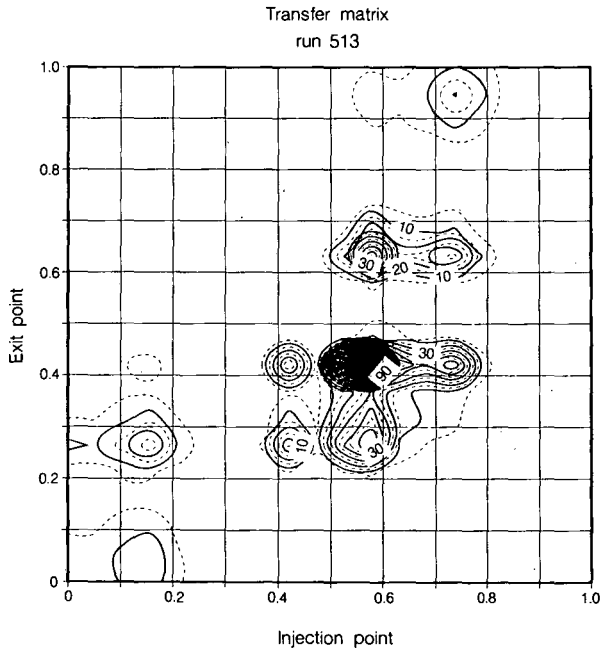

Figure 3. Contours of particle number as a function of tracer entrance location and collection location for a fracture with aperture variation as shown in Fig. 1a. [XBL 875-9677]

Based on our calculations in two dimensions, we may recommend point-injection measurements, such as those shown in Figs. 3 and 4, that probe the spatial correlation length of the aperture heterogeneities in the single fracture. Our calculations also show that if one employs line injection and line collection of tracers, where the measurement-line lengths cover a few correlation lengths, then the resultant breakthrough curves tend to be more stable and not so sensitive to the local heterogeneities and may therefore be analyzed to elucidate the dispersivity of the system.

REFERENCES

Moreno, L., Tsang, Y.W., Tsang, C.F., Hale, F.V., and Neretnieks, I., 1988. Flow and tracer transport in a single fracture: A Stochastic model and its relation to some field observations. Water Resour. Res., in press.

Tsang, Y.W., Tsang, C.F., Hale, F.V., Moreno, L., and Neretnieks, I., 1987. Channeling characteristics of flow and solute transport through a rough-surfaced fracture. Lawrence Berkeley Laboratory Report LBL-23195.

Tracer Transport in Fractured Media: A Variable-Aperture Channel Approach

Y.W. Tsang, and C.F. Tsang

There is field evidence that fluid flow in a fractured crystalline rock mass is very unevenly distributed and takes place along selected preferred paths. This is the flow-channeling phenomenon, which seems to be present both in three dimensions for a network of fractures and two dimensions in a single fracture. We have developed (Tsang and Tsang, 1987) a theoretical approach to treat the fluid flow as if it passes through a system of statistically equivalent 1-D flow channels. Each channel has along its length variable apertures that conform to a given aperture-density distribution and spatial-correlation length. By including only the essential physics of flow on a tight medium in this conceptual model, we seek to analyze flow and transport data in two and three dimensions in a highly heterogeneous medium by a system of independent 1-D channels, thus simplifying the computation effort enormously. In this report, we apply the 1-D channel model to the 2-D flow and tracer transport in a single fracture. Based on the insight gained, we discuss the implications of flow channeling to field measurements and data interpretations.

INTERPRETATION OF 2-D TRACER TRANSPORT BY THE CHANNEL MODEL

Results are presented in the preceding article of this Annual Report for flow and transport in two dimensions in a single fracture with spatially correlated variable apertures. The flow through such a heterogeneous system was obtained by solving the Laplace equation for the fluid potentials within the fracture, and the tracer breakthrough is obtained by tracking particles in the steady-state flow field using dye tracers. To analyze the 2-D results with the 1-D variable-aperture channel approach involves

1. Determining the apertures on the particle flow paths from the 2-D simulation. Figure 1 shows a typical normalized aperture density distribution for all the apertures in a fracture (broken curve) and for the subset of apertures specifically along the particle flow paths (solid curve). The figure illustrates clearly that the smallest apertures are avoided in 2-D flow through a fracture.

2. Employing the aperture-density distribution that characterizes the apertures on the particle flow paths derived from the previous step to generate 1-D statistically equivalent channels. A breakthrough curve is then derived from the residence times of the set of channels.

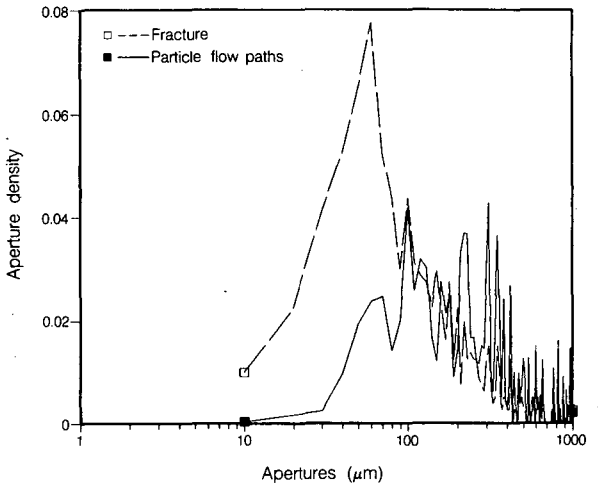

Figure 1. Aperture-density distributions for apertures along particle paths and over the entire fracture of Fig. 2a in the preceding article of this Annual Report. [XBL 875-9685]

3. Comparing the breakthrough curve derived from the channel model with that of the 2-D simulation, as shown in Fig. 2. The solid curve shows the results for the average of the 2-D simulations for eight realizations of aperture variations. The long-dash broken curve is for the averages of the 1-D channel model calculations using the aperture-density distributions as derived in step (2) above. The horizontal bars give the limits of the spread of values for the eight realizations. We also construct a system of constant-aperture channels using the aperture-density distribution from step (2). The resultant breakthrough is shown as the short-dash broken curve in Fig. 2. Finally, if the entire fracture has only one constant aperture, then the plot in Fig. 2 would be a step with tracer concentration equal to 0 before $t/t_m=1$ and 100% after, implying a piston flow with zero dispersivity. The breakthrough that results from such a parallel-plate representation of a single fracture is shown as the dot-and-dash curve in the figure.

Figure 2 is plotted with time on the horizontal axis normalized to the mean residence time t_m in

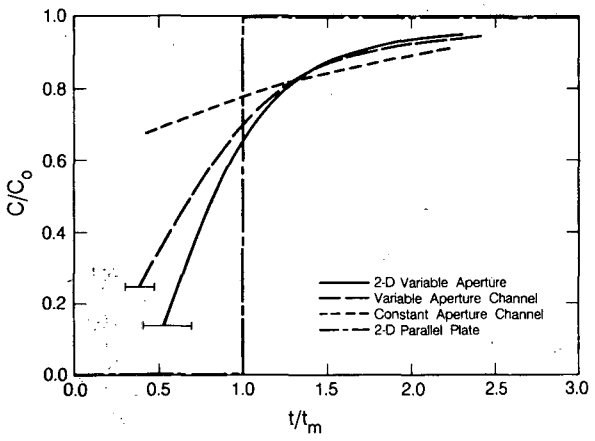

Figure 2. Tracer breakthrough curves from 2-D calculations, 1-D variable-aperture channel calculations, constant-aperture channel calculations, and parallel-plate fracture calculations. Horizontal bars give limits of values from different runs. [XBL 879-10383]

order to compare the dispersivity predicted from different models. The actual values of mean residence times from the different models are presented in Table 1. The second column gives the expected values obtained by dividing total fracture volume by the calculated total flow rates in two dimensions. The third column gives mean particle residence time from the breakthrough curves derived from particle tracking in two dimensions. These agree within a few percent with the values in column 2. The fourth column gives the mean residence time from the breakthrough curves derived from the 1-D variable-aperture channel model. These mean residence times are within a factor of 2 of those derived from the actual 2-D transport. The last column gives mean residence time obtained from the breakthrough curves derived from a system of constant-aperture channels. The mean residence times in this last column are typically two to three orders of magnitude smaller than those predicted from both the 2-D and 1-D variable-aperture channel representations. This is easy to understand, since, in the constant-aperture channel representation, the larger the aperture, the shorter the residence time. Therefore the average is weighted heavily by the residence times of the largest constant-aperture channels.

The qualitative agreement between the results from the 1-D variable-aperture channel model and the 2-D simulations in both Fig. 2 and Table 1 is good. Calculations (Tsang et al., 1988) show that if, in tracking the particles in the 2-D simulations, we have grouped the particles in quantiles according to their residence times within the fracture, and if the aperture parameters of the fastest quantile of particles are used to generate the variable-aperture chan-

Table 1. Mean residence times calculated from (a) fracture volume divided by total calculated flow rate, (b) mean particle-travel times from 2-D calculations, (c) mean residence times from a system of statistically equivalent 1-D variable-aperture channels, and (d) mean residence times from a system of constant-aperture 1-D channels.

	Mean residence time (arbitrary units)			
Realization	Fracture volume 2-D flow rate	2-D Particle tracking	Variable-aperture 1-D channels	Constant-aperture 1-D channels
511	0.59	0.59	0.82	0.004
512	1.46	1.49	1.64	0.012
513	0.35	0.34	0.39	0.007
514	0.33	0.33	0.41	0.006
541	0.07	0.07	0.06	0.0005
542	2.29	2.30	3.10	0.007
543	0.86	0.85	1.15	0.0047
544	0.30	0.30	0.35	0.003

nels, then the resultant breakthrough curves agree even better with those from the 2-D simulations. This result paved the way for an inverse calculation to be carried out. In this calculation we derive the aperture parameters that characterize the most conductive flow channels from the 2-D fracture-breakthrough data.

CONCLUSIONS

In analyzing tracer-breakthrough data from transport in a 2-D single fracture in terms of statistically equivalent 1-D channels, we derive the coefficient of variance for the aperture distribution along the most conductive flow channels. Furthermore, in the variable-aperture channel model, the mean residence time t_m from tracer measurements reflects the mean aperture of the actual flow channels.

The breakthrough data referred to in this report consist of the sum of measurements over a line covering a few correlation lengths. Channeling, by its very definition, implies that flow is very uneven spatially, and there may be a large percentage of areas where flow and transport is zero. No existing theoretical approach can deterministically predict the tracer flow paths and the tracer-breakthrough curve at one particular observation point. Point measurements are hard to interpret in a heterogeneous system. However, for tracer transport that sums over data from multiple-point measurements spanning a few correlation lengths, many channels will be involved, and we may be able to use the present model to predict the total tracer-breakthrough curve. This underlines the usefulness and importance of making tracer measurements with line tracer injection and line observation of tracer emergence.

REFERENCES

Tsang, Y.W., and Tsang, C.F., 1987. Channel model of flow through fractured media. Water Resour. Res., v. 23, no. 3, p. 467–479.

Tsang, Y.W., Tsang, C.F., Hale, F.V., Moreno, L., and Neretnieks, I., 1988. Channeling characteristics of flow and solute transport through a rough-surfaced fracture. *In* this Annual Report.

Tsang, Y.W., Tsang, C.F., Neretnieks, I., and Moreno, L., 1988. Flow and tracer transport in fractured media: A variable-aperture channel model and its properties. Water Resour. Res., in press.

Reservoir Studies of the Seltjarnarnes Geothermal Field, Iceland

H. Tulinius, A.L. Spencer, G.S. Bodvarsson, H. Kristmannsdottir,* T. Thorsteinsson,* and A.E. Sveinbjornsdottir†*

The Seltjarnarnes geothermal resource is located in Seltjarnarnes, a suburb of Reykjavik, the capital city of Iceland. The resource has been exploited for the past 16 years to provide hot fluids for the central heating of Seltjarnarnes. In the typical low-temperature field, temperatures of about 100°C have been encountered at 1000 m depth, and temperatures of over 140°C have been encountered at 2700 m depth. Drilling in the region started in 1965; a total of six wells had been drilled by 1985. Four of these wells are producing with a maximum capacity of 110 L/s, while the remaining two are used for observation.

During the sixteen years of production (1970 to 1986), the salinity within the system has increased. Although the salinity changes were relatively slow initially, an increase in production in 1972 (by 35 L/s), and again in 1981 (by 30 L/s), accelerated the increase. Changes in the average temperature of the produced fluids have been very small (< 2°C) throughout the production period. The pressure changes induced by production have also been small.

In the summer of 1986, all available data on the Seltjarnarnes field (geological, geophysical, and geochemical) were compiled and integrated into a conceptual model for reservoir-simulation studies. The main objective of this work was to develop a numerical model of the field that would be calibrated against the production history, interference-test data, and observed thermal and chemical changes. The model would then be used to predict changes in pres-

*Iceland National Energy Authority, Orkustofnun, Geothermal Division, Grensavegur 9, 108 Reykjavik, Iceland.

†Science Institute, University of Iceland, Dunhagi 3, 107 Reykjavik, Iceland.

sure, temperature, and chemical composition with future production. This paper summerizes the work done; a detailed description is given in Tulinius et al. (1987).

CONCEPTUAL MODEL

Since the drilling of the first well in 1965, considerable amounts of data have been collected, and several reports have been published describing the field (Tomasson et al., 1977; Palmason et al., 1983; Sigurdsson et al., 1985; Kristmannsdottir, 1986). Other, more specific reports on well drilling, fracturing, pressure testing, well tests, fluid chemistry, and other aspects of the Seltjarnarnes field include Thorsteinsson (1970, 1980, 1985), Tomasson and Saemundsson (1970), Thorsteinsson and Tomasson (1972), Kristmannsdottir (1983, 1984), Haraldsdottir (1984a,b,c), Kristmannsdottir and Tulinius (1984), Kristmannsdottir et al. (1984), Sveinbjornsdottir et al. (1984a,b), and Thorsteinsson et al. (1985). All available data were integrated to form a conceptual model of the field. Thermal-gradient and interference-test data suggest that low-permeability barriers limit the extent of the field to the east. Tests on shallow wells indicate that the top 100 m of the subsurface rocks are nearly impermeable. Most of the aquifers are located in the interval from about 400 to 2200 m depth (see Fig. 1).

Isotope studies also indicated the water to be of meteoric origin, probably percolating to a depth of some 3–4 km in the inland highlands, and some tens of kilometers to the north, and heating up due to the anomalous thermal conditions of the subsurface rocks (Arnason, 1976). The water then flows to the south and ascends under the Seltjarnarnes field through fissures that extend to considerable depth and are more permeable than in the surrounding areas. The small changes in oxygen-18 suggest that a large portion of the fluids recharging the field during exploration is meteoric.

The increase in most of the other chemical components is large, indicating that a portion of the recharge fluids consists of highly saline water. The source is most likely seawater recharging the reservoir at shallow depths (above 400 m). From the observed changes in the chemical composition of individual wells, it appears that the seawater is recharging from the southwest.

Figure 2 shows a top view of the conceptual model for the Seltjarnarnes area. Lines of equal

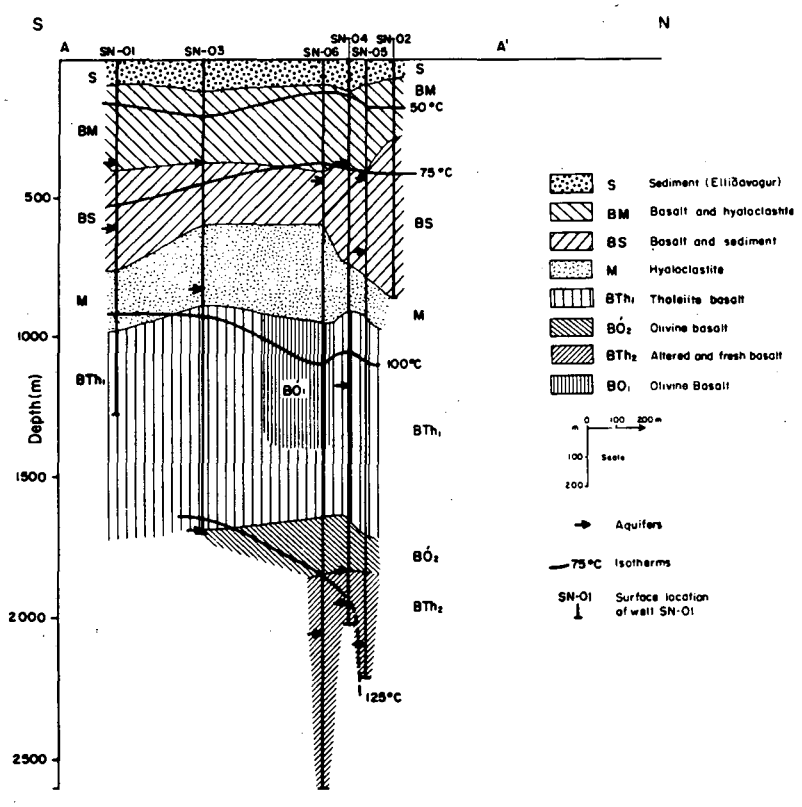

Figure 1. Geologic cross section through wells SN-01 to SN-06. [XBL 888-2810]

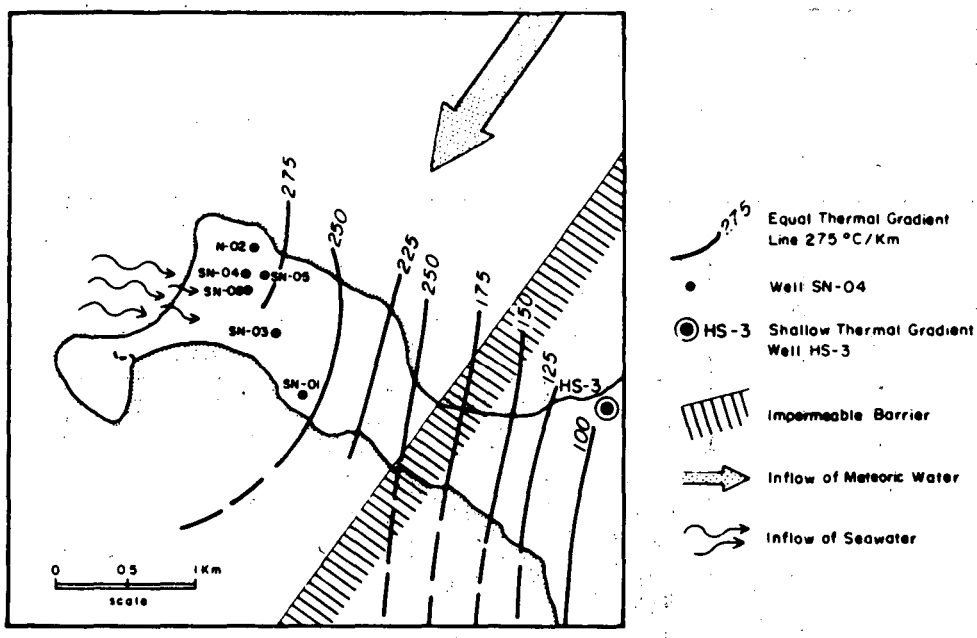

Figure 2. Conceptual model of the Seltjarnarnes geothermal field. [XBL 888-2811]

thermal gradient in the uppermost 200–300 m are plotted in the figure (Tulinius et al., 1986), along with suggested flow directions for the recharge water (plotted as arrows).

NUMERICAL SIMULATION

The single-phase three-dimensional numerical code PT (Bodvarsson, 1982) was used to simulate the interference tests and production history. A modified version of PT (Spencer, 1986), which allows for chemical transport modeling, was used to model the changes in chloride, sodium, silica, and oxygen-18 concentrations. The modified program is capable of modeling the convective transport of up to ten conservative (nonreactive) chemical species, as well as the kinetic reactions and convective transport of silica and oxygen-18.

The model used an 1800-m recharge layer representing the depth interval 400–2200 m. The mesh consisted of squares 50 × 50 m in size around the wells, increasing rapidly in size away from the wellfield (infinite reservoir system). The initial average pressure was estimated to be 123 bars, using the average depth of 1300 m and the density of water at 110°C. Trial-and-error simulations were carried out using permeability (k) and porosity (ϕ) as adjustable parameters. The compressibility of the rock (C) was held constant at 5×10^{-10} Pa^{-1}.

RESULTS

The best model derived from the match using the interference-test data consisted of six regions with different porosities and permeabilities. Figure 3 shows the central portion of the grid and the locations of the six regions. The area around all the wells except SN-01 (region 5) was found to have the largest permeability (80 md) and a porosity of 2%. The total volume of this region is about 0.8 km^3. The area around well SN-10 (region 1) has the lowest porosity (< 0.1%), and a permeability of 7 md. The porosity seems to increase away from the wellfield, with a value of 15% 4 km away from the wellfield (region 4, not shown in Fig. 3); the permeability of this region is about 10–15 md. The porosity and permeability near the wellfield (region 2) are estimated to be 3% and 10 md, respectively. To achieve a reasonable match with the pressure transients for both wells SN-01 and SN-02, another region between region 1(SN-01) and region 2, with a porosity of 0.3% and a permeability of 10 md, was necessary. This region (region 6) has a porosity of 4% and a permeability of 10 md.

After matching the interference data, the model had to be modified slightly to get a good match for the production history. The permeability away from the wellfield (regions 2, 4, and 6) had to be increased to 17 md, and the porosity in the region next to the

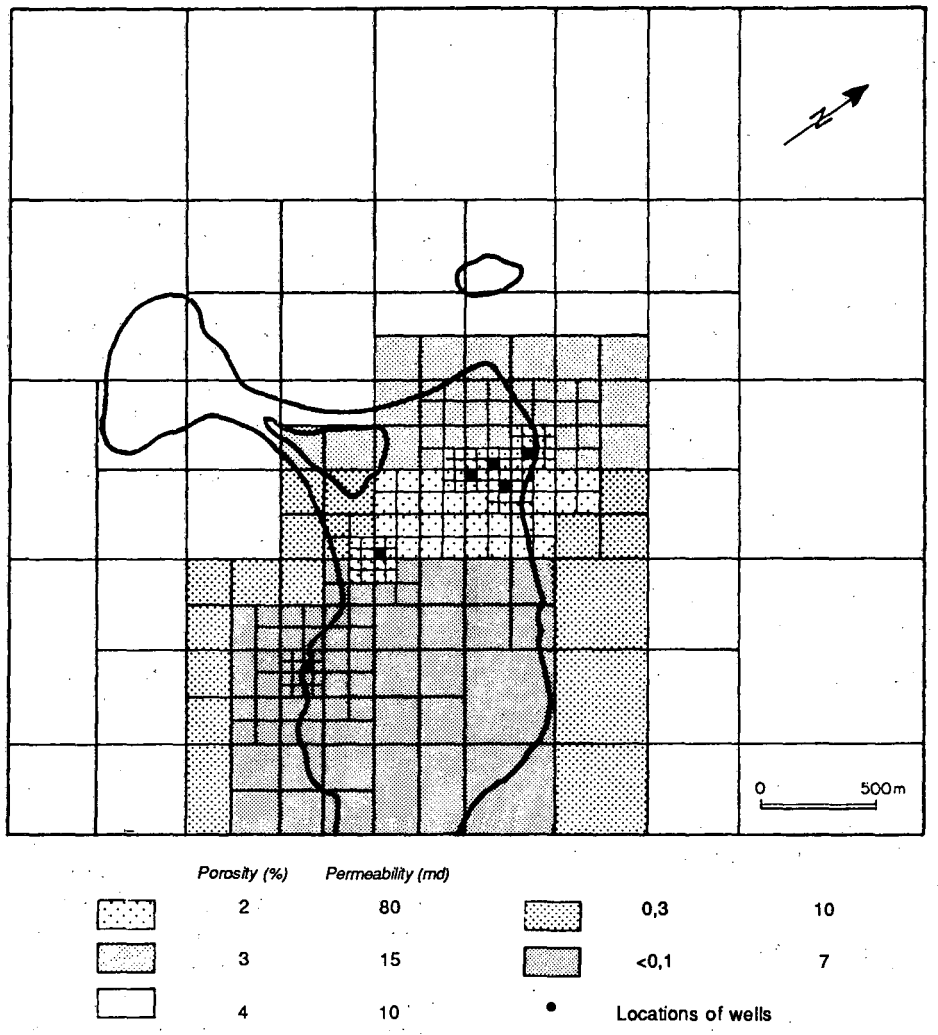

Figure 3. Mesh used in the simulation of the permeability and porosity values for five of the regions. [XBL 888-2882]

wellfield (region 3) was increased from 3 to 4%. All other parameters remained the same.

The fact that somewhat different models were needed to achieve a good match with both the interference-test data and the production history suggests that the effects of fractures may be important. Due to the short duration of the interference test, the overall permeability was most likely dominated by the fracture permeability. However, during the long-term production period, the matrix permeability becomes more important.

TEMPERATURE AND CHEMISTRY MATCH

After obtaining a match using only the pressure data, the temperature data were taken into account. The same grid was used, dividing the volume into two regions, a high-temperature region with an initial temperature of 110°C, and a low-temperature region with a temperature of 75°C. The high-temperature region includes the wellfield (region 5) and well SN-01. Using this temperature distribution, very little cooling was detected in the field (< 1°C) over the production history, which is in agreement with the observed data.

To achieve the most accurate results for the chemistry match, the calculated and observed data were matched individually for each well. The results for oxygen-18, chloride, sodium, and silica are plotted for well SN-03 in Fig. 4. For the best match, the seawater boundary approximately follows the land/sea boundary, surrounding the wells on three of four sides, and lying within 350 m of wells SN-02

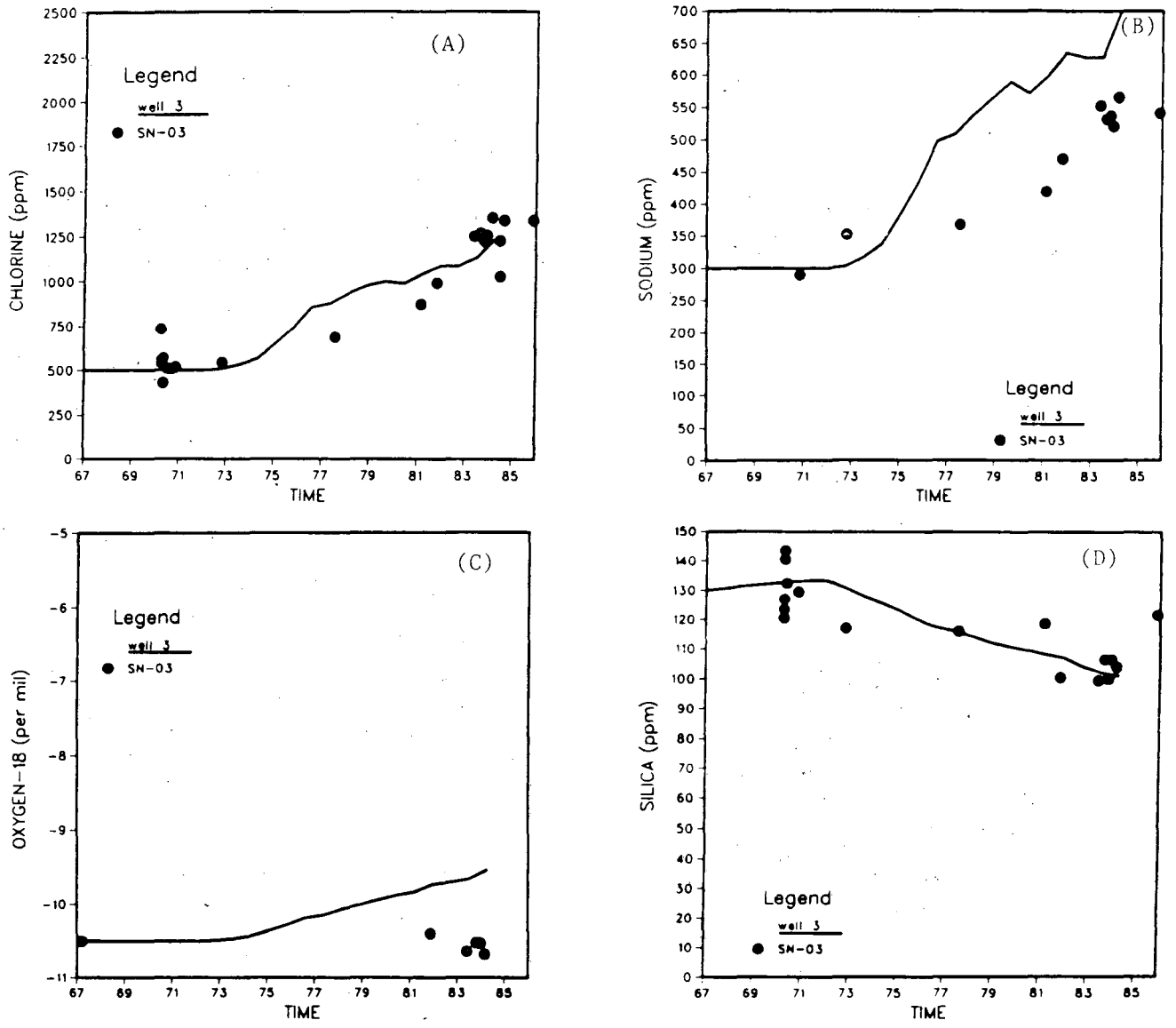

Figure 4. Results of chemistry matches for well SN-03 for **(A)** chloride, **(B)** sodium, **(C)** oxygen-18, and **(D)** silica. [XBL 888-2813]

and SN-05 to the northeast. Figure 5 shows the suggested seawater/meteoric-water boundary.

The results also raised several other points. The match with the chloride data was very good (Fig. 4A); however, the match with the sodium data was not (Fig. 4B). This suggests that the sodium cations in the system sustain significant ionic-exchange reactions and are not truly conservative, as was assumed in the present model. The matches with the oxygen-18 data for the individual wells were not good; the numerical model showed a much more rapid increase in oxygen-18 than indicated by field data (Fig. 4C). This could be due to three-dimensional effects, suggesting that fluid having a low oxygen-18 content (< -10.5 per mil) is recharging the system from either above or below. It is also possible that the fluid infiltrating the system is not seawater but is meteoric water that has flowed through a salty formation before entering the well-field region. This would make the recharge water saline, while the oxygen-18 content would remain low.

The results of the silica match (Fig. 4D) suggest that kinetic reactions play a strong role in the transport of silica in the Seltjarnarnes system. To achieve the best match for silica, the A/V (surface

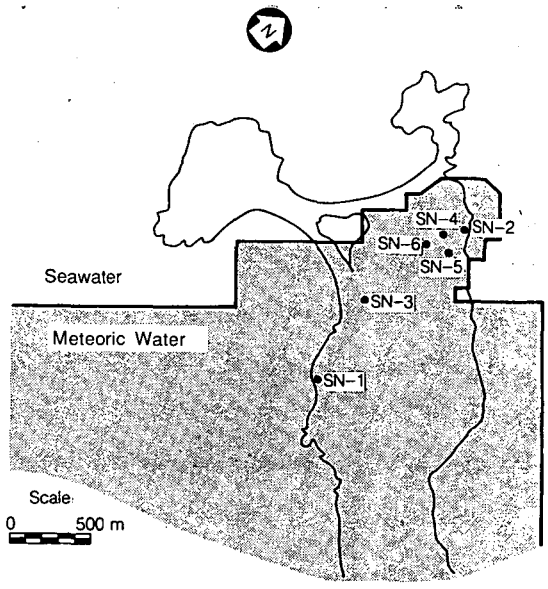

Figure 5. Suggested boundary between seawater and meteoric water. [XBL 8612-12846]

area open to reaction per volume) value was set at 25.0, indicating fairly rapid kinetic reactions (Spencer, 1986). The kinetic reactions do not appear significant in modeling the oxygen-18, probably due to the fractured nature of the reservoir.

Although the chemistry modeling has identified some shortcomings in the two-dimensional model, it can be used to roughly predict the future influence of the seawater on the system. Thus, an estimate of the amount of seawater influx in the future could be obtained. Then, potential corrosion problems may be identified and the necessary steps taken to minimize or alleviate these problems.

CONCLUSIONS

A two-dimensional model for the Seltjarnarnes geothermal field in Iceland has been developed, incorporating thermal, chemical, and pressure-transient data. Results of matching the model with the observed drawdown data revealed six regions of different permeabilities and porosities. The wellfield lies within a region of high permeability (80 md) and low porosity (2%). The porosities increase away from the field, up to 15% at a distance of 4 km. The model shows no thermal decline, in agreement with observed data. The performance predictions indicated a maximum drawdown of 15.5 bars over 20 years and a maximum temperature decline of 9°C, if the production of the field were to increase by 30 L/s every five years beginning in 1991. From the pattern of the observed chemical data, the salinity could increase greatly under this production scheme.

ACKNOWLEDGMENTS

The primary author would like to thank the National Energy Authority of Iceland for sponsoring her work at LBL, and the Earth Sciences Division of LBL for their cooperation during this work. The authors thank the Seltjarnarnes District Heating Service for allowing publication of the field data. This work was supported by the National Energy Authority of Iceland and the U.S. Department of Energy.

REFERENCES

Arnason, B., 1976. Groundwater systems in Iceland traced by deuterium. Soc. Sci. Isl., v. 42, 236 p.

Haraldsdottir, S.H., 1984a. Seltjarnarnes hola SN-1, borholumaelingar. Orkustofnun, Report OS-84059/JHD-19 B.

Haraldsdottir, S.H., 1984b. Seltjarnarnes hola SN-2, borholumaelingar. Orkustofnun, Report OS-84059/JHD-20 B.

Haraldsdottir, S.H., 1984c. Setjarnarnes hola SN-5, hitamaelingar. Orkustofnun, Report OS-84059/JHD-21 B.

Kristmannsdottir, H., 1983. Breytingar a efnasamsetningu jarohitavatns a Seltjarnarnesi a timabilinu 1970–1983. Orkustofnun, Report OS-83106/JHD-19.

Kristmannsdottir, H., 1984. Rannsoknir fyrir Hitaveitu Seltjarnarness, 1984. In-house Report, Orkustofnun, Iceland, HK-84/02.

Kristmannsdottir, H., 1986. Exploitation-induced infiltration of seawater into the Seltjarnarnes geothermal field, Iceland. Geoth. Resour. Counc. Trans., v. 10, p. 389–393.

Kristmannsdottir, H., and Tulinius, H., 1984. Fruminidurstodur maelinga og efnagreininga a djupsynum ur holu SN-4 a Seltjarnarnesi. In-house Report, Orkustofnun, Iceland, H.K.-H.Tul/8406.

Kristmannsdottir, H., Thorsteinsson, Th., and Tomasson, J., 1984. Varoar rannsoknir og borun fyrir hitaveitu Seltjarnarness. In-house Report, Orkustofnun, Iceland, 84.02.10.

Palmason, G., Stefansson, V., Thórhallsson, S., and Thorsteinsson, Th., 1983. Geothermal field developments in Iceland. *In* Proceedings, Ninth Workshop on Geothermal Reservoir Engineering, Stanford, California, December 13–15, 1983.

Sigurdsson, O., Kjaran, S.P., Thorsteinsson, Th., Stefansson, V., and Palmason, G., 1985. Experience of exploring Icelandic geothermal reservoirs. Proceedings, Geothermal Resources Council, 1985. International Symposium on

Geothermal Energy, Kailua-Kona, Hawaii, August 26–30, 1985.
Spencer, A., 1986. Development of a method to predict the temperature decline in low temperature geothermal systems under exploitation utilizing temperature, pressure and chemical transport data (M.S. thesis). University of California, Berkeley.
Sveinbjornsdottir, A.E., Tomasson, J., and Thorsteinsson, Th., 1984a. Seltjarnarnes, hola SN-05. Framkvaemd borunar, jardlagaskipan og orvunaradgerdir. Orkustofnun, Report OS-84091/JHD-41 B.
Sveinbjornsdottir, A.E., Sigursteinsson, D., Tulinius, H., Kristmannsdottir, H., and Benediktsson, H., 1984b. Seltjarnarnes hola SN-06. Borun fyrir 13 3/8″ fodringu i 416 m. Orkustofnun, Report OS-84081/JHD-34 B.
Thorsteinsson, Th., 1970. Vatnsvinnsla og vatnsstodumaelingar i borholum a Seltjarnarnesi i agust-sept 1970. Draft at Orkustofnun, Iceland.
Thorsteinsson, Th., 1980. Stadsetning holu S-5 a Seltjarnarnesi. In-house Report, Orkustofnun, Iceland, PTH.-80104.
Thorsteinsson, Th., 1985. Orvun og afkastageta holu SN-6 a Seltjarnarnesi. In-house Report, Orkustofnun, Iceland, PTH-85/06.
Thorsteinsson, Th., and Tomasson, J., 1972. Vatnsvinnsla ur holu S-4 a Seltjarnarnesi. In-house Report, Orkustofnun, PTh./J.T. 30.8.72.
Thorsteinsson, Th., Kristmannsdottir, H., Sveinbjornsdottir, A.E., and Tulinius, H., 1985. Aaetlun um loftdaelingar og pokkun i holu SNJ-6 a Seltjarnarnesi. In-house Report, Orkustofnun PTh-HK-AES-HTul-85/02.
Tomasson, J., and Saemundsson, K., 1970. Efnagreiningar a vatni ur holu S-3, a Seltjarnarnesi. In-house Report, Orkustofnun, Iceland, November.
Tomasson, J., Thorsteinsson, Th., Kristmannsdottir, H., and Fridleifsson, I.B., 1977. Hofudborgarsvaedi, Jardhitarannsoknir 1965-1973. Orkustofnun, Report OSJDH-7703. Prepared for Hitaveita Reykjavikur.
Tulinius, H., Smarasson, O.B., Tomasson, J., Fridleifsson, I.B., and Hermannsson, G., 1986. Hitastigulsboranir arid 1984 a hofudborgarsvaedinu, holur HS-14 til HS-22. Orkustofnun, Report OS-86060/JHD-22 B.
Tulinius, H., Spencer, A.L., Bodvarsson, G.S., Kristmannsdottir, H., Thorsteinsson, Th., and Sveinbjornsdottir, A.E., 1987. Reservoir studies of the Seltjarnarnes geothermal field, Iceland. National Energy Authority of Iceland, Report OS-870321/JHD-07, July 1987, 55 p.

Vertical and Lateral Movement of Partially Saturated Fluid Flow Near a Fault Zone

J.S.Y. Wang and T.N. Narasimhan

In modeling fluid movement, it is important to assess the impacts of fractures that traverse the media and faults that traverse the geological formations. Under partially saturated conditions, the distribution of fluid flow is governed by the balance between gravity and the capillary forces. The external gravitational force moves the water downward, and the internal capillary forces hold the water in place within the pores. The magnitude of the capillary force is inversely proportional to pore size, and the heterogeneity of rock pore structure controls distribution and movement of water through partially saturated formations. For meter-scale porous-matrix blocks separated by discrete fractures, the fractures represent openings with average apertures much larger than the average pore sizes of the matrix. The large pores can be easily drained, and small pores will hold the water (Wang and Narasimhan, 1985). An understanding of the drastic change in the role played by the fractures, from active main conduits for flow and transport in saturated conditions to passive dry pores in unsaturated conditions, is crucial for assessment of the partially saturated fluid-flow field at Yucca Mountain, a candidate repository site for high-level nuclear waste in southern Nevada.

In this study, we model the movement of water within the layered Yucca Mountain tuff system on the kilometer scale. The part of the system that we have chosen to study is bounded by vertical faults. Yucca Mountain consists of alternating units of

welded and nonwelded tuff. The candidate Topopah Spring Member (TSw) is a fractured, welded unit approximately 300 m thick, bounded above and below by nonwelded units several tens of meters thick. The upper nonwelded Paintbrush unit (PTn) can effectively damp out transient infiltration before infiltration moves down into TSw (Wang and Narasimhan, 1986). In this third phase of study, we extend the model laterally to cover the 1000-m scale of mountain width with a two-dimensional cross section bounded by vertical fault zones. The stratigraphic units at Yucca Mountain generally tilt eastward at 5–7°. The lateral component of the gravity gradient caused by the small tilt has been suggested as a possible mechanism for diverting some water laterally to a high-conductivity fault zone where vertical flow of diverted water can continue. If a substantial fraction of the net infiltration could be diverted away from dispersed vertical flows through unsaturated units to concentrated flow through a localized fault zone, the fault zone would likely constitute the fastest flow path from the repository to the water table. In saturated systems, an open fault with high conductivity is indeed likely to be the main conduit for fluid flow. However, the high saturated conductivity also implies that equivalent pores of the fault zone are larger than characteristic pore sizes of the formations. If we assume that the same capillary mechanism governing meter-scale fracture-matrix blocks is applicable to much larger fault-formation units, we may argue that the fault zone will be dry and that water will remain in the tuff units. The capillary mechanism can be applied only to systems with pores small enough to maintain a meniscus between rock surfaces. Without experimental studies of the unsaturated characteristics of fault-zone material, we cannot exclude other flow patterns, such as sheet flow, as mechanisms for effectively transporting fluid along a fault surface to the water table. In this study, we will not address the question of how fast water can travel along a fault. We will instead focus our attention on whether water can overcome capillary forces holding it in the unsaturated units so that water can exit laterally through formation-fault interfaces. The assumption is that once water leaves the formation it will freely fall into the water table. Instead of modeling the fault zone explicitly, we treat the formation-fault interface as a seepage boundary; i.e., we assume that the fault is so open that the face of the fault behaves as an open surface exposed to atmospheric pressure. It is well known in hillside studies that water will seep out of formations if the potential at the open-face boundary is lower than the potential inside the hill. If the potential near formation-fault interfaces can be increased to initiate seepage flow, the fault zone could become an important flow channel. However, if seepage flow cannot be initiated or is very small, the predominant flow pattern will remain downward within unsaturated units.

HYDROLOGICAL MODEL

We will model partially saturated fluid-flow behavior through portions of formation units in a section (A-A′) of Yucca Mountain (Fig. 1). A minor fault, Ghost Dance fault (GDF), inside the proposed repository area, will be a major hydrological concern if fault flow is an important transport mechanism. To focus on the impact of GDF on two-dimensional flow behavior, we will model the region west of GDF, treating GDF as an eastern seepage boundary. The location of the western no-flow boundary will be treated as variable, ranging from a few hundred meters to over half of 1266.5 m, which corresponds to the Solitario Canyon (SC) boundary. The unsaturated region is bounded at the top by the ground surface and on the bottom by the water table. To focus on the effect of interface tilting, we simplify the A-A′ section by neglecting topographic variations of the ground surface and treating the GDF boundary as vertical. We also assume that all interfaces tilt by 6°. Material properties for the different units and meshes for the different cases modeled are described in Wang and Narasimhan (1987).

First, we will review and discuss the results of one-dimensional vertical infiltration through a column. The stratigraphy of the column corresponds to the units above the water table at GDF. To properly model saturation, pressure, potential, and velocity variations, each unit is divided into grid blocks. Figure 2 compares results using a "coarse" grid with results using a "fine" grid. The fine grid was used for both 0.1- and 0.5-mm/yr infiltration-rate cases and for columns at other locations in section A-A′.

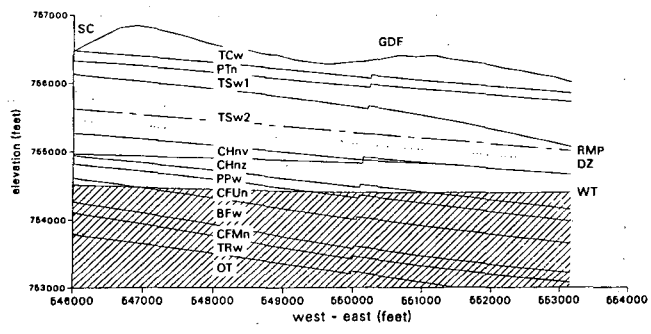

Figure 1. Hydrogeologic cross section A-A′ at Yucca Mountain. [XBL 887-2588]

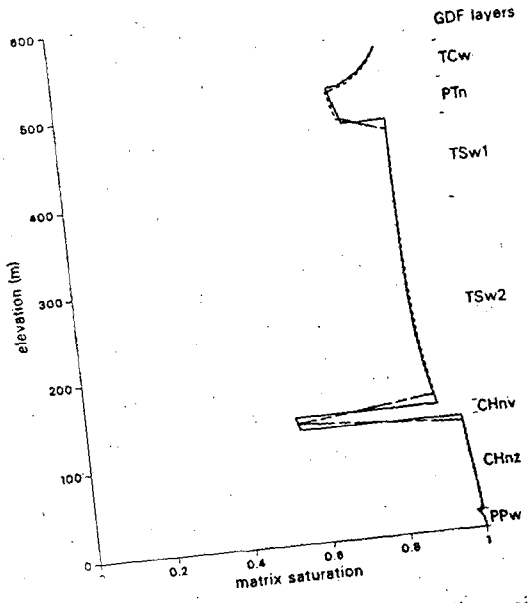

Figure 2. Matrix saturations for one-dimensional 0.1-mm/yr infiltration with fine and coarse meshes. |XBL 887-2589|

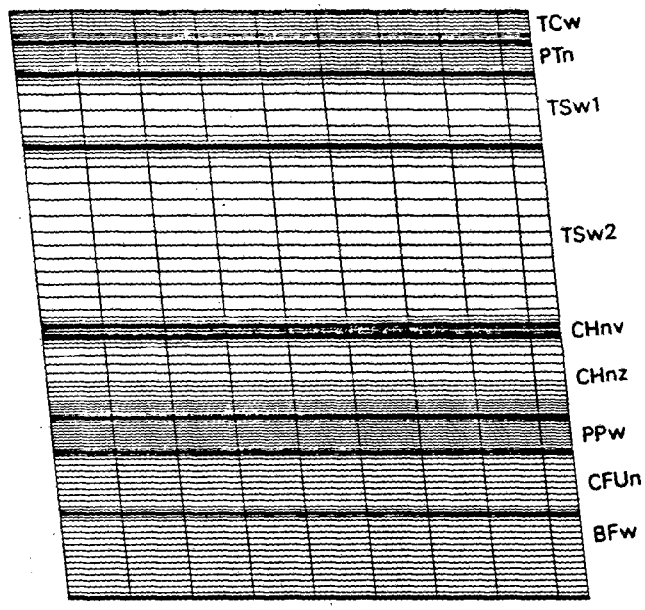

Figure 3. Two-dimensional grids for vertical- and lateral-flow models. |XBL 887-2590|

In one-dimensional vertical-column models, the main reason for using fine mesh near interfaces is the possibility of large variations in saturation, pressure, and potential (as water moves vertically) from one unit to another with very different material properties. The external driving force in the vertical column is gravity. Along the lateral direction in the two-dimensional models, there is only one interface: the formation-fault boundary. Furthermore, the external driving force, namely the lateral component of the gravity, is much weaker. For a 6° tilting, the sine of 6° is 0.1. So the external lateral driving force is approximately 10% of gravity. If the partially saturated flow movement is determined by the balance between the external force and the internal capillary forces, a weaker external force requires less capillary force to maintain the balance. Therefore, we may expect the variation in saturation, capillary pressure head, and potential to be smaller than the vertical variation.

LATERAL REDISTRIBUTION

Five meshes were constructed in the two-dimensional studies. Different meshes were used to evaluate lateral mesh-refining effects and to study the dependence of the results on the size of the modeled region. In this summary, we will mainly present the results for a nine-column model (Fig. 3). The nine-column model covers the 648-m section west of GDF. Figure 4 illustrates the matrix-saturation profiles along the nine columns with 0.1-mm/yr infiltration from above. Except for the elevation dependence, the vertical profiles of different columns are very similar to the one-column results in Fig. 2. Tilting of the units changes the vertical distributions very little. The matrix saturations along eastern columns closer to the GDF boundary are slightly higher than saturations along western columns. In Fig. 4, profiles of fracture saturations are also plotted. The fractures are dry except at the lowest nodes, which are connected to the water table.

Figure 5 shows that vertical Darcy velocities along eastern columns are higher than the 0.1-mm/yr infiltration rate; flows in the middle columns are approximately 0.1 mm/yr; and flows in western columns, away from the GDF boundary, are less than 0.1 mm/yr. In Fig. 5, lateral components of Darcy velocity from one column to its neighboring column are also plotted. In the slanted meshes used in this study, lateral fluxes between two neighboring columns are evaluated from both pressure and elevation differences of neighboring nodes. Since elevation differences are included in flux calculations, a lateral velocity is not a horizontal velocity. Lateral velocities measure flux magnitudes along layers parallel to tilted interfaces. Figure 5, in which lateral components are plotted in the same scale as vertical components, shows that lateral Darcy velocities are smaller than vertical Darcy velocities. Figure 6 illus-

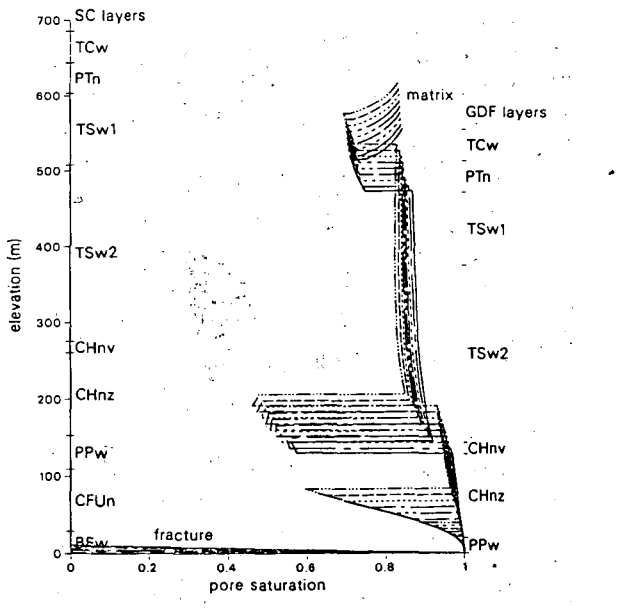

Figure 4. Saturations for two-dimensional 0.1-mm/yr infiltration with a nine-column 645-m section model. [XBL 887-2591]

trates column-to-column lateral Darcy velocities versus the horizontal coordinate for the nonwelded PTn unit for this nine-column model and other smaller or finer models. Lateral flow redistributes vertical infiltration by channeling water from the west to the east, so that vertical Darcy flux and saturation are higher in the east than in the west.

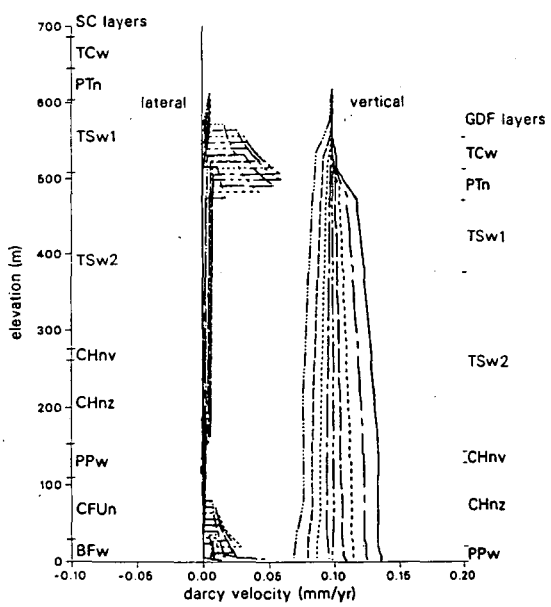

Figure 5. Darcy velocities for two-dimensional 0.1-mm/yr infiltration with a nine-column 645-m section model. [XBL 887-2592]

Lateral flows are higher in the middle of the cross section than near the side boundaries. For 0.1-mm/yr cases in Fig. 6, lateral flows are zero at $x = 0$, the seepage boundary. That is, water does not exit through the fault-formation boundary. The lateral gravity gradient associated with interface tilting cannot overcome the capillary forces that hold water in partially saturated formations.

The onset of seepage flows is simulated in the 0.5-mm/yr infiltration cases. With the material properties used in this study, we observe seepage flow between two lower nonwelded Calico Hill units (CHnv and CHnz) for the 0.5-mm/yr cases. Approximately 8% of infiltration on the ground surface exits at the CHnv-Chnz interface out of the two-dimensional section, and the remaining 92% moves down to the water table. With 0.5-mm/yr infiltration, the redistribution effects due to tilting are strong enough to increase pressure values to nonnegative ranges and induce seepage flows. In view of the material properties we used in this study, we should point out that saturation and pressure distributions with 0.5-mm/yr infiltration do not represent ambient partially saturated conditions at Yucca Mountain. Therefore, predictions of the existence of seepage flows in the 0.5-mm/yr cases are mainly modeling exercises.

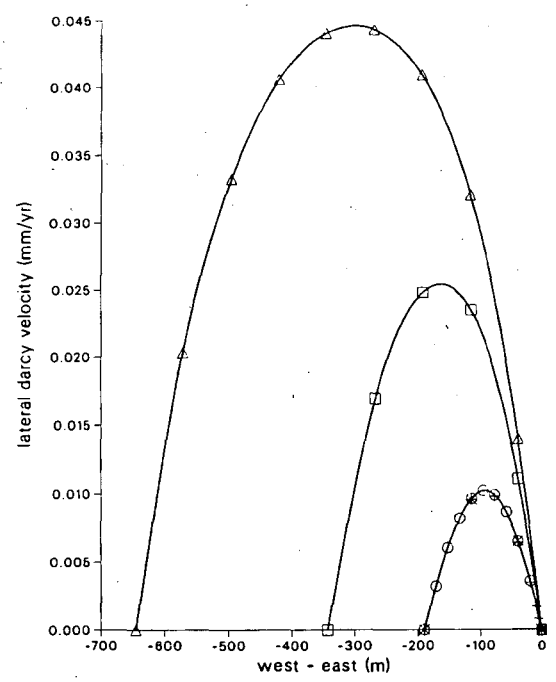

Figure 6. Lateral Darcy flow in the middle of the Paintbrush nonwelded unit with 0.1-mm/yr infiltration. [XBL 887-2593]

SUMMARY AND DISCUSSION

In modeling the hydrology of Yucca Mountain, it is important to assess the impacts of faults that traverse the alternating layers. If they are barriers to fluid flows, faults will partition the system into separate hydrologic blocks, and we can focus on the study of flows through block interiors. If faults are the main conduits for fluid flow, then we should focus on the study of fault flows. In saturated systems, we have a clear distinction between these two possibilities. A closed fault is treated as a no-flow boundary, and an open fault can be treated as a constant-potential boundary. In the latter case, faults may help transport water from a distant source or may help transport water to a deeper sink. In partially saturated systems, there may not be such a clear distinction between an open and a closed fault.

If a fault consists of brecciated mass, it will have very coarse openings that can easily drain and become dry. On the other hand, a dry opening is not a barrier to fluid flow; it will have high permeability and offer low resistance to fluid flow. Under partially saturated conditions, an "open" fault becomes a passive boundary that transports water but cannot hold it because of the very weak capillary force in large openings.

If a fault is sealed with gouge or other fine-grained materials, it can keep, and may even attract, water with the strong capillary force associated with small openings. However, small openings have low permeability and are not good conduits for transporting fluid. Under partially saturated conditions, a "closed" fault becomes a relatively wet zone that passively keeps water in nearly static conditions.

There is a third, remote, possibility that requires the fault to have a unique combination of saturated and unsaturated characteristics. If the fault material can maintain both strong capillary attractive force and large permeability, then the fault can pull water from the formation and transport it quickly away. We cannot rule out the existence of such a unique combination, wherein fault flow would control the partially saturated hydrology. There are no data for the fault-zone materials that clearly indicate whether faults in tuff formations have open, closed, or exotic characteristics with high saturated conductivity and strong suction characteristics.

In this study, we do not use material properties to represent the fault; instead we treat the fault-formation boundary as a seepage boundary. We assume that the fault is so open that capillary force is zero and the saturated permeability is infinite. The face of the fault behaves like a hillside (open surface) exposed to atmospheric pressure. We focus on the interior of the formation to determine whether water can overcome the capillary forces holding it inside the tuff matrix. If water does not exit through the fault-formation boundary, the seepage boundary is essentially closed. If water remains inside the formations, distribution of fluid flow will be independent of whether the fault is open or closed. The only possibility we do not model in this study is the third one, wherein the fault acts as a strong capillary suction sink as well as a high-permeability conduit under partially saturated conditions.

Based on results with two-dimensional cross-section models for alternating layers tilted toward the seepage boundary on the east, we may conclude that for 0.1-mm/yr infiltration:

1. Eastern tilting of units contributes to redistribution of flow, resulting in higher saturations and higher vertical velocities in the eastern side of a block bounded by faults. This redistribution effect is approximately proportional to cross-section width.
2. Nonwelded units are major channels for redistributing vertical infiltration. Lateral flows are higher in the middle of the cross section than near side boundaries.
3. Tilting itself is not a strong enough mechanism to induce the drastic changes in saturation, pressure, and potential distributions that would drive flows into fault zones.

The mild lateral variations in saturation, pressure, and potential indicate that one-dimensional results approximate ambient conditions fairly well. The lateral tilting mechanism is a second-order perturbation that does not globally change the downward, gravity-driven flow patterns. So long as fluid flow remains inside partially saturated units, redistribution effects due to tilting will not introduce order-of-magnitude differences in fluid-transport predictions. If the system is close to making a phase transition from partially saturated to fully saturated, as in the case of 0.5-mm/yr infiltration, the lateral tilting mechanism can perturb the system and change a fraction of fluid flow from dispersed slow flows percolating through the formations to concentrated fast flows rushing down the faults. If fault flow is important, the early-arrival portion of the groundwater travel-time distributions may be controlled by the fault characteristics. For ambient conditions with large negative pressures in all partially saturated units, it is unlikely that the lateral tilting mechanism can perturb the pressure and saturation field enough to overcome negative capillary forces holding water in formations and to change groundwater travel-time distributions drastically.

REFERENCES

Wang, J.S.Y., and Narasimhan, T.N., 1985. Hydrologic mechanisms governing fluid flow in partially saturated, fractured, porous tuff at Yucca Mountain. Water Resour. Res., v. 21, p. 1861–1874.

Wang, J.S.Y., and Narasimhan, T. N., 1986. Hydrologic mechanisms governing partially saturated fluid flow in fractured welded units and porous non-welded units at Yucca Mountain, Sandia National Laboratories Report SAND 86-7114. Lawrence Berkeley Laboratory Report LBL-21022, 74 p.

Wang, J.S.Y., and Narasimhan, T. N., 1987. Hydrologic modeling of vertical and lateral movement of partially saturated fluid flow near a fault zone at Yucca Mountain, Sandia National Laboratories Report SAND 87-7070. Lawrence Berkeley Laboratory Report LBL-23510, 122 p.

Monitoring of Subsurface Contaminants with Borehole/Surface Resistivity Measurements: Field Results

M.J. Wilt, C.F. Tsang, I. Javandel, S.C. Lee, and H.F. Morrison

The recent interest in mapping subsurface groundwater contaminant fronts using geophysical methods relates to the growing groundwater contamination problem and to federal and state mandates to identify and evaluate contaminant sources and contaminated sites preparatory to their cleanup. Initial studies have shown that many such sites have distinct geophysical anomalies relative to the surrounding area (Saunders and Stanford, 1984; Gilmer and Hebling, 1984). A wide variety of geophysical techniques, including seismic, potential-field, and electrical methods, have been successfully employed to detect contaminant plumes in groundwater (Rodriguez, 1984).

Of all the geophysical techniques available the electrical methods have had the most widespread use in the detection of groundwater contaminant plumes. Many sites have electrical-resistivity anomalies that may be directly attributable to the presence of an electrolytic contaminant (Saunders and Stanford, 1984). At present, the emphasis of field surveys has been on surface electrical techniques. The problem with this approach is that measurements are insensitive to contaminants if they are too deeply buried or if their concentrations are low (Wilt et al., 1983).

If the resistivity measurements are made using downhole, rather than surface, current sources, the situation improves dramatically. In a numerical study using three-dimensional resistivity models, Wilt and Tsang (1985) found that an order-of-magnitude increase in sensitivity can be achieved when the current source is placed downhole and within the contaminant zone. Figure 1 is a plot of

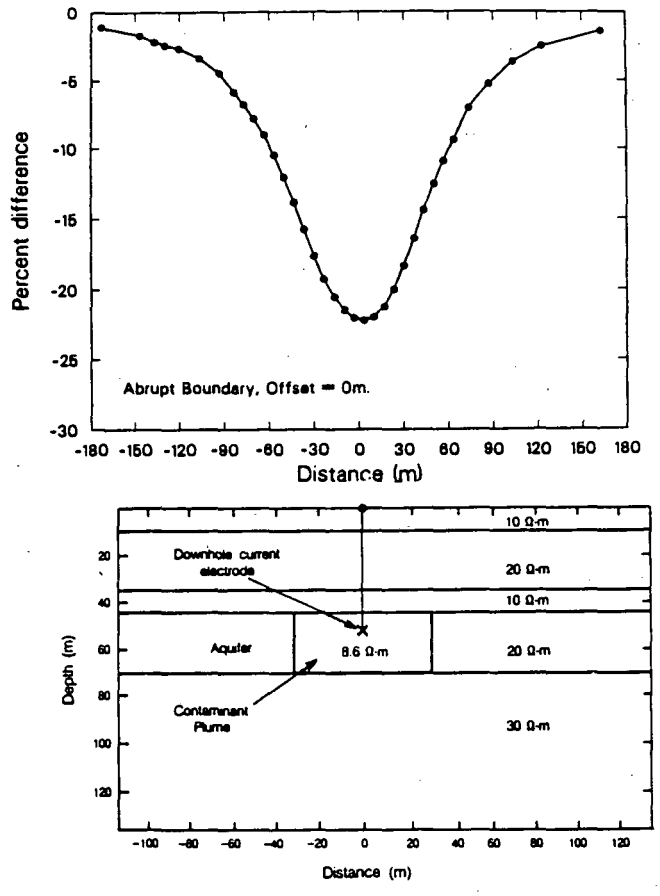

Figure 1. Model calculations of percent difference in apparent resistivity for a downhole electrode source. [XBL 887-2577]

the percent difference in apparent resistivity for a typical model before and after groundwater contamination (after Wilt and Tsang, 1985). The figure shows that the changes in apparent resistivity form an inverted Gaussian bell curve centered over the injection well, with a maximum change of 22%; this compares with a maximum change of about 3% for surface-array measurements.

Here we describe a companion field study to the above numerical modeling. In this field experiment saltwater was injected into a freshwater aquifer for three days, and the resistivity of the site was monitored concurrently using downhole/surface and surface/surface resistivity arrays. We give the results of these resistivity measurements, make some preliminary interpretations, and describe problems encountered during the field project.

EXPERIMENTAL SETTING

The field study took place in July and August of 1987 in the University of California Richmond Field Station, located in an industrial area adjacent to San Francisco Bay about 6 miles northwest of the University of California, Berkeley (Fig. 2). The site was chosen for its accessibility and suitable geological conditions and for the availability of saltwater for fluid injection.

For this study eight wells were drilled to depths ranging from 35 to 40 m through a section of unconsolidated clays and silt with intermittent lenses of sand and gravel. Analysis of the drillers logs shows that several of the clay horizons can be traced throughout the well field but that many sand and gravel bodies are lenticular, connecting three or four wells at most (Pouch, 1987). Pouch (1987) described the rocks as predominantly a deltaic sequence consisting of deposits from San Pablo and Wildcat Canyon Creeks.

The well field is located in an open area 400 m north of San Francisco Bay. In the center of the field we placed intersecting north-south and east-west profile lines for resistivity measurements; the lines are centered over well INJ (Fig. 2). A small building at the eastern end of the array of wells is used to house the instrumentation for the experiment. All electrodes are wired into the building, and resistivity measurement were made from this one location.

INJECTION EXPERIMENT

Saltwater for injection was obtained from from a pipe on a pier that extends one-half mile into San Francisco Bay at the Richmond Field Station. The saltwater was first pumped into a 50,000-gal holding

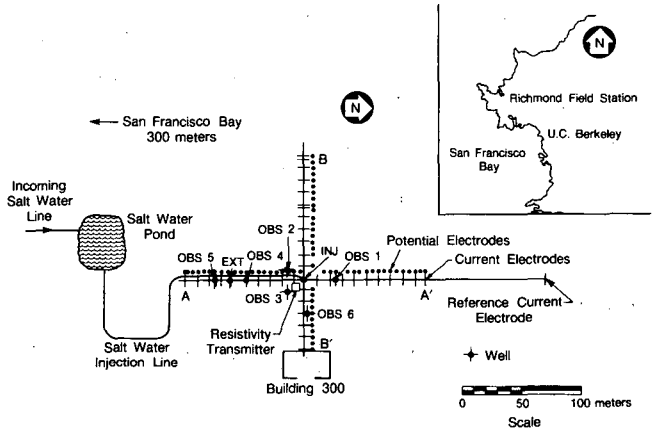

Figure 2. Site map of the Richmond Field Station experiment. [XBL 879-10347]

pond located 200 m south of well INJ (Fig. 2). After silt and mud had been allowed to settle out, the water was pumped through filters and then through 200 m of 1.5-in. plastic pipe into well INJ. The target injection rate was 7 gal/min, which was regulated by a diversion valve and measured by a flowmeter located adjacent to the wellbore. In practice it was difficult to maintain a steady 7-gal/min injection rate because the filters would periodically clog with silt and algae. The average flow rate for the 72 hours of injection was approximately 6 gal/min, for a total of over 26,000 gal injected.

The electrical conductivities of the injected saltwater and the native groundwater were measured with a conductance meter before injection, and the conductivity of the injected saltwater was continually monitored during injection. Conductivity probes were placed within well INJ just above the well screen and in observation wells OBS1, OBS2, OBS3, and OBS6.

The conductivity of the native groundwater was measured to be 0.046 mhos/m, and the injected saltwater was 3.4 mhos/m, or about 75 times higher. During the experiment the conductivity of the injected saltwater did not significantly change. In the observation wells the conductivity of the water at a depth of 30 m increased between 5% (OBS1 and OBS2) and 40% (OBS6) by the end of the injection period. Preliminary calculations indicated that the saltwater front extended 10–12 m from well INJ, or approximately halfway to the nearest observation well (OBS1).

After 72 hours of injection the filters were clogging continually due to the growth of algae in the saltwater holding pond, and the injection was stopped. For the next two days the injected plume was allowed to drift while well INJ was fitted with a

downhole pump to extract the saltwater at a rate of 20 gal/min, using the same pipe and holding pond used for injection. Water was extracted continuously from the well (for 7 days) until the outflowing fluid reached the same conductivity as the native groundwater before the injection. The total extracted fluid was more than 200,000 gal or about 8 times the amount injected.

RESISTIVITY MONITORING

Resistivity was measured using the pole-pole configuration. That is, for each current, electrode voltages were measured at each potential electrode with reference to a common distant potential electrode. Data could then be combined mathematically to give apparent resistivity for a wide variety of surface and downhole/surface configurations.

Base-line resistivity data were collected just before injection began. The full data set included 25 surface and borehole current electrodes along the two 100-m crossing profiles, with potentials recorded at all 82 electrodes for each current source. This complete data set was measured 7 times during the 13-day experiment; the full data set required almost 12 hours and resulted in more than 2000 averaged voltages. On each day at least a partial data set was collected. This partial set involved four downhole current electrodes (two each in wells INJ and EXT) and five surface current electrodes centered over well INJ.

Typically 20–24 averages of the 0.1-Hz square wave were taken for each potential measurement. Based on standard deviations and sequential measurements using the same current electrode, the predicted error in measuring the voltage ranged between 0.05–0.5%. In practice we found that when measurements were separated by more than a few hours they differed 0.2 to 2%, or about 4 times higher than predicted.

Figure 3 is a dipole-dipole apparent-resistivity pseudosection of the north-south profile line A-A′. The section indicates that, to a depth of about 50 m, the resistivity does not change very much along the profile line. Within the pseudosection, apparent resistivities range from 12 to 20 Ω-m, which are the typical values for deltaic clays and sands. The lower resistivity values usually correspond to smaller *n*-spacings, or shallower depths, and the higher values correspond to the greater *n*-spacings, or larger depths. The profile does not show any large lateral variations in resistivity, although there are indications of surface resistive inhomogeneities 0–20 m north of, and at both extremities of, the profile line. The east-west pseudosection (not shown) is similar

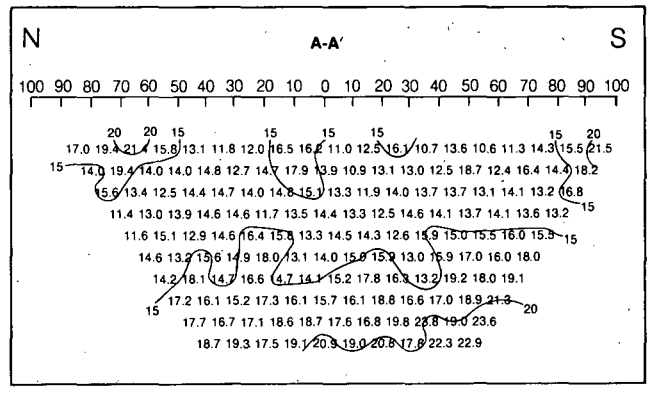

Figure 3. Dipole-dipole apparent resistivity pseudosection for north-south profile line A-A′. Dipole spacing is 10 m, apparent resistivity is in Ω-m. [XBL 879-10348]

to the above, showing no large lateral variation in resistivity but a gradual increase in resistivity with depth.

The increase in resistivity at depth is probably largely due to compaction; i.e., the weight of the overlying rock is decreasing the porosity. The local resistive inhomogeneities may represent zones of increased sand or gravel, since these tend to have higher resistivities than the clay horizons at the Richmond Field Station (Pouch, 1987).

RESISTIVITY CHANGES

Figure 4 shows the changes in apparent resistivity for the north-south profile line after 3 days of

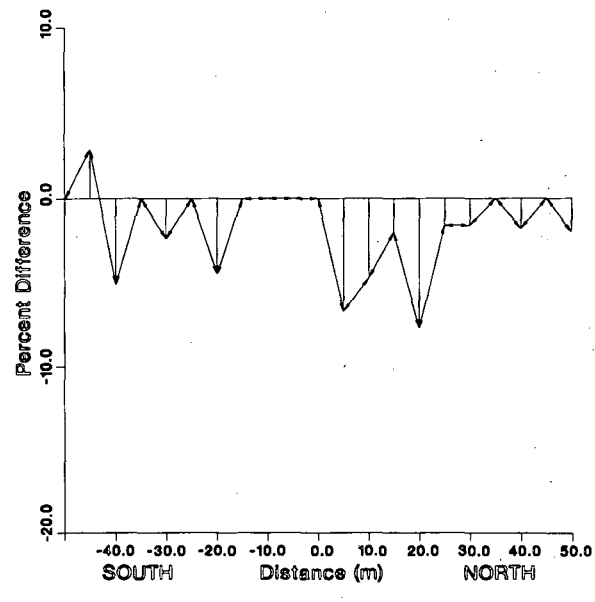

Figure 4. Plot of percent difference in apparent resistivity for north-south profile A-A′ after 3 days of saltwater injection. The current electrode is on the surface located at well INJ. [XBL 887-2578]

saltwater injection using a surface current electrode located at well INJ. The percent difference in apparent resistivity is defined as follows:

$$\text{percent diff} = \frac{\rho_a(2) - \rho_a(1)}{\rho_a(1)} \times 100\,,$$

where $\rho_a(2)$ refers to the apparent resistivity at time 2, and $\rho_a(1)$ is the apparent resistivity at time 1.

Only small changes in apparent resistivity due to the saltwater injection are seen for a current electrode on the surface. The maximum observed difference is about 5%, and the pattern of change is irregular, suggesting that system noise or surface inhomogeneities are responsible for much of it. These data are typical of what we observed from the surface current electrodes during this experiment; that is, at best the system and geological noise account for as much observed change as the injected fluid.

Figures 5 and 6 show the profiles of percent difference in apparent resistivity for the north-south and east-west lines. These were observed after 3 days of fluid injection using a downhole current source. In this case the current electrode is the metal screen in the open interval in the injection well. These figures show substantial changes in apparent resistivity after 3 days of saltwater injection. The resistivity changes form irregular inverted bell-shaped curves with a maximum decrease of almost 20%. The irregular shapes of the curves are mainly due to the influence of surface inhomogeneities and system noise. The effect of nonuniform spreading of the saltwater plume may be manifest in the extended tails on the southern area of the percent-difference profiles (Fig. 6). In general, the shape of the curves agrees with the numerical models of Wilt and Tsang (1985), but the noise in the profiles makes using these data to determine the plume boundaries very difficult.

REMARKS AND CONCLUSIONS

The field experiment described in this paper demonstrated that electrolytic contaminants may be detected with downhole/surface resistivity measurements even in areas where surface resistivity measurements alone provide little information. We were able to make the measurements mostly using existing equipment and computer software, and the extension of this type of measurement to an operating contaminant site would not be especially difficult.

The roughness of our field results demonstrates that much work must be done before such data can be used to determine plume boundaries. The influence of geological surface inhomogeneities must be mitigated, and the level of measurement uncertainty must be reduced before these data can be used in rigorous modeling.

Several longer-term fluid tests are being planned at the Richmond Field Station in the near future to

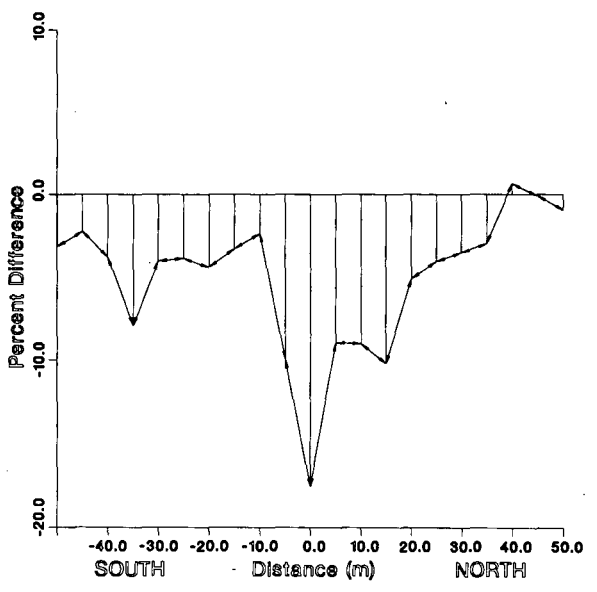

Figure 5. Plot of percent difference in apparent resistivity for north-south profile A-A′ after 3 days of saltwater injection. The current electrode is located 30 m deep in well INJ. [XBL 887-2579]

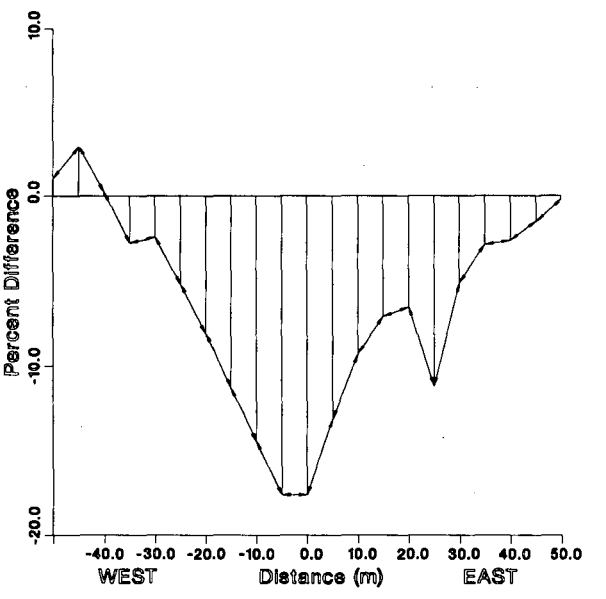

Figure 6. Plot of percent difference in apparent resistivity for east-west profile B-B′ after 3 days of saltwater injection. The current electrode is located 30 m deep in well INJ. [XBL 887-2580]

better match the fluid-injection results to the resistivity data. Tests will include a longer-term dilute saltwater injection, in which the advancing plume boundaries will be determined from the observation wells. The sensitivity and accuracy of the resistivity system have been improved, and the system is currently being further automated to speed up data acquisition.

REFERENCES

Gilmer, T.H., and Hebling, M.P., 1984. Geophysical investigations of a hazardous waste site, Massachusetts. *In* Proceedings from Surface and Borehole Geophysical Methods in Ground Water Investigation, San Antonio, Texas, February 6–9, 1984.

Pouch, G.W., 1987. Hydrogeologic site assessment of the engineering geoscience well field at the Richmond Field Station, Contra Costa County, California (M.S. thesis). Department of Engineering Geosciences, University of California, Berkeley.

Rodriguez, E.B., 1984. Ground water contamination studies in Ontario. *In* Proceedings from Surface and Borehole Geophysical Methods in Ground Water Investigations, San Antonio, Texas, February 6–9, 1984.

Saunders, W.R., and Stanford, J.A., 1984. Integration of individual geophysical techniques as a means to characterize an abandoned hazardous waste site, 1984. *In* Proceedings from Surface and Borehole Geophysical Methods in Ground Water Investigations, San Antonio, Texas, February 6–9, 1984.

Wilt, M.J., and Tsang, C.F., 1985. Monitoring of subsurface contaminants with borehole/surface resistivity measurements. *In* Proceedings from Surface and Borehole Geophysical Methods in Ground Water Investigation, National Water Well Association Conference, Fort Worth, Texas, February 12–14, 1985.

Wilt, M.J., Pruess, K., Bodvarsson, G.S., and Goldstein N.E., 1983. Geothermal injection monitoring with dc resistivity methods. *In* Proceedings of the Geothermal Resources Council Annual Meeting, Portland, Oregon, October 24–27, 1983.

APPENDIXES

APPENDIX A: ABSTRACTS OF JOURNAL ARTICLES

Bodvarsson, G.S., and Gaulke, S.W., 1987
Effects of noncondensible gases on fluid recovery in fractured geothermal reservoirs
SPE Reservoir Engineering, v. 2, no. 3, p. 335–342 (LBL-21112)

Numerical simulations are performed to investigate the effects of noncondensible gases (CO_2) on fluid recovery and matrix depletion in fractured geothermal reservoirs. The model is of a well producing at a constant bottomhole pressure (BHP) from a two-phase fractured reservoir. The recoverable fluid reserves are shown to depend strongly on the amount of CO_2 present in the reservoir system. The results obtained revealed a complex fracture/matrix interaction caused by the thermodynamics of H_2O/CO_2 mixtures. Although the matrix initially contributes fluids (liquid and gas) to the fractures, the flow directions later reverse and the fractures backflow fluids into the matrix. The amount of backflow depends primarily on the flowing gas saturation in the fractures; the lower the flowing gas saturation in the fractures, the more backflow. An analytic expression has been derived that allows for the determination of mass backflow on the basis of wellhead measurements of noncondensible gases and flowing enthalpy.

Bodvarsson, G.S., Pruess, K., Stefansson, V., Bjornsson, S., and Ojiambo, S.D., 1987
East Olkaria geothermal field, Kenya: 1. History match with production and pressure decline data
J. Geophys. Res., v. 92, no. B1, p. 521–539 (LBL-20337)

A detailed three-dimensional model of the present well field of the Olkaria geothermal field in Kenya (East Olkaria) has been developed. The model matches reasonably well flow rate and enthalpy data from all existing wells at East Olkaria. The history match shows that the effective permeabilities in the steam zone and the underlying liquid-dominated zone are 7.5 and 4.0 mdarcy, respectively. These values are somewhat higher than those inferred from well test data. The effective fracture porosity in the liquid-dominated zone is estimated to be 2% on the average, with spatial variations of 0.25–5%. The modeling studies suggest that the reservoir system is of rather uniform permeability and that no barriers to fluid flow are necessary to match the data. However, there appears to be a high permeability anomaly below a depth of 1000 m extending north-south through some of the more productive wells (wells 12, 15, 16, and 20).

Bodvarsson, G.S., Pruess, K., Stefansson, V., Bjornsson, S., and Ojiambo, S.D., 1987
East Olkaria geothermal field, Kenya: 2. Predictions of well performance and reservoir depletion
J. Geophys. Res., v. 92, no. B1, p. 541–554 (LBL-20338)

Performance predictions are presented for the East Olkaria geothermal field, using a three-dimensional well-by-well model calibrated against 6.5 years of production history. Various reservoir development schemes are investigated to study the effects of different well spacing on well deliverabilities, power production of 45 and 105 MW_e (megawatts electric), and the effects of injection on well performance and reservoir depletion. It is shown that the present well density at Olkaria (20 wells/km^2) is too high; recommended well density for future wells is 11 wells/km^2 (300-m well spacing). The present production area at East Olkaria (2 km^2) is capable of 45 MW_e power production for a 30-year period, but 105 MW_e power production requires a well field area of about 9.5 km^2, which may not exist. Injection can help sustain steam flow rates from wells, thus reducing the need for new development.

Gauglitz, P.A., St. Laurent, C.M., and Radke, C.J., 1987
An experimental investigation of gas-bubble breakup in constricted square capillaries
J. Pet. Technol., v. 39, p. 1137–1146 (LBL-25305)

Recent advances in EOR involve generating foam within underground porous media to displace the oil. We investigate the important snap-off mechanism of gas-bubble generation in constricted square capillaries experimentally. The snap-off of smaller bubbles from a larger bubble as it moves through the constriction is recorded on 16-mm movies. The time required for bubbles to snap off once they move past the constriction and the length of the generated bubbles are obtained from viewing the movie frames. The bubble capillary number, $\mu v_T/\sigma$, is varied from 10^{-5} to 5×10^{-3} by adjusting the wetting-fluid viscosity, μ, and the surface tension, σ, by adding aqueous surfactants to mixtures of glycerol and water, and by altering the bubble velocity, v_T.

Results show that a dimensionless time to snap-off depends weakly on the capillary number and that the generated bubble size increases almost linearly with increasing capillary number. Surfactants create dynamically immobile interfaces for surfactant solutions of 1 wt% sodium dodecyl benzene sulfonate (SDBS) and Chevron Chaser SD1000™. Compared with the surfactant-free solutions, the time to breakup with surfactants increases by a factor of about 3; generated bubble length increases by a factor of at most 3.

Henyey, T.E., Okaya, D.A., Frost, E.G., and McEvilly, T.V., 1987
CALCRUST (1985) seismic reflection survey, Whipple Mountains detachment terrane, California: An overview
Geophys. J.R. Astr. Soc., v. 89, p. 111–118 (LBL-25288)

CALCRUST is a new consortium of six academic institutions from California engaged in seismic reflection studies of the continental crust. CALCRUST activities are concentrated in the southwestern U.S. where a diversity of geotectonic styles occur which are fundamental to the evolution of continental margins. The good surface geologic control provided by excellent outcrop exposure and more than two decades of intensive mapping adds to the attractiveness of the region for deep-crustal investigation.

Current CALCRUST efforts are directed, in large part, toward development of a crustal transect from the Colorado Plateau (stable North American craton) to the Salton Trough/Gulf of California (continental rifting/transform). The transect crosses a variety of tectonic elements central to the Mesozoic and Cenozoic evolution of the continental margin of western North America.

Both compressional and extensional structures are involved. CALCRUST is not only addressing the seismic character and geometry of the individual elements or structures, but also relationships between them. The first work on the transect began during CALCRUST's pilot program from 1984 to 1986. It focussed on the detachment fault terrane of the Whipple Mountains in southeastern California. The Whipple Mountains are part of the "metamorphic core complex" of the North American Cordillera. Well exposed in the Whipple Mountains and common to the core complexes of Arizona and southeastern California is a series of low-angle normal or detachment faults of mid-Tertiary age, indicating appreciable crustal extension. Also exposed in the range are zones of pronounced mylonitic foliation, which are seen on a regional basis throughout large parts of the southwestern U.S. Finally, immediately south of the Whipple Mountains, Mesozoic thrusts and nappes are exposed in the Riverside and Big Maria Mountains.

Jensen, D.J., and Radke, C.J., 1987
The role of a bentonite-based packing in limiting steady radionuclide release from an underground high level waste repository
Ann. Nucl. Energy, v. 14, no. 3, p. 153–157 (LBL-21865)

Steady fractional release rates are calculated for an isolated waste canister protected by bentonite-based and alternative packing materials in both basalt and tuff repositories. The bentonite-based packing is shown to be superior to either crushed basalt or crushed tuff packing in reducing nuclide release. Additional fractional release rates assessing the role of the packing permeability, K_p, are also studied. Nuclide release is found to be insensitive to large changes in K_p, reducing concern over possible alteration of the bentonite to nonsmectite minerals.

Lange, R.A., and Carmichael, I.S.E., 1987
Densities of Na_2O-K_2O-CaO-MgO-FeO-Fe_2O_3-Al_2O_3-TiO_2-SiO_2 liquids: New measurements and derived partial molar properties
Geochim. Cosmochim. Acta, v. 51, p. 2931–2946 (LBL-24047)

The densities of 27 liquids in the system K_2O-Na_2O-CaO-MgO-FeO-Fe_2O_3-Al_2O_3-TiO_2-SiO_2 have been measured using the double-bob Archimedean technique. These results indicate that multicomponent silicate liquid volumes have a linear dependence on composition with the exception of the TiO_2 component. The equation:

$$V(T) = \Sigma X_i(T)\bar{V}_i(T) + X_{Na_2O}X_{TiO_2}\bar{V}_{Na_2O-TiO_2}$$

was used to derive values of the oxide partial molar volumes ($\bar{V}_i$) by the method of least squares. Regressions were made separately at 1573, 1673, 1773 and 1873 K (as liquid ferric-ferrous ratios change with temperature) with relative standard errors for each fit of 0.38%, 0.32%, 0.30% and 0.32%, respectively. Derived $d\bar{V}_i/dT$ values by separate least squares regression for each oxide component reproduce the measured dV/dT of the experimental liquids by 20.21% on average. The effects of iron redox state on the density of a variety of natural liquids are demonstrated and at most amount to a variation of 1%.

These new data on silicate liquid volumes were used to re-derive oxide partial molar compressibilities, $d\bar{V}_{i,T}/dP$ and $\beta_{i,T}$, at 1 bar from ultrasonic velocity and calorimetric data from the literature. The fits for $d\bar{V}_{i,T}/dP$ and $\beta_{i,T}$ at 1673 K have relative standard errors 3.9% and 1.8%, respectively, which represent substantial improvements over previous fits. Two applications of these volume data are given: firstly, the fusion curve of diopside is calculated up to 95 kbar using an equation of state for liquid volume expressed as:

$$V(T,P) = V(T)\exp\int -\beta(T)(1 - bP + cP^2)dP$$

(where $\beta = K'$ and therefore $dk/dP = K' = -\beta^{-2}\,d\beta/dP$); secondly, using a range of K' appropriate to a komatiite liquid, the pressure-temperature conditions where the density of the liquid equals that of its olivine phenocrysts are calculated.

Leonard, M.A., and Johnson, L.R., 1987
Velocity structure of Silent Canyon caldera, Nevada Test Site
Bull. Seismol. Soc. Am., v. 77, no. 2, p. 597–613 (LBL-21866)

A laterally averaged, one-dimensional P- and S-wave velocity structure is obtained for Silent Canyon Caldera, located beneath Pahute Mesa at the Nevada Test Site. The velocity models are derived from a linearized damped least-squares travel-time inversion for slowness gradient perturbations. A total of 72 P- and 20 S-wave travel times generated from 13 different explosions, obtained at locations above the caldera, are used in the inversion. The structure is modeled using linear velocity gradients in a series of horizontal layers. The inversion produces a model in which velocity for P waves increases from 1.5 km/sec at the surface to 4.5 km/sec at 2.3 km depth and from 1.0 km/sec at the surface to 2.3 km/sec at 2.0 km depth for S waves. The P- and S-wave models produce travel-time residuals which are typically less than 0.1 and 0.2 sec, respectively, which is within observational error. In an attempt to estimate the degree of lateral velocity variations over which the one-dimensional model averages, waveform data collected above the caldera are examined for indications of a laterally heterogeneous structure.

Lippmann, M.J., and Mañón, A., 1987
The Cerro Prieto geothermal field
Geoth. Sci. Technol., v. 1, no. 1, p. 1–38 (LBL-21796)

During the last 25 years the Salton Trough, a structural depression extending landward from the Gulf of California, has been extensively explored for geothermal energy, allowing the identification of a large resource base. Even though in 1959 a small pilot power plant operated for a few months in the Salton Sea area, the first geothermal system that was commercially developed for electrical production was Cerro Prieto in the Mexicali Valley, Baja California, Mexico.

Exploration in the Cerro Prieto area started in the late 1950's; the first deep exploration wells were drilled in 1960/61. By December 1984, 126 deep wells (up to almost 4 km in depth) had been completed, delineating a good portion of the geothermal reservoir. The Comisión Federal de Electricidad of Mexico (CFE), which operates and manages the field, began electrical power production in 1973; by late 1984 290 MW_e had been installed, and in 1986 the total installed capacity came to 620 MW_e. Other geothermal systems in the Salton Trough have not reached this level of development. In mid-1986, the net installed capacities at the Heber, Salton Sea and East Mesa geothermal areas, all located in the Imperial Valley of southern California, were about 92, 45 and 10 MW_e, respectively.

Long, J.C.S., and Billaux, D.M., 1987
From field data to fracture network modeling—An example incorporating spatial structure
Water Resour. Res., v. 23, no. 7, p. 1201–1216 (LBL-21730)

This paper describes a technique for processing field data for a fracture network model which accounts for observed spatial variability. This has been done generating a network subregion by subregion where the properties of each subregion are predicted through geostatistics. Once the geometry of a particular realization is specified, flow through the network is studied. We develop the method for a two-dimensional analysis based on data from Fanay-Augeres, a uranium mine in France. We plan to extend the analysis to three dimensions and compare the results with *in situ* test results. In particular, we have focused on the data collected in a long section of a drift where fractures have been mapped and steady state permeability tests have been performed in 10 boreholes. In order to generate fractures in a statistically heterogeneous region we first divided the region into statistically homogeneous subregions. In each subregion and for each fracture set we must specify the areal fracture density and the orientation, length, and aperture distributions. We divided the fractures into five sets based on tectonic history and observed that for each set, fractures spaced close together tended to have similar orientations. This was built into the simulation. An estimate of the aperture distribution for each set was made by assuming that the hydraulic apertures of the fractures intersecting a well test zone were proportional to the fracture opening observed in the core. Data input to the geostatistical analysis for each set consisted of 16 values of mean length and density of fractures in each 5 m by 2 m section of the drift wall. The results of the simulation are tables of values for mean length and fracture density for each of the five sets. The value of density simulated for each subregion was used directly to determine the number of fractures to be generated of that set in the subregion. The value of mean length was used as the mean of the length distribution in the subregion. The local coefficient of variation for length was the same in every subregion. Using the data described above, we generated a 100 m by 100 m fracture network in a series of 100 statistically homogeneous subregions. The fractured region generated has a total of 65,740 fractures. A 70 m by 70 m region was isolated for directional permeability testing. Results show that the system is barely connected. About 0.1% of the fractures essentially control permeability. In the language of percolation theory this mesh is close to the critical density for which infinite clusters of fractures are found. Problems remaining include that (1) the analysis should be extended to three dimensions, (2) the geostatistical simulation and network simulation should be combined, rather than used as two separate operations, and (3) the nature of flow through single fractures at Fanay-Augeres should be investigated.

Narasimhan, T.N., 1986
Evolution of the notion of time in hydrogeology
Eos: Trans. Am. Geophys. Union, v. 67, no. 41, p. 789–790 (LBL-22292)

The systematic study of the flow of fluids in geological systems commenced in the middle of the 19th century, following the seminal contribution of H. Darcy in France. Researchers in diverse disciplines, both in

Europe and in the United States, addressed problems related to seepage in soils, flow of groundwater in aquifers, migration of hydrocarbons, and the interaction of plants with soils. A new dimension was added to these researches when the advent of the 20th century ushered in the latent recognition that time and dynamics were crucial in all realistic field situations. This recognition took another quarter of a century to mature, leading to the remarkable decade of 1925–1935, when the nonlinear parabolic differential equation was recognized as the basis for formalizing the dynamic migration of fluids in geologic systems. What is even more remarkable is that the formalism was reached independently in parallel investigations in the fields of soil mechanics, hydrogeology, petroleum engineering, and soil physics. The decade of interest culminated in 1935 in a paper by C.V. Theis on nonsteady flow of water to a well, which is widely recognized as a landmark in groundwater hydrology. The special session thus also turned out to be a commemoration of the 50th anniversary of Theis' contribution, which appeared in the old *Transactions of the American Geophysical Union* (now *Eos*).

Nitsche, H., 1987
Effects of temperature on the solubility and speciation of selected actinides in near-neutral solution
Inorg. Chim. Acta, v. 127, p. 121–128 (LBL-21707)

The solubility and speciation predictions for actinide waste elements, needed to meet the requirements for licensing a high-level radioactive waste disposal, are made by utilizing thermodynamic solution data. Since elevated temperatures are expected in the repository and little or no information is available on thermodynamic solution data at temperatures above 25°C, one common method of prediction is to extrapolate thermodynamic functions to elevated temperatures from available data or reasonable estimates for 25°C.

The objective of this study was to determine experimentally the trends in the temperature dependence of the solubilities and speciation of neptunium, plutonium, and americium. In groundwaters hydroxide and carbonate anions are considered to play a most important role in the formation of insoluble precipitates and soluble complexes of actinides. Therefore, solubility measurements were made in 0.01 M noncomplexing $NaClO_4$ solution at pH 6.0 and 8.5 at both 25°C and 60°C. The total carbonate concentration was held constant at 120 ppm, a value close to that found in some groundwaters.

This study showed no clear change in solubility as the temperature changed from 25°C to 60°C. A summary of the results is given in Table 1. Many of the solid phases that formed, although crystalline, remain unidentified because of the lack of reference data in the literature. A comparison of the experimental results with solubility predictions from modeling calculations showed significant differences. These differences are probably caused by the existence in the experiment of unknown solubility-controlling solid phases that were not included in the modeling data base. The results of this study demonstrate the need to study radionuclide solubilities experimentally in groundwaters from a prospective repository site to accurately predict the solubility limits needed for licensing a nuclear waste repository.

Pabalan, R.T., and Pitzer, K.S., 1987
Thermodynamics of concentrated electrolyte mixtures and the prediction of mineral solubilities to high temperatures for mixtures in the system Na-K-Mg-Cl-SO_4-OH-H_2O
Geochim. Cosmochim. Acta, v. 51, p. 2429–2443 (LBL-22790)

Mineral solubilities in binary and ternary electrolyte mixtures in the system Na-K-Mg-Cl-SO_4-OH-H_2O are calculated to high temperatures using available thermodynamic data for solids and for aqueous electrolyte solutions. Activity and osmotic coefficients are derived from the ion-interaction model of Pitzer (1973, 1979) and co-workers, the parameters of which are evaluated from experimentally determined solution properties or from solubilities data in binary and ternary mixtures. Excellent to good agreement with experimental solubilities for binary and ternary mixtures indicates that the model can be successfully used to predict mineral-solution equilibria to high temperatures. Although there are currently no theoretical forms for the temperature dependencies of the various model parameters, the solubility data in ternary mixtures can be adequately represented by constant values of the mixing term θ_{ij} and values of ψ_{ijk} which are either constant or have a simple temperature dependence. Since no additional parameters are needed to describe the thermodynamic properties of more complex electrolyte mixtures, the calculations can be extended to equilibrium studies relevant to natural systems. Examples of predicted solubilities are given for the quaternary system NaCl-KCl-$MgCl_2$-H_2O.

Pabalan, R.T., and Pitzer, K.S., 1987
Thermodynamics of NaOH(aq) in hydrothermal solutions
Geochim. Cosmochim. Acta, v. 51, p. 829–837 (LBL-21631)

Apparent molar volumes and osmotic coefficients of NaOH solutions, calculated from critically evaluated literature data on volumes and vapor pressures, were used to fit the Pitzer equations to yield ion-interaction parameters as a function of temperature and pressure. These parameters allow the calculation of osmotic and activity coefficients from 0–350°C, saturation pressure to about 400 bars and 0–10 molal NaOH, and volumetric properties at saturation pressure over the same temperature and concentration range. Because the parameters for osmotic and activity coefficients above 300°C are based on less precise data, and because of possible ion-pairing above this temperature, calculated values above 300°C are considered only as best estimates available at this time. Partial molar volumes at infinite dilution calculated for NaOH are combined with literature data for NaCl, HCl, and H_2O to yield the pressure dependence of the ionization of water to 200°C, and are also combined with the potentiometric data of Sweeton et al. (1974) on the ionization of water to calculate the infinitely dilute partial molar volume of HCl to 300°C. Specific volumes of NaOH solutions at saturation pressure and up to 350°C are also calculated and tabulated.

Phutela, R.C., Pitzer, K.S., and Saluja, P.P.S., 1987
Thermodynamics of aqueous magnesium chloride, calcium chloride and strontium chloride at elevated temperatures
J. Chem. Eng. Data, v. 32, no. 1, p. 76–80 (LBL-21304)

Heat capacities and densities of aqueous $MgCl_2$, $CaCl_2$, and $SrCl_2$ from the accompanying paper are combined with literature data up to 473 K to yield temperature-dependent equations using the ion-interaction model of Pitzer. These heat capacity equations have been integrated to yield the enthalpy and the Gibbs energy. The enthalpy parameters for 298 K are evaluated in separate calculations using published high-temperature osmotic data as well as heats of dilution, while the Gibbs energy parameters for 298 K are taken from the literature. The range of validity of the final equations is described.

Pruess, K., Calore, C., Celati, R., and Wu, Y.S., 1987
An analytical solution for heat transfer at a boiling front moving through a porous medium
Int. J. Heat Mass Transfer, v. 30, no. 12, p. 2595–2602 (LBL-22513)

A problem of current interest in geothermal energy extraction is the injection of cold water into a porous medium containing superheated vapor. Such injection will cause a boiling front to move away from the injection point. When flow is approximated as being one-dimensional radial, it can be shown from similarity variable concepts that temperature, pressure, and boiling rate at the front are constant, independent of time. From heat and mass balance considerations an analytical solution is obtained for front temperature and evaporation rate. Comparison with detailed numerical simulations of the injection process shows excellent agreement.

Pyrak-Nolte, L.J., and Cook, N.G.W., 1987
Elastic interface waves along a fracture
Geophys. Res. Lett., v. 14, no. 11, p. 1107–1110 (LBL-24046)

Non-welded interfaces can be treated as a displacement discontinuity characterized by elastic stiffnesses. Applying this boundary condition to a generalized Rayleigh wave, it is shown that a fast and a slow dispersive wave can propagate along the fracture, even when the seismic properties of the rock on each side are identical.

Ransohoff, T.C., Gauglitz, P.A., and Radke, C.J., 1987
Snap-off of gas bubbles in smoothly constricted noncircular capillaries
AIChE J., v. 35, no. 5, p. 753–765 (LBL-22044)

A corner flow hydrodynamic theory is outlined for the time to snap-off of a gas bubble moving through a smoothly constricted noncircular capillary as a function of the pore geometry and the capillary number, Ca. Above a transition capillary number the time to snap-off is independent of Ca, while below it the time to snap-off is inversely proportional to the capillary number. Thin films of liquid deposited along the capillary walls are shown to play a minor role; they are accordingly neglected in the analysis. The

proposed theory is compared to new experimental results for snap-off in two constricted square capillaries (dimensionless constriction radii of 0.3 and 0.5) over a range of capillary numbers (10^{-5} to 10^{-3}), wetting-liquid viscosities (1.0 to 8.5 mPa · s), and surfactant types. Good agreement is found between theory and experiment.

Ransohoff, T.C., and Radke, C.J., 1987
Weeping flow around nonwetting bubbles trapped in constricted noncircular pores
PhysicoChemical Hydrodynamics, v. 8, no. 3, p. 255–263 (LBL-22077)

This paper addresses the "weeping" flow of a wetting liquid around a nonwetting bubble or droplet wrapped in a smoothly constricted noncircular capillary. We derive a theory that balances the hydrodynamic pressure drop in the wetting phase with the increase in curvature along the bubble/droplet interface. A weeping number, W_p, or modified capillary number arises in this problem. As the weeping number increases, the length of a bubble that can be mobilized becomes smaller and trapping of nonwetting bubbles becomes less likely. Also, the weeping flow theory explains the surprising observation of nonwetting-droplet snap off prior to invasion of the neck of a square pore constriction. We predict that pre-neck snap off occurs at a weeping number slightly lower than that required for droplet mobilization, which agrees with observed behavior.

Rivers, M.L., and Carmichael, I.S.E., 1987
Ultrasonic studies of silicate melts
J. Geophys. Res., v. 92, no. B9, p. 9247–9270 (LBL-21905)

The ultrasonic velocity and absorption of 32 silicate melts have been determined as a function of temperature (1175–1925 K) and frequency (3–12 MHz). The samples include the components SiO_2, TiO_2, Al_2O_3, FeO, MgO, CaO, SrO, BaO, Li_2O, Na_2O, K_2O, Rb_2O, and Cs_2O, and range from simple alkali silicates to multicomponent synthetic and natural melts. The relaxed sound speed varies systematically with substitution of the alkali and alkaline earth oxides, decreasing monotonically with increased cation radius. An algorithm for the compositional dependence of the ultrasonic velocity at 1673 K: $1/c = \Sigma\,(x_{i,v}/\overline{c_i})$, where $x_{i,v}$ is the volume fraction of component i and $\overline{c_i}$ is independent of composition, is capable of predicting relaxed melt velocities to within 4%. The temperature dependence of the sound speeds in the nondispersive region is quite small, $\approx$ 1 part in 10^4 K^{-1}. A simple linear model for the compositional dependence of the derived property $(\delta V/\delta P)_T$ has an uncertainty of 13%, approximately equal to that expected from the propagation of errors involving sound speed, density, thermal expansion, and heat capacity. The contributions of the changes in sound speed and density with temperature are nearly the same in their influence on the temperature dependence of the bulk modulus of natural melts. The relaxation properties c/c_0 (ratio of the sound speed to the low-frequency value) and $\alpha\lambda$ (absorption per wavelength) of all of the liquids studied are very similar when plotted against $\omega\tau$, the product of the angular frequency and the shear relaxation time. Both properties are consistent with τ equal to 1% of the product of the low-frequency shear viscosity and bulk modulus. Dispersion begins when $\omega\tau \approx 0.1$ and the limiting high-frequency sound speed c_∞ is about 2.3 times c_0. The product $\alpha\lambda$ attains a maximum value of about 1.4 when $\omega\tau \approx 0.8$. The data cannot be explained by a single relaxation time in the melts; rather, a spectrum of relaxation times is indicated.

Stebbins, J.F., Murdoch, J.B., Carmichael, I.S.E., and Pines, A., 1986
Defects and short-range order in nepheline group minerals: A silicon-29 nuclear magnetic resonance study
Phys. Chem. Miner., v. 13, p. 371–381 (LBL-20941)

^{29}Si magic-angle spinning *nuclear magnetic resonance* (NMR) spectra are presented for seven crystalline phases of the nepheline group: natural nephelines from a plutonic environment (Bancroft, Ontario) and a volcanic deposit (Mt. Somma, Italy), kalsilite, synthetic pure Na nepheline, carnegieite, and two samples of orthorhombic $KAlSiO_4$. In all phases, nearly all of the Si sites have four Al neighbors, indicating nearly complete Al-Si ordering. Excess Si over the 1:1 stoichiometric Si/Al ratio appears to substitute randomly for Al on an ordered lattice, adding Si sites with 3 and 0 Al neighbors in a 3:1 ratio. Various types of structural disorder, including Al-Si disorder, that are reported from some x-ray diffraction studies are probably long range in nature and are due to the presence of ordered domains.

In naturally occurring nepheline, the relative abundance of T sites with three-fold local symmetry is maintained at the ideal stoichiometric value of 1/4, even when the K/(K + Na) ratio is substantially lower. This is in agreement with conclusions reached about the average structure from x-ray data. The distinction between the two sites, at least in terms of the local structure that is reflected in ^{29}Si NMR chemical shifts, is lost in a pure Na nepheline sample.

Stebbins, J.F., Schneider, E., Murdoch, J.B., Pines, A., and Carmichael, I.S.E., 1986
New probe for high-temperature nuclear-magnetic-resonance spectroscopy with ppm resolution
Rev. Sci. Instrum., v. 57, no. 1, p. 39–42 (LBL-20940)

A new type of instrument has been designed and built to make Fourier transform nuclear-magnetic-resonance (NMR) spectroscopic measurements at temperatures to at least 1200°C, with a resolution of about 1 ppm. A sample is rapidly and repeatedly shuttled between the furnace and the radio frequency (rf) coil of the NMR probe (both located within a high field superconducting magnet), spending most of the time in the furnace. During each cycle, a series of rf pulses may be given and a single free-induction decay sampled. The rf coil is located outside of the furnace and is maintained at room temperature despite its close proximity to the sample. Electronic stability and coil "filling factor" are thus both optimized. The sample temperature drops below that of the furnace when cycling begins, but rapidly approaches a nearly constant value with only small fluctuations. 99% BN has been successfully used as a sample container in experiments on ^{27}Al, ^{29}Si, and ^{23}Na in molten silicates in the system Na_2O–Al_2O_3–SiO_2.

Tralli, D.M., and Johnson, L.R., 1986
Estimation of slowness-dependent source and receiver corrections for *P*-wave travel times
Bull. Seismol. Soc. Am., v. 76, no. 6, p. 1718–1738 (LBL-24561)

Tectonically regionalized tau estimates are used to obtain seismic *P*-wave travel-time corrections for lateral variations in the Earth's crust and shallow-mantle velocity structure. The corrections, in the form of estimates of tau perturbations, are functions of slowness and are assessed for both the source and receiver regions. The functional form is derived analytically and allows interpretations of causative velocity anomalies. Corrections for both ray path endpoints constrain effects typically assigned solely to the receiver, thereby helping assess systematic errors in hypocentral parameters. Over 1.25 million *ISC Bulletin P*-wave ray paths are used to estimate tau perturbation functions for seven types of tectonic regions. Particular attention is given to the problem of uniformly sampling all tectonic regions at all propagation depths in the mantle.

Estimates of source and receiver tau perturbations are consistently less than 1 sec and show a definite and systematic difference between the travel-time correction functions for oceans and continents. Source tau perturbations are indicative of negative velocity anomalies in the shallow mantle beneath oceanic regions and positive anomalies beneath continental regions and oceanic trenches. Heterogeneity confined to the upper 250 km of the mantle suggests velocity variations with ±5 per cent of the lateral mean over a depth interval of approximately 100 km. Differences between the receiver and source perturbations for a common tectonic region are attributed to variations in the characteristic crustal structure of the region, constrained by the receiver perturbation, and errors in origin time and or focal depth, determined from the source perturbation. The estimates of perturbation functions therefore suggest systematic regional biases in crustal structure and hypocentral parameters. A less than average crustal thickness in oceanic regions and greater thickness in stable continental regions is indicated. Furthermore, it appears that the origin times of sources in oceanic regions are systematically determined too late and/or focal depths located too shallow, whereas origin times of sources in continental regions are systematically determined too early and/or focal depths located too deep.

Tralli, D.M., and Johnson, L.R., 1986
Lateral variations in mantle *P* velocity from tectonically regionalized tau estimates
Geophys. J. R. Astron. Soc., v. 86, p. 475–489 (LBL-20316)

Estimates of tau functions for a tectonically regionalized earth are obtained from over 1.25 million seismic ray paths of *ISC Bulletin* data to study the correlation of potential lateral variations in mantle *P*-wave velocities with recognized surface heterogeneity. The use of regionalized travel-time data relies on statistical regularity criteria to check the consistency of

the global regionalization. Estimates of tau perturbations attributed to velocity structure at the seismic source and receiver regions are derived by a simple algebraic formulation. Contributions from near-surface heterogeneity are thereby removed and permit the assessment of lateral velocity variations at depth. Estimates of "single region" equivalent tau functions are constructed and inverted to obtain velocity–depth functions and extremal bounds at the 99.9% confidence level for seven different tectonic regions.

Deviations from a regionally weighted reference mean velocity function which agrees well with PREM (Dziewonski and Anderson) indicate significant differences, particularly between oceanic and continental tectonic regions, extending to a depth of 700 km. *P*-wave velocity anomalies are typically less than ± 1% of the reference velocity. The age-dependence of the shallow oceanic mantle is observed by increased velocities from young (< 25 Myr) to old (> 100 Myr) regions, and similarly from orogenic zones and magmatic belts to stable continental regions. Unlike for young and old oceanic regions, stable continental regions do not show a pronounced gradient in the mean velocity residuals above 250 km. Continental platforms and particularly shields, however, show a compensation in the sign of the mean velocity residual at depths between about 350 and 700 km. Evidence for a velocity anomaly between 700 and 950 km is indicated. Significant negative residuals are observed centered at a depth of about 780 km below oceanic ridges and about 880 km below active continental regions. This anomaly may be related to a boundary layer between the upper and lower mantle. The level of velocity variations decreases below 950 km. Lateral variations are also suggested within 250 km of the core boundary.

Tsang, C.F., 1987
Comments on model validation
Transport in Porous Media, v. 2, no. 6, p. 623–629, 1987 (LBL-23973)

The present paper points out the importance and usefulness of recognizing the separate roles of processes and geometric structures in predictive modeling of the performance of a nuclear waste repository or underground injection disposal of toxic wastes. Based on this, a validation procedure is proposed. Furthermore, two stages and three elements of validation are described and discussed. Finally, comments are made on the choice of measurables to be used to compare modeling results and field data in the validation procedure.

Tsang, Y.W., and Pruess, K., 1987
A study of thermally induced convection near a high-level nuclear waste repository in partially saturated fractured tuff
Water Resour. Res., v. 23, no. 10, p. 1958–1966 (LBL-21311)

We present simple estimates for velocities of buoyancy-driven flow of liquid and gas phases near a hypothetical high-level nuclear waste repository in partially saturated, fractured tuff. These estimates indicate that gas phase convection could take place with appreciable velocity, of the order of 20 m/year, while liquid convection is expected to be very slow, of the order of 0.1 mm/year. Detailed numerical simulations using an "effective continuum" approximation to represent fracture effects confirm these estimates and demonstrate a sensitivity of gas convection to the strength of binary diffusion.

Tsang, Y.W., and Tsang, C.F., 1987
Channel model of flow through fractured media
Water Resour. Res., v. 23, no. 3, p. 467–479 (LBL-21310)

On the basis of a review of recent theoretical and experimental studies of flow through fractured rocks, we have studied the fluid flow and solute transport in a tight fractured medium in terms of flow through channels of variable aperture. The channels are characterized by an aperture density distribution and a spatial correlation length. Aperture profiles along the channels are statistically generated and compared to laboratory measurements of fracture surfaces. Calculated tracer transport between two points in the fractured media is by way of a number of such channels. Tracer breakthrough curves display features that correspond well with recent data by Moreno et al., which lends support to the validity of our model. Calculated pressure profiles along the channels suggest possible measurements that may be useful in identifying the geometrical characteristics of the channels. Finally, predictions were made for tracer breakthrough curves in the case of single fractures under various degrees of normal stress. These suggest possible laboratory experiments which may be performed to validate this conceptual model.

Vasco, D.W., and Johnson, L.R., 1987
The correspondence between gravitational attraction and surface displacement due to volume expansion
Geophys. J. R. Astron. Soc., v. 89, p. 749–754 (LBL-22038)

It is shown that the formulas for the calculation of surface displacement due to a volume source in a half-space may be derived from a potential of the same form as the gravitational potential. The similarity between these expressions allows the use of methods developed for gravity in the study of surface displacement. As an example of the applicability of the correspondence, an efficient algorithm is developed for the calculation of uplift due to volume expansion within a homogeneous half-space. The method may be generalized to three-dimensional volumes undergoing expansion in a half-space.

White, A.F., and Chuma, N.J., 1987
Carbon and isotopic mass balance models of the Oasis-Fortymile Canyon groundwater basin, Southern Nevada
Water Resour. Res., v. 23, no. 4, p. 571–582 (LBL- 22791)

Environmental isotopes and carbon chemistry provide means of differentiating various recharge areas, flow paths, and ages of groundwater in portions of the Nevada Test Site and vicinity. Regional $\delta D/\delta^{18}O$ trends are offset from the present-day meteoric line by a deuterium depletion of 5‰, suggesting paleoclimatic changes. Partial pressures of CO_2 and the ^{18}O and ^{13}C data indicate solubility and isotopic equilibrium between the gas and water in the soil zone with progressive exchange with underlying groundwater in the shallow alluvium of Oasis Valley. Application of a closed system CO_2 model using the EQ3NR/EQ6 reaction path simulator successfully reproduces chemical compositions observed in the alluvium in the Amargosa Desert and in the deep tuff aquifer beneath Pahute Mesa and Yucca Mountain. Initial P_{CO_2} input to the soil zone during recharge was calculated to range from 0.03 to 0.10 atm, which is comparable to measured soil CO_2 pressures in Oasis Valley. Results are compared for ^{14}C ages using the $\delta^{13}C$ dilution correction and a mass action correction term relating predicted and calculated ionic activity products of $CaCO_3$. Results are generally comparable with discrepancies attributed to anomalous $\delta^{13}C$ values.

Wollenberg, H.A., and Smith, A.R., 1987
Radiogenic heat production of crustal rocks: An assessment based on geochemical data
Geophys. Res. Lett., v. 14, no. 3, p. 295–298 (LBL-22844)

A survey of the geochemical literature and unpublished data has resulted in the classification of U, Th, and K concentrations by rock type. Over 2500 data entries have been compiled, permitting calculation of their radiogenic heat production. In the igneous rocks mean heat production ranges from highs of 12–20 heat production units (HPU: μWm^{-3}) in some peralkaline intrusives, through ~ 4 HPU in acidic, ~ 2 in intermediate, and ~ 1 in basic rocks to a low of 0.3 HPU in ultramafic rocks. Siliceous clastic rocks generally have greater heat production (2 to 4 HPU) than do chemical sedimentary rocks, including the carbonates (0.4 to 2 HPU). The heat production of metamorphic rocks generally depends on the radioelement contents of their igneous and sedimentary predecessors, modified by metamorphic processes. Based on estimates of the proportion of the continental crust that specific rock types occupy, the weighted mean radiogenic heat production of the upper continental crust estimated from this data base is ~ 3 HPU.

Wollenberg, H.A., Sorey, M.L., Farrar, C.D., White, A.F., Flexser, S., and Bartel, L., 1987
A core hole in the southwestern moat of the Long Valley caldera
Eos: Trans. Am. Geophys. Union, v. 68, no. 20, p. 529–534 (LBL-23116)

A continuously cored hole penetrated 715 m into the southwestern moat of the Long Valley caldera. Temperatures in the postcaldera deposits increased rapidly with depth over the upper 335 m to 202°C, then remained nearly isothermal into the Bishop Tuff to the bottom of the hole. The depth to the Bishop Tuff is the shallowest, and the temperatures observed are among the highest in holes drilled in the caldera. The hole identifies a potential geothermal resource for the community of Mammoth Lakes, constrains the position of the principal heat source for the caldera's hydrothermal system, and serves as access for monitoring changes in water level, temperatures, and fluid chemistry.

APPENDIX B: LBL REPORTS, BOOK CONTRIBUTIONS, CONFERENCE PAPERS

LBL REPORTS

LBL-19515
Gilmour, H.M.P., Billaux, D., and Long, J.C.S., 1986. Models for calculating flow in randomly generated three-dimensional networks of disc-shaped fractures: Theory and design of FMG3D, DISCEL, and DIMES.

LBL-19516
Gilmour, H.M.P., Billaux, D., and Long, J.C.S., 1986. Models for calculating flow in randomly generated three-dimensional networks of disc-shaped fractures: User's manuals and listings for FMG3D, DISCEL, and DIMES.

LBL-20700
Pruess, K., 1987. TOUGH User's guide.

LBL-21442
Karasaki, K., 1987Rev. Well test analysis in fractured media (Ph.D. thesis).

LBL-21806
Chambré, P.L., Lee, W.W.-L., Kim, C.L., and Pigford, T.H., 1986. Steady-state and transient radionuclide transport through penetrations in nuclear waste containers.

LBL-21859
Weres, O., Peiper, J.C., Pitzer, K.S., and Pabalan, R., 1987. Documentation for computer code NACL.

LBL-21985
Zhou, Q., Lee, K.H., Goldstein, N.E., and Morrison, H.F., 1986. Fracture detection using a grounded subsurface vertical electric dipole.

LBL-22090
Earth Sciences Division, 1987. Annual Report 1986.

LBL-22361
Noorishad, J., and Carnahan, C.L., 1987. Development of the non-equilibrium reactive chemical transport code CHMTRNS.

LBL-22641
Morrison, H.F., Becker, A., and Lee, K.H., 1986. Measurements of electrical conductivity for characterizing and monitoring nuclear waste repositories.

LBL-22719
Spencer, A.L., 1986. Modeling of thermodynamic and chemical changes in low-temperature geothermal systems (M.S. thesis).

LBL-23069
Tsang, C.F. (principal investigator) and others, 1986. Geotechnical support and topical studies for nuclear waste geologic repositories: Annual report, fiscal year 1986.

LBL-23175
Narasimhan, T.N., 1987. Hydrodynamics of a vertical hydraulic fracture.

LBL-23195
Tsang, Y.W., Tsang, C.F., Hale, F.V., Moreno, L., and Neretnieks, I., 1987. Channeling characteristics of flow and solute transport through a rough-surfaced fracture.

LBL-23425
Ahn, J., Chambré, P.L., Pigford, T.H., and Lee, W.W.-L., 1986. Radionuclide dispersion from multiple patch sources into a rock fracture.

LBL-23497
Mangold, D.C., and Tsang, C.-F., 1987. Summary of hydrologic and hydrochemical models with potential application to deep underground injection performance.

LBL-23717
Prucha, R.H., 1987. Heat and mass transfer in the Klamath Falls, Oregon, geothermal system.

LBL-23888
Severson, L.K., 1987. Interpretation of shallow crustal structure of the Imperial Valley, California, from seismic reflection profiles (master's thesis).

BOOK CONTRIBUTIONS

Carnahan, C.L., 1987. Simulation of chemically reactive solute transport under conditions of changing temperature. *In* C.F. Tsang (ed.), Coupled Processes Associated with Nuclear Waste Repositories. Academic Press, Orlando, Florida, p. 249–257 (LBL-21486).

Cook, N.G.W., 1987. Coupled processes in geomechanics. *In* C.F. Tsang (ed.), Coupled Processes Associated with Nuclear Waste Repositories. Academic Press, Orlando, Florida, p. 39–66 (LBL-25130).

Hestir, K., Chiles, J.-P., Long, J., and Billaux, D., 1987. Three-dimensional modeling of fractures in rock: From data to a regionalized parent-daughter model. *In* D. Evans and J. Nicholson (eds.), Flow and Transport through Unsaturated Fractured Rock (Geophysical Monograph 42). American Geophysical Union, Washington, D.C., p. 141–148 (LBL-22116).

Jahnke, F.M., and Radke, C.J., 1987. Electrolyte diffusion in compacted montmorillonite engineered barriers. *In* C.F. Tsang (ed.), Coupled Processes Associated with Nuclear Waste Repositories. Academic Press, Orlando, Florida, p. 287–297 (LBL-25131).

Jensen, D.J., and Radke, C.J., 1987. Steady radionuclide release rates from a bentonite protected waste canister. *In* C.F. Tsang (ed.), Coupled Processes Associated with Nuclear Waste Repositories. Academic Press, Orlando, Florida, p. 299–307 (LBL-25132).

Mishra, S., Bodvarsson, G.S., and Attanayake, M.P., 1987. Injection and falloff test analysis to estimate properties of unsa-

turated fractures. *In* D. Evans and J. Nicholson (eds.), Flow and Transport through Unsaturated Fractured Rock (Geophysical Monograph 42). American Geophysical Union, Washington, D.C., p. 149–156 (LBL-22102).

Muralidhar, K., and Long, J.C.S., 1987. A new approach to characterizing flow in single fractures. *In* D. Evans and J. Nicholson (eds.), Flow and Transport through Unsaturated Fractured Rock (Geophysical Monograph 42). American Geophysical Union, Washington, D.C., p. 115-120 (LBL-22114).

Narasimhan, T.N., 1987. Some thoughts on model verification. *In* D. Evans and J. Nicholson (eds.), Flow and Transport through Unsaturated Fractured Rock (Geophysical Monograph 42). American Geophysical Union, Washington, D.C., p. 185–187 (LBL-23021).

Noorishad, J., and Tsang, C.F., 1987. Simulation of coupled thermal-hydraulic-mechanical interactions in fluid injection of fractured rocks. *In* C.F. Tsang (ed.), Coupled Processes Associated with Nuclear Waste Repositories. Academic Press, Orlando, Florida, p. 673–678 (LBL-25134).

Pitzer, K.S., 1987. A thermodynamic model for aqueous solutions of liquid-like density. *In* I.S.E. Carmichael and H.P. Eugster (eds.), Thermodynamic Modeling of Geologic Materials: Minerals, Fluids and Melts (Reviews in Mineralogy, Vol. 17), Mineralogical Society of America, p. 97–142 (LBL-23554).

Pruess, K., and Wang, J.S.Y., 1987. Numerical modeling of isothermal and nonisothermal flow in unsaturated fractured rock—A review. *In* D. Evans and J. Nicholson (eds.), Flow and Transport through Unsaturated Fractured Rock (Geophysical Monograph 42). American Geophysical Union, Washington, D.C., p. 11–22 (LBL-22773).

Shimo, M., and Long, J.C.S., 1987. A numerical study of transport parameters in fracture networks. *In* D. Evans and J. Nicholson (eds.), Flow and Transport through Unsaturated Fractured Rock (Geophysical Monograph 42). American Geophysical Union, Washington, D.C., p. 121–132 (LBL-22115).

Verma, A., and Pruess, K., 1987. Effects of silica redistribution on performance of high-level nuclear waste repositories in saturated geologic formations. *In* C.F. Tsang (ed.), Coupled Processes Associated with Nuclear Waste Repositories. Academic Press, Orlando, Florida, p. 541–563 (LBL-25133).

White, A.F., 1986. Surface reactions of natural glasses; effects on radionuclide transport. *In* D.E. Clark, W.B. White, and A.J. Machiels (eds.), Nuclear Waste Management II (Advances in Ceramics, Vol. 20). American Ceramic Society, Westerville, Ohio, p. 713–722 (LBL-22290).

White, A.F., and Yee, A., 1986. Near-surface alkali diffusion into glassy and crystalline silicates at 25°C to 100° (Chapter 28). *In* J.A. Davis and K.F. Hayes (eds.), Geochemical Processes at Mineral Surfaces (American Chemical Society Symposium Series, No. 323). American Chemical Society, Washington, D.C., p. 587–598 (LBL-22291).

CONFERENCE PAPERS

Ahn, J., Chambré, P.L., Pigford, T.H., and Lee, W.W.-L., 1987. Transport of radionuclides released from a multiple-patch source into a planar fracture with transverse hydrodynamic dispersion. Presented at the Annual Meeting of the American Nuclear Society, Dallas, Texas, June 7–11, 1987. Trans. Am. Nucl. Soc., v. 54, p. 107 (LBL-22770).

Ahn, J., Chambré, P.L., Pigford, T.H., and Lee, W.W.-L., 1987. Nuclide migration from areal sources into a fracture. Presented at the American Society of Civil Engineers Engineering Hydrology Symposium, Williamsburg, Virginia, August 3–7, 1987. *In* R.M. Ragan (ed.), Proceedings, 1987 National Conference on Hydraulic Engineering. American Society of Civil Engineers, New York, p. 913 (LBL-23370).

Apps, J.A., 1987. Alteration of natural glass in radioactive waste repository host rocks: A conceptual review. Presented at the Symposium on Glass and Ceramics for Nuclear Repositiories, Madrid, Spain, May 21–22, 1987 (LBL-22871).

Benson, S.M., Daggett, J.S., Iglesias, E., Arellano, V., and Ortiz-Ramirez, J., 1987. Analysis of thermally induced permeability enhancement in geothermal injection wells. Presented at the Twelfth Workshop on Geothermal Reservoir Engineering, Stanford, California, January 20–22, 1987 (LBL-23022).

Bjornsson, G, and Bodvarsson, G.S., 1987. A multi-feedzone wellbore simulator. Presented at the 1987 Annual Meeting of the Geothermal Resources Council, Sparks, Nevada, October 12–14, 1987. Geoth. Resour. Counc. Trans., v. 11, p. 503507 (LBL-23723).

Bodvarsson, G.S., 1987. Numerical modeling of geothermal systems with applications to Krafla, Iceland, and Olkaria, Kenya. Presented at the NATO Conference on Advanced Geothermal Reservoir Engineering, Antalya, Turkey, July 1–10, 1987 (LBL-23950).

Bodvarsson, G.S., and Stefansson, V., 1987. Reinjection into geothermal reservoirs. Presented at the NATO Conference on Advanced Geothermal Reservoir Engineering, Antalya, Turkey, July 1–10, 1987 (LBL-23949).

Bodvarsson, G.S., Cox, B.L., and Ripperda, M., 1987. Effects of steam-liquid counterflow on pressure transient data from two-phase geothermal reservoirs. Presented at the 1987 SPE Annual Technical Conference and Exhibition, Dallas, Texas, September 27–30, 1987 (LBL-23719).

Carle, S.F., and Goldstein, 1987. A three-dimensional gravity model of the geologic structure of Long Valley caldera. Presented at the Symposium on the Long Valley Caldera: A Pre-Drilling Data Review, Berkeley, California, March 17–18, 1987 (LBL-24572).

Carle, S.F., and Goldstein, N.E., 1987. Gravity and fault structures, Long Valley caldera, California. Presented at the 1987 Annual Meeting of the Geothermal Resources Council, Sparks, Nevada, October 12–14, 1987. Geoth. Resour. Counc. Trans., v. 11, p. 327–332 (LBL-23648).

Carnahan, C.L., 1986. Simulation of uranium transport with variable temperature and oxidation potential: The computer program THCC. Presented at the Materials Research Society Fall Meeting, Symposium L, Boston, Massacachusetts, December 1–4, 1986. *In* J.K. Bates and W.B. Seefeldt (eds.), Scientific Basis for Nuclear Waste Management X (Materials Research Society Symposia Proceedings, Vol. 84). Materials Research Society, Pittsburgh, Pennsylvania, p. 713–721, 1987 (LBL-21639).

Carnahan, C.L., 1987. Effects of coupled thermal, hydrological and chemical processes on nuclide transport. Presented at the GEOVAL-87 Symposium on Verification and Validation

of Geosphere Performance Assessment Models, Stockholm, Sweden, April 7–9, 1987 (LBL-23186).

Carnahan, C.L., 1987. Some effects of data base variations on numerical simulations of uranium migration. Presented at the International Conference on Chemistry and Migration Behavior of Actinides and Fission Products in the Geosphere, Munich, Federal Republic of Germany, September 14–18, 1987 (LBL-24537).

Carnahan, C.L., 1987. Simulation of effects of redox and precipitation on diffusion of uranium solution species in backfill. Presented at the Materials Research Society Fall Meeting, Symposium P: Scientific Basis for Nuclear Waste Management XI, Boston, Massachusetts, November 30–December 3, 1987 (LBL-24538).

Chambré, P.L., Kang, C.H., Lee, W.W.-L., and Pigford, T.H., 1986. Mass transfer of soluble species into backfill and rock. Presented at the American Nuclear Society Winter Meeting, Washington, D.C., November 16–20, 1986 (LBL-21807).

Chambré, P.L., Lee, W.W.-L., Kim, C.L., and Pigford, T.H., 1986. Radionuclide transport through penetrations in nuclear waste containers. Presented at the American Nuclear Society Winter Meeting, Washington, D.C., November 16–20, 1986 (LBL-21809).

Chambré, P.L., Lee, W.W.-L., Kim, C.L., and Pigford, T.H., 1986. Transient and steady-state radionuclide transport through penetrations in nuclear waste containers. Presented at the Materials Research Society Fall Meeting, Symposium L, Boston, Massachusetts, December 1–4, 1986. *In* J.K. Bates and W.B. Seefeldt (eds.), Scientific Basis for Nuclear Waste Management X (Materials Research Society Symposia Proceedings, Vol. 84). Materials Research Society, Pittsburgh, Pennsylvania, p. 131–140 (LBL-21697).

Ewy, R.T., Kemeny, J.M., Zheng, Z., and Cook, N.G.W., 1987. Generation and analysis of stable excavation shapes under high rock stresses. Presented at the Sixth International Congress on Rock Mechanics, Montreal, Quebec, Canada, August 30–September 3, 1987 (LBL-22747).

Flexser, S., Wollenberg, H.A., and Smith, A.R., 1987. Radon in groundwater of the Long Valley caldera, California. Presented at the Conference on Radon, Radium, and other Radioactivity in Ground Water: Hydrogeologic Impact and Application to Indoor Airborne Contamination, Somerset, New Jersey, April 7–9, 1987 (LBL-23301).

Goldstein, N.E., 1986. Perspective and Trends: Future of geothermal exploration technology. Presented at the Symposium on the Future of Geothermal Energy, San Diego, California, November 17–18, 1986 (LBL-22487).

Goldstein, N.E., 1987. Introduction: Potential field and electromagnetic studies. Presented at the Symposium on the Long Valley Caldera: A Pre-Drilling Data Review, Berkeley, California, March 17–18, 1987 (LBL-24570).

Goldstein, N.E. (ed.), 1987. Proceedings of the Symposium on the Long Valley Caldera: A Pre-Drilling Data Review, Lawrence Berkeley Laboratory, March 17–18, 1987 (LBL-23940).

Hopkins, D.L., Cook, N.G.W., and Myer, L.R., 1987. Fracture stiffness and aperture as a function of applied stress and contact geometry. *In* I.W. Farmer et al. (eds.), Proceedings, 28th U.S. Symposium on Rock Mechanics, Tucson, Arizona, June 29–July 1, 1987. A.A. Balkema, Rotterdam, Netherlands, p. 673–680 (LBL-25312).

Kemeny, J.M., and Cook, N.G.W., 1987. Crack models for the failure of rocks in compression. *In* C.S. Desai et al. (eds.), Constitutive Laws for Engineering Materials: Theory and Applications (Vol. II), Proceedings, Second International Conference on Constitutive Laws for Engineering Materials: Theory and Applications, Tucson, Arizona, January 5–8, 1987, p. 879–887 (LBL-25311).

Kemeny, J.M., and Cook, N.G.W., 1987. Determination of rock fracture parameters from crack models for failure in compression. *In* I.W. Farmer et al. (eds.), Proceedings, 28th U.S. Symposium on Rock Mechanics, Tucson, Arizona, June 29–July 1, 1987. A.A. Balkema, Rotterdam, Netherlands, p. 367–374 (LBL-25309).

Kim, C.L., Chambré, P.L., Lee, W.W.-L., and Pigford, T.H., 1987. Radionuclide transport from an array of waste packages in a geologic repository. Presented at the Annual Meeting of the American Nuclear Society, Dallas, Texas, June 7–11, 1987. Trans. Am. Nucl. Soc., v. 54, p. 109 (LBL-22772).

Kim, C.L. Chambré, P.L., Lee, W.W.-L., and Pigford, T.H., 1987. Contaminant transport from an array of sources. Presented at the American Society of Civil Engineers Engineering Hydrology Symposium, Williamsburg, Virginia, August 3–7, 1987. *In* R.M. Ragan (ed.), Proceedings, 1987 National Conference on Hydraulic Engineering. American Society of Civil Engineers, New York, p. 1022 (LBL-23371).

Lee, W.W.-L., Kim, C.L., Chambré, P.L., and Pigford, T.H., 1986. Cumulative releases of radionuclides from uncontained waste packages. Presented at the American Nuclear Society Winter Meeting, Washington, D.C., November 16–20, 1986 (LBL-21808).

Light, W.B., Lee, W.W.-L., Chambré, P.L., and Pigford, T.H., 1987. The effects of sorption and decay on steady-state radionuclide release rates. Presented at the Annual Meeting of the American Nuclear Society, Dallas, Texas, June 7–11, 1987. Trans. Am. Nucl. Soc., v. 54, p. 108 (LBL-22771).

Lippmann, M.J., 1987. Brine injection studies at the Lawrence Berkeley Laboratory. Presented at the Fifth Annual DOE Geothermal Program Review, Washington, D.C., April 14–15, 1987 (LBL-23230).

Lippmann, M.J., 1987. Reservoir technology research at Lawrence Berkeley Laboratory. Presented at the Fifth Annual DOE Geothermal Program Review, Washington, D.C., April 14–15, 1987 (LBL-23231).

Majer, E.L., 1987. The application of high frequency seismic monitoring methods for the mapping of fluid injections. Presented at the Workshop on Forced Fluid Flow through Fractured Rock, Paris, France, April 13–16, 1987 (LBL-24048).

Narasimhan, T.N., and Pruess, K., 1987. MINC: An approach for analyzing transport in strongly heterogeneous systems. Presented at the NATO Advanced Research Workshop on Advances in Analytical and Numerical Modeling, Lisbon, Portugal, June 2–6, 1987. *In* E. Custodio et al., Groundwater Flow and Quality Modeling, Proceedings of the NATO-ARW Conference on Advances in Analytical and Numerical Groundwater Flow and Quality Modeling, Lisbon, Portugal, June 2–6, 1987. D. Reidel Publ. Co., Hingam, Massachusetts, p. 375–391 (LBL-23477).

Nitsche, H., Lee, S.C., and Gatti, R.C., 1987. Determination of plutonium oxidation states at trace levels pertinent to nuclear waste disposal. Presented at the American Nuclear Society

International Topical Conference on the Methods and Applications of Radioanalytical Chemistry, Kona, Hawaii, April 5–10, 1987 (LBL-23158).

Pabalan, R.T., and Pitzer, K.S., 1987. Prediction of thermodynamic properties, including solubility equilibria and vapor pressures, for mixed aqueous electrolytes to high temperatures. Presented at the Conference on Thermodynamics of Aqueous Systems with Industrial Applications, Warrenton, Virginia, May 10–14, 1987 (LBL-24601).

Pabalan, R.T., and Pitzer, K.S., 1987. Prediction of high-temperature thermodynamic properties of mixed electrolyte solutions including solubility equilibria, vapor pressure depression and boiling point elevation. Presented at the Symposium on Chemistry in High Temperature Aqueous Solutions, Provo, Utah, August 25–27, 1987 (LBL-24627).

Prucha, R.H., Benson, S.M., and Witherspoon, P.A., 1987. Conceptual model of the Klamath Falls, Oregon, geothermal area. Presented at the Twelfth Workshop on Geothermal Reservoir Engineering, Stanford, California, January 20–22, 1987 (LBL-23115).

Pruess, K., Celati, R., Calore, C., and Capetti, G., 1987. On fluid and heat flow in deep zones of vapor-dominated geothermal reservoirs. Presented at the Twelfth Workshop on Geothermal Reservoir Engineering, Stanford, California, January 20–22, 1987 (LBL-22810).

Pyrak-Nolte, L.J., Cook, N.G.W., and Witherspoon, P.A., 1987. Hydraulic and mechanical properties of natural fractures in low-permeability rock. Presented at the Sixth International Conference on Rock Mechanics, Montreal, Quebec, Canada, August 3–September 3, 1987 (LBL-22718).

Ransohoff, T.C., and Radke, C.J., 1986. Mechanisms of foam generation in glass bead packs. Presented at the 61st Annual Meeting of the Society of Petroleum Engineers, New Orleans, Louisiana, October 5–8, 1986 (LBL-21845).

Ripperda, M., and Bodvarsson, G.S., 1987. Decline curve analysis of production data from The Geysers geothermal field. Presented at the Twelfth Workshop on Geothermal Reservoir Engineering, Stanford, California, January 20–22, 1987 (LBL-22987).

Sorey, M.L., Farrar, C.D., and Wollenberg, H.A., 1986. Proceedings of the Second Workshop on Hydrologic and Geochemical Monitoring in the Long Valley Caldera, Mammoth Lakes, California, July 15–17, 1986 (LBL-22852).

Tsang, C.F., 1986. Coupled processes in single fractures, double fractures and fractured porous media. Presented at the Workshop on Numerical Modeling for Radioactive Waste Repositories, Madrid, Spain, December 10–12, 1986 (LBL-22559).

Tulinius, H., Kristmansdottir, H., Thorsteinsson, T., Spencer, A. L., and Bodvarsson, G.S., 1987. Reservoir studies of the Seltjarnarnes geothermal field, Iceland. Presented at the Twelfth Workshop on Geothermal Reservoir Engineering, Stanford, California, January 20–22, 1987 (LBL-22461).

Vasco, D.W., Johnson, L.R., and Goldstein, N.E., 1987. Using surface displacement to constrain deformation at Long Valley caldera, CA. Presented at the Symposium on the Long Valley Caldera: A Pre-Drilling Data Review, Berkeley, California, March 17–18, 1987 (LBL-24571).

Witherspoon, P.A., and Long, J.C.S., 1987. Some recent developments in understanding the hydrology of fractured rocks. *In* Proc., 28th US Symposium on Rock Mechanics, Tucson, Arizona, June 29–July 1, 1987, p. 421–432 (LBL-23464).

Witherspoon, P.A., Long, J.C.S., Majer, E.L., and Myer, L.R., 1987. A new seismic-hydraulic approach to modeling flow in fractured rocks. Presented at the NWAA/NGWMA Conference on Solving Ground Water Problems with Models, Denver, Colorado, February 10–12, 1987 (LBL-22794).

Witherspoon, P.A., Long, J.C.S., Majer, E.L., and Myer, L.R., 1987. Combined seismic and hydraulic method of modeling flow in fractured low permeability rocks. *In* E. Custodio et al., Groundwater Flow and Quality Modeling, Proceedings of the NATO-ARW Conference on Advances in Analytical and Numerical Groundwater Flow and Quality Modeling, Lisbon, Portugal, June 2–6, 1987. D. Reidel Publ. Co., Hingam, Massachusetts (LBL-24324).

Witherspoon, P.A., Shikari, Y., Radke, C.J., Pruess, K., Persoff, P., Benson, S.M., and Wu, Y.S., 1987. Feasibility analysis and development of a foam-protected underground natural gas storage facility. Presented at the 1987 Distribution/Transmission Conference, Las Vegas, Nevada, May 4–6, 1987 (LBL-23500).

Wollenberg, H., White, A., Flexser, S., Sorey, M., and Farrar, C., 1987. A core hole into the hydrothermal system at the Long Valley caldera. Presented at the Symposium on the Long Valley Caldera: A Pre-Drilling Data Review, Berkeley, California, March 17–18, 1987 (LBL-24569).

Zhou, Q., Becker, A., Morrison, H.F., Goldstein, N.E., and Lee, K.H., 1987. Fracture detection using subsurface electromagnetic techniques. *In* I.W. Farmer et al. (eds.), Proceedings, 28th U.S. Symposium on Rock Mechanics, Tucson, Arizona, June 29–July 1, 1987. A.A. Balkema, Rotterdam, Netherlands, p. 5–17 (LBL-22614).

LAWRENCE BERKELEY LABORATORY
TECHNICAL INFORMATION DEPARTMENT
UNIVERSITY OF CALIFORNIA
BERKELEY, CALIFORNIA 94720